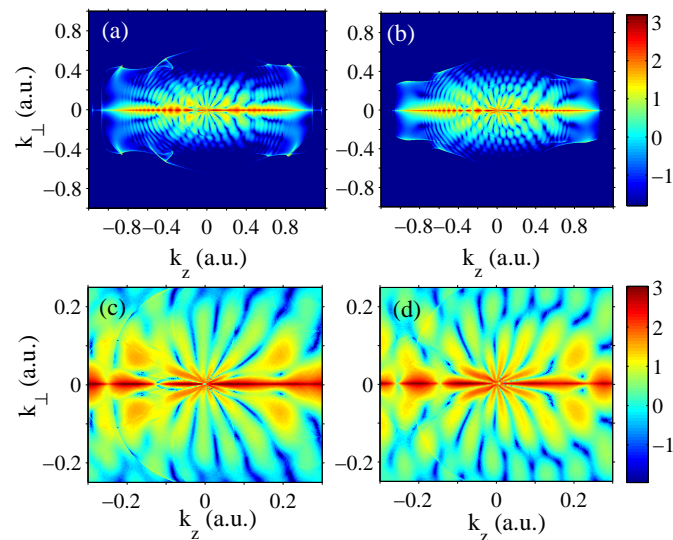# DEVELOPMENT AND APPLICATION OF SEMICLASSICAL MODELS FOR STRONG-FIELD PHENOMENA

Von der Fakultät für Mathematik und Physik
der Gottfried Wilhelm Leibniz Universität Hannover zur
Erlangung des Grades

Dr. rer. nat. habil.

genehmigte Habilitationsschrift von

Dr. Nikolay Shvetsov-Shilovskiy

2023

Datum des Vollzugs der Habilitation: 14.11.2023

To Elizaveta, Alexei, and Maria

CONTENTS

ACKNOWLEDGEMENTS

SUMMARY

Semiclassical models based on classical trajectories for the description of the electron motion in the continuum are a powerful tool of strong-field, ultrafast, and attosecond physics. The semiclassical models allow us to identify the specific mechanism of a phenomenon of interest and visualize it in terms of classical trajectories. Often these models are also computationally simple. In the present work we developed a range of new semiclassical models and applied them to various strong-field phenomena. Among these are: capture of electrons into Rydberg states, sequential multiple ionization, above-threshold ionization of the hydrogen molecule, multielectron effects due to the laser-induced polarization of the atomic ion, and strong-field holography with photoelectrons. We also used the semiclassical simulations to understand the results obtained using quantum optimal control theory, namely, optimization of the high-harmonic yield by shaping of the driving pulse. We developed a method capable of retrieving effective single-active electron potentials, which are required for semiclassical simulations. In this method the single-active electron potential is found as the result of an optimization procedure aimed at reproducing given photoelectron momentum distributions. Finally, we applied deep learning to retrieve the internuclear distance in a molecule ionized by a strong laser pulse from the photoelectron momentum distribution. The results of this thesis will serve as a basis for development of new generation of semiclassical models that are expected to combine accurate description of the ionization step, the ability to account for interference and multielectron effects, and numerical efficiency. The emergence of such models will open new perspectives in the theory of laser-matter interaction.

1. INTRODUCTION

Strong-field physics is a fascinating field of research that has emerged due to the outstanding progress in laser technologies during last decades. This area of modern physics focuses on highly nonlinear phenomena emerging as a result of interaction of strong laser pulses with atoms, molecules, nanostructures, etc. The most well-known examples of these phenomena are: Above-threshold ionization (ATI) along with formation of the plateau at high energies in the photoelectron energy spectrum (high-order ATI), high-order harmonic generation (HHG), and nonsequential double ionization (NDSI), see Refs. [1–6] for reviews. Many different theoretical approaches to strong-field processes have been developed so far. Most of these approaches are based on the strong-field approximation (SFA) [7–9], direct numerical solution of the time-dependent Schrödinger equation (TDSE), see, e.g., Refs. [10–13], and the semiclassical models, such as the widely known two-step [14–16] and the three-step models [17, 18].

In many cases the numerical solution of the TDSE in the single-active electron approximation provides a good agreement with experimental results. Presently the TDSE in three spatial dimensions for an atom interacting with a strong laser pulse can be solved at moderate computational costs. However, it is often difficult to understand the physical mechanism responsible for the process under study based on the numerical wave function. Furthermore, computational power of modern computers is not infinite. Already the direct numerical solution of the three-dimensional (3D) TDSE for a molecule ionized by a strong laser pulse is a very difficult task. This TDSE can be solved only for the simplest molecules and with selection of the most important degrees of freedom, see Refs. [19, 20]. Moreover, such problems as, e.g., NSDI in molecules, or the same process in atoms caused by elliptically polarized laser pulse, are far beyond the reach of modern computer clusters.

The SFA describes ionization as a direct quantum transition from an initial bound state to the Volkov state. Since the Volkov state is the wave function of an electron in an electromagnetic wave and the initial state is assumed to be unaffected by the laser field, the SFA neglects both the Coulomb field in the final state and the intermediate bound states. The role of the SFA in studies of strong-field phenomena and the transparent physical pic-

ture of these phenomena provided by the SFA could not be overemphasized, see, e.g., Refs. [1, 2, 6]. In many cases this method allows to obtain analytic or semi-analytic solutions. Nevertheless, the approximations used in the SFA are severe, and, in some cases, may lead to wrong results. The well-known example is the fourfold symmetry of the electron angular distributions predicted by the SFA [21]. However, the distributions observed experimentally possess only the inversion symmetry, i.e., they are asymmetric in any half of the polarization plane, see Ref. [22]. It was shown that the fourfold symmetry arises from neglecting the effect of the Coulomb field of the parent ion on the electron motion in the continuum [23–28].

The semiclassical models employ a classical description of the electron after it has been released from an atom or molecule, often by tunneling ionization. These models have a number of important advantages compared to other theoretical approaches. First, the trajectory-based models allow us to reveal the specific mechanism underlying the strong-field process under study and to interpret this mechanism in terms of classical trajectories. Second, these models are often computationally simple. Finally, for some strong-field processes the semiclassical models are the only feasible approach as, e.g., for the above-mentioned NSDI process in molecules. All this explains a wide use of semiclassical models in intense laser-matter physics.

The trajectory-based models have allowed to obtain invaluable information about strong-field processes. First of all, this applies to the ATI process. In ATI an electron absorbs more photons than necessary to overcome the ionization threshold. As a result, the ionized electrons are detected with energies larger than the one corresponding to the threshold channel. It was found that the typical electron energy spectrum consists of two different parts. The first rapidly decaying part of the spectrum ends at an energy close to $2U_p$, where $U_p = F^2/4\omega^2$ is the ponderomotive energy (atomic units are used throughout the thesis unless indicated otherwise). Here, in turn, F and ω are the amplitude and the frequency of the laser field, respectively. This first part is called the direct ionization spectrum. The second part that is often referred to as the high-energy plateau extends up to $10U_p$. The high-energy plateau is often several orders of magnitude lower than the maximum of the low-energy part.

The direct ionization spectrum can be described by the two-step model. In the first step of the two-step model an electron tunnels out of an atom, and in the second step it moves towards a detector along a classical trajectory in the laser field. The high-energy plateau is qualitatively described within the three-step model. The three-step model involves the interaction of the returning electron with the parent ion as the third step. Indeed, along with the electrons that do not return to the parent ions, i.e., direct electrons

contributing to the direct ionization spectrum, there are also rescattered electrons that are driven back by the alternating laser field to their ions and rescatter off them by large angles. These rescattered electrons are responsible for the formation of the high-energy plateau. The three-step model also allows us to understand the HHG and the NSDI processes. Specifically, the returning electron can recombine with the parent ion accompanied by emission of a high-frequency photon (harmonic radiation). On the other hand, if the energy of the returning electron is sufficient, it can liberate a second electron from the ion.

The three-step model has explained many important features of the processes induced by rescattering, i.e., ATI, HHG, and NSDI. Among these are: the cutoffs in both the high-order ATI [29] and HHG spectra (see Refs. [17, 30]), the maximal allowed angles in photoelectron angular distributions from rescattering [31], and characteristic cutoffs of the NSDI distributions [32, 33]. The two-step model accounting for the Coulomb potential has revealed the Coulomb focusing effect [34]. The semiclassical models including the ionic force in the Newton's equations of motion have also been used to study the Coulomb cusp in photoelectron angular distributions [35], the low-energy structures in the electron spectra produced by strong midin-frared pulses [36–44] (i.e., the widely known ionization surprise that was for the first time observed in the experiment of Ref. [45]), and the nonadiabatic effects in ionization [46–48].

The present work focuses on the development and application of novel semiclassical models for strong-field, ultrafast, and attosecond physics. Simultaneously, the thesis is not restricted by this topic only. Three different problems closely related to the semiclassical simulations are also considered in the present work. These problems are: optimization of the strong-field phenomena using quantum optimal control theory, reconstruction of the effective single-active-electron potential from observables, and the retrieval of the internuclear distance in a molecule interacting with a strong laser field. The results included in this cumulative habilitation thesis were obtained during the applicant's work at the Moscow Engineering Physics Institute (National Research Nuclear University), Frierdrich-Schiller University Jena, Aarhus University, Tampere University of Technology, and Leibniz University Hannover in the period of 2009–2022.

The thesis is organized as follows. In Chapter 2 we first discuss the general formulation of semiclassical models used in strong-field physics. We next discuss development and application of the semiclassical models to the capture into Rydberg states and sequential multiple ionization. We also consider the applicability conditions of the trajectory-based approaches. In Chapter 3 we discuss the semiclassical two-step model (SCTS) describing

quantum interference effects and its modifications: the semiclassical two-step model with quantum input and the SCTS model for ionization of the hydrogen molecule. Semiclassical models describing polarization-type multelectron effects and the algorithm for retrieving the effective single-active electron potential are discussed in Chapter 4. Chapter 5 focuses on the application of the semiclassical models for understanding the results obtained from quantum optimal control theory. This applies to the optimization of the HHG yield and ionization suppression in atoms and molecules. In Chapter 6 we discuss the application of the SCTS model to strong-field holography with photoelectrons, as well as the retrieval of the internuclear distance in a molecule from interference patterns in electron momentum distributions. The conclusions and perspectives of the thesis are given in Chapter 7.

2. SEMICLASSICAL SIMULATIONS OF STRONG-FIELD PROCESSES

2.1 Semiclassical models: Theoretical background

In any semiclassical model accounting for the ionic potential $V(\vec{r}, t)$ the electron trajectory $\vec{r}(t)$ is found from Newton's equation of motion:

$$\frac{d^2\mathbf{r}}{dt^2} = -\mathbf{F}(t) - \nabla V(\mathbf{r}, t), \qquad (2.1)$$

where $\mathbf{F}(t)$ is the electric field of the laser pulse. In order to integrate Eq. (2.1), we need to specify the initial conditions: The initial electron velocity and the starting point of the trajectory. Actually, the initial conditions are the weak point of the semiclassical models. Indeed, the choice of the initial conditions that are to connect classical and quantum descriptions of strong-field phenomena is a nontrivial task. It is usually assumed that the electron starts with zero initial velocity along the laser field $v_{0,||} = 0$, whereas it can have an arbitrary initial velocity $v_{0,\perp}$ in the transverse direction. It should be noted that the SFA implies a nonzero initial longitudinal velocity, see, e.g., Refs. [38, 49, 50]. The effect of the nonzero initial parallel velocity in semiclassical simulations is discussed in Ref. [P1]

It is natural to treat the tunnel exit point as the starting point of the electron trajectory. The corresponding potential barrier is formed by ionic potential and the electric field of the laser pulse. If this potential is considered in *a 1D cut along the field direction*, the resulting approach is often called the field direction model (FDM), see Ref. [P2]. This model is used in many studies applying trajectory-based simulations, see, e.g., Refs. [34, 35, 40, 51] and [P3]. Within the FDM the tunnel exit point is determined by the equation:

$$V(\mathbf{r}) + F(t_0) z_e = -I_p, \qquad (2.2)$$

where I_p is the ionization potential. In the simplest version of the FDM, the ionic potential is neglected in Eq. (2.2), i.e., it is assumed that the potential barrier is formed by the laser field and the ground-state energy only. The

exit point for the corresponding triangular barrier is given by

$$|z_e(t_0)| = \frac{I_p}{F(t_0)}. \tag{2.3}$$

Here the sign of $z_e(t_0)$ is to be chosen from the condition that the electron tunnels in the direction opposite to the electric field $\mathbf{F}(t_0)$ at the time of ionization.

If the ionic potential is modeled by the Coulomb one, the tunnel exit point can be found using the separation of the corresponding static problem in the parabolic coordinates. Let us assume that the static electric field acts along the z-axis, i.e., $\mathbf{F} = F\mathbf{e}_z$ with $F > 0$, and define the parabolic coordinates as $\xi = r + z$, $\eta = r - z$, and $\varphi = \arctan(y/x)$. The tunnel exit coordinate $\eta_e > 0$ is then determined by the equation

$$-\frac{\beta_2(F)}{2\eta} + \frac{m^2 - 1}{8\eta^2} - \frac{F\eta}{8} = -\frac{I_p(F)}{4}, \tag{2.4}$$

see, e.g., Ref. [52], and the tunnel exit point is found as $z_e \approx -\eta_e/2$. In Eq. (2.4) m is the magnetic quantum number of the initial state, $I_p(F)$ is the Stark-shifted ionization potential, and

$$\beta_2(F) = Z - (1 + |m|) \frac{\sqrt{2I_p(F)}}{2} \tag{2.5}$$

is the separation constant, see, e.g., Ref. [53]. The ionization potential $I_p(F)$ accounting for the Stark shift is given by

$$I_p(F) = I_p(0) + (\boldsymbol{\mu}_N - \boldsymbol{\mu}_I) \cdot \mathbf{F} + \frac{1}{2}(\alpha_N - \alpha_I)\mathbf{F}^2, \tag{2.6}$$

where $I_p(0)$ is the field-free ionization potential, and $\boldsymbol{\mu}_{N,I}$ and $\alpha_{N,I}$ are the static dipole moments and polarizabilities, respectively. The index N stands for a neutral atom or molecule, and the index I refers to its ion. We note that for atoms the second (i.e., linear in F) term is absent in Eq. (2.6) provided the atom is placed at the origin. It should be also stressed that quasistatic approximation is assumed in Eqs. (2.4)-(2.6), i.e., the field F is to be interpreted as the instantaneous field value at the time of ionization t_0.

It is obvious that the trajectories, which form the electron wave packet produced in the ionization process, have different weights. These weights are determined by the corresponding ionization instants and initial velocities. Specifically, the static ionization rate (see Ref. [21, 52, 54, 55]) is often employed to distribute the times of ionization and the initial transverse momenta:

$$w(t_0, v_{0,\perp}) \sim \exp\left(-\frac{2\kappa^3}{3F(t_0)}\right) \exp\left(-\frac{\kappa v_{0,\perp}^2}{F(t_0)}\right), \tag{2.7}$$

with $\kappa = \sqrt{2I_p}$. For simplicity, the preexponential factor is omitted in Eq. (2.7). This is justified, as long as ionization of atoms is considered. Indeed, for atoms this factor only slightly affects the shape of the resulting photoelectron momentum distributions, which we are interested in. However, in contrast to the atomic case, this preexponential factor should be taken into account if the ionization of molecule is considered (see Sec. 3.3).

After the end of the laser pulse the electron moves in the ionic potential only. For simplicity, we assume this potential to be the Coulomb one. If the electron energy E at the end of the laser pulse $t = t_f$ is negative, the electron should be considered as captured into a Rydberg state. In this case it will move along an elliptical orbit. It is clear that ionized electrons correspond to $E > 0$ (hyperbolic trajectories). The asymptotic momentum of an ionized electron can be completely determined from its position $\mathbf{r}\,(t_f)$ and momentum $\mathbf{p}\,(t_f)$ at the end of the laser pulse:

$$\mathbf{k} = k\frac{k\,(\mathbf{L} \times \mathbf{a}) - \mathbf{a}}{1 + k^2 L^2}, \tag{2.8}$$

see Refs. [P4,P2] (the misprint in this formula obtained in Ref. [P4] was corrected in Ref. [P2]). Here $\mathbf{L} = \mathbf{r}\,(t_f) \times \mathbf{p}\,(t_f)$ and $\mathbf{a} = \mathbf{p}\,(t_f) \times \mathbf{L} - Z\mathbf{r}\,(t_f)\,/r\,(t_f)$ are the conserved angular momentum and Runge-Lenz vector, respectively. The absolute value of the final momentum that is present in Eq. (2.8) is found from the energy conservation:

$$\frac{k^2}{2} = \frac{\mathbf{p}^2\,(t_f)}{2} - \frac{Z}{r\,(t_f)}. \tag{2.9}$$

The semiclassical models often operate with large ensembles of classical trajectories. These ensembles are propagated in the continuum till the end of the laser pulse and, in this way, the final asymptotic momenta of all the trajectories are found. Thereafter the trajectories are binned in accord to their final momenta in bins in momentum space, and the contributions associated with the trajectories reaching the same bin are summed. This approach is sometimes referred to as "shooting method" [38]. However, this is not the only possible approach to the semiclassical simulations. Alternatively, we can solve the so-called inverse problem, i.e., find all the trajectories corresponding to a given final momentum. This approach was used, e.g., in Refs. [56–60]. The advantage of this approach is that it allows to avoid large ensembles of trajectories. Furthermore, by solving the inverse problem, we can establish a better control over cusps and caustics that are always present in classical simulations [P5]. However, this method can often be less versatile, and the solution of the inverse problem is often a difficult task. For these reasons,

in this work we use the standard approach based on ensembles of classical trajectories.

2.2   Capture into Rydberg states

Stabilization in strong-field ionization refers to a decrease of the total ionization yield when the laser field strength exceeds a certain value. This phenomenon was intensively studied both experimentally and theoretically in the 1980s and 1990s (see Refs. [1, 61] for reviews). It was found that there are two different mechanisms responsible for the stabilization effect: adiabatic stabilization, which is often called stabilization in the Kramers-Henneberger regime, and interference stabilization. The adiabatic stabilization can be observed for the laser frequency exceeding the ionization potential, $\omega > I_p$. In this case there is a single-photon coupling between the states of the discrete spectrum and the continuum states. In experiment this stabilization regime can be realized by populating Rydberg states. In contrast to this, the interference stabilization occurs due to multiple Raman-type transitions between the Rydberg states and the common continuum. In interference stabilization ionization is suppressed due to destructive interference of the transition amplitudes from these coherently populated states to the continuum.

The renewed interest in the studies of the neural atoms produced in ionization by a strong laser field was caused by the results obtained in Ref. [62]. The experimental study of Ref. [62] focuses on the yield of neutral excited He atoms produced in ionization of a gaseous target by laser pulses with the wavelength 800 nm, pulse duration 30 fs, and intensities up to 10^{15} W/cm^2. It was shown that at relatively low laser intensities the observed excited neutral atom yield is about 20 % of the ion yield. For higher intensities this yield decreases to about 10 %. The experimental data were compared with the direct numerical solution of the TDSE and with the results of a semiclassical model that accounts for both the laser field and the Coulomb potential of the atomic residual [62]. In the latter approach the electrons with negative total energies at the end of the laser pulse were considered as captured into bound states. The corresponding distribution over the effective principal quantum number is in quantitative agreement with the quantum results [62].

The production of the substantial number of neutral atoms in the tunneling ionization regime was named in Ref. [62] frustrated tunneling ionization (FTI). The FTI process was extensively studied over the last years. One of the first theoretical studies of the FTI phenomenon was done in Ref. [P4]. This study also applies a semiclassical model. However, it is mainly focused on the mechanism responsible for the production of neutral excited atoms and

the derivation of the scaling of this yield with the laser-atom parameters. In addition to this, the impact of the FTI on the momentum distributions of the ionized electrons is studied in Ref. [P4].

The following quasistatic tunneling rate was used in Ref. [P4] instead of Eq. (2.7):

$$w\left(t_0, v_{0,\perp}\right) \sim \frac{\left(2I_p\right)^3}{F^2\left(t_0\right)\sqrt{1 + v_{0,\perp}^2/2I_p}} \exp\left\{-\frac{2\kappa^3}{3F\left(t_0\right)}\left[1 + \frac{v_{0,\perp}^2}{2I_p}\right]^{3/2}\right\} \quad (2.10)$$

This expression can be obtained from the standard SFA amplitude by using the saddle-point method in the tunneling regime when the Keldysh parameter $\gamma = \omega\sqrt{2I_p}/F \ll 1$ (see Refs. [63, 64] for details of the derivation). It is assumed that the electron tunnels with zero initial velocity along the laser field polarization direction, see Sec. 2.1. The tunnel exit point is given by Eq. (2.3). The initial conditions fully determine the electron trajectory in the continuum, i.e., the time-dependent electron position $\mathbf{r}\left(t\right) = \mathbf{r}\left(t, t_0, v_{0,\perp}\right)$ and momentum $\mathbf{p}\left(t\right) = \mathbf{q}\left(t, t_0, v_{0,\perp}\right)$. As in Ref. [62], the electrons with negative total energies at the end of the laser pulse, $t = t_f$, are considered as captured in Rydberg states:

$$E\left(\tau_f\right) = \frac{\mathbf{q}^2}{2} - \frac{1}{r} < 0, \quad (2.11)$$

where $\mathbf{q}$ and r are the electron velocity and the distance from the ion at the end of the laser pulse, respectively. The results of the semiclassical simulations based on this model are in a good agreement with those obtained in Ref. [62]. This is true for both the relative yield of the neutral atoms and the distribution of the captured electrons over the principal quantum number [P4].

The in-depth analysis of the electron trajectories has shown that only those electrons are captured into Rydberg states that (i) have moderate initial transverse velocities at the time of ionization and (ii) avoid strong interactions with the ion, i.e., "hard collisions" (see Ref. [P4] for details). This analysis allows us to derive the analytical scaling for the ratio of the neutral excited atoms and singly charged ions with laser-atom parameters [P4]. Indeed, the electron momentum at the end of the laser pulse can be written as

$$\mathbf{q} = -\mathbf{A}\left(t_0\right) + \mathbf{v}_{0,\perp} + \mathbf{p}_C\left(t_0, \mathbf{v}_{0,\perp}\right), \quad (2.12)$$

where $\mathbf{A}\left(t_0\right)$ is the vector potential of the laser pulse at the time of start, and $\mathbf{p}_C\left(t_0, \mathbf{v}_{0,\perp}\right)$ is the contribution due to the Coulomb field. For the parameters used in Ref. [62] the Coulomb force is small compared to the laser field

already at the tunnel exit and decreases further along the trajectory. There-
fore, the Coulomb contribution to the final momentum can be calculated by
integration of the Coulomb force along the trajectory in the laser field only:

$$\mathbf{p}_C\left(t_0, \mathbf{v}_{0,\perp}\right) = -\int_{t_0}^{+\infty} \frac{\mathbf{r}_L\left(t\right)}{r_L^3\left(t\right)}, \tag{2.13}$$

Only the first initial part of the trajectory adjacent to the exit point con-
tributes significantly to the integral of Eq. (2.13). This part of trajectory can
be approximated by the electron trajectory in the constant field equal to the
instantaneous field strength at the time of ionization:

$$\mathbf{r}_L\left(t\right) = \left\{x_0 + \frac{1}{2}F\left(t_0\right)\left(t-t_0\right)^2\right\}\mathbf{e}_x + v_{0,\perp}\left(t-t_0\right)\mathbf{e}_y. \tag{2.14}$$

We note that similar approach was used in Ref. [63]. The following estimate
for the relative yield of neutral excited atoms N^* and singly charged ions N^+
was derived in Ref. [P4]:

$$\frac{N^*}{N^+} \sim \frac{\omega}{F^{3/2}\tau_L^{2/3}}\left(1 - 2\frac{F}{\left(2I_p\right)^2}\right)^{-1}. \tag{2.15}$$

This scaling with respect to the laser parameters and ionization potential
agrees well with the semiclassical simulations.

Finally, the capture into Rydberg states has a pronounced effect on
the photoelectron momentum distribution, especially on its low-energy part.
Specifically, it is correlated with the formation of the widely discussed "dip"
in the longitudinal momentum distributions (see, e.g., Refs. [35, 65–69]). It
should be noted that the approach developed in Ref. [P4] is extensively used
in many other studies of the FTI. The findings of the study [P4] has been
substantially extended (see Ref. [70] and references therein).

2.3 Sequential multiple ionization

Theoretical description of double and multiple ionization is one of the most
difficult problems in strong-field physics. These processes have been inten-
sively studied over the last decades and two different physical mechanisms
responsible for the production of doubly and multiply charged ions were
revealed. These are nonsequential and sequential double (or multiple) ion-
ization. The term nonsequential double (multiple) ionization is used in the
situation when two (or more) electrons are ionized as a result of one cor-
related process. Therefore, electron-electron correlation is necessary for the

nonsequential ionization. The mechanism of this correlation has been intensively studied over the last two decades. By now it is established that inelastic recollision of the ionized electron with the parent ion underlies the nonsequential ionization and this process can be visualized by the three-step model, see Chapter 1. However, the actual details depend on the specific atom (molecule), see Ref. [4, 71, 72] for reviews. It is obvious that the rate of the nonsequential process cannot be calculated as the product of single ionization rates and more sophisticated models are required (see, e.g, Refs. [4, 73]).

In contrast to this, in sequential double (multiple) ionization electrons are ionized sequentially and independently of one another. While the nonsequential ionization dominates at relatively low laser intensities, the sequential mechanism becomes important at higher intensities, where the product of two (or several) large ionization rates exceeds the contribution of the nonsequential channel. The studies of sequential ionization are important in view of the constant increase in the intensity of the available laser systems. Furthermore, the availability of the cold-target recoil-ion momentum spectroscopy (COLTRIMS), which is also known as reaction microscope (REMI) allows us to measure not only the total ion yields, but also the momentum distributions of the product ions [66, 74–79].

The sequential mechanism also dominates for elliptically (circularly) polarized laser fields. In this case the nonsequential mechanism is suppressed for a different reason. In order to return to the parent ion in elliptically polarized field, an ionized electron has to start with a nonzero initial transverse velocity. This velocity decreases the ionization yield, see Eq. (2.7). We note that all the recollision-induced processes are suppressed with the increase of the ellipticity of the incident field [80].

The sequential process may appear trivial compared to the nonsequential one. The yields of the multiply charged ions generated in sequential ionization process were calculated in many works, see, e.g., Refs. [81–89]. However, the primary interest was in empirical formulas capable to describe the well-known "knee" in the ion yield originating from the nonsequential ionization. Furthermore, there is a lack of studies of momentum distributions of multiply charged ions. The distributions along the polarization direction for doubly charged ions of noble gas atoms ions were studied experimentally in Refs. [76, 77]. In Ref. [90] these distributions are observed for Ar and Ne ions with the charges up to $Z = 4$, and the experimental study of Ref. [89] analyzes momentum distributions of Ar^{n+}, Kr^{m+}, and Xe^{l+} ions with $n \leq 9$, $m \leq 9$, and $l \leq 12$, respectively. It was shown that the momentum distributions have a Gaussian-like shape with its center (maximum) at zero momentum. The longitudinal momentum distributions of multiply

charged ions of Ne, Ar, and Kr were observed and simulated numerically in Refs. [91, 92] for laser pulses with durations of 200 fs and intensities of $5 - 7 \times 10^{15}$ W/cm^2. For calculation of the ion momentum distributions the classical trajectory Monte-Carlo method including tunneling (CTMC-T, see Refs. [35, 93]) was used in Refs. [91, 92]. It has been revealed that the width of the longitudinal ion momentum distributions is almost a linear function of the ionization potential. This dependence of the width can be explained using the SFA and the electron kinematics in the laser pulse [91]. The study of Ref. [P6] focuses on the momentum distributions of highly charged Xe ions with $Z > 8$. Furthermore, sequential multiple ionization by short laser pulses including the CEP effects was for the first time investigated in Ref. [P6].

The yields of the highly charged ions produced in sequential ionization by a laser field can be calculated by solving the system of rate equations. This approach is used in the vast majority of the studies of the sequential ionization process, see, e.g., [81–83, 86, 87, 89]. This system was also solved in Ref. [P6] accounting for both the envelope and the oscillations of the laser field. The solution of the rate equations requires well-defined ionization rates. The static tunneling rate [21, 52, 54]

$$
\begin{aligned}
W_{l,m} &= (2I_p)(2l+1)\frac{(l+m)!}{2^m m!\,(l-m)!}C_{\kappa l}^2 2^{2n^*-m}\left(\frac{F}{F_a}\right)^{m+1-2n^*}\\
&\times \exp\left(-\frac{2F_a}{3F}\right)
\end{aligned}
\tag{2.16}
$$

and the barrier-suppression ionization rate [94, 95]

$$
\begin{aligned}
W_{l,m} &= \sqrt{\pi}\,(2I_p)(2l+1)\frac{(l+m)!}{2^m m!\,(l-m)!}C_{\kappa l}^2 2^{2n^*+\frac{14}{3}-m}\\
&\times \left(\frac{F}{F_a}\right)^{m+\frac{1}{6}-2n^*}\int_0^\infty \mathrm{Ai}^2\left(k^2+x^2\right)x^2 dx
\end{aligned}
\tag{2.17}
$$

with $F = F(t_0)$ were used in Ref. [P6]. Here $n^* = Z/\sqrt{2I_p}$ is the effective quantum number, $C_{\kappa l}$ is the assymptotic coefficient of the atomic wave function (see, e.g., Ref. [96]), $F_a = (2I_p)^{3/2}$ is the atomic field, $k = 2I_p/(2F)^{2/3}$, and l and m are the orbital and magnetic quantum numbers, respectively.

We note in passing that the system of rate equations is stiff because two tunneling rates entering the same rate equation usually can differ even by more than one order of magnitude. Therefore, it is impractical to solve the rate equations using the standard numerical methods, such as the Runge-Kutta method with adaptive step size control [97]. The Gear method [98] aimed at the solution of stiff differential equations was used in Ref. [P6]. The
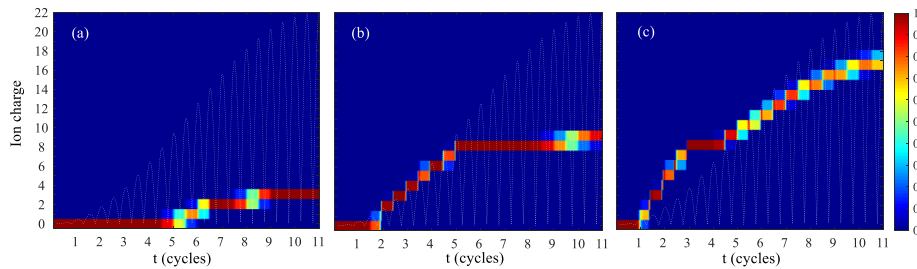
Fig. 2.1: Results of the numerical solution of the rate equations for Xe ions. The panels (a), (b), and (c) correspond to peak intensities of 0.8, 60, and 500×10^{14} W/cm^2, respectively. The color scale depicts the time-dependent ionization state distribution. In all cases, the pulse duration is 30 fs at FWHM and the white line is the instantaneous intensity. Taken from Ref. [P6].

results of the solution of the rate equations are shown in Figs. 2.1 (a)-(c), which show the probability for an ion to have a specific charge as a function of time for three different laser intensities (see Ref. [P6] for details). The numerical analysis has shown that ions with $Z > 2$ are ionized before the field strength reaches the corresponding barrier-suppression regime, and therefore tunneling rates determined by Eq. (2.16) can be used for simulations. However, it is not possible to calculate the ion momentum distributions by solving the system of rate equations. In order to calculate these distributions, a simple semiclassical model was developed in Ref. [P6]. This model is based on the calculation of the ion trajectory in the laser field allowing for the possibility of a single or multiple ionization during the laser pulse. More specifically, the time axis is subdivided into small intervals, and the ion trajectory is considered in each of these intervals. The neutral atom $(Z = 0)$ starts its motion with zero initial velocity along the polarization direction $P_x = 0$. It is clear that the laser pulse cannot act on the neutral particle. Let us assume that Z and $P_x(t_0)$ are the charge and the momentum of the ion at time t_0, respectively. The ion momentum at the end of the interval is calculated using the Newton's equation of motion

$$P_x(t_0 + \Delta t) = P_x(t_0) + Z \int_{t_0}^{t_0+\Delta t} F(t')\, dt', \qquad (2.18)$$

and the probability for the ion to be ionized during the time interval is equal to $\int_{t_0}^{t_0+\Delta t} W_Z(t)\, dt$. This probability is compared with a random number $0 \leq r \leq 1$. If the ionization probability is larger than this random number, the ion is again ionized and the charge Z should be increased by one. In this case the motion of the ion with the charge $(Z + 1)$ is considered in the next
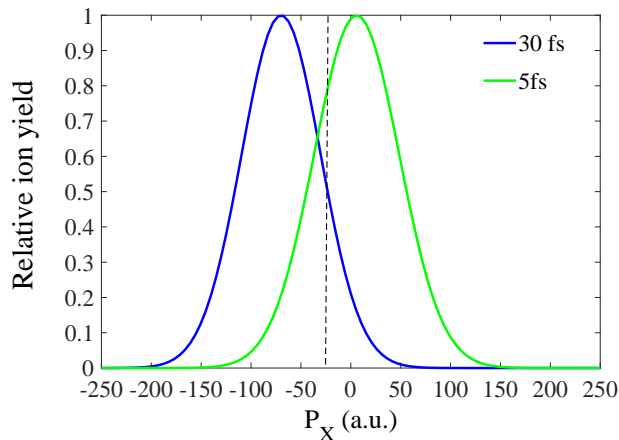
Fig. 2.2: Ion momentum distribution of Xe^{21+} at the intensity of 1.5×10^{18} W/cm^2 for two different pulse durations at FWHM. The shift of the maximum is clearly seen from the figure. From Ref. [P6].

time interval. If the ionization probability is less than r, no ionization occurs for $t_0 \leq t \leq t_0 + \Delta t$. In both these cases the initial momentum of the ion for the next time interval is equal to $P_x(t_0 + \Delta t)$ determined by Eq. (2.18). At the end of the pulse, the ion has a certain charge Z_F and a certain momentum $P_{x,F}$. By doing these simulations for an ensemble of particles we obtain the ion momentum distributions.

Examples of the resulting longitudinal ion momentum distributions are shown in Fig. 2.2. It is seen that the distributions have Gaussian shape. In what follows we discuss the momentum distributions of the ions that have the maximum yield at a given laser intensity. The simulations performed in Ref. [P6] show that the width of the ion momentum distributions is proportional to $I_p^{1.4}$ within a wider range of intensities $(10^{14} - 10^{18}$ W/cm$^2)$ than the one considered in Ref. [91]. Moreover, a new effect was predicted in Ref. [P6]: It is found that the maxima of the ion momentum distributions shift from zero momenta. The shift of the maxima originates from the finite duration of the ionizing field, and therefore, it cannot be observed in a monochromatic field [P6]. This shift also disappears in the distributions averaged over the carrier envelope phase (CEP). It is shown that the magnitude of this shift is proportional to the field strength and inversely proportional to the pulse duration. However, in order to reliably estimate the position of the maxima in the ion momentum distributions at given parameters, it is necessary to know the subcycle ionization dynamics, i.e., to solve rate equations (see Ref. [P6] for details). The intensity and CEP dependence of the position of
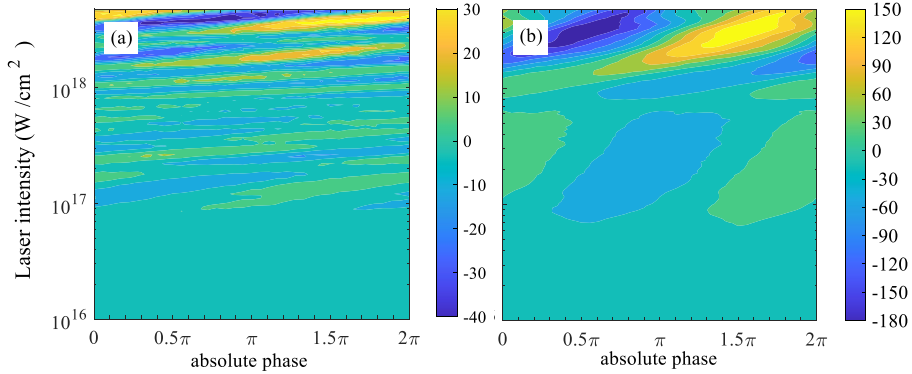
Fig. 2.3: The shift of the centroid in atomic units as a function of the CEP and the intensity. At any given intensity only the distribution of the ion with the highest yield is considered. The two panels (a) and (b) correspond to the pulse duration of 30 and 6.7 fs at FHWH, respectively. Modified from Fig. 6 in Ref. [P6].

the maxima was also studied, see Fig. 2.3. It is found that at high intensities the shift of the maxima can be observed in long laser pulses [up to 30 fs at full with at half maximum (FWHM)]. The pronounced dependence on the CEP originates due to different ionization dynamics that corresponds to different temporal evolution of the varying field. This temporal evolution, in turn, depends strongly on the absolute phase. We note that CEP effects for relatively long pulses were observed in HHG, see Ref. [99]. However, the mechanism responsible for these effects, i.e., interference of the contributions from different recolliding trajectories, is substantially different from the one discussed here.

It appears easier to observe CEP effects in the total yields of multiply charged ions than the CEP-dependent shift of the maxima of the ion momentum distributions. The effect of the absolute phase on the yields of multiply charged ions produced in sequential ionization was studied in Ref. [P7]. It is found that the ion yields oscillate as functions of the CEP if the pulse length is no more than $6-7$ fs at FWHM. A surprising property of this effect is that it can only be observed, if at the end of the ionizing pulse the yields of at least two ions are comparable to each other. The analytic model describing the basic features of this effect was also developed in Ref. [P7]. Although the oscillations of the yields strongly depend on the laser intensity, the predicted effect survives averaging over the focal volume. It should be experimentally observable for the noble gas atoms.

2.4 Applicability of trajectory-based models

Although the semiclassical models had been widely used in strong-field physics, for a long time there were no systematic studies of their applicability regions. Such a study was for the first time performed in Ref. [P8] that focuses on the applicability of the two-step model [14, 15]. The approach of Ref. [P8] is based on Ehrenfest's theorem (see, e.g., Ref. [100] for a text-book treatment). Ehrenfest's theorem formulates the quantum-mechanical counterpart to the Newton's equation of motion. More specifically, Ehrenfest's theorem establishes the equation of motion obeyed by the mean values of the spatial and momentum coordinates of the quantum system. Let us consider a single-particle quantum system with the Hamiltonian

$$\hat{H} = -\frac{1}{2}\nabla_{\mathbf{r}}^2 + V\left(\mathbf{r}, t\right), \tag{2.19}$$

where $V\left(\mathbf{r}, t\right)$ is the potential. In accord with Ehrenfest's theorem, the equations for the mean values of the position and momentum operators read as

$$\frac{d\langle\mathbf{r}\rangle}{dt} = \langle\mathbf{p}\rangle \tag{2.20}$$

and

$$\frac{d\langle\mathbf{p}\rangle}{dt} = \langle-\nabla_{\mathbf{r}}V\left(\mathbf{r}, t\right)\rangle, \tag{2.21}$$

respectively. At first glance, it seems that the averaged values $\langle\mathbf{r}\rangle$ and $\langle\mathbf{p}\rangle$ satisfy classical equations of motion. However, this is not true, since the term $\langle-\nabla_{\mathbf{r}}V\left(\mathbf{r}, t\right)\rangle$ in the right-hand side of Eq. (2.21) is the average value of the force acting on the particle, but not *the force at the average position*. Let us call the equations

$$\frac{d\langle\mathbf{r}\rangle}{dt} = \langle\mathbf{p}\rangle \tag{2.22}$$

and

$$\frac{d\langle\mathbf{p}\rangle}{dt} = -\nabla_{\mathbf{r}}V\left(\mathbf{r}, t\right)\big|_{\mathbf{r}=\langle\mathbf{r}\rangle}. \tag{2.23}$$

the *strict* form of Ehrenfest's theorem. It is seen from Eqs. (2.22) and (2.23) that if the quantum system satisfies the strict form of the Ehrenfest's theorem, the mean values of the position and momentum operators obey the classical equations of motion. We have found a correlation between the inapplicability of the two-step model and the deviation from the strict form of the Ehrenfest's theorem for an ensemble of classical trajectories [P8].

Simple analysis based on the Taylor expansion shows that quantum systems with potentials linear or quadratic in $\mathbf{r}$ satisfy the strict form of Ehrenfest's theorem, as, e.g., the free particle in the external laser field or the

3D harmonic oscillator. All other quantum systems, including atoms and molecules in a laser field, do not satisfy Eqs. (2.23) and (2.23). Indeed, in case of strong-field ionization of an atom or molecule the potential V reads as

$$V\left(\mathbf{r}, t\right) = V_0 + \mathbf{F}\left(t\right) \cdot \mathbf{r}, \tag{2.24}$$

where V_0 is the atomic (molecular) potential and $\mathbf{F}\left(t\right)$ is the electric field of the pulse. In general, the first term of Eq. (2.24) is not linear or quadratic in r, and therefore, it does not satisfy the strict form of the Ehrenfest's theorem.

The deviation of a given quantum system from the strict form of Ehrenfest's theorem can be quantified by the following measure:

$$R_q\left(t\right) = \frac{\left|\nabla_{\mathbf{r}} V\left(\mathbf{r}, t\right)\right|_{\mathbf{r}=\langle \mathbf{r}\rangle} - \left\langle \nabla_r V\left(\mathbf{r}, t\right)\right\rangle\right|}{\left\langle \nabla_r V\left(\mathbf{r}, t\right)\right\rangle}. \tag{2.25}$$

Equation (2.25) is the relative deviation between the force at the average position of the system and the average value of the force. The averaged values in Eq. (2.25) should be calculated quantum mechanically what requires the exact solution of the TDSE at all times and makes the application of the measure (2.25) impractical. It is useful to possess a method that (i) is capable to estimate the applicability of a semiclassical model for description of quantum phenomena, and (ii) does not need the numerical solution of the TDSE. It was shown that the average values of the coordinate and momentum for a probability distribution of a classical ensemble satisfying the Liouville equation obey the Ehrenfest's theorem, but violates its strict form, see Ref. [101].

In Ref. [P8] the validity of the strict form of the Ehrenfest's theorem is monitored using a classical ensemble, i.e., the relative deviation $R\left(t\right)$ is defined as:

$$R\left(t\right) = \frac{\left|\nabla_{\mathbf{r}} V\left(\mathbf{r}, t\right)\right|_{\mathbf{r}=\langle \mathbf{r}(t)\rangle} - \sum_{\mathcal{A}} w_i \nabla_{\mathbf{r}} V\left(\mathbf{r}, t\right)\right|}{\left|\sum_{\mathcal{A}} w_i \nabla_{\mathbf{r}} V\left(\mathbf{r}, t\right)\right|}. \tag{2.26}$$

Here $\langle \mathbf{r}\rangle$ is the average position of the ensemble $\mathcal{A}$ of classical trajectories at time t, and w_i is a weight of the i-th trajectory in the ensemble. The relative deviation (2.26) should be monitored for the whole duration of the laser pulse. The maximal relative deviation $R\left(t\right)$ was used in Ref. [P8] as the measure of violation of the strict form of Ehrenfest's theorem. However, this measure alone is not sufficient to gauge the validity of the two-step model. It was shown that the time at which the maximum is achieved, i.e., the time of maximal relative deviation, is equally important [P8]. It turns out that even

substantial deviations from the strict form of Ehrenfest's theorem at times close to the electron ejection, as well as at the end of the pulse, do not affect the agreement between the two-step model and the exact quantum results. This can be attributed to the following. At times close to the ionization time the quantum part of the semiclassical model (i.e., initial conditions) is interfacing the classical propagation of the electron trajectory. On the other hand, when the laser pulse is over, the ensemble of classical trajectories represents both ionized and excited atoms (see Ref. [P8] for details).

However, we have found that a substantial deviation from the strict form of Ehrenfest's theorem at any other time during the laser pulse is a manifestation of the inapplicability of the two-step model. As an example, let us compare the PMDs calculated from the two-step model and the solution of the TDSE for ionization by a laser pulse with peak intensity 2.0×10^{14} W/cm^2, ellipticity 0.5, and pulse duration $n_p = 3$ cycles for two different wavelengths: 800 nm and 400 nm, see Figs. 2.4 and 2.5, respectively. It is seen that at 800 nm the two-step model shows a good qualitative agreement with the TDSE. Simultaneously, there is a substantial discrepancy between the predictions of the semiclassical model and the TDSE result at 400 nm: Even the maxima of the distributions shown in Figs. 2.5 (a) and (b) are in different quadrants of the (k_x, k_y) plane. The relative deviations that correspond to these two cases as functions of time are shown in Fig. 2.6 (a) and (b), respectively. It is seen that for the wavelength of 800 nm the maximal relative deviation does not exceed 0.1 and occurs at the half cycle where the trajectories are launched. In contrast to this, for 400 nm the maximal relative deviation exceeds 0.25 and occurs at the next half cycle after the trajectories of the ensemble were launched, i.e., at a later stage of the time evolution. Therefore, there is indeed a correlation between the inapplicability of the two-step model and the violation of the strict form of the Ehrenfest's theorem along the lines discussed here.

The maximal relative deviations and the times of these deviations are calculated as functions of parameters of the laser field and the atomic target: ellipticity, intensity, wavelength, ionization potential, and the range of the potential, see Ref. [P8]. Therefore, the study of Ref. [P8] investigates the trends of the applicability of the two-step model. Moreover, this study is not restricted to the hydrogen atom: The applicability of the two-step model is investigated for Mg, Xe, Kr, Ar, Ne, and He. In all these cases the corresponding Stark-shifts and the polarization-induced dipole potentials (as in Refs. [102–104] and [P2]) are taken into account.

It should be mentioned that the study of Ref. [P8] is based on the 2D implementation of the two-step model. Therefore, the limitations that should be imposed on the laser-atom parameters for the model to be applicable in the
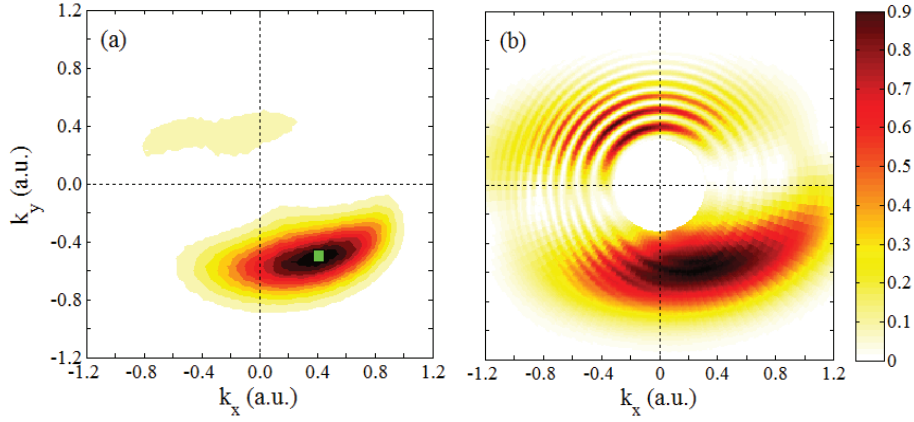
Fig. 2.4: Momentum distribution (normalized to the peak value) for the H atom in the polarization plane using a laser pulse with wavelength $\lambda = 800$ nm, peak intensity 2×10^{14} W/cm^2, ellipticity $\epsilon = 0.5$ and a laser pulse duration of $n_p = 3$ cycles, obtained (a) using the semiclassical two-step model, and (b) by numerical solution of the TDSE (the size of the spatial box $X_{max} = 600$ a.u., the maximum angular momentum $l_{max} = 60$). The maximum of the semiclassical momentum distribution is qualitatively indicated by a (green) square in (a). Taken from Ref. [P8]
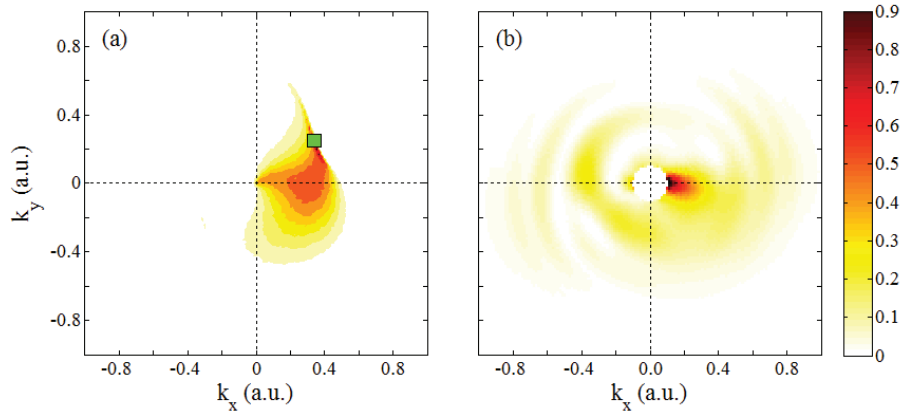
Fig. 2.5: Momentum distribution (normalized to the peak value) for the H atom in the polarization plane using a laser pulse with wavelength $\lambda = 400$ nm, peak intensity 2×10^{14} W/cm^2, ellipticity $\epsilon = 0.5$ and a laser pulse duration of $n_p = 3$ cycles, obtained (a) using the semiclassical two-step model, and (b) by numerical solution of the TDSE (the size of the spatial box $X_{max} = 400$ a.u., the maximum angular momentum $l_{max} = 40$). The maximum of the semiclassical momentum distribution is qualitatively indicated by a (green) square in (a). Taken from Ref. [P8].
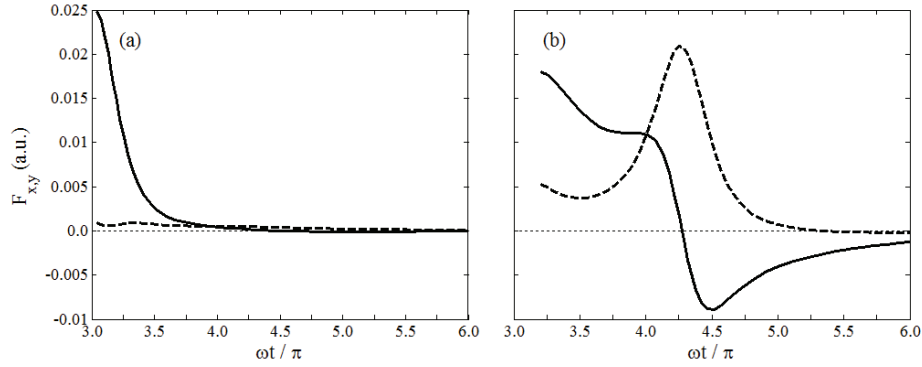
Fig. 2.6: Time-dependence of the x-components (full curves) and the y-components (long-dashed curves) of the Coulomb force for trajectories that lead to final momenta corresponding to the maxima of the momentum distributions in (a) Fig. 2.4 (a) and (b) Fig. 2.5 (a). The pulse parameters are as in Figs. 2.4 and 2.5, respectively. In (b) the time axis is given in units of half-cycle duration, the pulse starts at time zero, and $\omega t/\pi$ corresponds to the center of the pulse. From Ref. [P8].

real 3D case might not be as strict as predicted in Ref. [P8]. Nevertheless, the results obtained in Ref. [P8] can be used as a guideline for the applicability of the two-step semiclassical model for ionization by a strong laser pulse.

3. SEMICLASSICAL TWO-STEP MODEL AND ITS MODIFICATIONS

3.1 *Semiclassical two-step model*

For a long time, the semiclassical models were not able to describe quantum interference. A substantial progress in this direction has been achieved in the last years: new trajectory-based models capable of accounting for the quantum interference effects have been developed. Among these are: The trajectory-based Coulomb SFA (TCSFA) [105, 106], the quantum trajectory Monte Carlo model (QTMC) [107], the Coulomb quantum orbit strong-field approximation (CQSFA) [56–60, 108], and the semiclassical two-step model (SCTS) [P1]. All these approaches assign certain phases to electron trajectories, and the contributions of the trajectories corresponding to the same final momentum are to be added coherently.

The TCSFA is a further development of the CCSFA model [49, 50]. In contrast to the CCSFA approach, in the TCSFA model the laser field and the Coulomb force of the ionic residual are treated on an equal footing in the Newton's equations of motion. However, the first-order semiclassical perturbation theory (see Ref. [109]) is used in the TCSFA model to account for the Coulomb potential in the phase assigned to the trajectory. The semiclassical perturbation theory was also applied in the phase of the QTMC model. The other two models capable to describe quantum interference effects, i.e., CQSFA and SCTS, account for the ionic potential in the phase beyond the semiclassical perturbation theory.

The phase used in the SCTS model coincides with the phase of the matrix element of the semiclassical propagator between the initial state of a quantum system at time t_1 and its final state at time t_2 [110–112] (see Refs. [113, 114] for a text-book treatment). There are four different expressions for this semiclassical propagator U_{SC} for different variables describing the initial and

final states of a quantum system:

$$\langle \mathbf{r}_2 | U_{\text{SC}}(t_2, t_1) | \mathbf{r}_1 \rangle = \left[-\frac{\det \left(\partial^2 \phi_1 (\mathbf{r}_1, \mathbf{r}_2) / \partial \mathbf{r}_1 \partial \mathbf{r}_2 \right)}{(2\pi i)^3} \right]^{1/2}$$
$$\times \exp \left[i \phi_1 (\mathbf{r}_1, \mathbf{r}_2) \right], \qquad (3.1a)$$

$$\langle \mathbf{r}_2 | U_{\text{SC}}(t_2, t_1) | \mathbf{p}_1 \rangle = \left[-\frac{\det \left(\partial^2 \phi_2 (\mathbf{p}_1, \mathbf{r}_2) / \partial \mathbf{p}_1 \partial \mathbf{r}_2 \right)}{(2\pi i)^3} \right]^{1/2}$$
$$\times \exp \left[i \phi_2 (\mathbf{p}_1, \mathbf{r}_2) \right], \qquad (3.1b)$$

$$\langle \mathbf{p}_2 | U_{\text{SC}}(t_2, t_1) | \mathbf{r}_1 \rangle = \left[-\frac{\det \left(\partial^2 \phi_3 (\mathbf{r}_1, \mathbf{p}_2) / \partial \mathbf{r}_1 \partial \mathbf{p}_2 \right)}{(2\pi i)^3} \right]^{1/2}$$
$$\times \exp \left[i \phi_3 (\mathbf{r}_1, \mathbf{p}_2) \right], \qquad (3.1c)$$

$$\langle \mathbf{p}_2 | U_{\text{SC}}(t_2, t_1) | \mathbf{p}_1 \rangle = \left[-\frac{\det \left(\partial^2 \phi_4 (\mathbf{p}_1, \mathbf{p}_2) / \partial \mathbf{p}_1 \partial \mathbf{p}_2 \right)}{(2\pi i)^3} \right]^{1/2}$$
$$\times \exp \left[i \phi_4 (\mathbf{p}_1, \mathbf{p}_2) \right]. \qquad (3.1d)$$

In Eqs. (3.1a)-(3.1d) $\mathbf{r}_1 (\mathbf{r}_2)$ and $\mathbf{p}_1 (\mathbf{p}_2)$ are the initial (final) sets of positions and momenta, respectively. For example, the phase ϕ_1 in Eq. (3.1a) corresponds to the transition from the initial state described by the coordinate $\mathbf{r}_1$ to the final state described by the coordinate $\mathbf{r}_2$. This phase is determined by the classical action

$$\phi_1 (\mathbf{r}_1, \mathbf{r}_2) = \int_{t_1}^{t_2} \left\{ \mathbf{p}(t) \dot{\mathbf{r}}(t) - H [\mathbf{r}(t), \mathbf{p}(t)] \right\} dt, \qquad (3.2)$$

Here $H [\mathbf{r}(t), \mathbf{p}(t)]$ is the classical Hamiltonian function that depends on both the canonical coordinates and momenta. The canonical transformations

$$\phi_2 (\mathbf{p}_1, \mathbf{r}_2) = \phi_1 (\mathbf{r}_1, \mathbf{r}_2) + \mathbf{p}_1 \cdot \mathbf{r}_1, \qquad (3.3a)$$
$$\phi_3 (\mathbf{r}_1, \mathbf{p}_2) = \phi_1 (\mathbf{r}_1, \mathbf{r}_2) - \mathbf{p}_2 \cdot \mathbf{r}_2, \qquad (3.3b)$$
$$\phi_4 (\mathbf{p}_1, \mathbf{p}_2) = \phi_1 (\mathbf{r}_1, \mathbf{r}_2) + \mathbf{p}_1 \cdot \mathbf{r}_1 - \mathbf{p}_2 \cdot \mathbf{r}_2, \qquad (3.3c)$$

relate the phases ϕ_2, ϕ_3, and ϕ_4 to the phase ϕ_1 [110].

The phase ϕ_3 is used in the SCTS model. This choice is justified by the following considerations. For a given ionization time t_0 the starting point of the electron trajectory (the tunnel exit point) is localized in space [see, e.g., Eqs. (2.2), (2.3), and (2.4)]. In contrast to this, the initial electron velocity is distributed in accord with Eq. (2.7). Simultaneously, the final state is characterized by the asymptotic electron momentum $\mathbf{k}$. It should

be noted that the ionization by a strong laser field can be considered as a half-scattering process, in which an electron is initially located near the atom (molecule) and detected with the given asymptotic momentum [P1]. For zero initial longitudinal velocity $v_{0,\|} = 0$, the initial electron position vector is orthogonal to the initial momentum, i.e., $\mathbf{p}_1 \cdot \mathbf{r}_1 = 0$. In this case the phases ϕ_3 and ϕ_4 are equal to each other. For nonzero initial longitudinal velocity, the term $\mathbf{p}_1 \cdot \mathbf{r}_1$ is not equal to zero and should be included in the phase. However, it does not substantially affect the resulting photoelectron momentum distribution (see Ref. [P1] for details).

The phase used in the SCTS model is given by:

$$\Phi^{SCTS}(t_0, \mathbf{v}_0) = -\mathbf{v}_0 \cdot \mathbf{r}(t_0) + I_p t_0$$
$$- \int_{t_0}^{\infty} dt \left\{ \dot{\mathbf{p}}(t) \cdot \mathbf{r}(t) + H[\mathbf{r}(t), \mathbf{p}(t)] \right\}, \tag{3.4}$$

To arrive at Eq. (3.4) we have used an integration by parts. It is also assumed that the electron trajectory possesses the initial phase $\exp(iI_p t_0)$. This initial phase describes the time evolution of the initial state. By using Newton's equation of motion and the explicit form of the Hamiltonian for an arbitrary effective potential $V(\mathbf{r})$

$$H[\mathbf{r}(t), \mathbf{p}(t)] = \frac{\mathbf{p}^2(t)}{2} + \mathbf{F}(t) \cdot \mathbf{r}(t) + V(\mathbf{r}), \tag{3.5}$$

we can rewrite Eq. (3.4) as follows

$$\Phi^{SCTS}(t_0, \mathbf{v}_0) = -\mathbf{v}_0 \cdot \mathbf{r}(t_0) + I_p t_0$$
$$- \int_{t_0}^{\infty} dt \left\{ \frac{\mathbf{p}^2(t)}{2} + V[\mathbf{r}(t)] - \mathbf{r}(t) \cdot \nabla V[\mathbf{r}(t)] \right\}. \tag{3.6}$$

It should be emphasized that this expression can be applied for any single-active-electron potential (or pseudopotential, see, e.g., Ref. [115]) describing the multielectron atom or molecule. For the Coulomb potential the phase (3.6) is given by:

$$\Phi^{STCS}(t_0, \mathbf{v}_0) = -\mathbf{v}_0 \cdot \mathbf{r}(t_0) + I_p t_0 - \int_{t_0}^{\infty} dt \left\{ \frac{\mathbf{p}^2(t)}{2} - \frac{2Z}{r(t)} \right\} \tag{3.7}$$

The corresponding expression used in the QTMC model reads as:

$$\Phi^{STCS}(t_0, \mathbf{v}_0) = -\mathbf{v}_0 \cdot \mathbf{r}(t_0) + I_p t_0 - \int_{t_0}^{\infty} dt \left\{ \frac{\mathbf{p}^2(t)}{2} - \frac{Z}{r(t)} \right\}. \tag{3.8}$$

The QTMC phase coincides with the SCTS phase if the term $\mathbf{r}(t) \cdot \nabla V[\mathbf{r}(t)]$ is neglected in Eq. (3.6). The presence of this term leads to the double weight of the Z/r term in the phase of the SCTS model. This double contribution of the Coulomb term ensures better agreement with the numerical solution of the TDSE [P1].

It should be noted that the SCTS phase diverges when $t \to \infty$. A regularization of the phase was performed in Ref. [P1]. This regularization is based on the following decomposition of the SCTS phase

$$\Phi^{SCTS}(t_0, \mathbf{v}_0) = -\mathbf{v}_0 \cdot \mathbf{r}(t_0) + I_p t_0 - \int_{t_0}^{t_f} \left\{ \frac{p^2(t)}{2} - \frac{2Z}{r(t)} \right\}$$
$$- \int_{t_f}^{\infty} dt \left\{ E - \frac{Z}{r(t)} \right\} \tag{3.9}$$

and the separation of the time-independent part of the integrand in the last term of Eq. (3.9), see Ref. [P1] for details. As a result, the contribution to the phase accumulated due to the Coulomb potential in the time interval between t_f and ∞ is given by

$$\tilde{\Phi}_f^C(t_f) = -Z\sqrt{b} \left[\ln g + \text{arsinh} \left\{ \frac{\mathbf{r}(t_f) \cdot \mathbf{p}(t_f)}{g\sqrt{b}} \right\} \right]. \tag{3.10}$$

Here $b = 1/(2E)$ and $g = \sqrt{1 + 2EL^2}$. This asymptotic correction to the phase, which is referred to as post-pulse phase in Ref. [P1], is absent in both the QTMC and TCSFA models.

In Ref. [P1] the STCS model was compared with the direct numerical solution of the TDSE and the QTMC model. The photoelectron momentum distributions calculated within the three approaches are shown in Figs. 3.1 (a)-(c). It is seen that both the QTMC and SCTS models reproduce the most important features of the TDSE result: elongation of the PMDs along the polarization direction, the ATI rings, and a central interference structure at small momenta. It should be noted that both semiclassical approaches underestimate the width of the distributions along the polarization axis. This underestimate occurs due to the zero initial longitudinal velocity $v_{0,\parallel}$ (see Ref. [P1] for details). Nevertheless, a closer look at the low-energy parts of the PMDs shows significant deviations. For $|k| < 0.3$ a.u., i.e., electron energies well below $U_p = 0.2$ a.u., the 2D momentum distributions show pronounced fanlike interference structures, see Figs. 3.2 (a)-(c). These structures are similar to that of Ramsauer-Townsend diffraction oscillations, see Refs. [116–119]. It is seen from Figs. 3.2 (a)-(c) that the SCTS model reproduces the nodal pattern on the TDSE. In contrast to this, the QTMC model
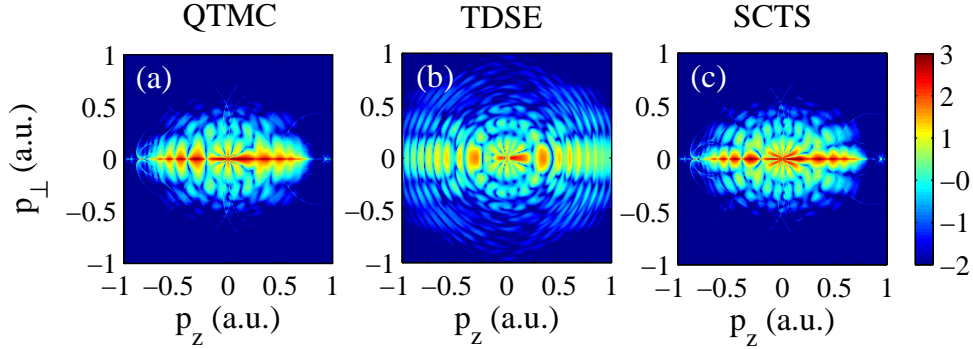
Fig. 3.1: Vectorial electron momentum distributions for the H atom ionized by a laser pulse with a duration of $n = 8$ cycles, wavelength of $\lambda = 800$ nm, and peak intensity of $I = 0.9 \times 10^{14}$ W/cm^2 obtained from (a) the QTMC model, (b) solution of the TDSE, and (c) the present SCTS model. The distributions are normalized to the total ionization yield. A logarithmic color scale in arbitrary units is used. The laser field is linearly polarized along the z-axis. From [P1].

yields fewer nodal lines. This fact was explained by the underestimate of the Coulomb contribution in the QTMC interference phase, see Eq. (3.8). The comparison of the electron energy spectra dR/dE and photoelectron angular distributions $dR/(\sin\theta d\theta)$ calculated using the QTMC and the SCTS models shows that the semiclassical approaches qualitatively reproduce the ATI peaks. However, quantitative agreement between the semiclassical models and the TDSE results can be achieved only for the low-order peaks [P1]. This is due to the fact that the initial conditions [see Eq. (2.7)] allow for insufficient number of trajectories with large initial momenta along the polarization direction (see Ref. [P1] for details). This lack of trajectories with large initial longitudinal momenta is also responsible for the too rapid fall down of the electron energy spectra predicted by the semiclassical approaches. It was shown that the main reason of deviations between the SCTS model and the TDSE are the inaccuracies in description of the initial tunneling step rather than the semiclassical treatment of the electron motion in the continuum [P1].

It should be noted that an efficient extension of the STCS model was proposed recently, see Ref. [120]. This study focuses on the effect of the preexponential factor of the semiclassical matrix element that is neglected in other versions of the SCTS model. The SFA and the saddle-point approximation were used in Ref. [120] to implement the SCTS model. Furthermore,

QTMC   TDSE   SCTS
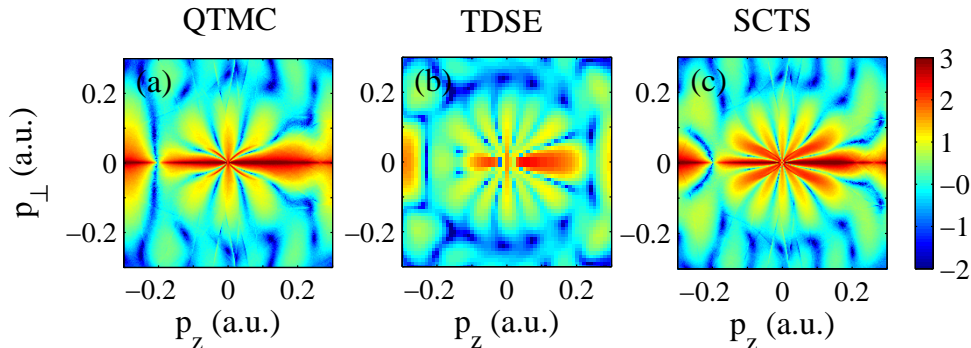
Fig. 3.2: Magnification of Fig. 3.1 for $|k_z|, |k_\perp| < 0.3$ a.u. Taken from Ref. [P1].

the inverse problem was solved in [120]. The resulting model shows an excellent agreement with the TDSE. Nevertheless, here we improve the SCTS model by combining it with the exact numerical solution of the TDSE.

3.2 Semiclassical two-step model with quantum input

The semiclassical two-step model with quantum input (SCTSQI) combines the SCTS model with the initial conditions for classical trajectories obtained from the numerical solution of the TDSE. The SCTSQI model was proposed and implemented in the one-dimensional (1D) case in Ref. [P9]. For the 1D model atom, the TDSE in the velocity gauge is given by:

$$i\frac{\partial}{\partial t}\Psi\left(x,t\right) = \left\{\frac{1}{2}\left(-i\frac{\partial}{\partial x} + A_x\left(t\right)\right)^2 + V\left(x\right)\right\}\Psi\left(x,t\right), \qquad (3.11)$$

where

$$V\left(x\right) = -\frac{1}{\sqrt{x^2 + a_0}} \qquad (3.12)$$

is the soft-core Coulomb potential with the soft-core parameter a_0.

It is clear that a unification of the direct solution of the TDSE with the trajectory-based approach is a highly non-trivial task. Indeed, in order to unambiguously determine the classical trajectory, we need to specify both the initial velocity and the starting point. It is known, however, that the Heisenberg's uncertainty principle imposes a fundamental limit to the precision with which position and momentum (as canonically conjugated variables) can be simultaneously known. A position-momentum quasiprobability distribution allows to extract information about both the position and momentum of a

quantum particle from a known wavefunction. The Wigner function and the Husimi distribution [121] (see, e.g., Ref. [122] for a textbook treatment) are the most well-known examples of the quasiprobability distributions. In Ref. [P9] we used the Gabor transform of the wave function $\Psi(x, t)$:

$$G(x_0, p_x, t) = \frac{1}{\sqrt{2\pi}} \int_{-\infty}^{\infty} \Psi(x', t) \exp\left[-\frac{(x' - x_0)^2}{2\delta_0^2}\right] \exp(-ip_x x') \, dx', \quad (3.13)$$

Here x_0 is the point near which the Gabor transform is calculated, p_x is the electron momentum, and δ_0 is the width of the Gaussian window. The square modulus of $G(x_0, p_x, t)$ corresponds to the momentum distribution of the electron in the vicinity of the point x_0 at time t. It should be noted that $|G(x_0, p_x, t)|^2$ is actually the Husimi distribution, which can be obtained by the Gaussian smoothing of the Wigner function.

In Ref. [P9] the Gabor transform (3.13) was combined with the absorbing boundaries used in the solution of the TDSE. The absorbing boundaries prevent unphysical reflections of the wave function from the boundary of the computational grid. More specifically, in the SCTSQI model the Gabor transformation is applied to the part of the wave function that is absorbed at every step of the time propagation of the TDSE. An example of the corresponding Husimi distribution is shown in Fig. 3.3. This absorbed part of the wave function is transformed into an ensemble of classical trajectories. The latter is then propagated using the Newton's equation of motion in both the laser field $F_x(t)$ and the soft-core potential:

$$\frac{d^2 x}{dt^2} = -F_x(t) - \frac{x}{(x^2 + a^2)^{3/2}}, \quad (3.14)$$

Therefore, in the SCTSQI model the initial conditions of the classical trajectories are determined by the exact quantum dynamics. Furthermore, every trajectory is assigned with the SCTS phase

$$\Phi(t_0, v_0) = -\int_{t_0}^{\infty} dt \left\{ \frac{v_x^2(t)}{2} - \frac{x^2}{(x^2 + a^2)^{3/2}} - \frac{1}{\sqrt{x^2 + a^2}} \right\} dt \quad (3.15)$$

and the quantum amplitude $G(x, p_x, t)$. It should be noted that the amplitude is a complex function that has both absolute value and phase. As in every semiclassical model describing quantum interference effects, the contributions of different trajectories reaching the same bin centered at k_x have to be added coherently. Therefore, the ionization probability in the SCTSQI
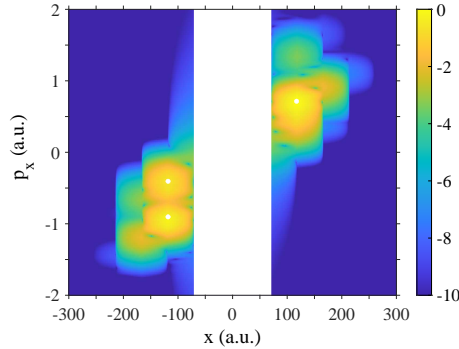
Fig. 3.3: The Husimi distribution $|G(x, p_x, t)|^2$ in the absorbing mask regions calculated for ionization of 1D model atom at the end of the laser pulse with a duration of 4 optical cycles, intensity of 2.0×10^{14} W/cm^2, and a wavelength of 800 nm. A logarithmic color scale is used. The three main maxima of the Husimi distribution are shown by white circles. Modified from Fig. 10 in [P10].

model reads as

$$R(k_x) = \left| \sum_{m=1}^{N_T} \sum_{j=1}^{n_{k_x}} G\left(t_0^m, x_0^j, p_{x,0}^j\right) \exp\left[i\Phi_0\left(t_0^m, x_0^j, p_{x,0}^j\right)\right] \right|^2. \tag{3.16}$$

Here N_T is the number of the time steps needed to solve the TDSE and n_{k_x} is the number of the trajectories leading to the same final momentum k_x. It is clear that convergence with respect to the number of trajectories launched at each time step and the positions of the absorbing boundaries should be carefully checked in the SCTSQI.

As noted above, the SCTS phase is divergent at $t \to \infty$. The regularization procedure for the 1D case slightly differs from the one used in the full 3D case (see Ref. [P9] for details). In the 1D case the corresponding post-pulse phase is given by:

$$\tilde{\tilde{\Phi}}_f^V = \int_{t_f}^{\infty} \left[\frac{x^2}{(x^2 + a^2)^{3/2}} - \frac{2Et^2}{(2Et^2 + a^2)^{3/2}} \right] dt. \tag{3.17}$$

This converging integral depends on the electron position $x(t_f)$ and velocity $p_x(t_f)$ at the end of the laser pulse and can be calculated numerically.

The SCTSQI model was compared with the SCTS model and the direct solution of the TDSE, see Fig. 3.4 and Ref. [P9]. It is seen that the SCTSQI model provides not only qualitative, but also quantitative agreement

with the exact quantum results. This applies for the width of the electron momentum distributions and the positions of the interference maxima and minima. There is, however, a small discrepancy in the heights of some interference maxima, see Fig. 3.4 (b). This discrepancy is attributed to the neglected preexponential factor of the semiclassical matrix element $U_{SC}(t_2, t_1)$, see Eq. (3.4). The agreement between the energy spectra obtained within the SCTSQI model and from the solution of the TDSE is almost perfect, see Fig. 3.4 (c). In contrast to this, and similarly to the 3D case, the SCTS model only qualitatively reproduces the TDSE spectrum. Again, the energy spectrum calculated within the SCTS model falls off too rapidly with increasing energy compared to the spectrum obtained from the TDSE.
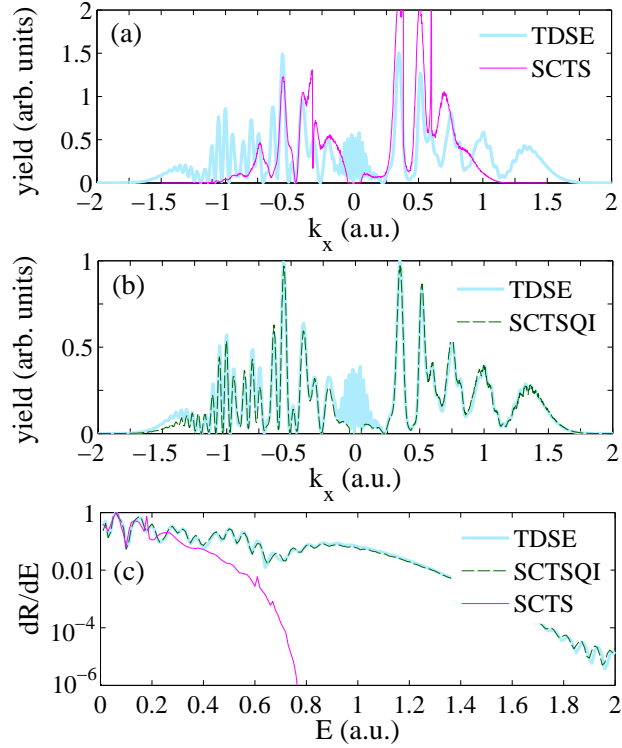
Fig. 3.4: Comparison of the semiclassical models with the TDSE for ionization of
a 1D model atom by the laser pulse with a duration of 4 cycles, intensity
of 2.0×10^{14} W/cm^2, and a wavelength of 800 nm. (a) The photoelectron
momentum distributions for ionization of a one-dimensional model atom
obtained from the SCTS model (thin magenta curve) and the solution
of the TDSE (thick light blue curve). The distributions are normalized
to the total ionization yield. (b) The electron momentum distributions
calculated using the present SCTSQI model (dashed dark green curve)
and the TDSE (thick light blue curve). The distributions are normalized
to the peak values. (c) Electron energy spectra obtained from the TDSE
(thick light blue curve), SCTSQI (dashed dark green curve), and the
SCTS (thin magenta curve). The spectra are normalized to the peak
values. Taken from Ref. [P9].

It was shown in Ref. [P9] that the phase of the Gabor transform $G(x, p_x, t)$
is very important in the SCTSQI model. Without this phase the SCTSQI
cannot provide even a qualitative agreement with quantum results. This
is easy to understand, if we take into account that the complex amplitude
$G(x, p_x, t)$ contains all the information about the quantum dynamics of the
absorbed part of the electron wave function before its transformation into

the ensemble of trajectories.

The SCSTQI model can be further developed to make it applicable to rescattering-induced phenomena: high-order ATI, HHG, and NSDI. As other semiclassical models, the SCTSQI model allows to obtain a valuable physical picture of the phenomena of interest using classical trajectories. What is even more important, the initial conditions of these trajectories are determined by the exact quantum mechanical calculations. Indeed, the SCTSQI model demonstrates a way to circumvent a non-trivial problem of choosing the initial conditions in trajectory-based models of strong-field processes. Therefore, it corrects the inaccuracies of the standard semiclassical models in description of ionization steps. Nevertheless, further work is needed to (i) extend the SCTSQI model to the 3D case, (ii) make it computationally more efficient, i.e., to decrease the number of trajectories launched at every time step by applying more sophisticated sampling techniques, and (iii) develop a way of efficient visualization of the strong-field processes with this model, see Ref. [P9].

3.3   Semiclassical two-step model for the H_2 molecule

It is clear that strong-field ionization of a molecule is much more involved than the same process for an atom. This is due to the necessity to account for the nuclear motion (extra degrees of freedom and the associated time scales) and complicated shape of the orbitals. Indeed, it should be noted that the nuclear motion period of the proton is about 10-15 fs. This is comparable to the characteristic pulse length. Simultaneously, the rich nuclear structure in molecules leads to orbitals of diverse symmetries. In principle, all these features can be taken into account by the direct numerical solution of the TDSE in three spatial dimensions. However, this is a very complicated task. The numerical solution of the 3D TDSE is possible only for the simplest molecules and with selection of the most important degrees of freedom [19, 20]. Therefore, approximate semianalytical models such as, e.g., the molecular strong-field approximation (MO-SFA) [123, 124] and the molecular Ammosov-Delone-Krainov (MO-ADK) theory [125] are very valuable for providing insight into ionization of molecules by strong laser fields. The same is also true for the semiclassical models. Presently there are only a few studies that apply trajectory-based models with interference to strong-field ionization of molecules [126, 127] and [P3]. In Refs. [126, 127] the QTMC model was extended to the molecular case. The study of Ref. [P3] applies the SCTS model to ionization of the hydrogen molecule.

The effective SAE potential for an outer electron in the H_2 molecule reads

as

$$V\left(\mathbf{r}\right) = -\frac{Z_1}{|\mathbf{r} - \mathbf{R}/2|} - \frac{Z_2}{|\mathbf{r} + \mathbf{R}/2|} \tag{3.18}$$

where $\mathbf{R}$ is the vector pointing from one nucleus to another, and Z_1 and Z_2 are the effective charges. These charges are chosen to be equal to 0.5. a.u. (see Refs. [126, 127]). The key question emerging in semiclassical simulations of ionization of a molecule is how to choose initial conditions for classical trajectories. There are two well-known approaches to this problem, namely the molecular quantum-trajectory Monte-Carlo model (MO-QTMC) [126, 127] and the partial Fourier transform for molecules (MO-PFT), see Refs. [127–129]. While the MO-QTMC approach is based on the MO-SFA, the MO-PFT model considers the wave function in mixed (coordinate-momentum) representation and uses the Wentzel-Kramers-Brillouin approximation. The work [P3] applies the MO-PFT approach.

The bound-state orbital of the H_2 molecule is given by the bonding superposition of the two 1s atomic orbitals located at the positions of the nuclei:

$$\Psi_{H_2}\left(\mathbf{r}\right) = \frac{1}{\sqrt{2\left(1 + S_{\mathrm{OI}}\right)}} \left[\psi_{\mathrm{atom}}\left(\mathbf{r} - \mathbf{R}/2\right) + \psi_{\mathrm{atom}}\left(\mathbf{r} + \mathbf{R}/2\right)\right], \tag{3.19}$$

where S_{OI} is the atomic overlap integral. The partial Fourier transform of the wave function (3.19) reads as:

$$
\begin{aligned}
\Pi_{H_2}\left(p_x, p_y, z\right) = \exp\Bigg(&-\frac{i}{2}R\sin\theta_m \left[p_x\cos\varphi_m\right. \\
+ \quad &\left. p_y\sin\varphi_m\right]\Bigg) \Pi_{\mathrm{atom}}\left(p_x, p_y, z - \frac{R}{2}\cos\theta_m\right) \\
+ \quad &\exp\Bigg(\frac{i}{2}R\sin\theta_m\left[p_x\cos\varphi_m\right. \\
+ \quad &\left. p_y\sin\varphi_m\right]\Bigg) \Pi_{\mathrm{atom}}\left(p_x, p_y, z + \frac{R}{2}\cos\theta_m\right).
\end{aligned}
\tag{3.20}
$$

see Ref. [126]. Here $\Pi_{\mathrm{atom}}\left(p_x, p_y, z\right)$ is the partial Fourier transform of the 1s orbital, and θ_m and φ_m are the polar and azimuthal angles of the molecular axis, respectively. By using the explicit formula for $\Pi_{atom}\left(p_x, p_y, z\right)$ derived in Ref. [128], the following mixed-representation wave function is obtained

in Ref. [P3]:

$$
\begin{aligned}
\Pi\left(p_x, p_y, z_e\right) & \\
\sim \Bigg\{ & \exp\left(-\frac{i}{2}R\sin\theta_m\left[p_x\cos\varphi_m + p_y\sin\varphi_m\right]\right) \times \exp\left(-\frac{1}{2}\kappa R\cos\theta_m\right) \\
+ \quad & \exp\left(\frac{i}{2}R\sin\theta_m\left[p_x\cos\varphi_m + p_y\sin\varphi_m\right]\right) \times \exp\left(-\frac{1}{2}\kappa R\cos\theta_m\right)\Bigg\} \\
\times & \exp\left[-\frac{\kappa^3}{3F} - \frac{\kappa\left(p_x^2 + p_y^2\right)}{2F}\right].
\end{aligned}
\tag{3.21}
$$

We note that this expression is valid just beyond the tunnel exit point. Similar to the study of Ref. [127], Eq. (3.21) is used as a complex ionization amplitude [P3]. This amplitude corresponds to ionization of an electron at time t_0 with initial transverse velocity $v_{0,\perp} = p_y$. The study of Ref. [P3] focuses on the simplest case where the molecule is oriented along the polarization direction: $\theta_m = \varphi_m = 0$. In this case the preexponential factor in brackets in Eq. (3.21) is a constant for the fixed internuclear distance and, therefore, it is sufficient to account for the exponent only [P3]. Both triangular and the FDM potential barriers were used in Ref. [P3] to find the tunnel exit point.

The SCTS phase for the H_2 molecule reads as:

$$
\begin{aligned}
\Phi_{H_2}^{SCTS}\left(t_0, \mathbf{v}_0\right) = & -\mathbf{v}_0 \cdot \mathbf{r}(t_0) + I_p t_0 \\
& -\int_{t_0}^{\infty} dt \left\{ \frac{p^2(t)}{2} - \frac{Z_1\left(\mathbf{r} - \mathbf{R}/2\right) \cdot \left(2\mathbf{r} - \mathbf{R}/2\right)}{\left|\mathbf{r} - \mathbf{R}/2\right|^3} \right. \\
& \left. - \frac{Z_2\left(\mathbf{r} + \mathbf{R}/2\right) \cdot \left(2\mathbf{r} + \mathbf{R}/2\right)}{\left|\mathbf{r} + \mathbf{R}/2\right|^3} \right\},
\end{aligned}
\tag{3.22}
$$

In order to arrive at Eq. (3.22) the potential (3.18) is to be substituted in the general expression for the SCTS phase (3.6). For $r_f \gg R$ the phase (3.22) coincides with the SCTS phase for the Coulomb potential $-Z/r$, where $Z = Z_1 + Z_2$. We note that the corresponding QTMC phase is given by:

$$
\begin{aligned}
\Phi_{H_2}^{QTMC}\left(t_0, \mathbf{v}_0\right) = & -\mathbf{v}_0 \cdot \mathbf{r}(t_0) + I_p t_0 \\
& -\int_{t_0}^{\infty} dt \left\{ \frac{p^2(t)}{2} - \frac{Z_1}{\left|\mathbf{r} - \mathbf{R}/2\right|} - \frac{Z_2}{\left|\mathbf{r} + \mathbf{R}/2\right|} \right\}.
\end{aligned}
\tag{3.23}
$$

Assuming that at the end of the laser pulse the ionized electron is far away from the molecule, the asymptotic momentum and the post-pulse phase can be found from Eqs. (1) and (3.10), respectively [P3].

The comparison of the predictions of the SCTS model for the H atom and the H_2 molecule was performed in Ref. [P3], see Figs. 3.5 (a)-(c). Figure 3.5 (a) shows the electron momentum distribution for H, whereas Figs. 3.5 (b) and (c) presents the same distributions for H_2. The triangular potential barrier was used to calculate the distributions of Figs. 3.5 (a) and (b). Nevertheless, the molecular potential (3.18) was fully taken into account in Newton's equation of motion (2.1) and in the phase when calculation the PMD shown in Fig. 3.5 (b), see Ref. [P3]. The distribution of Fig. 3.5 (c) was obtained using the FDM expression for the tunnel exit point. It is seen that the PMDs of Figs. 3.5 (a) and (b) are similar to each other. Therefore, it is found that the effects of the molecular structure are not visible in electron momentum distributions, if the molecular potential is not taken into account in the expression for the exit point [P3]. We note that this result can be expected. Indeed, $r_0 = I_p/F_0 \gg R/2$ for the parameters of Fig. 3.5. Moreover, the distance between the molecular ion and the ionized electron increases further when the electron starts its motion in the continuum. Therefore, if the expression (2.3) is used to calculate the tunnel exit point, the electron moves in the same Coulomb potential as in the case of the H atom.

The application of the FDM model leads to smaller exit points compared to the triangular barrier formula [P3]. As a result, the effects of the molecular potential become visible in Fig. 3.5 (c). It is seen that the PMD is more extended in the polarization direction compared to the atomic hydrogen case. For this reason, the electron energy spectra for H_2 fall off slower with increasing energy than the ones for the H atom, and the photoelectron angular distributions are more aligned along the laser polarization direction (see Ref. [P3] for details). The comparison of the PMDs calculated within the STCS and the QTMC models has show that, similar to the atomic case, the QTMC model predicts fewer nodal lines in the interference structure in the low-energy part of the distributions than the SCTS. This is again attributed to the underestimation of the potential in the phase of the QTMC model (3.8), see Ref. [P3].
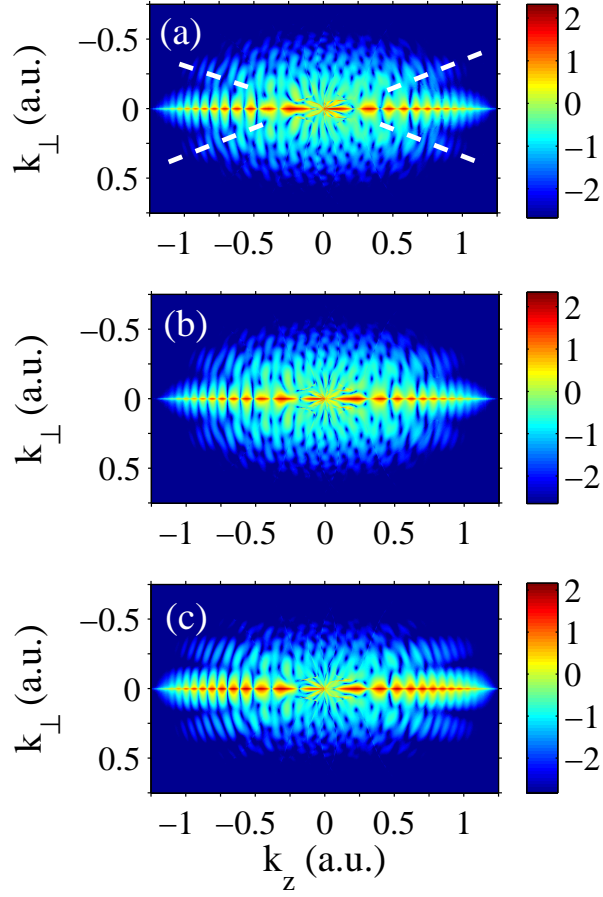
Fig. 3.5: The two-dimensional photoelectron momentum distributions for the H atom [panel (a)] and the H_2 molecule [panels (b) and (c)] ionized by a laser pulse with a sine square envelope, duration of $n = 8$ cycles, wavelength of $\lambda = 800$ nm, and intensity of 2.0×10^{14} W/cm^2. The panels (a) and (b) show the distributions calculated for the exit point given by Eq. (2.3). The panel (c) correspond to the exit point found in accord with the FDM [Eq. (2.2)]. The holographic fringes are indicated by white dashed lines in panel (a). The distributions are normalized to the total ionization yield. A logarithmic color scale in arbitrary units is used. The laser field is linearly polarized along the z axis. From Ref. [P3].

4. SEMICLASSICAL MODELS AND MULTIELECTRON EFFECTS

4.1 Multielectron polarization effects

The theoretical approaches used to analyze strong-field physics problems are usually based on the single-active electron approximation (SAE). The SAE treats the ionization as a one-electron process, i.e., an atom or molecule interacting with the laser field is replaced by a single electron that moves in the laser field and in an effective potential. This effective potential has to be optimized to reproduce the ground state and the excited states of a real atom (molecule). The SAE allows to understand many features of ATI, HHG, and other processes (see, Refs. [2, 114] and references therein). However, multielectron effects (ME) in strong-field phenomena have been attracting considerable attention recently, see, e.g., Refs. [130, 131]. There exist many theoretical methods capable of accounting for ME effects in strong-field physics. Among these are: time-dependent density functional theory [132] (see Refs. [133, 134] for a text-book treatment), multiconfiguration time-dependent Hartree-Fock theory [135, 136], time-dependent restricted-active-space and time-dependent complete-active-space self-consistent-field theories (see Refs. [137] and [138], respectively), time-dependent R-matrix theory [139, 140], the R-matrix method with time dependence [141, 142], time-dependent configuration interactions singles [143, 144], time-dependent restricted-active space configuration-interaction methods [145, 146], time-dependent analytical R-matrix theory [147], and various semiclassical approaches [P2], [44, 103, 130, 148, 149]. The advantages of the semiclassical models discussed in the Introduction are particularly important in studies of the ME effects.

Laser-induced polarization of the parent atomic or molecular ion is one of the most well-known and intensively studied ME effects [44, 103, 130, 148–150] and [P2]. In Refs. [151, 152] and [150] the effective potential for the outer electron was found within the adiabatic approximation. The potential

derived in Refs. [150–152] reads as

$$V\left(\mathbf{r}, t\right) = -\frac{Z}{r} - \frac{\alpha_I \mathbf{F}\left(t\right) \cdot \mathbf{r}}{r^3} \tag{4.1}$$

In Eq. (4.1) the ME effect is accounted through the induced dipole potential $\alpha_I \mathbf{F}\left(t\right) \cdot \mathbf{r}/r^3$, where α_I is the static polarizability of the ion. This potential takes into account the external laser field, the Coulomb potential, and the polarization of the ionic core. In the study of Ref. [103] it was for the first time shown that the time-independent Schrödinger equation with this effective potential and accounting for the Stark shift of the ionization potential can be approximately separated in the parabolic coordinates. This separation procedure leads to a certain tunneling geometry. The resulting physical picture is called tunnel ionization in parabolic coordinates with induced dipole and Stark shift (TIPIS). In the TIPIS model the tunnel exit point is calculated as $z_e \approx -\eta_e/2$, where η_e is the solution of the equation:

$$-\frac{\beta_2\left(F\right)}{2\eta} + \frac{m^2 - 1}{8\eta^2} - \frac{F\eta}{8} + \frac{\alpha_I F}{\eta^2} = -\frac{I_p\left(F\right)}{4}, \tag{4.2}$$

see Refs. [P2,P11]. It is possible to develop semiclassical models based on the TIPIS approach. These models disregarding the interference effects are in a good agreement with the TDSE results [P2], [103] and experimental data (see Refs. [103, 148, 149]).

    We note that the effective potential of Refs. [150–152] is applicable only at large and intermediate distances from the ionic core. For this reason, most of the studies applying this potential were done for circularly or elliptically polarized laser pulses. Indeed, the rescattering-induced processes are suppressed in close to circularly polarized fields, and, as a result, most of the electrons do not return to the vicinity of the parent ion. We note that strong-field processes in elliptically polarized pulses have been attracted particular interest for a number of reasons. First, evolution of the electron momentum distributions, electron energy and high-order harmonics spectra with increasing ellipticity provides additional information about the process under study. Second, the electron kinematics in an elliptically polarized laser pulse is essentially two-dimensional (2D), which is not the case for linearly polarized pulse. This 2D kinematics leads to features and properties that are absent with a linearly polarized field. Indeed, the first observation of the CEP effect was performed using the ATI by a circularly polarized laser pulse [153]. Other examples are the photoelectron angular distributions produced by an elliptically polarized field [22–28, 63, 154, 155], predominant emission when the laser field points along the major axis of the polarization ellipse

leading to the peaks in the PMD along the minor axis [154, 156, 157], and attosecond angular streaking [158, 159].

It was shown that the electron momentum distributions produced in ionization of various atoms and molecules (Ar, Mg, CO, naphthalene, etc.) by elliptically or circularly polarized pulses are very sensitive to the ME effects caused by the induced dipole moment of the ionic core, see Refs. [P2], [44, 103, 148, 149]. In particular, the study of Ref. [P2] focuses on the role of the multielectron effects in the formation of the PMDs. This role is revealed and investigated over a wide range of laser wavelengths and intensities for ionization of Mg. The choice of Mg is due to the following reasons. Along with the inapplicability of the potential (4.1) for small r, the range of applicability of the TIPIS model is also restricted by the two following conditions. On the one hand, the intensity of the laser pulse should not be too high, and the third term of Eq. (2.6) should not exceed 10-20 % of the first one. On the other hand, the Keldysh parameter $\gamma = \omega \sqrt{2I_p}/F$ has to be less or order of unity, and, thus, the laser pulse should be strong enough. Therefore, for each atomic species and fixed wavelength there exist a range of intensities, within which the TIPIS model is applicable. At the first glance, alkali metals seems to be ideal candidates for studies of the ME effects, since they have high values of α_N and low values of α_I. However, alkali metals have very low ionization potentials, and therefore they will be ionized before the laser intensity reaches its maximum. Elements such as Mg, Cu, Zn have relatively high ionization potentials and static polarizabilities. What is also important, the polarizabilities of these elements are substantially different from those of their ions. For Mg, $I_p = 0.28$ a.u., $\alpha_N = 71.33$ a.u., and $\alpha_I = 35.00$ a.u. Finally, multiphoton ionization of the Mg atom has been intensively studied both experimentally [160–164] and theoretically [165–169]. For the Mg atom ionized by a laser pulse with the a wavelength of 1600 nm, intensity of 5.0×10^{13} W/cm^2 and ellipticity of 0.78, the quadratic in F term in Eq. (2.6) is about 6% of the field-free ionization potential $I_p(0)$, and the Keldysh parameter is $\gamma = 0.7$. On the other hand, for the intensity of 2.35×10^{13} W/cm^2, the same wavelength and ellipticity, the third term is about 3% of the frst one in Eq. (2.6), and the Keldysh parameter $\gamma = 1.05$. Therefore, we did the semiclassical simulations for Mg within the intensity range $2.35 \times 10^{13} - 5.0 \times 10^{13}$ W/cm^2, see Ref. [P2].

The results of the simulations of Ref. [P2] are shown in Figs. 4.1 (a)-(i). Figure 4.1 presents the 2D PMDs at three different laser intensities obtained within the three different semiclassical models. The left column [panels (a), (d), and (g)] show the distributions obtained ignoring the ionic potential after tunneling, i.e., within the two-step model. These distributions are similar to those predicted by the SFA. The central column, i.e., the panels (b), (e),

and (h), present the same distributions, but accounting for the Coulomb potential. The right column shows the results of the full TIPIS model, within which an electron moves in the laser field and in the potential of Eq. (4.1). In all three cases the Stark shift is taken into account. It is seen that at low intensities the ME term does not affect the electron momentum distributions. However, with increasing intensity the offset angle, i.e., the angle between the maximum of the PMD and the minor axis of the polarization ellipse, decreases compared to the case where the ME term is neglected. This is clearly seen from the comparison of Figs. 4.1 (e) and 4.1 (f), as well as of Figs. 4.1 (h) and (i). The decrease of the offset angle is due to the fact that in the initial stage of the electron motion in the continuum the Coulomb and the ME forces act in opposite directions.

The decrease of the offset angle is further confirmed by the analytic estimates obtained in Ref. [P2]. These estimates allowed to understand better the underlying physics. As in Ref. [P4], the asymptotic momentum of an electron ionized at time t_0 can be written as:

$$\mathbf{P}\left(t_0, \mathbf{v}_0\right) = -\mathbf{A}\left(t_0\right) + \mathbf{v}_0 + \mathbf{P}_{\mathrm{C}}\left(t_0, \mathbf{v}_0\right) + \mathbf{P}_{\mathrm{ME}}\left(t_0, \mathbf{v}_0\right), \qquad (4.3)$$

Here $\mathbf{v}_0$ is the initial electron velocity, and $\mathbf{P}_{\mathrm{C}}$ and $\mathbf{P}_{\mathrm{ME}}$ are the contributions due to the Coulomb force and the ME force, respectively. By treating both the Coulomb and the ME potentials as perturbations, the contributions $\mathbf{P}_{\mathrm{C}}$ and $\mathbf{P}_{\mathrm{ME}}$ can be calculated by integrating the respective forces along the electron trajectory in the laser field only (see Sec. 2.2):

$$\mathbf{P}_{\mathrm{C}} = -\int_{t_0}^{\infty} dt \frac{\mathbf{r}_L\left(t\right)}{r_L^3\left(t\right)}, \qquad (4.4)$$

$$\mathbf{P}_{\mathrm{ME}} = \int_{t_0}^{\infty} dt \left(\frac{\alpha_I \mathbf{F}\left(t\right)}{r_L^3} - \frac{3\alpha_I \left[\mathbf{F}\left(t\right) \cdot \mathbf{r}_L\right] \mathbf{r}_L}{r_L^5} \right). \qquad (4.5)$$

Furthermore, both contributions can be estimated by calculating the integrals along the trajectory in the constant field $\mathbf{F} = \mathbf{F}\left(t_0\right)$, see Ref. [P2]. These estimates can be improved by considering the trajectory in the field $\mathbf{F}\left(t_0\right) \approx \mathbf{F}\left(t_0\right) + \mathbf{F}'\left(t_0\right)\left(t - t_0\right)$. In Ref. [P2] the improved estimates were obtained only for one single trajectory that corresponds to the maximum of the electric field. The latter is defined as follows:

$$\mathbf{F}\left(t\right) = \frac{F_0}{\sqrt{1 + \epsilon^2}} \sin^2\left(\frac{\pi t}{\tau_L}\right) \left[\cos\left(\omega t + \varphi\right) \mathbf{e}_x + \epsilon \sin\left(\omega t + \varphi\right) \mathbf{e}_y\right], \qquad (4.6)$$

where τ_L is the pulse duration, ϵ is the ellipticity, n_p is the number of cycles, and φ is related to the CEP. For the trajectory corresponding to the field
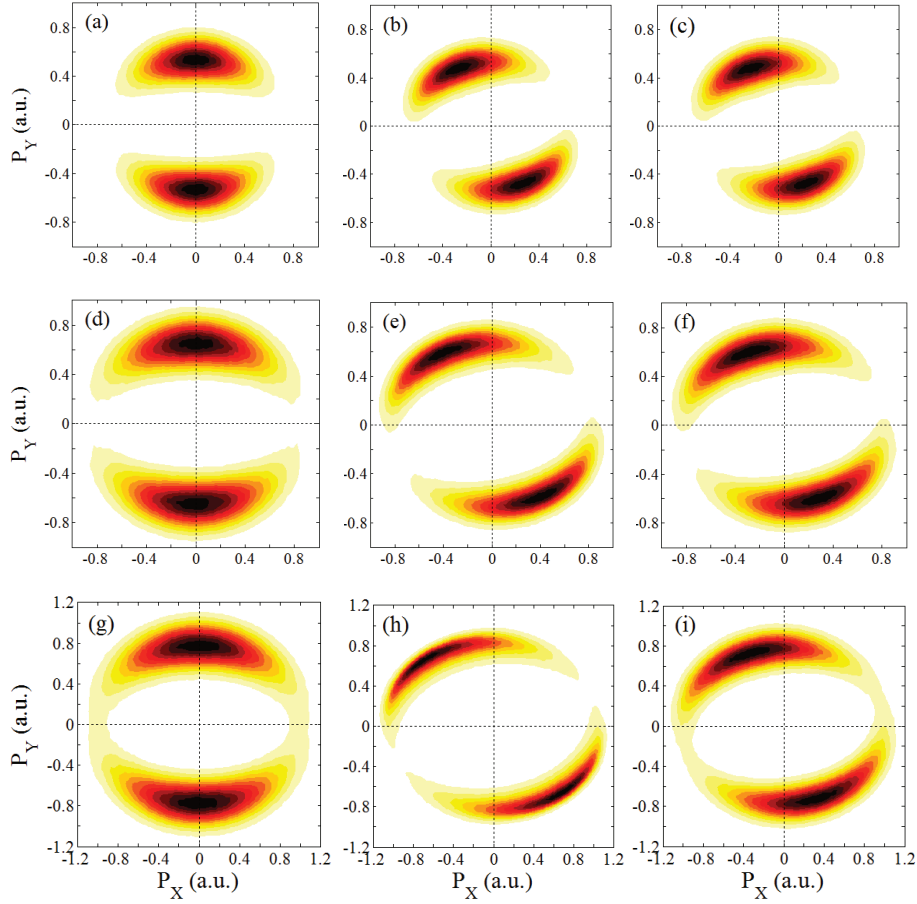
Fig. 4.1: Momentum distributions of the photoelectrons emitted from Mg at a wavelength of 1600 nm calculated within the three different versions of semiclassical approaches. The left column, i.e., the panels (a), (d), and (g), shows the distributions, calculated ingnoring the ionic potential after tunneling, when the tunneled electron moves in the laser field only. The middle column (panels (b), (e), and (h)) depicts the same distributions, but with consideration for the Coulomb field. The right column (panels (c), (f), and (i)) presents the results of the full TIPIS model, when both terms are taken into account in Eq. (4.1). The distributions (a)-(c), (d)-(f), and (g)-(i) correspond to the intensity of 2.35, 3.5, and 5.0×10^{13} W/cm^2, and to the Keldysh parameter of 1.05, 0.85, and 0.7, respectively. The same color scale is used for all the distributions. Taken from Ref. [P2].

maximum the Coulomb contribution $\mathbf{P}_C$ is given by

$$\mathbf{P}_C \left(t_0 = \tau_L/2, \mathbf{v}_{0,\perp} = 0 \right) = - \left(\frac{\pi}{4} \sqrt{\frac{2}{F r_0^3}} \mathbf{e}_x + \frac{\epsilon \omega}{6 F r_0} \mathbf{e}_y \right), \qquad (4.7)$$

whereas the total correction to the final momentum due to the ion potential $\mathbf{P}_I = \mathbf{P}_C + \mathbf{P}_{ME}$ reads as

$$\mathbf{P}_I\left(t_0 = \tau_L/2, \mathbf{v}_{0,\perp} = 0\right) = \frac{\pi}{4}\sqrt{\frac{2}{Fr_0^3}}\left(\frac{3\alpha_I F}{2r_0} - 1\right)\mathbf{e}_x - \frac{\epsilon\omega}{6Fr_0}\mathbf{e}_y. \qquad (4.8)$$

Here r_0 is absolute value of the tunnel exit point. It is seen that the x-components of the Coulomb and ME contributions have opposite signs. This explains the decrease of the offset angle. Furthermore, both $\mathbf{P}_C$ and $\mathbf{P}_{ME}$ increase with increasing intensity, but the ME contribution increases faster due to the presence of the additional factor of r_0 in the denominator. Although the estimates (4.7) and (4.8) do not quantitatively agree with the simulation results, they provide valuable insight into the properties and evolution of the PMDs (see Ref. [P2] for details). It was shown that the ME potential affects both the exit point and electron dynamics in the continuum. The calculations of Ref. [P2] were done for random CEP. Therefore, the obtained theoretical results can be relatively easily checked in an experiment.

4.2 Combination of the SCTS model and the TIPIS approach

The TIPIS approach was combined with the SCTS model in Ref. [P11]. The semiclassical approach developed in Ref. [P11] describes interference effects and accounts for the Stark shift, the Coulomb potential, and the polarization induced dipole potential [P11]. The phase used in this approach is determined by Eq. (3.6) with the potential given by Eq. (4.1):

$$\Phi^{SCTS}\left(t_0, \mathbf{v}_0\right) = -\mathbf{v}_0 \cdot \mathbf{r}\left(t_0\right) + I_p t_0$$
$$- \int_{t_0}^{\infty} dt \left\{\frac{\mathbf{p}^2(t)}{2} - \frac{2Z}{r} - \frac{3\alpha_I \mathbf{F}\left(t\right) \cdot \mathbf{r}}{r^3}\right\} . \qquad (4.9)$$

Furthermore, the study of Ref. [P11] analyses the applicability of the TIPIS model for linearly polarized fields. It is clear that application of the potential (4.1) at small distances should be avoided. To this end, a special cutoff radius r_C was introduced. Classical trajectories entering the sphere $r < r_C$ were not taken into account. The rest of trajectories do not come close to the parent ion. Therefore, the application of the potential (4.1) is justified for these trajectories. It is clear, that the elimination of the whole class of the returning trajectories will lead to the depletion of certain parts of the resulting electron momentum distributions [P11]. However, it was shown that for the parameters of interest these parts usually correspond to the boundary of the direct ionization spectrum. As a result, the depletion of the PMDs

caused by elimination of returning trajectories does not affect the main part of the momentum distributions (see Ref. [P11] for details).

The combined semiclassical model was applied to the cases of Mg and Ca atoms. These atoms have similar ionization potentials, but their static ionic polarizabilities are different by approximately of factor of two. Indeed, for the Ca atom, $I_p = 0.22$ a.u., $\alpha_N = 169.0$ a.u., and $\alpha_I = 74.11$ a.u. The resulting 2D electron momentum distributions are displayed in Figs. 4.2 (a)-(d). The distributions of Figs. 4.2 (a),(c) are calculated by taking into account the laser and the Coulomb fields only, whereas the PMDs of Figs. 4.2 (b) and (d) show the results of the combined TIPIS+SCTS approach, i.e., with the account of the ME potential. The panels [(a),(b)] and [(c),(d)] display the PMDs for ionization of Mg and Ca, respectively. It is seen that the presence of the ME term in the potential leads to the two following effects: (i) narrowing of the distributions in the longitudinal direction, and (ii) modification of the interference patterns. Both effects were analyzed in Ref. [P11].

The narrowing of the longitudinal momentum distribution is a kinematic effect [P11]. It was found that there are different groups of trajectories leading to a bin centered at some final momentum **k**. One of these groups of classical trajectories is strongly affected by induced polarization of atomic core. The trajectories of this group start their motion closer to the parent ion than other trajectories. Simultaneously, their initial transverse velocities are small. Since the ME force acting on the electron decreases as $1/r^2$ with increasing r, this force affects the electron motion only at the initial part of the trajectory. For the dominant trajectories the ME force effectively reduces both longitudinal and transverse electron momentum components. As a result, the electrons belonging to the discussed group lead to the bins with smaller value of k_z (see Ref. [P11] for details).

For Mg and Ca the interference effect caused by the presence of the polarization-induced dipole potential is not very strong. The interference structure changes only in the vicinity of the k_z axis and for the first and the second ATI peaks, see Figs. 4.2 (a)-(d). It was found that the modification of the interference patterns is mostly due to the presence of the ME term in the Newton's equation rather than due to the additional term $-3\alpha_I \mathbf{F} \cdot \mathbf{r}/r^3$ in the phase. Indeed, the contributions

$$-\int_{t_0}^{\infty} dt \frac{3\alpha_I \mathbf{F} \cdot \mathbf{r}(t)}{r^3(t)} \tag{4.10}$$

to the phase of trajectories leading to a given bin in the momentum space are often close to each other. Therefore, the difference between the ME contributions is small. However, a noticeable phase difference is an important precondition for observation of any interference effect. The similarity of the
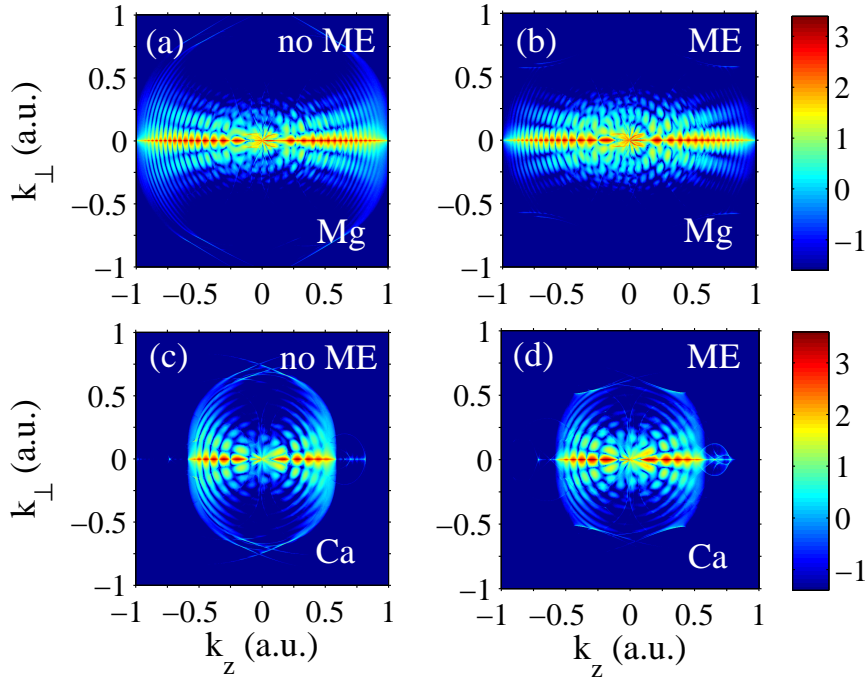
Fig. 4.2: The two-dimensional photoelecton momentum distributions for Mg [(a),
(b)] and Ca [(c), (d)] ionized by a laser pulse with a duration of $n = 8$
cycles at a wavelength of 1600 nm. Panels (a,b) and (c,d) correspond
to the intensities 3.0×10^{13} W/cm^2 and 1.0×10^{13} W/cm^2, respectively,
implying the Keldysh parameters 0.71 and 1.13. The left column [panels
(a) and (c)] show the distributions calculated ignoring the ME terms
in Eqs. (4.1), (4.2), and (4.9). The right column [panels (b) and (d)]
displays the distributions obtained with account of the ME terms in all
equations. The distributions are normalized to the total ionization yield.
A logarithmic color scale in arbitrary units is used. The laser field is
linearly polarized along the z axis. Modified from Ref. [P11].

ME contributions to the phase from different trajectories interfering in the
same bin can be understood as follows. The tunneling rate (2.7) is very sen-
sitive to the field strength $F(t_0)$. In order to have similar weights, which
is also necessary for the interference effect to be observable, the interfering
trajectories should start at times that correspond to close values of the field
strength. The starting point of the electron trajectory depends only on the
field $\mathbf{F}(t_0)$ and the parameters of the atom (molecule), and the main con-
tribution to the integral (4.10) is made by the initial part of the electron
trajectory.

However, the situation changes for atoms and molecules with high values

of the ionic polarizability α_I. In this case, the difference of the ME contributions to the phase is large enough, and modification of the interference structures caused by the ME effect can be highly pronounced, see Figs. 4.3 (a)-(d). It is seen that the number of radial nodal lines in the fanlike interference structure at low energies is different for the PMD's obtained with and without the ME term in the phase (3.6).
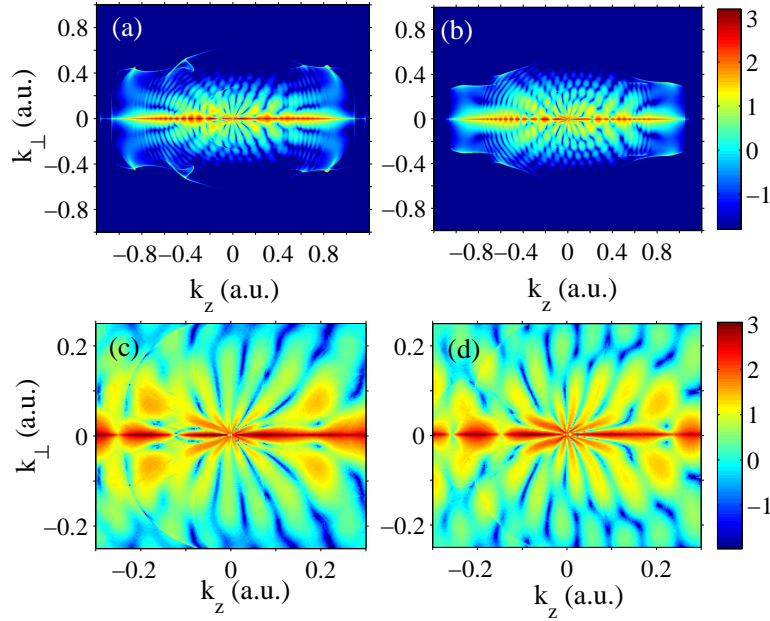
Fig. 4.3: Two-dimensional electron momentum distributions for the Ba atom ($\alpha_N = 273.9$ a.u., $\alpha_I = 124.15$ a.u.) ionized by a laser pulse with a duration of $n = 4$ cycles, wavelength of 1600 nm and an intensity of 3.0×10^{13} W/cm^2 calculated [(a),(c)] disregarding the ME term in the phase [Eq. (4.9)], and [(b),(d)] with the ME term. Panels (c) and (d) show the magnification for $|k_z| \leq 0.3$ a.u and $|k_\perp| \leq 0.25$ a.u. of the distributions shown in (a) and (b), respectively. For both distributions the ME force is included in the equations of motion. The distributions are normalized to the total ionization yield. A logarithmic color scale in arbitrary units is used. Modified from Ref. [P11].

4.3 Retrieval of single-active-electron potentials from photoelectron momentum distributions

As discussed above, the SAE approximation provides a reliable basis for studies of many strong-field phenomena. The semiclassical approaches discussed in this thesis are based on the SAE. Moreover, in the cases, where the multielectron effects are important, the SAE provides a necessary benchmark for the comparison with the results of multielectron approaches. However, the multielectron calculations are not always possible and, in such situations, the SAE is the only possible approach. It is therefore important to be able to obtain suitable SAE potentials for various atomic and molecular systems. However, the calculation of these potentials is a difficult task. This is true even in the atomic case. The SAE potential for a multielectron atom should account for both the atomic nuclei and, within some approximation, the effect of the other electrons. The well-known potential proposed by Tong and Lin [170], which is obtained on the basis of density functional theory, has a singularity at $r \to 0$. The same singularity is characteristic to the other widely used potential of Ref. [171], and the SAE potentials obtained by fitting to the effective Kohn-Sham potentials. This singularity often causes problems in numerical solution of the TDSE. The approach proposed by Troullier and Martins (see Ref. [172]) avoids this singularity by converting the SAE potential into a pseudopotential. The resulting pseudopotentials are applicable for the description of the direct electrons. However, the application of the pseudopotentials to the rescattered electrons can be problematic [173].

Often the SAE potentials are heuristically constructed as analytic functions depending on one or a few parameters. These parameters are adjusted using an optimization technique. The resulting potential is usually capable of reproducing the energy of one (if the potential is determined by only one parameter) or a few different bound states (for a potential determined by several parameters). Therefore, it appears natural to obtain the SAE potential as a result of some optimization process. This idea was exploited in Ref. [174]. It was shown that the atomic potential can be reconstructed from the differential electron scattering cross section by using a genetic algorithm. In turn, the differential cross sections are extracted from the PMDs of rescattered electrons. The potential experienced by the ionized electron directly affects the corresponding momentum distributions. Therefore, the unknown SAE potential can be retrieved in an optimization procedure aimed at reproducing a given PMD generated in strong-field ionization process. We have developed the corresponding optimization procedure, see Ref. [P12].

In Ref. [P12] this procedure was implemented in the case of a 1D model

atom, and the optimization method is based on the direct numerical solution of the TDSE. It is clear that application of any optimization-based approach requires specification of a measure that allows to identify whether the optimization target is achieved. The momentum distributions in the 1D case are functions of only one variable. The following metric is widely used to calculate the distance between continuous functions $f(x)$ and $g(x)$ that are defined for $x \in [a, b]$:

$$\rho\left[f\left(x\right), g\left(x\right)\right] = \left\{\int_a^b dx\left[f\left(x\right) - g\left(x\right)\right]^2\right\}^{1/2}. \qquad (4.11)$$

This metric was used in Ref. [P12] to measure the difference between two distributions: the result of the current iteration and the optimization target that is to be achieved. The derivatives of this similarity measure with respect to the potential parameters can be calculated only numerically. For this reason, derivative-free optimization techniques were used in [P12] (see Refs. [175, 176] for recent reviews of these techniques). It is shown that the proposed method demonstrates a high accuracy in the retrieval of the potential [P12]. This is true for different ways used to represent the SAE potential sought, including parameterization or specification of the potential by its values on a spatial grid, see, e.g., Fig. 4.4. In the latter case an effective way to improve the spatial resolution is found in Ref. [P12]: The optimization results on a sparse grid can be used as an initial approximation for further optimization on the dense grid.

The method of Ref. [P12] can be extended to the 3D case. It is clear that this extension will require a reliable measure for comparison of different PMDs, at least the 2D ones. Since the 2D electron momentum distribution is a picture (image), the tools used in image analysis and pattern recognition can be applied. The well-known examples of such measures are the mean squared error, structural similarity index (SSIM) [177], and perceptual hash functions (see, e.g., Ref. [178]). The technique of Ref. [P12] is based on optimization of only one part of the PMD created by the direct electrons. Simultaneously, our preliminary results show that the momentum distributions of the rescattered electrons can be used as more sensitive optimization targets. It is therefore of interest to develop a method based on the optimization of the PMDs for rescattered electrons. Finally, the experimental momentum distributions are affected by focal volume averaging. The developed optimization technique allows us to reconstruct not only the SAE potential, but also the actual laser intensity. Nevertheless, the question how sensitive is the proposed method to the focal averaging is to be investigated. Finally, the method of Ref. [P12] has not been applied to molecular potentials
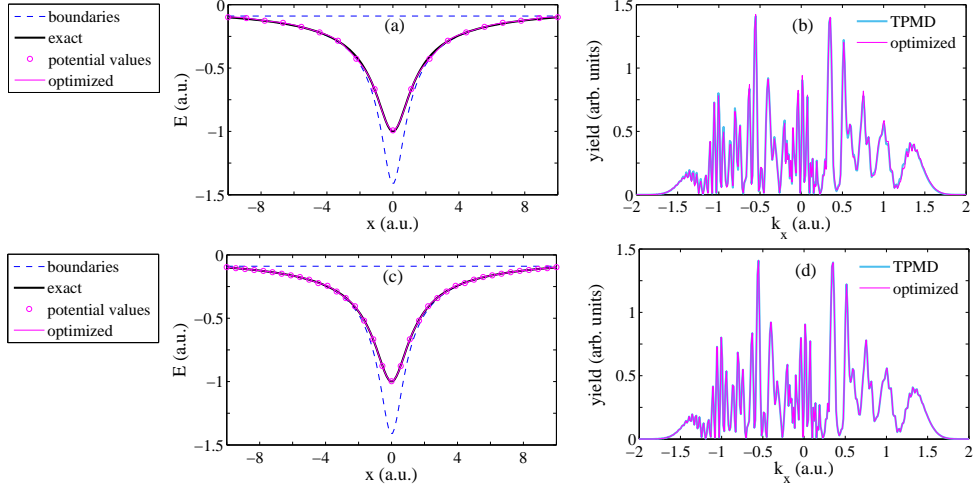
Fig. 4.4: (a),(c) The values of the SAE potential (magenta circles) reconstructed
by optimization of the electron momentum distribution, boundaries for
the allowed potential values (dashed blue curves), the potential obtained
by spline interpolation using the reconstructed values (thin magenta
curve), and the soft-core Coulomb potential (thick black curve). (b),(d)
The PMD calculated using the optimized potential (thin magenta curve)
and the target PMD (TPMD) that is to be reproduced (thick light-blue
curve). Panels (a) and (b) show the optimization results for the potential
determined by its values on a uniform grid consisting of 10 points between
0 and 10.0 a.u. Panels (c) and (d) display the optimization results for the
same grid consisting of 20 points. The PMDs correspond to ionization of
a 1D atom by a laser pulse with a duration of $n_p = 4$ cycles, wavelength
of 800 nm, phase $\varphi = 0$, and intensity of 2.0×10^{14} W/cm^2. Taken from
Ref. [P12].

yet. Further studies are needed to address the questions listed here. Never-
theless, the obtained results suggest that the optimization-based method for
reconstruction of the SAE potential has prospects of becoming a powerful
tool for studies of strong-field processes.

5. QUANTUM OPTIMAL CONTROL AND SEMICLASSICAL SIMULATIONS

5.1 Optimal control of high-harmonic generation

Monitoring and control of electron dynamics on its natural time scale would ideally be based on pulses with duration of only a few dozen attoseconds (see, e.g., Ref. [179]). However, generation of such pulses is a non-trivial task. Indeed, ultrashort pulses can be produced by using large and expensive free-electron laser facilities or with table-top intense optical lasers. In the latter case ultrashort pulses are produced due to the HHG process. However, the pulses obtained in HHG are often too long and weak.

Similar to the electron energy spectrum of high-order ATI, the spectrum of high-order harmonics has a range of a nearly constant yield (harmonic plateau) that ends at a certain cutoff. Attosecond pulses are created from superposition of high harmonics. Therefore, the low yield of high-order harmonics results in the low amplitude of the attosecond pulses. Furthermore, the duration of the ultrashort pulses is determined by the plateau cutoff: the higher the cutoff energy, the shorter the pulse. Therefore, it is important to increase the harmonic yield and extend the plateau in the HHG spectrum. Recently both problems have attracted considerable attention. The cutoff extension can be achieved by using two-color laser fields [180, 181], chirped pulses [182–184], steepening of the carrier wave [185], a sawtooth pulse [186], or combined temporal and spatial synthesis of the driving pulse [187]. The harmonic yield can be increased in two-color fields [188–193] or by HHG in a mixture of two target cases. The goal of a simultaneous enhancement of both the harmonic yield and the cutoff energy can be achieved by temporal shaping of the initial driving pulse. The temporal shaping of strong laser pulses is experimentally feasible nowadays [194, 195]. The required shape of the driving pulse can be obtained using quantum optimal control theory (QOCT). QOCT [196, 197] is the theoretical approach to the control of various quantum phenomena (see Refs. [198] and [199] for reviews).

In the early work of Ref. [200], QOCT was applied to the problem at hand and a cutoff extension was achieved. However, the yield of the high-order

harmonics in the optimized pulse remained relatively low. The application of QOCT requires the specification of the target functional that is to be maximized. The ground-state occupation at the end of the laser pulse was maximized in Ref. [200]. In contrast to this, in Ref. [P13] we used the following target functional:

$$J_1\left[\epsilon\right] = \int_{\omega_a}^{\omega_b} \left|\ddot{d}\left[F\right]\left(\omega\right)\right|^2 d\omega. \tag{5.1}$$

Here $[\omega_a, \omega_b]$ is the frequency range within which the enhancement of the HHG spectrum is desired, $F\left(t\right)$ is the laser pulse, and $\ddot{d}\left[F\right]\left(\omega\right)$ is the Fourier transform of the dipole acceleration. We define the harmonic spectrum as $S\left(\omega\right) = \left|\ddot{d}\left(\omega\right)\right|^2 / \omega^2$ (see Ref. [201]). The study of Ref. [P13] focuses on the 1D model atom with the soft-core potential $V\left(x\right) = -1/\sqrt{x^2 + 1}$. The laser field $F\left(t\right)$ that is to be optimized is represented by a number of parameters. Therefore, maximization of the functional (5.1) can be viewed as an optimization of these parameters under some constraints. These constraints include (i) discrete number of frequencies contained in the laser pulse and a maximum allowed frequency, (ii) a fixed length of the pulse, and (iii) a fixed pulse fluence (integrated intensity). The latter was taken to be equal to that of the reference single-frequency pulse. A gradient-free algorithm (NEWUOA, see Ref. [202]) and the gradient based Broyden-Fletcher-Goldfarb-Shannon (BFGS) algorithm [203] were used for the optimization. Both algorithms lead to similar results. The optimization involves the direct numerical solution of the 1D TDSE.

The optimization goals have been fully achieved, see Figs. 5.1 and 5.2. The optimized pulse provides a remarkable cutoff extension and enhancement of the harmonic yield (see Ref. [P13] for details). It is shown that the physical mechanisms underlying the cutoff extension and the yield enhancement are essentially different. The yield enhancement was shown to have a quantum origin. Specifically, it was attributed to the increased tunneling probability in the optimized pulses compared to the reference pulses [P13].

In contrast to the yield enhancement, the semiclassical simulations allowed us to reveal that the extension of the plateau has a classical origin. More specifically, 1D semiclassical simulations were performed in Ref. [P13]. The ionization times of trajectories were distributed either uniformly, or in accord with the tunneling rate $w\left(t_0\right) \sim \exp(-[2\left(2I_p\right)^{3/2}]/[3\left|F\left(t_0\right)\right|])$ with the ionization potential $I_p = 0.669$ a.u. The tunnel exit was found using the FMD model, i.e., from the equation $V\left(x\right) + F_x\left(t\right)x = -I_p$ and the initial velocity was set to zero. It as assumed that a photon is emitted upon the return of the electron to the origin. The frequency of this photon is equal to

the electron energy at the time of return. The late returns were also taken into account. It should be emphasized that the electron motion in both the laser field and the effective 1D potential was considered in Ref. [P13]. The three-step model, which neglects the atomic potential, underestimates the cutoff of the HHG plateau severely, see Ref. [P13] for details. The predictions of the semiclassical model are in a good agreement with the quantum results, see Fig. 5.1 (c) and Fig 5.2 (c), which is the decisive argument in favor of the classical origin of the cutoff extension.

The optimized pulse produced by using the BFGS-algorithm allows multiple returns of the electron, see Fig. 5.2 (c). The corresponding classical energies were obtained for the case where the ionization times are distributed in accord to the tunneling rate. This rate underestimates some ionization events. As a result, not all the maxima of the spectrotemporal plot can be reproduced by the semiclassical model, see Fig. 5.2 (c). The effect of the multiple returns was also analyzed by using the semiclassical model [P13]. It is shown that for longer pulses the second return of the electron is important for the enhancement of the HHG process. The optimization scheme developed in Ref. [P13] is straightforwardly applicable to more realistic models.

5.2 Suppression of strong-field ionization

The ability to control the electron dynamics in real time provided by the strong-field, ultrafast, and attosecond physics implies plenty of possible applications, and, especially, in femtochemistry. Femtochemistry is the area of physical chemistry that studies chemical reactions on the femtosecond or, in some cases, the attosecond time scale (see, e.g., Ref. [204]). The laser control of chemical dynamics is an important problem in femtochemistry. Among the applications of such control are photoassociation [205], control of branching ratios in photofragmentation processes [206–208], enhancement of molecular bond breaking in the electronic ground state [209, 210], and possible creation of molecules that cannot be created without the action of the laser source. It is conventional to distinguish between weak-field and strong-field laser control. The latter one is often more efficient. For example, the branching ratios in photofragmentation of CH_2BrCl can be more efficiently controlled (compared to the case of relatively weak laser fields) using intensities higher than 10^{13} W/cm^2, see Refs. [208, 211, 212]. However, the strong-field control is often accompanied by undesired ionization. Indeed, it was experimentally shown in Ref. [211] that the fragments of the molecule emerging in the photofragmentation process are ionized by the strong laser pulse. The same problem occurs in the control of electron localization in
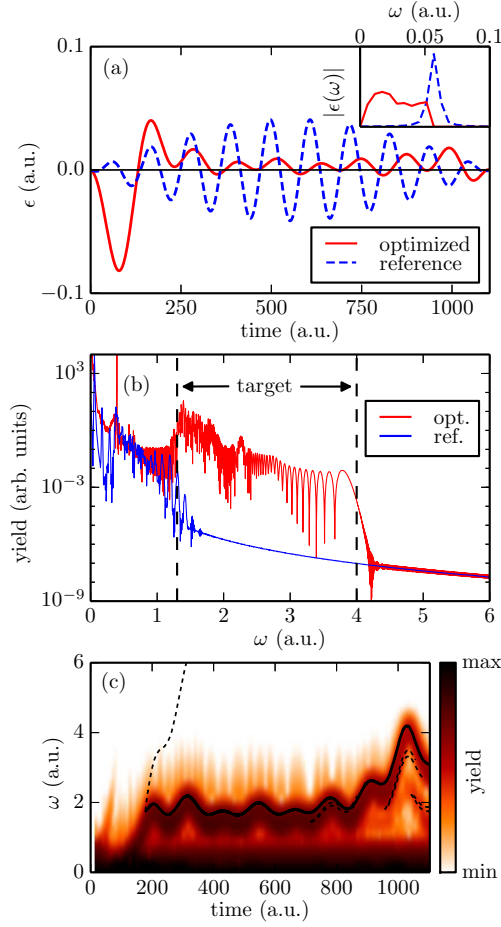
Fig. 5.1: Optimization results with the NEWUOA algorithm for pulse length $T = 1104$ a.u. (26.7 fs) and reference pulse peak intensity of 6×10^{13} W/cm^2. The maximum frequency of the optimal pulse is $\omega_{\mathrm{max}} = 0.0569$ a.u. (800 nm). (a) Pulses and their frequencies (inset) for optimized (solid black) and reference (dashed blue) pulses. (b) High-harmonic spectra for optimized (black) and reference (blue) pulses. The target range is shown with vertical dashed lines. (c) Quantum mechanical time-dependent harmonic spectrum in log-scale (the color image) and classical return energies using an exponential tunneling rate (solid line). Spurious branches from a uniform tunneling rate are shown with dashed lines. Modified from [P13].

molecular dissociation [213]. Therefore, for applications in femtochemistry it is necessary to develop a tool capable to suppress the undesired ionization process. In order to control ionization, laser pulses of specific shape can be used. The optimal shape of the laser pulse can be obtained using QOCT.
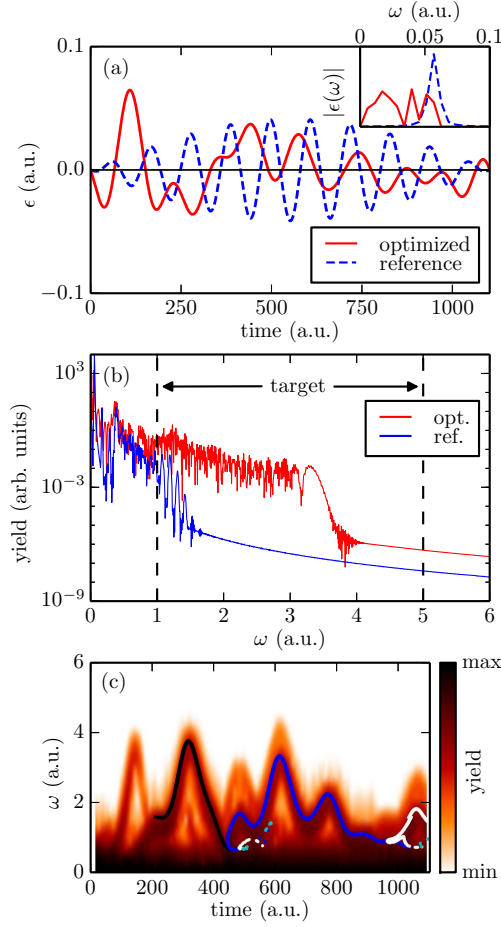
Fig. 5.2: Same as Fig. 5.1 but for an extended target range (up to $\omega = 5$ a.u.) and
for the gradient-based BFGS optimization algorithm. In (c), energies of
an electron calculated from the semiclassical model upon its first, second,
third, and fourth return to the origin are shown with black, blue, white,
and cyan curves, respectively. Modified from Ref. [P13].

In Ref. [200] the QOCT was applied to suppress ionization of a 1D model
H atom. The inverse problem, i.e., enhancement of ionization using QOCT
was considered in Ref. [214] for the H_2^+ molecular ion with fixed internuclear
distance in the 3D case.

The ability to suppress strong-field ionization of the hydrogen atom and
the H_2^+ molecule by optimal pulse shaping was investigated in Ref. [P14].
The first term of the functional minimized in QOCT, i.e., the optimization
target, is given by:

$$J_1 = \left\langle \Psi\left(T\right) \left| \hat{O} \right| \Psi\left(T\right) \right\rangle = \left| \left\langle \Psi\left(T\right) \left| \Psi_0 \right\rangle \right|^2 , \right. \tag{5.2}$$

where Ψ_0 is the ground state, $\hat{O}$ is the target operator (projection onto the ground state), $\Psi(t)$ is the time-dependent wave function, and the laser pulse terminates at $t = T$, see Ref. [P14]. It should be noted that different parametrizations and different QOCT algorithms have to be used for high and low laser frequencies, i.e., ultraviolet and infrared laser fields (see Ref. [P14] for details). Both these cases were considered in Ref. [P14] for the H atom, whereas the ionization suppression in the H_2^+ molecule was studied only in the low-frequency regime and in the fixed-nuclei approximation due to the computational complexity of the problem [P14]. Considerable suppression of the ionization yield for both H and H_2^+ can be achieved for fixed fluence and length of the laser pulse [P14]. However, the mechanisms responsible for ionization suppression are substantially different for ultraviolet and infrared pulses. It is shown that in the high-frequency regime the ionization can be suppressed by using a resonance population transfer between the ground $(1s)$ state and excited states $(2p$ and $3p)$, see Fig. 5.3. This mechanism cannot be reproduced by a semiclassical model.

Fig. 5.3: (a) Initial laser pulse with $F_0 = 0.15$ a.u. and $\omega = 0.4$ a.u. (dashed blue curve) and the optimized pulse (full red curve) with a fixed fluence equal to 1.16 a.u. (b) Fourier spectra of the pulses. (c) The occupations of some of the bound states during the optimized pulse. (d) The total bound-state occupation and the population in the continuum during the optimized pulse. From Ref. [P14].

The situation is different in the low-frequency case. The corresponding QOCT results are shown in Figs. 5.4 (a)-(d). In order to decrease the strong yield keeping the fluence constant, the optimized pulse suppresses the highest peaks of the laser field, see Fig. 5.4 (a). This can be understood even without trajectory-based simulations. Indeed, the tunneling rate is proportional to $\exp\left(-2\kappa^3/3F\right)$ with $F = F\left(t_0\right)$, where t_0 is the time of ionization. It is clear that a lower amplitude of the laser field results in a smaller ionization yield in an exponentially sensitive manner [P14]. Therefore, QOCT leads to an overall flatter profile of the laser pulse. Since the pulse fluence is fixed, the peaks at the beginning and at the end of the laser pulse become larger [Fig. 5.4 (a)], and Fourier spectrum of the pulse shifts towards lower frequencies, see Fig. 5.4 (b). The remarkable technological progress that has been achieved in generation of strong few-cycle pulses with a predefined shape allows us to hope that the experimental realization of the results obtained in Ref. [P14] will become possible.
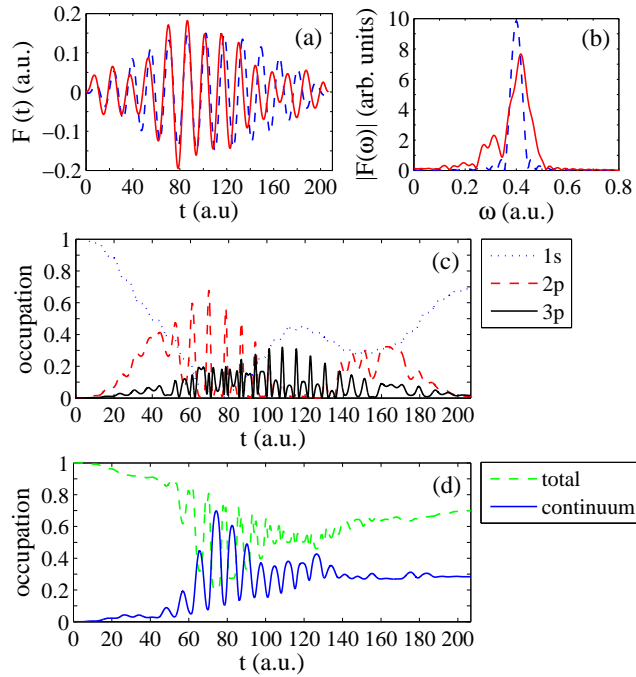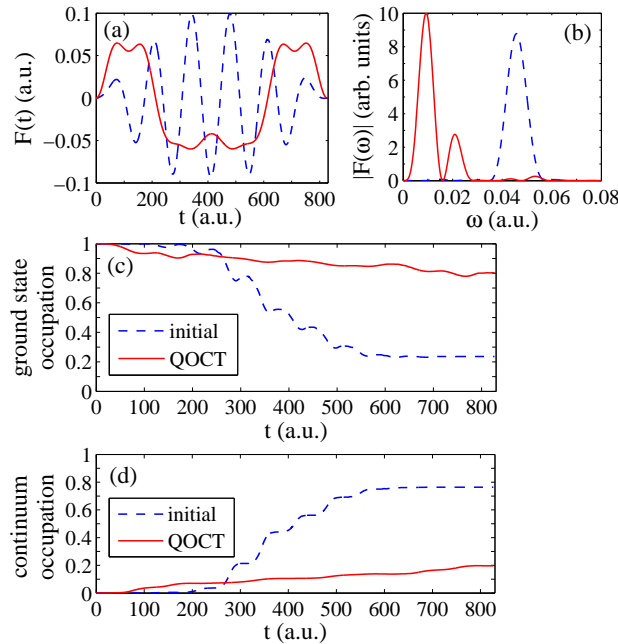

Fig. 5.4: (a) Initial laser pulse with $F_0 = 0.1$ a.u. and $\omega = 0.0459$ a.u. (dashed blue curve) and the optimized pulse (full red curve). The pulse fluence is fixed to 2.07 a.u. (b) Fourier spectra of the pulses. (c) Time-dependence of the ground state occupation in an H atom for the initial pulse (dashed blue curve) and the same dependence for the optimized one (full red curve). (d) Continuum occupation during the initial (dashed blue curve) and the optimized (full red curve) laser pulses. Taken from Ref. [P14].

6. STRONG-FIELD HOLOGRAPHY WITH PHOTOELECTRONS

6.1 Time-resolved molecular imaging

The ability to visualize electronic and molecular dynamics in real time will lead to a revolution in chemistry, biology, and material science. Many techniques for time-resolved molecular imaging have been developed so far, see Ref. [215] for a review. These techniques employ the remarkable achievements in laser technologies and, especially, the emergence of free-electron lasers and development of the technology for pulse compression. The availability of table-top intense femtosecond laser systems operating at various wavelengths has opened new perspectives for time-resolved molecular imaging. Several new time-resolved imaging techniques based on strong-field processes have recently emerged. The well-known examples of these techniques are laser-induced Coulomb explosion imaging [216–219], laser-assisted electron diffraction [220, 221], high-order harmonic orbital tomography [222, 223], laser-induced electron diffraction (LIED) [224–226], and strong-field holography with photoelectrons [227].

The strong-field holography with photoelectrons (SFPH) puts the idea of holography [228] into practice in strong-field physics. It was for the first time shown by Y. Huismans and co-authors [227] that a holographic pattern in electron momentum distributions can be clearly observed in experiment. This hologram is created by the interference of the direct (reference) electrons with the rescattered (signal) ones. It was found that the SFPH method has several important advantages. First, this technique can be implemented using a table-top laser system. Second, the recorded hologram contains a wealth of spatio-temporal information not only about the electrons, but also about the parent ions. Finally, attosecond time resolution is accessible for the imaging of the electron dynamics. For these reasons, the SFPH has been extensively studied recently. This applies both to theory [56–60, 227, 229–236] and experiment (see Refs. [229, 230, 237, 238] and [P15]).

However, most of the SFPH experiments [227, 229–231, 237] have provided valuable insights into the ionization process and the electron wave

packet dynamics, but not the molecular structure or dynamics. The reason for this is that for diatomic and small molecules the holographic structures are mostly governed by the long-range and alignment-independent Coulomb potential of the ion. Therefore, the short-range effects that reflect the molecular structure are not visible in the holographic patterns on the background of the order-of-magnitude stronger contribution. A simple and elegant solution of this problem was found in the experimental study of Ref. [238]. The approach of Ref. [238] uses the fact that for large scattering angles the differential cross section deviates from that of the Coulomb potential and depends on the molecular alignment. Therefore, the alignment independent interference can be removed by calculating the difference between the normalized PMDs for aligned and antialigned molecules. A similar method was also used in the experiment [P15].

Different theoretical approaches were applied in the studies of SFPH. Among these are: the three-step model, the modified SFA capable to describe rescattering process [227, 231], the CCSFA [227, 231], direct numerical solution of the TDSE [232], the CQSFA [56–60], etc. (see Ref. [239] for a recent review). The SCTS model was also applied to SFPH, see Refs. [P15, P16].

6.2   Experimental holographic patterns and the SCTS model

In Ref. [P15] the SCTS model was used to simulate the experimental holographic patterns emerging in ionization of the NO molecule. Since the experiment [P15] applies the same approach to the long-range Coloumb potential problem as Ref. [238], the corresponding PMDs were calculated for two different cases, where the electron density of the highest occupied molecular orbital (HOMO) is aligned in two different perpendicular directions. We note that for application of the SCTS to both these cases the corresponding distributions over the initial transverse velocities are necessary. These distributions were calculated using the MO-PFT approach. In turn, the MO-PFT requires the corresponding HOMO's. The latter were calculated using the GAMESS package [240].

The distributions calculated using the SCTS model and their normalized difference are shown in Figs. 6.1 (a)-(c). The semiclassical results are in excellent agreement with the experimental data. The simulations within the SCTS model allow us to reproduce all characteristic properties of the holographic patterns, see Fig. 6.1 (c). Simultaneously, the calculations based on the three-step model neglecting the Coulomb potential (see Ref. [232]) overestimate the spacing between the interference maxima (minima) in the

direction perpendicular to the laser polarization. Therefore, the improved agreement between the experiment and trajectory-based modelling originates from the account of the Coulomb potential in the SCTS model.
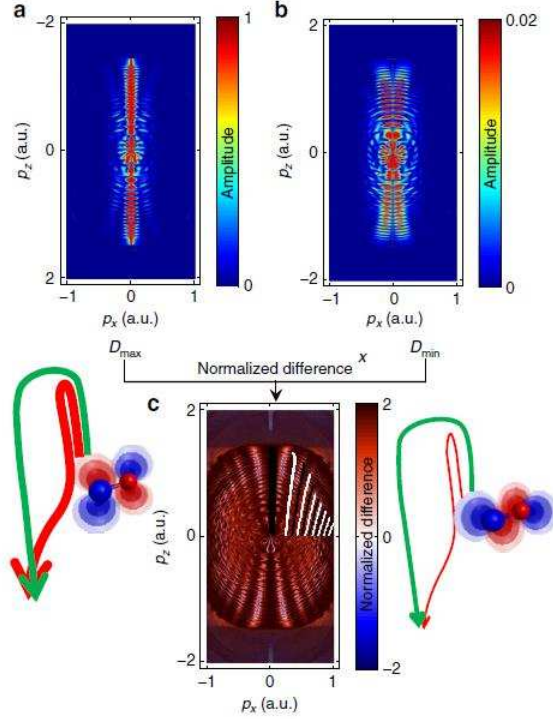

Fig. 6.1: Calculated momentum distribution for ionization of the NO molecule by a laser pulse with a duration of 35 fs, wavelength of 800 nm, and intensity of 2.3×10^{14} W/cm^2. The panels (a) and (b) show the distributions calculated for the cases where the electron density of the HOMO is aligned in two different perpendicular directions. Panel (c) displays the normalized difference of the momentum distributions shown in (a) and (b). Taken from Ref. [P15].

6.3   Effects of the Coulomb potential

Several different types of holographic structures were predicted within the three-step model [232]. Indeed, the signal and reference electrons can be ionized not only in the same quarter cycle of the laser field, but also in different quarter cycles. The simulations of SFPH in the three-step model are usually performed under the assumption that the starting points of the electron trajectories do not depend on the instantaneous value of the laser field. Rather, the starting points are determined by the field amplitude [107, 232–234] and the sub-cycle variation is neglected. In contrast to this,

in Ref. [P16] we obtained the holographic patterns of various types assuming that the tunnel exit point depends on time. It is found that the interference structures change significantly when the time dependence of the exit point is taken into account. This is due to the substantial change in kinematics of the signal electron.

For every kind of the holographic structure predicted by the three-step model we calculated its counterpart emerging in the presence of the Coulomb potential of the parent ion. To this end, we used an adapted version of the SCTS model. Specifically, we used the tunnel exit point (2.3), in order to directly compare the resulting holographic patterns with the ones predicted by the three-step model. Moreover, we disregarded the weights of classical trajectories and distributed them uniformly. Therefore, the study of Ref. [P16] focuses on the shape and location of interference fringes, i.e., on holographic patterns instead of the full momentum distributions. For every bin in the momentum space only one kind of direct and only one kind of rescattered trajectories were considered. This is necessary to prevent a mixture of different types of holographic interferences. The isolation of the single direct and rescattered contributions is not a simple task if both the laser field and the Coulomb force are taken into account in equations of motion. Indeed, it is not obvious how to distinguish between the direct and rescattered electrons in the presence of the Coulomb potential. It is clear that all the trajectories are to some extent affected by the Coulomb force. The study of Ref. [P16] defines the direct trajectories as those that pass the ion at large distances. These trajectories experience only small-angle scattering and obey the condition $v_{0,\perp} k_y \geq 0$. In contrast to this, the rescattered trajectories pass the parent ion at small distances. They undergo large-angle scattering. Therefore, the condition $v_{0,\perp} k_y \leq 0$ is met for the rescattered trajectories. However, these conditions are not sufficient for accurate calculation of the holographic patterns.

In the presence of the Coulomb potential the mapping from the initial condition plane $(t_0, v_{0,\perp})$ to the final momentum components plane (k_x, k_y) is a complicated function. Specifically, this mapping is not bijective (one-to-one) in the domain defined by the condition $v_{0,\perp} k_y \leq 0$ that correspond to signal trajectories. As a result, different sets of initial condition lead to the same final momentum. The necessary separation of the corresponding trajectories can be achieved by using machine learning, namely, by applying the clusterization algorithms. However, in Ref. [P16] the trajectories were separated manually by identifying the domains of initial conditions where the mapping $(t_0, v_{0,\perp}) \rightarrow (k_x, k_y)$ is bijective.

We have found that the presence of the Coulomb potential modifies the holographic patterns significantly. In addition to changing the width and the

positions of the interference stripes, the Coulomb potential manifests itself in three other effects. The first effect is the shift of the interference pattern as a whole. The second effect is the filling of the parts of the holographic structure that are unfilled when the Coulomb potential is not taken into account. Finally, the Coulomb potential is responsible for the characteristic kink of the interference stripes at zero transverse momentum, see Figs. 6.2 (a) and (b). However, it should be studied how sensitive are these Coulomb effects to focal averaging. This study is needed to understand which of the predicted effects can be observed in an experiment.
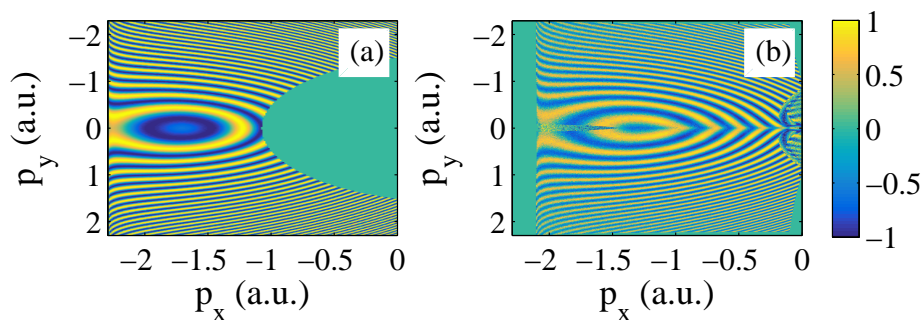

Fig. 6.2: Holographic patterns emerging due to interference of a direct electron with a rescattered electron that has the shortest travel time (see Ref. [P16]) calculated (a) using the three-step model with time-dependent exit point, and (b) accounting for the Coulomb potential of the ion. The interference patterns are calculated for ionization of the H atom at a wavelength of 800 nm and intensity of 6.0×10^{14} W/cm^2. Taken from [P5].

6.4 Deep learning and retrieval of the internuclear distance in a molecule

The new and promising methods for time-resolved molecular imaging, namely, LIED and SFPH analyze electron momentum distributions produced in ionization by a strong laser field. The remarkable experimental achievements of these methods suggest that in the nearest future we can expect new experiments aimed at extracting the information about the motion of the nuclei and many-electron dynamics from the PMDs. The understanding of the existing and forthcoming experiments requires theoretical analysis of the effect of the nuclear motion in the electron momentum distributions. The work in this direction has already begun. For example, it was shown that the different dynamics of the nuclear wave packets in hydrogen and deuterium leads to a

difference in bond length [238]. In turn, this difference transforms into a shift of the holographic fringes that can be observed at certain electron momenta.

Before studying the effects of the nuclear motion on the momentum distributions, it is useful to consider changes of the PMDs calculated for fixed nuclei positions with varying internuclear distance. This problem was addressed in Ref. [P17] by using methods of machine learning (see, e.g., Refs. [241–243] for a textbook treatment). We note that machine learning and, more precisely, deep learning has been successfully applied to many sophisticated problems of strong-field, ultrafast, and attosecond physics. Among these are: prediction of the ground-state energy for various 2D potentials [244], prediction of the flux of high-order harmonics for different experimental parameters [245], reconstruction of the intensity and the CEP of ultrashort laser pulses from frequency-resolved optical gating traces [246] and dispersion scan traces [247], prediction of the HHG spectra for model di- and triatomic molecules for randomly chosen parameters (laser intensity, internuclear distance, and molecular orientation) [248]. Convolutional neural network (CNN) can be used for solving inverse problems, e.g., determination of laser and molecular parameters or classification of molecules using the HHG spectra [248]. It should be emphasized that a deep neural network was also used to implement the TCSFA efficiently, see Ref. [249].

In Ref. [P17] we trained a CNN capable to retrieve the internuclear distance in the H_2^+ molecule using electron momentum distributions. This problem is hard to solve by manually inspecting a variety of PMDs. The distributions that are required to train the CNN were calculated by the numerical solution of the 2D TDSE. The deep neural network applied to retrieval of the internuclear distance consists of five nonreducing convolutional layers, each followed by a reducing average pooling layer (see Ref. [P17] for details). The results of the application of the neural network to the test data are shown in Fig. 6.3 (a). The CNN trained on a few thousand images can predict the internuclear distance with a mean absolute error (MAE) less than 0.1 a.u. Furthermore, we use deep learning to retrieve more than one parameter from a given PMD [P17]. Specifically, we used the CNN to retrieve both the internuclear distance and the laser intensity. Moreover, we have found that the ability of the CNN to retrieve both parameters does not affect the accuracy with which the internuclear distance is obtained, see Ref. [P17].

It is evident that the shape of momentum distributions depends not only on the internuclear distance. This shape is also affected by the laser parameters and, especially, the intensity of the pulse. In order to understand how the focal averaging affects the performance of the CNN, we obtained a number of focal volume averaged PMDs and used them to test the CNN, which is trained on the distributions calculated for fixed laser intensities.
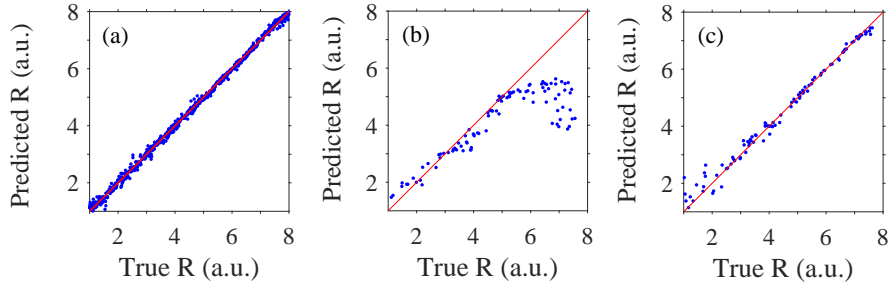
Fig. 6.3: Plot of predicted vs. true internuclear distances illustrating the performance of neural networks. (a) Neural network trained on a set of distributions that were calculated with fixed laser intensities (not focal averaged), see text. (b) The same neural network as in (a), but receiving focal averaged momentum distributions as test images. (c) The neural network trained on a set of focal averaged distributions and tested on another independent set of focal averaged distributions. Taken from Ref. [P17].

The performance of the CNN on this test set is not as good as for the non-averaged distributions, see Fig. refdeep (b). The corresponding MAE is equal to 0.83 a.u. This raises the question: Can the internuclear distance be reliably retrieved from the focal averaged PMDs by using deep learning? To answer this question, we trained another CNN on a set of focal volume averaged PMDs, see Ref. [P17] for details. This CNN also shows an excellent performance: it retrieves the internuclear distance with a MAE less than 0.2 a.u., see Fig. 6.3 (c).

For application of the CNN to experimental data, it should possess some transferability. This means that the CNN should be able to predict correct internuclear distances even for distributions obtained at parameters that it has not been trained for. The CNNs trained in Ref. [P17] show only limited transferability. This problem can be solved by using the transfer learning technique, see, e.g. Ref. [250]. We note that the transfer learning was used in the study of Ref. [248]. The application of this technique to the problem at hand will be a subject of further studies. Another important question that is planned to be investigated is to understand, how the neural network, a "blackbox" by its nature, takes its decisions [P17]. Indeed, it would be beneficial to know what features of the holographic structures allow the CNN to predict the corresponding internuclear distance. This problem can be solved by application of the so-called visualization methods of deep neural networks (see, e.g., Ref. [251] for a review). To summarize, the results obtained in Ref. [P17] suggest that deep learning has a high potential for

retrieving various molecular properties from the electron momentum distributions generated by strong laser pulses.

7. CONCLUSIONS AND PERSPECTIVES

Semiclassical models applying classical mechanics to describe the motion of an electron after it has been freed by a strong laser field are widely used in the studies of laser-matter interaction. In many cases, the semiclassical simulations provide deeper insight into the physical mechanism of a strong-field process under consideration than the direct numerical solution of the time-dependent Schrödinger equation (TDSE) and the strong-field approximation (SFA). The trajectory-based models are also invaluable tools for the investigation and development of techniques for time-resolved molecular imaging, interpretation of the outcomes of quantum optimal control theory (QOCT), and the studies of multielectron effects in strong-field physics. In the present work we have developed several new semiclassical approaches and applied them to investigations of capture into Rydberg states, sequential multiple ionization, above-threshold ionization (ATI) in molecules, multielectron polarization effects, and strong-field photoelectron holography. We applied deep learning to retrieve the internuclear distance in a molecule from holographic interference patterns. Furthermore, we used semiclassical simulations to reveal the specific mechanisms responsible for the optimization of the high-harmonic emission by optimal pulse shaping. Finally, we developed a method for retrieval of effective single-active electron (SAE) potentials that are needed for semiclassical simulations. The method is based on reproducing given electron momentum distributions produced by a strong laser pulse.

The semiclassical simulations of the capture into Rydberg states in ionization by a strong laser pulse have led us to a simple physical picture of this process. We were able to identify the class of trajectories that can be captured by the ionic potential. This, in turn, allowed us to obtain analytic estimates and scaling relations. Furthermore, we developed the semiclassical model for sequential multiple ionization by a short intense laser pulse. The model allows us to obtain both the relative yield and momentum distributions of multiply charged ions. Two new effects were predicted on the basis of the semiclassical simulations. The first effect is the substantial shift of the maximum of the ion momentum distribution along the laser polarization direction. This shift depends on the laser intensity and the CEP ("absolute phase") of the pulse. The CEP dependence is visible even for relatively long

pulses. The second effect is also CEP dependent. It is shown that the ion yield oscillates as a function of the absolute phase. This effect can only be observed if the yields of at least two ions are comparable at the end of the laser pulse.

We have investigated the validity of the semiclassical model for strong-field ionization accounting for the atomic potential. It is found that the discrepancy between the semiclassical model and the solution of the TDSE correlates with the situations where the dynamics of an ensemble of classical trajectories deviates from the so-called strict form of the Ehrenfest's theorem. We proposed a measure of this deviation for classical dynamics of an ensemble of trajectories. This measure has allowed us to identify the general trends for the applicability of the trajectory-based models in terms of laser intensity, wavelength, ellipticity, and parameters of the atomic potential.

The semiclassical two-step (SCTS) model developed within the present work is one of the few modern semiclassical approaches aimed at the description of quantum interference effects. The SCTS reproduces interference patterns in momentum distributions, energy spectra, and angular distributions of photoelectrons produced in ATI and accounts for the ionic potential beyond the semiclassical perturbation theory. The SCTS model shows better agreement with the numerical solution of the TDSE than, e.g., the well-known quantum trajectory Monte Carlo (QTMC) model. The reason for this is that the QTMC uses the first-order semiclassical perturbation theory to describe the Coulomb potential of the parent ion in the phase.

Initially the SCTS model was applied to ionization of atomic hydrogen. We have extended this model to the molecular case and used it to describe the strong-field ionization of the H_2 molecule. We have found significant deviations in the electron momentum distributions and energy spectra from the case of the H atom. It is shown that for the H_2 molecule the electron energy spectra fall off slower with increasing energy for the same parameters of the laser pulse. Simultaneously, the holographic interference fringes in the photoelectron momentum distributions (PMDs) are more pronounced for the H_2 molecule than that for the hydrogen atom. The SCTS model can be also generalized to an arbitrary polarization of the laser pulse and orientation of the molecule. The same also applies for heteronuclear and polyatomic molecules.

Recently we have developed the SCTS model further to improve the description of its first step, i.e., ionization. The resulting SCTSQI model allows to overcome deficiencies of standard semiclassical approaches in the description of the ionization step: In this model the initial conditions for classical trajectories are determined by the exact quantum dynamics. Specifically, we have solved the TDSE with absorbing boundary conditions in a restricted

part of space, applied the Gabor transform to the part of the electron wave packet absorbed at each time step, and transformed this absorbed part into an ensemble of classical trajectories. In the SCTSQI model the Gabor transform determines quantum amplitudes that are assigned to trajectories of the ensemble. The model was implemented for a 1D model atom and tested by comparison of its outcomes with the solution of the TDSE. It is shown that the SCTSQI model yields quantitative agreement with the full quantum results. Further work in needed to improve the efficiency of the SCTSQI model and to generalize it to the 3D case.

The semiclassical approaches were used for studies of multielectron polarization effects in ATI. We have used the semiclassical model accounting for the Stark shift of the initial state, the Coulomb potential, and the polarization induced dipole potential to study the PMDs in strong elliptically polarized laser pulse. It is shown that the momentum distributions are highly sensitive to the tunneling exit point, the Coulomb field, and the multielectron polarization potential. We have investigated the PMDs over a wide range of laser intensities and wavelengths and identified the role of the ME effects in the formation of the electron momentum distributions. Analytic estimates for the position of the maximum in the PMD were obtained. Furthermore, the SCTS model was modified to take into account the multielectron polarization potential. The semiclassical simulations within the combined model have predicted a pronounced narrowing of the PMDs in the direction parallel to the laser polarization. It is shown that this narrowing occurs due to the focusing of the electron by the induced dipole potential. Moreover, the induced polarization of the ionic core also modifies interference patterns in electron momentum distributions. Specifically, the number of fanlike interference fringes at low energies of the 2D PMD may change.

Any semiclassical model requires specification of an effective SAE potential simulating an atom or molecule under consideration. We have developed a method for retrieving of such a potential from a given electron momentum distribution produced by strong-field ionization. In this method the potential is determined as the result of the optimization procedure aimed at reproducing the given PMD. The optimization procedure based on the solution of the TDSE has been implemented in the 1D case. The proposed method allows us to reconstruct the SAE potential with high accuracy. It is planned to extend this method to the 3D case.

The semiclassical simulations were used to understand the results and the mechanisms of optimization of strong-field processes. For example, we developed and applied the trajectory-based model to get insight into the QOCT-based optimization of the high-order harmonic generation (HHG) process in a 1D atom. The optimization of the driving pulse using the QOCT has al-

lowed us both to extend the cutoff of the HHG spectrum and to enhance the harmonic yield. The semiclassical simulations have revealed that the cutoff extension is a classical effect. In contrast to this, the harmonic yield increases due to the increase of the tunneling probability. The developed optimization scheme can be applied to real 3D atoms and molecules.

The SCTS model was used in the study of the strong-field holography with photoelectrons. We have shown that semiclassical simulations performed within the SCTS are in excellent agreement with the recent experimental results. This model has reproduced all main features of the observed holographic structures. We have also used the SCTS model to study the effects of the Coulomb potential in the strong-field photoelectron holography (SFPH). Three main characteristic effects of the Coulomb potential have been predicted: the shift of the whole interference pattern, the filling of the parts of the interference pattern that are missing if the Coulomb potential is not taken into account, and the kink of the interference stripes at zero perpendicular momentum. It needs to be studied which of these effects are less vulnerable to focal averaging and, therefore, can be observed in an experiment.

Continuing our studies of the SFPH that we began with the trajectory-based model, we applied machine learning to retrieval of the internuclear distance in a molecule ionized by a strong laser pulse. In particular, we applied a convolutional neural network to predict the internuclear distance in the 2D H_2^+ molecule based on the electron momentum distribution. It is shown that the neural network trained on a dataset consisting of a few thousand images can efficiently predict the internuclear distance with a mean absolute error of about 0.1 a.u. Furthermore, it is possible to retrieve more than one parameter from a given PMD: we have shown that both the internuclear distance and the laser intensity can be predicted simultaneously. We have studied the effect of the focal volume averaging on the retrieval of the internucnear distance. The neural network trained on a set of focal averaged PMDs also shows an excellent performance. Nevertheless, future work is required to achieve transferability of the trained neural networks. This is planned to be done by using the transfer learning technique.

The results obtained in the present work clearly show that in the foreseeable future the semiclassical models will remain an important tool in studies of strong-field phenomena. Moreover, we can expect soon the emergence of a new generation of these models, namely combining more accurate description of the ionization step, ability to describe interference effects, and numerical efficiency. The development of such approaches, as well as wide application of machine learning, modern optimization techniques, and pattern recognition tools will provide the basis for new achievements in strong-field, ultrafast, and attosecond physics.

BIBLIOGRAPHY

[1] N. B. Delone and V. P. Krainov, *Multiphoton Processes in Atoms* (Springer, Berlin, 2000).

[2] W. Becker, F. Grasbon, R. Kopold, D. Milošević, G. Paulus, and H. Walther, Adv. At. Mol. Opt. Phys. **48**, 35 (2002).

[3] A. Becker and F. H. M. Faisal, Journal of Physics B: Atomic, Molecular and Optical Physics **38**, R1 (2005).

[4] C. Faria and X. Liu, J. Mod. Opt. **58**, 1076 (2011).

[5] M. Kitzler and S. Gräfe, eds., *Ultrafast Dynamics Driven by Intense Light Pulses (From Atoms to Solids, from Lasers to Intense X-Rays* (Berlin: Springer, 2016).

[6] C. D. Lin, A.-T. Le, C. Jin, and H. Wei, *Attosecond and Strong-Field Physics (Principles and Applications)* (Cambridge: Cambridge University Press, 2018).

[7] L. V. Keldysh, JETP **20**, 1307 (1965).

[8] F. H. M. Faisal, J. Phys. B: At. Mol. Opt. Phys. **6**, L89 (1973).

[9] H. R. Reiss, Phys. Rev. A **22**, 1786 (1980).

[10] H. G. Muller, Laser Phys. **9**, 138 (1999).

[11] D. Bauer and P. Koval, Computer Physics Communications **174**, 396 (2006), ISSN 0010-4655.

[12] L. B. Madsen, L. A. A. Nikolopoulos, T. K. Kjeldsen, and J. Fernández, Phys. Rev. A **76**, 063407 (2007).

[13] S. Patchkovskii and H. Muller, Comput. Phys. Commun. **199**, 153 (2016), ISSN 0010.

[14] H. B. van Linden van den Heuvell and H. G. Müller, *Multiphoton Processes* (Cambridge University Press, Cambridge, UK, 1988).

[15] T. F. Gallagher, Phys. Rev. Lett. **61**, 2304 (1988).

[16] P. B. Corkum, N. H. Burnett, and F. Brunel, Phys. Rev. Lett. **62**, 1259 (1989).

[17] J. L. Krause, K. J. Schafer, and K. C. Kulander, Phys. Rev. Lett. **68**, 3535 (1992).

[18] P. B. Corkum, Phys. Rev. Lett. **71**, 1994 (1993).

[19] A. Palacios, H. Bachau, and F. Martín, Phys. Rev. Lett. **96**, 143001 (2006).

[20] J. Förster, Y. V. Vanne, and A. Saenz, Phys. Rev. A **90**, 053424 (2014).

[21] A. M. Perelomov, V. S. Popov, and M. V. Terent'ev, Sov. Phys. JETP **23**, 924 (1966).

[22] M. Bashkansky, P. H. Bucksbaum, and D. W. Schumacher, Phys. Rev. Lett. **60**, 2458 (1988).

[23] S. Basile, F. Trombetta, and G. Ferrante, Phys. Rev. Lett. **61**, 2435 (1988).

[24] P. Lambropoulos and X. Tang, Phys. Rev. Lett. **61**, 2506 (1988).

[25] H. G. Muller, G. Petite, and P. Agostini, Phys. Rev. Lett. **61**, 2507 (1988).

[26] P. Krstić and M. H. Mittleman, Phys. Rev. A **44**, 5938 (1991).

[27] A. Jaroń, J. Kamiński, and F. Ehlotzky, Optics Communications **163**, 115 (1999), ISSN 0030-4018.

[28] N. L. Manakov, M. V. Frolov, A. F. Starace, and I. I. Fabrikant, Journal of Physics B: Atomic, Molecular and Optical Physics **33**, R141 (2000).

[29] G. G. Paulus, W. Nicklich, H. Xu, P. Lambropoulos, and H. Walther, Phys. Rev. Lett. **72**, 2851 (1994).

[30] M. Lewenstein, P. Balcou, M. Y. Ivanov, A. L'Huillier, and P. B. Corkum, Phys. Rev. A **49**, 2117 (1994).

[31] G. G. Paulus, W. Becker, W. Nicklich, and H. Walther, Journal of Physics B: Atomic, Molecular and Optical Physics **27**, L703 (1994).

[32] C. Faria and W. Becker, Laser Phys. **13**, 1196 (2003).

[33] D. B. Milošević and W. Becker, Phys. Rev. A **68**, 065401 (2003).

[34] T. Brabec, M. Y. Ivanov, and P. B. Corkum, Phys. Rev. A **54**, R2551 (1996).

[35] K. I. Dimitriou, D. G. Arbó, S. Yoshida, E. Persson, and J. Burgdörfer, Phys. Rev. A **70**, 061401 (2004).

[36] W. Quan, Z. Lin, M. Wu, H. Kang, H. Liu, X. Liu, J. Chen, J. Liu, X. T. He, S. G. Chen, et al., Phys. Rev. Lett. **103**, 093001 (2009).

[37] C. Liu and K. Z. Hatsagortsyan, Phys. Rev. Lett. **105**, 113003 (2010).

[38] T.-M. Yan, S. V. Popruzhenko, M. J. J. Vrakking, and D. Bauer, Phys. Rev. Lett. **105**, 253002 (2010).

[39] A. Kästner, U. Saalmann, and J. M. Rost, Phys. Rev. Lett. **108**, 033201 (2012).

[40] C. Lemell, K. I. Dimitriou, X.-M. Tong, S. Nagele, D. V. Kartashov, J. Burgdörfer, and S. Gräfe, Phys. Rev. A **85**, 011403 (2012).

[41] C. Lemell, J. Burgdörfer, S. Gräfe, K. I. Dimitriou, D. G. Arbó, and X.-M. Tong, Phys. Rev. A **87**, 013421 (2013).

[42] B. Wolter, C. Lemell, M. Baudisch, M. G. Pullen, X.-M. Tong, M. Hemmer, A. Senftleben, C. D. Schröter, J. Ullrich, R. Moshammer, et al., Phys. Rev. A **90**, 063424 (2014).

[43] W. Becker, S. P. Goreslavski, D. B. Milošević, and G. G. Paulus, J. Phys. B: At. Mol. Opt. Phys. **47**, 204022 (2014).

[44] D. Dimitrovski and L. B. Madsen, Phys. Rev. A **91**, 033409 (2015).

[45] C. I. Blaga, F. Catoire, P. Colosimo, G. G. Paulus, H. G. Muller, P. Agostini, and L. F. DiMauro, Nat. Phys **5**, 335 (2009).

[46] R. Boge, C. Cirelli, A. S. Landsman, S. Heuser, A. Ludwig, J. Maurer, M. Weger, L. Gallmann, and U. Keller, Phys. Rev. Lett. **111**, 103003 (2013).

[47] C. Hofmann, A. S. Landsman, A. Zielinski, C. Cirelli, T. Zimmermann, A. Scrinzi, and U. Keller, Phys. Rev. A **90**, 043406 (2014).

[48] J.-W. Geng, L. Qin, M. Li, W.-H. Xiong, Y. Liu, Q. Gong, and L.-Y. Peng, Journal of Physics B: Atomic, Molecular and Optical Physics **47**, 204027 (2014).

[49] S. V. Popruzhenko and D. Bauer, J. Mod. Opt. **55**, 2573 (2008).

[50] S. V. Popruzhenko, G. G. Paulus, and D. Bauer, Phys. Rev. A **77**, 053409 (2008).

[51] J. Chen and C. H. Nam, Phys. Rev. A **66**, 053415 (2002).

[52] L. D. Landau and E. M. Lifshitz, *Quantum Mechanics Nonrelativistic Theory*, v. 3 (Pergamon Oxford, 1965).

[53] C. Z. Bisgaard and L. B. Madsen, Am. J. Phys. **72**, 249 (2004).

[54] M. V. Ammosov, N. B. Delone, and V. P. Krainov, Sov. Phys. JETP **64**, 1191 (1986).

[55] N. B. Delone and V. P. Krainov, J. Opt. Soc. Am. B **8**, 1207 (1991).

[56] X. Lai, S. Yu, Y. Huang, L. Hua, C. Gong, W. Quan, C. Faria, and X. Liu, Phys. Rev. A **96**, 013414 (2017).

[57] A. S. Maxwell, A. Al-Jawahiry, T. Das, and C. Faria, Phys. Rev. A **96**, 023420 (2017).

[58] A. S. Maxwell, A. Al-Jawahiry, X. Y. Lai, and C. Faria, J. Phys. B: At. Mol. Opt. Phys. **51**, 044004 (2018).

[59] A. S. Maxwell, S. V. Popruzhenko, and C. Faria, Phys. Rev. A **98**, 063423 (2018).

[60] A. S. Maxwell and C. Faria, J. Phys. B: At. Mol. Opt. Phys. **51**, 124001 (2018).

[61] M. V. Fedorov, *Atomic and Free Electrons in a Strong Laser Field* (World Sci., Singapore, 1997).

[62] T. Nubbemeyer, K. Gorling, A. Saenz, U. Eichmann, and W. Sandner, Phys. Rev. Lett. **101**, 233001 (2008).

[63] S. P. Goreslavski, G. G. Paulus, S. V. Popruzhenko, and N. I. Shvetsov-Shilovski, Phys. Rev. Lett. **93**, 233002 (2004).

[64] N. I. Shvetsov-Shilovski, S. P. Goreslavski, S. V. Popruzhenko, and W. Becker, Phys. Rev. A **77**, 063405 (2008).

[65] J. Chen and C. H. Nam, Phys. Rev. A **66**, 053415 (2002).

[66] A. Rudenko, K. Zrost, C. D. Schröter, V. L. B. de Jesus, B. Feuerstein, R. Moshammer, and J. Ullrich, Journal of Physics B: Atomic, Molecular and Optical Physics **37**, L407 (2004).

[67] F. H. M. Faisal and G. Schlegel, J. Phys. B: At. Mol. Opt. Phys. **38**, L223 (2005).

[68] A. S. Alnaser, C. M. Maharjan, P. Wang, and I. V. Litvinyuk, J. Phys. B: At. Mol. Opt. Phys. **39**, L323 (2006).

[69] C. M. Maharjan, A. S. Alnaser, I. Litvinyuk, P. Ranitovic, and C. L. Cocke, J. Phys. B: At. Mol. Opt. Phys. **39**, 1955 (2006).

[70] L. Ortmann, Ph.D. thesis, Technische Universität Dresden (2019).

[71] R. Dörner, T. Weber, M. Weckenbrock, A. Staudte, M. Hattass, H. Schmidt-Böcking, R. Moshammer, and J. Ullrich, **48**, 1 (2002), ISSN 1049-250X.

[72] A. Becker, R. Dörner, and R. Moshammer, J. Phys. B: At. Mol. Opt. Phys. **38**, S753 (2005).

[73] W. Becker, X. Liu, P. J. Ho, and J. H. Eberly, Rev. Mod. Phys. **84**, 1011 (2012).

[74] T. Weber, M. Weckenbrock, A. Staudte, L. Spielberger, O. Jagutzki, V. Mergel, F. Afaneh, G. Urbasch, M. Vollmer, H. Giessen, et al., Phys. Rev. Lett. **84**, 443 (2000).

[75] R. Moshammer, B. Feuerstein, W. Schmitt, A. Dorn, C. D. Schröter, J. Ullrich, H. Rottke, C. Trump, M. Wittmann, G. Korn, et al., Phys. Rev. Lett. **84**, 447 (2000).

[76] T. Weber, H. Giessen, M. Weckenbrock, G. Urbasch, A. Staudte, L. Spielberger, O. Jagutzki, V. Mergel, M. Vollmer, and R. Dörner, Nature (London) **405**, 658 (2000).

[77] T. Weber, M. Weckenbrock, A. Staudte, L. Spielberger, O. Jagutzki, V. Mergel, F. Afaneh, G. Urbasch, M. Vollmer, H. Giessen, et al., J. Phys. B: At. Mol. Opt. Phys. **33**, L127 (2000).

[78] B. Feuerstein, R. Moshammer, and J. Ullrich, J. Phys. B: At. Mol. Opt. Phys. **33**, L823 (2000).

[79] R. Moshammer, J. Ullrich, B. Feuerstein, D. Fischer, A. Dorn, C. D. Schröter, J. R. Crespo Lopez-Urrutia, C. Hoehr, H. Rottke, C. Trump, et al., Phys. Rev. Lett. **91**, 113002 (2003).

[80] P. Dietrich, N. H. Burnett, M. Ivanov, and P. B. Corkum, Phys. Rev. A **50**, R3585 (1994).

[81] P. Lambropoulos and X. Tang, J. Opt. Soc. Am. B **4**, 821 (1987).

[82] B. Chang, P. R. Bolton, and D. N. Fittinghoff, Phys. Rev. A **47**, 4193 (1993).

[83] S. Augst, A. Talebpour, S. L. Chin, Y. Beaudoin, and M. Chaker, Phys. Rev. A **52**, R917 (1995).

[84] S. Larochelle, A. Talebpour, and S. L. Chin, J. Phys. B: At. Mol. Opt. Phys. **31**, 1201 (1998).

[85] A. Becker and F. H. M. Faisal, Phys. Rev. A **59**, R3182 (1999).

[86] A. Becker and F. H. M. Faisal, J. Phys. B: At. Mol. Opt. Phys. **32**, L335 (1999).

[87] H. Maeda, M. Dammasch, U. Eichmann, W. Sandner, A. Becker, and F. H. M. Faisal, Phys. Rev. A **62**, 035402 (2000).

[88] H. Maeda, M. Dammasch, U. Eichmann, and W. Sandner, Phys. Rev. A **63**, 025401 (2001).

[89] S. Palaniyappan, A. DiChiara, I. Ghebregziabher, E. L. Huskins, A. Falkowski, D. Pajerowski, and B. C. Walker, J. Phys. B: At. Mol. Opt. Phys. **39**, S357 (2006).

[90] A. Rudenko, K. Zrost, B. Feuerstein, V. L. B. de Jesus, C. D. Schröter, R. Moshammer, and J. Ullrich, Phys. Rev. Lett. **93**, 253001 (2004).

[91] K. I. Dimitriou, S. Yoshida, J. Burgdörfer, H. Shimada, H. Oyama, and Y. Yamazaki, Phys. Rev. A **75**, 013418 (2007).

[92] S. Yoshida, K. I. Dimitriou, J. Burgdörfer, H. Shimada, H. Oyama, and Y. Yamazaki, Journal of Physics: Conference Series **163**, 012009 (2009).

[93] J. S. Cohen, Phys. Rev. A **64**, 043412 (2001).

[94] V. P. Krainov and S. B., JETP **80**, 657 (1995).

[95] V. P. Krainov, J. Opt. Soc. Am. B **14**, 425 (1997).

[96] V. S. Popov, Usp. Fiz. Nauk **174**, 921 (2004).

[97] W. H. Press, S. A. Teukolsky, W. T. Vetterling, and B. P. Flannery, *Numerical Recipes in Fortran 77: The art of scientific computing* (Cambridge University Press, Cambridge, 1992), 2nd ed.

[98] C. W. Gear, *Numerical Initial Value Problems in Ordinary Differential Equations* (Prentice-Hall, Englewood Cliffs, NJ, 1971).

[99] G. Sansone, C. Vozzi, S. Stagira, M. Pascolini, L. Poletto, P. Villoresi, G. Tondello, S. De Silvestri, and M. Nisoli, Phys. Rev. Lett. **92**, 113904 (2004).

[100] A. Messiah, *Quantum Mechanics* (Wiley, New York, 1966).

[101] L. E. Ballentine, Y. Yang, and J. P. Zibin, Phys. Rev. A **50**, 2854 (1994).

[102] C. Lemell, K. I. Dimitriou, X.-M. Tong, S. Nagele, D. V. Kartashov, J. Burgdörfer, and S. Gräfe, Phys. Rev. A **85**, 011403 (2012).

[103] A. N. Pfeiffer, C. Cirelli, M. Smolarski, D. Dimitrovski, M. Abu-Samha, L. B. Madsen, and U. Keller, Nat. Phys. p. 76 (2012).

[104] J. Maurer, D. Dimitrovski, L. Christensen, L. B. Madsen, and H. Stapelfeldt, Phys. Rev. Lett. **109**, 123001 (2012).

[105] T.-M. Yan, S. V. Popruzhenko, M. J. J. Vrakking, and D. Bauer, Phys. Rev. Lett. **105**, 253002 (2010).

[106] T.-M. Yan and D. Bauer, Phys. Rev. A **86**, 053403 (2012).

[107] M. Li, J.-W. Geng, H. Liu, Y. Deng, C. Wu, L.-Y. Peng, Q. Gong, and Y. Liu, Phys. Rev. Lett. **112**, 113002 (2014).

[108] X.-Y. Lai, C. Poli, H. Schomerus, and C. Faria, Phys. Rev. A **92**, 043407 (2015).

[109] A. M. Perelomov and V. S. Popov, Sov. Phys. JETP **25**, 336 (1967).

[110] W. H. Miller, Adv. Chem. Phys. **25**, 69 (1974).

[111] M. W. Walser and T. Brabec, J. Phys. B: At. Mol. Opt. Phys. **36**, 3025 (2003).

[112] M. Spanner, Phys. Rev. Lett. **90**, 233005 (2003).

[113] D. J. Tannor, *Introduction to Quantum Mechanics. A Time-Dependent Perspective* (University Science Books, Sausalito, 2007).

[114] F. Grossmann, *Theoretical Femtosecond Physics. A Time-Dependent Perspective* (Springer-Verlag, Berlin, Heidelberg, 2008).

[115] X.-M. Tong, G. Wachter, S. A. Sato, C. Lemell, K. Yabana, and J. Burgdörfer, Phys. Rev. A **92**, 043422 (2015).

[116] D. G. Arbó, E. Persson, and J. Burgdörfer, Phys. Rev. A **74**, 063407 (2006).

[117] R. Gopal, K. Simeonidis, R. Moshammer, T. Ergler, M. Dürr, M. Kurka, K.-U. Kühnel, S. Tschuch, C.-D. Schröter, D. Bauer, et al., Phys. Rev. Lett. **103**, 053001 (2009).

[118] D. G. Arbó, S. Yoshida, E. Persson, K. I. Dimitriou, and J. Burgdörfer, Phys. Rev. Lett. **96**, 143003 (2006).

[119] D. G. Arbó, K. I. Dimitriou, E. Persson, and J. Burgdörfer, Phys. Rev. A **78**, 013406 (2008).

[120] S. Brennecke, N. Eicke, and M. Lein, Phys. Rev. Lett. **124**, 153202 (2020).

[121] K. Husimi, Proc. Phys. Math. Soc. Jpn. **22**, 264 (1940).

[122] L. E. Ballentine, *Quantum Mechanics: A Modern Development* (World Scientific, Singapore, 1998).

[123] J. Muth-Böhm, A. Becker, and F. H. M. Faisal, Phys. Rev. Lett. **85**, 2280 (2000).

[124] T. K. Kjeldsen and L. B. Madsen, J. Phys. B: At. Mol. Opt. Phys. **37**, 2033 (2004).

[125] X. M. Tong, Z. X. Zhao, and C. D. Lin, Phys. Rev. A **66**, 033402 (2002).

[126] M.-M. Liu, M. Li, C. Wu, Q. Gong, A. Staudte, and Y. Liu, Phys. Rev. Lett. **116**, 163004 (2016).

[127] M.-M. Liu and Y. Liu, J. Phys. B: At. Mol. Opt. Phys. **50**, 105602 (2017).

[128] R. Murray, W.-K. Liu, and M. Y. Ivanov, Phys. Rev. A **81**, 023413 (2010).

[129] M. Liu and Y. Liu, Phys. Rev. A **93**, 043426 (2016).

[130] H.-P. Kang, S.-P. Xu, Y.-L. Wang, S.-G. Yu, X.-Y. Zhao, X.-L. Hao, X.-Y. Lai, T. Pfeifer, X.-J. Liu, J. Chen, et al., J. Phys. B: At. Mol. Opt. Phys. **51**, 105601 (2018).

[131] C.-T. Le, V.-H. Hoang, L.-P. Tran, and V.-H. Le, Phys. Rev. A **97**, 043405 (2018).

[132] E. Runge and E. K. U. Gross, Phys. Rev. Lett. **52**, 997 (1984).

[133] C. A. Ullrich, *Time-Dependent Density-Functional Theory: Concepts and Applications* (Oxford University Press, Oxford, 2012).

[134] M. A. L. Marques, N. T. Maitra, F. M. S. Nogueira, E. K. U. Gross, and A. Rubio, eds., *Fundamentals of Time-Dependent Density-Functional Theory* (Oxford University Press, Oxford, 2014).

[135] J. Zanghellini, M. Kitzler, T. Brabec, and A. Scrinzi, J. Phys. B: At. Mol. Opt. Phys. **37**, 763 (2004).

[136] J. Caillat, J. Zanghellini, M. Kitzler, O. Koch, W. Kreuzer, and A. Scrinzi, Phys. Rev. A **71**, 012712 (2005).

[137] H. Miyagi and L. B. Madsen, Phys. Rev. A **87**, 062511 (2013).

[138] T. Sato and K. L. Ishikawa, Phys. Rev. A **88**, 023402 (2013).

[139] P. G. Burke and V. M. Burke, J. Phys. B: At. Mol. Opt. Phys. **30**, L383 (1997).

[140] M. A. Lysaght, H. W. van der Hart, and P. G. Burke, Phys. Rev. A **79**, 053411 (2009).

[141] L. A. A. Nikolopoulos, J. S. Parker, and K. T. Taylor, Phys. Rev. A **78**, 063420 (2008).

[142] L. R. Moore, M. A. Lysaght, L. A. A. Nikolopoulos, J. S. Parker, H. W. van der Hart, and K. T. Taylor, Journal of Modern Optics **58**, 1132 (2011).

[143] N. Rohringer, A. Gordon, and R. Santra, Phys. Rev. A **74**, 043420 (2006).

[144] S. Pabst, L. Greenman, D. A. Mazziotti, and R. Santra, Phys. Rev. A **85**, 023411 (2012).

[145] D. Hochstuhl and M. Bonitz, Phys. Rev. A **86**, 053424 (2012).

[146] S. Bauch, L. K. Sørensen, and L. B. Madsen, Phys. Rev. A **90**, 062508 (2014).

[147] L. Torlina and O. Smirnova, Phys. Rev. A **86**, 043408 (2012).

[148] D. Dimitrovski, J. Maurer, H. Stapelfeldt, and L. B. Madsen, Phys. Rev. Lett. **113**, 103005 (2014).

[149] D. Dimitrovski, J. Maurer, H. Stapelfeldt, and L. B. Madsen, J. Phys. B: At. Mol. Opt. Phys. **48**, 121001 (2015).

[150] D. Dimitrovski, C. P. J. Martiny, and L. B. Madsen, Phys. Rev. A **82**, 053404 (2010).

[151] T. Brabec, M. Côté, P. Boulanger, and L. Ramunno, Phys. Rev. Lett. **95**, 073001 (2005).

[152] Z. Zhao and T. Brabec, J. Mod. Opt. **54**, 981 (2007).

[153] G. G. Paulus, F. Grasbon, H. Walther, P. Villoresi, M. Nisoli, S. Stagira, E. Priori, and S. D. Silvestri, Nature (London) **414**, 182 (2001).

[154] A. M. Perelomov, V. S. Popov, and M. V. Terent'ev, Sov. Phys. JETP **24**, 207 (1967).

[155] G. G. Paulus, F. Grasbon, A. Dreischuh, H. Walther, R. Kopold, and W. Becker, Phys. Rev. Lett. **84**, 3791 (2000).

[156] S. P. Goreslavski and S. V. Popruzhenko, Sov. Phys. JETP **83**, 661 (1996).

[157] G. G. Paulus, F. Zacher, H. Walther, A. Lohr, W. Becker, and M. Kleber, Phys. Rev. Lett. **80**, 484 (1998).

[158] P. Eckle, A. N. Pfeiffer, C. Cirelli, A. Staudte, R. Dörner, H. G. Muller, M. Büttiker, and U. Keller, Science **322**, 1525 (2008).

[159] P. Eckle, M. Smolarski, P. Schlup, J. Biegert, A. Staudte, M. Schöffler, H. G. Muller, R. Dörner, and U. Keller, Nat. Phys. **8**, 76 (2012).

[160] D. Kim, S. Fournier, M. Saeed, and L. F. DiMauro, Phys. Rev. A **41**, 4966 (1990).

[161] N. J. van Druten, R. Trainham, and H. G. Muller, Phys. Rev. A **50**, 1593 (1994).

[162] D. Xenakis, N. E. Karapanagioti, D. Charalambidis, H. Bachau, and E. Cormier, Phys. Rev. A **60**, 3916 (1999).

[163] G. D. Gillen, M. A. Walker, and L. D. Van Woerkom, Phys. Rev. A **64**, 043413 (2001).

[164] G. D. Gillen and L. D. Van Woerkom, Phys. Rev. A **68**, 033401 (2003).

[165] J. Zhang and P. Lambropoulos, Phys. Rev. Lett. **77**, 2186 (1996).

[166] L. A. A. Nikolopoulos, G. Buică-Zloh, and P. Lambropoulos, Eur. Phys. J. D **26**, 245 (2003).

[167] I. Liontos, A. Bolovinos, S. Cohen, and A. Lyras, Phys. Rev. A **70**, 033403 (2004).

[168] T. Nakajima and G. Buica, Phys. Rev. A **74**, 023411 (2006).

[169] G. Buica and T. Nakajima, Phys. Rev. A **79**, 013419 (2009).

[170] X. M. Tong and C. D. Lin, J. Phys. B: At. Mol. Opt. Phys. **38**, 2593 (2005).

[171] H. G. Muller and F. C. Kooiman, Phys. Rev. Lett. **81**, 1207 (1998).

[172] N. Troullier and J. L. Martins, Phys. Rev. B **43**, 1993 (1991).

[173] N. T. Eicke, Ph.D. thesis, Leibniz Universität Hannover (2020).

[174] J. Xu, H.-L. Zhou, Z. Chen, and C. D. Lin, Phys. Rev. A **79**, 052508 (2009).

[175] L. M. Rios and N. V. Sahinidis, J. Glob. Optim **56**, 1247 (2013).

[176] J. Larson, M. Menickelly, and S. M. Wild, Acta Numer. **28**, 287 (2019).

[177] Z. Wang, A. C. Bovik, H. R. Sheikh, and E. P. Simoncelli, IEEE Transactions on Image Processing **13**, 600 (2004).

[178] A. Buldas, A. Kroonmaa, and R. Laanoja, *SignaturesÍnfrastructure: How to Build Global Distributed Hash-Trees* (Springer, Berlin, Heidelberg, 2013).

[179] P. B. Corkum and F. Krausz, Nat. Phys. **3**, 381 (2007).

[180] T. Shao, G. Zhao, B. Wen, and H. Yang, Phys. Rev. A **82**, 063838 (2010).

[181] Z. Zeng, Y. Cheng, X. Song, R. Li, and Z. Xu, Phys. Rev. Lett. **98**, 203901 (2007).

[182] D. G. Lee, J.-H. Kim, K.-H. Hong, and C. H. Nam, Phys. Rev. Lett. **87**, 243902 (2001).

[183] J. J. Carrera and S.-I. Chu, Phys. Rev. A **75**, 033807 (2007).

[184] Y. Xiang, Y. Niu, and S. Gong, Phys. Rev. A **79**, 053419 (2009).

[185] S. B. P. Radnor, L. E. Chipperfield, P. Kinsler, and G. H. C. New, Phys. Rev. A **77**, 033806 (2008).

[186] L. E. Chipperfield, J. S. Robinson, J. W. G. Tisch, and J. P. Marangos, Phys. Rev. Lett. **102**, 063003 (2009).

[187] J. A. Pérez-Hernández, M. F. Ciappina, M. Lewenstein, L. Roso, and A. Zaïr, Phys. Rev. Lett. **110**, 053001 (2013).

[188] K. Ishikawa, Phys. Rev. Lett. **91**, 043002 (2003).

[189] K. L. Ishikawa, Phys. Rev. A **70**, 013412 (2004).

[190] I. J. Kim, C. M. Kim, H. T. Kim, G. H. Lee, Y. S. Lee, J. Y. Park, D. J. Cho, and C. H. Nam, Phys. Rev. Lett. **94**, 243901 (2005).

[191] E. Mansten, J. M. Dahlström, P. Johnsson, M. Swoboda, A. L'Hiullier, and J. Mauritsson, New J. Phys. **10**, 083041 (2008).

[192] A. Fleischer and N. Moiseyev, Phys. Rev. A **77**, 010102 (2008).

[193] F. Brizuela, C. M. Heyl, P. Rudawski, D. Kroon, L. Rading, J. M. Dahlström, J. Mauritsson, P. Johnsson, C. L. Arnold, and A. L'Huillier, Sci. Rep. **3**, 1410 (2013).

[194] A. Wirth, M. T. Hassan, I. Grguraš, J. Gagnon, A. Moulet, T. T. Luu, S. Pabst, R. Santra, Z. A. Alahmed, A. M. Azzeer, et al., Science **334**, 195 (2011).

[195] H. Fattahi, H. G. Barros, M. Gorjan, T. Nubbemeyer, B. Alsaif, C. Y. Teisset, M. Schultze, S. Prinz, M. Haefner, M. Ueffing, et al., Optica **1**, 45 (2014).

[196] R. Kosloff, S. Rice, P. Gaspard, S. Tersigni, and D. Tannor, Chemical Physics **139**, 201 (1989), ISSN 0301-0104.

[197] A. P. Peirce, M. A. Dahleh, and H. Rabitz, Phys. Rev. A **37**, 4950 (1988).

[198] J. Werschnik and E. K. U. Gross, J. Phys. B: At. Mol. Opt. Phys. **40**, R175 (2007).

[199] C. Brif, R. Chakrabarti, and H. Rabitz, New J. Phys. **12**, 075008 (2010).

[200] E. Räsänen and L. B. Madsen, Phys. Rev. A **86**, 033426 (2012).

[201] J. C. Baggesen and L. B. Madsen, J. Phys. B: At. Mol. Opt. Phys. **44**, 115601 (2011).

[202] M. J. D. Powell, IMA Journal of Numerical Analysis **28**, 649 (2008), ISSN 0272-4979.

[203] R. Fletcher, ed., *Practical Methods of Optimization* (Wiley, New York, 2000), 2nd ed.

[204] M. F. Kling and M. J. Vrakking, Annu. Rev. Phys. Chem. **59**, 463 (2008).

[205] C. Koch and M. Shapiro, Chem. Rev. **112**, 4928 (2012).

[206] T. S. Rose, M. J. Rosker, and A. H. Zewail, J. Chem. Phys. **88**, 6672 (1988).

[207] A. K. Tiwari, K. B. Møoller, and N. E. Henriksen, Phys. Rev. A **78**, 065402 (2008).

[208] C. C. Shu, T. Rozgonyi, L. Gonzáles, and N. E. Henriksen, J. Chem. Phys. **136**, 174303 (2012).

[209] S. Chelkowski, A. D. Bandrauk, and P. B. Corkum, Phys. Rev. Lett. **65**, 2355 (1990).

[210] T. Witte, T. Hornung, L. Windhorn, D. Proch., R. de Vivie-Riedle, M. Motzkus, and K. L. Kompa, J. Chem. Phys. **118**, 2021 (2003).

[211] N. H. Damrauer, C. Dietl, G. Krampert, S.-H. Lee, K.-H. Jung, and G. Gerber, Eur. Phys. J D **20**, 71 (2002).

[212] N. E. Henriksen, Chemical Physics **442**, 2 (2014), ISSN 0301-0104.

[213] M. F. Kling, C. Siedschlag, A. J. Verhoef, J. I. Khan, M. Schultze, T. Uphues, Y. Ni, M. Uiberacker, M. Drescher, F. Krausz, et al., Science **312**, 246 (2006).

[214] A. Castro, E. Räsänen, A. Rubio, and E. K. U. Gross, EPL **87**, 53001 (2009).

[215] J. Xu, C. I. Blaga, P. Agostini, and L. F. DiMauro, J. Phys. B: At. Mol. Opt. Phys. **49**, 112001 (2016).

[216] L. J. Frasinski, K. Codling, P. Hatherly, J. Barr, I. N. Ross, and W. T. Toner, Phys. Rev. Lett. **58**, 2424 (1987).

[217] C. Cornaggia, J. Lavancier, D. Normand, J. Morellec, P. Agostini, J. P. Chambaret, and A. Antonetti, Phys. Rev. A **44**, 4499 (1991).

[218] J. H. Posthumus, L. J. Frasinski, A. J. Giles, and K. Codling, J. Phys. B: At. Mol. Opt. Phys. **28**, L349 (1995).

[219] C. Cornaggia, M. Schmidt, and D. Normand, Phys. Rev. A **51**, 1431 (1995).

[220] R. Kanya, Y. Morimoto, and K. Yamanouchi, Phys. Rev. Lett. **105**, 123202 (2010).

[221] Y. Morimoto, R. Kanya, and K. Yamanouchi, J. Chem. Phys. **140**, 064201 (2014).

[222] J. Itatani, L. J., D. Zeidler, H. Niikura, H. Pépin, J. C. Kieffer, P. B. Corkum, and D. M. Villeneuve, Nature **432**, 867 (2004).

[223] S. Haessler, J. Caillat, W. Boutu, C. Giovanetti-Teixeira, T. Ruchon, T. Auguste, Z. Diveki, P. Breger, A. Maquet, B. Carré, et al., Nat. Phys. **6**, 200 (2010).

[224] M. Meckel, D. Comtois, D. Zeidler, A. Staudte, D. Pavičić, H. C. Bandulet, H. Pépin, J. C. Kieffer, R. Dörner, D. M. Villeneuve, et al., Science **320**, 1478 (2008).

[225] C. I. Blaga, J. Xu, A. D. DiChiara, E. Sistrunk, K. Zhang, P. Agostini, T. A. Miller, L. F. DiMauro, and C. D. Lin, Nature **483**, 194 (2012).

[226] M. G. Pullen, B. Wolter, A.-T. Le, M. Baudisch, M. Hemmer, A. Senftleben, C. D. Schröter, J. Ullrich, R. Moshammer, C. D. Lin, et al., Nat. Commun **6**, 7262 (2015).

[227] Y. Huismans, A. Rouzée, A. Gijsbertsen, J. H. Jungmann, A. S. Smolkowska, P. S. W. M. Longman, F. Lépine, C. Cauchy, S. Zamith, T. Marchenko, et al., Science **331**, 61 (2011).

[228] D. Gabor, *Nobel Lectures, Physics, 1971-1980*, v. 3 (World Scientific, Singapore, ????).

[229] T. Marchenko, Y. Huismans, K. J. Schafer, and M. J. J. Vrakking, Phys. Rev. A **84**, 053427 (2011).

[230] D. D. Hickstein, P. Ranitovic, S. Witte, X.-M. Tong, Y. Huismans, P. Arpin, X. Zhou, K. E. Keister, C. W. Hogle, B. Zhang, et al., Phys. Rev. Lett. **109**, 073004 (2012).

[231] Y. Huismans, A. Gijsbertsen, A. S. Smolkowska, J. H. Jungmann, A. Rouzée, P. S. W. M. Logman, F. Lépine, C. Cauchy, S. Zamith, T. Marchenko, et al., Phys. Rev. Lett. **109**, 013002 (2012).

[232] X.-B. Bian, Y. Huismans, O. Smirnova, K.-J. Yuan, M. J. J. Vrakking, and A. D. Bandrauk, Phys. Rev. A **84**, 043420 (2011).

[233] X.-B. Bian and A. D. Bandrauk, Phys. Rev. Lett. **108**, 263003 (2012).

[234] X.-B. Bian and A. D. Bandrauk, Phys. Rev. A **89**, 033423 (2014).

[235] M. Li, J. Yuan, X. Sun, J. Yu, Q. Gong, and Y. Liu, Phys. Rev. A **89**, 033425 (2014).

[236] M. Li, X. Sun, X. Xie, Y. Shao, Y. Deng, C. Wu, Q. Gong, and Y. Liu, Sci. Rep. **5**, 8519 (2015).

[237] M. Meckel, A. Staudte, S. Patchkovskii, D. M. Villeneuve, P. B. Corkum, R. Dörner, and M. Spanner, Nat. Phys **10**, 594 (2014).

[238] M. Haertelt, X.-B. Bian, M. Spanner, A. Staudte, and P. B. Corkum, Phys. Rev. Lett. **116**, 133001 (2016).

[239] C. Faria and A. S. Maxwell, Rep. Prog. Phys. **83**, 034401 (2020).

[240] M. S. Gordon, J. H. Jensen, S. Koseki, N. Matsunaga, K. A. Nguen, S. Su, T. L. Windus, M. Dupuis, and M. J. A., J. Comput. Chem. **14**, 1347 (1993).

[241] A. W. Trask, *Grokking Deep Learning* (Manning, Shelter Island, NY, 2019).

[242] S. Raschka, *Python Machine Learning* (Packt, Birmingham, UK, 2016).

[243] P. Kim, *MATLAB Deep Learning: With Machine Learning, Neural Networks and Artificial Intelligence* (Apress, Seoul, South Korea, 2017).

[244] K. Mills, M. Spanner, and I. Tamblyn, Phys. Rev. A **96**, 042113 (2017).

[245] A. M. M. Gherman, K. Kovács, M. V. Cristea, and V. Toșa, Applied Sciences **8** (2018), ISSN 2076-3417, URL `https://www.mdpi.com/2076-3417/8/11/2106`.

[246] T. Zahavy, A. Dikopoltsev, D. Moss, G. I. Haham, O. Cohen, S. Mannor, and M. Segev, Optica **5**, 666 (2018).

[247] S. Kleinert, A. Tajalli, T. Nagy, and U. Morgner, Opt. Lett. **44**, 979 (2019).

[248] M. Lytova, M. Spanner, and I. Tamblyn (2021), `arXiv:2012.10328`.

[249] X. Liu, G. Zhang, J. Li, G. Shi, M. Zhou, B. Huang, Y. Tang, X. Song, and W. Yang, Phys. Rev. Lett. **124**, 113202 (2020).

[250] I. Goodfellow, Y. Benqio, and A. Courville, *Deep Learning* (The MIT Press, Cambridge, MA, 2016).

[251] M. Lytova, M. Spanner, and I. Tamblyn (2021), `arXiv:2102.01792`.

8. PUBLICATIONS

[P1] N. I. Shvetsov-Shilovski, M. Lein, L. B. Madsen, E. Räsänen, C. Lemell, J. Burgdörfer, D. G. Arbó, and K. Tőkési, Phys. Rev. A **94**, 013415 (2016).

[P2] N. I. Shvetsov-Shilovski, D. Dimitrovski, and L. B. Madsen, Phys. Rev. A **85**, 023428 (2012).

[P3] N. I. Shvetsov-Shilovski, M. Lein, and K. Tőkési, Eur. Phys. J. D **73**, 37 (2019).

[P4] N. I. Shvetsov-Shilovski, S. P. Goreslavski, S. V. Popruzhenko, and W. Becker, Laser Phys. **19**, 1550 (2009).

[P5] N. I. Shvetsov-Shilovski, Eur. Phys. J D **75**, 130 (2021).

[P6] N. I. Shvetsov-Shilovski, A. M. Sayler, T. Rathje, and G. G. Paulus, Phys. Rev. A **83**, 033401 (2011).

[P7] N. I. Shvetsov-Shilovski, A. M. Sayler, T. Rathje, and G. G. Paulus, New J. Phys. **13**, 123015 (2011).

[P8] N. I. Shvetsov-Shilovski, D. Dimitrovski, and L. B. Madsen, Phys. Rev. A **87**, 013427 (2013).

[P9] N. I. Shvetsov-Shilovski and M. Lein, Phys. Rev. A **100**, 053411 (2019).

[P10] C. Hofmann, A. Bray, W. Koch, H. Ni, and N. I. Shvetsov-Shilovski, Eur. Phys. J D **75**, 208 (2021).

[P11] N. I. Shvetsov-Shilovski, M. Lein, and L. B. Madsen, Phys. Rev. A **98**, 023406 (2018).

[P12] N. I. Shvetsov-Shilovski, J. Phys. B: At. Mol. Opt. Phys. **54**, 105601 (2021).

[P13] J. Solanpää, J. A. Budagosky, N. I. Shvetsov-Shilovski, A. Castro, A. Rubio, and E. Räsänen, Phys. Rev. A **90**, 053402 (2014).

[P14] N. I. Shvetsov-Shilovski, L. B. Madsen, and E. Räsänen, Phys. Rev. A **91**, 023425 (2015).

[P15] S. G. Walt, N. Ram, M. Atala, N. I. Shvetsov-Shilovski, A. von Conta, D. Baykusheva, and H. J. Wörner, Nat. Commun. **8**, 15651 (2017).

[P16] N. I. Shvetsov-Shilovski and M. Lein, Phys. Rev. A **97**, 013411 (2018).

[P17] N. I. Shvetsov-Shilovski and M. Lein, Phys. Rev. A **105**, L021102 (2022).

8.1 Semiclassical two-step model for strong-field ionization

Semiclassical two-step model for strong-field ionization

N. I. Shvetsov-Shilovski,[1,*] M. Lein,[1] L. B. Madsen,[2] E. Räsänen,[3] C. Lemell,[4]
J. Burgdörfer,[4,5] D. G. Arbó,[6] and K. Tőkési[5,7]

[1]*Institut für Theoretische Physik and Centre for Quantum Engineering and Space-Time Research,*
Leibniz Universität Hannover, D-30167 Hannover, Germany
[2]*Department of Physics and Astronomy, Aarhus University, 8000 Århus C, Denmark*
[3]*Department of Physics, Tampere University of Technology, FI-33101 Tampere, Finland*
[4]*Institute for Theoretical Physics, Vienna University of Technology, A-1040 Vienna, Austria, European Union*
[5]*Institute for Nuclear Research, Hungarian Academy of Sciences, H-4001 Debrecen, Hungary, European Union*
[6]*Institute for Astronomy and Space Physics, IAFE (UBA-Conicet), Buenos Aires, Argentina*
[7]*ELI-HU Nonprofit Ltd., Dugonics tér 13, 6720 Szeged, Hungary*
(Received 18 April 2016; published 19 July 2016)

We present a semiclassical two-step model for strong-field ionization that accounts for path interferences of tunnel-ionized electrons in the ionic potential beyond perturbation theory. Within the framework of a classical trajectory Monte Carlo representation of the phase-space dynamics, the model employs the semiclassical approximation to the phase of the full quantum propagator in the exit channel. By comparison with the exact numerical solution of the time-dependent Schrödinger equation for strong-field ionization of hydrogen, we show that for suitable choices of the momentum distribution after the first tunneling step, the model yields good quantitative agreement with the full quantum simulation. The two-dimensional photoelectron momentum distributions, the energy spectra, and the angular distributions are found to be in good agreement with the corresponding quantum results. Specifically, the model quantitatively reproduces the fanlike interference patterns in the low-energy part of the two-dimensional momentum distributions, as well as the modulations in the photoelectron angular distributions.

I. INTRODUCTION

Strong-field physics is concerned with highly nonlinear phenomena originating from the interaction of strong laser radiation with atoms and molecules. Above-threshold ionization (ATI), high-order harmonic generation, and nonsequential double ionization are the most well-known examples (see Refs. [1–5] for reviews). Among the main theoretical approaches used to understand these diverse phenomena are the direct numerical solution of the time-dependent Schrödinger equation (TDSE), the strong-field approximation (SFA) [6–8], and semiclassical models applying a classical description of an electron after it has been released from an atom, e.g., by tunneling ionization [9–11]. The most widely known examples of semiclassical approaches are the two-step model for ionization [12–14] and the three-step models for harmonic radiation and rescattering [15,16]. In the first step of the two-step model an electron tunnels out of an atom, and in the second step it propagates in the laser field. The third step involves the rescattering of the returning electron with the residual ion. Thus, the three-step model allows for a qualitative description of rescattering-induced processes: high-order ATI, high-order harmonic generation, and nonsequential double ionization.

Although significant progress has been made over the last two decades in development of the theoretical approaches based on the SFA and, particularly, on the TDSE (see, e.g., Refs. [17,18] and references therein), the semiclassical models are still extensively used in strong-field physics. The reason is

that these models have a number of advantages. Indeed, semiclassical simulations can help to identify the specific mechanisms responsible for the phenomena under consideration and provide an illustrative picture in terms of classical trajectories. For example, the three-step model explained the cutoffs in high-order harmonic generation [19,20] and high-order ATI spectra [21], the maximum angles in the photoelectron angular distributions [22], and the characteristic momenta of recoil ions of the nonsequential double ionization [23,24].

In their original formulation, the two-step and three-step models do not take into account the effect of the Coulomb potential of the parent ion on the electron motion after ionization. The inclusion of the Coulomb potential into the two-step model made it possible to reveal the so-called Coulomb focusing effect [25]. Employing classical trajectory Monte Carlo (CTMC) simulations for the second step, the Coulomb cusp in the angular distribution of strong-field ionized electrons could be identified [26]. Among the more recent examples of application of the semiclassical models with the Coulomb potential are the investigation of the so-called "ionization surprise" [27], i.e., the low-energy structures in strong-field ionization by midinfrared pulses [28–36], the study of the angular shifts of the photoelectron momentum distributions in close to circularly polarized laser fields [37–39], and the analysis of the nonadiabatic effects in strong-field ionization (see, e.g., Refs. [40–42]). Semiclassical simulations are often (but not necessarily always) computationally much simpler than the direct numerical solution of the TDSE. Sometimes rather large ensembles of classical trajectories are needed (e.g., in the present case about 10^9 trajectories) in order to get statistically reliable results or resolve fine details of the photoelectron differential distributions. Nevertheless,

---
*n79@narod.ru

semiclassical models remain powerful tools even in this situation, since trajectory-based simulations can be easily and very efficiently parallelized even on modest computer clusters. Moreover, there are still many strong-field problems, for which semiclassical models are the only feasible approach. Well-known examples of the latter category include the non-sequential double ionization of atoms by elliptically [43–45] and circularly [46] polarized fields as well as the nonsequential double ionization of molecules [47]. Therefore, improvements of the semiclassical models of strong-field phenomena are being sought with the goal to render them quantitatively predictive.

Recently, some progress among these lines has been achieved. For example, a criterion of applicability of the two-step model with the Coulomb potential of the parent ion was formulated in Ref. [48]. Within a purely classical treatment of the electron dynamics subsequent to tunnel ionization, interference structures in the photoelectron spectrum and two-dimensional momentum distribution [49–52] cannot be reproduced. This deficiency has been overcome by a semiclassical model denoted by the authors of [53] as the "quantum trajectory Monte Carlo (QTMC)."[1] This model makes it possible to include interference effects into the two-step model with the Coulomb potential. Accordingly, each classical trajectory is associated with a phase determined by the classical action, and the contributions of all trajectories leading to a given final momentum calculated by a CTMC approach are added coherently. The QTMC model has already been used in the study of nonadiabatic effects in tunneling ionization of atoms in elliptically polarized laser fields [42]. A similar approach, but disregarding the Coulomb potential, was used in Ref. [55] to investigate the holographic interference patterns in strong-field ionization of N_2, O_2, and CO_2. Very recently, the QTMC model has been applied to the identification of resonance structures in the low-energy part of the photoelectron spectra [56] and to the study of the nonadiabatic subcycle electron dynamics in orthogonally polarized two-color laser fields [57].

The Coulomb-corrected strong-field approximation (CCSFA) [30,58,59] has been applied to analyze results of experiment and theory. The CCSFA invokes first-order perturbation theory [60] to include the Coulomb potential. Likewise, according to the Supplemental Material in Ref. [53], the QTMC model includes the Coulomb effect in a perturbative manner, a point that we discuss below. It is, therefore, of interest to formulate a semiclassical two-step (SCTS) model that accounts for the Coulomb potential beyond the semiclassical perturbation theory. Our present approach is based on the theory of semiclassical time-dependent propagators (see, e.g., Refs. [61,62] for a textbook treatment). Here we derive a semiclassical expression for the transition amplitude for strong-field ionization that differs from the

one used in the QTMC and CCSFA models improving the agreement with full quantum simulations.

The paper is organized as follows. In Sec. II we briefly review previous two-step models that invoke semiclassical approximations at various stages of their development. In Sec. III we present our semiclassical two-step model that combines the CTMC method for trajectory sampling with the phase of the semiclassical propagator and discuss its numerical implementation. The application to the benchmark case of strong-field ionization of atomic hydrogen and the comparison with TDSE results are presented in Sec. IV, followed by concluding remarks in Sec. V. Atomic units are used throughout the paper unless indicated otherwise.

II. TWO-STEP MODELS

The two-step models for direct strong-field ionization as well as their three-step extensions typically invoke semiclassical approximations to the full quantum dynamics at various levels. We briefly sketch the major steps involved in order to delineate the point of departure of the present SCTS model. It should be stressed that our model is different from SFA-type models such as the CCSFA model [30,58,59] as the latter are applicable for arbitrary values of the Keldysh parameter $\gamma = \omega\kappa/F$ [6] (here ω is the angular frequency of the laser field, F is the field amplitude, and $\kappa = \sqrt{2I_p}$, where I_p is the ionization potential). In contrast to this, we employ instantaneous tunneling ionization rates. The description of the ionization step by tunneling is expected to be accurate only for small values of the Keldysh parameter, $\gamma \ll 1$.

The starting point of the semiclassical approximation is the assumption that the (classical) action in the Feynman propagator is asymptotically large compared to the quantum action $\hbar$ such that the path integral over (in general, nonclassical) paths can be performed by the saddle-point approximation. Equivalently, the semiclassical approximation can be viewed as the leading term in an $\hbar^n$ expansion as $\hbar \to 0$. Accordingly, the expression for the matrix element of the semiclassical propagator U_{SC} between the initial state at time t_1 and the final state at time $t_2 (t_2 > t_1)$ reads [63–65] (see Refs. [61] and [62] for a textbook treatment)

$$\langle \vec{r}_2 | U_{SC}(t_2, t_1) | \vec{r}_1 \rangle = \left[-\frac{\det(\partial^2 \phi_1(\vec{r}_1, \vec{r}_2)/\partial \vec{r}_1 \partial \vec{r}_2)}{(2\pi i)^3} \right]^{1/2}$$
$$\times \exp[i\phi_1(\vec{r}_1, \vec{r}_2)]. \quad (1)$$

Here $\vec{r}_1$ and $\vec{r}_2$ are the spatial coordinates of a particle at times t_1 and t_2, respectively, and the phase $\phi_1(\vec{r}_1, \vec{r}_2) = S_1(\vec{r}_1, \vec{r}_2)/\hbar$ is given in terms of the action S_1,

$$S_1(\vec{r}_1, \vec{r}_2) = \int_{t_1}^{t_2} \{\vec{p}(t)\dot{\vec{r}}(t) - H[\vec{r}(t), \vec{p}(t)]\}dt, \quad (2)$$

where, in turn, $H[\vec{r}(t), \vec{p}(t)]$ is the classical Hamiltonian function as a function of the canonical coordinates $\vec{r}(t)$ and momenta $\vec{p}(t)$. In dipole approximation the Hamiltonian function of an electron moving in laser and Coulomb fields is

---

[1]This model should not be confused with another approach termed quantum trajectory Monte Carlo that was used for the solution of the Liouville equation for open quantum systems [54]. It is based on an ensemble of solutions of a stochastic Schrödinger equation, each of which corresponds to a quantum trajectory in Hilbert space.

given by

$$H[\vec{r}(t), \vec{p}(t)] = \frac{p^2(t)}{2} + \vec{F}(t) \cdot \vec{r}(t) - \frac{Z}{r(t)}, \qquad (3)$$

where $\vec{F}(t)$ is the electric field and Z is the ionic charge. The prefactor in Eq. (1) contains the determinant of $-\partial^2 S_1 / \partial \vec{r}_1 \partial \vec{r}_2$, frequently referred to as the van Vleck (vV) determinant for multidimensional systems, which is independent of $\hbar$. The phase factor $\exp(i\phi_i)$ is nonanalytic as $\hbar \to 0$ and accounts for the nonuniform approach to the classical limit via increasingly fast oscillations (see Ref. [66]).

For classically allowed processes, the vV-determinant governs the classical phase-space density (or probability density) for the phase flow from $\vec{r}_1$ to $\vec{r}_2$ within the time interval $t_2 - t_1$. Higher-order corrections in $\hbar$ are neglected in Eq. (1) from the outset. Using atomic units in the following we do not display the $\hbar$ dependence explicitly but, instead, express the semiclassical limit in terms of the de Broglie wavelength λ_{dB} exploiting the equivalence of vanishing de Broglie wavelength $\lambda_{dB} \to 0$ and the limit $\hbar \to 0$.

The point to be emphasized is that the applicability of the saddle-point approximation, and, in turn, the semiclassical limit for the ionization process in the presence of laser and Coulomb fields is, *a priori*, not obvious. The tunneling process is intrinsically nonclassical and the de Broglie wavelength $\lambda_{dB}(E)$ of slow electrons close to the tunneling exit is, in general, not small compared to the exit coordinate η or the width of the barrier; i.e., the semiclassical relation $\lambda_{dB} \ll \eta$ is violated.

A. Semiclassical approximation for the first step

The starting point for the first step of strong-field ionization, the tunneling through the barrier formed by the atomic (ionic) potential and the interaction with the electromagnetic field, is the quantum transition matrix element in distorted-wave Born approximation (SFA)

$$M_{\mathrm{SFA}}(\vec{k}) = -i \int_{-\infty}^{\infty} dt \langle \psi_{\vec{k}}(t) | V_L(t) | \psi_i(t) \rangle, \qquad (4)$$

where $|\psi_i(t)\rangle$ is the bound initial state and $|\psi_{\vec{k}}(t)\rangle$ is the Volkov state after tunneling with the asymptotic momentum $\vec{k}$,

$$\psi_{\vec{k}}(\vec{r},t) = \exp\left\{ i[\vec{k} + \vec{A}(t)/c]\vec{r} - \frac{i}{2} \int_{-\infty}^{t} dt'[\vec{k} + \vec{A}(t')/c]^2 \right\}. \qquad (5)$$

Equation (4) is referred to as the strong-field approximation as in the final state the ionic potential is considered to be negligible in comparison to the interaction $V_L(t) = \vec{F}(t) \cdot \vec{r}$. Note that we use a length gauge in Eqs. (4) and (5) and define the strong electric field $\vec{F}(t) = -\frac{1}{c}\frac{d\vec{A}}{dt}$ through the vector potential $\vec{A}(t)$. The time integral is evaluated within the framework of the saddle-point approximation assuming that the effective phase (or action)

$$S(\vec{k},t) = \int_{-\infty}^{t} dt' \left\{ \frac{1}{2}[\vec{k} + \vec{A}(t')/c]^2 - \varepsilon_i \right\} \qquad (6)$$

is large and rapidly varying with t, thereby invoking the semiclassical (SC) limit. The prerequisites for the applicability

of this semiclassical limit are the ponderomotive energy U_p and the ionization potential $I_p = -\varepsilon_i$ to be large compared to the photon energy ω, $U_p/\omega \gg 1$ and $I_p/\omega \gg 1$. Unlike Eq. (1), the semiclassical approximation is applied to the transition matrix element [Eq. (4)] rather than to the propagator. Accordingly (see, e.g., [67,68]),

$$M_{\mathrm{SFA}}^{\mathrm{SC}} = \sum_j \frac{\exp\left[i S(\vec{k}, t_s^j) \right]}{\left[\frac{\partial^2}{\partial t^2} S(\vec{k}, t_s^j) \right]^{1/2}} V_{\vec{k}}^j, \qquad (7)$$

with $V_{\vec{k}}^j$ containing the spatial dependencies of the transition matrix element. The saddle-point equation

$$\frac{\partial}{\partial t} S(\vec{k}, t_s) = \frac{1}{2}[\vec{k} + \vec{A}(t_s)/c]^2 + I_p = 0 \qquad (8)$$

has complex solutions in t, $t_s^j = t_0^j + i t_t^j$, where the real part t_0 is referred to as the ionization time and the imaginary part t_t as the tunneling time. Because of the complex solutions, the emerging trajectories are often referred to as quantum trajectories; see Refs. [67,69]. When more than one saddle point contributes ($j = 1, \ldots$), Eq. (7) can give rise to semiclassical path interferences.

Frequently employed approximate evaluations of Eq. (7) include the Perelomov-Popov-Terent'ev or Ammosov-Delone-Krainov rates for adiabatic tunneling in which t_0 coincides with the extremum of the electric field F [9–11]:

$$w(t_0, v_{0,\perp}) \sim \left| M_{\mathrm{SFA}}^{\mathrm{SC}} \right|^2$$

$$\sim \exp\left[-\frac{2\kappa^3}{3F(t_0)} \right] \exp\left[-\frac{\kappa v_{0,\perp}^2}{F(t_0)} \right]. \qquad (9)$$

For simplicity, we omit the preexponential factor in Eq. (9). Although this factor changes the total ionization rate by several orders of magnitude, for atoms it only slightly affects the shape of the photoelectron momentum distributions. When applying Eq. (9), a simple and frequently used choice is that the electron emerges with vanishing velocity component along the laser polarization direction $v_{0,z} = 0$, while $v_{0,\perp}$ is Gaussian distributed. It is common to apply Eq. (9) as a quasistatic rate [70], i.e., for tunneling ionization for laser phases other than the field extremum, with $F(t_0)$ in Eq. (9) denoting the instantaneous field. Nonzero longitudinal velocity components $v_{0,z} \neq 0$ appear near the tunnel exit when the subbarrier motion is modeled by the strong-field approximation [71].

The coordinates of the tunneling exit can be conveniently determined by using the fact that for an electron in a time-independent electric field F and the Coulomb potential, $-Z/r$, both the classical Hamilton-Jacobi equation [72] and the stationary Schrödinger equation are separable in parabolic coordinates (see Refs. [9,73])

$$\xi = r + z, \quad \eta = r - z, \quad \phi = \arctan\left(\frac{y}{x}\right). \qquad (10)$$

If the electric field points along the positive z direction, the electron is trapped by an attractive potential along the ξ coordinate and can tunnel out only in the η direction. The

tunnel exit coordinate η is then obtained from the equation

$$-\frac{\beta_2(F)}{2\eta} + \frac{m^2 - 1}{8\eta^2} - \frac{F\eta}{8} = -\frac{I_p(F)}{4}, \qquad (11)$$

where

$$\beta_2(F) = Z - (1 + |m|)\frac{\sqrt{2I_p(F)}}{2} \qquad (12)$$

is the separation constant (see, e.g., Ref. [74]) and m is the magnetic quantum number of the initial state. In Eq. (12) we have allowed for the Stark shift of the initial state, i.e., of the ionization potential,

$$I_p(F) = I_p + \tfrac{1}{2}(\alpha_N - \alpha_I)F^2, \qquad (13)$$

where F is the instantaneous field amplitude at the ionization time t_0 and α_N and α_I are the static polarizabilities of an atom and of its ion, respectively [75]. With Eqs. (11) and (9), the initial conditions for the propagation of trajectories subsequent to tunneling ionization, i.e., for the second step, are determined.

As the focus of the present work is the improved semiclassical description of the second step, we treat in the following the output of the first step, in particular the initial velocity (or momentum) distribution at the tunneling exit [see, e.g., Eq. (9)] as adjustable input. We use two different initial phase-space distributions resulting from the tunneling step as initial conditions for the post-tunneling semiclassical propagation. Both choices of distributions are described by Eq. (9). The difference is that in one case, the initial parallel velocity $v_{0,z}$ is set to zero, whereas in the other case, it is set to a nonzero value predicted by the SFA [71].

B. Semiclassical approximation for the second step

The position and momentum distributions at the tunneling exit serve as initial conditions for the propagation of classical trajectories in the second step. In the simplest approximation, the quiver motion for a selected set of trajectories for free electrons in the electromagnetic field is treated, thereby neglecting the atomic force field [14–16,20]. More advanced descriptions employ full CTMC simulations treating the laser field and the atomic force field on equal footing by solving Newton's equation of motion,

$$\frac{d^2\vec{r}(t)}{dt^2} = -\vec{F}(t) - \frac{Z\vec{r}(t)}{r^3(t)}, \qquad (14)$$

for a large number of initial conditions (typically $\geqslant 10^7$), thereby sampling the initial phase-space distribution after tunneling [26].

For the propagation of the electron in the combined fields [Eq. (14)], a semiclassical approximation in terms of a coherent superposition of amplitudes appears justified since classical-quantum correspondence holds separately for both the propagation in the Coulomb field and in the laser field. For the linear potential of a charged particle in the external field, $V_L = \vec{F} \cdot \vec{r}$, the Ehrenfest theorem holds for Newton's law, $\langle \vec{\nabla} V_L \rangle = \vec{\nabla} V_L(\langle \vec{r} \rangle)$. For the long-range Coulomb potential $\lambda_{dB}(E)$ is negligible compared to the infinite range of the potential at any energy E. However, an extension of CTMC simulations to the semiclassical domain faces considerable

difficulties in view of the intrinsic numerical instability, which is closely related to the nonuniform convergence to the classical limit mentioned above. Superposition of a large number of amplitudes associated with trajectories with rapidly oscillating phases fails to yield converged scattering amplitudes in the asymptotic limit $t \to \infty$ [66]. One key ingredient is therefore the binning of the trajectories according to the appropriate final canonical momenta and restricting coherent superpositions to those trajectories within each bin. For bound-state excitation driven by ultrashort pulses this corresponds to binning of the action variable, i.e., to a quantization of classical trajectories. This quantized classical trajectory Monte Carlo method [76] can accurately account for quantum revivals and dephasing in Rydberg manifolds.

For strong-field ionization, the final states lie in the continuum and are binned according to their momenta in cells in momentum space [42,57], $[k_i, k_i + \Delta k_i]$, with $i = x, y, z$. Accordingly, the amplitudes associated with all n_p trajectories taking off at t_0^j with initial velocity $\vec{v}_0^j$ ($j = 1, \ldots, n_p$) reaching the same bin centered at $\vec{k} = (k_x, k_y, k_z)$ are added coherently. Thus, the ionization probability $R(\vec{k})$ for this final momentum $\vec{k}$ is given by

$$R(\vec{k}) = \left| \sum_{j=1}^{n_p} \sqrt{w(t_0^j, \vec{v}_0^j)} \exp\left[i \Phi(t_0^j, \vec{v}_0^j) \right] \right|^2, \qquad (15)$$

where $w(t_0^j, v_0^j)$ is the probability density of the initial conditions. The sum over j samples the classical phase flow from $\vec{v}_0$ to the bin $\vec{k}$ corresponding to the vV determinant as determined by CTMC. $\Phi(t_0^j, \vec{v}_0^j)$ is the phase that each trajectory carries. When the interference phases of trajectories reaching the same bin are neglected, the classical CTMC probability density

$$R(\vec{k}) = \sum_{j=1}^{n_p} w(t_0^j, \vec{v}_0^j) \qquad (16)$$

emerges. In the QTMC model [53], the phase in Eq. (15) was approximated by

$$\Phi^{\text{QTMC}}(t_0^j, \vec{v}_0^j) \approx I_p t_0^j - \int_{t_0^j}^{\infty} \left[\frac{p^2(t)}{2} - \frac{Z}{r(t)} \right] dt. \qquad (17)$$

We relate the phase in Eq. (17) to our semiclassical phase in Sec. III A.

III. FORMULATION OF THE MODEL

A. Semiclassical expression for the phase

The two key ingredients of the present semiclassical two-step model are the choice of an initial momentum distribution emerging from the first tunneling step based on SFA estimates and a proper semiclassical description for the second step. This approach accounts for the expectation that the semiclassical limit is applicable for the evolution of the liberated electron in the combined laser and ionic force fields. We describe the second step of the two-step model using the expression for the matrix element of the semiclassical propagator U_{SC}.

In addition to its coordinate representation [Eq. (1)], three equivalent forms involving different combinations of phase-space coordinates exist [63,77]:

$$\langle \vec{r}_2 | U_{\text{SC}}(t_2,t_1) | \vec{p}_1 \rangle = \left[-\frac{\det(\partial^2 \phi_2(\vec{p}_1,\vec{r}_2)/\partial \vec{p}_1 \partial \vec{r}_2)}{(2\pi i)^3} \right]^{1/2}$$
$$\times \exp[i\phi_2(\vec{p}_1,\vec{r}_2)], \qquad (18a)$$

$$\langle \vec{p}_2 | U_{\text{SC}}(t_2,t_1) | \vec{r}_1 \rangle = \left[-\frac{\det(\partial^2 \phi_3(\vec{r}_1,\vec{p}_2)/\partial \vec{r}_1 \partial \vec{p}_2)}{(2\pi i)^3} \right]^{1/2}$$
$$\times \exp[i\phi_3(\vec{r}_1,\vec{p}_2)], \qquad (18b)$$

$$\langle \vec{p}_2 | U_{\text{SC}}(t_2,t_1) | \vec{p}_1 \rangle = \left[-\frac{\det(\partial^2 \phi_4(\vec{p}_1,\vec{p}_2)/\partial \vec{p}_1 \partial \vec{p}_2)}{(2\pi i)^3} \right]^{1/2}$$
$$\times \exp[i\phi_4(\vec{p}_1,\vec{p}_2)]. \qquad (18c)$$

They describe the propagation from the initial position $(\vec{r}_1)$ or momentum coordinate $(\vec{p}_1)$ to a final position $(\vec{r}_2)$ or momentum coordinate $(\vec{p}_2)$ within the time interval $t_2 - t_1$. The phases ϕ_i, $i = 2,3,4$ in Eqs. (18a)–(18c) are given by the classical action associated with the corresponding canonical transformations,

$$\phi_2(\vec{p}_1,\vec{r}_2) = \phi_1(\vec{r}_1,\vec{r}_2) + \vec{p}_1 \cdot \vec{r}_1, \qquad (19a)$$

$$\phi_3(\vec{r}_1,\vec{p}_2) = \phi_1(\vec{r}_1,\vec{r}_2) - \vec{p}_2 \cdot \vec{r}_2, \qquad (19b)$$

$$\phi_4(\vec{p}_1,\vec{p}_2) = \phi_1(\vec{r}_1,\vec{r}_2) + \vec{p}_1 \cdot \vec{r}_1 - \vec{p}_2 \cdot \vec{r}_2, \qquad (19c)$$

with $\phi_1(\vec{r}_1,\vec{r}_2)$ given by Eq. (2).

It is now of interest to inquire which of the propagator matrix elements is appropriate for the second step of strong-field ionization. Semiclassical scattering characterized by a transition from momentum $\vec{p}_1$ at $t \to -\infty$ to $\vec{p}_2$ at $t \to \infty$ is described by the propagator Eq. (18c) with the compensated action ϕ_4 given by [Eq. (19c)]:

$$\phi_4(\vec{p}_1,\vec{p}_2) = \int_{t_1}^{t_2} \{-\vec{r}(t) \cdot \dot{\vec{p}}(t) - H[\vec{r}(t),\vec{p}(t)]\} dt. \qquad (20)$$

For strong-field ionization representing a half-scattering process of an electron initially located near the nucleus and emitted with final momentum $\vec{p}_2(t \to \infty)$, the propagator Eq. (18b) with action ϕ_3 should be applicable for trajectories launched with initial phase $\exp(i I_p t_0)$ according to the time evolution of the ground state. This choice is based on the assumption of well-localized starting points in coordinate space $\vec{r}_1$ near the tunnel exit [Eq. (11)] with negligible phase accumulation under the barrier in position-space representation. We have

$$\phi_3(\vec{r}_1,\vec{p}_2) = \phi_4(\vec{p}_1,\vec{p}_2) - \vec{p}_1 \cdot \vec{r}_1. \qquad (21)$$

Since in length gauge $\vec{v}_0 = \vec{p}_1$, $\vec{p}_1$ is orthogonal to $\vec{r}_1$ in the limit of vanishing longitudinal velocity at the tunneling exit ($v_{0,z} = 0$) and, hence, ϕ_3 and ϕ_4 coincide. In the following we include the phase contribution $\vec{p}_1 \cdot \vec{r}_1$ for nonzero $v_{0,z}$. Its contribution to the interference pattern discussed below is numerically found, however, to be of minor importance.

In our model we restrict ourselves to exponential accuracy. Thus, we ignore the preexponential factor of the matrix element. Using $\phi_3(\vec{r}_1,\vec{p}_2)$ in Eq. (15) yields the semiclassical approximation for the phase corresponding to a given

trajectory

$$\Phi(t_0^j,\vec{v}_0^j) = -\vec{v}_0^j \cdot \vec{r}(t_0^j) + I_p t_0^j$$
$$- \int_{t_0^j}^{\infty} dt \{\dot{\vec{p}}(t) \cdot \vec{r}(t) + H[\vec{r}(t),\vec{p}(t)]\}$$
$$= -\vec{v}_0^j \cdot \vec{r}(t_0^j) + I_p t_0^j - \int_{t_0^j}^{\infty} dt \left\{ \frac{p^2(t)}{2} - \frac{2Z}{r(t)} \right\}. \qquad (22)$$

To arrive at this result, $\dot{\vec{p}}$ is expressed in terms of the negative gradient of the total potential containing the electric field and the Coulomb potential. In the case of an arbitrary effective potential $V(\vec{r})$, the Hamiltonian function $H[\vec{r}(t),\vec{p}(t)]$ reads

$$H[\vec{r}(t),\vec{p}(t)] = \frac{p^2(t)}{2} + \vec{F}(t) \cdot \vec{r}(t) + V(\vec{r}) \qquad (23)$$

and Newton's equation of motion,

$$\dot{\vec{p}} = -\vec{F}(t) - \vec{\nabla} V[\vec{r}(t)]. \qquad (24)$$

Using Eqs. (23) and (24) to derive the integrand in Eq. (20) we obtain from Eq. (21) the following expression for the phase:

$$\Phi(t_0^j,\vec{v}_0^j) = -\vec{v}_0^j \cdot \vec{r}(t_0^j) + I_p t_0^j$$
$$- \int_{t_0^j}^{\infty} dt \left\{ \frac{p^2(t)}{2} + V[\vec{r}(t)] - \vec{r}(t) \cdot \vec{\nabla} V[\vec{r}(t)] \right\}. \qquad (25)$$

Equation (22) is a special case of Eq. (25) when $V(\vec{r})$ is set to the Coulomb potential $-Z/r$. Equation (25) is applicable to effective one-electron descriptions of ionization of multi-electron systems employing model or pseudopotentials [78]. It should be noted, however, that in the presence of a strong short-ranged contribution to $V(\vec{r})$ the validity of the underlying semiclassical approximation, $\lambda_{dB} \ll R$, where R is the range of the short-ranged contribution, is not obvious and remains to be verified.

For the Coulomb potential $V(\vec{r}) = -Z/r$, the phase of the QTMC model can be obtained from Eq. (25) by omitting the term $\vec{r}(t) \cdot \vec{\nabla} V[\vec{r}(t)]$ in the integrand of Eq. (25). Thus, the semiclassical phase given by Eq. (22) differs from that of the QTMC model [Eq. (17)]: The Coulomb interaction enters with doubled weight. The factor 2 originates from properly accounting for elastic scattering in Eqs. (19b) and (25), i.e., from fully accounting for the Coulomb potential in the compensated action $\phi_4(\vec{p}_1,\vec{p}_2)$. Note, that this compensated action accounts for elastic scattering also in the absence of time-dependent processes. By contrast, Eq. (17) yields for any time-independent Hamiltonian only a trivial trajectory-independent phase $\sim \int dt (H + I_p)$. The QTMC phase can therefore be viewed as an approximation to the full semiclassical phase, Eq. (22).

B. Numerical implementation

In the presence of long-range interactions the calculation of the semiclassical transition amplitude [Eq. (15)] for strong-field ionization requires special care in view of divergent phases and the large number of trajectories for a dense

N. I. SHVETSOV-SHILOVSKI *et al.*

sampling of phase space needed for achieving sufficient resolution for the multidifferential ionization probability.

We subdivide the integration interval $[t_0^j, \infty]$ into two intervals, $[t_0^j, \tau_f]$ and $[\tau_f, \infty]$, where τ_f is the time at which the laser pulse has concluded and beyond which the energy $H(\tau_f) = E$ is conserved along the outgoing Kepler hyperbola. For pure Coulomb potentials the asymptotic phase-space coordinates $(\vec{k})$ can be determined by the analytic Coulomb mapping of the coordinates $[\vec{r}(\tau_f), \vec{p}(\tau_f)]$ for given energy E,

$$\frac{k^2}{2} = \frac{p^2(\tau_f)}{2} - \frac{1}{r(\tau_f)}, \tag{26}$$

the angular momentum,

$$\vec{L} = \vec{r}(\tau_f) \times \vec{p}(\tau_f), \tag{27}$$

and the Runge-Lenz vector,

$$\vec{a} = \vec{p}(\tau_f) \times \vec{L} - \vec{r}(\tau_f)/r(\tau_f). \tag{28}$$

The asymptotic momentum follows from (see Ref. [39], which corrects the misprint in [79])

$$\vec{k} = k \frac{k(\vec{L} \times \vec{a}) - \vec{a}}{1 + k^2 L^2}. \tag{29}$$

The phase Eq. (22) can be analogously decomposed as

$$\Phi(t_0^j, \vec{v}_0^j) = -\vec{v}_0^j \cdot \vec{r}(t_0^j) + I_p t_0^j - \int_{t_0^j}^{\tau_f} dt \left\{ \frac{p^2(t)}{2} - \frac{2Z}{r(t)} \right\}$$
$$- \int_{\tau_f}^{\infty} dt \left\{ E - \frac{Z}{r(t)} \right\}. \tag{30}$$

We furthermore separate the last term in Eq. (30) representing the scattering phase accumulated in the asymptotic interval $[\tau_f, \infty]$ into the parts with time-independent and time-dependent integrand. The first part yields the linearly divergent contribution

$$\lim_{t \to \infty} E(t - \tau_f). \tag{31}$$

Since only the relative phase between those trajectories arriving in the same bin contribute to the probability (15) whose final momenta and, therefore, energies coincide, the relative phase $(E_j - E_{j'})(t - \tau_f)$ vanishes. This allows for the reduction of the integral for the interval $[\tau_f, \infty]$ to the Coulomb phase,

$$\Phi_f^C(\tau_f) = Z \int_{\tau_f}^{\infty} \frac{dt}{r(t)}, \tag{32}$$

which is still divergent. The regularization of this integral can be performed by analytic Coulomb mapping for Kepler hyperbolae: The distance from the Coulomb center (i.e., from the ion) at a given time t reads (see, e.g., Ref. [80])

$$r(t) = b(g \cosh \xi - 1), \tag{33}$$

where $b = 1/(2E)$, $g = \sqrt{1 + 2EL^2}$, and the parameter $\xi = \xi(t)$ is determined from

$$t = \sqrt{b^3}(g \sinh \xi - \xi) + C. \tag{34}$$

The constant C in Eq. (34) can be found from the initial conditions for the motion in the Coulomb field, i.e., from the

position $\vec{r}(\tau_f)$ and momentum $\vec{p}(\tau_f)$ of an electron at $t = \tau_f$. With Eqs. (33) and (34) the integral in Eq. (32) gives

$$\Phi_f^C(\tau_f) = Z\sqrt{b}[\xi(\infty) - \xi(\tau_f)]. \tag{35}$$

Thus, for every trajectory we need to calculate $\xi(\infty)$ and $\xi(\tau_f)$. Since $\xi \to \infty$ for $t \to \infty$, we can discard the decaying exponent in $\sinh \xi = [\exp(\xi) + \exp(-\xi)]/2$ and neglect both C and ξ compared to $\exp(\xi)$ in the asymptotic limit [Eq. (34)]. Consequently, we find for asymptotically large ξ

$$t \approx \sqrt{b^3} g \exp(\xi)/2, \tag{36}$$

from which follows

$$\xi(t \to \infty) \approx \ln\left(\frac{2t}{g\sqrt{b^3}}\right). \tag{37}$$

It is clear that $\xi(t)$ diverges at $t \to \infty$. However, we can isolate the divergent part of Eq. (37), which is common for all the trajectories interfering in a given bin of momentum space, from the finite contributions specific for every individual trajectory. Indeed, we are interested in the relative phases of the interfering trajectories within the same bin, and b depends only on the energy E. Therefore, the common divergent part is given by $\ln(2t/\sqrt{b^3})$, and the finite contribution of every trajectory to the phase [Eq. (30)] is equal to $-\ln(g)$. Note that g depends on both electron energy and angular momentum L. The latter is different for different interfering trajectories within a given bin of the momentum space. For the lower boundary in Eq. (35) we find from Eq. (33)

$$\xi(\tau_f) = \pm \operatorname{arcosh}\left\{\frac{1}{g}\left[\frac{r(\tau_f)}{b} + 1\right]\right\}, \tag{38}$$

where the sign still needs to be determined. Taking into account that $dr/dt = \vec{r}\vec{v}/r$ and $dr/dt = (dr/d\xi)/(dt/d\xi)$ and using Eqs. (33) and (34), we find for $\xi(\tau_f)$

$$\xi(\tau_f) = \operatorname{arsinh}\left\{\frac{\vec{r}(\tau_f) \cdot \vec{p}(\tau_f)}{g\sqrt{b}}\right\}. \tag{39}$$

Thus, the finite interference contribution $\tilde{\Phi}_f^C(\tau_f)$ from the Coulomb phase becomes

$$\tilde{\Phi}_f^C(\tau_f) = -Z\sqrt{b}\left[\ln g + \operatorname{arsinh}\left\{\frac{\vec{r}(\tau_f) \cdot \vec{p}(\tau_f)}{g\sqrt{b}}\right\}\right]. \tag{40}$$

We note that such asymptotic Coulomb phase contributions are missing in the QTMC model [53].

In order to achieve convergent semiclassical amplitudes based on Monte-Carlo sampling of a large number of classical trajectories, efficient sampling of initial conditions is essential. One possible method employs initial sets of t_0 and $\vec{v}_0$ that are either uniformly randomly distributed or distributed on a uniform grid (e.g., in Ref. [53]). This results in sampling of a large number of trajectories with relatively small weights [see, e.g., Eq. (9)], which contribute to the final momentum distribution only to a small extent.

Here we implement an alternative Monte Carlo algorithm based on importance sampling. Accordingly, the importance (weight) of a given trajectory is accounted already at the sampling stage, i.e., before the integration of the equations of motion (14). This means that initial sets of t_0 and $\vec{v}_0$ are distributed taking into account the tunneling probability

$w(t_0,v_{0,\perp})$. Importance sampling is a standard method in Monte Carlo integration [81] and is also used in many semiclassical simulations of above-threshold ionization disregarding interference effects (see, e.g., Refs. [22,79]). In the absence of interference effects, the classical probability density $R(\vec{k})$ is calculated within the importance sampling approach as a number of trajectories ending up in a given bin [instead of using Eq. (16) for uniformly distributed initial sets].

Importance sampling is particularly significant in the presence of interference because typically many more trajectories are needed to resolve fine interference structures compared to CTMC simulations without interference (see Sec. IV). Calculation of the ionization probability with trajectories selected by importance sampling is given [instead of Eq. (15)] by

$$R\left(\vec{k}\right) = \left| \sum_{j=1}^{n_p} \exp\left[i\,\Phi\left(t_0^j, \vec{v}_0^j\right)\right] \right|^2, \qquad (41)$$

with ionization times t_0^j and initial velocities $\vec{v}_0^j$ distributed according to the *square root* of the tunneling probability, $\sqrt{w(t_0,\vec{v}_0)}$ [Eq. (9)]. Depending on the laser parameters and tunneling probabilities this importance sampling algorithm can significantly increase the computational speed and convergence as a function of the number of simulated trajectories.

IV. RESULTS AND DISCUSSION

In our simulations we use a few-cycle linearly polarized laser pulse defined in terms of a vector potential that is present between $t = 0$ and $t = \tau_f$,

$$\vec{A}(t) = (-1)^{n+1}\frac{cF_0}{\omega}\sin^2\left(\frac{\omega t}{2n}\right)\sin(\omega t)\vec{e}_z. \qquad (42)$$

Here $\vec{e}_z$ is the unit vector pointing in polarization direction and n is the number of optical cycles of the field with $\tau_f = 2\pi n/\omega$. The electric field is obtained from Eq. (42) by $\vec{F}(t) = -\frac{1}{c}\frac{d\vec{A}}{dt}$. We define the vector potential $\vec{A}(t)$ with a prefactor $(-1)^{n+1}$ [Eq. (42)] in order to ensure that the electric field has its maximum at the center of the pulse at $\omega t = \pi n$ for both even and odd numbers of cycles n. We solve Newton's equations of motion using a fourth-order Runge-Kutta method with adaptive step size [81] and calculate the phase [Eq. (22)] by adding an extra equation to the system of equations of motion.

Because of the rotational symmetry with respect to the polarization direction of the laser pulse the semiclassical simulations for a linearly polarized field can be performed employing only two degrees of freedom $(z, r_\perp)$. This reduces the numerical complexity of the problem significantly. Indeed, in order to achieve convergence of the interference oscillations, we need about 1.6×10^9 trajectories (for a comparison, 1.5×10^6 trajectories were sufficient in the CTMC simulation to calculate electron momentum distributions without interference [39]). Nearly the same number of trajectories is used in CCSFA calculations (see, e.g., Ref. [30]). Thus, about 1000 times more trajectories are needed for the semiclassical simulations when interference is included. Simulations of

interactions with elliptically or circularly polarized laser fields will require an even larger number of trajectories.

Importance sampling reduces the number of trajectories required to reach convergence of the photoelectron spectrum by a factor 4–5. Typically, we need with importance sampling 4×10^8 trajectories at 800 nm and 1.6×10^9 trajectories at 1200 and 1600 nm. It should be stressed, however, that the performance of numerical approaches employing a uniform distribution of the initial conditions strongly depends on the distribution of initial conditions. The maximum modulus of the initial transverse velocity $v_{0,\perp}$ in the aforementioned example is chosen to correspond to an ionization probability of 10^{-6} of the maximum value of $w(t_0,v_{0,\perp})$ [the latter is achieved for $v_{0,\perp} = 0$; see Eq. (9)] when considering ionization at the field maximum. Moreover, the efficiency depends also on the laser-atom parameters and the calculated observable.

We benchmark our present SCTS model against the exact numerical solution of the time-dependent Schrödinger equation and also compare with results of the previous QTMC model. In order to numerically solve the TDSE

$$i\frac{\partial|\psi(t)\rangle}{\partial t} = \left\{-\frac{\Delta}{2} + V(r) + zF(t)\right\}|\psi(t)\rangle \qquad (43)$$

in the dipole approximation for a single active electron, we employ the generalized pseudospectral method [82–84]. This method combines the discretization of the radial coordinate optimized for the Coulomb singularity with quadrature methods to allow stable long-time evolution using a split-operator representation of the time-evolution operator. Both the bound as well as the unbound parts of the wave function $|\psi(t)\rangle$ can be accurately represented. The atomic potential $V(r)$ is taken to be the Coulomb potential, $V(r) = -1/r$. Propagation of the wave function is started from the ground state of hydrogen. Due to the cylindrical symmetry of the system, the magnetic quantum number $m = 0$ is conserved. After the end of the laser pulse the wave function is projected on eigenstates $|k,\ell\rangle$ of the free atomic Hamiltonian with positive eigenenergy $E = k^2/2$ and orbital quantum number ℓ to determine the transition probabilities $R(\vec{k})$ to reach the final state $|\phi_{\vec{k}}\rangle$ (see Refs. [85–87]):

$$R(\vec{k}) = \frac{1}{4\pi k}\left| \sum_l e^{i\delta_\ell(k)}\sqrt{2l+1}\,P_\ell(\cos\theta)\langle k,\ell|\psi(t_f)\rangle \right|^2. \qquad (44)$$

In Eq. (44), $\delta_\ell(k)$ is the momentum-dependent atomic phase shift, θ is the angle between the electron momentum $\vec{k}$ and the polarization direction of the laser field $\vec{e}_z$ and P_ℓ is the Legendre polynomial of degree ℓ. In order to avoid unphysical reflections of the wave function at the boundary of the system, the length of the computing box was chosen to be 1200 a.u. ($\sim$65 nm), which is much larger than the maximum quiver amplitude $\alpha = F_0/\omega^2 = 62$ a.u. at the intensity of 0.9×10^{14} W/cm^2 and the wavelength of 1600 nm. The maximum angular momentum included was $\ell_{\max} = 300$.
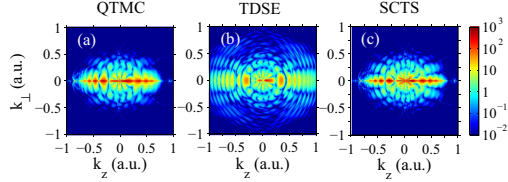
FIG. 1. Vectorial momentum distributions for the H atom ionized by a laser pulse with a duration of $n = 8$ cycles, wavelength of $\lambda = 800$ nm, and peak intensity of $I = 0.9 \times 10^{14}$ W/cm^2 obtained from (a) the QTMC model, (b) solution of the TDSE, and (c) the present SCTS model. The distributions are normalized to the total ionization yield. A logarithmic color scale in arbitrary units is used. The laser field is linearly polarized along the z axis.

We first turn our attention to the vectorial photoelectron momentum distribution in the $(k_z, k_\perp)$ plane (Fig. 1). For the semiclassical simulations we first employ the initial distribution [Eq. (9)] with zero initial parallel velocity. Important features of the TDSE momentum distribution are reproduced by both the SCTS and the QTMC models: The distributions are stretched along the polarization axis with clear ATI rings and a central interference structure at small momenta. The spread of the distribution along the polarization axis is underestimated by both semiclassical models due to the initial condition $v_{0,z} = 0$ (see below).

A close-up of the low-energy spectrum (Fig. 2) shows marked differences between the different models. For $|k| \leqslant 0.3$ a.u. and energies well below $U_p = 0.2$ a.u., the vectorial momentum distribution displays a fanlike interference structure similar to that of Ramsauer-Townsend diffraction oscillations [50,51,88,89]. The number of radial nodal lines is controlled by the dominant partial-wave angular momentum ℓ_c in Eq. (44); i.e., $R(\vec{k}) \sim |P_{l_c}(\cos\theta)|^2$ (see Refs. [88,89]). While the SCTS model closely matches the nodal pattern of the TDSE, the QTMC model yields fewer nodal lines, which is a direct consequence of the underestimate of the Coulomb interaction in the QTMC treatment of the interference phase. This effect of neglecting the elastic scattering in the Coulomb field occurs both during the laser pulse [Eq. (30)] and after [Eq. (40)]. The magnitude of the latter is illustrated in Fig. 3 where we display the effect of $\tilde{\Phi}_f^C(\tau_f)$ for both an ultrashort single-cycle pulse and the longer eight-cycle pulse. The postpulse Coulomb phase is more pronounced for shorter τ_f as the electron is still closer to the nucleus at the end of the pulse.
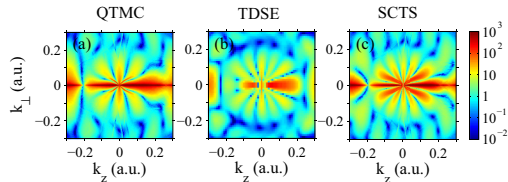

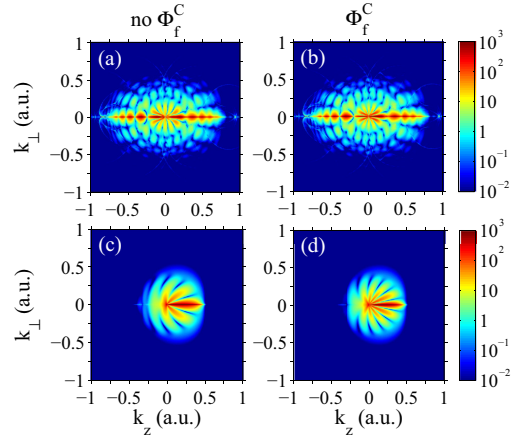FIG. 2. Magnification of Fig. 1 for $|k_z|, |k_\perp| < 0.3$ a.u.

FIG. 3. Vectorial momentum distribution from the present SCTS model for low-energy electrons without (a),(c) and with (b),(d) inclusion of the postpulse Coulomb phase $\tilde{\Phi}_f^C(\tau_f)$ [Eq. (40)] for the eight-cycle pulse of Fig. 1 (a),(b) and a single-cycle pulse (c),(d) with all other laser parameters identical. The distributions are normalized to the total ionization yield. A logarithmic color scale in arbitrary units is used.

For a quantitative comparison of different methods we consider the singly differential angular distribution (Fig. 4)

$$\frac{dR}{\sin\theta \, d\theta} = 2\pi \int_0^\infty dE \sqrt{2E} R[\vec{k}(E)] \qquad (45)$$

and the photoelectron spectrum

$$\frac{dR}{dE} = 2\pi \sqrt{2E} \int_0^\pi d\theta \sin\theta \, R[\vec{k}(\theta)]. \qquad (46)$$

The energy spectra feature pronounced ATI peaks. These are qualitatively reproduced by the semiclassical methods. However, only for the low-order peaks can the semiclassical approximation quantitatively reproduce the amplitude of the oscillations [52]. This is closely related to the fact that the initial conditions from the tunneling step [Eq. (9)] provide too few trajectories with large longitudinal momenta that could account for intercycle interferences, the semiclassical origin of the ATI modulation at large momenta. For the same reason the photoelectron spectrum dR/dE falls off too rapidly for energies exceeding $\sim U_p$. The semiclassical angular distributions reproduce the Ramsauer-Townsend diffraction oscillations [88,89]. The modulation amplitude as well as the position of the minima of the SCTS agree better with the TDSE compared to the QTMC model because of the improved interference phase. The difference is more pronounced for the angular distribution of low-energy electrons (Fig. 5).

Obviously, further improvement of the semiclassical description of the energy and angular distributions of photoelectrons require an improved initial distribution emerging from the tunneling step. To this end, we set the initial conditions for the propagation of classical trajectories, we
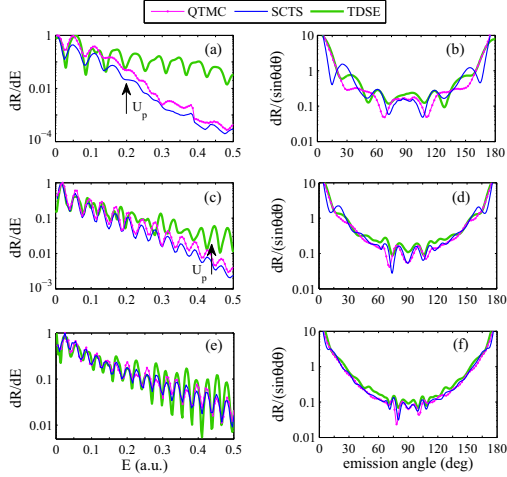
FIG. 4. Energy spectra (a),(c),(e) and angular distributions (b),(d),(f) of the photoelectrons for ionization of H at an intensity of 9×10^{13} W/cm^2 and a pulse duration of eight cycles obtained from the QTMC model [thin (magenta) curve with solid circles], the SCTS model [solid (blue) curve], and TDSE [thick (green) curve]. The distributions [(a),(b)], [(c),(d)], and [(e),(f)] correspond to the wavelengths of 800, 1200, and 1600 nm, with Keldysh parameters of 1.12, 0.75, and 0.56, respectively. The energy spectra are normalized to the peak value; the angular distributions are normalized to the total ionization yield and show the spectrum for electrons with asymptotic energies $E < U_p$. The energy equal to U_p is shown by arrows in panels (a) and (c).

set the initial parallel velocity $v_{0,z}$ at every ionization time t_0 in Eq. (9) to a nonzero value predicted by the strong-field approximation (see Refs. [30,58,59,71]). For the pulse defined in Eq. (42) it can be, for a sufficiently long pulse, approximated by

$$v_{z,0}(t_0) = -\frac{1}{c} A_z(t_0)[\sqrt{1 + \gamma^2(t_0, v_{0,\perp})} - 1], \quad (47)$$

where

$$\gamma(t_0, v_{0,\perp}) = \frac{\omega\sqrt{2I_p + v_{0,\perp}^2}}{F_0 \sin^2\left(\frac{\omega t_0}{2n}\right)|\cos(\omega t_0)|} \quad (48)$$

is the effective Keldysh parameter [71]. In the tunneling limit $\gamma(t_0, v_{0,\perp}) \to 0$ the longitudinal initial velocity $v_{z,0}(t_0)$ vanishes.

Employing Eq. (47) as initial condition for CTMC trajectories taking off at t_0 at the tunneling exit yields improved agreement between the SCTS model and the TDSE for both the vectorial momentum distribution (Fig. 6) and the singly differential distributions dR/dE and $dR/(\sin\theta d\theta)$ (Fig. 7).

Indeed, the SCTS model can now better reproduce the energy spectrum obtained from the TDSE; see Fig. 7(a). For angular distribution the agreement between the QTMC and the TDSE worsens, whereas the agreement between the SCTS and the TDSE improves [compare Fig. 7(b) with Fig. 4(b)]. These
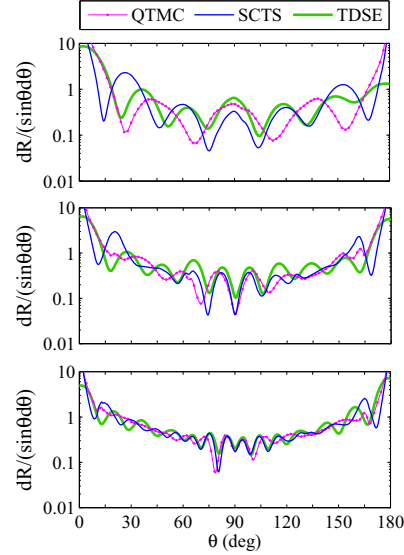

FIG. 5. Angular distributions for low-energy electrons (inner-most fanlike structure; cf. Fig. 2): (a) $E < 0.022$ a.u. for $\lambda = 800$ nm, (b) $E < 0.031$ a.u. for $\lambda = 1200$ nm, and (c) $E < 0.036$ a.u. for $\lambda = 1600$ nm. Cutoff energies have been determined from TDSE results.

results clearly suggest that the main source of deviations of the SCTS model from the TDSE are the errors in treating the tunneling step rather than the semiclassical description of the post-tunneling propagation.

V. CONCLUSIONS AND OUTLOOK

We have developed a semiclassical two-step model for strong-field ionization that describes quantum interference and accounts for the Coulomb potential beyond the semiclassical perturbation theory. In the SCTS model the phase associated with every classical trajectory is calculated using the semi-classical expression for the matrix element of the quantum mechanical propagator. For identical initial conditions after
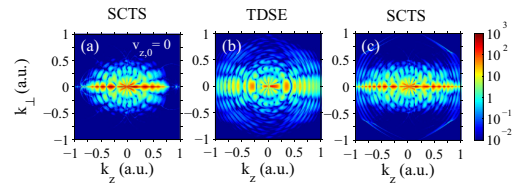

FIG. 6. Vectorial momentum distributions obtained from (a) SCTS model with zero initial parallel velocity, (b) solution of the TDSE, and (c) the SCTS model with nonzero initial parallel velocity. The parameters are the same as in Fig. 1. Panel (a) is the same as Fig. 1(c). A logarithmic color scale in arbitrary units is used.
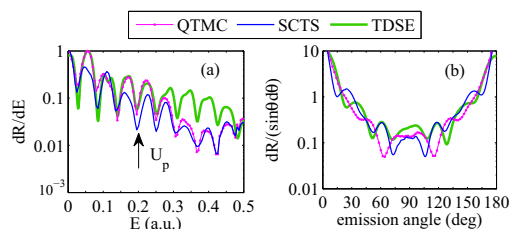
N. I. SHVETSOV-SHILOVSKI *et al.*

FIG. 7. Same as Fig. 4 for $\lambda = 800$ nm with nonzero initial parallel velocity.

the tunneling ionization step taken from standard tunnel ionization rates [1], the SCTS model yields closer agreement with the exact solution of the Schrödinger equation than the previously proposed QTMC model. Furthermore, after improving the input from the tunneling ionization step by including nonzero parallel velocities in the initial conditions for the motion after tunneling, the SCTS model yields significantly improved agreement in the angular distribution, i.e., the position of interference fringes with the TDSE results. Remaining differences in the intensity of energy distributions are traced back to improvable starting conditions (in particular the choice of parallel velocities) of classical trajectories.

The present SCTS model can be extended to multielectron targets in a straightforward fashion by the inclusion of dynamical Stark shifts and polarization-induced dipole potentials. To this end, the SCTS model can be combined with the semiclassical approach developed in Refs. [37,39]

that is based on the effective potential for the outer electron [75]. This effective potential includes the laser field, the Coulomb field, and the polarization effects of the inner core. Semiclassical models of this type will make it possible to investigate the role of the multielectron polarization effect in the formation of the interference structure in the electron momentum distributions. Since the multielectron potential affects both the exit point and the electron dynamics in the continuum, pronounced imprints of the polarization effects in the interference patterns are expected. Finally, the two-step semiclassical models accounting for both the interference and the multielectron effects can provide a valuable tool for investigation of the delays in photoemission, which is presently one of the most intensively studied problems in strong-field physics and attosecond science.

[1] N. B. Delone and V. P. Krainov, *Multiphoton Processes in Atoms* (Springer, Berlin, 2000), Chap. 9.

[2] W. Becker, F. Grasbon, R. Kopold, D. B. Milošević, G. G. Paulus, and H. Walther, Above-threshold ionization: from classical features to quantum effects, Adv. At. Mol. Opt. Phys. **48**, 35 (2002).

[3] D. B. Milošević and F. Ehlotzky, Scattering and reaction processes in powerful laser fields, Adv. At. Mol. Opt. Phys. **49**, 373 (2003).

[4] A. Becker and F. H. M. Faisal, Intense-field many-body S-matrix theory, J. Phys. B: At. Mol. Opt. Phys. **38**, R1 (2005).

[5] C. Figueira de Morisson Faria and X. Liu, Electron-electron correlation in strong laser fields, J. Mod. Opt. **58**, 1076 (2011).

[6] L. V. Keldysh, Ionization in the field of a strong electromagnetic wave, Zh. Eksp. Teor. Fiz. **47**, 1945 (1964) [Sov. Phys. JETP **20**, 1307 (1965)].

[7] F. H. M. Faisal, Multiple absorption of laser photons by atoms, J. Phys. B: At. Mol. Opt. Phys. **6**, L89 (1973).

[8] H. R. Reiss, Effect of an intense electromagnetic field on a weakly bound system, Phys. Rev. A **22**, 1786 (1980).

[9] L. D. Landau and E. M. Lifshitz, *Quantum Mechanics Non-relativistic Theory*, 2nd ed. (Pergamon, Oxford, U.K., 1965).

[10] A. M. Perelomov, V. S. Popov, and M. V. Terent'ev, Ionization of atoms in an alternating electric field, Zh. Eksp. Teor. Fiz. **50**, 1393 (1966) [Sov. Phys. JETP **23**, 924 (1966)].

[11] M. V. Ammosov, N. B. Delone, and V. P. Krainov, Tunnel ionization of complex atoms and of atomic ions in an alternating electromagnetic field, Zh. Eksp. Teor. Fiz. **91**, 2008 (1986) [Sov. Phys. JETP **64**, 1191 (1986)].

[12] H. B. van Linden van den Heuvell and H. G. Muller, in *Multiphoton Processes*, edited by S. J. Smith and P. L. Knight (Cambrige University Press, Cambrige, U.K., 1988).

[13] T. F. Gallagher, Above-Threshold Ionization in Low-Frequency Limit, Phys. Rev. Lett. **61**, 2304 (1988).

[14] P. B. Corkum, N. H. Burnett, and F. Brunel, Above-Threshold Ionization in the Long-Wavelength Limit, Phys. Rev. Lett. **62**, 1259 (1989).

[15] K. C. Kulander, K. J. Schafer, and J. L. Krause, in *Super-Intense Laser-Atom Physics*, edited by B. Piraux, A. L'Hullier, and K. Rzazewski (Plenum, New York, 1993).

[16] P. B. Corkum, Plasma Perspective on Strong Field Multiphoton Ionization, Phys. Rev. Lett. **71**, 1994 (1993).

[17] H. G. Muller, An efficient propagation scheme for the time-dependent Schrödinger equation in the velocity gauge, Laser Phys. **9**, 138 (1999).

[18] D. Bauer and P. Koval, Qprop: A Schrödinger-solver for intense laseratom interaction, Comput. Phys. Commun. **174**, 396 (2006).

[19] J. L. Krause, K. J. Schafer, and K. C. Kulander, High-Order Harmonic Generation from Atoms and Ions in the High Intensity Regime, Phys. Rev. Lett. **68**, 3535 (1992).

[20] M. Lewenstein, Ph. Balcou, M. Yu. Ivanov, A. L'Huillier, and P. B. Corkum, Theory of high-harmonic generation by low-frequency laser fields, Phys. Rev. A **49**, 2117 (1994).

[21] G. G. Paulus, W. Nicklich, H. Xu, P. Lambropoulos, and H. Walther, Plateau in Above Threshold Ionization Spectra, Phys. Rev. Lett. **72**, 2851 (1994).

[22] G. G. Paulus, W. Becker, W. Nicklich, and H. Walther, Rescattering effects in above-threshold ionization: A classical model, J. Phys. B **27**, L703 (1994).

[23] C. Figueira de Morisson Faria and W. Becker, Quantum-orbit analysis of nonsequential double ionization, Laser Phys. **13**, 1196 (2003).

[24] D. B. Milošević and W. Becker, Classical cutoffs for laser-induced nonsequential double ionization, Phys. Rev. A **68**, 065401 (2003).

[25] T. Brabec, M. Yu. Ivanov, and P. B. Corkum, Coulomb focusing in intense field atomic processes, Phys. Rev. A **54**, R2551(R) (1996).

[26] K. Dimitriou, D. G. Arbó, S. Yoshida, E. Persson, and J. Burgdörfer, Origin of the double-peak structure in the momentum distribution of ionization of hydrogen atoms driven by strong laser fields, Phys. Rev. A **70**, 061401(R) (2004).

[27] C. I. Blaga, F. Catoire, P. Colosimo, G. G. Paulus, H. G. Muller, P. Agostini, and L. F. DiMauro, Strong-field photoionization revisited, Nat. Phys. **5**, 335 (2009).

[28] W. Quan, Z. Lin, M. Wu, H. Kang, H. Liu, X. Liu, J. Chen, J. Liu, X. T. He, S. G. Chen *et al.*, Classical Aspects in Above-Threshold Ionization with a Midinfrared Strong Laser Field, Phys. Rev. Lett. **103**, 093001 (2009).

[29] C. Liu and K. Z. Hatsagortsyan, Origin of Unexpected Low Energy Structure in Photoelectron Spectra Induced by Midinfrared Strong Laser Fields, Phys. Rev. Lett. **105**, 113003 (2010).

[30] T.-M. Yan, S. V. Popruzhenko, M. J. J. Vrakking, and D. Bauer, Low-Energy Structures in Strong Field Ionization Revealed by Quantum Orbits, Phys. Rev. Lett. **105**, 253002 (2010).

[31] A. Kästner, U. Saalmann, and J. M. Rost, Electron-Energy Bunching in Laser-Driven Soft Recollisions, Phys. Rev. Lett. **108**, 033201 (2012).

[32] C. Lemell, K. I. Dimitriou, X. M. Tong, S. Nagele, D. V. Kartashov, J. Burgdörfer, and S. Gräfe, Low-energy peak structure in strong-field ionization by midinfrared laser pulses: Two-dimensional focusing by the atomic potential, Phys. Rev. A **85**, 011403(R) (2012).

[33] C. Lemell, J. Burgdörfer, K. I. Dimitriou, D. G. Arbó, and X.-M. Tong, Classical-quantum correspondence in atomic ionization by midinfrared pulses: Multiple peak and interference structures, Phys. Rev. A **87**, 013421 (2013).

[34] B. Wolter, C. Lemell, M. Baudish, M. G. Pullen, X.-M. Tong, M. Hemmer, A. Senftleben, C. D. Schröter, J. Ullrich, R. Moshammer, J. Biegert, and J. Burgdörfer, Formation of very-low-energy states crossing the ionization threshold of argon atoms in strong mid-infrared fields, Phys. Rev. A **90**, 063424 (2014).

[35] W. Becker, S. P. Goreslavski, D. B. Milošević, and G. G. Paulus, Low-energy electron rescattering in laser-induced ionization, J. Phys. B: At. Mol. Opt. Phys. **47**, 204022 (2014).

[36] D. Dimitrovski and L. B. Madsen, Theory of low-energy photoelectrons in strong-field ionization by laser pulses with large ellipticity, Phys. Rev. A **91**, 033409 (2015).

[37] A. N. Pfeiffer, C. Cirelli, M. Smolarski, D. Dimitrovski, M. Abu-Samha, L. B. Madsen, and U. Keller, Attoclock reveals geometry for laser-induced tunneling, Nat. Phys. **8**, 76 (2012).

[38] J. Maurer, D. Dimitrovski, L. Christensen, L. B. Madsen, and H. Stapelfeldt, Molecular-Frame 3D Photoelectron Momentum Distributions by Tomographic Reconstruction, Phys. Rev. Lett. **109**, 123001 (2012).

[39] N. I. Shvetsov-Shilovski, D. Dimitrovski, and L. B. Madsen, Ionization in elliptically polarized pulses: Multielectron polarization effects and asymmetry of photoelectron momentum distributions, Phys. Rev. A **85**, 023428 (2012).

[40] R. Boge, C. Cirelli, A. S. Landsman, S. Heuser, A. Ludwig, J. Maurer, M. Weger, L. Gallmann, and U. Keller, Probing Nonadiabatic Effects in Strong-Field Tunnel Ionization, Phys. Rev. Lett. **111**, 103003 (2013).

[41] C. Hofmann, A. S. Landsman, A. Zielinski, C. Cirelli, T. Zimmermann, A. Scrinzi, and U. Keller, Interpreting electron-momentum distributions and nonadiabaticity in strong-field ionization, Phys. Rev. A **90**, 043406 (2014).

[42] J.-W. Geng, L. Qin, M. Li, W.-H. Xiong, Y. Liu, Q. Gong, and L.-Y. Peng, Nonadiabatic tunneling ionization of atoms in elliptically polarized laser fields, J. Phys. B: At. Mol. Opt. Phys. **47**, 204027 (2014).

[43] N. I. Shvetsov-Shilovski, S. P. Goreslavski, S. V. Popruzhenko, and W. Becker, Ellipticity effects and the contributions of long orbits in nonsequential double ionization of atoms, Phys. Rev. A **77**, 063405 (2008).

[44] X. Wang and J. H. Eberly, Effects of Elliptical Polarization on Strong-Field Short-Pulse Double Ionization, Phys. Rev. Lett. **103**, 103007 (2009).

[45] X. L. Hao, G. Q. Wang, X. Y. Jia, W. D. Li, J. Liu, and J. Chen, Nonsequential double ionization of Ne in an elliptically polarized intense laser field, Phys. Rev. A **80**, 023408 (2009).

[46] F. Mauger, C. Chandre, and T. Uzer, Recollisions and Correlated Double Ionization with Circularly Polarized Light, Phys. Rev. Lett. **105**, 083002 (2010).

[47] A. Emmanouilidou and D. S. Tchitchekova, Strongly driven molecules: Traces of soft recollisions for intermediate intensities in the over-the-barrier regime, Phys. Rev. A **84**, 033407 (2011).

[48] N. I. Shvetsov-Shilovski, D. Dimitrovski, and L. B. Madsen, Ehrenfest's theorem and the validity of the two-step model for strong-field ionization, Phys. Rev. A **87**, 013427 (2013).

[49] Ph. A. Korneev, S. V. Popruzhenko, S. P. Goreslavski, T.-M. Yan, D. Bauer, W. Becker, M. Kübel, M. F. Kling, C. Rödel, and G. G. Paulus, Interference Carpets in Above-Threshold Ionization: From the Coulomb-Free to the Coulomb-Dominated Regime, Phys. Rev. Lett. **108**, 223601 (2012).

[50] D. G Arbó, E. Persson, and J. Burgdörfer, Time double-slit interferences in strong-field tunneling ionization, Phys. Rev. A **74**, 063407 (2006).

[51] R. Gopal, K. Simeonidis, R. Moshammer, Th. Ergler, M. Dürr, M. Kurka, K.-U. Kühnel, S. Tschuch, C.-D. Schröter, D. Bauer, and J. Ullrich, Three-Dimensional Momentum Imaging of Electron Wave Packet Interference in Few-Cycle Laser Pulses, Phys. Rev. Lett. **103**, 053001 (2009).

[52] D. G Arbó, K. L. Ishikawa, K. Schiessl, E. Persson, and J. Burgdörfer, Intracycle and intercycle interferences in above-threshold ionization: The time grating, Phys. Rev. A **81**, 021403(R) (2010).

[53] M. Li, J.-W. Geng, H. Liu, Y. Deng, C. Wu, L.-Y. Peng, Q. Gong, and Y. Liu, Classical-Quantum Correspondence for Above-Threshold Ionization, Phys. Rev. Lett. **112**, 113002 (2014).

[54] T. Minami, C. O. Reinhold, and J. Burgdörfer, Quantum-trajectory Monte Carlo method for internal-state evolution of fast ions traversing amorphous solids, Phys. Rev. A **67**, 022902 (2003).

[55] M. Li, X. Sun, X. Xie, Y. Shao, Y. Deng, C. Wu, Q. Gong, and Y. Liu, Revealing backward rescattering photoelectron interference of molecules in strong infrared laser fields, Sci. Rep. **5**, 8519 (2015).

[56] Y. Shao, M.-M. Liu, X. Sun, X. Xie, P. Wang, Y. Deng, C. Wu, Q. Gong, and Y. Liu, Isolating resonant excitation from above-threshold ionization, Phys. Rev. A **92**, 013415 (2015).

[57] J.-W. Geng, W.-H. Xiong, X.-R. Xiao, L.-Y. Peng, and Q. Gong, Nonadiabatic Electron Dynamics in Orthogonal Two-Color Laser Fields with Comparable Intensities, Phys. Rev. Lett. **115**, 193001 (2015).

[58] S. V. Popruzhenko and D. Bauer, Strong field approximation for systems with Coulomb interaction, J. Mod. Opt. **55**, 2573 (2008).

[59] S. V. Popruzhenko, G. G. Paulus, and D. Bauer, Coulomb-corrected quantum trajectories in strong-field ionization, Phys. Rev. A **77**, 053409 (2008).

[60] A. M. Perelomov and V. S. Popov, Ionization of atoms in an alternating electrical field III, Zh. Eksp. Teor. Fiz. **52**, 514 (1967) [Sov. Phys. JETP **25**, 336 (1967)].

[61] D. J. Tannor, *Introduction to Quantum Mechanics: A Time-Dependent Perspective* (University Science Books, Sausalito, California, 2007).

[62] F. Grossmann, *Theoretical Femtosecond Physics. Atoms and Molecules in Srong Laser Fields* (Springer-Verlag, Berlin, Heidelberg, 2008).

[63] W. H. Miller, Classical-limit quantum mechanics and the theory of molecular collisions, Adv. Chem. Phys. **25**, 69 (1971).

[64] M. Walser and T. Brabec, Semiclassical path integral theory of strong-laser-field physics, J. Phys. B **36**, 3025 (2003).

[65] M. Spanner, Strong Field Tunnel Ionization by Real-Valued Classical Trajectories, Phys. Rev. Lett. **90**, 233005 (2003).

[66] S. Yoshida, F. Grossmann, E. Persson, and J. Burgdörfer, Semiclassical analysis of quantum localization of the periodically kicked Rydberg atom, Phys. Rev. A **69**, 043410 (2004).

[67] D. B. Milošević, G. G. Paulus, D. Bauer, and W. Becker, Above-threshold ionization by few-cycle pulses, J. Phys. B **39**, R203 (2006).

[68] T. Yan and D. Bauer, Sub-barrier Coulomb effects on the interference pattern in tunneling-ionization photoelectron spectra, Phys. Rev. A **86**, 053403 (2012).

[69] P. Salières, B. Carré, L. Le Déroff, F. Grasbon, G. G. Paulus, H. Walther, R. Kopold, W. Becker, D. B. Milošević, A. Sanpera, and M. Lewenstein, Feynman's path-integral approach for intense-laser-atom interactions, Science **292**, 902 (2001).

[70] G. L. Yudin and M. Yu. Ivanov, Nonadiabatic tunnel ionization: Looking inside a laser cycle, Phys. Rev. A **64**, 013409 (2001).

[71] M. Li, J.-W. Geng, M. Han, M.-M. Liu, L.-Y. Peng, Q. Gong, and Y. Liu, Subcycle nonadiabatic strong-field tunneling ionization, Phys. Rev. A **93**, 013402 (2016).

[72] M. Born, *Vorlesungen über Atommechanik* (Springer, Berlin, 1925), p. 243.

[73] E. Schrödinger, Ann. Phys. (Berlin, Ger.) **385**, 437 (1926).

[74] C. Z. Bisgaard and L. B. Madsen, Tunneling ionization of atoms, Am. J. Phys. **72**, 249 (2004).

[75] D. Dimitrovski, C. P. J. Martiny, and L. B. Madsen, Strong-field ionization of polar molecules: Stark-shift-corrected strong-field approximation, Phys. Rev. A **82**, 053404 (2010).

[76] C. Reinhold, S. Yoshida, J. Burgdörfer, B. Wyker, J. Mestayer, and F. Dunning, Large-scale quantum coherence of nearly circular wave packets, J. Phys. B **42**, 091003 (2009).

[77] K. G. Kay, Semiclassical initial value treatments of atoms and molecules, Annu. Rev. Phys. Chem. **56**, 255 (2005).

[78] X.-M. Tong, G. Wachter, S. Sato, C. Lemell, K. Yabana, and J. Burgdörfer, Application of norm-conserving pseudopotentials to intense laser-matter interactions, Phys. Rev. A **92**, 043422 (2015), and references therein.

[79] N. I. Shvetsov-Shilovski, S. P. Goreslavski, S. V. Popruzhenko, and W. Becker, Capture into Rydberg states and momentum distributions of ionized electrons, Laser Phys. **19**, 1550 (2009).

[80] L. D. Landau and E. M. Lifshitz, *Mechanics*, 2nd ed. (Pergamon, Oxford, U.K., 1969).

[81] W. H. Press, S. A. Teukolsky, W. T. Vetterling, and B. P. Flannery, *Numerical Recipes in Fortran 77: The Art of Scientific Computing*, 2nd ed. (Cambridge University Press, Cambridge, U.K., 1992).

[82] X.-M. Tong and S. I. Chu, Theoretical study of multiple high-order harmonic generation by intense ultrashort pulsed laser fields: A new generalized pseudospectral time-dependent method, Chem. Phys. **217**, 119 (1997).

[83] X.-M. Tong and S.-I Chu, Time-dependent approach to high-resolution spectroscopy and quantum dynamics of Rydberg atoms in crossed magnetic and electric fields, Phys. Rev. A **61**, 031401(R) (2000).

[84] X.-M. Tong and C. D. Lin, Empirical formula for static field ionization rates of atoms and molecules by lasers in the barrier-suppression regime, J. Phys. B **38**, 2593 (2005).

[85] O. Schöller, J. S. Briggs, and R. M. Dreizler, Coherent excitation of hydrogen atoms by proton impact, J. Phys. B **19**, 2505 (1986).

[86] A. Messiah, *Quantum Mechanics 1* (North-Holland, New York, 1965).

[87] S. Dionissopoulou, Th. Mercouris, A. Lyras, and C. A. Nicolaides, Strong laser-field effects in hydrogen: High-order above-threshold ionization and photoelectron angular distributions, Phys. Rev. A **55**, 4397 (1997).

[88] D. G Arbó, S. Yoshida, E. Persson, K. I. Dimitriou, and J. Burgdörfer, Interference Oscillations in the Angular Distribution of Laser-Ionized Electrons Near Ionization Threshold, Phys. Rev. Lett. **96**, 143003 (2006).

[89] D. G Arbó, E. Persson, K. I. Dimitriou, and J. Burgdörfer, Sub-Poissonian angular momentum distribution near threshold in atomic ionization by short laser pulses, Phys. Rev. A **78**, 013406 (2008).

8.2   Multielectron effects in elliptically polarized pulses

Ionization in elliptically polarized pulses: Multielectron polarization effects and asymmetry of photoelectron momentum distributions

N. I. Shvetsov-Shilovski, D. Dimitrovski, and L. B. Madsen

Lundbeck Foundation Theoretical Center for Quantum System Research, Department of Physics and Astronomy,
Aarhus University, 8000 Århus C, Denmark

In the tunneling regime we present a semiclassical model of above-threshold ionization with inclusion of the Stark shift of the initial state, the Coulomb potential, and a polarization induced dipole potential. The model is used for the investigation of the photoelectron momentum distributions in close to circularly polarized light, and it is validated by comparison with *ab initio* results and experiments. The momentum distributions are shown to be highly sensitive to the tunneling exit point, the Coulomb force, and the dipole potential from the induced dipole in the atomic core. This multielectron potential affects both the exit point and the dynamics, as illustrated by calculations on Ar and Mg. Analytical estimates for the position of the maximum in the photoelectron distribution are presented, and the model is compared with other semiclassical approaches.

I. INTRODUCTION

The interaction of a strong laser field with atoms and molecules gives rise to a variety of phenomena, including above-threshold ionization (ATI) along with the formation of the high-energy plateau in the electron spectrum, excessive yield of doubly and multiply charged ions, and the generation of the high-order harmonics of the incident field (see, e.g., Refs. [1–6] for reviews). The theoretical approaches used to describe all of these phenomena are based on the numerical solution of the time-dependent Schrödinger equation (TDSE) (see, e.g., Refs. [7–11] and references therein), the strong-field approximation (SFA) [12–14], and the semiclassical model for strong-field ionization [15–19], with the initial step being tunneling ionization [20–22] and the subsequent dynamics described by classical equations of motion. When all other interactions but that of the laser field are ignored in this propagation, this latter approach is known as the simpleman's model.

Although the solution of the TDSE in most cases gives good agreement with the experimental data, it is often very difficult to reconstruct the mechanism of the phenomena under consideration. In the SFA the initial bound state of the atom is unaffected by the laser field, whereas the final continuum state does not feel the binding potential of the parent ion. Despite the appealing physical picture of many laser-atom phenomena provided by the SFA, it has been known for many years that neglecting the binding potential is severe [23–31].

The three-step model [15–19] has given great insight into strong-field phenomena. Presently semiclassical simulations based on the three-step model are widely used due to (i) their numerical simplicity and (ii) the physical picture of strong-field phenomena. For some laser-atom problems, the semiclassical simulations are, in fact, the only feasible approach, for example, for the nonsequential double ionization of molecules [32] and atoms by elliptically [33–36] and circularly polarized fields [37]. For a linearly polarized field the three-step model is equivalent to the following simple picture. At some time an electron tunnels out of the atom and moves along a classical trajectory in the laser field. The tunneling

rate is calculated in the static limit [20] with a field strength set equal to the instantaneous value of the oscillating laser field. The description of the ionization step by tunneling is expected to be accurate when the Keldysh parameter $\gamma = \omega\varkappa/F \ll 1$ [12], where ω is the carrier angular frequency, F is the field strength, and $\varkappa = \sqrt{2I_p}$ with I_p the ionization potential (atomic units are used throughout this paper). In most cases the tunneled electrons reach the detector without recolliding with their parent ions. These direct electrons have energies below $2U_p$, where $U_p = F^2/4\omega^2$ is the ponderomotive energy. There are also electrons which are driven back by the laser field to rescatter on their parent ions by angles close to $180°$. These backscattered electrons are responsible for the formation of the high-energy plateau of the ATI spectrum, which is usually 4–6 orders of magnitude lower than the maximum of the low-energy spectrum. In this work we focus on the direct electrons, that is on the low-energy spectrum, therefore the model that we use consists of essentially two steps: Ionization and propagation. In the following we shall refer to this situation where recollision has been switched off as the two-step model. An example where recollision is absent is the case of ionization in close to circularly polarized fields considered here.

Above-threshold ionization, as well as other strong-field phenomena generated by elliptically polarized fields, has attracted particular attention for a number of reasons. First, the evolution of the distributions with increasing ellipticity from linear to circular gives additional information about the process under consideration. Second, in the experiment it is easier to control the ellipticity than the intensity of the fluctuating laser pulse. Finally, the kinematics caused by an elliptically polarized field is essentially two dimensional (2D), in contrast to the case of linear polarization, when the laser field acts only along one spatial direction. The 2D nature, in turn, gives rise to features and properties which are not accessible with a linearly polarized laser field. For example, the ATI by a circularly polarized laser pulse was used in the first observation of the carrier-envelope effect in [38], see also theoretical studies [39,40].

Another example is the angular distribution of photoelectrons generated by an elliptically polarized field. While

the SFA predicts a fourfold symmetry of the photoelectron angular distribution with respect to the both main axes of polarization ellipse [41], the experimentally observed distributions possess only inversion symmetry, see Refs. [23–25]. This was soon realized to be an effect of the Coulomb potential [26–28,42–44]. Other examples are the predominant ionization when the field points along the major axis resulting in peaks in the photoelectron momentum distribution along the minor axis [41,45,46], asymmetries in the photoelectron angular distributions resulting from the ionization of the oriented molecules [47–52], attosecond angular streaking [53,54], and the possibility of detailed exploration of Stark and polarization effects in the initial tunneling step [55].

In Ref. [56] the molecular SFA was extended to include the linear and quadratic Stark shifts. The adiabatic approximation was made in order to find the effective potential for the outer electron, which includes the laser field and the polarization effects of the inner core. It was found in Ref. [55] that the parabolic coordinates approximately separate the Schrödinger equation with this effective potential. This separation procedure defines a certain tunneling geometry, that is, identifies the flow of the electron charge associated with the tunneling electron in parabolic coordinates. The emerging physical picture is referred to as tunnel ionization in parabolic coordinates with induced dipole and Stark shift (TIPIS). Here we describe the TIPIS model and explore its predictions.

In the study of Ref. [55] the offset angle θ, that is, the angle between the maximum of the momentum distribution and the minor axes of the polarization ellipse (see Fig. 1), was in focus. It was found that for Ar in the tunneling regime this angle is of the order of $10°$–$15°$ and decreasing with laser intensity, whereas for He the angle was $5°$–$10°$ and less sensitive to the laser intensity. The difference between Ar and He was related to the difference in polarizability of the two systems. It is interesting to find a situation where the offset angle is larger, that is, the effect of rotation away from the minor axis is more pronounced. Here we consider not only the offset angle, but the shape of the whole distribution and its evolution with the intensity and wavelength.

In this paper we (i) present an exhaustive derivation of the TIPIS model; (ii) validate the semiclassical approach by comparing with TDSE results; (iii) analyze momentum distribution generated by an elliptically polarized laser field; (iv) further investigate the role of the polarization effects; and (v) compare different approaches to the semiclassical simulations of the ATI.

The paper is organized as follows. In Sec. II we discuss approaches to the classical simulation of the momentum distribution, present a detailed derivation of the TIPIS model, and discuss its range of applicability. Our results are discussed in Sec III and conclusions are given in Sec. IV.

II. SEMICLASSICAL MODELS

In the semiclassical approach to ATI, the electron is ejected from the atom by tunneling [20–22]. Subsequently, Newton's equations of motion are solved for the electron, starting out at the exit of the tunnel in the combined atomic or ionic potential $V(\mathbf{r})$ and the electric field $\mathbf{F}(t)$ of the laser pulse,

$$\frac{d^2\mathbf{r}}{dt^2} = -\boldsymbol{\nabla}V(\mathbf{r}) - \mathbf{F}(t). \tag{1}$$

Semiclassical models have been successfully used to explain various strong-field phenomena involving single ionization (see, e.g. [55,57–64]) and double ionization [34–37,65,66]. The abovementioned models vary greatly with respect to the particular implementation. Here we present the semiclassical model referred to as TIPIS [55].

To solve Eq. (1) one needs to specify the initial conditions for the electron in phase-space just after the escape from the atom. The static tunneling rate with which the classical trajectories are weighted is a quantum input in the semiclassical model. The exit point at the outer turning point of the barrier also depends critically on the quantum model used to solve the tunneling problem—a key point that we come back to below. To start, we consider the static problem of an electron, bound by $V(\mathbf{r})$ in the presence of the static electric field $\mathbf{F}$ (which should be interpreted as the instantaneous value of the laser field at the time of ionization and it is assumed to point in the positive z direction) [67],

$$\left(-\tfrac{1}{2}\Delta + V(\mathbf{r}) + \mathbf{F} \cdot \mathbf{r} \right)\Psi = -I_p(F)\Psi. \tag{2}$$

In Eq. (2) we have included the static Stark shifts [50,56],

$$I_p(F) = I_p(0) + \tfrac{1}{2}(\alpha_N - \alpha_I)F^2, \tag{3}$$

where $I_p(0)$ is the field-free ionization potential and α_N and α_I are the static polarizabilies of the atomic system with charge $Z-1$ and the Z-charged atomic ion, respectively. We have specialized to the case of atoms, with no permanent dipole moment and therefore no linear Stark shift is present in Eq. (3). The above perturbative expansion of the Stark-shifted ionization potential holds for shifts that are small compared to the field-free ionization potential $I_p(0)$. In all cases presented in this paper, this requirement is satisfied.

Following the ionization step, we will consider propagation in the potential $V(\mathbf{r})$,

$$V(\mathbf{r},t) = -\frac{Z}{r} - \frac{\alpha_I\mathbf{F}(t) \cdot \mathbf{r}}{r^3}, \tag{4}$$

which is valid at large and intermediate distances [56,67], and where the multielectron effect expressed through the induced dipole of the ion $[\alpha_I\mathbf{F}(t)]$ is taken into account [55,56]. We refer to the second term of Eq. (4) as the multielectron (ME) term.

In semiclassical simulations it is important to find the tunnel exit point z_e, from where the classical trajectory starts. In the next two subsections we present two possible approximate separations of the static tunneling problem that lead to different values of the tunnel exit point, and therefore different results in the semiclassical model.

A. Field direction model

The simplest and most widely used approach to determine the tunneling path and z_e is to consider the potential barrier formed by the atomic potential and the electric field of the laser in a 1D cut *along the direction of the field*. We denote

this approach as the field direction model (FDM) (see, e.g., Refs. [57,58,63,68,69]), where this model was used. The tunnel exit point is found from

$$V(z_e) + Fz_e = -I_p(F). \tag{5}$$

However, in this approach, it is implicitly assumed that the tunneling problem can be treated as one dimensional along the field direction. The direction along the field can be separated from the transverse coordinates in Eq. (2) if the potential does not depend on the transverse dimension, that is when $V(\mathbf{r}) = V(z)$. Then the wave function can be sought as a product $\Psi(x,y,z) = \Psi_2(z)\Psi_1(x,y)$, and Eq. (2) is separated as follows:

$$-\frac{1}{2}\left(\frac{\partial^2}{\partial x^2} + \frac{\partial^2}{\partial y^2}\right)\Psi_1(x,y) = \lambda_1 \Psi_1(x,y), \tag{6}$$

$$\lambda_1 = \frac{p_x^2 + p_y^2}{2} = \frac{p_\perp^2}{2}, \tag{7}$$

$$\left(-\frac{1}{2}\frac{\partial^2}{\partial z^2} + V(z) + Fz\right)\Psi_2(z) = \lambda_2 \Psi_2(z), \tag{8}$$

where λ_1 and λ_2 are the separation constants. The sum of the separation constants is equal to the energy of the initial state

$$\lambda_1 + \lambda_2 = -I_p(F), \tag{9}$$

and therefore

$$\lambda_2 = -\left(I_p(F) + \frac{p_\perp^2}{2}\right). \tag{10}$$

Equation (6) states the fact that because the artificial potential used in the FDM does not depend on the transverse dimension, the electron can be described as a free particle in these degrees of freedom. On the other hand, Eq. (8) gives the effective 1D tunneling problem where Eq. (10) shows that the effective ionization potential is increased by the transverse kinetic energy of the particle [70]. The minimal ionization potential that occurs for transverse energy zero is taken into the equation for the tunnel exit point in FDM (5).

It is clear that the potential in Eq. (4), even without the ME term, is not in the form required for a separation in the FDM. A much more accurate approach is to use parabolic coordinates as discussed in the next subsection.

B. Separated problem in parabolic coordinates and TIPIS model

To separate the problem of an electron bound by a pure Coulomb potential in a static field, parabolic coordinates are used [20]:

$$\xi = r + z, \quad \eta = r - z, \quad \phi = \arctan(y/x). \tag{11}$$

Under the assumption that the electric field vector points in the positive z direction, the separation results in two 1D problems: in the ξ coordinate the electron is trapped in an attractive potential without the possibility to tunnel out, whereas in the η coordinate a potential barrier exists that enables tunneling [20]. However, for the potential in Eq. (4), where the ME term is included, and also, in general for atomic and molecular potentials, such a separation is not possible. In Ref. [55] an *approximate* separation in the limit $\xi/\eta \ll 1$ was carried out. As the external field is increased, the exit point moves to

smaller distances. Hence, the approximate separation becomes inaccurate if the field strength becomes too large.

To perform the separation we seek the solution to Eq. (2) in the product form $\Psi(\mathbf{r}) = (1/\sqrt{\xi\eta})f_1(\xi)f_2(\eta)e^{im\phi}/\sqrt{2\pi}$, and after retaining the lowest-order term in ξ/η coming from $\alpha_I \mathbf{F} \cdot \mathbf{r}/r^3$ we arrive at two separated equations

$$\frac{d^2 f_1(\xi)}{d\xi^2} + 2\left(-\frac{I_p(F)}{4} - V_1(\xi,F)\right)f_1(\xi) = 0, \tag{12}$$

$$\frac{d^2 f_2(\eta)}{d\eta^2} + 2\left(-\frac{I_p(F)}{4} - V_2(\eta,F)\right)f_2(\eta) = 0. \tag{13}$$

The potentials V_1 and V_2 are

$$V_1(\xi,F) = -\frac{\beta_1(F)}{2\xi} + \frac{m^2 - 1}{8\xi^2} + \frac{F\xi}{8}, \tag{14}$$

$$V_2(\eta,F) = -\frac{\beta_2(F)}{2\eta} + \frac{m^2 - 1}{8\eta^2} - \frac{F\eta}{8} + \frac{\alpha_I F}{\eta^2}, \tag{15}$$

where $\beta_1(F)$ and $\beta_2(F)$ are the separation constants fulfilling

$$\beta_1(F) + \beta_2(F) = Z, \tag{16}$$

$$\beta_2(F) = Z - (1 + |m|)\frac{\sqrt{2I_p(F)}}{2}. \tag{17}$$

Again, the potential $V_1(\xi,F)$ along the ξ coordinate is a bound one, while $V_2(\eta,F)$ shows that along the η coordinate tunneling is possible. To lowest order in ξ/η, the potential (14) is identical to the potential obtained for ξ when separating the pure Coulomb plus field problem. In addition to the terms that appear for pure Coulomb potential and a field, the potential (15) along the η direction contains the multielectron term $\alpha_I F/\eta^2$. The sum of the separation constants gives the nuclear charge Z [Eq. (16)], in contrast to the FDM where the sum of the separation constants gives the Stark-shifted eigenenergy of the initial state [Eq. (9)].

The separation in parabolic coordinates is not to be understood as a coordinate transformation from the FDM since Eqs. (13) and (8) define different tunneling problems. The tunneling occurs through the η coordinate; this defines the geometry of tunneling, that is, the "natural" path of the tunneling current flow in atoms [55]. The tunnel exit point z_e is obtained as $z_e \approx -\eta_e/2$, where η_e is obtained by equating the potential V_2 of Eq. (15) with the energy term $-I_p/4$, that is,

$$V_2(\eta_e, F) = -\frac{I_p(F)}{4}. \tag{18}$$

The approximate separation of the tunneling problem in parabolic coordinates, together with the inclusion of Stark shifts and the ME term, are the essential ingredients of the TIPIS model. We note that, contrary to the FDM, in this treatment no unphysical assumption about free motion in the transverse degrees of freedom is introduced.

Equation (18) for η_e is a cubic equation. However, for exit points that are sufficiently far away from the origin, that is, for

$$\eta_e \gg \frac{2[\alpha_I F + (m^2 - 1)/8]}{\beta_2(F)}, \tag{19}$$

Eq. (18) becomes quadratic and the exit point η_e is well approximated by

$$\eta_e \approx \frac{I_p(F) + \sqrt{I_p^2(F) - 4\beta_2(F)F}}{F}. \tag{20}$$

In Cartesian coordinates, using $z_e \approx -\eta_e/2$,

$$z_e \approx -\frac{I_p(F) + \sqrt{I_p^2(F) - 4\beta_2(F)F}}{2F}, \tag{21}$$

which is different from the corresponding exit point in FDM, following from (5)

$$z_e \approx -\frac{I_p(F) + \sqrt{I_p^2(F) - 4ZF}}{2F}. \tag{22}$$

Below we show examples highlighting that the final momentum depends very sensitively on the use of either Eq. (18) or Eq. (22) for the exit point.

C. Details of the classical simulations

In our calculations we consider the following short laser pulse elliptically polarized in the (x, y) plane:

$$\begin{aligned} \mathbf{F}(t) = \frac{F_0}{\sqrt{1+\epsilon^2}} &\sin^2(\pi t/\tau_L) \\ &\times [\cos(\omega t + \varphi)\mathbf{e}_x + \epsilon \sin(\omega t + \varphi)\mathbf{e}_y], \end{aligned} \tag{23}$$

with the duration $\tau_L = (2\pi/\omega)n_p$ and a sine-square envelope, and where n_p is the number of cycles, ϵ is the ellipticity, and φ is the carrier-envelope phase. As in recent experiments [55] we use $\epsilon = 0.78$ throughout. Note that the rescattering process is suppressed for close to circularly polarized field (see, e.g., [71]), and direct electrons, which we are interested in, dominate in the ATI spectrum.

In the present studies we assume that the electron has zero initial velocity in the direction of the laser field $v_\parallel = 0$, however, we include an initial transverse velocity $v_{0\perp}$. The ionization instant and this initial transverse velocity are distributed according to the static ionization rate in the tunneling regime [21,22,68]:

$$w(t_0, v_0) \sim \exp\left(-\frac{2\varkappa^3}{3F}\right) \exp\left(-\frac{\varkappa v_{0\perp}^2}{F}\right), \tag{24}$$

where $F = F(t_0)$. For simplicity, we omit the preexponential factor in Eq. (24). Although this factor changes the total ionization rate by several orders of magnitude, its effect on the shape of the final momentum distributions, which we are interested in, is weak for atoms. Moreover, analysis of the transverse momentum distributions in terms of the Siegert eigenfunctions [72] showed that the Gaussian shape of the distribution in Eq. (24) holds if the laser field is less than 0.2 a.u., which is the regime of interest in our case.

An ensemble of 1.5×10^6 trajectories weighted with the probability given by Eq. (24) was used to calculate the momentum distributions. Equation (1) was solved using a fourth-order Runge-Kutta method with adaptive stepsize control [73]. It is necessary to soften the $1/r^2$ ME term in numerical simulations because it tends to the infinity as $r \to 0$. To do so we multiply this term by the factor $\exp(-b_0/r)$,

where $b_0 = 0.1$ a.u. Otherwise, nonphysical bursts can appear in the momentum distributions. Bearing in mind that it is often very difficult to stabilize the carrier-envelope phase in the experiment, we choose φ in Eq. (23) randomly for each trajectory. The distributions calculated in this way are, however, very similar to those with $\varphi = \pi$ (or $\varphi = 0$) since the absolute maximum of the field (23) occurs at that particular phase and according to Eq. (24) the absolute maximum of the field is strongly favored. We typically use $n_p = 6$.

The calculation of the momentum distributions of the photoelectrons must take into account the possible population of Rydberg orbits, see [59,74]. So we follow the procedure of Ref. [74] and exclude trajectories with negative energy at the end of the pulse, and take into account the subsequent motion of electrons with positive energies in the Coulomb field of the atomic residual. The electron momentum $\mathbf{q} = \mathbf{q}(t_0, v_0, \tau_L)$ and its position $\mathbf{r} = \mathbf{r}(t_0, v_0, \tau_L)$ at *the end of the laser pulse* uniquely determine the asymptotic momentum:

$$\mathbf{P} = P\frac{P(\mathbf{L} \times \mathbf{a}) - \mathbf{a}}{1 + p^2L^2}. \tag{25}$$

Here $\mathbf{L} = \mathbf{r} \times \mathbf{q}$ and $\mathbf{a} = \mathbf{q} \times \mathbf{L} - \mathbf{r}/r$ are the conserved angular momentum and Runge-Lenz vector, respectively. The above equation corrects a misprint in Ref. [74]. The absolute value P of the asymptotic momentum, appearing in Eq. (25), is found from energy conservation:

$$\frac{q^2}{2} - \frac{Z}{r} = \frac{P^2}{2}. \tag{26}$$

D. Analytical estimates

Numerical simulations give valuable insights into the properties and evolution of the momentum distributions. Nevertheless, it would be desirable to have some analytical estimates for better understanding of the underlying physics. Let us then write the asymptotic momentum of an electron tunneling at time t_0 with nonzero initial velocity $\mathbf{v}_0$ as a sum:

$$\begin{aligned} \mathbf{P}(t_0, \mathbf{v}_0) = \mathbf{P}_L(t_0) + \mathbf{v}_0 &+ \mathbf{P}_C(t_0, \mathbf{v}_0) \\ &+ \mathbf{P}_{ME}(t_0, \mathbf{v}_0). \end{aligned} \tag{27}$$

Here $\mathbf{P}_C$ and $\mathbf{P}_{ME}$ are the contributions of the Coulomb force $\mathbf{F}_C = -\mathbf{r}/r^3$ and of the multielectron force $\mathbf{F}_{ME} = \nabla[\alpha_I \mathbf{F}(t) \cdot \mathbf{r}/r^3]$, respectively, and $\mathbf{P}_L(t_0) = -\int_{t_0}^{\tau_L} \mathbf{F}(t)dt$ is the integral of the force due to the external field $\mathbf{F}(t)$ from the time of ionization. In the simpleman's model $\mathbf{P}_L$ is the estimate of the final momentum. Here, however, the effects of other force terms are significant. In order to estimate $\mathbf{P}_C$ and $\mathbf{P}_{ME}$, one can use the approach of Refs. [25,74]. Hence we treat the Coulomb and ME potentials as perturbations and calculate each contribution by integrating the respective force along a trajectory $\mathbf{r}_L(t) = \int_{t_0}^{t} \mathbf{P}_L(t')dt' + \mathbf{v}_0(t - t_0)$ governed by the laser field only:

$$\mathbf{P}_C = -\int_{t_0}^{+\infty} dt \frac{\mathbf{r}_L(t)}{r_L^3(t)}, \tag{28}$$

$$\mathbf{P}_{ME} = \int_{t_0}^{+\infty} dt \left(\frac{\alpha_I \mathbf{F}(t)}{r_L^3} - \frac{3\alpha_I[\mathbf{F}(t) \cdot \mathbf{r}_L]\mathbf{r}_L}{r_L^5}\right), \tag{29}$$

where the upper integration limit is extended to infinity. We restrict our consideration to sufficiently large ellipticities. Therefore, the trajectory of an electron will not come very close to the atomic residual for the vast majority of initial conditions. Already at the exit of the tunnel the Coulomb and ME forces are small as compared to that of the laser field and they decrease further along the trajectory [25].

Estimates for both contributions can be obtained by calculating the integrals in Eqs. (28) and (29) along the trajectory generated by a constant field $\mathbf{F}(t) = \mathbf{F}(t_0)$. Then, for small initial velocities, $v_0 \ll \varkappa$, the main contributions are given by

$$\mathbf{P}_C = -\frac{\pi}{4}\sqrt{\frac{2}{r_0^3 F(t_0)}}\mathbf{n}_F(t_0) - \frac{v_{0\perp}}{2r_0^2 F(t_0)}\mathbf{n}_\perp(t_0) \quad (30)$$

and

$$\mathbf{P}_{ME} = \frac{3\pi\alpha_I}{8}\sqrt{\frac{2F(t_0)}{r_0^5}}\mathbf{n}_F(t_0) + \frac{\alpha_I v_{0\perp}}{r_0^3}\mathbf{n}_\perp(t_0), \quad (31)$$

where r_0 is the absolute value of the tunnel exit point, $\mathbf{n}_F(t_0)$ is a unit vector along the laser field at time t_0, and $\mathbf{n}_\perp(t_0)$ is a unit vector in the polarization plane perpendicular to the laser field at t_0.

One can improve the estimate of Eq. (30) by evaluating the integral in Eq. (28) along a trajectory in the field $\mathbf{F}(t) \approx \mathbf{F}(t_0) + \mathbf{F}'(t_0)(t - t_0)$. For simplicity, in this analytical development let us consider only a single electron trajectory, corresponding to the maximum of the field. For such a trajectory and for carrier-envelope phase $\varphi = \pi$ one has $t_0 = \tau_L/2$, and, therefore, $\mathbf{n}_F = \mathbf{e}_x, \mathbf{n}_\perp = \mathbf{e}_y$, and $F = F_0/\sqrt{1 + \varepsilon^2}$. Then, one has the following estimate of the Coulomb contribution:

$$\mathbf{P}_C(t_0 = \tau_L/2, v_{0\perp} = 0) = -\left(\frac{\pi}{4}\sqrt{\frac{2}{Fr_0^3}}\mathbf{e}_x + \frac{\epsilon\omega}{6Fr_0}\mathbf{e}_y\right). \tag{32}$$

Let us also introduce the total correction $\mathbf{P}_I = \mathbf{P}_C + \mathbf{P}_{ME}$ due to the ion potential to the electron momentum:

$$\mathbf{P}_I(t_0 = \tau_L/2, v_{0\perp} = 0) = \frac{\pi}{4}\sqrt{\frac{2}{Fr_0^3}}\left(\frac{3\alpha_I F}{2r_0} - 1\right)\mathbf{e}_x$$
$$- \frac{\epsilon\omega}{6Fr_0}\mathbf{e}_y. \tag{33}$$

For the parameters considered here $3\alpha_I F/2r_0 \ll 1$ so the estimates Eqs. (32) and (33) show that the contribution of the ME term is small compared to the Coulomb correction. Both contributions increase with increasing intensity, but $\mathbf{P}_{ME}$ increases faster than $\mathbf{P}_C$ due to the additional factor of r_0 in the denominator, see Eq. (33). As we shall see in Sec. III B the estimates provided by Eqs. (32) and (33) underestimate the effect of the ME term and do not account quantitatively for the momentum distributions. However, they do provide valuable insight in the evolution and properties of the momentum distributions.

III. RESULTS AND DISCUSSION

In the following, using our semiclassical model, we consider the momentum distributions from elliptically polarized
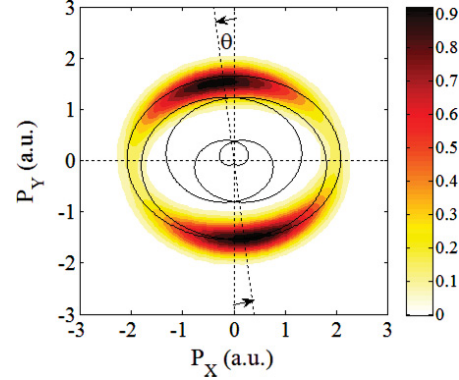

FIG. 1. (Color online) The 2D electron momentum distribution for ionization of Ar by a Ti:sapphire laser pulse ($\lambda = 800$ nm) with a duration $n_p = 6$ cycles, peak intensity of 0.8×10^{15} W/cm^2, and ellipticity $\epsilon = 0.78$. The Keldysh parameter is $\gamma = 0.5$. The offset angle θ is shown on the figure. The black curve represents $-\mathbf{A}(t)$, where $\mathbf{A}(t)$ is the vector potential corresponding to the field (23).

pulses, compare them with the solution of the TDSE, and consider the differences between the FDM and TIPIS model. In Ref. [55] the TIPIS model was already compared with experimental data for the rotation (offset) angle of the momentum distribution generated by elliptically polarized field, that is, the angle θ between the maximum of the distribution and the minor axes of the polarization ellipse. In Fig. 1 we present the momentum distribution in the polarization plane for ionization of Ar by the field of Ti:sapphire laser. The figure shows the main characteristics of the momentum distribution consisting of two main lobes rotated by the angle θ with respect to the minor axis, and that the distribution peaks at $-\mathbf{A}(t)$.

A. Validation of the TIPIS model

We establish the validity of our semiclassical model by comparison with the experiment and an *ab initio* solution of the TDSE. In Fig. 2 we present the momentum distribution in the polarization plane for the case of ionization of the hydrogen atom. In Ref. [75] the solution of the TDSE for the case of the hydrogen atom in a few-cycle circularly polarized laser pulse was presented. The distribution now only has a single main lobe. This is due to the short duration of the phase-stabilized pulse. Calculations in our semiclassical model for the exact same parameters as in Ref. [75] yielded the momentum distribution in Fig. 2. Comparing the momentum distributions obtained with the TDSE, the distributions in Fig. 2 look qualitatively very similar. The interference pattern that is present in the TDSE momentum distribution is not reproducible by our semiclassical model. A quantitative comparison of the distributions can be made by calculating the offset angle: for the TDSE the offset angle is 23° for 5.0×10^{13} W/cm^2 and 12° for 10^{14} W/cm^2 [75], while the offset angles calculated at these intensities within the semiclassical model are 18° and 15°, respectively. The agreement is quite good, also for lower intensity where $\gamma = 1.5$, and the application of tunneling
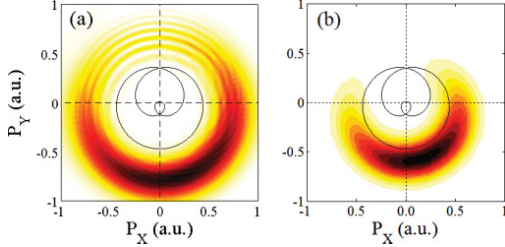
FIG. 2. (Color online) The 2D electron momentum distributions in the polarization plane for ionization of H($1s$) by circularly polarized Ti:sapphire laser pulse with a duration $n_p = 3$ cycles and peak intensity of 10^{14} W/cm^2. Panels (a) and (b) show results obtained by solving the TDSE, and using the classical simulations within the TIPIS model, respectively. The curves represent $-\mathbf{A}(t)$, where $\mathbf{A}(t)$ is the vector potential, defined as in Ref. [75] for this particular figure.

theory for the description of the initial tunneling step is expected to be less accurate.

B. Momentum distributions for λ = 1600 and λ = 800 nm: Difference between the FDM and the TIPIS model, and the role of the ME term

We are interested in a situation where the offset angle θ is larger than for noble gases, that is, when the rotation of the momentum distribution is more pronounced, so that any differences between the semiclassical approaches and also the role of the ME term could be more easily observed. At first glance it would seem that alkali metals are suitable candidates for a large θ. Indeed, the static polarizabilities of the Ar and Ar$^+$ atom are $\alpha_N = 11.08$ a.u. and $\alpha_I = 7.2$ a.u, and, for example, in the case of Li the same quantities are equal to 164.2 and 0.1883 a.u., respectively [76,77]. However, alkali metals have very low ionization potential (for Li $I_0 = 5.39$ eV) and this prevents us from using them in our simulations. In order to understand this fact, let us discuss the applicability conditions of the TIPIS model in more detail.

The validity range of the simulations based on the TIPIS approach is restricted by the two following conditions. On one hand, the laser intensity should not be too high: The second term of Eq. (3) should be not more than $10-20\%$ of the first one. On the other hand, the laser field needs to be strong enough to keep the Keldysh parameter less than or of the order of unity, such that the ionization probability can be described by tunneling. Thus for each atomic species and given wavelength (in our case $\lambda = 1600$ or $\lambda = 800$ nm) the aforementioned conditions define a range of acceptable intensities. In the case of Li and $\lambda = 800$ nm, this range of intensities is $8.7 \times 10^{12} - 8.7 \times 10^{13}$ W/cm^2, which corresponds to the following interval of the Keldysh parameter: $\gamma = 4.8 - 1.6$. Although the tunneling ionization rate often works even when the Keldysh parameter is several times greater than unity (see, e.g., Ref. [78]), we do not consider alkali metals here.

A close inspection of the ionization potentials and static polarizabilities of different atomic species shows that elements as Mg, Cu, or Zn can be used for the present purpose. Indeed, these elements have higher ionization potentials than the

alkali metals. Simultaneously, their polarizabilities are high and substantially different from those of the corresponding ions. We perform our simulations for Mg since multiphoton ionization of this atom has already attracted attention in experiment [79–83] and theory [84–88]. For Mg, $I_p = 0.28$ a.u., $\alpha_N = 71.33$ a.u., and $\alpha_I = 35.00$ a.u., and at the wavelength of 800 nm, our simulation technique is applicable at the intensities of $2.35 \times 10^{13} - 1.0 \times 10^{14}$ W/cm^2, for which the Keldysh parameter is $\gamma = 2.0 - 1.0$.

The results of our simulations for Mg are shown in Figs. 3–5. First we turn our attention to Figs. 3 and 4 where 2D momentum distributions at three different intensities calculated within three different semiclassical models at two wavelengths are shown. The difference between the semiclassical models compared in Figs. 3 and 4 is the potential $V(\mathbf{r})$ in which the classical trajectories (1) are propagated. The first column of Figs. 3 and 4, that is, panels (a), (d), and (g), presents the distributions, calculated ignoring the influence of the ionic potential on the electron motion after tunneling, that is, the tunneled electron moves only in the laser field (the simpleman's model). It is reasonable therefore that these distributions are very similar to those obtained within the SFA (see, e.g. Ref. [78]). The second column of Figs. 3 and 4 shows the same distributions, but now including the Coulomb potential. Finally, the third column presents the results of the full TIPIS model when an electron moves under the action of the laser field and the potential of Eq. (4). It should be stressed that in all three cases the exit points were calculated with the account of the Stark shift, while for the distributions in the first and the second columns of Figs. 3 and 4, the ME term was omitted in Eq. (18). Moreover, the effect of the capture into Rydberg states was taken into account while calculating the distributions of Figs. 3 and 4, see Sec. II above.

The distributions of Fig. 3 are similar to those for Ar at 800 nm, see Fig. 1 and Ref. [55]. As expected, the effect of the rotation is more pronounced, now $\theta \in [30°; 40°]$, whereas for Ar it was $\theta \in [10°; 15°]$ (see Fig. 1). At the same intensities the shape of the distributions at a wavelength of 800 nm differs from that at a wavelength of 1600 nm, compare Fig. 3 and Fig. 4. The reason is that the Keldysh parameter at $\lambda = 800$ nm is two times greater than at $\lambda = 1600$ nm. This, in turn, has two consequences. First, for larger γ the 2D distribution calculated within the plain SM [see Figs. 4(a), 4(d), and 4(g)] is two times closer to the origin of the (p_x, p_y) plane because one has $\mathbf{P} = \mathbf{P}_L \sim (F/\omega, \epsilon F/\omega) = (\varkappa/\gamma, \epsilon\varkappa/\gamma)$. Conversely, at $\lambda = 800$ nm the relative yield of neutral excited atoms N^* with respect to the number of singly charged ions N^+ is larger than at a wavelength of 1600 nm in accordance with Ref. [74], where $N^*/N^+ \sim 1/\lambda^{5/2}$, provided the field strength F is the same for the two wavelengths.

In the first column of Figs. 3 and 4 the momentum distributions consist of two lobes along the minor polarization axis (along the P_y axis), that peak at P_y equal to the value of the vector potential at the time of maximum emission [the time when the electric field (23) points along the major polarization axis]. In the second and third columns of Figs. 3 and 4, the momentum distributions are shifted with respect to the minor polarization axis of the field by some offset angle, discussed above in connection with Fig. 1. By comparison between the second and third columns in Figs. 3 and 4 we
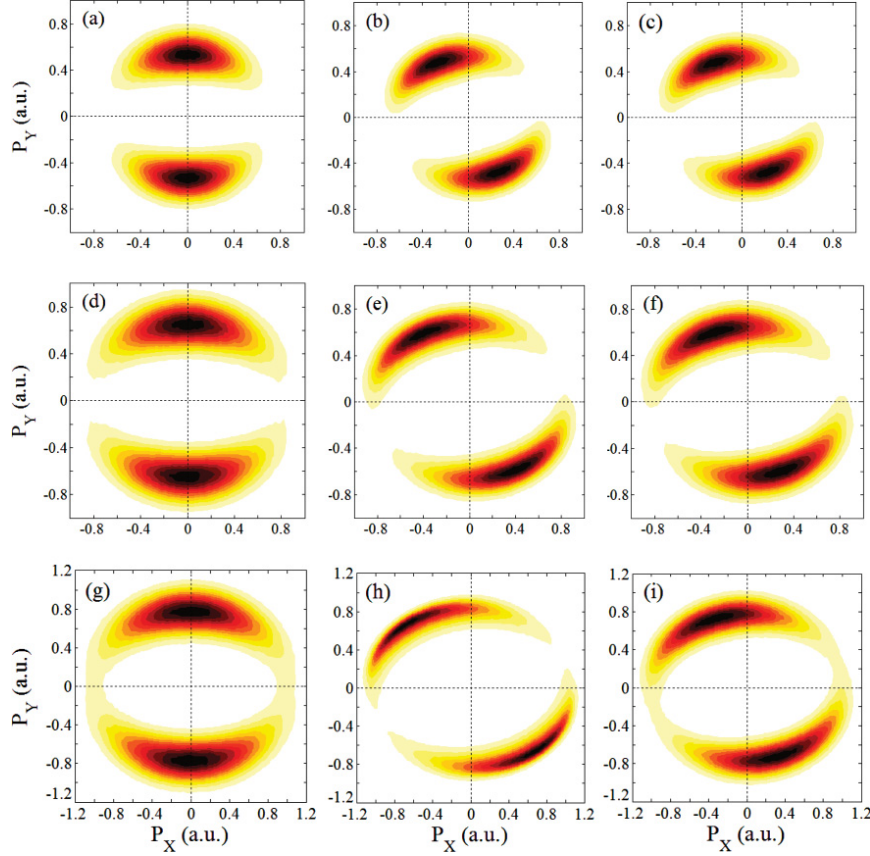
FIG. 3. (Color online) Momentum distributions of the photoelectrons emitted from Mg at a wavelength of 1600 nm and ellipticity $\epsilon = 0.78$ calculated within the three different versions of semiclassical approaches. The left column, that is, panels (a), (d), and (g), shows the distributions, calculated ignoring the ionic potential after tunneling, when the tunneled electron moves in the laser field only. The middle column [panels (b), (e), and (h)] depicts the same distributions, but with consideration for the Coulomb field. The right column [panels (c), (f), and (i)] presents the results of the full TIPIS model, when both terms are taken into account in Eq. (4). The distributions (a)–(c), (d)–(f), and (g)–(i) correspond to the intensity of 2.35, 3.5, and 5.0×10^{13} W/cm^2, and to the Keldysh parameter of 1.05, 0.85, and 0.7, respectively. The same color scale is used for all the distributions.

can gauge the influence of the ME term. At low intensities [Figs. 3(b), 3(c), 4(b), and 4(c)] the ME term does not play any noticeable role: there is hardly any difference whether the ME term is taken into account or not. However, the situation changes with increasing intensity: The offset angles θ of the distributions of Figs. 3(f) and 3(i) are smaller than those of Figs. 3(e) and 3(h). This is so because in the initial stages of the propagation the ME and Coulomb forces act in opposite directions, which results in a smaller offset angle when the ME term is taken into account. This feature is also captured in the analytic estimates: the x components of the Coulomb and ME corrections of the electron momentum have different signs, see Eq. (33). Next, detailed comparison of the semiclassical calculations and the analytic estimates

show that the estimate of Eq. (31) for the contribution of the ME term is quite good. For example, at the intensity of 5.0×10^{13} W/cm^2 and at a wavelength of 800 nm, for $\varphi = \pi$ and $I_p = 7.64$ eV (Mg atom), and for initial conditions, which correspond to the maximum of the field Eq. (23), that is, for $t_0 = \tau_L/2$ and $\mathbf{v}_0 = 0$, one has $\mathbf{P}_{\mathrm{ME}} = (0.058,0)$ from the estimate Eq. (31), whereas exact numerical solution of Newton's equations gives $(0.046, -0.01)$. Contrary to this, the estimate of the Coulomb contribution Eq. (30) is not accurate. The latter does not describe a decrease in the P_y component due to the Coulomb field (along minor axis), see Fig. 4, which is clear from the following example: For the same initial conditions and field parameters as above, the estimate Eq. (30) gives $\mathbf{P}_C = (-0.27,0)$, whereas the numerical solution gives
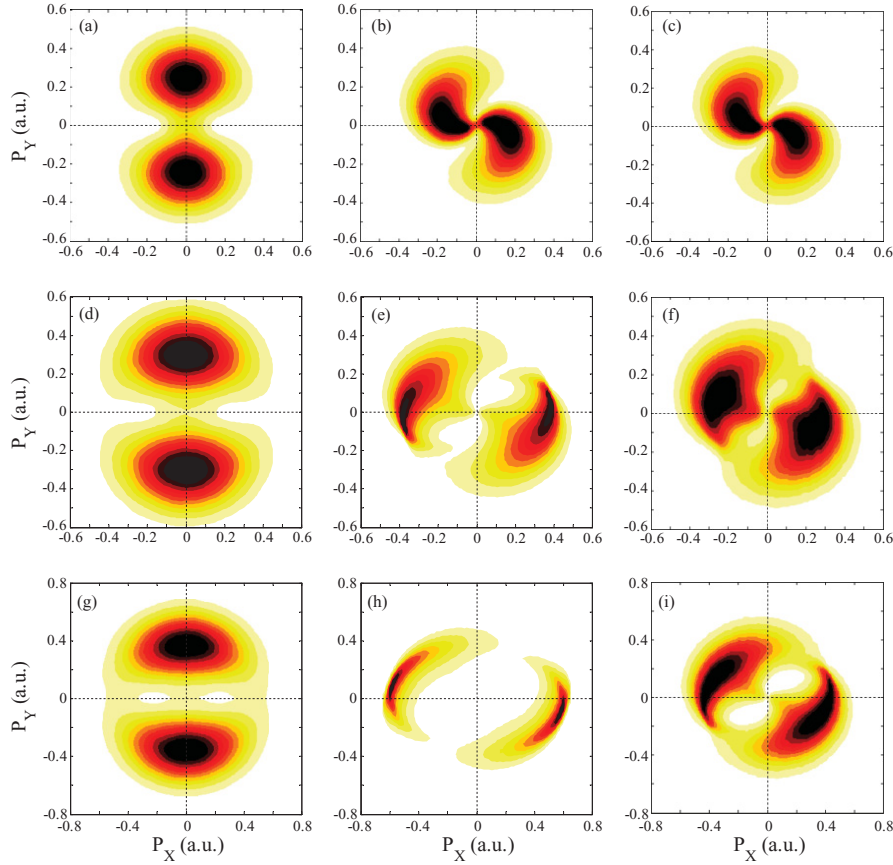
FIG. 4. (Color online) Momentum distributions of the photoelectrons emitted from Mg at a wavelength of 800 nm and ellipticity $\epsilon = 0.78$ calculated within the three different versions of semiclassical approaches. The left column, that is, panels (a), (d), and (g), shows the distributions, calculated ignoring the ionic potential after tunneling, when the tunneled electron moves in the laser field only. The middle column [panels (b), (e), and (h)] depicts the same distributions, but with consideration for the Coulomb field. The right column [panels (c), (f), and (i)] presents the results of the full TIPIS model, when both terms are taken into account in Eq. (4). The distributions (a)–(c), (d)–(f), and (g)–(i) correspond to the intensity of 2.35, 3.5, and 5.0×10^{13} W/cm^2, and to the Keldysh parameter of 2.1, 1.7, and 1.4, respectively. The same color scale is used for all the distributions.

$(-0.31, -0.19)$ with a nonvanishing y component. Therefore the estimate of Eq. (32) is to be used instead of Eq. (30).

The evolution of the distributions at $\lambda = 800$ nm with increasing intensity is more dramatic since not only do the angular offset changes, but also the shapes of the momentum distributions. The two main lobes in the momentum distribution, although distorted, are still present, but also a substantial amount of probability is located in the low-energy part of the distribution. The central (low energy) part of the distribution shown in Fig. 4(e) is more depleted than that of Fig. 4(f). One could expect that this depletion results from the more effective capture into bound states in the absence of the ME force. This is, however, not true. From the estimate (33) one can see that

the magnitude of the final electronic momentum is slightly decreased when the ME term is taken into account. This leads to a larger number of electronic trajectories finishing with smaller radial momenta and, in accord with Eq. (26), more trajectories will finish with negative energy and be captured. Hence the effect of capture after the end of the pulse is stronger when the ME term is taken into account in the potential of Eq. (4): The relative yields of the captured trajectories associated with the momentum distributions of Figs. 4(e) and 4(f) are equal to 0.06 and 0.13, respectively. As expected from Eq. (15), it is seen from Figs. 3 and 4 that the influence of the ME term increases with increasing intensity, which is again consistent with the estimate of Eq. (31).
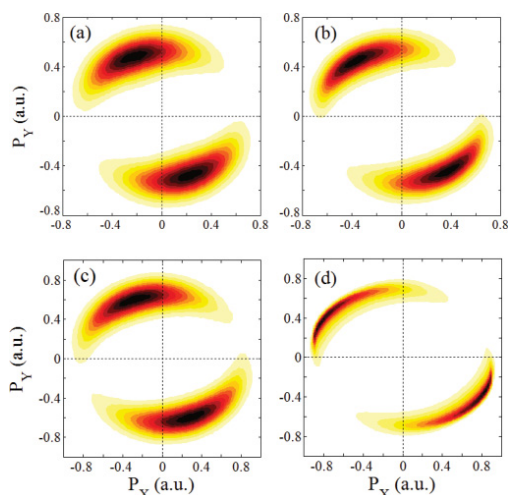
FIG. 5. (Color online) The electron momentum distributions for ionization of Mg at a wavelength of 1600 nm for the ellipticity $\epsilon = 0.78$ and two different intensities: (a), (b) 2.35×10^{13} W/cm^2 and (c), (d) 3.5×10^{13} W/cm^2, which corresponds to the Keldysh parameter γ of 1.05 and 0.85, respectively. The left column of the panels corresponds to the TIPIS model, whereas the right one presents the results of the FDM with the potential given by Eq. (4). In both cases Stark shifts and ME terms are included. The color scale is the same for all the panels.

Next we test to which extent the separation procedure of the static problem of an atom plus field into an one-dimensional tunneling problem, described in Secs. II A and II B, can influence the outcome of the semiclassical simulation. Momentum distributions calculated according to the full TIPIS approach and within the FDM with all force terms are shown in Fig. 5 for three different laser intensities at wavelengths of 1600 nm. The only difference between these approaches is the position of the exit point, which is different in TIPIS and in FDM. We note that in all cases in Fig. 5 the tunneling occurs below the barrier, calculated in FDM or TIPIS. Figure 5 illustrates that the exit point plays a crucial role in semiclassical simulations.

Since $\beta_2(F) < Z$ [see Eq. (17)], and comparing Eqs. (21) and (22), it is evident that the exit point evaluated with the TIPIS model is larger than in the FDM. This is true whether the inequality Eq. (19) is valid (as in the case of Figs. 3–5) or not. Smaller exit points result in larger influence of the

parent ion potential on the trajectory of the tunnelled electron and therefore larger offset angle. This explains why the offset angle is larger in the FDM. At the lower intensity [Figs. 5(a) and 5(b)], the difference between the exit points in the FDM and the TIPIS model is small and therefore the differences between the momentum distributions [Figs. 5(a) and 5(b)] are small. Increasing the intensity [Figs. 5(c) and 5(d)], the tunnel exit point moves closer to the origin and simultaneously the difference between the exit points obtained with the FDM and the TIPIS model increases. Hence, there is a large difference between the offset angles in Figs. 5(c) and 5(d). These trends are correctly captured in the analytic estimates (30)–(31) and (33): they are all inverse proportional to powers of the tunnel exit point r_0. In the final expression of Eq. (33), the ratio between the x and the y component of final momentum is inverse proportional to the tunnel exit point, which gives correct dependence of the offset angle on the tunnel exit point.

IV. CONCLUSIONS

In conclusion, we have investigated in detail a recently introduced physical picture of above-threshold ionization [55]: Tunnel ionization in parabolic coordinates with induced dipole and Stark shift followed by classical propagation in all force fields. We have tested this model by applying it for the investigation of the photoelectron momentum distributions in elliptically polarized field. The present approach demonstrates good agreement with recent experimental data [55] and with TDSE [75]. The role of the multielectron effects in the formation of the photoelectron momentum distributions is clearly identified and investigated over a wide range of laser intensities and wavelengths. The tunnel exit point, and with it the separation procedure yielding the one-dimensional tunneling problem, are clearly demonstrated to have a profound influence on the momentum distributions. The evolution of the momentum distributions with respect to the intensity, the terms in the atomic (ionic) potential, and the tunnel exit point are correctly captured by the analytic estimates and scalings proposed here. Finally, all the effects presented here are studied using pulses with random carrier-envelope phase and therefore can be easily checked in an experiment.

[1] M. V. Fedorov, *Atomic and Free Electrons in a Strong Laser Field* (World Scientific, Singapore, 1997).

[2] N. B. Delone and V. P. Krainov, *Multiphoton Processes in Atoms* (Springer, Berlin, 2000), Chap. 9.

[3] W. Becker, F. Grasbon, R. Kopold, D. B. Milošević, G. G. Paulus, and H. Walther, Adv. At. Mol. Opt. Phys. **48**, 35 (2002).

[4] D. B. Milošević and F. Ehlotzky, Adv. At. Mol. Opt. Phys. **49**, 373 (2003).

[5] A. Becker and F. H. M. Faisal, J. Phys. B **38**, R1 (2005).

[6] C. Figueira de Morisson Faria and X. Liu, J. Mod. Opt. **58**, 1076 (2011).

[7] E. Cormier and P. Lambropoulos, J. Phys. B **30**, 77 (1997).

[8] M. Nurhuda and F. H. M. Faisal, Phys. Rev. A **60**, 3125 (1999).

[9] H. G. Muller, Laser Phys. **9**, 138 (1999).

[10] D. Bauer and P. Koval, Comput. Phys. Commun. **174**, 396 (2006).

[11] T. K. Kjeldsen, Ph.D. thesis, University of Århus, Århus, Denmark, 2007.

[12] L. V. Keldysh, Zh. Eksp. Teor. Fiz. **47**, 1945 (1964) [Sov. Phys. JETP **20**, 1307 (1965)].

[13] F. H. M. Faisal, J. Phys. B **6**, L89 (1973).

[14] H. R. Reiss, Phys. Rev. A **22**, 1786 (1980).

[15] H. B. van Linden van den Heuvell and H. G. Muller, in *Multiphoton Processes*, edited by S. J. Smith and P. L. Knight (Cambridge University Press, Cambridge, 1988).

[16] T. F. Gallagher, Phys. Rev. Lett. **61**, 2304 (1988).

[17] P. B. Corkum, N. H. Burnett, and F. Brunel, Phys. Rev. Lett. **62**, 1259 (1989).

[18] K. C. Kulander, K. J. Schafer, and J. L. Krause, in *Super-Intense Laser-Atom Physics*, edited by B. Piraux, A. L'Hullier, and K. Rzazewski (Plenum, New York, 1993).

[19] P. B. Corkum, Phys. Rev. Lett. **71**, 1994 (1993).

[20] L. D. Landau and E. M. Lifschitz, *Quantum Mechanics Non-relativistic Theory*, 2nd ed. (Pergamon, Oxford, 1965).

[21] A. M. Perelomov, V. S. Popov, and M. V. Terent'ev, Zh. Eksp. Teor. Fiz. **50**, 1393 (1966) [Sov. Phys. JETP **23**, 924 (1966)].

[22] M. V. Ammosov, N. B. Delone, and V. P. Krainov, Zh. Eksp. Teor. Fiz. **91**, 2008 (1986) [Sov. Phys. JETP **64**, 1191 (1986)].

[23] M. Bashkansky, P. H. Bucksbaum, and D. W. Schumacher, Phys. Rev. Lett. **60**, 2458 (1988).

[24] G. G. Paulus, F. Grasbon, A. Dreischuh, H. Walther, R. Kopold, and W. Becker, Phys. Rev. Lett. **84**, 3791 (2000).

[25] S. P. Goreslavski, G. G. Paulus, S. V. Popruzhenko, and N. I. Shvetsov-Shilovski, Phys. Rev. Lett. **93**, 233002 (2004).

[26] S. Basile, F. Trombetta, and G. Ferrante, Phys. Rev. Lett. **61**, 2435 (1988).

[27] P. Lambropoulos and X. Tang, Phys. Rev. Lett. **61**, 2506 (1988).

[28] H. G. Muller, G. Petite, and P. Agostini, Phys. Rev. Lett. **61**, 2507 (1988).

[29] S. V. Popruzhenko and D. Bauer, J. Mod. Opt. **55**, 2573 (2008).

[30] S. V. Popruzhenko, G. G. Paulus, and D. Bauer, Phys. Rev. A **77**, 053409 (2008).

[31] T.-M. Yan, S. V. Popruzhenko, M. J. J. Vrakking, and D. Bauer, Phys. Rev. Lett. **105**, 253002 (2010).

[32] A. Emmanouilidou and D. S. Tchitchekova, Phys. Rev. A **84**, 033407 (2011).

[33] N. I. Shvetsov-Shilovski, S. P. Goreslavski, S. V. Popruzhenko, and W. Becker, Phys. Rev. A **77**, 063405 (2008).

[34] X. Wang and J. H. Eberly, Phys. Rev. Lett. **103**, 103007 (2009).

[35] X. Wang and J. H. Eberly, Phys. Rev. Lett. **105**, 083001 (2010).

[36] X. Wang and J. H. Eberly, New J. Phys. **12**, 093047 (2010).

[37] F. Mauger, C. Chandre, and T. Uzer, Phys. Rel. Lett. **105**, 083002 (2010).

[38] G. G. Paulus, F. Grasbon, H. Walther, P. Villoresi, M. Nisoli, S. Stagira, E. Priori, and S. De. Silvestri, Nature (London) **414**, 182 (2001).

[39] D. B. Milošević, G. G. Paulus, and W. Becker, Phys. Rev. Lett. **89**, 153001 (2002).

[40] D. B. Milošević, G. G. Paulus, and W. Becker, Laser Phys. **13**, 948 (2003).

[41] A. M. Perelomov, V. S. Popov, and M. V. Terent'ev, Zh. Eskp. Teor. Fiz. **51**, 309 (1966) [Sov. Phys. JETP **24**, 207 (1967)].

[42] P. Krstic and M. H. Mittleman, Phys. Rev. A **44**, 5938 (1991).

[43] A. Jaron, J. Z. Kaminski, and F. Ehlotzky, Opt. Commun. **163**, 115 (1999).

[44] N. L. Manakov, M. V. Frolov, B. Borca, and A. F. Starace, J. Phys. B **33**, R141 (2000).

[45] S. P. Goreslavski and S. V. Popruzhenko, Zh. Eksp. Teor. Fiz. **110**, 1200 (1996) [Sov. Phys. JETP **83**, 661 (1996)].

[46] G. G. Paulus, F. Zacher, H. Walther, A. Lohr, W. Becker, and M. Kleber, Phys. Rev. Lett. **80**, 484 (1998).

[47] M. Busuladžić, A. Gazibegović-Busuladžić, and D. B. Milošević, Phys. Rev. A **80**, 013420 (2009).

[48] M. Busuladžić, A. Gazibegović-Busuladžić, and D. B. Milošević, Laser Phys. **20**, 1001 (2010).

[49] L. Holmegaard, J. L. Hansen, L. Kalhøj, S. L. Kragh, H. Stapelfeldt, F. Filsinger, J. Küpper, G. Meijer, D. Dimitrovski, M. Abu-samha, C. P. J. Martiny, and L. B. Madsen, Nat. Phys. **6**, 428 (2010).

[50] D. Dimitrovski, M. Abu-samha, L. B. Madsen, F. Filsinger, G. Meijer, J. Küpper, L. Holmegaard, L. Kalhøj, J. H. Nielsen, H. Stapelfeldt, Phys. Rev. A **83**, 023405 (2011).

[51] J. L. Hansen, L. Holmegaard, L. Kalhøj, S. L. Kragh, H. Stapelfeldt, F. Filsinger, G. Meijer, J. Küpper, D. Dimitrovski, M. Abu-samha, C. P. J. Martiny, and L. B. Madsen, Phys. Rev. A **83**, 023406 (2011).

[52] J. L. Hansen and H. Stapelfeldt, D. Dimitrovski, M. Abu-samha, C. P. J. Martiny, and L. B. Madsen, Phys. Rev. Lett. **106**, 073001 (2011).

[53] P. Eckle, A. N. Pfeiffer, C. Cirelli, A. Staudte, R. Dörner, H. G. Muller, M. Büttiker, and U. Keller, Science **322**, 1525 (2008).

[54] P. Eckle, M. Smolarski, P. Schlup, J. Biegert, A. Staudte, M. Schöffler, H. G. Muller, R. Dörner, and U. Keller, Nat. Phys. **4**, 565 (2008).

[55] A. N. Pfeiffer, C. Cirelli, M. Smolarski, D. Dimitrovski, M. Abu-samha, L. B. Madsen, and U. Keller, Nat. Phys. **8**, 76 (2012).

[56] D. Dimitrovski, C. P. J. Martiny, and L. B. Madsen, Phys. Rev. A **82**, 053404 (2010).

[57] T. Brabec, M. Yu. Ivanov, and P. B. Corkum, Phys. Rev. A **54**, R2551 (1996).

[58] J. Chen and C. H. Nam, Phys. Rev. A **66**, 053415 (2002).

[59] T. Nubbemeyer, K. Gorling, A. Saenz, U. Eichmann, and W. Sandner, Phys. Rev. Lett. **101**, 233001 (2008).

[60] C. Liu and K. Z. Hatsagortsyan, J. Phys. B **44**, 095402 (2011).

[61] C. Liu and K. Hatsagortsyan, e-print arXiv: 1109.5645v1 [physic.atom-ph] (2011).

[62] A. Kästner, U. Saalmann, and J. M. Rost, Phys. Rev. Lett. **108**, 033201 (2012).

[63] C. Lemell, K. I. Dimitriou, X.-M. Tong, S. Nagele, D. V. Kartashov, J. Burgdörfer, and S. Gräfe, Phys. Rev. A **85**, 011403(R) (2012).

[64] A. Kästner, U. Saalmann, and J. M. Rost, Phys. Rev. Lett. **108**, 033201 (2012).

[65] J. Chen, J. Liu, L. B. Fu, and W. M. Zheng, Phys. Rev. A **63**, 011404(R) (2000).

[66] L. B. Fu, J. Liu, J. Chen, and S. G. Chen, Phys. Rev. A **63**, 043416 (2001).

[67] T. Brabec, M. Côté, P. Boulanger, and L. Ramunno, Phys. Rev. Lett. **95**, 073001 (2005).

[68] N. B. Delone and V. P. Krainov, J. Opt. Soc. Am. B **8**, 1207 (1991).

[69] K. I. Dimitriou, D. G. Arbo, S. Yoshida, E. Persson, and J. Burgdörfer, Phys. Rev. A **70**, 061401(R) (2004).

[70] M. Yu. Ivanov, M. Spanner, and O. Smirnova, J. Mod. Opt. **52**, 165 (2005).

[71] M. Abu-samha and L. B. Madsen, Phys. Rev. A **84**, 023411 (2011).

[72] P. A. Batishchev, O. I. Tolstikhin, and T. Morishita, Phys. Rev. A **82**, 023416 (2010).

[73] W. H. Press, S. A. Teukolsky, W. T. Vetterling, and B. P. Flannery, *Numerical Recipes in Fortran 77: The Art of Scientific Computing*, 2nd ed. (Cambridge University Press, Cambridge, 1992).

[74] N. I. Shvetsov-Shilovski, S. P. Goreslavski, S. V. Popruzhenko, and W. Becker, Laser Phys. **19**, 1550 (2009).

[75] C. P. J. Martiny, M. Abu-samha, and L. B. Madsen, J. Phys. B **42**, 161001 (2009).

[76] J. Mitroy, M. S. Safronova, and C. W. Clark, J. Phys. B **43**, 202001 (2010).

[77] M. P. F. Bristow and I. I. Glas, Phys. Fluids **15**, 2066 (1972).

[78] V. S. Popov, Usp. Fiz. Nauk **174**, 921 (2004) [Phys. Usp. **47**, 855 (2004)].

[79] D. Kim, S. Fournier, M. Saeed, and L. F. DiMauro, Phys. Rev. A **41**, 4966 (1990).

[80] N. J. van Druten, R. Trainham, and H. G. Muller, Phys. Rev. A **50**, 1593 (1994).

[81] D. Xenakis, N. E. Karapanagioti, D. Charalambidis, and H. Bachau, and E. Cormier, Phys. Rev. A **60**, 3916 (1999).

[82] G. D. Gillen, M. A. Walker, and L. D. Van Woerkom, Phys. Rev. A **64**, 043413 (2001).

[83] G. D. Gillen and L. D. Van Woerkom, Phys. Rev. A **68**, 033401 (2003).

[84] J. Zhang and P. Lambropoulos, Phys. Rev. Lett. **77**, 2186 (1996).

[85] L. A. A. Nikolopoulos, G. Buica-Zloh, and P. Lambropoulos, Eur. Phys. J. D **26**, 245 (2003).

[86] I. Liontos, A. Bolovinos, S. Cohen, and A. Lyras, Phys. Rev. A **70**, 033403 (2004).

[87] T. Nakajima and G. Buica, Phys. Rev. A **74**, 023411 (2006).

[88] G. Buica and T. Nakajima, Phys. Rev. A **79**, 013419 (2009).

8.3 *Semiclassical two-step model for the hydrogen molecule*

THE EUROPEAN
PHYSICAL JOURNAL D

Regular Article

Semiclassical two-step model for ionization of the hydrogen molecule by a strong laser field[*]

Nikolay I. Shvetsov-Shilovski[1,a], Manfred Lein[1], and Karoly Tőkési[2,3]

[1] Institut für Theoretische Physik, Leibniz Universität Hannover, 30167 Hannover, Germany
[2] Institute for Nuclear Research, Hungarian Academy of Sciences, 4001 Debrecen, Hungary
[3] ELI-HU Nonprofit Ltd., Dugonics tér 13, 6720 Szeged, Hungary

Abstract. We extend the semiclassical two-step model for strong-field ionization that describes quantum interference and accounts for the Coulomb potential beyond the semiclassical perturbation theory to the hydrogen molecule. In the simplest case of the molecule oriented along the polarization direction of a linearly polarized laser field, we predict significant deviations of the two-dimensional photoelectron momentum distributions and the energy spectra from the case of atomic hydrogen. Specifically, for the hydrogen molecule the electron energy spectrum falls off slower with increasing energy, and the holographic interference fringes are more pronounced than for the hydrogen atom at the same parameters of the laser pulse.

1 Introduction

Strong-field physics focuses on the interaction of intense laser radiation with atoms and molecules. This interaction leads to such phenomena as above-threshold ionization (ATI), formation of the high-energy plateau in the electron energy spectrum, generation of high-order harmonics, sequential and nonsequential double and multiple ionization, etc. (see Refs. [1–4] for reviews). Among the main theoretical approaches used in strong-field laser-atom physics are the direct numerical solution of the time-dependent Schrödinger equation (TDSE) (see, e.g., Refs. [5–7]), the strong-field approximation (SFA) [8–10], and the semiclassical models (see, e.g., Refs. [11–14]) applying a classical description of an electron after it has been released from an atom, e.g., by tunneling ionization [15–17].

However, ionization of a molecule by a strong laser pulse is much more complicated than the same process for an atom. This is due to the presence of extra degrees of freedom (nuclear motion), the corresponding time scales, and complicated shape of the electronic orbitals. In order to fully consider all the features of the molecular ionization, the TDSE in three spatial dimensions should be solved. This is a very difficult task, which is possible only for the simplest molecules and under selection of the most

relevant degrees of freedom (see Refs. [18,19]). Therefore, approximate semianalytic models that can provide the basic physical insight are very important for theoretical description of molecules in strong laser fields. The molecular strong-field approximation (MO-SFA) [20,21] and the molecular tunneling theory, i.e., the molecular Ammosov-Delone-Krainov (MO-ADK) theory [22], are the most widely known examples of such models. MO-SFA is a generalization of the atomic SFA onto the case of molecules. In turn, the MO-ADK is the extension of the Perelomov-Popov-Terent'ev [16] or ADK [17] tunneling formulas. In both MO-SFA and MO-ADK (as well as in the SFA and ADK) ionization is described as a transition from an initial field-free state to a Volkov state (the wave function for an electron in an electromagnetic field). As a result, intermediate bound states and the Coulomb interaction in the final state are completely neglected in the MO-SFA and MO-ADK.

In contrast to this, the semiclassical approaches allow to account for the effects of the Coulomb potential. In addition to this, the trajectory-based models do not usually require as high computational costs as the numerical solution of the TDSE. Finally, by analyzing classical trajectories these models are able to illustrate the mechanism underlying the strong-field phenomena of interest. For these reasons, the semiclassical model accounting for the ionic potential has become one of the powerful tools of the strong-field physics. However, presently there are only a few studies applying these models to describe strong-field ionization of molecules, see, e.g., references [23–26].

Until recently, trajectory-based models have not been able to account for quantum interference and to describe

---

[*] Contribution to the Topical Issue "Many Particle Spectroscopy of Atoms, Molecules, Clusters and Surfaces (2018)", edited by Károly Tőkési, Béla Paripás, Gábor Pszota, and Andrey V. Solov'yov.

[a] e-mail: nikolay.shvetsov@itp.uni-hannover.de

interference effects in photoelectron spectra and momentum distributions. This drawback has been overcome by a quantum trajectory Monte Carlo (QTMC) [27] and semiclassical two-step (SCTS) [28] models. In these models each classical trajectory is associated with a certain phase, and the contributions of all the trajectories leading to a given final (asymptotic) momentum are added coherently. In the SCTS model the phase is calculated from the semiclassical expression for the matrix element of the quantum mechanical propagator. Therefore, the SCTS model accounts for the Coulomb potential beyond the semiclassical perturbation theory. The phase used in the QTMC model can be viewed as an approximation to the full semiclassical phase of the SCTS. As a result, the SCTS model yields better agreement with the direct numerical solution of the TDSE than previously developed QTMC model, see reference [28]. While the QTMC model was applied to strong-field ionization of molecules (see Refs. [24,25]), the SCTS model has not been generalized to the molecular case so far.

In this paper, we extend the SCTS model to molecular hydrogen. We calculate two-dimensional momentum distributions, energy spectra, and angular distributions of ionized electrons, and compare them to the case of atomic hydrogen. We reveal significant differences in momentum distributions and electron energy spectra. Then we compare our molecular SCTS to the predictions of the QTMC model for molecules.

The paper is organized as follows. In Section 2 we formulate the SCTS model for the hydrogen molecule. In Section 3 we compare the results of the SCTS model for the H_2 molecule and the H atom. The conclusions are given in Section 4. Atomic units are used throughout the paper unless indicated otherwise.

2 Semiclassical two-step model for H_2 molecule

Any semiclassical approach to a strong-field process is based on propagation of an ensemble of classical trajectories that obey Newton's equation of motion. We treat the electric field of the laser pulse $\mathbf{F}(t)$ and the ionic potential $V(\mathbf{r}, t)$ on equal footing, and, therefore, the equation of motion reads as:

$$\frac{d^2\mathbf{r}}{dt^2} = -\mathbf{F}(t) - \nabla V(\mathbf{r}, t). \tag{1}$$

For the H_2 molecule the ionic potential reads as

$$V(\mathbf{r}) = -\frac{Z_1}{|\mathbf{r} - \mathbf{R}/2|} - \frac{Z_2}{|\mathbf{r} + \mathbf{R}/2|}, \tag{2}$$

where $\mathbf{R}$ is the vector that points from one nucleus to another. Here we assume that the origin of the coordinate system is placed in the center of the molecule. Following references [24,25], we choose the effective charges Z_1 and Z_2 to be equal to 0.5 a.u.

In order to find the trajectory $\mathbf{r}(t)$ and momentum $\mathbf{p}(t)$ by integrating equation (1), we need to specify the initial velocity of the electron and the starting point of its trajectory. As in many trajectory-based models, we assume that the electron starts with zero initial velocity along the laser field $v_{0,z} = 0$, but can have a nonzero initial velocity $\mathbf{v}_{0,\perp} = v_{0,x}\mathbf{e}_x + v_{0,y}\mathbf{e}_y$ in the perpendicular direction. (We imply that the field is polarized along the z axis.) Various approaches are used to obtain the starting point of the trajectory, i.e., the tunnel exit point z_e. For the H atom the tunnel exit can be found using the separation of the tunneling problem for the Coulomb potential in parabolic coordinates [15]. However, in the case of the H atom we use the simplest formula for z_e neglecting the Coulomb potential, i.e., assuming triangular potential barrier formed by the laser field and the ground state energy:

$$r_e(t_0) = \frac{I_p}{F(t_0)}, \tag{3}$$

where I_p is the ionization potential, $r_e(t_0) = |z_e(t_0)|$, and the sign of $z_e(t_0)$ is chosen the ensure that the electron tunnels out from under the barrier in the direction opposite to the laser field $\mathbf{F}(t_0)$ at the time of ionization. For the H_2 molecule we use and compare two different approaches to determine z_e. The first one applies equation (3) neglecting the molecular potential, and the second approach considers the potential barrier formed by the molecular potential and the electric field of the laser *in a 1D cut along the field direction*. This latter approach is often called the field direction model (FDM), see [29]. Thus in the FDM the tunnel exit point is found from the equation:

$$V(\mathbf{r}) + F(t_0)z_e = -I_p. \tag{4}$$

The electron trajectory $\mathbf{r}(t)$ is completely determined by the ionization time t_0 and initial transverse velocity $\mathbf{v}_{0,\perp}$. However, in contrast to the atomic case, for ionization of a molecule it is not obvious how to distribute the times of ionization and the initial transverse momenta.

The two main approaches to this problem are presently used in semiclassical simulations of the ATI in molecules: Molecular quantum-trajectory Monte-Carlo model (MO-QTMC) [24,25] and partial Fourier transform approach for molecules (MO-PFT), see references [25,30,31]. The MO-QTMC approach is based on the MO-SFA, whereas the MO-PFT introduces the wave function in mixed representation and applies the Wentzel-Kramers-Brillouin (WKB) approximation. For the parameters of interest both approaches yield similar results when combined with the QTMC model (see Ref. [25]). In the present paper we use the MO-PFT model. This model is based on the partial Fourier transform (PFT) approach for atoms [32]. In order to make the presentation self-contained, here we repeat the main points of the PFT and MO-PFT.

The mixed representation wave function $\Pi(p_x, p_y, z)$ of an electron in a zero-range potential and a static electric field that points in the direction of the z axis is given by

$$\Pi_{H_2}\left(p_x, p_y, z\right) = \exp\left(-\frac{i}{2}p_x R \sin\theta_m \cos\varphi_m - \frac{i}{2}p_y R \sin\theta_m \sin\varphi_m\right) \Pi_{atom1}\left(p_x, p_y, z - \frac{R}{2}\cos\theta_m\right)$$
$$+ \exp\left(\frac{i}{2}p_x R \sin\theta_m \cos\varphi_m + \frac{i}{2}p_y R \sin\theta_m \sin\varphi_m\right) \Pi_{atom2}\left(p_x, p_y, z + \frac{R}{2}\cos\theta_m\right) \quad (10)$$

(see Ref. [32]):

$$\Pi\left(p_x, p_y, z\right) = \Pi\left(p_x, p_y, z_0\right) \sqrt{\frac{p_z\left(z_0\right)}{p_z\left(z\right)}}$$
$$\times \exp\left\{i\left[S\left(p_x, p_y, z\right) - S\left(p_x, p_y, z_0\right)\right]\right\}. \quad (5)$$

Here $p_z\left(z\right) = \left|\partial S\left(p_x, p_y, p_z\right)/\partial z\right|$ is the electron momentum in the z direction, $S\left(p_x, p_y, z\right)$ is the classical action, and $z_0 < 0$ is the point (for $F > 0$) in the classically forbidden region, where the one-dimensional WKB solution for the motion along the z axis is matched to the wave function of the initial bound state. We note that since z_0 is not a turning point, the wave function and its derivatives are continuous at z_0. The exponential of equation (5) can be found by integration of the Hamilton-Jacobi equation:

$$S\left(p_x, p_y, z\right) - S\left(p_x, p_y, z_0\right)$$
$$= \frac{1}{3F}\left(2E' - 2Fz\right)^{3/2} - \frac{1}{3F}\left(2E' - 2Fz_0\right)^{3/2}. \quad (6)$$

Here $E' = -\left(I_p + p_\perp^2/2\right)$ and $p_\perp = \sqrt{p_x^2 + p_y^2}$. Assuming that $|z_0| \ll |z_e|$, where $z_e = -I_p/F < 0$ is the exit point from the triangular barrier, we expand the expression in the right-hand side of equation (6) in powers of z_0 up to the first order:

$$S\left(p_x, p_y, z_e\right) - S\left(p_x, p_y, z_0\right) = i\frac{\kappa^3}{3F} + i\frac{\kappa p_\perp^2}{2F} - i\kappa\left|z_0\right|, \quad (7)$$

where $\kappa = \sqrt{2I_p}$. Inserting this expression into equation (5) and replacing the momentum $p_z\left(z_0\right)$ with κ, we obtain the following expression for the wave function in mixed representation (see Ref. [32]):

$$\Pi\left(p_x, p_y, z\right) = \Pi\left(p_x, p_y, z_0\right) \sqrt{\frac{\kappa}{p_z\left(z\right)}}$$
$$\times \exp\left[-\frac{\kappa^3}{3F} - \frac{\kappa p_\perp^2}{2F} + \kappa\left|z_0\right|\right]. \quad (8)$$

For the H_2 molecule the bound-state orbital is the bonding superposition of the two $1s$ atomic orbitals at the atomic centers (see, e.g., Ref. [33]).

$$\Psi_{H_2}\left(\mathbf{r}\right) = \frac{1}{\sqrt{2\left(1 + S_{OI}\right)}}\left[\psi_{atom1}\left(\mathbf{r} - \mathbf{R}/2\right)\right.$$
$$\left. + \psi_{atom2}\left(\mathbf{r} + \mathbf{R}/2\right)\right], \quad (9)$$

where S_{OI} is the atomic overlap integral. In what follows we omit the coefficient before the sum of two atomic orbitals in equation (9), since it has no effect on the shape of the momentum distributions that we are interested in. The partial Fourier transform of this molecular orbital reads as (see Ref. [31]):

See equation (10) *above*

where θ_m and φ_m are the polar and azimuthal angles of the molecular axis, respectively (see Fig. 1). Inserting the partial Fourier transforms of the $1s$ orbitals (see Ref. [32]) into equation (10) and taking into account that the new matching points z_1 and z_2 for atoms 1 and 2 are $z_{1,2} = z_0 \pm R\cos\theta_m/2$, we arrive at the following expression for the wave function of the H_2 molecule in mixed representation just beyond the tunnel exit:

See equation (11) *next page.*

Following reference [25], we use expression (11) as a complex amplitude for ionization at t_0 and $\mathbf{v}_{0,\perp}$, without adding prefactors. Thus, we put $F = F\left(t_0\right)$, $p_x = v_{0,x}$, and $p_y = v_{0,y}$ in equation (11). Furthermore, we concentrate on the case when the H_2 molecule is oriented along the polarization direction of the laser field, i.e., $\theta_m = \varphi_m = 0$. Then the factor in the curly brackets in equation (11) is a constant for a fixed R. Therefore, in our simulations we use only the exponential part of the amplitude (11). We use the ionization potential $I_p = 0.60$ a.u., what corresponds to the vertical ionization potential of H_2 molecule, i.e., to the case when the H_2^+ ion has the same internuclear distance R as the neutral hydrogen molecule. Since in our model the positions of the nuclei are fixed, we disregard the vibrational energy levels when calculating the ionization potential.

For not too short laser pulses the ionized electron is far away from both nuclei at the time instant t_f when the pulse terminates: $r\left(t_f\right) \gg R/2$. Therefore, we can assume that after the end of the pulse the electron moves in the Coulomb field only. Indeed, the potential of equation (2) tends to Z/r for $r \to \infty$, where $Z = Z_1 + Z_2$. Therefore, the asymptotic momentum $\mathbf{k}$ of the electron is uniquely determined by its momentum and position at the end of the pulse [29,34]. The magnitude of the final momentum can be found from energy conservation:

$$\frac{k^2}{2} = \frac{p^2(t_f)}{2} - \frac{Z}{r(t_f)}, \quad (12)$$

whereas its orientation is determined by the following expression:

$$\mathbf{k} = k\frac{k\left(\mathbf{L} \times \mathbf{a}\right) - \mathbf{a}}{1 + k^2 L^2}. \quad (13)$$

$$\Pi\left(p_x, p_y, z_e\right) \sim \left\{ \begin{array}{l} \exp\left(-\dfrac{i}{2}p_x R \sin\theta_m \cos\varphi_m - \dfrac{i}{2}p_y R \sin\theta_m \sin\varphi_m\right)\exp\left(-\dfrac{1}{2}\kappa R\cos\theta_m\right) \\[2mm] + \exp\left(\dfrac{i}{2}p_x R \sin\theta_m \cos\varphi_m + \dfrac{i}{2}p_y R \sin\theta_m \sin\varphi_m\right)\exp\left(\dfrac{1}{2}\kappa R\cos\theta_m\right) \end{array} \right\}$$

$$\times \exp\left[-\frac{\kappa^3}{3F} - \frac{\kappa\left(p_x^2 + p_y^2\right)}{2F}\right] \qquad (11)$$

Here $\mathbf{L} = \mathbf{r}(t_f) \times \mathbf{p}(t_f)$ and $\mathbf{a} = \mathbf{p}(t_f) \times \mathbf{L} - Z\mathbf{r}(t_f)/r(t_f)$ are the conserving angular momentum and the Runge-Lenz vector, respectively. For a single-cycle or two-cycle pulse the condition $r(t_f) \gg R/2$ is not true for a substantial number of trajectories. In this case the asymptotic momenta are to be found by numerical integration of equation (1) up to times substantially exceeding the duration of the pulse.

In order to accomplish the generalization of the SCTS model to the hydrogen molecule, we need to derive the corresponding expression for the phase associated with a classical trajectory. In the case of an arbitrary effective potential $V(\mathbf{r}, t)$ the SCTS phase reads as:

$$\Phi^{SCTS}(t_0, \mathbf{v}_0) = -\mathbf{v}_0 \cdot \mathbf{r}(t_0) + I_p t_0$$
$$- \int_{t_0}^{\infty} dt \left\{\frac{p^2(t)}{2} + V[\mathbf{r}(t)] - \mathbf{r}(t) \cdot \nabla V[\mathbf{r}(t)]\right\} \qquad (14)$$

see reference [28]. For the molecular potential $V(\mathbf{r})$ (Eq. (2)) the phase $\Phi(t_0, \mathbf{v}_0)$ is given by

$$\Phi_{H_2}^{SCTS}(t_0, \mathbf{v}_0) = -\mathbf{v}_0 \cdot \mathbf{r}(t_0) + I_p t_0$$
$$- \int_{t_0}^{\infty} dt \left\{\frac{p^2(t)}{2} - \frac{Z_1\left(\mathbf{r} - \mathbf{R}/2\right) \cdot \left(2\mathbf{r} - \mathbf{R}/2\right)}{|\mathbf{r} - \mathbf{R}/2|^3} \right.$$
$$\left. + \frac{Z_2\left(\mathbf{r} + \mathbf{R}/2\right) \cdot \left(2\mathbf{r} + \mathbf{R}/2\right)}{|\mathbf{r} + \mathbf{R}/2|^3}\right\}. \qquad (15)$$

It is easy to see that for $r \gg R/2$

$$\Phi_H^{SCTS}(t_0, \mathbf{v}_0) \approx -\mathbf{v}_0 \cdot \mathbf{r}(t_0) + I_p t_0$$
$$- \int_{t_0}^{\infty} dt \left\{\frac{p^2(t)}{2} - \frac{2Z}{r(t)}\right\}. \qquad (16)$$

Equation (16) coincides with the SCTS phase for the Coulomb potential, $-Z/r$ (see Ref. [28]). Assuming that $r(t_f) \gg R/2$ we can use the expression for the phase accumulated in the asymptotic interval $[t_f, \infty]$ for the Coulomb potential (see Ref. [28]):

$$\tilde{\Phi}_f^C(t_f) = -Z\sqrt{b}\left[\ln g + \mathrm{arcsinh}\left\{\frac{\mathbf{r}(t_f) \cdot \mathbf{p}(t_f)}{g\sqrt{b}}\right\}\right], \quad (17)$$

where $b = 1/2E$ and $g = \sqrt{1 + 2EL^2}$. Here, in turn, E is the conserving energy of the electron moving along
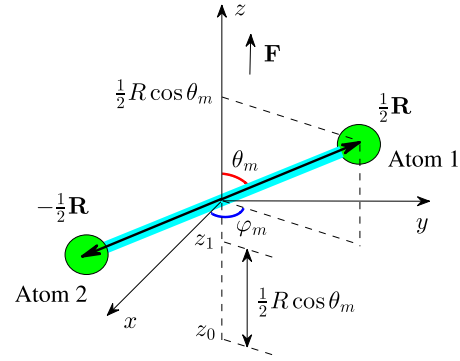

Fig. 1. The sketch of the hydrogen molecule. The thick blue line depicts the molecular axis. Its orientation is determined by the polar θ_m and azimuthal φ_m angles. The positions of the first and the second atoms are given by the vectors $-\mathbf{R}/2$ and $\mathbf{R}/2$, respectively. The laser field $\mathbf{F}$ points towards z direction. The longitudinal displacement $R\cos\theta_m/2$ and the new matching point z_1 for atom 1 are shown on the z-axis.

the outgoing Kepler hyperbola. Equation (17) allows to decompose the integral in equation (15) into two integrals over the intervals $[t_0, t_f]$ and $[t_f, \infty]$. The first integral over $[t_0, t_f]$ can be readily calculated numerically knowing the position vector $\mathbf{r}(t)$ and momentum $\mathbf{p}(t)$ of the electron.

In contrast to this, the phase associated with each trajectory in the molecular QTMC model reads as:

$$\Phi_{H_2}^{QTMC}(t_0, \mathbf{v}_0) = -\mathbf{v}_0 \cdot \mathbf{r}(t_0) + I_p t_0$$
$$- \int_{t_0}^{\infty} dt \left\{\frac{p^2(t)}{2} - \frac{Z_1}{|\mathbf{r} - \mathbf{R}/2|} - \frac{Z_2}{|\mathbf{r} + \mathbf{R}/2|}\right\}, \qquad (18)$$

see references [24,25]. At large distances equation (18) recovers the QTMC phase for the H atom (see Ref. [27]):

$$\Phi_H^{QTMC}(t_0, \mathbf{v}_0) \approx -\mathbf{v}_0 \cdot \mathbf{r}(t_0) + I_p t_0$$
$$- \int_{t_0}^{\infty} dt \left\{\frac{p^2(t)}{2} - \frac{Z}{r(t)}\right\}. \qquad (19)$$

For the simulations we apply an importance sampling implementation of both QTMC and SCTS models. Within the importance sampling approach the initial conditions

t_j^0 and v_0^j $(j = 1, \ldots, n_p)$ for all n_p trajectories of the ensemble are distributed according to the square root of the probability (Eq. (11)). We propagate the trajectories of the ensemble using equation (1) and bin them in cells in momentum space in accord with their asymptotic momenta. The amplitudes that correspond to the trajectories reaching the same cell are added coherently, and the ionization probability reads as:

$$\frac{dR}{d^3k} = \left| \sum_{j=1}^{n_p} \exp\left[i\Phi\left(t_0^j, \mathbf{v}_0^j\right) \right] \right|^2, \qquad (20)$$

see reference [28]. It should be stressed that it is necessary to achieve convergence both with respect to the size of the momentum cell in and the number of the trajectories in the ensemble.

3 Results and discussion

We define a few-cycle linearly polarized laser pulse in terms of a vector potential:

$$\mathbf{A} = \frac{F_0}{\omega} f(t) \sin(\omega t) \mathbf{e}_z. \qquad (21)$$

Here F_0 is the field strength, ω is the carrier angular frequency, $\mathbf{e}_z$ is the unit vector in the polarization direction, and $f(t)$ is the envelope function. The pulse is present between for $0 \leq t \leq t_f$. Here $t_f = nT$, where, in turn, n is the number of cycles within the pulse, and $T = 2\pi/\omega$ is the laser period. The electric field can be obtained from the vector potential (21) by $\mathbf{F} = -d\mathbf{A}/dt$. In our simulations we consider a pulse with $n = 8$ optical cycles and use two different envelope functions:

$$f_1(t) = \sin^2\left(\frac{\omega t}{16}\right), \qquad (22)$$

for a sine squared pulse, and

$$f_2(t) = \begin{cases} t/2T, & t < 2T \\ 1, & 2T \leq t < 6T \\ (8T - t)/2T, & 6T \leq t \leq 8T \end{cases} \qquad (23)$$

for a trapezoidal pulse.

We first compare the results of the SCTS model for the H atom and the H_2 molecule. In Figure 2 we present the two-dimensional (2D) photoelectron momentum distributions in the $(k_z, k_\perp)$ plane for H (Fig. 2a) and H_2 (Figs. 2b and 2c). The tunnel exit point for the H atom was calculated from equation (3) (triangular potential barrier). For the H_2 molecule we show the momentum distribution calculated for the exit point given by equation (3) (see Fig. 2b), as well as the distribution obtained for z_e found in accord with the FDM (see Fig. 2c). It is seen that the distributions of Figures 2a and 2b are rather similar to each other. It should be stressed that the potential of equ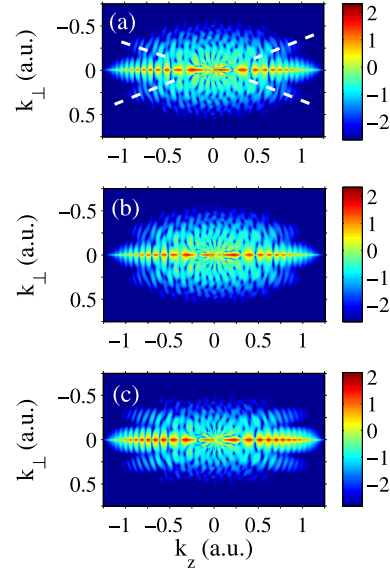ation (2) is fully taken into account in Newton's equations of motion and the expression for the phase when calculating of Figure 2b. These results show that the effects of molecular structure are not pronounced in the photoelectron momentum distributions if the molecular potential is neglected in finding the starting point of the trajectory. This fact is easy to understand taking into account that for the parameters of Figure 2 the characteristic exit for the triangular barrier $r_0 = I_p/F_0 \gg R/2$. Indeed, for the H molecule at the intensity of $2.0 \cdot 10^{14}$ W/cm^2 $z_{e,c} \approx 7.94$ a.u. (cf. with $R/2 = 0.71$ a.u.). We note that the distance between the released electron and the nuclei increases further when the electron moves along the trajectory. Therefore, if the tunnel exit point is calculated from equation (3), the ionized electron is actually moving in the same Coulomb potential as in the case of the atomic hydrogen. For the H_2 molecule and the parameters of Figure 2 the FDM predicts the tunnel exit point at 5.48 a.u. at the maximum of the laser field. In Figure 3 we show the tunnel exit points corresponding to the maximum value of the pulse calculated from equation (3) and in accord with the FDM as functions of the laser intensity.
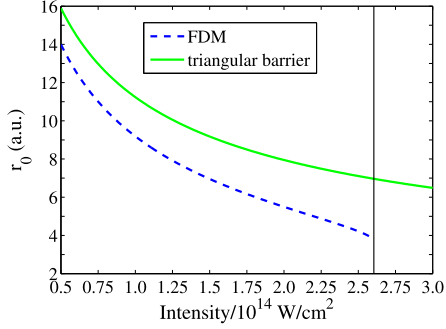

Fig. 2. The two-dimensional photoelectron momentum distributions for the H atom (a) and the H_2 molecule (b) and (c) ionized by a laser pulse with a sine square envelope (Eq. (22)), duration of $n = 8$ cycles, wavelength of $\lambda = 800$ nm, and intensity of 2.0×10^{14} W/cm^2. The panels (a) and (b) show the distributions calculated for the exit point given by equation (3). The panel (c) corresponds to the exit point found in accord with the FDM (Eq. (4)). The holographic fringes are indicated by white dashed lines in panel (a). The distributions are normalized to the total ionization yield. A logarithmic color scale in arbitrary units is used. The laser field is linearly polarized along the z axis.

Fig. 3. The tunnel exit point as a function of laser intensity. The parameters are as in Figure 2. The blue (dashed) and green (solid) curves correspond to the triangular potential barrier (Eq. (3)) and the FDM model, respectively. The critical (threshold) intensity in the FDM model is shown by a thin black (solid) line.

It is seen that the exit point from under the triangular potential barrier is larger than the result of the FDM that accounts for the molecular potential (Eq. (2)). Moreover, for the parameters of Figure 2 the FDM with the potential of equation (2) yields the critical (threshold) field that corresponds to the barrier-suppression regime $F_C = 0.086$ a.u. This value of the critical field corresponds to the peak intensity of 2.60×10^{14} W/cm^2 (see Fig. 3), which is close to the widely known estimate for the critical field based on the one-dimensional consideration (see Ref. [35]):

$$F_C = \frac{\kappa^4}{16Z} \qquad (24)$$

that predicts $F_C = 0.09$ a.u. for a model atom with $I_p = 0.60$ a.u. equal to the one for H$_2$. For these reasons, in what follows we use the FDM for calculation of the exit point for the H$_2$ molecule. The comparison of Figures 2a and 2c shows that the molecular potential has a pronounced effect on the shape of the momentum distribution and its interference structure. Indeed, the 2D momentum distribution for the H$_2$ molecule is more extended along the polarization direction that the one for the H atom. It is seen that the interference pattern contains well-resolved side lobes (fringes) marked by white (dashed) lines in Figure 2a. These fringes result from holographic interference (see Ref. [36]). It is seen that at the same laser parameters the holographic fringes are more pronounced for the hydrogen molecule than for the H atom.

The photoelectron energy spectra and angular distributions calculated for H and H$_2$ are shown in Figures 4a and 4b, respectively. It is seen that the energy spectrum for the H$_2$ molecule falls off slower than the spectrum for the H atom. This is a direct consequence of the fact that the 2D momentum distribution for the hydrogen molecule is more extended along the polarization direction, where the signal is maximal. Accordingly, the angular distribution for H$_2$ is
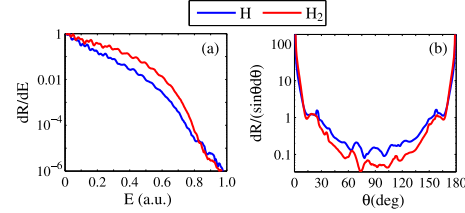

Fig. 4. Energy spectra (a) and and angular distributions (b) of the photoelectrons for ionization of H and H$_2$. The parameters are the same as in Figure 2. The energy spectra are normalized to the peak value, and the angular distributions are normalized to the total ionization yield.
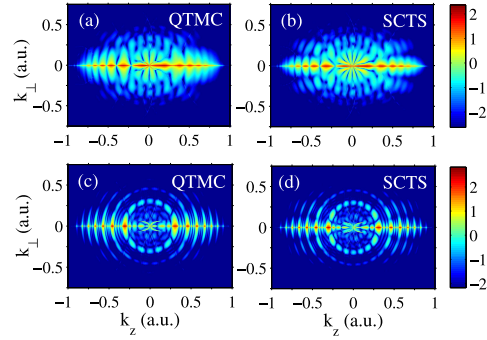

Fig. 5. The two-dimensional photoelectron momentum distributions for H$_2$ ionized by a laser pulse with an intensity of 1.2×10^{14} W/cm^2. The rest of parameters is the same as in Figure 2. The left column [panels (a) and (c)] shows the predictions of the QTMC model. The right column [panels (b) and (d)] displays the results of the SCTS model. Panels (a,b) and (c,d) correspond to the sine squared (Eq. (22)) and trapezoidal (Eq. (23)) pulse, respectively. The distributions are normalized to the total ionization yield. A logarithmic color scale in arbitrary units is used. The laser field is linearly polarized along the z axis.

more aligned along the polarization axis than that for the H atom, see Figure 4b. Up to this point we have discussed the results of the SCTS model. It is instructive to compare these results with the predictions of the QTMC model. In Figures 5a–5d we present the 2D electron momentum distributions for the H$_2$ molecule calculated in accord with the QTMC (Figs. 5a and 5c) and the SCTS (Figs. 5b and 5d). The first and the second row of Figure 5, i.e., the panels (Figs. 5a and 5b) and (Figs. 5c and 5d) show the results for the sine squared (Eq. (22)) and trapezoidal (Eq. (23)) pulse, respectively. Figures 6a–6d show the magnification of the distributions of Figures 5a–5d for $|k_z|$, $|k_\perp| < 0.35$ a.u. It is seen from Figures 6a and 6b that in their low-energy part the 2D momentum distributions display fan-like interference structures. For the trapezoidal pulse the interference structure in the low-energy part of the distributions consists of a number of blobs on a circle of the radius $k \approx 0.30$ a.u. (see Figs. 6c and 6d). These
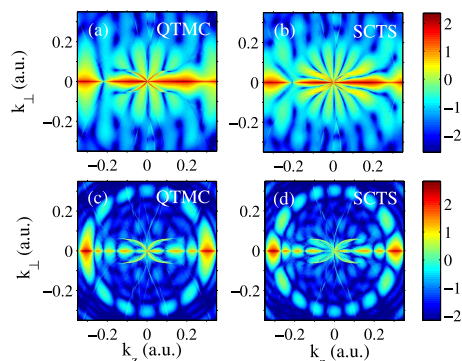
Fig. 6. Magnification of Figure 5 for $|k_z| < 0.35$ a.u. and $|k_\perp| < 0.3$ a.u.

structures are similar to that of Ramsauer-Townsend diffraction oscillations were thoroughly studied in references [37–40]. It is seen that similar to the atomic case [28], the QTMC predicts for the H_2 molecule fewer nodal lines in the low-energy interference structure than the SCTS model. As in the case of atomic hydrogen, we attribute this fact to the underestimation of the Coulomb interaction in the QTMC treatment of the interference phase.

4 Conclusions

In conclusion, we have extended the SCTS model of reference [28] to ionization of the hydrogen molecule by a strong few-cycle laser pulse. We have restricted ourselves to the simplest case when the H_2 molecule is oriented along the direction of a linearly polarized laser field. In our simple implementation of the molecular SCTS model the ionized electron moves in the laser field and in the Coulomb fields of the two fixed atomic nuclei with equal effective charges of 0.5 a.u.

We have compared the 2D photoelectron momentum distributions calculated for the H_2 molecule and the hydrogen atom. We have found that for the same laser parameters the distributions for H_2 are more extended along the polarization axis than the ones for H. As the result, the energy spectrum for the H_2 molecule falls off slower with electron energy than for the hydrogen atom. Furthermore, the holographic interference fringes in the 2D electron momentum distributions are more pronounced for the hydrogen molecule than for the H atom.

By comparing with the predictions of the QTMC model for H_2 we have found that similar to the atomic case, the QTMC yields fewer nodal lines in the interference structure that is characteristic for the low-energy part of the momentum distributions. As in the case of the H atom, we attribute this to the fact that the QTMC model underestimates the Coulomb interaction in the phase associated with each classical trajectory.

The present SCTS model for H_2 can be straightforwardly extended to an arbitrary orientation of the molecule and polarization of the laser field, as well as to other molecules, including heteronuclear and polyatomic ones. We believe that this further development of the molecular SCTS model will help to understand better the complicated highly nonlinear phenomena originating from the interaction of intense laser radiation with molecules.

Author contribution statement

All authors discussed the results and contributed to the final manuscript. Nikolay Shvetsov-Shilovski performed the calculations.

References

1. W. Becker, F. Grasbon, R. Kopold, D.B. Milošević, G.G. Paulus, H. Walther, Adv. At. Mol. Opt. Phys. **48**, 35 (2002)
2. D.B. Milošević, F. Ehlotzky, Adv. At. Mol. Opt. Phys. **49**, 373 (2003)
3. A. Becker, F.H.M. Faisal, J. Phys. B: At. Mol. Opt. Phys. **38**, R1 (2005)
4. C. Figueira de Morisson Faria, X. Liu, J. Mod. Opt. **58**, 1076 (2011)
5. H.G. Muller, Laser Phys. **9**, 138 (1999)
6. D. Bauer, P. Koval, Comput. Phys. Commun. **174**, 396 (2006)
7. L.B. Madsen, L.A.A. Nikolopoulos, T.K. Kjeldsen, J. Fernández, Phys. Rev. A **76**, 063407 (2007)
8. L.V. Keldysh, Zh. Eksp. Teor. Fiz. **47**, 1945 [Sov. Phys. JETP **20**, 1307 (1964)]
9. F.H.M. Faisal, J. Phys. B: At. Mol. Opt. Phys. **6**, L89 (1973)
10. H.R. Reiss, Phys. Rev. A **22**, 1786 (1980)
11. H.B. van Linden, van den Heuvell, H.G. Muller, in *Multiphoton processes*, edited by S.J. Smith, P.L. Knight (Cambridge University, Cambridge, 1988)
12. T.F. Gallagher, Phys. Rev. Lett. **61**, 2304 (1988)
13. P.B. Corkum, N.H. Burnett, F. Brunel, Phys. Rev. Lett. **62**, 1259 (1989)
14. P.B. Corkum, Phys. Rev. Lett. **71**, 1994 (1993)
15. L.D. Landau, E.M. Lifshitz, *Quantum Mechanics Non-relativistic Theory* (Pergamon Oxford, 1965)
16. A.M. Perelomov, V.S. Popov, M.V. Terent'ev, Zh. Eksp. Teor. Fiz. **50**, 1393 (1966) [Sov. Phys. JETP **23**, 924 (1966)]
17. M.V. Ammosov, N.B. Delone, V.P. Krainov, Zh. Eksp. Teor. Fiz. **91**, 2008 (1986) [Sov. Phys. JETP **64**, 1191 (1986)]
18. A. Palacios, H. Bachau, F. Martin, Phys. Rev. Lett. **96**, 143001 (2006)
19. J. Förster, Y.V. Vanne, A. Saenz, Phys. Rev. A **90**, 053424 (2014)
20. J. Muth-Böhm, A. Becker, F.H.M. Faisal, Phys. Rev. Lett. **85**, 2280 (2000)

21. T.K. Kjeldsen, L.B. Madsen, J. Phys. B: At. Mol. Opt. Phys. **37**, 2033 (2004)
22. X.M. Tong, Z.X. Zhao, C.D. Lin, Phys. Rev. A **66**, 033402 (2002)
23. K. Doblhoff-Dier, K.I. Dimitriou, A. Staudte, S. Gräfe, Phys. Rev. A **88**, 033411 (2013)
24. M.-M. Liu, M. Li, C.Y. Wu, Q.H. Gong, A. Staudte, Y.Q. Liu, Phys. Rev. Lett. **116**, 163004 (2016)
25. M.-M. Liu, Y. Liu, J. Phys. B: At. Mol. Opt. Phys. **50**, 105602 (2017)
26. A. Emmanouilidou, D.S. Tchitchekova, Phys. Rev. A **84**, 033407 (2011)
27. M. Li, J.-W. Geng, H. Liu, Y. Deng, C. Wu, L.-Y. Peng, Q. Gong, Y. Liu, Phys. Rev. Lett. **112**, 113002 (2014)
28. N.I. Shvetsov-Shilovski, M. Lein, L.B. Madsen, E. Räsänen, C. Lemell, J. Burgdörfer, D.G. Arbó, K. Tőkési, Phys. Rev. A **94**, 013415 (2016)
29. N.I. Shvetsov-Shilovski, D. Dimitrovski, L.B. Madsen, Phys. Rev. A **85**, 023428 (2012)
30. R. Murray, M. Spanner, S. Patchkovskii, M.Y. Ivanov, Phys. Rev. A **106**, 173001 (2011)
31. M.M. Liu, Y.Q. Liu, Phys. Rev. A **93**, 043426 (2016)
32. R. Murray, W.K. Liu, M.Y. Ivanov, Phys. Rev. A **81**, 023413 (2010)
33. D.A. McQuarrie, J.D. Simon, *Physical chemistry: A molecular approach* (University Science Books, Sausalito, 1997)
34. N.I. Shvetsov-Shilovski, S.P. Goreslavski, S.V. Popruzhenko, W. Becker, Laser Phys. **19**, 1550 (2009)
35. H.A. Bethe, E.E. Salpeter, *Quantum Mechanics of One- and Two-Electron Atoms* (Springer-Verlag, Berlin, Heidelberg, 1957)
36. Y. Huismans, A. Rouzée, A. Gijsbertsen, J.H. Jungmann, A.S. Smolkowska, P.S.W.M. Logman, F. Lépine, C. Cauchy, S. Zamith, T. Marchenko et al., Science **331**, 61 (2011)
37. D.G. Arbó, S. Yoshida, E. Persson, K.I. Dimitriou, J. Burgdörfer, Phys. Rev. Lett. **96**, 143003 (2006)
38. D.G. Arbó, E. Persson, K.I. Dimitriou, J. Burgdörfer, Phys. Rev. A **78**, 013406 (2008)
39. R. Gopal, K. Simeonidis, R. Moshammer, T. Ergler, M. Dürr, M. Kurka, K.-U. Kühnel, S. Tschuch, C.-D. Schröter, D. Bauer, J. Ullrich, Phys. Rev. Lett. **103**, 053001 (2009)
40. D.G. Arbó, K.L. Ishikawa, K. Schiessl, E. Persson, J. Burgdörfer, Phys. Rev. A **81**, 021403(R) (2010)

8.4   *Capture into Rydberg states*

TUNNELING

Capture into Rydberg States and Momentum Distributions of Ionized Electrons[1]

N. I. Shvetsov-Shilovski[a], S. P. Goreslavski[a], S. V. Popruzhenko[a], and W. Becker[b]

[a] *Moscow State Engineering Physics Institute, Kashirskoe sh. 31, Moscow, 115409 Russia*
[b] *Max-Born-Institut, Max-Born-Str. 2a, Berlin, 12489 Germany*
e-mail: n79@narod.ru
Received March 13, 2009; in final form March 17, 2009

Abstract—The yield of neutral excited atoms and low-energy photoelectrons generated by the electron dynamics in the combined Coulomb and laser field after tunneling is investigated. We present results of Monte-Carlo simulations built on the two-step semiclassical model, as well as analytic estimates and scaling relations for the population trapping into the Rydberg states. It is shown that mainly those electrons are captured into bound states of the neutral atom that due to their initial conditions (i) have moderate drift momentum imparted by the laser field and (ii) avoid strong interaction ("hard" collision) with the ion. In addition, it is demonstrated that the channel of capture, when accounted for in semiclassical calculations, has a pronounced effect on the momentum distribution of electrons with small positive energy. For the parameters that we investigated its presence leads to a dip at zero momentum in the longitudinal momentum distribution of the ionized electrons.

PACS numbers: 32.80.Rm, 42.50.Hz

DOI: 10.1134/S1054660X09150377

1. INTRODUCTION

The interaction of strong laser radiation with atoms and molecules generates a variety of highly nonlinear phenomena. These include the extended photoelectron spectrum of above-threshold ionization (ATI), the excessive yield of doubly and multiply charged ions, the generation of very high harmonics of the driving field, and the yield of neutral atoms in excited Rydberg states (see [1—5] for reviews). The generally recognized transparent physical picture of the first three phenomena is based on the so-called direct ionization and rescattering scenario. According to it, electrons are promoted to the continuum via tunneling ionization and, while oscillating in the laser field, interact with their parent ions. Most of the ionized electrons, i.e., the "direct" electrons, are decelerated and deflected by the ion at small angles and finally contribute to the low-energy part of the photoelectron spectrum. In some rare cases, the ionized electron returns close to its parent ion and recombines emitting a high-frequency harmonic photon or kicks out one or several electrons, producing thereby a doubly or multiply charged ion. Yet another opportunity upon the close encounter is that the electron is elastically backscattered and thereafter acquires additional energy from the laser field. Such electrons contribute to the high-energy part of the photoelectron spectrum. The rescattering picture is explicitly realized in terms of complex "quantum orbits" or even simpler in terms of the two- and three-step semi-classical models. In the

latter, real electron trajectories after ionization are calculated with Newton's equations.

The interpretation of the afore-mentioned processes is largely classical, based on trajectories obtained from Newton's equations. Population trapping in Rydberg states resulting in an excited neutral atom at the end of the laser pulse is an exception because until recently its interpretation was purely quantum mechanical. The effect was considered as evidence of the existence of stabilization against ionization and studied theoretically and experimentally in many papers (see [4, 5] and references therein). It is generally believed that there are two different mechanisms of stabilization: adiabatic stabilization (stabilization in the Kramers–Henneberger regime) and interference stabilization. The adiabatic approach is appropriate when the field frequency ω exceeds the atomic ionization potential I so that the states in the discrete spectrum and the continuum are coupled by one-photon transitions. In experiments with optical lasers, such conditions were realized by initially populating Rydberg states. The physical mechanism behind interference stabilization is associated with multiple Raman-type transitions between the Rydberg levels and the common continuum. Destructive interference of the transition amplitudes from these coherently populated states to the continuum suppresses ionization and, hence, serves to retain population in Rydberg states.

The recent paper [6] reports data on the yield of neutral excited He* atoms and singly charged ions He$^+$ from a gaseous target irradiated by 30-fs Tita-

---

[1] The article is published in the original.

nium–Sapphire (Ti:Sa) laser pulses with intensities up to 10^{15} W/cm². The data, corrected for the radiative decay of neutral excited atoms on the way to the detector, fairly well agree with the results of extensive quantum-mechanical calculations. The latter were accomplished in two ways: by approximately solving the two-electron TDSE for helium exposed to a laser field and in single-active-electron (SAE) approximation. The excited neutral atom yield is roughly 20% of the ion yield at lower intensities decreasing to about 10% at higher intensities.

In addition, a two-step semiclassical model was employed for the first time for providing a simple picture of the dynamics resulting in the population of Rydberg states. Monte Carlo calculations were performed with classical trajectories in the combined Coulomb potential and electric laser field. Those electrons are captured into bound states of the neutral atom that have negative total (kinetic plus Coulomb) energy at the end of the laser pulse. The energy distribution in the subset of bound trajectories was converted into the distribution in an effective principal quantum number ($E = -1/2n^2$) and the latter was found to be in qualitative and even quantitative agreement with the one deduced from quantum calculations.

The implication of this study is that in Monte-Carlo simulations with classical trajectories in the laser field and the ionic Coulomb field not all electrons that tunneled out at some time are actually ionized after the end of the laser pulse. Some may be captured back into bound states. This outcome of the electron motion in the continuum was dubbed frustrated tunneling ionization (FTI) in [6]. Transient trapping in Rydberg states during the laser pulse was mentioned earlier in [7]. However, to the best of our knowledge, there are no comments on the formation of excited neutral atoms at the end of the pulse in the papers where Monte Carlo simulation of classical trajectories after tunneling was used to model the effect of Coulomb focusing on the rescattering processes [7–9] or to investigate the low-energy photoelectron spectra [10–12].

In this paper, we further exploit the semiclassical model: (i) to get deeper insight into the mechanism responsible for the yield of neutral exited atoms; (ii) to find out the scaling of this yield with the laser-atom parameters; and (iii) to understand the impact of the population trapping on the momentum distributions of the ionized electrons.

2. MODEL

In this section we will sketch our simulation technique with special emphasis on the details that are essential for the following.

Let us consider a neutral atom with the ionization potential I, irradiated by a short laser pulse with the duration $\tau_L = (2\pi/\omega)n_p$ and sine-square envelope, linearly polarized along the x axis:

$$F(t) = F_0 \sin^2(\pi t/\tau_L)\cos(\omega t), \tag{1}$$

where n_p is the number of cycles and ω is the carrier frequency. At time t_0 the bound electron tunnels out of the atom quasistatically with the rate

$$w(t_0, v_0) \sim \left(\frac{F_a}{F(t_0)}\right)^2 \frac{1}{\sqrt{1 + v_0^2/2I}}$$

$$\times \exp\left\{-\frac{2F_a}{3F(t_0)}\left[1 + \frac{v_0^2}{2I}\right]^{3/2}\right\}. \tag{2}$$

Here, I and $F_a = (2I)^{3/2}$ are the ionization potential and the characteristic atomic force of the bound state ($I = 1/2$, $F_a = 1$ for the ground state of hydrogen). The rate (2) is obtained from the standard strong-field ionization amplitude [13, 14] calculated by the saddle-point method in the tunneling regime, when the Keldysh parameter $\gamma = \omega\sqrt{2I}/F \ll 1$. Details of the calculations are presented elsewhere (see [15, 16]). Atomic units $e = m = \hbar = 1$ are used.

At the tunnel exit $x_0 = I/F(t_0)$ the electron has zero longitudinal and nonzero initial transverse velocity v_0. The released electron moves along a classical trajectory under the action of the laser field and the Coulomb force of its residual ion. The initial conditions unambiguously determine its position $\mathbf{r}(t) = \mathbf{r}(t_0, v_0, t)$ and velocity $\mathbf{q}(t) = \mathbf{q}(t_0, v_0, t)$ at any time instant t. In the limit of large t, one obtains the asymptotic momentum $\mathbf{p} = \mathbf{q}(t_0, v_0, t \longrightarrow \infty)$, which is identical with the momentum measured by the detector. During the whole laser pulse $0 \leq t_0 \leq \tau_L$, an ensemble of trajectories is launched corresponding to different pairs (t_0, v_0) weighted with the probability (2). No interference effects are accounted for. In our simulations we employed about 1.5×10^6 trajectories regardless of the intensity. By solving the respective Newton equations one obtains $\mathbf{r}(t)$ and $\mathbf{q}(t)$ for each trajectory. The ratio of the number of trajectories in a particular bin of momentum space to the total number of trajectories is the momentum distribution at given time t normalized to unity. It evolves in time and in the limit $t \longrightarrow \infty$ can be compared with the experimental data.

The picture described in the previous paragraph is not complete, however. Indeed, if the Coulomb field of the nucleus is included into the Newton equations then, for some initial conditions (t_0, v_0), the electron's momentum simply does not converge to any constant value but keeps oscillating in the limit $t \longrightarrow \infty$. Such trajectories correspond to those electrons whose total energy after the end of the laser pulse is negative

$$E(\tau_L) = \frac{\mathbf{q}^2}{2} - \frac{1}{r} < 0, \tag{3}$$
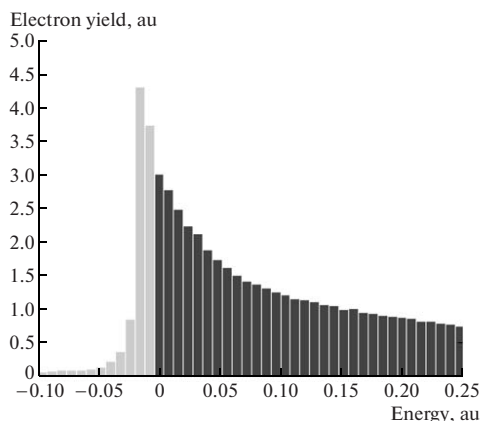
Electron yield, au

Fig. 1. The distribution of the total energy $E = \mathbf{q}^2/2 - 1/r$ of electrons tunneling out of an H-atom ($I = 13.6$ eV) at the end of a laser pulse with a duration of $n_p = 5$ cycles, frequency $\omega = 0.05$ au and an intensity of 3.5×10^{14} W/cm^2. The number of electrons with negative energy (shown by green bars) is estimated at about 15%, which is consistent with [6].

so that they never reach a detector. Following [6] we interpret these electrons as trapped in Rydberg states (captured electrons). Here, $\mathbf{q} = \mathbf{q}(v_0, t_0, \tau_L)$ and $\mathbf{r} = \mathbf{r}(v_0, t_0, \tau_L)$ are the electron velocity and its distance from the ion at the end of the laser pulse, respectively. Starting with the time τ_L the electron moves only in the Coulomb field, and its energy as well as the angular momentum are conserved. Thus, since this time the whole ensemble of trajectories can be subdivided into two subsets. The subset of trajectories satisfying condition (3) specifies the distribution of the bound electrons over the principal and the angular quantum numbers n and l. The subset of trajectories with positive total energy determines the distribution of ionized electrons.

3. RESULTS AND DISCUSSION

The results of our simulations are presented in Figs. 1, 2, and 3.

The energy distribution of the electrons at the time τ_L is shown in Fig. 1. It can be seen from the figure that the number of captured electrons corresponds to approximately 15% of the number of ions, which agrees with the results obtained in [6]. The distribution of the trapped electrons over the principal quantum number is depicted in Fig. 2. This distribution is similar to those evaluated in [6] by the solution of the time-dependent Schrödinger equation and by Monte Carlo simulations: the maximum of the distribution corresponds to $n = 6$.
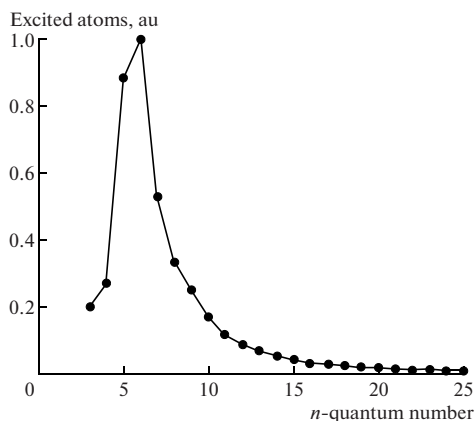
Excited atoms, au

Fig. 2. The distribution of the captured electrons over the principal quantum number n. The parameters are those of Fig. 1.

Finally, Fig. 3 exhibits the areas of the plane (t_0, v_0) of initial conditions that lead to capture of the electron into Rydberg states. The profile of the laser pulse is also shown in the figure. Figure 3 reveals two main features. First, the capture does not take place for any initial velocity. It occurs only when $|v_0|$ is less than some maximum value (approximately 0.3 for the parameters of Fig. 3). But this is not yet a sufficient condition. Such a condition will be formulated in the next section, in which Fig. 3 is explained and all necessary estimates are done.

3.1. Mechanism and Scalings of Population Trapping

To understand the results of Fig. 3 one should keep in mind that the momentum (velocity) $\mathbf{q}$ and the distance $\mathbf{r}$ in the capture condition (3) are actually correlated. The larger the momentum, the larger is the electron distance and the smaller is the potential energy and, hence, the electron cannot be trapped. With the equality sign, Eq. (3) sets an upper limit for q. Regarding smaller values for q, the electron can have a small drift momentum at the end of the laser pulse only under certain conditions. The trajectories of electrons ionized near the field extrema with initially small drift momentum along the laser field and with small transverse velocity are strongly affected by the attraction of the Coulomb field. While such an electron oscillates in the laser field, a single "hard" collision or a sequence of "soft" collisions [7] are likely to increase its drift momentum so that, with very high probability, it is not a candidate for capture anymore. On closer inspection, this holds for electrons that start their orbit *after* an extremum of the field. In this case, the drift momentum imparted by the laser field is directed

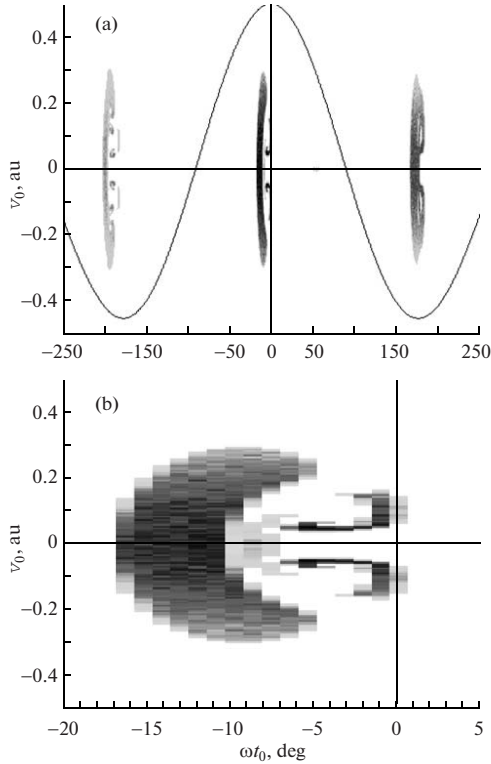CAPTURE INTO RYDBERG STATES AND MOMENTUM DISTRIBUTIONS 1553

Fig. 3. (a) The 2D distribution of the captured electrons over the time of tunneling t_0 and initial velocity v_0 for the parameters of Fig. 1. The laser field (1) is shown by a blue line; (b) The same as in (a), but for the dominant maximum of the pulse. Dark means high electron yield.

Fig. 4. Two electron trajectories in the field $F(t) = F_0\cos(\omega t)$ corresponding to two instants of ionization before and after the field maximum: $\omega t_0 = -0.1$ (dashed curve) and $\omega t_0 = 0.1$ (solid curve) for the parameters of Fig. 1. The coordinate is scaled by the amplitude $A_0 = F_0/\omega^2$ of the electron oscillation in the laser field.

towards the ion. The net effect of the laser field is that these electrons are driven back to the ion at least once if not many times. An example of such a trajectory is shown in Fig. 4 by the solid line. The Coulomb force still further increases the drift momentum in the direction towards the ion. Inevitably electrons with large drift momentum return back to the ion and scatter depending on the magnitude of their impact parameter. The opportunity to avoid strong interaction with the ion and have sufficiently small drift momentum at the end of the laser pulse exists for electrons which start in the continuum *before* the field extremum. Without the Coulomb field, while oscillating in the laser field they drift away from their parent ion and never return to its vicinity (the trajectory shown by the dashed line in Fig. 4). The Coulomb attraction reduces the drift momentum without reversing its direction, so that the trajectory remains "on the aver-
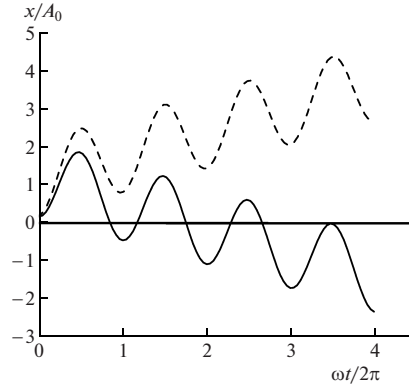
age outgoing." This classification of trajectories is illustrated by Fig. 4.

To support this general conclusion, let us consider the contribution to the capture process from a single half cycle of the laser field, for example, from the central maximum of the field (1). With time counted from this maximum and for phases within the interval $-\pi/2 < \omega t < \pi/2$, the field and its vector potential are simplified as $F(t) = F\cos(\omega t)$ and $A(t) = -(F/\omega)\sin(\omega t)$. The momentum at the end of the laser pulse of an electron tunneling at time t_0 with nonzero transverse velocity can be written as

$$\mathbf{q} \equiv \mathbf{q}(t_0, \mathbf{v}_0, \tau_L) = \mathbf{A}(t_0) + \mathbf{v}_0 + \mathbf{p}_C(t_0, \mathbf{v}_0). \qquad (4)$$

At $t > \tau_L$ the momentum (4) evolves in the Coulomb field. The trajectory starts at the tunnel exit $x_0 = I/F(t_0)$ and the field $F(t_0)$ accelerates the electron away from it. For the laser-atom parameters of interest, the Coulomb force is small in comparison to the laser field already at the tunnel exit and rapidly decreases when the electron departs from the ion. For example, with the parameters of Figs. 1 and 4 and not too far from the field maximum one has $x_0 \approx 5$ au, while the oscillation amplitude $A_0 = F_0/\omega^2$ is about 40 au. This allows us to evaluate the contribution of the Coulomb force in Eq. (4)

$$\mathbf{p}_C(t_0, \mathbf{v}_0) = -\int_{t_0}^{+\infty} dt \frac{\mathbf{r}_L(t)}{r_L^3(t)} \qquad (5)$$

as the integral along the initial part of the electron trajectory

$$\mathbf{r}_L(t) = \left\{ x_0 + \frac{1}{2} F(t_0)(t - t_0)^2, \ v_0(t - t_0) \right\},$$

and to extend the upper integration limit to infinity [15]. Evaluation of the integral (5) for not very large transverse velocities, $v_0 < \sqrt{2I}$, gives the drift momentum (4) in the plane defined by the directions of the field (x axis) and of the transverse initial velocity ($\perp$ axis):

$$q_x = -\frac{F}{\omega} \sin(\omega t_0) - \pi \frac{F \cos(\omega t_0)}{(2I)^{3/2}}, \qquad (6)$$

$$q_\perp = v_0 - 2 v_0 \frac{|F(t_0)|}{(2I)^2}. \qquad (7)$$

Except for the numerical factor, the Coulomb contribution to the drift momentum (6) is just the product of the Coulomb force at the tunnel exit, $-1/x_0^2$, and the time interval $\Delta t = \sqrt{2x_0/F(t_0)}$ over which the electron-ion distance doubles. Not surprisingly, this time interval coincides with the time of flight under the potential barrier, $x_0/\sqrt{2I}$, introduced by Keldysh.

For the next half period, the laser field changes its direction and pulls the outgoing electron back to the ion.

But, for $q_x > 0$, the minimum distance in the x direction between the electron and the ion will be larger than the tunnel exit x_0 by the drift displacement q_x/ω. So, if this displacement is of the order of or larger than x_0, the Coulomb force upon the closest approach is less than the one at the time of tunneling, and its effect can be neglected. In such cases, the drift momentum given by (6) and (7) remains practically constant during the rest of the laser pulse. This allows us to estimate the electron-ion distance at the end of the laser pulse in Eq. (3) as

$$r = q(\tau_L - t_0), \qquad (8)$$

where $q = \sqrt{q_x^2 + q_\perp^2}$. With the momentum and the distance at the end of the laser pulse known as functions of t_0 and v_0, the condition (3) determines the subspace of the initial parameters that result in capture to the bound states:

$$q < \left(\frac{2}{\tau_L - t_0} \right)^{1/3}. \qquad (9)$$

It is immediately obvious that the number of trapped electrons decreases with increasing time that the electron spends in the laser field after ionization. This explains the difference in the number of electrons cap-

tured from identical laser half-periods before and after the field maximum, which is seen in Fig. 3a.

Next, we try to obtain a rough analytical estimate for the relative yield of neutral excited atoms with respect to singly charged ions, i.e., the ratio N^*/N^+, in a short laser pulse. The numbers N^* and N^+ can be evaluated by integrating the rate (2) over the respective parts of the (t_0, v_0)-plane shown in Fig. 3a. To a fair approximation, the integration can be performed over the initial conditions related to the central maximum of the field. Furthermore, applying the theorem of the mean to both integrals, we assume that the rates (2) do not differ essentially and cancel out in their ratio, which thereby is estimated as $N^*/N^+ \approx \Sigma^*/\Sigma^+$. Here, Σ^* and Σ^+ are the areas of the (t_0, v_0) plane effective for population trapping and real ionization, respectively. For ions from the central maximum of the field we have $\Sigma^+ \approx \pi \times \sqrt{2I}\sqrt{F/F_a}$, where the second factor is the width of the rate (2) in the initial velocity.

For the neutrals, Σ^* is just the area of the crescent-shaped region in Fig. 3b. First, we find the interval of start times that are favorable for capture for $v_0 = 0$. Its left end $t_{0<}$ is found by equating the two sides of Eq. (9) under the assumption that we deal with an "on the average outgoing trajectory", i.e., $q_x > 0$. The resulting equation is

$$-\sin(\omega t_0) - \lambda \cos(\omega t_0) = \frac{\omega}{F} \left(\frac{2}{\tau_L - t_0} \right)^{1/3}, \qquad (10)$$

where $\lambda = \pi \omega/(2I)^{3/2}$. In the middle of the laser pulse, $\tau_L - t_0 \approx \tau_L/2$, and, typically, the r.h.s. of Eq. (10) is small in comparison with unity. To first order in $\omega t_0 < 1$, the solution within the interval $-\pi/2 < \omega t_0 < \pi/2$ is

$$\omega t_0 \equiv \omega t_{0<} \approx -\lambda - \frac{\omega}{F} \left(\frac{4}{\tau_L} \right)^{1/3}. \qquad (11)$$

The momentum (6) decreases when the start time $t_0 > t_{0<}$ moves away from the left end of the favorable interval. If it is recalled that trajectories with very small momenta are strongly perturbed by the Coulomb field and do not contribute to the process of capture, then the upper end of the window can be estimated from the equation $q_x(t_{0>}, v_0, \tau_L) = 0$. For $\lambda < 1$, one easily finds

$$\omega t_{0>} \approx -\lambda. \qquad (12)$$

For the parameters of Fig. 3, the predictions of Eqs. (11) and (12), i.e., $\omega t_{0<} \approx -15°$ and $\omega t_{0>} \approx -9°$, respectively, agree nicely with the results of the Monte Carlo simulations presented in the lower panel of this figure.

It can be seen that the transverse width of the crescent-like shape in Fig. 3b, i.e., the maximum transverse velocity allowing for the capture of electrons into the bound states, is more or less the same for start times within the favorable window. To estimate this

CAPTURE INTO RYDBERG STATES AND MOMENTUM DISTRIBUTIONS   1555

width, we consider the condition (9) for the case when $q_x(t_{0>}, v_0, \tau_L) = 0$ and for times in the middle of the laser pulse so that $\tau_L - t_0 \approx \tau_L/2$. With account of (7), it immediately takes the form $|v_0| < v_{max}$, where

$$v_{max} = \left(\frac{4}{\tau_L}\right)^{1/3} \Big/ \left(1 - 2\frac{F}{(2I)^2}\right). \qquad (13)$$

Actually, in (13) we have neglected terms of the order of $\lambda^2 \ll 1$. In Fig. 3, the transverse velocity does not exceed 0.30 au whereas, for the same parameters, one has from Eq. (13) $v_{max} = 0.23$ au. Again, the agreement is quite reasonable.

By roughly estimating the capture area in Fig. 3 as $\Sigma^* \approx \omega(t_{0>} - t_{0<}) \times 2v_{max}$ and dividing it by the area Σ^+ effective for ionization (see above) we have for the relative yield of neutral excited atoms with respect to singly charged ions

$$\frac{N^*}{N^+} \propto \frac{\omega}{F^{3/2}\tau_L^{2/3}}\left(1 - 2\frac{F}{(2I)^2}\right)^{-1}. \qquad (14)$$

The scaling with the laser parameters given by Eq. (14) was correlated with the results of the Monte Carlo simulations. According to the latter, when the field strength varies from $F = 0.1$ to $F = 0.07$ the ratio N^*/N^+ rises from 0.18 to 0.41, i.e., by a factor of 2.3, while Eq. (14) predicts a factor of 1.7. Agreement is even better with respect to pulse duration. When the pulse duration is doubled from 5 to 10 cycles, then for the field strength of $F = 0.1$ au the relative yield drops from 0.18 to 0.11, i.e., by a factor of 1.64, which is practically equal to the factor of $2^{2/3}$ expected from (14). The general tendency of an increasing percentage of bound electrons for shorter pulses and lower intensities was observed in the Monte Carlo simulations of [6].

Experimentally, a strong decrease of the yield of neutral excited atoms with increasing pulse duration was reported in an early paper [17]. When the scaling of Eq. (14) is applied to analyze ionization of He atoms with their high ionization potential, the very last factor can be dropped. Then it follows from (14) that an-order-of-magnitude increase of the laser intensity will reduce the relative yield by a factor of 5 to 6. The relative yield reported in [6] decreases over such a range by approximately a factor of 2. The origin of this discrepancy is not presently clear.

According to [6], the maximum of the n-distribution scales with $\sqrt{F}/\omega$. The derivation of this dependence presented there was based on the heuristic assumption that the radial expectation value of the final Rydberg atom, $\langle r \rangle \propto n^2$, is proportional to the amplitude of electron oscillation in the laser field, $A_0 = F/\omega^2$. Our idea is that the quantum-mechanical mean distance of a captured orbit is determined by the electron distance (8) at the end of the laser pulse, $\langle r \rangle \approx$ $r(t_0)$. From Monte Carlo simulations with the parameters of Fig. 1, we found that the distribution of the distances of trapped electrons (not shown here) has a maximum around $r_{max} = 60$ au. The relation $r_{max} = \langle r \rangle = 3n^2/2$ then gives $n_{max} \approx 6$, which agrees nicely with the results of Fig. 2. The distance (8) indeed becomes proportional to the oscillation amplitude if one factors out the dimensional factor F/ω from the momentum and converts time into the field phase.

3.2. The Capture into Rydberg States and the Distribution of the Ionized Electrons

The fact that a substantial part of the tunneled electrons end up in bound states with $E < 0$ after the end of the pulse should affect the energy-angular spectrum of direct ionization, particularly its low-energy part. This raises the question of a possible relation between the capture into Rydberg states and the dip (minimum) at $p = 0$ in the momentum distribution of ionized electrons along the laser polarization, which was for the first time observed in [18]. The origin of this dip has been the object of intense investigations [10, 11, 19–22]. In this section we analyze momentum distributions of the ionized electrons, calculated taking into account the capture into bound states.

First, however, we address the photoelectron momentum distribution *at the end of the pulse (not at infinity)* (see Fig. 5), calculated with the assumption that all electrons are ionized, regardless of whether the total energy $E(\tau_L)$ (Eq. (3)) is positive or negative [10]. Note, that in the presence of the Coulomb field such a distribution is not an observable, since the momentum is not conserved. However, the momentum distribution at the end of the pulse is instructive for understanding the influence of the Coulomb force on the electron dynamics. The distribution evaluated without taking the Coulomb field of the atomic residual into account is also shown in the figure. Figure 5 demonstrates that the Coulomb force severely modifies the central part of the longitudinal momentum distribution. Incidentally, the asymmetry of the dip is due to the small (5 optical cycles) duration of the laser pulse.

Figure 6 illustrates the evolution of the distribution of p_x calculated considering all launched trajectories, including those with $E(\tau_L) < 0$ at the end of the pulse, under the action of the Coulomb force. One observes that the dip in the longitudinal distribution is gradually filled in and a narrow maximum develops in its place. Our simulations show that the dip in this approach also vanishes with increasing laser intensity and pulse duration. We should focus our attention on the fact that the latter result coincides with a conclusion of [11], which, however, concerned the *asymptotic* distribution of the ionized electrons. It is very important to note that the *asymptotic* distribution, by which we understand the distribution to be measured by a detector far away from the ion, has to be calculated *by*
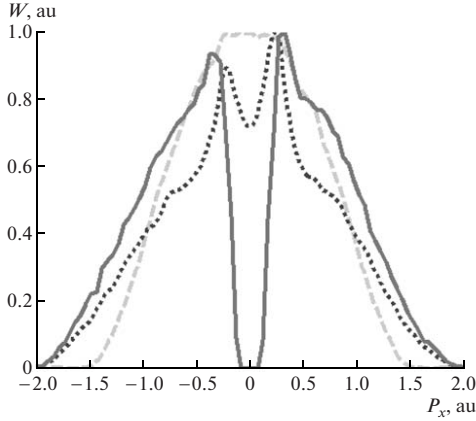
Fig. 5. The longitudinal momentum distribution evaluated by Monte Carlo simulations at the end of the laser pulse at time τ_L. Dotted blue curve: All launched trajectories, including those with $E(\tau_L) < 0$, are accounted for. Solid red curve: The trajectories with negative energies are excluded. Dashed green curve: The result of simulations with the Coulomb field entirely turned off. The parameters are those of Fig. 1.

Fig. 6. The longitudinal momentum distributions, calculated taking into consideration all launched trajectories, at $t = 2\tau_L$ (dotted blue curve), $t = 3\tau_L$ (dashed green curve), $t = 4\tau_L$ (dash-dotted magenta curve). The red curve shows the asymptotic distribution, which was evaluated by excluding the trajectories with $E(\tau_L) < 0$, as discussed in the text.

excluding the trajectories with $E(\tau_L) < 0$. Since the latter are trapped into Rydberg states they will never reach the detector. If nevertheless they are included into the asymptotic distribution, their momenta will not converge to definite values as time goes to infinity or, depending on the numerical accuracy, they will contribute to a spurious accumulation of events with very low momenta. Indeed, the asymptotic distribution obtained *by excluding the trajectories with negative energy* (the solid red curve in Fig. 6) has a distinct minimum at zero longitudinal momentum.

Let us summarize the results shown in Figs. 5 and 6. A dip in the longitudinal momentum distribution generated by a relatively short laser pulse is already seen at the end of the pulse. A comparison of the two curves calculated with and without the Coulomb field suggests that the Coulomb field is responsible for the formation of this dip [10, 11]. However, Fig. 6 shows that this dip is washed out if we allow the distribution to continue developing under the action of the Coulomb field after the end of the laser field. Our definition of the asymptotic distribution discards the contribution of those electrons with negative energy at the end of the pulse. Remarkably, the asymptotic distribution again exhibits a dip. The obvious conclusion is that the mechanism responsible for the formation of the dip at zero momentum is closely related to the one that governs the electron capture into Rydberg states. Both effects are caused by the Coulomb field and occur in adjacent energy intervals. We notice in pass-
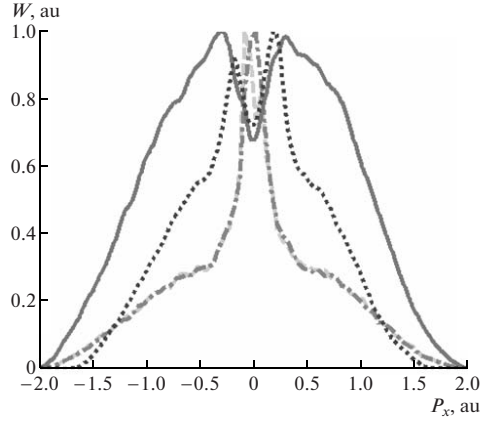
ing that the observed structure also survives focal averaging, which is inevitable in real experimental conditions.

Hence, the calculation of the momentum distribution of ionized electrons must take into account the possible population of Rydberg orbits with negative total energy. The two-dimensional momentum distribution, which disregards electrons with $E(t) < 0$ at $t = \tau_L$, is depicted in Fig. 7a. One can see from the figure that the central part of the distribution is completely unpopulated. Simulations for $t > \tau_L$ show that the subsequent motion in the Coulomb field partly fills in this hole, see below.

The asymptotic distribution at $t \longrightarrow \infty$ can be obtained without calculations up to a large time instant t_{end}, which guarantees the asymptotic regime for the vast majority of launched trajectories. Indeed, the electron momentum $\mathbf{q}(t_0, v_0, \tau_L)$ and its position vector $\mathbf{r}(t_0, v_0, \tau_L)$ at the end of the laser pulse uniquely determine the subsequent trajectory in the Coulomb field of the parent ion. Standard formulas of classical mechanics for hyperbolic motion (see, for example [23]), allow straightforward analytical evaluation of the electronic asymptotic momentum

$$\mathbf{p} = p\frac{p(\mathbf{A} \times \mathbf{M}) - \mathbf{A}}{1 + p^2 M^2}, \qquad (15)$$

where $\mathbf{M} = \mathbf{r} \times \mathbf{q}$ and $\mathbf{A} = \mathbf{q} \times \mathbf{M} - \mathbf{r}/r$ are the conserved angular momentum and Runge–Lenz vector, respec-
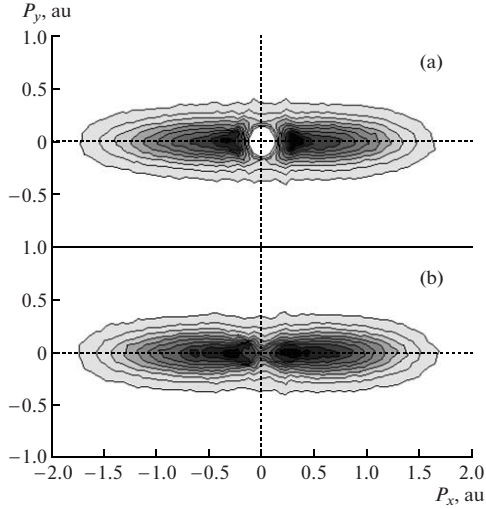
CAPTURE INTO RYDBERG STATES AND MOMENTUM DISTRIBUTIONS 1557

Fig. 7. (a) The 2D momentum distribution for the parameters of Fig. 1 resulting from Monte Carlo simulations at the end of the laser pulse, where the trajectories with negative total energy $E = \mathbf{q}^2/2 - 1/r < 0$ are discarded. (b) The same distribution in the asymptotic limit after its subsequent evolution in the Coulomb field.

Fig. 8. Asymptotic momentum distributions along laser polarization for different laser intensities (in W/cm^2) for the parameters of Fig. 1.

tively. The absolute value p of the asymptotic momentum can be determined from the energy conservation law:

$$\frac{\mathbf{q}^2}{2} - \frac{1}{r} = \frac{p^2}{2}. \tag{16}$$

It should be noticed that Eq. (16) can also be used to explain the origin of the unpopulated area in Fig. 7a.

In fact, at the end of the laser pulse electrons can be found at various finite distances from the ion. The positivity of the total energy imposes a lower limit on the value of the electron momentum at that instant of time. In contrast, the electron does not feel the Coulomb field at $t \longrightarrow \infty$, and its momentum can be arbitrarily small.

The distribution evaluated by this approach is shown in Fig. 7b. Together with Fig. 8 it demonstrates that the dip is not smeared out by the evolution in the Coulomb field after the end of the laser pulse and, moreover, its shape is not very sensitive to the laser intensity. The same holds for the behavior of the distribution with increasing pulse duration.

Thus, depletion of the low-energy part of the ionization spectrum due to the capture into Rydberg states is a possible mechanism for the formation of a dip in the momentum distribution along the polarization direction.
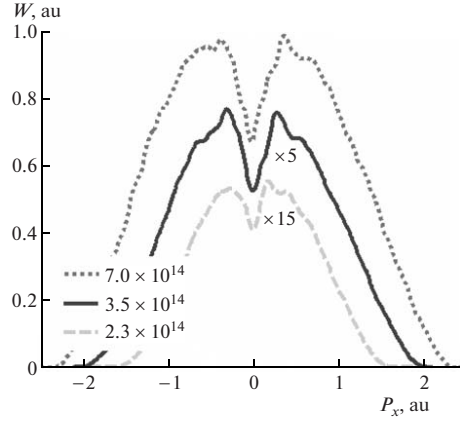
4. CONCLUSIONS

Based on the two-step semiclassical model, we have investigated the electron motion after tunneling in a strong laser field considering the interaction with the Coulomb field of the parent ion. The focus of attention is on the mechanism governing the yield of neutral excited atoms from a gaseous target irradiated by a short laser pulse. A simple physical picture emerges from Monte Carlo simulations with classical trajectories after tunneling. With account of the Coulomb field, not all tunneled electrons are actually ionized since some of them are captured back into bound atomic states after the end of the laser pulse. Obviously, an electron remains bound if its total energy at the end of the laser pulse is negative. Furthermore, we show that for an electron to be captured it (i) has to have moderate drift momentum at the time of tunneling and (ii) has to avoid strong interaction ("hard" collision) with the ion. Such trajectories do exist when electrons are released within a narrow time window before the extrema of the oscillating laser field having a not too large transverse velocity $\mathbf{v}_0$. Understanding these features has allowed us to derive the scaling of the ratio of neutral excited atoms and singly charged ions with the laser-atom parameters in analytic form. Its prediction, that the percentage of neutrals increases with decreasing intensity or pulse duration, fits into the general physical picture. In both cases, the electron drifts away from the ion by a smaller distance during the laser pulse and experiences a stronger Coulomb attraction. This distance is smaller at lower intensity because of a reduced drift momentum imparted by the laser field and, in the other case of a shorter pulse, because of a smaller travel time. In addi-

1558   SHVETSOV-SHILOVSKI et al.

tion, it has been demonstrated that the channel of cap-
ture, when accounted for in semiclassical calculations,
has a pronounced effect on the momentum distribu-
tion of electrons with small positive energy. In partic-
ular, it is correlated with the formation of a "dip" at
zero momentum in the distribution of the longitudinal
momentum.

REFERENCES

 1. W. Becker, F. Grasbon, R. Kopold, et al., Adv. At. Mol.
    Opt. Phys. **48**, 35 (2002).

 2. A. Becker and F. H. M. Faisal, J. Phys. B: At. Mol. Opt.
    Phys. **38**, R1 (2005).

 3. D. B. Milošević and F. Ehlotzky, Adv. At. Mol. Opt.
    Phys. **49**, 373 (2003).

 4. M. V. Fedorov, *Atomic and Free Electrons in a Strong
    Light Field* (World Sci., Singapore, 1997).

 5. N. B. Delone and V. P. Krainov, *Multiphoton Processes
    in Atoms*, Ch. 9 (Springer, Berlin, 2000).

 6. T. Nubbemeyer, K. Gorling, A. Saenz, et al., Phys. Rev.
    Lett. **101**, 233001 (2008).

 7. G. L. Yudin and M. Yu. Ivanov, Phys. Rev. A **63**, 033404
    (2001).

 8. T. Brabec, M. Yu. Ivanov, and P. B. Corkum, Phys. Rev.
    A **54**, R2551 (1996).

 9. D. Comtois, D. Zeidler, H. Pepin, et al., J. Phys. B: At.
    Mol. Opt. Phys. **38**, 1923 (2005).

10. J. Chen and C. H. Nam, Phys. Rev. A **66**, 053415
    (2002).

11. K. I. Dimitriou, D. G. Arbo, S. Yoshida, et al., Phys.
    Rev. A **70**, 061401(R) (2004).

12. D. G. Arbo, S. Yoshida, E. Persson, et al., Phys. Rev.
    Lett. **96**, 143003 (2006).

13. L. V. Keldysh, Zh. Eksp. Teor. Fiz. **47**, 1945 (1964)
    [Sov. Phys. JETP **20**, 1307 (1965)].

14. F. H. M. Faisal, J. Phys. B **6**, L89 (1973); H. R. Reiss,
    Phys. Rev. A **22**, 1786 (1980).

15. S. P. Goreslavski, G. G. Paulus, S. V. Popruzhenko, and
    N. I. Shvetsov-Shilovski, Phys. Rev. Lett. **93**, 233002
    (2004).

16. N. I. Shvetsov-Shilovski, S. P. Goreslavski, S. V. Popru-
    zhenko, and W. Becker, Phys. Rev. A **77**, 063405 (2008).

17. R. R. Jones, D. W. Schumacher, and P. H. Bucksbaum,
    Phys. Rev. A **47**, R49 (1993).

18. R. Moshammer, J. Ullrich, B. Feuerstein, et al., Phys.
    Rev. Lett. **91**, 113002 (2002).

19. A. Rudenko, K. Zrost, C. D. Schröter, et al., J. Phys. B:
    At. Mol. Opt. Phys. **37**, L407 (2004).

20. F. H. M. Faisal and G. Schlegel, J. Phys. B: At. Mol.
    Opt. Phys. **38**, L323 (2006).

21. A. S. Alnaser, C. M. Maharjan, P. Wang, and I. V. Lit-
    vinyuk, J. Phys. B: At. Mol. Opt. Phys. **39**, L323 (2006).

22. C. M. Maharjan, A. S. Alnaser, I. V. Litvinyuk, et al.,
    J. Phys. B: At. Mol. Opt. Phys. **39**, 1955 (2006).

23. L. D. Landau and E. M. Lifshitz, *Mechanics* (Perga-
    mon, Oxford, 1976).

8.5 Semiclassical two-step model: further developments

THE EUROPEAN PHYSICAL JOURNAL D

Colloquium - Ultraintense and Ultrashort Laser Fields

Semiclassical two-step model for ionization by a strong laser pulse: further developments and applications

N. I. Shvetsov-Shilovski[a]

Institut für Theoretische Physik, Leibniz Universität Hannover, Hannover 30167, Germany

Abstract. We review the semiclassical two-step model for strong-field ionization. The semiclassical two-step model describes quantum interference and accounts for the ionic potential beyond the semiclassical perturbation theory. We discuss formulation and implementation of this model, its further developments, as well as some of the applications. The reviewed applications of the model include strong-field holography with photoelectrons, multielectron polarization effects in ionization by an intense laser pulse, and strong-field ionization of the hydrogen molecule.

1 Introduction

Strong-field physics studies phenomena arising from the interaction of strong laser pulses with atoms and molecules. The most well-known examples of these highly nonlinear phenomena are above-threshold ionization (ATI), formation of the high-energy plateau in the electron energy spectrum (High-order ATI), generation of high-order harmonics (HHG) and nonsequential double ionization (NSDI), see Refs. [1–5] for reviews. Both experimental and theoretical approaches used to analyze these processes are constantly being improved. The vast majority of the modern theoretical methods used in strong-field physics are based on the strong-field approximation SFA [6–8], the direct numerical solution of the time-dependent Schrödinger equation (see Refs. [9–12] and references therein), and the semiclassical models applying classical mechanics to describe the electron motion in the continuum. The widely known examples of the semiclassical models are the two-step model [13–15] and the three-step model [16,17].

In the SFA ionization is described as a transition from an initial state unaffected by the laser field to a Volkov state, i.e., the wave function of an electron in an electromagnetic field. Therefore, the SFA neglects the intermediate bound states and the Coulomb interaction in the final state. The SFA provides the illustrative physical picture of many strong-field phenomena and often allows for the analytic solutions. Nevertheless, the approximations used in the SFA are strong enough and may sometimes lead to wrong results. The widely known example is the fourfold symmetry of the photoelectron angular distributions in the elliptically polarized field predicted by the SFA [18]. In contrast to this,

the experimental angular distributions show only the inversion symmetry: They are asymmetric in any half of the polarization plane [19]. The theoretical studies [20–25] have shown that the fourfold symmetry of the angular distributions is a direct consequence of neglecting the effect of the Coulomb potential on the electron motion in the continuum.

In most cases the direct numerical solution of the TDSE provides a good agreement with the experimental results. However, it is often difficult to understand the physical mechanism of the phenomena under study with only the numerical wave function. What is also important, the capabilities of modern computers are not unlimited. One of the most prominent examples is the strong-field ionization of molecules. The solution of the TDSE in three spatial dimensions is possible only for the simplest molecules and with selection of the most relevant degrees of freedom [26,27]. Indeed, ionization of a molecule by an intense laser pulse is much more complicated than ionization of an atom. This is because of the existence of additional degrees of freedom (nuclear motion), the associated time scales, and the complex shape of the electronic orbitals. For typical laser parameters used in experiments nuclear motion should be treated on an equal footing with the processes induced by a strong laser field. Simultaneously, the rich nuclear structure of molecules results in orbitals of diverse symmetries.

Although the first semiclassical model (i.e., the two-step model) was formulated in 1988-1989 [13–15], the trajectory-based models are still widely used for description of various strong-field phenomena. This is due to a number of important advantages characteristic to the semiclassical approaches. The semiclassical models provide a great insight into strong-field processes. They allow to reveal the specific mechanism responsible for the process under investigation, as well as visualize

[a] e-mail: nikolay.shvetsov@itp.uni-hannover.de (corresponding author)

Ⓐ Springer

it using classical trajectories. This point needs to be discussed in more details.

In the ATI an electron absorbs more photons than necessary for ionization. The studies of the ATI have revealed that the majority of the ionized electrons do not experience hard recollisions with their parent ions. These electrons are referred to as direct electrons. They contribute to the low energy part of the ATI energy spectrum $E < 2U_p$, where $U_p = F_0^2/4\omega^2$ is the ponderomotive energy. Here, in turn, F_0 and ω are the amplitude and the frequency of the laser field (atomic units are used throughout the paper). The two-step model allows to describe the spectrum of the direct electrons. In the first step of the this model an electron tunnels out of an atom. In the second step it moves along a classical trajectory in the laser field towards a detector.

There are also rescattered electrons that are driven back by the laser field to their parent ions. Upon their returns the rescattered electrons scatter from the parent ions by large angles close to $180°$. These electrons form the high-energy plateau of the ATI spectrum. The rescattering scenario provides the basis for an understanding of the HHG and NSDI. Indeed, the returning electron can recombine to the parent ion and as the result of the recombination a high-frequency photon (harmonic) radiation is emitted. Alternatively, if the energy of the scattered electron is sufficient enough, it can release the second electron from the ion, e.g., by impact ionization. The three-step model comprises the interaction of the rescattered electron with the parent ion as the third step. As the result, the three-step model provides the qualitative description of the rescattering-induced processes.

The three-step model explained a number of features revealed in the studies of the high-order ATI, HHG, and NSDI: the cutoffs in high-order ATI spectrum [28] and HHG [16,29], the maximum angles of the angular distributions of ionized electrons [30], the characteristic recoil ion momenta in NSDI [31,32], etc. Originally the two-step and the three-step models did not account for the effect of the ionic potential on the electron motion in the continuum. The inclusion of the ionic force in the Newton's equation of motions allowed to uncover the Coulomb focusing effect [33], study the Coulomb cusp in the angular distributions of the photoelectrons [34], investigate the low-energy structures in ionization by the strong midinfrared pulses [35–43] (the so-called ionization surprise observed for the first time in experiment [44]), explore the nonadiabatic effects in ionization by intense laser pulses (see, e.g., Refs. [45–47]), etc.

The trajectory-based simulations are often (although not always) computationally less expensive than the solution of the TDSE. Furthermore, for some strong-field processes the semiclassical simulations are presently the only feasible approach. The most well-known example of such process is the NSDI of atoms by circularly [48] or elliptically polarized pulses [49–51], as well as the NSDI in molecules [52]. Therefore, further development of the semiclassical approaches to strong-field phenomena is an important objective.

Until recently the trajectory-based models were not able to describe quantum interference effects. However, a significant progress along these lines has been made in the last decade. The trajectory-based Coulomb SFA (TCSFA) [37,53], the quantum trajectory Monte Carlo model (QTMC) [54], the semiclassical two-step model (SCTS) [55], and the Coulomb quantum orbit strong-field approximation (CQSFA) [56–60] (see Ref. [61] for the foundations of the CQSFA approach) are recent trajectory-based models that are capable to reproduce interference structures in photoelectron momentum distributions of the ATI process. These models assign certain phases to classical trajectories, and the contributions of different trajectories leading to the same final momentum are added coherently.

The TCSFA is an extension of the CCSFA [62,63] that on an equal footing accounts the laser field and the Coulomb force in the Newton's equation for electron motion in the continuum. The TCSFA applies the first-order semiclassical perturbation theory [64] to account the Coulomb potential in the phase associated with every trajectory. The same first-order semiclassical perturbation theory was used in the phase of the QTMC model. In contrast to this, the SCTS and the CQSFA approaches go beyond the perturbation theory.

The SCTS model operates with large ensembles of classical trajectories that are propagated in the continuum to find the final asymptotic momenta and bin them (and, therefore, the corresponding contributions assigned to these trajectories) in bins in momentum space. This approach is often referred to as "shooting method" (see, e.g., Ref. [37]). Instead, the CQSFA model solves the so-called inverse problem, i.e., finds all the trajectories leading to a given final momentum. This allows to avoid large ensembles of trajectories and establish a better control over cusps and caustics that are inevitable in trajectory-based simulations. The price that is to be paid is that the solution of the inverse problem is a difficult task. In addition to this, the approach with the inverse problem can often be less versatile.

In this paper we review the SCTS model, as well as two recent implementations of this model. We also discuss some of the applications of the SCTS. The SCTS model has been applied to the investigation of the intra-half-cycle interference of photoelectrons with low energies [65], to the studies of the interference patterns arising in the strong-field photoelectron holography [66–68], to the analysis of the sub-cycle interference in ionization by counter-rotating two-color fields [69], to the investigation of sideband modulation by subcycle interference in ionization by circularly polarized two-color laser fields [70], etc. Here we focus on the applications of the SCTS to the strong-field photoelectron holography, study of the multielectron polarization effects, and the ionization of the H_2 molecule.

The paper is organized as follows. In Sect. 2 we review the SCTS and discuss different approaches used to implement this model numerically. In Sect. 3 we discuss the further modifications of the SCTS model: the semiclassical two-step model with quantum input and

the SCTS model accounting for the preexponential factor of the semiclassical propagator. In Sect. 4 we briefly review applications of the SCTS model to the strong-field photoelectron holography. The application of the SCTS to the study of the multielectron polarization effects in the ATI are discussed in Sect. 5. In Sect. 6 we review the usage of the SCTS model to describe the strong-field ionization of the H_2 molecule. The conclusions of this colloquia paper are given in Sect. 7.

2 Semiclassical two-step model

2.1 Formulation of the semiclassical two-step model

As any semiclassical model, the electron trajectory in SCTS is calculated using classical equation of motion:

$$\frac{d^2r}{dt^2} = -F(t) - \nabla V(r,t), \tag{1}$$

where $\mathbf{F}(t)$ is the laser field and $V(\mathbf{r},t)$ is the ionic potential. In order to find the trajectory from Eq. (1), we need to specify the initial conditions, i.e., the initial velocity of the departing electron and the starting point. In the original version of the SCTS model it is assumed that the electron starts with zero initial velocity along the laser field $v_{0,z} = 0$, but it can have a nonzero initial velocity $v_{0,\perp}$ in the perpendicular direction. We note that the application of the SFA to describe the electron motion under the potential barrier leads to a nonzero initial longitudinal velocity $v_{0,z} \neq 0$. The effect of the nonzero $v_{0,z}$ will be discussed later. Let us first assume that the interaction of the ionized electron with the ion is modelled by the Coulomb potential. Then the starting point of the trajectory, i.e., the tunnel exit point, can be obtained using the separation of the static tunneling problem in parabolic coordinates. For the static field polarized along the z-axis we define the parabolic coordinates as $\xi = r + z$, $\eta = r - z$, and $\varphi = \arctan(y/x)$ and find the tunnel exit coordinate η_e from the following equation:

$$-\frac{\beta_2(F)}{2\eta} + \frac{m^2-1}{8\eta^2} - \frac{F\eta}{8} = -\frac{I_p(F)}{4}. \tag{2}$$

Here m is the magnetic quantum number of the initial state, $I_p(F)$ is the Stark-shifted ionization potential, and

$$\beta_2(F) = Z - (1+|m|)\frac{\sqrt{2I_p(F)}}{2}. \tag{3}$$

The tunnel exit point is given by $z_e = -\eta_e/2$. In the general case, the ionization potential $I_p(F)$ in Eq. (2) is given by

$$I_p(F) = I_p(0) + (\boldsymbol{\mu}_N - \boldsymbol{\mu}_I) \cdot \mathbf{F} + \frac{1}{2}(\alpha_N - \alpha_I)\mathbf{F}^2. \tag{4}$$

Here $I_p(0)$ is the ionization potential in the absence of the field, and $\boldsymbol{\mu}_{N,I}$ and $\alpha_{N,I}$ are the dipole moments and static polarizabilities, respectively. The index N refers to the neutral atom (molecule), and the index I stands for its ion. We note that for atom the term linear with respect to F is absent in Eq. (4). The static field F in Eqs. (2), (3), and (4) should be replaced by the instantaneous value of the laser field at the time of ionization t_0.

The instants of ionization and the initial transverse velocities are distributed in accord with the static ionization rate [71]:

$$w(t_0, v_{0,\perp}) \sim \exp\left(-\frac{2\kappa^3}{3F(t_0)}\right)\exp\left(-\frac{\kappa v_{0,\perp}^2}{F(t_0)}\right), \tag{5}$$

where $\kappa = \sqrt{2I_p}$. Following the original formulation of the SCTS model we omit the preexponential factor in Eq. (5). For atoms it only slightly affects the shape of the electron momentum distributions.

After the laser pulse terminates an electron moves in the Coulomb field only. If the electron energy at the time $t = t_f$ at which the laser pulse terminates is negative $E < 0$, the electron moves along the elliptical orbit, and it should be treated as captured into a Rydberg state [72,73]. The corresponding process is often referred to as frustrated tunnel ionization, see, e.g., Refs. [74–77]. It is clear that the trajectories with $E < 0$ should be excluded from consideration, if we are interested in ionized electrons. The latter obviously correspond to the hyperbolic trajectories ($E > 0$). The asymptotic momentum $\mathbf{k}$ of the electron is determined by its position $\mathbf{r}(t_f)$ and momentum $\mathbf{p}(t_f)$ at the time $t = t_f$:

$$\mathbf{k} = k\frac{k(\mathbf{L}\times\mathbf{a}) - \mathbf{a}}{1 + k^2L^2}, \tag{6}$$

see Refs. [73,78]. In Eq. (6) $\mathbf{L} = \mathbf{r}(t_f) \times \mathbf{p}(t_f)$ and $\mathbf{a} = \mathbf{p}(t_f) \times \mathbf{L} - Z\mathbf{r}(t_f)/r(t_f)$ are the angular momentum and the Runge-Lenz vector, respectively. The magnitude of the momentum k is determined by the energy conservation:

$$\frac{k^2}{2} = \frac{\mathbf{p}^2(t_f)}{2} - \frac{Z}{r(t_f)}. \tag{7}$$

The key ingredient of the SCTS model is the expression for the phase associated with every trajectory. This phase corresponds to the phase of the matrix element of the semiclassical propagator $U_{SC}(t_2, t_1)$ between the initial state at time t_1 and the final state at time t_2 [79–81] (for a text-book treatment see Refs. [82,83]). Depending on the variables used to describe the initial and final states there exist four equivalent forms of the semiclassical propagator U_{SC}:

$$\langle r_2| U_{\mathrm{SC}}(t_2,t_1)|r_1\rangle = \left[-\frac{\det\left(\partial^2\phi_2(r_1,r_2)/\partial r_1\partial r_2\right)}{(2\pi i)^3}\right]^{1/2}$$

$$\times \, exp[i\phi_1(r_1, r_2)], \quad (8a)$$

$$\langle \mathbf{r}_2| U_{\mathrm{SC}}(t_2, t_1) |\mathbf{p}_1\rangle = \left[-\frac{\det\left(\partial^2 \phi_2\left(\mathbf{p}_1, \mathbf{r}_2\right)/\partial \mathbf{p}_1 \partial \mathbf{r}_2\right)}{(2\pi i)^3}\right]^{1/2}$$
$$\times \exp\left[i\phi_2\left(\mathbf{p}_1, \mathbf{r}_2\right)\right], \quad (8b)$$

$$\langle \mathbf{p}_2| U_{\mathrm{SC}}(t_2, t_1) |\mathbf{r}_1\rangle = \left[-\frac{\det\left(\partial^2 \phi_3\left(\mathbf{r}_1, \mathbf{p}_2\right)/\partial \mathbf{r}_1 \partial \mathbf{p}_2\right)}{(2\pi i)^3}\right]^{1/2}$$
$$\times \exp\left[i\phi_3\left(\mathbf{r}_1, \mathbf{p}_2\right)\right], \quad (8c)$$

$$\langle \mathbf{p}_2| U_{\mathrm{SC}}(t_2, t_1) |\mathbf{p}_1\rangle = \left[-\frac{\det\left(\partial^2 \phi_4\left(\mathbf{p}_1, \mathbf{p}_2\right)/\partial \mathbf{p}_1 \partial \mathbf{p}_2\right)}{(2\pi i)^3}\right]^{1/2}$$
$$\times \exp\left[i\phi_4\left(\mathbf{p}_1, \mathbf{p}_2\right)\right]. \quad (8d)$$

Here $\mathbf{r}_1$ ($\mathbf{r}_2$) and $\mathbf{p}_1$ ($\mathbf{p}_2$) are the initial (final) coordinates and momenta, respectively. The phase ϕ_1 that corresponds to the transition from the initial state to the final state, which are both described by the position, is determined by the classical action:

$$\phi_1\left(\mathbf{r}_1, \mathbf{r}_2\right) = \int_{t_1}^{t_2} \left\{\mathbf{p}\left(t\right) \dot{\mathbf{r}}\left(t\right) - H\left[\mathbf{r}\left(t\right), \mathbf{p}\left(t\right)\right]\right\} dt, \quad (9)$$

where $H\left[\mathbf{r}\left(t\right), \mathbf{p}\left(t\right)\right]$ is the classical Hamiltonian function that depends on the canonical coordinates $\mathbf{r}\left(t\right)$ and momenta $\mathbf{p}\left(t\right)$. The other three phases ϕ_2, ϕ_3, and ϕ_4 are related to ϕ_1 by the canonical transformations:

$$\phi_2\left(\mathbf{p}_1, \mathbf{r}_2\right) = \phi_1\left(\mathbf{r}_1, \mathbf{r}_2\right) + \mathbf{p}_1 \cdot \mathbf{r}_1, \quad (10a)$$
$$\phi_3\left(\mathbf{r}_1, \mathbf{p}_2\right) = \phi_1\left(\mathbf{r}_1, \mathbf{r}_2\right) - \mathbf{p}_2 \cdot \mathbf{r}_2, \quad (10b)$$
$$\phi_4\left(\mathbf{p}_1, \mathbf{p}_2\right) = \phi_1\left(\mathbf{r}_1, \mathbf{r}_2\right) + \mathbf{p}_1 \cdot \mathbf{r}_1 - \mathbf{p}_2 \cdot \mathbf{r}_2, \quad (10c)$$

Then the question arises: Which of these phases should be chosen for description of the strong-field ionization process? On the assumption that for a given ionization time the starting-point of the electron trajectory is localized in space [see Eq. (2)] and the final state is characterized by the asymptotic momentum $\mathbf{k}$, the phase ϕ_3 is used in the SCTS model. Indeed, the strong-field ionization can be viewed as a half-scattering process of an electron that is initially localized near the atom (molecule) and detected with the final momentum $\mathbf{k}$. We note that if the initial longitudinal velocity is equal to zero, the initial electron momentum $\mathbf{p}_1$ is orthogonal to the initial position vector $\mathbf{r}_1$ (i.e., $\mathbf{p}_1 \cdot \mathbf{r}_1 = 0$), and therefore, the phases ϕ_3 and ϕ_4 coincide with each other. For nonzero $v_{0,z}$ the term $\mathbf{p}_1 \cdot \mathbf{r}_1$ is to be accounted in the phase. However, in most cases this term almost does not affect the resulting electron momentum distributions.

As the result, after a partial integration, the phase corresponding to a given trajectory in the SCTS model is given by:

$$\Phi^{SCTS}\left(t_0, \mathbf{v}_0\right) = -\mathbf{v}_0 \cdot \mathbf{r}(t_0) + I_p t_0$$
$$- \int_{t_0}^{\infty} dt \,\left\{\dot{\mathbf{p}}(t) \cdot \mathbf{r}(t) + H[\mathbf{r}(t), \mathbf{p}(t)]\right\}, \quad (11)$$

where it is assumed that the trajectory has also the initial phase $\exp\left(iI_p t_0\right)$ that describes the time evolution of the ground state. The expression (11) can be also written as follows:

$$\Phi^{SCTS}\left(t_0, \mathbf{v}_0\right) = -\mathbf{v}_0 \cdot \mathbf{r}(t_0) + I_p t_0$$
$$- \int_{t_0}^{\infty} dt \,\left\{\frac{p^2(t)}{2} + V[\mathbf{r}(t)] - \mathbf{r}(t) \cdot \boldsymbol{\nabla} V[\mathbf{r}(t)]\right\}. \quad (12)$$

To arrive at the expression (12), we use the explicit form of the Hamiltonian for an arbitrary effective potential

$$H\left[r\left(t\right), p\left(t\right)\right] = \frac{p^2\left(t\right)}{2} + F\left(t\right) \cdot r\left(t\right) + V\left(r\right) \quad (13)$$

and employed Newton's equation of motion (1). This formula is applicable for any single-active-electron potential used to describe the multielectron system (atom or molecule), including pseudopotentials (see, e.g., Ref. [84] and references therein). For the specific case of the Coulomb potential, the phase (12) reads as

$$\Phi^{STCS}\left(t_0, \mathbf{v}_0\right) = -\mathbf{v}_0 \cdot \mathbf{r}(t_0) + I_p t_0$$
$$- \int_{t_0}^{\infty} dt \,\left\{\frac{p^2(t)}{2} - \frac{2Z}{r\left(t\right)}\right\}. \quad (14)$$

This formula should be compared with the phase used in the QTMC model:

$$\Phi^{QTMC}\left(t_0, \mathbf{v}_0\right) = -\mathbf{v}_0 \cdot \mathbf{r}(t_0) + I_p t_0$$
$$- \int_{t_0}^{\infty} dt \,\left\{\frac{p^2(t)}{2} - \frac{Z}{r\left(t\right)}\right\}. \quad (15)$$

It is seen that the QTMC phase can be obtained from Eq. (14) by neglecting the term $\mathbf{r}(t) \cdot \boldsymbol{\nabla} V[\mathbf{r}(t)]$ in the integrand. This term leads to the double weight of the Coulomb term in the SCTS compared to the QTMC. Therefore, the QTMC phase can be considered as an approximation to the SCTS one. The double weight of the Coulomb contribution leads to a better agreement with the TDSE results [55].

The SCTS phase (14) is divergent at $t \to \infty$, and therefore, it is to be regularized. The regularization (see Ref. [55]) can be accomplished by decomposing the SCTS phase as

$$\Phi^{SCTS}\left(t_0, \mathbf{v}_0\right) = -\mathbf{v}_0 \cdot \mathbf{r}(t_0) + I_p t_0$$
$$- \int_{t_0}^{t_f} \left\{\frac{p^2\left(t\right)}{2} - \frac{2Z}{r\left(t\right)}\right\} - \int_{t_f}^{\infty} dt \,\left\{E - \frac{Z}{r\left(t\right)}\right\} \quad (16)$$

and separating the time-independent part of the integrand in the term $\int_{t_f}^{\infty} dt \,\{E - Z/r\left(t\right)\}$. Although this time-independent part leads to the contribution $\lim\limits_{t \to \infty} E\left(t - t_f\right)$ that diverges linearly when $t \to \infty$, it

does not produce a phase difference for electron trajectories ending up in the same bin. Indeed, the final momenta of such trajectories (and, therefore, their energies) should be considered as equal. Using the solution of the Kepler problem (see, e.g., Ref. [85]) we calculate the divergent integral

$$\Phi_f^C\left(t_f\right) = Z \int_{t_f}^{\infty} \frac{dt}{r\left(t\right)} \tag{17}$$

analytically: $\Phi_f^C\left(\tau_f\right) = Z\sqrt{b}\left[\xi\left(\infty\right) - \xi\left(t_f\right)\right]$. The parameter ξ is used to parametrize the time t and the distance r from the Coulomb center:

$$\begin{aligned} r\left(t\right) &= b\left(g\cosh\xi - 1\right), \\ t &= \sqrt{b^3}\left(g\sinh\xi - \xi\right) + C \end{aligned} \tag{18}$$

Here, in turn, $b = 1/\left(2E\right)$ and $g = \sqrt{1 + 2EL^2}$. The constant C in Eq. (18) is to be found using the initial conditions, i.e, $\mathbf{r}\left(t_f\right)$ and $\mathbf{p}\left(t_f\right)$. It is easy to verify that

$$\xi\left(t_f \to \infty\right) = \ln\left(\frac{2t}{g\sqrt{b^3}}\right), \tag{19}$$

see Ref. [55]. Therefore, for trajectories arriving at the same bin, we can discriminate between the common divergent part $\ln\left(2t/\sqrt{b^3}\right)$ and the finite contributions determined by $-\ln\left(g\right)$. We note that the latter depends not only on the energy, but also on the angular momentum L, and thus is different for different trajectories interfering in a given bin. Since

$$\xi\left(t_f\right) = \operatorname{arsinh}\left\{\frac{\mathbf{r}\left(t_f\right) \cdot \mathbf{p}\left(t_f\right)}{g\sqrt{b}}\right\}, \tag{20}$$

we obtain the following contribution to the phase accumulated in the time interval $[t_f, \infty]$ due to the Coulomb potential (see Ref. [55]):

$$\tilde{\Phi}_f^C\left(t_f\right) = -Z\sqrt{b}\left[\ln g + \operatorname{arsinh}\left\{\frac{\mathbf{r}(t_f) \cdot \mathbf{p}(t_f)}{g\sqrt{b}}\right\}\right] \tag{21}$$

This asymptotic correction of the phase which we call post-pulse phase is missing in the QTMC model.

2.2 Implementation of the semiclassical two-step model

The expression for the phase can be conveniently treated as an additional equation in the system of the first-order ordinary differential equations for electron coordinates and velocity components following from (1). This system can be solved using the fourth-order Runge–Kutta method with adaptive step size [86]. The ability of the numerical method to change the integration step is particularly important at small distances from the Coulomb center.

It is clear that the convergence of the results must be controlled with respect to both the size of the bin in the momentum space and the number of trajectories. It is particularly convenient to control convergence by using the energy spectra. In contrast to the three-dimensional (3D) differential momentum distributions or their two-dimensional (2D) cuts, the spectra are functions of only one variable. They can be easily compared to each other in, e.g., logarithmic scale.

Already the first practical application of the SCTS model has shown that a large number of trajectories is needed for convergence (see Ref. [55] for details). Typically, for the same laser parameters a thousand times more trajectories are needed for the simulations with the phase compared to a semiclassical model disregarding the interference effect. This can be expected taking into account the fine interference details of electron momentum distributions generated in ionization by strong laser pulses. For this reason, it is important to consider optimization of the codes implementing the SCTS model. The most obvious way to speed up the SCTS calculations is to use parallelization. Indeed, any trajectory-based simulation can be very easily and efficiently implemented on a computer cluster by paralleling the loop over the number of trajectories.

Another approach consists in an efficient sampling of the initial conditions, i.e., times of ionization t_0^j and initial velocities v_0^j, where index j enumerates the trajectories of an ensemble. In a standard trajectory-based approach the initial conditions are chosen either randomly or from a certain uniform grid. Neglecting interference effect the ionization probability $R\left(\mathbf{k}\right)$ for the final momentum $\mathbf{k}$ that corresponds to the bin $[k_i, k_i + \Delta k_i]$ $(i = x, y, z)$ is calculated as

$$R\left(\mathbf{k}\right) = \sum_{j=1}^{n_p} w\left(t_0^j, v_0^j\right), \tag{22}$$

while the similar formula for the SCTS model reads as

$$\begin{aligned} &R\left(\mathbf{k}\right) \\ &= \sum_{j=1}^{n_p}\left|\sqrt{w\left(t_0^j, v_0^j\right)}\exp\left[i\Phi^{SCTS}\left(t_0^j, v_0^j\right)\right]\right|^2 \end{aligned} \tag{23}$$

The sums in Eqs. (22) and (23) are calculated over all n_p trajectories arriving at the given bin. However, the approach sketched here is not the only possible one. Importance sampling widely used in Monte-Carlo integration (see, e.g., Ref. [86]) can be used to implement the SCTS model.

We turn first to the semiclassical simulations disregarding interference. In the important sampling approach the weights (importance) of classical trajectories are accounted already at the sampling stage. More specifically, the sets of initial conditions $\left(t_0^j, v_0^j\right)$ are distributed in accord with the tunneling rate $w\left(t_0^j, v_0^j\right)$

and the ionization probability $R(\mathbf{k})$ is given by a number of trajectories reaching the bin corresponding to the final momentum $\mathbf{k}$. It is easy to see that the ionization probability in the SCTS model based on the importance sampling reads as

$$R(\mathbf{k}) = \sum_{j=1}^{n_p} \left| \exp\left[i\Phi^{SCTS}\left(t_0^j, v_0^j\right)\right]\right|^2. \quad (24)$$

with the initial conditions distributed in accord to the square root of the ionization probability. In many situations the important sampling technique provides faster convergence compared to the standard approach of Eqs. (22–23). Its performance, however, depends on the laser-atom parameters and the specific part of photoelectron momentum distribution under study.

2.3 Benchmark case: ionization of the H atom

The SCTS model was compared with the QTMC approach and direct numerical solution of the TDSE for ionization of the hydrogen atom (see Ref. [55]). The 2D electron momentum distributions calculated in accord to the all three approaches are shown in Fig. 2a–c. The simulations are done for ionization by a few-cycle laser pulse linearly polarized along the z-axis and defined through the vector-potential:

$$\mathbf{A}(t) = (-1)^n \frac{F_0}{\omega} \sin^2\left(\frac{\omega t}{2n}\right) \sin(\omega t + \varphi)\,\mathbf{e}_z. \quad (25)$$

Here n is the number of optical cycles within the pulse, and $\mathbf{e}_z$ is the unit vector in the polarization direction. The pulse (25) is present between $t = 0$ and $t = t_f = (2\pi/\omega) \cdot n$. The laser field is to be calculated from Eq. (25) as $\mathbf{F}(t) = -d\mathbf{A}(t)/dt$. The factor $(-1)^n$ in (25) ensures that $F_z(t)$ for $\varphi = 0$ has its maximum (equal to F_0) for $\omega t = \pi n$, i.e., at the center of the pulse. We do calculations for $\varphi = 0$.

It is seen that the most important features of the TDSE result are reproduced by the semiclassical models (see Fig. 1a, c, e). Indeed, the electron momentum distributions are stretched along the z-axis and show clear ATI rings as well as the pronounced interference structure in their low-energy parts. The width of the momentum distributions along the polarization direction is obviously underestimated by both semiclassical models. This is due to the initial condition $v_{0,z} = 0$ (see Ref. [55] for details).

However, a closer examination of the low-energy parts of the distributions reveals remarkable deviations Indeed, for $|k| < 0.3$ a.u. the photoelectron momentum distributions demonstrate pronounced fanlike interference structures, see Fig 1b, d, f. These structures are similar to the ones of Ramsauer-Townsend diffraction oscillations, see Refs. [87–90]. It is seen that the SCTS model reproduces the interference pattern of the TDSE, whereas the QTMC model predicts fewer nodal lines. This fact was attributed to the underestimate of the
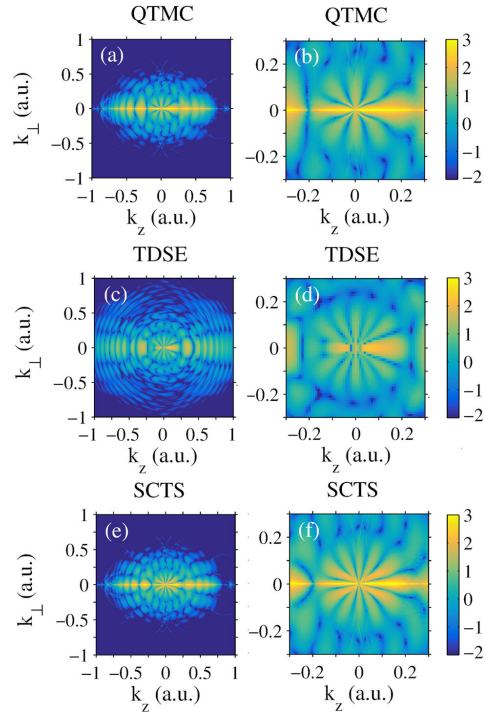
Fig. 1 Two-dimensional electron momentum distributions for ionization of the H atom by a laser pulse with a duration of $n = 8$ cycles, peak intensity of 0.9×10^{14} W/cm^2, and wavelength of 800 nm calculated from the QTMC model [**a**, **b**], numerical solution of the TDSE [**c**, **d**], and the SCTS [**e**, **f**]. Panels **b**, **d**, and **f** display the magnifications for $|k_z|, |k_\perp| < 0.3$ a.u. of the distributions shown in (**a**), (**c**), and (**d**), respectively. The laser pulse is linearly polarized along the z axis. The distributions are normalized to the total ionization yield. A logarithmic color scale in arbitrary units is used

Coulomb potential in the expression for the phase used in the QTMC model. The comparison of the photoelectron energy spectra dR/dE shows that the QTMC and the SCTS qualitatively reproduce the ATI peaks, see Fig. 2a–c. However, both semiclassical approaches can quantitatively reproduce the amplitude of interference oscillations only for a few low-order peaks. This is related to the fact that due to the initial conditions [Eq. (5)] used in both semiclassical models too few trajectories with large initial momenta in the polarization direction are launched. This also explains why the semiclassical energy spectra fall off too rapidly with the increase of energy. In order to test this hypothesis, the initial longitudinal velocity for every ionization time is set to the value predicted by the SFA, see, e.g. Ref. [37]. This change in initial conditions leads to a better
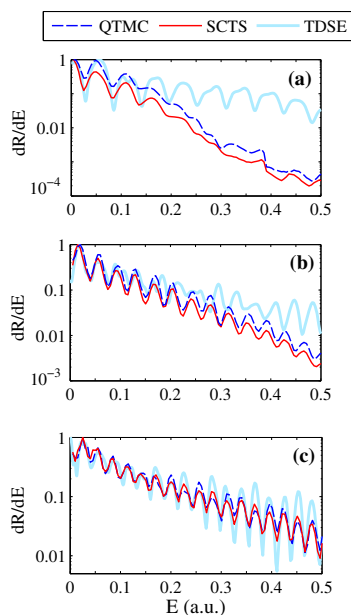
Fig. 2 Photoelectron energy spectra for ionization of the H atom by a laser pulse with a duration of $n = 8$ cycles and peak intensity of 0.9×10^{14} W/cm^2 calculated using the TDSE (thick light blue curve), the QTMC (dashed blue curve) and the SCTS (solid red curve). Panels **a**, **b**, and **c** correspond to the wavelengths of 800 nm, 1200 nm, and 1600 nm, respectively. The spectra are normalized to the peak value
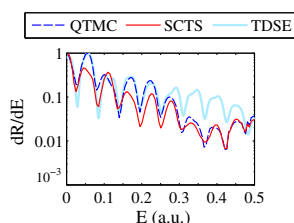

Fig. 3 Photoelectron energy spectra calculated from the TDSE (thick light blue curve), the QTMC model (dashed blue curve) and the SCTS (solid red curve). A nonzero initial parallel velocity predicted by the SFA is used in both the QTMC and SCTS simulations. The pulse parameters are as in Fig 2a

agreement between the SCTS model and the TDSE, see Fig. 3 and Ref. [55]. Therefore, the main reason of deviations of the SCTS results from the TDSE solutions is not the semiclassical treating of the electron motion in the continuum, but the fact that the SCTS model does not describe the tunneling step accurately enough.

Here we compare the semiclassical simulations with the direct numerical solution of the TDSE assuming that the latter approach is exact. However, it should be noted that the numerical solution of the TDSE can sometimes have its own limitations. This is also true for the extraction of the photoelectron momentum distributions from the time-dependent wave function, which is a non-trivial problem. Some methods used for this purpose can cause wrong results (see Ref. [91] for details).

3 Modifications of semiclassical two-step model

Substantial efforts have been recently made to modify the SCTS model. These modifications are aimed at providing not only a qualitative, but also a quantitative agreement with the TDSE. To achieve this goal, it is necessary to overcome the deficiencies of the SCTS model (as well as of any other semiclassical model) in description of the ionization step. The simplest way is to use the SFA formulas to distribute the initial conditions of classical trajectories. This approach dates back to the studies of Refs. [92,93]. It is used in the various semiclassical models (see, e.g., Refs. [37,45–47]), as well as in the implementations of the SCTS model developed in Refs. [70,94]. We note, however, that the validity of the SFA formulas used as initial conditions for classical trajectories requires a systematic study. To the best of our knowledge, such a study has not been accomplished so far. Here we discuss two modifications of the SCTS model: The semiclassical two-step model with quantum input (SCTSQI) [95] and the SCTS model with the prefactor [94].

3.1 Semiclassical two-step model with quantum input

The SCTSQI model combines the SCTS with initial conditions obtained from the solution of the TDSE. Such a combination leads to a novel quantum-classical approach. The SCTSQI model is formulated for ionization of a one-dimensional (1D) model atom. Therefore, before reviewing the SCTSQI, we briefly discuss the solution of the 1D TDSE, as well as the application of the SCTS model in 1D case.

For the 1D model, the TDSE in the velocity gauge is given by

$$i\frac{\partial}{\partial t}\Psi\left(x,t\right) = \left\{\frac{1}{2}\left(-i\frac{\partial}{\partial x} + A_x\left(t\right)\right)^2 + V\left(x\right)\right\}\Psi\left(x,t\right),$$

(26)

where $\Psi(x, t)$ is the wave function in coordinate space. The 1D soft-core Coulomb potential

$$V = -\frac{1}{\sqrt{x^2 + a^2}} \qquad (27)$$

with $a = 1.0$ (see Ref. [96]) is used in Ref. [95]. The corresponding time-independent Schrödinger equation reads as:

$$\left\{ -\frac{1}{2}\frac{d^2}{dx^2} + V(x) \right\} \Psi(x) = E\Psi(x). \qquad (28)$$

Equation (28) can be easily solved on a grid using, e.g., the well-known three-step formula for approximation of the second derivative and subsequent diagonalization. In Ref. [95] the TDSE (26) is solved using slit-operator method [97]. In the regions $x_b \leq |x| \leq x_{\max}$ the wave function is multiplied by a mask

$$M(x) = \cos^{1/6}\left[\frac{\pi(|x| - x_b)}{2(x_{\max} - x_b)} \right], \qquad (29)$$

where $x = \pm x_b$ correspond to the internal boundaries of the absorbing regions, and $x_{\max}$ is the size of the computational box. The mask prevents unphysical reflections of the propagating wave function from the grid boundary and allows to calculate the electron momentum distributions using the mask method [98].

In the 1D case the Newton's equation for an electron moving in the laser field and the field of the potential (27) reads as

$$\frac{d^2 x}{dt^2} = -F_x(t) - \frac{x}{(x^2 + a^2)^{3/2}}. \qquad (30)$$

The corresponding SCTS phase is given by (see Ref. [95]):

$$\Phi^{SCTS}(t_0, \mathbf{v}_0) = I_p t_0$$
$$- \int_{t_0}^{\infty} dt \left\{ \frac{v_x^2(t)}{2} - \frac{x^2}{(x^2 + a^2)^{3/2}} - \frac{1}{\sqrt{x^2 + a^2}} \right\}. \qquad (31)$$

We note that the ionization rate (5) in the 1D case is to be replaced by

$$w(t_0) \sim \exp\left(-\frac{2(2|E_0|)^{3/2}}{3F(t_0)} \right), \qquad (32)$$

where $E_0 = -0.6698$ a.u. is the ground-state energy in the potential (27). Equation (30) is to be numerically integrated up to the end of the laser pulse at $t = t_f$. The asymptotic momentum of the photoelectron can be found from $x(t_f)$ and $p_x(t_f)$ using the energy conservation law. We note that after the end of the pulse the

unbound electron cannot change its direction of motion, and, therefore, k_x has the same sign as that of $p_x(t_f)$.

In order to correctly apply the SCTS model in the 1D case, the post-pulse phase is to be calculated. This calculation can be performed as follows (see Ref. [95]). At first, we decompose the phase as:

$$\Phi^{SCTS}(t_0, \mathbf{v}_0) = I_p t_0$$
$$- \int_{t_0}^{t_f} dt \left\{ \frac{v_x^2(t)}{2} - \frac{x^2}{(x^2 + a^2)^{3/2}} - \frac{1}{\sqrt{x^2 + a^2}} \right\}$$
$$+ \Phi_f^V, \qquad (33)$$

As in the 3D case, we separate the post-pulse phase into parts with time-dependent and time-independent integrands and disregard the linearly divergent contribution from the first part. As the result, the post-pulse phase is determined by:

$$\tilde{\Phi}_f^V = \int_{t_f}^{\infty} \frac{x^2(t)}{[x^2(t) + a^2]^{3/2}} dt. \qquad (34)$$

The divergent part of this integral can be efficiently isolated. Indeed, Eq. (34) can be equivalently rewritten as follows:

$$\tilde{\Phi}_f^V = \int_{t_f}^{\infty} \left[\frac{x^2}{(x^2 + a^2)^{3/2}} - \frac{2Et^2}{(2Et^2 + a^2)^{3/2}} \right] dt$$
$$+ \int_{t_f}^{\infty} \frac{2Et^2}{(2Et^2 + a^2)^{3/2}} dt. \qquad (35)$$

Since the second divergent term in Eq. (35) depends on the electron energy E and the parameter a, it is the same for every trajectory that arrives at a given bin $[k_x - \Delta k_x, k_x + \Delta k_x]$. Therefore, it does not affect the resulting interference pattern and can be omitted [95]. The post-pulse phase is determined by the first term in Eq. (35). This converging integral is easily calculated numerically. It depends on the position $x(t_f)$ and velocity $p_x(t_f)$ at the end of the laser pulse what suggests an efficient way to calculate it by interpolation [95].

This is not a simple task to unify the direct solution of the TDSE and the trajectory-based approach in one single model. The main problem of such combination has a fundamental origin. Indeed, both the starting point and the initial velocity are needed to uniquely determine the classical trajectory. On the other hand, the Heisenberg's uncertainty principle imposes a limit to the precision with which position and momentum (as other canonically conjugated variables) can be simultaneously known. The application of quasiprobability distribution allows to extract the information from the wave function about both the coordinate and momentum.

The most widely-known examples of the quasiprobability distributions are the Wigner function and Husimi

distribution [99] (see Ref. [100] for a textbook treatment). The latter can be obtained by smoothing of the Wigner function with a Gaussian weight. The Gabor transformation [101] was used in Ref. [95]. The Gabor transformation is presently widely used in studies of the ATI (see, e.g., Ref. [102]) and, especially, the HHG (see, e.g., Refs. [103–105]). The Gabor transform of the wave function $\tilde{\Psi}(x,t)$ near the point x_0 is given by:

$$
G(x_0, p_x, t) = \frac{1}{\sqrt{2\pi}} \int_{-\infty}^{\infty} \tilde{\Psi}(x', t) \exp\left[-\frac{(x'-x_0)^2}{2\delta_0^2}\right]
$$
$$
\times \exp(-i p_x x') \, dx', \tag{36}
$$

where δ_0 is the width of the Gaussian window. The square modulus $|G(x_0, p_x, t)|^2$ corresponds to the momentum distribution of the particle in the vicinity of $x = x_0$ at time t and is just the Husimi distribution [99]. The Husimi distribution is a positive semidefinite function, which helps to interpret it as a quasiprobability distribution.

The SCTSQI model employs the solution of the TDSE in the length gauge:

$$
i\frac{\partial}{\partial t}\Psi(x, t)
$$
$$
= \left\{-\frac{1}{2}\frac{\partial^2}{\partial x^2} + V(x) + F_x(t)x\right\}\Psi(x, t). \tag{37}
$$

Two additional spatial grids containing N points are introduced the absorbing regions $|x| \geq x_b$:

$$
x_{0,\pm}^j = \mp(x_b + \Delta x \cdot j), \tag{38}
$$

Here $j = 0, ..., N$ and $\Delta x = (x_{max} - x_b)/N$. In the SCTSQI the Gabor transforms of the absorbed part of the wave function $\tilde{\Psi}(x,t) = [1 - M(x)]\Psi(x,t)$ are calculated at every time at the points $x_{0,-}^j$ and $x_{0,+}^j$ of the grids (38). The value of the Gabor transformation at an arbitrary point belonging to D_1 or D_2 can be obtained by interpolation (see Ref. [95] for a details of the implementation of the SCTSQI model). Hence, at every time t the Gabor transform $G(x, p_x, t)$ is known on the grids in the phase-space domains $D_1 = [-x_{max}, -x_b] \times [-p_{x,max}, p_{x,max}]$ and $D_2 = [x_b, x_{max}] \times [-p_{x,max}, p_{x,max}]$. An example of the Husimi distribution obtained in the domains D_1 and D_2 at $t = 3t_f/2$ is shown in Fig. 4. It should be stressed that the size of the computational box x_{max} used in the SCTSQI can be much smaller than the one required to obtain accurate momentum distributions by using the mask method.

At every time t_0 an ensemble of n_p classical trajectories with random initial positions x_0^j and momenta $p_{x,0}^j$ ($j = 1, ..., n_p$) is launched in the SCTSQI model. Every trajectory of the ensemble is assigned with the
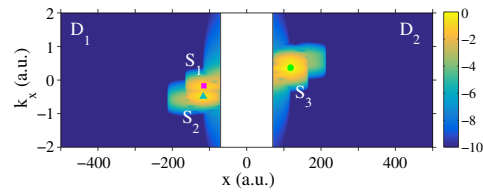

Fig. 4 The Husimi quasiprobability distribution $|G(x, p_x, t)|^2$ at $t = 3t_f/2$ calculated for ionization of 1D model atom by a laser pulse with a duration of $n = 4$ cycles, wavelength of 800 nm, and peak intensity of 2.0×10^{14} W/cm^2. The distribution is calculated in the phase space domains D_1 and D_2 (see text). The points S_1, S_2, and S_3 depicted by a magenta square, cyan triangle, and green circle, respectively show the three main maxima of the Husimi distribution. A logarithmic color scale is used

amplitude $G\left(t_0, x_0^j, p_{x,0}^j\right)$ and the SCTSQI phase

$$
\Phi_0^{SCTSQI}\left(t_0, x_0^j, p_{x,0}^j\right)
$$
$$
= -\int_{t_0}^{\infty} dt \left\{\frac{v_x^2(t)}{2} - \frac{x^2}{(x^2 + a^2)^{3/2}}\right.
$$
$$
\left. - \frac{1}{\sqrt{x^2 + a^2}}\right\}. \tag{39}
$$

This phase coincides with the phase of the semiclassical propagator describing a transition from an initial state characterized by the momentum to a final state, which is also described by the momentum value. The ionization probability $R(k_x)$ is calculated as:

$$
R(k_x) = \left|\sum_{m=1}^{N_T}\sum_{j=1}^{n_{k_x}} G\left(t_0^m, x_0^j, p_{x,0}^j\right)\right.
$$
$$
\left. \times \exp\left[i\Phi^{SCTSQI}\left(t_0^m, x_0^j, p_{x,0}^j\right)\right]\right|^2, \tag{40}
$$

where N_T is the number of steps that is used in the TDSE propagation and n_k is the number of trajectories arriving at the same bin centered at k_x. It is important to stress that $G\left(t_0^m, x_0^j, p_{x,0}^j\right)$ is a complex function having both modulus and the phase.

The SCTSQI model was tested by comparing its predictions with the numerical solution of the TDSE and the SCTS model, see Fig. 5a, b. It is seen that the SCTSQI provides not only qualitative, but also quantitative agreement with the TDSE result. This is true for both the width of the electron momentum distributions and the positions of the interference maxima and minima. The small discrepancy in the heights of some interference peaks (see Fig. 5a) is attributed to the fact that the SCTSQI model does not account for the pre-exponential factor of the semiclassical matrix element.
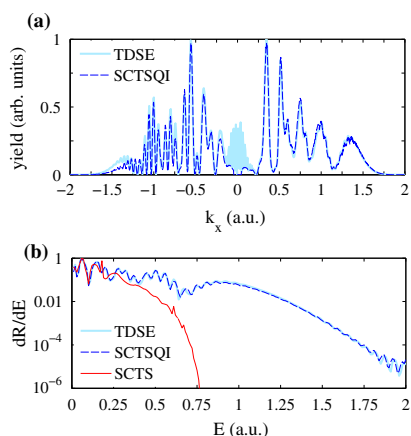
Fig. 5 a The photoelectron momentum distributions for ionization of a 1D atom by a laser pulse with a duration of $n = 4$ cycles, wavelength of 800 nm, and peak intensity of 2.0×10^{14} W/cm^2 calculated from the solution of the TDSE (thick light blue curve) and the SCTSQI model (dashed green curve). **b** Electron energy spectra obtained from the TDSE (thick light blue curve), SCTSQI (dashed blue curve), and the SCTS (red curve). The distributions and spectra are normalized to the peak values

We note that as in the 3D case (see Sect. 2.3) the 1D SCTS model shows only a qualitative agreement with the fully quantum results, see Fig. 5b. Specifically, the SCTS model underestimates the width of the momentum distributions. The electron energy spectra calculated within the SCTSQI model and from the solution of the TDSE are in almost perfect agreement. Simultaneously, the spectrum calculated using the SCTS model falls off too rapidly with the increase of the energy. This is caused by the underestimation of the width of the electron momentum distributions in the SCTS model. It was shown that the phase of the Gabor transform is very important in the SCTSQI [95]. Without this phase the SCTSQI model does not provide even a qualitative agreement with the TDSE result. This could be expected, since the amplitude $G(t, x, p_x)$ contains all the information about the quantum dynamics of the absorbed part of the wave function before it was transformed in an ensemble of trajectories. In a way the term $I_p t_0$ in the phase (11) of the SCTS model plays the same role as the phase of $G(t, x, p_x)$ in the SCTQI approach.

As any semiclassical approach, the SCTSQI model can visualize the physical mechanism responsible for the strong-field process under study using classical trajectories (see Ref. [95] for details). Since the initial conditions in the SCTSQI model are determined from the direct solution of the TDSE, we expect that this model will be able to provide more accurate trajectory-based pictures of strong-field phenomena compared to the standard semiclassical approaches. This advantage of the

SCTSQI model should be used in studies of complicated strong-field processes. In addition to this, after some modification the SCTSQI model can be applied to studies of the rescattering-induced phenomena, especially the high-order ATI and the HHG. The ways of this modification are suggested in Ref. [95]. Finally, the extension of the SCTSQI model to the three-dimensional (3D) case is straightforward and developments in this direction are on the way. Most importantly, the model solves the non-trivial problem how to choose initial conditions for classical trajectories. In the SCTSQI model these initial conditions are determined by the exact quantum dynamics.

3.2 SCTS model with preexponential factor

An efficient modification and extension of the SCTS model was proposed recently in Ref. [94]. This study for the first time investigates systematically the influence of the preexponential factor of the semiclassical matrix element (8c) (see Refs. [106,107]) that was not explicitly considered in all other versions of the SCTS. This preexponential factor for strong-field processes was calculated in Appendix B of Ref. [108]. The modulus of this prefactor that corresponds to the mapping from initial conditions to the final momentum components influences the weights of the classical trajectories. Its phase known as the Maslov phase can be identified as a case of Gouy's phase anomaly and modifies the interference structures [94]. In addition, the authors propose a novel way of solving the so-called inverse problem based on a clustering algorithm.

Since the SCTS implementation of Ref. [94] employs the SFA and the saddle-point approximation to calculate the ionization weight of the classical trajectories and their initial positions, the ionization time t_0 for each initial electron momentum $\mathbf{k}'$ is determined by the real part of the corresponding saddle-point time $t_s = t_0 + i t_1$. The saddle point t_s satisfies the equation:

$$\frac{1}{2}\left[\mathbf{k}' + \mathbf{A}(t_s)\right]^2 + I_p = 0. \tag{41}$$

The ionization probability is calculated as:

$$
R(\mathbf{k}) = \left| \sum \frac{D C_{\text{Coul}}}{\sqrt{|J(t \to \infty)|}} \exp\left[i\left(S_\downarrow^0 + S_\to - \frac{\nu \pi}{2}\right)\right] \right|^2. \tag{42}
$$

Here, the summation is over all the initial momenta $\mathbf{k}'$ leading to the final momentum $\mathbf{k}$. D is the matrix element emerging when the saddle-point method is applied to calculate the SFA ionization amplitude and C_{Coul} is the Coulomb correction of the ionization rate [64]. The phase associated with every trajectory is decomposed in Eq. (42) as $S_\downarrow^0 + S_\to$, where

$$S_{\downarrow}^{0} = I_p t_s - \frac{1}{2} \int_{t_s}^{t_0} dt \left[\mathbf{k}' + \mathbf{A}\left(t\right)\right]^2 \qquad (43)$$

corresponds to the ionization step (motion under the potential barrier), and

$$S_{\rightarrow} = \\ -\int_{t_0}^{\infty} dt \left\{ \frac{p^2(t)}{2} + V[\mathbf{r}(t)] - \mathbf{r}(t) \cdot \boldsymbol{\nabla} V[\mathbf{r}(t)] \right\} \\ \qquad (44)$$

accounts for the electron motion in the continuum. We note that the phase $S_{\rightarrow}$ coincides with the third term of the SCTS phase [see Eq. (12)]. The Jacobian J is calculated as

$$J\left(t\right) = \det\left(\frac{\partial \mathbf{k}\left(t\right)}{\partial \mathbf{k}'}\right). \qquad (45)$$

The Maslov index ν changes at focal points, i.e, at times T when the Jacobian is zero $J\left(T\right) = 0$. The change (jump) of the Maslov index when the trajectory passes through a focal point is calculated as:

$$\Delta\nu\left(T\right) = m - 1 + \text{sgn}\det\left(g\right), \qquad (46)$$

where the $m \times m$ matrix g is given by

$$g_{i,j} = \delta\mathbf{r}^{(i)} \cdot \text{Hesse}_{\mathbf{r},\mathbf{r}}\left(H\right)\delta\mathbf{r}^{(j)} \qquad (47)$$

Here, in turn, m is the number of linearly independent directions $\mathbf{d}^{(i)}$ $(i = 1, ..., m)$, which can be found at the focal points, such that infinitesimal changes of the initial momenta in these directions $\mathbf{k}' \rightarrow \mathbf{k}' + \epsilon\mathbf{d}^{(i)}$ do not affect $\mathbf{k}\left(T\right)$ in the first order of ϵ. These changes of the initial momenta correspond to the changes of the position

$$\delta\mathbf{r}^{(i)} = \epsilon \sum_j \frac{\partial \mathbf{r}\left(T\right)}{\partial k_j'} d_j^{(i)}, \qquad (48)$$

see Eq. (47). The Hessian $\text{Hesse}_{r,r}\left(H\right)$ of the Hamiltonian function

$$H = \frac{1}{2}\left[\mathbf{k} + \mathbf{A}\left(t\right)\right]^2 + V\left(\mathbf{r}\right) \qquad (49)$$

is calculated with respect to the position vector $\mathbf{r}$.

The inverse problem is solved in Ref. [94] by using clustering algorithms. More specifically, density-based spatial clustering of applications with noise algorithms was applied. The solution of inverse problem with clustering shows an example of the application of machine learning (see Ref. [109] for a text-book treatment) to strong-field phenomena. Other recent applications of the machine learning in strong-field physics are discussed in, e.g., Refs. [110,111].

The fact that the Jacobian is explicitly taken into account in Eq. (42) along with the solution of the inverse problem ensures the correct preexponential weight of every trajectory, namely, $1/\sqrt{|J|}$. It should be emphasized that this weight cannot be reproduced in "shooting method", since the distribution of the trajectories over the cells in accord with their final momenta automatically creates a factor of $1/|J|$ instead of the $1/\sqrt{|J|}$. This problem was ignored in the implementation of the SCTS [55], since the implementation of Ref. [55] accounts only for the exponential factors in the trajectories weights.

The simple relation between the Jacobian in the 3D case and the corresponding Jacobian for two spatial dimensions was derived in [94] for systems (ionic potential and the laser field) with cylindrical symmetry:

$$|J_{3D}| = \frac{k_\perp}{k_\perp'}|J_{2D}|, \qquad (50)$$

where $k_\perp = \sqrt{k_x^2 + k_y^2}$ (the field is polarized along the z-axis). This correction weight allows to obtain the results for the 3D system performing only the 2D simulations, and, by doing so, reduce the computational costs of the SCTS model significantly. We note that Eq. (50) has been already used in the SCTS simulations of Ref. [55].

The modified version of the SCTS is in excellent agreement with solution of the TDSE. This applies for both electron momentum distributions and energy spectra [94]. It is shown that the inclusion of the preexponential factors is crucial for quantitative agreement with the TDSE results. The extended version of the SCTS can be applied not only to the linearly polarized pulses, but also to non-cylindrically-symmetric laser fields, e.g., bicircular ones, see Ref. [94]. Undoubtedly the version of the SCTS developed in [94] is a valuable tool that is extremely useful in studies of strong-field ionization.

4 Semiclassical two-step model and the strong-field holography with photoelectrons

Development of the techniques capable to image the atomic positions that change in time in a chemical reaction will lead to a revolution in chemistry, biology, nanoscience, etc. At present there are many methods for time-resolved molecular imaging (see Ref. [112] for a review). These methods have been developed due to the prominent progress in laser technologies. This applies above all to the development of the technology for pulse compression and the emergence of free-electron lasers. Moreover, the availability of table-top intense femtosecond lasers, which led to the emergence of strong-field, ultrafast, and attosecond physics, gave a strong impulse to the development of new techniques for time-resolved molecular imaging. Among these techniques are: laser-induced Coulomb-explosion imaging [113–116], laser-assisted electron diffraction [117,118], high-order har-

monic orbital tomography [119,120], laser-induced electron diffraction (see, e.g., Refs. [121–123]), and strong-field photoelectron holography (SFPH) [124].

The SFPH method implements the widely-known idea of holography (1971 Nobel Prize in Physics awarded to Dennis Gabor, see Ref. [125]) in strong-field physics. It was for the first time shown in 2011 by Y. Huismans et al. [124] that a holographic pattern can be clearly recorded in experiment. This pattern in the electron momentum distributions is created by the signal (rescattered) and reference (direct) electrons. The SFPH can be implemented in a table-top experiment. It was shown that the holographic patterns encode a lot of spatio-temporal information about both the parent ion and the recolliding electron [124]. Last but not least, the electron dynamics can be imaged with sub-cycle (i.e., attosecond) time resolution. These advantages have triggered extensive studies of the SFPH, both experimental [66,126–129] and theoretical [56–60,124,126,127,130–135].

However, the first SFPH experiments [124,126–128, 130] investigated the ionization process and the dynamics of the electron wave packet rather than molecular structure or dynamics. This is because of the fact that for diatomic and small molecules the holographic structures are mostly determined by the long-range and the alignment-independent Coulomb potential. As the result, the short-range effect reflecting the molecular structure cannot be observed on the background of the more intense Coulomb contribution. This problem was elegantly solved in experiment of Ref. [129] by considering the difference between the normalized photoelectron holograms for aligned and antialigned molecules. This approach is based on the fact that for large scattering angles the differential cross section deviates from the Coulomb one and depends on the alignment of the molecule at the ionization instant. A similar method was also used in Ref. [66]. Various approaches were used for theoretical analysis of the SFPH: the three-step model [131–133,135], the SFA version that accounts for rescattering [124,130], the Coulomb-corrected strong-field approximation [124,130], the CQSFA [56,57,59, 60], etc. (see Ref. [136] for recent review).

4.1 SCTS model and experimental holographic patterns

The SCTS model was applied to the simulations of the holographic interference patterns observed in the experiment [66]. In the study [66] the electron momentum distribution produced in ionization of the NO molecule were calculated for two different cases. In the first case the electron density of the highest occupied molecular orbital (HOMO) is aligned along the polarization direction, whereas in the second case this density is orthogonal to it. These distributions, as well as their normalized difference are shown in Fig. 6. To apply the SCTS model, the distributions over the initial transverse velocities are needed for both these cases. These distributions were determined using the approach based
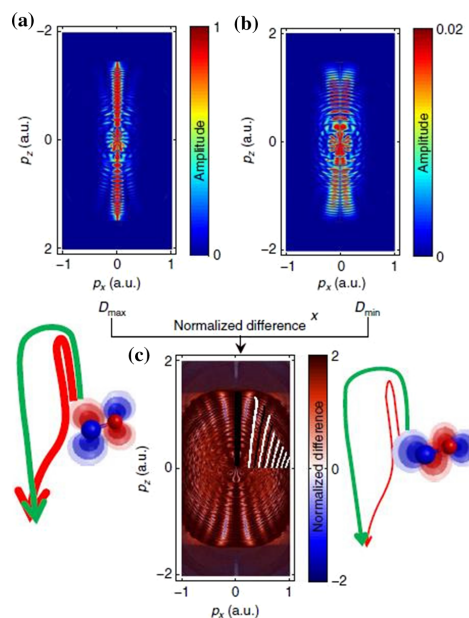

Fig. 6 Photoelectron momentum distributions for ionization of the NO molecule by a laser pulse with a duration of 35 fs, intensity of 2.3×10^{14} W/cm^2, and wavelength of 800 nm calculated using the SCTS model. The panels **a** and **b** show the distributions obtained in the cases where the electron density of the HOMO is aligned along the laser polarization direction and perpendicular to it, respectively. Panel **c** presents the normalized difference of the distributions shown in (**a**) and (**b**). The figure is reprinted from Ref. [66]

on partial Fourier transform generalized to molecules (MO-PFT) [137–139]. The MO-PFT approach works with the electron wave function in mixed (coordinate-momentum) representation and uses the Wentzel-Kramers-Brillouin (WKB) approximation. The MO-PFT requires the corresponding HOMO's that were obtained using the GAMESS package [140]. The semiclassical simulations are in a perfect agreement with the experimental results [66]. The simulations within the SCTS model reproduce all characteristic features of the holographic patterns. The regions of constructive and destructive interference predicted by the model of Ref. [131] that neglects the Coulomb potential are shown in Fig. 6 with white and black color, respectively. It is seen that the three-step model overestimates the spacing between the holographic fringes in the direction perpendicular to laser polarization. Therefore, the account of the Coulomb potential leads to the improved agreement between the experiment and the semiclassical simulations.

4.2 Effects of the Coulomb potential and the strong-field photoelectron holography

The three-step semiclassical model predicts different types of subcycle interferometric structures, see Ref. [131]. Various types of the holographic structures arise due to the fact that the reference and signal electrons can start from different quarter cycles of the laser field. In Ref. [67] the various types of the subcycle interference patterns revealed in [131] were calculated accounting for the Coulomb potential of the ion with the adapted version of the SCTS model. Here we sketch the main points of this adapted SCTS.

First, an ensemble of classical trajectories is launched only from the central period of a long (8 optical cycles) laser pulse. Second, the simple formula entirely neglecting the Coulomb potential, i.e., considering triangular potential barrier formed by the laser field and the ground state energy, is used for the tunnel exit point:

$$|z_e(t_0)| = -\frac{I_p}{F(t_0)}, \qquad (51)$$

where the sign of $z_e(t_0)$ is to be chosen to ensure the electron tunnels in the direction opposite to the instantaneous field $\mathbf{F}(t_0)$. This makes it possible to directly compare the resulting interference patterns with the patterns of the three-step model. Third, the weights (5) of classical trajectories were not taken into account, and the trajectories were distributed uniformly, which is justified by the fact that holographic patterns and not electron momentum distributions were calculated in Ref. [67]. Finally, a special approach instead of Eq. (23) has to be used in the semiclassical model to obtain the phase difference between the signal and reference electrons. Indeed, to calculate the phase difference we need to isolate only one kind of rescattered trajectories and only one kind of the direct ones. This is a complicated task if the Newton's equation of motion (1) is solved treating the laser field and the Coulomb force on equal footing. First of all, it is necessary to answer the question: How to distinguish between the direct and rescattered electron trajectories in the presence of the Coulomb field? Indeed, all the trajectories are, to some extent, affected by the Coulomb potential.

The following simple recipe is used in Ref. [67]. The reference trajectories were defined as those passing the ionic core at large distances and thus experiencing small-angle scattering only. More precisely, the reference electrons obey the condition $v_{0,\perp}k_y \geq 0$. In contrast to them, the signal trajectories come close to the parent ion and undergo large-angle scattering that changes direction of the k_y component compared to the initial one. Therefore, the signal trajectories can be defined as obeying the condition $v_{0,\perp}k_y \leq 0$. However, these conditions are not sufficient to calculate the holographic structures correctly. The fact is that in the presence of the Coulomb field the mapping from the plane of initial conditions $(t_0, v_{0,\perp})$ to the (k_x, k_y) plane is a complicated function. For example, in the domain
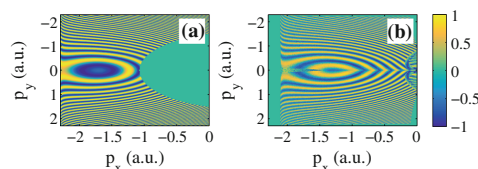

Fig. 7 Holographic patterns emerging due to interference of a direct electron with a rescattered one that has the shortest travel time (see Ref. [67]) calculated **a** using the three-step model with time-dependent exit point, and **b** accounting for the Coulomb potential of the ion. The interference patterns are calculated for ionization of the H atom at a wavelength of 800 nm and intensity of 6.0×10^{14} W/cm^2

where the condition $v_{0,\perp}k_y \leq 0$ defining the signal trajectories is fulfilled, this mapping is not one-to-one: Different sets of initial conditions lead to the same momentum $\mathbf{k}$, see Ref. [67] for details. The separation of trajectories of different kinds can be efficiently done by using the clusterization algorithms. In Ref. [67] this trajectory separation was accomplished manually by careful inspection of the mapping $(t_0, v_{0,\perp}) \rightarrow (k_x, k_y)$.

It was found that the Coulomb potential changes interference patterns significantly. Three main effects of the Coulomb field in the holographic patterns were identified in Ref. [67]. These are: shift of the interference pattern as a whole, filling of the parts of the pattern that are unfilled when the Coulomb potential is disregarded, and the characteristic kink of the interference pattern in the vicinity of $k_y = 0$ (cf. Fig. 7a, b). This kink at zero transverse momenta was attributed to the Coulomb focusing effect [141]. However, the question remains, how sensitive are the predicted Coulomb effects to focal averaging. Therefore, further studies are required to understand which of these effects can be observed in experiment.

5 Semiclassical two-step model and multielectron polarization effects

The theoretical methods used in strong-field physics usually employ the single-active electron approximation (SAE). In the SAE an atom or molecule interacting with the laser pulse is replaced by a single electron. This single electron moves in the laser field and in the field of an effective potential. Therefore, the ionization is treated as a one-electron process. The SAE is a basis for understanding of many strong-field processes, including ATI and HHG [2,83]. Nevertheless, the role of the multielectron effects (ME) in strong-field and ultrafast physics has been attracting particular attention (see, e.g., Refs. [142,143] and references therein). By now many theoretical approaches aimed at the description of the ME effects have been developed. The most well-known and widely used of them are: the time-dependent density-functional theory [144] (see

Refs. [145,146] for a text-book treatment), multiconfiguration time-dependent Hartree-Fock theory [147,148], time-dependent restricted-active-space [149] and time-dependent complete-active-space self-consistent field theory [150], time-dependent R-matrix theory [151,152] and R-matrix theory with time-dependence [153,154], time-dependent analytical R-matrix theory [155], etc. (see Ref. [156]). There are also many semiclassical approaches capable to account for the ME effects, see, e.g. Refs. [43,78,142,157–159]. The advantages of the trajectory-based models discussed in Sect. 1 are particularly valuable in studies of complex ME effects.

One of the most well-known ME effects in strong-field ionization is laser-induced polarization of the parent ion. Recently the polarization effects in the ATI have been actively studied, see, e.g., Refs. [43,78,142,157–160]. In Refs. [161,162] and [160] the effective potential for the outer electron that accounts for the external laser field, the Coulomb interaction, and the polarization effects of the ionic core, is derived in the adiabatic approximation. It was for the first time found in Ref. [157] that the time-independent Schrodinger equation with this effective potential and accounting for the Stark-shift of the ionization potential can be approximately separated in parabolic coordinates. This separation determines a certain tunneling geometry. The emerging physical picture of the flow of the electron charge associated with the tunneling electron is referred to as tunnel ionization in parabolic coordinates with induced dipole and Stark shift (TIPIS). The semiclassical model based on the TIPIS approach and disregarding the interference effect has shown a good agreement with experimental data (see Refs. [157–159]) and the TDSE results [78,157].

The electron momentum distributions generated in ionization of different atoms and molecules, including Ar, Mg, CO, naphthalene, etc., are very sensitive to the ME effects accounted by the induced dipole of the ionic core [43,78,157–159]. These studies consider ionization by circularly or elliptically polarized laser pulses. This is due to the fact that the effective potential derived in Refs. [161,162] and [160] is valid only at large and intermediate distances from the ionic core. In close to circularly polarized laser fields the rescattering-induced processes are suppressed (see Ref. [163]), and, therefore, the vast majority of the ionized electrons do not return to the parent ion. However, this is not true for linearly polarized field, and the applicability of the TIPIS approach in semiclassical simulations in the case of linear polarization raised questions. This problem is addressed in Ref. [156]. Furthermore, the study [156] combines the TIPIS approach with the SCTS model. The resulting two-step semiclassical model for strong-field ionization is capable to describe quantum interference and accounts for the Stark-shift, the Coulomb potential, and the polarization induced dipole potential.

5.1 Combination of the TIPIS model and the STCS

The ionic potential derived in Refs. [160–162] reads as:

$$V(\mathbf{r}, t) = -\frac{Z}{r} - \frac{\alpha_I \mathbf{F}(t) \cdot \mathbf{r}}{r^3}, \qquad (52)$$

where ME effect is accounted through the induced dipole potential $\left[\alpha_I \mathbf{F}(t) \cdot \mathbf{r}/r^3\right]$. For the potential of Eq. (52) the starting point of a classical trajectory can be obtained as the tunnel exit in the TIPIS model. More specifically, the tunnel exit point is given by $z_e \approx -\eta_e/2$, where η_e satisfies the equation:

$$-\frac{\beta_2(F)}{2\eta} + \frac{m^2 - 1}{8\eta^2} - \frac{F\eta}{8} + \frac{\alpha_I F}{\eta^2} = -\frac{I_p(F)}{4}, \quad (53)$$

It is seen that Eq. (53) has the additional ME term in the left-hand side compared to the equation (2). Since the ME term in the potential (52) is proportional to the laser field $\mathbf{F}(t)$, it is absent at $t > t_f$. Therefore, after the laser pulse terminates, the electron moves in the Coulomb field only. This makes it possible to use Eq. (6) for calculation of the asymptotic momentum of the electron from its position and momentum at $t = t_f$. The SCTS phase (12) with the potential $V(\mathbf{r}, t)$ defined by Eq. (52) reads as:

$$\Phi^{SCTS}(t_0, \mathbf{v}_0) = -\mathbf{v}_0 \cdot \mathbf{r}(t_0) + I_p t_0$$
$$- \int_{t_0}^{\infty} dt \left\{ \frac{p^2(t)}{2} - \frac{2Z}{r} - \frac{3\alpha_I \mathbf{F}(t) \cdot \mathbf{r}}{r^3} \right\} . \quad (54)$$

In order to implement the resulting semiclassical model, the importance sampling method was used in Ref. [156]. We note that in addition to the inapplicability of the potential (52) at small distances, there exist other conditions that restrict the range of applicability of the TIPIS model (see Refs. [78,156] for details). The study [156] focuses on the cases of Mg ($I_p = 0.28$ a.u., $\alpha_N = 71.33$ a.u., $\alpha_I = 35.00$ a.u.) and Ca ($I_p = 0.22$ a.u., $\alpha_N = 169.0$ a.u., $\alpha_I = 74.11$ a.u.) atoms, which have similar ionization potentials. But their static ionic polarizabilities are different by approximately two times.

In order to avoid the application of the potential (52) at small distances, a special cutoff radius r_C was introduced in Ref. [156], and all the trajectories entering the sphere $r < r_C$ were ignored. The remaining trajectories do not reach the vicinity of the ion. It is clear that the elimination of the whole class of the trajectories (the returning ones) depletes some parts of electron momentum distributions. However, these depleted parts usually correspond to the boundary of the direct ionization spectrum. Therefore, they do not affect the main part of the momentum distributions that provides major contribution to the ionization yield, see Ref. [156] for details.

5.2 Application of the combined semiclassical model

The 2D photoelectron momentum distributions calculated in accord with the resulting semiclassical model are shown in Fig. 8a–d. Figure 8a, c correspond to the
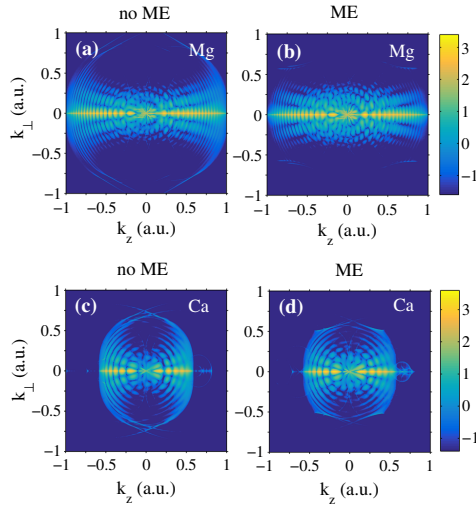
Fig. 8 Two-dimensional electron momentum distributions for the Mg [**a**, **b**] and Ca [**c**, **d**] atoms calculated by combining the TIPIS approach with the SCTS model. The wavelength is 1600 nm and the pulse duration is $n = 8$ cycles. Panels [**a**, **b**] and [**c**, **d**] show the distributions calculated at the intensities of 3.0×10^{13} W/cm^2 and 1.0×10^{13} W/cm^2, respectively. The distributions [**a**, **c**] are obtained neglecting the ME terms in Eqs. (52), (53), and (54), whereas the distributions [**b**, **d**] are calculated accounting the ME terms in all these equations. The momentum distributions are normalized to the total ionization yield. A logarithmic color scale in arbitrary units is used

Fig. 9 **a**, **c** Electron momentum distributions in the longitudinal direction, and **b**, **d** energy spectra. Panels [**a,b**] and [**c,d**] correspond to the ionization of Mg and Ca, respectively. Thick green curve and thin blue curve show the semiclassical results obtained with and without ME terms, respectively. The wavelength and duration of the pulse are as in Fig. 8. The panels [**a**, **b**] and [**c**, **d**] are calculated for the intensities of 3.0×10^{13} W/cm^2 and 1.0×10^{13} W/cm^2, respectively. The longitudinal distributions and energy spectra are normalized to the maximum value

distributions calculated accounting for the laser and Coulomb fields. Figure 8b, d display the results of the combined TIPIS + SCTS model, i.e., with the account of the ME potential. The panels (a, b) and (c, d) correspond to ionization of Mg and Ca, respectively. It is seen that the presence of the ME term in the potential of Eq. (52) results in a narrowing of the longitudinal momentum distributions and modification of the interference structures.

We first discuss the narrowing of the longitudinal distributions. This effect is further illustrated in Fig. 9a, c that show the longitudinal momentum distributions obtained with and without the ME term for Mg and Ca, respectively. Since the widths of the distributions do not change due to the interference effects, the phase is disregarded in the calculations of Fig. 9a, c. The corresponding electron energy spectra are shown in Fig. 9b, d. It is seen that the spectra calculated accounting for the ME term fall off more rapidly with increase of the energy than the ones obtained neglecting the ME effects. This is a direct consequence of the narrowing of the corresponding 2D electron momentum distributions.

The mechanism underlying the narrowing effect has a kinematic origin [156]. The analysis of classical trajec-

tories has shown that there is a certain class of trajectories strongly affected by the induced polarization of the ionic core. The trajectories of this class start closer to the parent ion that other trajectories and their initial transverse velocities are not too large (see Ref. [156] for details). Indeed, the force acting on the electron due to the ME polarization effect (the ME force) decays as $1/r^2$ with increasing r. Therefore, this force can change the electron motion only at the initial part of the trajectory adjacent to the tunnel exit. The ME force reduces both longitudinal and transverse components of the electron final momentum, and, as the result, the trajectories belonging to this class lead to the bins with smaller **k**. We note that for close to circularly polarized laser pulses the ME effects result in the rotation of the 2D electron momentum distributions towards the small axis of polarization ellipse [157].

It is seen that the presence of the ME term in the equations of motion and the phase does not dramatically change the interference patterns. The interference structure is modified only in the first and the second ATI peaks and also in the vicinity of the k_z axis. The analysis of the mechanism behind the polarization-induced interference effect showed that the changes in interference patterns are mostly caused by the ME term in the equation of motion, whereas the presence of the term $-3\alpha_I \mathbf{F} \cdot \mathbf{r}/r^3$ in the phase (54) does not play a substantial role [156].

It was found that the trajectories interfering in a given bin often have similar ME contributions to the phase
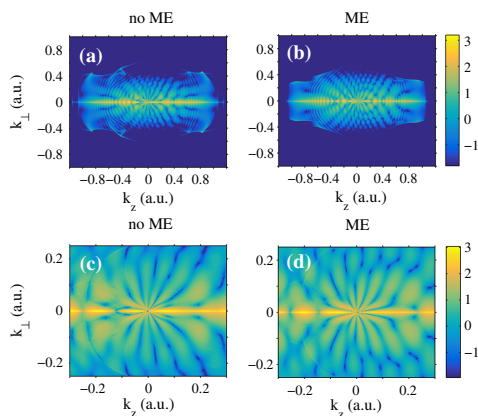
Fig. 10 Two-dimensional photoelectron momentum distributions for the Ba atom ionized by a laser pulse with a duration of $n = 4$ cycles, intensity of 3.0×10^{13} W/cm^2 and a wavelength of 1600 nm obtained by semiclassical simulations neglecting the ME term in the phase (54) [**a, c**] and including this term [**b, d**]. Panels (**c**) and (**d**) display the magnification for $|k_z| \leq 0.3$ a.u. and $|k_\perp| \leq 0.25$ a.u. of the momentum distributions shown in (**a**) and (**b**), respectively. In both cases the ME force is included in the Newton's equation of motion. The normalization to the total ionization yield is used. The color scale is logarithmic with arbitrary units

$$-\int_{t_0}^{\infty} dt \frac{3\alpha_I \mathbf{F} \cdot \mathbf{r}(t)}{r^3(t)}, \tag{55}$$

and therefore, the difference of these contributions is small. This difference is the only important quantity for the interference effect. The ME contributions to the phase are similar due to the combination of the following reasons: (i) the tunneling probability is a sharp function of the laser field $F(t_0)$ at time of ionization, (ii) the tunnel exit depends only on $F(t_0)$ and the parameters of the atom (molecule), and (iii) only the initial part of the electron trajectory is relevant in the integral (55). Nevertheless, for atoms and molecules with large values of the ionic polarizability α_I, the difference of the ME contributions to the phase is essential. As the result, the changes in the interference patters due to the ME effect can be significant. This is illustrated in Fig. 10a–d. It is seen that the number of radial nodal lines in the fanlike interference pattern at low energies is different when calculated with and without the ME term in the phase of Eq. (54). In Fig. 10c there are six nodal lines for positive $k_\perp$, while in the presence of the ME term only five such lines are visible [see Fig. 10d].

6 Semiclassical two-step model for H$_2$ molecule

To the best of our knowledge, there are only a few works that apply semiclassical models accounting for the quantum interference effect to describe strong-field ionization of molecules, see Refs. [139,164,165]. The studies [139,164] extend the QTMC model to the molecular case. The SCTS model was applied to the hydrogen molecule in Ref. [165]. Two-dimensional electron momentum distributions, energy spectra, and angular distributions were compared to the ones calculated for ionization of the atomic hydrogen. The study [165] revealed substantial differences in electron momentum distributions and energy spectra as compared to the atomic case.

6.1 SCTS model for hydrogen molecule

The ionic potential experienced by a single-active-electron in the H$_2$ molecule is given by

$$V(\mathbf{r}) = -\frac{Z_1}{|\mathbf{r} - \mathbf{R}/2|} - \frac{Z_2}{|\mathbf{r} + \mathbf{R}/2|} \tag{56}$$

Here $\mathbf{R}$ is the vector pointing from one nucleus to another. It is assumed that the origin of the coordinate system is located in the center of the molecule. The effective charges Z_1 and Z_2 are chosen to be equal to 0.5 a.u. [139,164]. It is obvious that the question how to distribute initial conditions of classical trajectories is more complicated for a molecule than for an atom. Presently there are two well-known approaches to this problem: Molecular quantum-trajectory Monte-Carlo model (MO-QTMC) [139,164] and MO-PFT [137–139]. The MO-QTMC model applies expressions of the molecular strong-field approximation (MO-SFA) [166,167]. The MO-SFA is a generalization of the SFA that was initially developed for atoms to the case of molecules. The MO-PFT model was used in Ref. [165].

The bound state orbital in the H$_2$ molecule is the bonding superposition of the two 1s atomic orbitals located at the centers of the atoms:

$$\Psi_{H_2}(\mathbf{r}) = \frac{1}{\sqrt{2(1 + S_{OI})}} [\psi_{atom1}(\mathbf{r} - \mathbf{R}/2)$$
$$+ \psi_{atom2}(\mathbf{r} + \mathbf{R}/2)]. \tag{57}$$

The corresponding partial Fourier transform is given by (see Ref. [138]):

$$
\boldsymbol{\Pi}_{H_2}(p_x, p_y, z) = \exp\left(-\frac{i}{2}R\sin\theta_m\left[p_x\cos\varphi_m\right.\right.
$$
$$
\left.\left. + p_y\sin\varphi_m\right]\right)\Pi_{atom1}\left(p_x, p_y, z - \frac{R}{2}\cos\theta_m\right)
$$
$$
+ \exp\left(\frac{i}{2}R\sin\theta_m\left[p_x\cos\varphi_m\right.\right.
$$
$$
\left.\left. + p_y\sin\varphi_m\right]\right)\boldsymbol{\Pi}_{atom2}\left(p_x, p_y, z + \frac{R}{2}\cos\theta_m\right). \quad (58)
$$

Here θ_m and φ_m are the polar and azimuthal angles of the molecular axis, respectively, and $\Pi_{atom}(p_x, p_y, z)$ is the partial Fourier transform of the $1s$ orbital. Substituting the expression for $\Pi_{atom}(p_x, p_y, z)$ (see Ref. [137]) in Eq. (58) we obtain the following formula for the mixed-representation wave function of the H_2 molecule applicable just beyond the tunnel exit:

$$
\Pi(p_x, p_y, z_e)
$$
$$
\sim \left\{\exp\left(-\frac{i}{2}R\sin\theta_m\left[p_x\cos\varphi_m + p_y\sin\varphi_m\right]\right)\right.
$$
$$
\times \exp\left(-\frac{1}{2}\kappa R\cos\theta_m\right)
$$
$$
+ \exp\left(\frac{i}{2}R\sin\theta_m\left[p_x\cos\varphi_m + p_y\sin\varphi_m\right]\right)
$$
$$
\left.\times \exp\left(-\frac{1}{2}\kappa R\cos\theta_m\right)\right\}
$$
$$
\times \exp\left[-\frac{\kappa^3}{3F} - \frac{\kappa\left(p_x^2 + p_y^2\right)}{2F}\right]. \quad (59)
$$

As in Ref. [139], this expression (without prefactor) was used in [165] as a complex amplitude describing ionization at time t_0 with initial transverse velocity $v_{0,\perp} = p_{0,\perp}$. In the simplest case analyzed in Ref. [165] the molecule is oriented along the laser polarization direction ($\theta_m = \varphi_m = 0$), and the factor in brackets in Eq. (59) is constant for a fixed internuclear distance R. This allows to use only the exponential factor of Eq. (59).

Different approaches can be used to find the tunnel exit point, i.e., the starting point of the trajectory, in the molecular case. The simplest one consists in neglecting the molecular potential, i.e., considering triangular potential barrier (51). An alternative approach, the so-called field direction model (FDM) (see Ref. [78]), accounts for the molecular potential. The potential barrier in the FDM model is formed by the molecular potential and the laser field in a 1D cut along the field direction. Therefore, the tunnel exit point in the FDM model is defined by the equation:

$$
V(\mathbf{r}) + F(t_0)z_e = -I_p. \quad (60)
$$

To finalize the generalization of the SCTS model to the case of the H_2 molecule, we need to obtain the phase, which is assigned to a classical trajectory. This phase is derived by substituting the potential (56) in Eq. (12):

$$
\Phi_{H_2}^{SCTS}(t_0, \mathbf{v}_0) = -\mathbf{v}_0 \cdot \mathbf{r}(t_0) + I_p t_0
$$
$$
- \int_{t_0}^{\infty} dt \left\{\frac{p^2(t)}{2} - \frac{Z_1(\mathbf{r} - \mathbf{R}/2)\cdot(2\mathbf{r} - \mathbf{R}/2)}{|\mathbf{r} - \mathbf{R}/2|^3}\right.
$$
$$
\left.+ \frac{Z_2(\mathbf{r} + \mathbf{R}/2)\cdot(2\mathbf{r} + \mathbf{R}/2)}{|\mathbf{r} + \mathbf{R}/2|^3}\right\}, \quad (61)
$$

see Ref. [165]. It is seen that for $r \gg R/2$ this phase corresponds to the SCTS phase for the Coulomb potential $-Z/r$ with the effective charge $Z = Z_1 + Z_2$. In contrast to this, the QTMC phase for the H_2 molecule is given by:

$$
\Phi_{H_2}^{QTMC}(t_0, \mathbf{v}_0) = -\mathbf{v}_0 \cdot \mathbf{r}(t_0) + I_p t_0
$$
$$
- \int_{t_0}^{\infty} dt \left\{\frac{p^2(t)}{2} - \frac{Z_1}{|\mathbf{r} - \mathbf{R}/2|} - \frac{Z_2}{|\mathbf{r} + \mathbf{R}/2|}\right\}. \quad (62)
$$

The expression (61) can be simplified at large distances and, as the result, the SCTS phase for the H atom is reproduced. Finally, it is assumed in Ref. [165] that at the end of the laser pulse the ionized electron is far enough from both nuclei, i.e., $r(t_f) \gg R$. If this condition is met, after the end of the pulse the electron moves in the Coulomb field with the effective charge Z. Therefore, its asymptotic momentum can be calculated from Eq. (6), and the post-pulse phase is determined by Eq. (21).

6.2 Application of the SCTS model to H_2 molecule

In Fig. 11 we compare the photoelectron momentum distributions calculated within the SCTS model for the hydrogen atom (Fig. 11a) and hydrogen molecule (Fig. 11b, c), see Ref. [165]. The starting point of the trajectory for H is calculated using the triangular potential barrier (51). The distribution of Fig. 11b for H_2 is also obtained for the exit point calculated from Eq (51). We note that the molecular potential is fully taken into account in the classical equations of motion (1) and in the phase (12) when calculating Fig. 11b. The electron momentum distribution of Fig. 11c corresponds to the tunnel exit obtained by using the FDM model. The electron momentum distributions shown in Fig. 11a, b are similar to each other. Therefore, it can be concluded that if the molecular potential is not accounted in calculating the starting point, the effects of the molecular structure are not visible in electron momentum distributions. This result can be expected bearing in mind that $r_0 = I_p/F_0 \gg R/2$ for the parameters of Fig. 11, and the distance between the ionized electron and the molecular ion increases further when the electron moves along the trajectory. As the result, the departing electron feels only the Coulomb asymptotic instead of the full molecular potential. The FDM model

predicts smaller exit points as compared to the triangular barrier formula (51), see Ref. [165]. For this reason, the effects of the molecular potential (56) are visible in Fig. 11c. First, the photoelectron momentum distribution is more extended in the polarization direction. As the result, the energy spectra for the hydrogen molecule falls off slower with the increase of energy than the ones for the H atom. Simultaneously, the angular distributions in the molecular case are more aligned along the polarization direction. Second, at the same parameters of the laser pulse the holographic interference fringes are more pronounced for H_2 than for H (see Fig. 11). The comparison of the distributions calculated using the SCTS and QTMC models for ionization of the H_2 molecule is presented in Fig. 12a–d. Two different pulse envelopes were used in Fig. 12a–d. Figure 12a, b corresponds to the sine squared pulse, whereas Figure 12c, d shows the distributions obtained for the trapezoidal pulse (see Ref. [165] for details). Figure 12a, c display the momentum distributions calculated within the QTMC model, and Fig. 12b,d show the corresponding SCTS results. For the sine squared pulse these distributions have a pronounced fan-like structure in their low-energy part. For the trapezoidal envelope the fans are substituted by the characteristic blobs (see Fig. 12c, d) lying on a circle with the radius $k = 0.30$ a.u. Similar to the atomic case, the QTMC predicts fewer nodal lines in the interference structure at low energies than the SCTS model. This fact can be again attributed to the underestimation of the Coulomb potential in the QTMC phase [165].

7 Conclusions

The semiclassical models using classical mechanics to describe the electron motion after it has been released from an atom or molecule are one of the powerful methods of strong-field, ultrafast, and attosecond physics. The standard formulation of the trajectory-based models does not allow to describe the effects of quantum interference. Nevertheless, a substantial progress in simulations of the interference effects using the semiclassical models has been achieved recently. By present several trajectory-based models capable to describe the interference effects have been developed and successfully applied to the studies of the ATI. Here we discuss one of these models, namely, the SCTS.

The SCTS model allows to reproduce interference patterns of the ATI process and accounts for the ionic potential beyond the semiclassical perturbation theory. In the SCTS the phase assigned to every classical trajectory is calculated using the semiclassical expression for the matrix element of the quantum mechanical propagator [79–81]. As the result, the SCTS model yields a good agreement with the direct numerical solution of the TDSE, better than, e.g., the QTMC model applying the first-order semiclassical perturbation theory to account for the Coulomb potential in the phase.
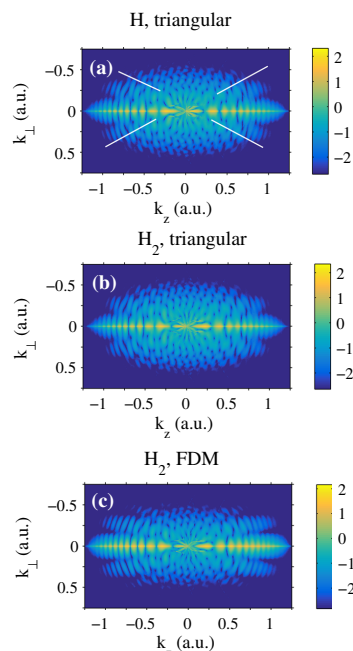
Fig. 11 Two-dimensional electron momentum distributions for ionization of **a** the H atom and **b, c** the H_2 molecule by a laser pulse with the duration of $n = 4$ cycles, intensity of 2.0×10^{14} W/cm^2, and wavelength of 800 nm. The distributions shown in panels **a** and **b** correspond to the tunnel exit point calculated from Eq. (51). The distribution of panel **c** is obtained using the FDM expression for the tunnel exit. The H_2 molecule is oriented along the polarization direction of the laser field (z-axis). The holographic fringes are shown by white lines in panel (**a**). The normalization to the total ionization yield is used. The color scale is logarithmic with arbitrary units

Here we review further developments and applications of the SCTS. At first, we review the formulation of the SCTS and its numerical implementation. The application of the model was illustrated in the case of the H atom. We next turn to the further developments of the SCTS: the SCTSQI model [95] and the SCTS model with the prefactor [94]. In the SCTSQI model the initial conditions for classical trajectories are determined from the exact quantum dynamics of the wavepacket. For ionization of the 1D atom the SCTSQI model yields not only qualitative, but also quantitative agreement with the numerical solution of the TDSE. Further work is needed to accomplish the generalization of the SCTSQI on the 3D case. The developments in this direction have already begun. The quantitative agreement with the TDSE was also achieved by the extension of the SCTS model that accounts for the pref-
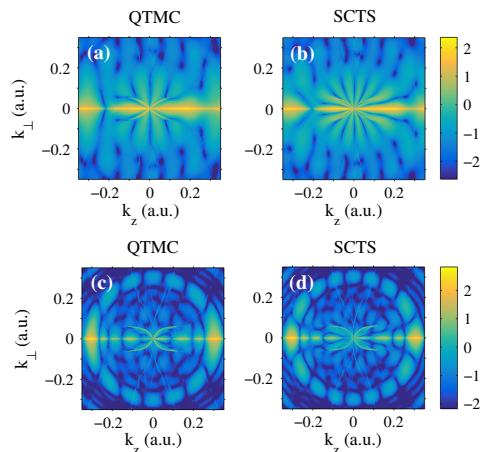
Fig. 12 The low-energy parts of the two-dimensional photoelectron momentum distributions for the H_2 molecule ionized by a laser pulse with a duration of $n = 4$ cycles, wavelength of 800 nm, and peak intensity of 1.2×10^{14} W/cm^2. The left column panels **a** and **c** show the results of the QTMC model. The right column panels **b** and **d** present the distributions calculated within the SCTS model. Panels [**a**, **b**] and [**c**, **d**] are calculated for the sine squared and trapezoidal envelopes of the laser pulse, respectively (see Ref. [165]). The molecule is oriented along the laser polarization direction (z-axis). A logarithmic color scale in arbitrary units is used

of the ionic core can also modify the interference patterns in electron momentum distributions.

Finally, we briefly reviewed the extension of the SCTS model to ionization of the hydrogen molecule. The SCTS model for the H_2 can be generalized to an arbitrary laser polarization and orientation of the molecule, as well as to heteronuclear and polyatomic molecules. We believe that these generalizations being combined with the extended versions of the SCTS will result to an emergence of powerfool tools for studies of the strong-field processes.

Data Availibility Statement This manuscript has no associated data or the data will not be deposited. [Authors' comment: All data included in this manuscript can be reproduced by performing simulations in accord with the approaches described here, or are available upon request by contacting the corresponding author.]

actor of the semiclassical matrix element. Furthermore, the 3D implementation of the SCTS [94] has a number of other important modifications.

We discuss the application of the SCTS approach to the SFPH. The semiclassical simulations within the SCTS model are in perfect agreement with the results of the recent experiment [66]. The model is able to reproduce all characteristic features of the observed holographic patterns. The SCTS model also allows to investigate the effect of the Coulomb potential on the holographic structures. Three main Coulomb effects in the interference patterns were predicted [67]. However, it should be investigated how sensitive are these Coulomb effects to focal averaging. This further work will allow to understand, which of the predicted effects can be observed.

We also present a quick review of the application of the SCTS to study of the multielectron polarization effects. We discuss the modification of the SCTS model accounting for the multielectron polarization-induced dipole potential. The semiclassical simulations predict narrowing of the electron momentum distributions along the polarization direction. This narrowing arises due to the focusing of the ionized electrons by the induced dipole potential. Furthermore, the polarization

References

1. N.B. Delone, V.P. Krainov, *Multiphoton Processes in Atoms. Chap. 9* (Springer, Berlin, 2000)
2. W. Becker, F. Grasbon, R. Kopold, D.B. Milošević, G.G. Paulus, H. Walther, Adv. At. Mol. Opt. Phys. **48**, 35 (2002)
3. D.B. Milošević, F. Ehlotzky, Adv. At. Mol. Opt. Phys. **49**, 373 (2003)
4. A. Becker, F.H.M. Faisal, J. Phys. B: At. Mol. Opt. Phys. **38**, R1 (2005)
5. C. Faria, X. Liu, J. Modern Opt. **58**, 1076 (2011)

6. L.V. Keldysh, Zh. Eksp. Teor. Fiz. **47**, (1945). [Sov. Phys. JETP **20**, 1307](1964)
7. F.H.M. Faisal, J. Phys. B.: At. Mol. Opt. Phys. **6**, L89 (1973)
8. H.R. Reiss, Phys. Rev. A **22**, 1786 (1980)
9. H.G. Muller, Laser Phys. **9**, 138 (1999)
10. D. Bauer, P. Koval, Comput. Phys. Commun. **174**, 396 (2006)
11. L.B. Madsen, L.A.A. Nikolopoulos, T.K. Kjeldsen, J. Fernández, Phys. Rev. A **76**, 063407 (2007)
12. S. Patchkovskii, H.G. Muller, Comput. Phys. Commun. **199**, 153 (2017)
13. H.B. van Linden, van den Heuvell, H.G. Muller, In Multiphoton processes, edited by S. J. Smith and P. L. Knight (Cambrige University, Cambrige, 1988)
14. T.F. Gallagher, Phys. Rev. Lett. **61**, 2304 (1988)
15. P.B. Corkum, N.H. Burnett, F. Brunel, Phys. Rev. Lett. **62**, 1259 (1989)
16. J.L. Krause, K.J. Schafer, K.C. Kulander, Phys. Rev. Lett. **68**, 3535 (1992)
17. P.B. Corkum, Phys. Rev. Lett. **71**, 1994 (1993)
18. A.M. Perelomov, V.S. Popov, M.V. Terent'ev, Zh. Eksp, Teor. Fiz. **51**, 309 (1966). [Sov. Phys. JETP **24**, 207] (1966)
19. M. Bashkansky, P.H. Bucksbaum, D.W. Schumacher, Phys. Rev. Lett. **60**, 2458 (1988)
20. S. Basile, F. Trombetta, G. Ferrante, Phys. Rev. Lett. **61**, 2435 (1988)
21. P. Lambropoulos, X. Tang, Phys. Rev. Lett. **61**, 2506 (1988)
22. H.G. Muller, G. Petite, P. Agostini, Phys. Rev. Lett. **61**, 2507 (1988)
23. P. Krstic, M.H. Mittleman, Phys. Rev. A **44**, 5938 (1991)
24. A. Jaron, J.Z. Kaminski, F. Ehlotzky, Opt. Commun. **163**, 115 (1999)
25. N.L. Manakov, M.V. Frolov, B. Borca, A.F. Starace, J. Phys. B **33**, R141 (2000)
26. A. Palacios, H. Bachau, F. Martin, Phys. Rev. Lett. **96**, 143001 (2006)
27. J. Förster, Y.V. Vanne, A. Saenz, Phys. Rev. A **90**, 053424 (2014)
28. G.G. Paulus, W. Nicklich, H. Xu, P. Lambropoulos, H. Walther, Phys. Rev. Lett. **72**, 2851 (1994)
29. M. Lewenstein, P. Balcou, M. Ivanov, A. L'Huillier, P.B. Corkum, Phys. Rev. A **49**, 2117 (1994)
30. G.G. Paulus, W. Becker, W. Nicklich, H. Walther, J. Phys. B **27**, L703 (1994)
31. C. Faria, W. Becker, Laser Phys. **13**, 1196 (2003)
32. D.B. Milošević, W. Becker, Phys. Rev. A **68**, 065401 (2003)
33. T. Brabec, M. Ivanov, P.B. Corkum, Coulomb focusing in intense field atomic processes. Phys. Rev. A **54**, R2551(R) (1996)
34. K. Dimitriou, D.G. Arbó, S. Yoshida, E. Persson, J. Burgdörfer, Phys. Rev. A **70**, 061401(R) (2004)
35. W. Quan, Z. Lin, M. Wu, H. Kang, H. Liu, X. Liu, J. Chen, J. Liu, X.T. He, S.G. Chen, H Xiong, L. Guo, H. Xu, Y. Fu, Y. Cheng, Z.Z. Xu, Phys. Rev. Lett. **103**, 093001 (2009)
36. C. Liu, K.Z. Hatsagortsyan, Phys. Rev. Lett. **105**, 113003 (2010)
37. T.-M. Yan, S.V. Popruzhenko, M.J.J. Vrakking, D. Bauer, Phys. Rev. Lett. **105**, 253002 (2010)
38. A. Kästner, U. Saalmann, J.M. Rost, Phys. Rev. Lett. **108**, 033201 (2012)
39. C. Lemell, K.I. Dimitriou, X.M. Tong, S. Nagele, D.V. Kartashov, J. Burgdörfer, S. Gräfe, Phys. Rev. A **85**, 011403(R) (2012)
40. C. Lemell, J. Burgdörfer, K.I. Dimitriou, D.G. Arbó, X.-M. Tong, Phys. Rev. A **87**, 013421 (2013)
41. B. Wolter, C. Lemell, M. Baudish, M.G. Pullen, X.-M. Tong, M. Hemmer, A. Senftleben, C.D. Schröter, J. Ullrich, R. Moshammer, J. Biegert, J. Burgdörfer, Phys. Rev. A **90**, 063424 (2014)
42. W. Becker, S.P. Goreslavski, D.B. Milošević, G.G. Paulus, J. Phys. B: At. Mol. Opt. Phys. **47**, 204022 (2014)
43. D. Dimitrovski, L.B. Madsen, Phys. Rev. A **91**, 033409 (2015)
44. C.I. Blaga, F. Catoire, P. Colosimo, G.G. Paulus, H.G. Muller, P. Agostini, L.F. DiMauro, Nat. Phys. **5**, 335 (2009)
45. R. Boge, C. Cirelli, A.S. Landsman, S. Heuser, A. Ludwig, J. Maurer, M. Weger, L. Gallmann, U. Keller, Phys. Rev. Lett. **111**, 103003 (2013)
46. C. Hofmann, A.S. Landsman, A. Zielinski, C. Cirelli, T. Zimmermann, A. Scrinzi, U. Keller, Phys. Rev. A **90**, 043406 (2014)
47. J.-W. Geng, L. Qin, M. Li, W.-H. Xiong, Y. Liu, Q. Gong, L.-Y. Peng, J. Phys. B: At. Mol. Opt. Phys **47**, 204027 (2014)
48. F. Mauger, C. Chandre, T. Uzer, Phys. Rev. Lett. **105**, 083002 (2010)
49. N.I. Shvetsov-Shilovski, S.P. Goreslavski, S.V. Popruzhenko, W. Becker, Phys. Rev. A **77**, 063405 (2008)
50. X. Wang, J.H. Eberly, Phys. Rev. Lett. **103**, 103007 (2009)
51. X.L. Hao, G.Q. Wang, X.Y. Jia, W.D. Li, J. Liu, J. Chen, Phys. Rev. A **80**, 023408 (2009)
52. A. Emmanouilidou, D.S. Tchitchekova, Phys. Rev. A **84**, 033407 (2011)
53. T.M. Yan, D. Bauer, Phys. Rev. A **86**, 053403 (2012)
54. M. Li, J.-W. Geng, H. Liu, Y. Deng, C. Wu, L.-Y. Peng, Q. Gong, Y. Liu, Phys. Rev. Lett. **112**, 113002 (2014)
55. N.I. Shvetsov-Shilovski, M. Lein, L.B. Madsen, E. Räsänen, C. Lemell, J. Burgdörfer, D.G. Arbó, K. Tőkési, Phys. Rev. A **94**, 013415 (2016)
56. X.-Y. Lai, S.-G. Yu, Yi.-Yi. Huang, L.-Q. Hua, C. Gong, W. Quan, C. Faria, X.-J. Liu, , Phys. Rev. A **96**, 013414 (2017)
57. A.S. Maxwell, A. Al-Jawahiry, T. Das, C. Faria, Phys. Rev. A **96**, 023420 (2017)
58. A.S. Maxwell, A. Al-Jawahiry, X.-Y. Lai, C. Faria, J. Phys. B: At. Mol. Opt. Phys. **51**, 044004 (2018)
59. A.S. Maxwell, S.V. Popruzhenko, C. Faria, Phys. Rev. A **98**, 063423 (2018)
60. A.S. Maxwell, C. Faria, J. Phys. B: At. Mol. Opt. Phys. **51**, 124001 (2018)
61. X.-Y. Lai, C. Poli, H. Schomerus, C. Faria, Phys. Rev. A **92**, 043407 (2015)
62. S.V. Popruzhenko, D. Bauer, J. Mod. Opt. **55**, 2573 (2008)

63. S.V. Popruzhenko, G.G. Paulus, D. Bauer, Phys. Rev. A **77**, 053409 (2008)
64. A.M. Perelomov, V.S. Popov, Sov. Phys. JETP **25**, 336 (1967)
65. H. Xie, M. Li, Y. Li, Y. Zhou, P. Lu, Opt. Express. **24**, 27726 (2016)
66. S.G. Walt, N. Ram, M. Atala, N.I. Shvestov-Shilovski, A. von Conta, D. Baykusheva, M. Lein, H.J. Wörner, Nat. Commun. **8**, 15651 (2017)
67. N.I. Shvetsov-Shilovski, M. Lein, Phys. Rev. A **97**, 013411 (2018)
68. S.D. López, D.G. Arbó, Phys. Rev. A **100**, 023419 (2019)
69. S. Eckart, M. Kunitski, I. Ivanov, M. Richter, K. Fehre, A. Hartung, J. Rist, K. Henrichs, D. Trabert, N. Schlott, L. Ph. H. Schmidt, T. Jahnke, M.S. Schöffler, A. Kheifets, R. Dörner, Phys. Rev. A **97**, 041402 (2018)
70. S. Eckart, D. Trabert, K. Fehre, A. Geyer, J. Rist, K. Lin, F. Trinter, L. Ph, H. Schmidt, M.S. Schöffler, T. Jahnke, M. Kunitski, R. Dörner, Phys. Rev. A **102**, 043115 (2020)
71. N.B. Delone, V.P. Krainov, J. Opt. Soc. Am. B **8**, 1207 (1991)
72. T. Nubbemeyer, K. Gorling, A. Saenz, U. Eichmann, W. Sandner, Phys. Rev. Lett. **101**, 233001 (2008)
73. N.I. Shvetsov-Shilovski, S.P. Goreslavski, S.V. Popruzhenko, W. Becker, Laser Phys. **19**, 1550 (2009)
74. J. McKenna, A.M. Sayler, B. Gaire, N.G. Kling, B.D. Esry, K.D. Carnes, I. Ben-Itzhak, New. J. Phys. **14**, 103029 (2012)
75. A. Emmanouilidou, C. Lazarou, A. Staudte, U. Eichmann, Phys. Rev. A **85**, 011402(R) (2012)
76. H. Price, C. Lazarou, A. Emmanouilidou, Phys. Rev. A **90**, 053419 (2014)
77. S.V. Popruzhenko, J. Phys. B: At. Mol. Opt. Phys. **51**, 014002 (2018)
78. N.I. Shvetsov-Shilovski, D. Dimitrovski, L.B. Madsen, Phys. Rev. A **85**, 023428 (2012)
79. W.H. Miller, Adv. Chem. Phys. **25**, 69 (1974)
80. M. Walser, T. Brabec, J. Phys. B **36**, 3025 (2003)
81. M. Spanner, Phys. Rev. Lett. **90**, 233005 (2003)
82. D.J. Tannor, *Introduction to Quantum Mechanics (A Time-Dependent Perspective* (University Science Books, Sausalito, 2007)
83. F. Grossmann, *Theoretical Femtosecond Physics (Atoms and Molecules in Srong Laser Fields* (Springer-Verlag, Berlin, Heidelberg, 2008)
84. X.-M. Tong, G. Wachter, S. Sato, C. Lemell, K. Yabana, J. Burgdörfer, Phys. Rev. A **92**, 043422 (2015)
85. L.D. Landau, E.M. Lifshitz, *Mechanics*, 2nd edn. (Pergamon, Oxford, 1969)
86. W.H. Press, S.A. Teukolsky, W.T. Vetterling, B.P. Flannery, *Numerical Recipes in Fortran 77: The Art of Scientific Computing*, 2nd edn. (Cambridge University Press, Cambridge, 1992)
87. D.G. Arbó, E. Persson, J. Burgdörfer, Phys. Rev. A **74**, 063407 (2006)
88. R. Gopal, K. Simeonidis, R. Moshammer, Th. Ergler, M. Dürr, M. Kurka, K.-U. Kühnel, S. Tschuch, C.-D. Schröter, D. Bauer et al., Phys. Rev. Lett. **103** 053001 (2009)
89. D.G. Arbó, S. Yoshida, E. Persson, K.I. Dimitriou, J. Burgdörfer, Phys. Rev. Lett. **96**, 143003 (2006)
90. D.G. Arbó, E. Persson, K.I. Dimitriou, J. Burgdörfer, Phys. Rev. A **78**, 013406 (2008)
91. B. Fetić, W. Becker, D.B. Milošević, Phys. Rev. A **102**, 023101 (2020)
92. G.L. Yudin, M. Ivanov, Phys. Rev. A **64**, 013409 (2001)
93. D.I. Bondar, Phys. Rev. A **78**, 015405 (2008)
94. S. Brennecke, N. Eicke, M. Lein, Phys. Rev. Lett. **124**, 153202 (2020)
95. N.I. Shvetsov-Shilovski, M. Lein, Phys. Rev. A **100**, 053411 (2019)
96. J. Javanainen, J.H. Eberly, Q. Su, Phys. Rev. A **38**, 3430 (1988)
97. M.D. Feit, J.A. Fleck, A. Steiger, J. Comput. Phys. **47**, 412 (1982)
98. X.M. Tong, K. Hino, N. Toshima, Phys. Rev. A **74**, 031405(R) (2006)
99. K. Husimi, Proc. Phys. Math. Soc. Jpn. **22**, 264 (1940)
100. L.E. Ballentine, *Quantum Mechanics* (World Scientific Publishing Co., Pte. Ltd., Singapore, A Modern Development, 1998)
101. D. Gabor, J. Inst. Electr. Eng. **93**, 429 (1946)
102. X.F. Shu, S.B. Liu, H.Y. Song, Mod. Phys. Lett. B **30**, 1650147 (2016)
103. C.C. Chirilă, I. Dreissigacker, E.V. van der Zwan, M. Lein, Phys. Rev. A **81**, 033412 (2010)
104. K.-J. Yuan, A.D. Bandrauk, J. Phys. B: At. Mol. Opt. Phys. **45**, 074001 (2012)
105. J. Wu, B.B. Augstein, C. Faria, Phys. Rev. A **88**, 023415 (2013)
106. S. Levit, U. Smilansky, Ann. Phys. (N.Y.) **108**, 165 (1977)
107. S. Levit, K. Möhring, U. Smilansky, T. Dreyfus, Ann. Phys. (N.Y.) **114**, 223 (1978)
108. D.B. Milošević, Phys. Rev. A **96**, 023413 (2017)
109. S. Raschka, *Python Machine Learning* (Packt Publishing Ltd., Birmingham, 2016)
110. X. Liu, G. Zhang, J. Li, G. Shi, M. Zhou, B. Huang, Y. Tang, X. Song, W. Yang, Phys. Rev. Lett. **124**, 113202 (2020)
111. M. Lytova, M. Spanner, I. Tamblyn. arXiv: 2012.10328 (2021)
112. J. Xu, C.I. Blaga, P. Agostini, L.F. DiMauro, J. Phys. B.: At. Mol. Opt. Phys. **49**, 112001 (2016)
113. L.J. Frasinski, K. Codling, P. Hatherly, J. Barr, I.N. Ross, W.I. Toner, Phys. Rev. Lett. **58**, 2424 (1987)
114. C. Cornaggia, J. Lavancier, D. Normand, J. Morellec, P. Agostini, J.P. Chambaret, A. Antonetti, Phys. Rev. A **44**, 4499 (1991)
115. J.H. Posthumus, L.J. Frasinski, A.J. Giles, K. Codling, J. Phys. B: At. Mol. Opt. Phys. **28**, L349 (1995)
116. C. Cornaggia, M. Schmidt, D. Normand, Phys. Rev. A **51**, 1431 (1995)
117. R. Kanya, Y. Morimoto, K. Yamanouchi, Phys. Rev. Lett. **105**, 123202 (2010)
118. Y. Morimoto, R. Kanya, K. Yamanouchi, J. Chem. Phys. **140**, 064201 (2014)
119. J. Itatani, J. Levesque, D. Zeidler, H. Niikura, H. Pépin, J.C. Kieffer, P.B. Corkum, D.M. Villeneuve, Nature **432**, 867 (2004)
120. S. Haessler, J. Caillat, W. Boutu et al., Nat. Phys. **6**, 200 (2010)
121. M. Meckel, D. Comtois, D. Zeidler et al., Science **320**, 1478 (2008)

122. C.I. Blaga, J. Xu, A.D. DiChiara, E. Sistrunk, K. Zhang, P. Agostini, T.A. Miller, L.F. DiMauro, C.D. Lin, Nature **194** (2012)

123. M.G. Pullen, B. Wolter, A.T. Le et al., Nat. Commun. **6**, 7262 (2015)

124. Y. Huismans, A. Rouzée, A. Gijsbertsen, J.H. Jungmann, A.S. Smolkowska, P.S.W.M. Logman, F. Lépine, C. Cauchy, S. Zamith, T. Marchenko et al., Science **331**, 61 (2011)

125. D. Gabor, *Nobel Lectures, Physics 1971–1980* (World Scientific, Singapore)

126. T. Marchenko, Y. Huismans, K.J. Schafer, M.J.J. Vrakking, Phys. Rev. A **84**, 053427 (2011)

127. D.D. Hickstein, P. Ranitovic, S. Witte, X.-M. Tong, Y. Huismans, P. Arpin, X. Zhou, K.E. Keister, C.W. Hogle, B. Zhang et al., Phys. Rev. Lett **109**, 073004 (2012)

128. M. Meckel, A. Staudte, S. Patchkovskii, D.M. Villeneuve, P.B. Corkum, R. Dörner, M. Spanner, Nat. Phys. **10**, 594 (2014)

129. M. Haertelt, X.-B. Bian, M. Spanner, A. Staudte, P.B. Corkum, Phys. Rev. Lett. **116**, 133001 (2016)

130. Y. Huismans, A. Gijsbertsen, A.S. Smolkowska, J.H. Jungmann, A. Rouzée, P.S.W.M. Logman, F. Lépine, C. Cauchy, S. Zamith, T. Marchenko et al., Phys. Rev. Lett. **109**, 013002 (2012)

131. X.-B. Bian, Y. Huismans, O. Smirnova, K.-J. Yuan, M.J.J. Vrakking, A.D. Bandrauk, Phys. Rev. A **84**, 043420 (2011)

132. X.-B. Bian, A.D. Bandrauk, Phys. Rev. Lett **108**, 263003 (2012)

133. X.-B. Bian, A.D. Bandrauk, Phys. Rev. A **89**, 033423 (2014)

134. M. Li, J. Yian, X. Sun, J. Yu, Q. Gong, Y. Liu, Phys. Rev. A **89**, 033425 (2014)

135. M. Li, X. Sun, X. Xie, Y. Shao, Y. Deng, C. Wu, Q. Gong, Y. Liu, Sci. Rep. **5**, 8519 (2015)

136. C. Faria, A.S. Maxwell, Rep. Prog. Phys. **83**, 034401 (2020)

137. R. Murray, W.K. Liu, M. Ivanov, Phys. Rev. A **81**, 023413 (2010)

138. M.M. Liu, Y.Q. Liu, Phys. Rev. A **93**, 043426 (2016)

139. M.-M. Liu, Y. Liu, J. Phys. B: At. Mol. Opt Phys. **50**, 105602 (2017)

140. M.S. Gordon, J.H. Jensen, S. Koseki, N. Matsunaga, K.A. Nguyen, S. Su, T.L. Windus, M. Dupuis, J.A. Montgomery, J. Comput. Chem. **14**, 1347 (1993)

141. T. Brabec, M. Ivanov, P.B. Corkum, Phys. Rev. A **54**, R2551 (1996b)

142. H.-P. Kang, S.-P. Xu, Y.-L. Wang, S.-G. Yu, X.-Y. Zhao, X.-L. Hao, X.-Y. Lai, T. Pfeifer, X.-J. Liu, J. Chen, Ya. Cheng, Z.-Z. Xu, J. Phys. B: At. Mol. Opt. Phys. **51**, 105601 (2018)

143. C.-T. Le, V.-H. Hoang, L.-P. Tran, V.-H. Le, Phys. Rev. A **97**, 043405 (2018)

144. E. Runge, E.K.U. Gross, Phys. Rev. Lett. **52**, 997 (1984)

145. C.A. Ullrich, *Time-Dependent Density-Functional Theory: Concepts and Applications* (Oxford University Press, Oxford, 2012)

146. M.A.L. Marques, N.T. Maitra, F.M.S. Nogueira, E.K.U. Gross, A. Rubio (eds.), *Fundamentals of Time-Dependent Density Functional Theory* (Springer, Berlin, 2012)

147. J. Zanghellini, M. Kitzler, T. Brabec, A. Scrinzi, J. Phys. B: At. Mol. Opt. Phys. **37**, 763 (2004)

148. J. Caillat, J. Zanghellini, M. Kitzler, O. Koch, W. Kreuzer, A. Scrinzi, Phys. Rev. A **71**, 012712 (2012)

149. H. Miyagi, L.B. Madsen, Phys. Rev. A **87**, 062511 (2013)

150. T. Sato, K.L. Ishikawa, Phys. Rev. A **88**, 023402 (2013)

151. P.G. Burke, V.M. Burke, J. Phys. B **30**, L383 (1997)

152. M.A. Lysaght, H.W. van der Hart, P.G. Burke, Phys. Rev. A **79**, 053411 (2009)

153. L.A.A. Nikolopoulos, J.S. Parker, K.T. Taylor, Phys. Rev. A **78**, 063420 (2008)

154. L.R. Moore, M.A. Lysaght, L.A.A. Nikolopoulos, J.S. Parker, H.W. van der Hart, K.T. Taylor, J. Mod. Opt. **58**, 1132 (2011)

155. L. Torlina, O. Smirnova, Phys. Rev. A **86**, 043408 (2012)

156. N.I. Shvetsov-Shilovski, M. Lein, L.B. Madsen, Phys. Rev. A **98**, 023406 (2018)

157. A.N. Pfeiffer, C. Cirelli, M. Smolarski, D. Dimitrovski, M. Abu-samha, L.B. Madsen, U. Keller, Nat. Phys. **8**, 76 (2012)

158. D. Dimitrovski, J. Maurer, H. Stapelfeldt, L.B. Madsen, Phys. Rev. Lett. **113**, 103005 (2014)

159. D. Dimitrovski, J. Maurer, H. Stapelfeldt, L.B. Madsen, J. Phys. B: At. Mol. Opt. Phys. **48**, 121001 (2015)

160. D. Dimitrovski, C.P.J. Martiny, L.B. Madsen, Phys. Rev. A **82**, 053404 (2010)

161. T. Brabec, M. Côté, P. Boulanger, L. Ramunno, Phys. Rev. Lett. **95**, 073001 (2005)

162. Z.X. Zhao, T. Brabec, J. Mod. Opt. **54**, 981 (2007)

163. P. Dietrich, N.H. Burnett, M. Ivanov, P.B. Corkum, Phys. Rev. A **50**, R3585 (1994)

164. M.-M. Liu, M. Li, C.Y. Wu, Q.H. Gong, A. Staudte, Y.Q. Liu, Phys. Rev. Lett. **116**, 163004 (2016)

165. N.I. Shvetsov-Shilovski, M. Lein, K. Tőkési, Eur. Phys. J. D **73**, 37 (2019)

166. J. Muth-Böhm, A. Becker, F.H.M. Faisal, Phys. Rev. Lett. **85**, 2280 (2000)

167. T.K. Kjeldsen, L.B. Madsen, J. Phys. B: At. Mol. Opt. Phys. **37**, 2033 (2004)

8.6   *Momentum distributions of sequential ionization*

Momentum distributions of sequential ionization generated by an intense laser pulse

N. I. Shvetsov-Shilovski,[1,2,3] A. M. Sayler,[1,2] T. Rathje,[1,2] and G. G. Paulus[1,2,4]

[1]*Institute for Optics and Quantum Electronics, Friedrich-Schiller-University, Max-Wien-Platz 1, D-07743 Jena, Germany*
[2]*Helmholtz Institut Jena, Max-Wien-Platz 1, D-07743 Jena, Germany*
[3]*National Research Nuclear University MEPI, Kashirskoe shosse 31, Moscow, Russia*
[4]*Department of Physics, Texas A&M University, College Station, Texas 77843, USA*

The relative yield and momentum distributions of all multiply charged atomic ions generated by a short (30 fs) intense (10^{14}–5×10^{18} W/cm^2) laser pulse are investigated using a Monte Carlo simulation. We predict a substantial shift in the maximum (centroid) of the ion-momentum distribution along the laser polarization as a function of the absolute phase. This effect should be experimentally detectable with currently available laser systems even for relatively long pulses, such as 25–30 fs. In addition to the numerical results, we present semianalytical scaling for the position of the maximum.

I. INTRODUCTION

The interaction of strong laser pulses with atoms and molecules results in a large number of different phenomena, among which are the formation of the high-energy plateau in the above-threshold ionization (ATI) spectrum, the generation of high harmonics of the incident field (HHG), and the excessive yield of doubly and multiply charged ions (see reviews [1–5]). The respective phenomena have been studied extensively in the last two decades, both theoretically and experimentally. These investigations were initially concerned with the total ion yield and the dependence of this yield on the intensity. Most of them dealt with double ionization and two different mechanisms underlying the production of doubly (or multiply) charged ions were revealed: nonsequential and sequential double (multiple) ionization.

The term nonsequential double (or multiple) ionization refers to the situation in which two (or more) electrons are ionized in one coherent process and the rate is not the product of single ionization rates. Hence, electron-electron correlation is a necessary condition of the nonsequential double ionization process. Nonsequential ionization is observed at relatively low laser intensities. It was first proposed in Refs. [6,7] that a nonsequential channel contributes to double ionization. The actual mechanism of this correlation was investigated and debated for many years. Finally, a consensus (i.e., that the dominating contribution to nonsequential double ionization is due to recollision [8,9]) has been achieved. The recollision process is also responsible for the ATI plateau and the HHG [9,10]. However, the details strongly depend on the atomic species (see [11] for reviews). When intensities increase such that the magnetic components of the electromagnetic field become significant, nonsequential ionization is suppressed. As a consequence, sequential ionization is predicted to dominate. This process is of considerable importance in view of the rapid increase in the intensity of currently available lasers. Another situation where sequential ionization may dominate is ionization by a circularly polarized field. For elliptical polarization, electrons have to start with nonzero initial velocity perpendicular to the main axis of the polarization ellipse in order to return to the position of the ion. However, this initial velocity decreases the tunneling rate. As a consequence,

the levels of the ATI plateau as well as the nonsequential double ionozation (NSDI) rate decrease quickly with increasing ellipticity. Thus, in the case of a circular polarization, the nonsequential channel is essentially suppressed.

Due to the capabilities of modern experiments (especially since the advent of cold-target recoil-ion-momentum spectroscopy), both the total yield and the ion-momentum distributions can be measured [12–18]. It was found that, at high laser intensities, momentum distributions of multiply charged ions along the polarization direction have a Gaussian-type shape with the maximum at zero momentum [14,15,19].

In our laboratory, an experiment aimed at investigating the ionization dynamics with ion beams of well-defined charge state is under construction. In order to establish what to expect based on the current understanding of multiple ionization at high intensities, we investigate sequential ionization theoretically. Clearly, we do not expect perfect agreement between the forthcoming experimental data and the predictions of any model based on the sequential mechanism, especially at relatively low intensities. Nevertheless, such a model will provide a necessary benchmark for the data analysis and, no doubt, will help to understand the real pathways of the multiple ionization process.

At first glance, sequential ionization may appear trivial as compared to the nonsequential process. Consequently, most studies have focused on the latter ionization mechanism and there is, in fact, a lack of theoretical studies of sequential multiple ionization. Although the sequential ion yield was calculated by many groups (see [20–27] and references therein), emphasis has been put on the derivation of empirical formulas, which can describe the well-known "knee" in the ion yield, caused by the presence of the nonsequential channel. The aforementioned lack of relevant theory becomes particularly evident in the case of momentum distributions. Momentum distribution of multiply charged ions up to $Z = 8$ produced by a strong laser pulse with duration of 200 fs and maximum intensity of 5–7 $\times 10^{15}$ W/cm^2 were recently measured and calculated in Refs. [28,29]. To the best of our knowledge, Refs. [28,29] are the only theoretical studies of the momentum distributions of the highly charged ions. Ionization dynamics was simulated using the classical trajectory Monte Carlo method including tunneling (CTMC-T method, see [30,31]). It

has been found experimentally that the width of the momentum distribution along the polarization direction is almost a linear function of the ionization potential. This linear dependence was explained on the basis of the strong-field approximation and electron kinematics in the laser field.

Nevertheless, the momentum distributions of highly charged ions have not been analyzed so far. This requires analyzing the subcycle ionization dynamics, whereas previous work has concentrated on the pulse envelope. Moreover, sequential multiple ionization by *short* laser pulses has not been investigated including the corresponding carrier-envelope phase (CEP) effects (see review [32] and references therein). In this paper, we further explore the sequential ionization in order to (i) calculate momentum distributions of ion with $Z \geqslant 8$; (ii) consider the ion production by a short laser pulse, when the CEP effects may be relevant; and (iii) find out the scaling of momentum distributions with laser-atom parameters.

II. EXPERIMENTAL SETUP

In this section, we briefly describe the experimental setup under construction in our laboratory and that we have in mind in our theoretical study. An ion beam is produced in an EBIT (electron beam ion trap) that is kept at a potential of approximately 5 kV, and which can produce xenon ions with charges ranging from Xe^{1+} to around Xe^{20+}.

Selecting the desired initial charge state with a Wienfilter (WF) [33] allows for determining the effects of the initial charge state on the subsequent laser-induced ionization. Einzel lenses (EL1, EL2), deflector plates (DF1, DF2, DF3), and adjustable pinholes (AP1, AP2) shown in Fig. 1 are used to produce a well-collimated ion beam at the laser interaction point (IA).

The focused laser beam is linearly polarized in the x direction, which is orthogonal to the ion beam propagation in the y direction, and hits the ion beam in the interaction region (IA). The momentum distribution of the ions in the y direction arises from the acceleration of the charged nuclei in the laser field.

After the laser interaction, the charge separator (CS) deflects the ions in the z directon using an electrostatic field. The nonionized portion of the ion beam is collected in a Faraday cup (FC), while the different ionization states are separated in space. The charge state and momentum distributions are then
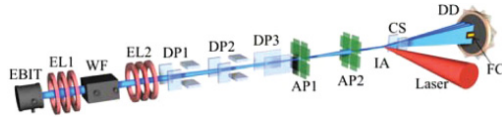
FIG. 1. (Color online) Experimental setup of the ion beam apparatus, which includes an electron beam ion trap (EBIT), two Einzel lenses (EL1, EL2), a Wienfilter (WF), three deflector plates (DF1, DF2, DF3), two adjustable pinholes (AP1, AP2), an interaction region (IA), a charge separator (CS), a Faraday cup (FC), and a delay-line detector (DD). The laser beam is focused vertically linear polarized into the ion beam.

detected using a time- and position-sensitive microchannel plate (MCP) delay-line detector (DD).

III. MODEL

In this section, we will sketch our numerical technique with special emphasis on the details that are essential for the following. Let us consider a short laser pulse with the duration $\tau_L = (2\pi/\omega)\, n_p$ and a sine-square envelope, linearly polarized along the x axis:

$$F(t) = F_0 \sin^2(\pi t/\tau_L) \cos(\omega t + \varphi), \qquad (1)$$

where n_p is the number of cycles within the pulse and ω is the carrier frequency.

In a strong field of laser radiation, an ionized electron can obtain relativistic energy in the final continuum state that is on the order of its rest energy. Taking into account that the oscillation energy of a free electron is $F^2/4\omega^2$, one can easily find that relativistic effects occur for radiation of the Ti:Sa laser at the intensity greater than 5×10^{18} W/cm^2 (see Ref. [2]). In our study, we will not consider intensities exceeding this value. More importantly, we consider the ion momentum, which will remain nonrelativistic even for much higher intensities.

A. Rate equations

Consider neutral atoms with a charge $Z = 0$ and initial momentum $\mathbf{P}_0$ exposed to a short intense laser pulse. Let N be the maximal ion charge that can be achieved for a given laser intensity and $R_Z(t)$ denote the probability for an ion to have charge Z at a given time instant t. Let $W_Z(t) \equiv W_Z(F(t), I_Z)$ be the ionization rate for an ion with the charge Z and ionization potential I_Z. Assuming that ions are created in a sequential process, we obtain the following system of rate equations:

$$\frac{dR_0}{dt} = -W_0 R_0,$$
$$\frac{dR_1}{dt} = W_0 R_0 - W_1 R_1,$$
$$\frac{dR_2}{dt} = W_1 R_{Z+1} - W_2 R_2, \qquad (2)$$
$$\cdots,$$
$$\frac{dR_N}{dt} = W_N R_{N-1}.$$

The initial conditions read as $R_0(0) = 1$ and $R_Z(0) = 0$ for $Z = 1, 2, \ldots, N$. Adding all the equations of the system (2), we get the conserved quantity

$$R_0(t) + R_1(t) + \cdots + R_N(t) = 1. \qquad (3)$$

Equation (3) is a constraint under which the system of rate equations (2) needs to be solved. A glance at the result (see Fig. 2) that will be obtained reveals that only two to three terms that sum in Eq. (3) differ from zero at any given time instant.

The system of equations (2) has already been solved by many authors (see [20–22,24–26] and references therein) for different atomic species and within a wide range of laser parameters. Particularly worth noting is the semianalytical
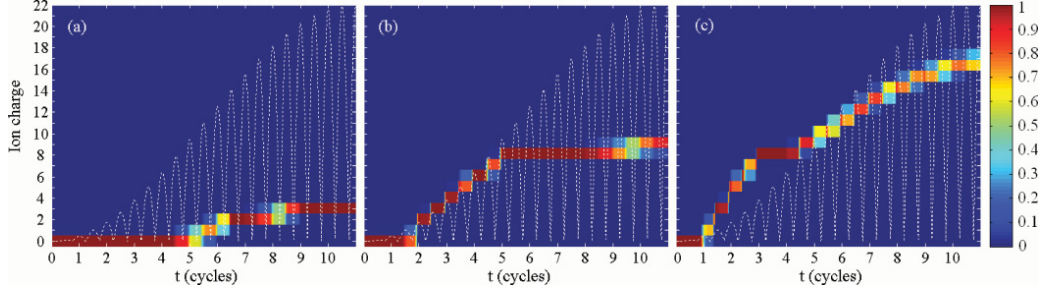
FIG. 2. (Color online) Results of the numerical solution of the rate equations (2) for Xe ions. Three panels (a), (b), and (c) correspond to peak intensities of 0.8, 60, and 500×10^{15} W/cm^2, respectively. The color scale depicts the time-dependent ionization state distribution. In all cases, the pulse duration is 30 fs at FWHM and the white line is the instantaneous intensity.

approach developed in [21], based on the following formal solution of Eqs. (2):

$$R_0(t) = \exp\left\{-\int_{-\infty}^{t} W_0(t')\,dt'\right\},$$

$$R_1(t) = \exp\left\{-\int_{-\infty}^{t} W_1(t')\,dt'\right\} \int_{-\infty}^{t} \exp\left\{\int_{-\infty}^{s} W_1(t')\,dt'\right\}$$
$$\times R_0(s)W_0(s)\,ds,$$

$$R_2(t) = \exp\left\{-\int_{-\infty}^{t} W_2(t')\,dt'\right\} \int_{-\infty}^{t} \exp\left\{\int_{-\infty}^{s} W_2(t')\,dt'\right\}$$
$$\times R_1(s)W_1(s)\,ds,$$
$$\ldots,$$

$$R_N(t) = \int_{-\infty}^{t} W_{N-1}(s)R_{N-1}(s)\,ds. \qquad (4)$$

After some approximations, this formal solution (4) can be simplified, and, by doing so, analytic estimates can be derived [21].

The aforementioned solutions of rate equations were obtained for Gaussian [22,24], Lorentzian [25,26], and hyperbolic-secant [21] pulse envelopes. To the best of our knowledge, the oscillations of the laser field have not been taken into account for solving Eqs. (2). However, knowing the cycle-resolved ionization dynamics is necessary to compute the momentum distribution of a given ion. Due to these reasons, we start our theoretical study from the solution of the rate equations (2).

B. Ionization rates

In order to solve system (2), one needs to know the ionization probabilities $W_Z(t)$. For such probabilities, we can use the ionization probability by a static field [34] or by Perelomov-Popov-Terent'ev [35] or Ammosov-Delone-Krainov (ADK) [36] formulas. Then, the tunneling rate for a level with ionization potential I_p reads as

$$W_{l,m} = (2I_p)(2l+1)\frac{(l+m)!}{2^m m!(l-m)!}C_{\kappa l}^2 2^{2n^*-m}$$
$$\times \left(\frac{F}{F_a}\right)^{m+1-2n^*} \exp\left(-\frac{2F_a}{3F}\right). \qquad (5)$$

Here $F_a = (2I_p)^{3/2}$ is the atomic feld, $n^* = Z/\sqrt{2I_p}$ is the effective quantum number, $C_{\kappa l}^2$ is the asymptotic coefficient of the atomic wave function (see [37] for details), and l and m are the angular and magnetic quantum numbers, respectively. Atomic units ($e = m = \hbar = 1$) are used throughout the paper. We omit the Keldysh parameter $\gamma = \omega\sqrt{2I_p}/F$ in the exponent of Eq. (5), and, of course, the pre-exponential factor $\sqrt{3\pi/F}$, because the latter arises from the averaging over the laser period.

Simple estimates show, however, that neutral Xe atoms, as well as Xe^{1+} and Xe^{2+} ions, are ionized in the barrier-suppression regime even at an intensity of 10^{14} W/cm^2. This means that, strictly speaking, we need to use ionization rates suitable for barrier suppression ionization in Eqs. (2).

Ionization by a field $F \geqslant F_{\mathrm{BSI}}$, where F_{BSI} is the field strength, when the perturbed energy of the initial state exceeds the maximum of an effective potential barrier was analyzed by many authors (see Refs. [38–42]). However, it is well known that, presently, no universal nonempirical formulas for the ionization probability in the barrier-suppression regime are in agreement with solutions of the time-dependent Schrödinger equation (TDSE) (see Ref. [40]).

An exception, however, is the result by V. S. Popov *et al.* [37,41] based on the investigation of the Stark effect [43–46], i.e., the probability was calculated as a width of the corresponding Stark level. However, these results are appropriate for atomic hydrogen only and their generalization to other atomic species is not obvious.

A simple empirical formula (both for the tunneling and the barrier-suppression regime) with only one free parameter has recently been proposed by X. M. Tong and C. D. Lin [42]. This parameter, however, must be computed by comparing with the TDSE solution for any given initial state.

For low-frequency laser fields, the barrier-suppression ionization rate was calculated by V. P. Krainov [38,39] on the basis of the strong-field approximation. This rate reduces to the usual ADK rate [36] in the tunneling limit when the laser field is relatively weak: $F \ll F_{\mathrm{BSI}}$. Note that the Stark shift of the initial bound state was not taken into account in the derivation of the formulas in Refs. [38,39]. As a consequence, this formula can give results only in qualitative agreement with the solution of TDSE, considerably overestimating the

ionization probability in the above barrier region [40]. In addition, the result of Refs. [38,39] is averaged over one laser cycle and valid only for s and p states (in the latter, the averaging over $m = -1,0,1$ is performed).

Let us generalize the rate [38,39] for the case of an arbitrary orbital momentum of the initial state and avoid averaging over the laser period. By doing so, we get the following expression:

$$W_{l,m} = \sqrt{\pi}(2I_p)(2l+1)\frac{(l+m)!}{2^m m!(l-m)!}C_{\kappa l}^2 2^{2n^* + \frac{14}{3} - m}$$

$$\times \left(\frac{F}{F_a}\right)^{m + \frac{1}{6} - 2n^*} \int_0^\infty \mathrm{Ai}^2(k^2 + x^2)x^2\,dx, \qquad (6)$$

where $k = 2I_p/(2F)^{2/3}$ and Ai denotes the Airy function.

In the following, we will use mainly the probability Eq. (6). However, as we will see below in Sec. IV A, there is no essential difference as to which formula [Eq. (5) or (6)] is used in the calculations. Moreover, we will consider these expressions as the ionization probabilities by a static field. In other words, for solving the rate equations, we will substitute not the envelope, as was done before in Refs. [21,25,26], but the instantaneous laser field in the formulas for $W_{l,m}$. To be more specific, we will use the modulus of Eq. (1), i.e., $F_0 \sin^2(\pi t/\tau_L)\,|\cos(\omega t + \varphi)|$, instead of F in the ionization rates [Eqs. (5) and (6)].

C. Derivation of the momentum distributions

The calculation of the ion-momentum distribution is not quite as simple as it may appear at first glance. The fact is that the depletion of the ions with the preceding charge $(Z-1)$ should be taken into account when calculating the distributions of ions with charge Z.

Our solution of the problem is based on a Monte Carlo algorithm, which has some important peculiarities that are briefly described here. The simulations are based on the calculation of the trajectory of a particle (the ion) in the laser field taking into account the possibility for this particle to be ionized by the field once, or many times, during the pulse. For the simulation, the temporal axis is discretized, i.e., subdivided into small intervals. The trajectory of the ion must be analyzed in each of the intervals. We start from the neutral atom $Z = 0$ with zero initial velocity along the laser polarization $P_x = 0$. Obviously, the laser field does not act on the neutral particle, but it will act on the particle, as soon as it is ionized.

Assume that $P_x(t_0)$ and Z are the momentum and the charge of the particle at a certain instant t_0, respectively. Let us then take a look at the interval $(t_0, t_0 + \Delta t)$. The ion momentum at the end of this interval can be calculated according to Newton's equation

$$P_x(t_0 + \Delta t) = P_x(t_0) + Z \int_{t_0}^{t_0 + \Delta t} F(t')\,dt'. \qquad (7)$$

On the other hand, the probability for an ion of charge Z to be ionized during the interval Δt_i can be calculated as $W_Z(t_i)\,\Delta t_i$ or, more exactly, as $\int_{t_0}^{t_0 + \Delta t} W_Z(t)\,dt$. This probability is evaluated and compared with a random number $0 \leqslant x \leqslant 1$. If the probability is greater than the random number, then the

next ionization occurs and the charge of Z is increased by one. This means that, for the next time interval $(t_0 + \Delta t, t_0 + 2\Delta t)$, we consider the motion of an ion with charge $(Z+1)$. In the opposite case, when the ionization probability is smaller than our random number x, the particle is not ionized during the interval $(t_0, t_0 + \Delta t)$. In both cases, the particle starts its motion on the next time interval with the momentum $P_x(t_0 + \Delta t)$ [see Eq. (7)]. Thus, at the end of the pulse, we obtain an ion of a certain charge Z_F and with a certain momentum $P_{F,x}$. By using an ensemble of such trajectories, one can get the necessary statistics to calculate momentum distributions.

IV. RESULTS AND DISCUSSION

A. Solution of the rate equations

For solving system (2), one can use the standard numerical method such as the Runge-Kutta method with adaptive step-size control (see, e.g., [47]). However, the rate equations are stiff [21] because the tunneling rates $W_{k-1}(t)$ and $W_k(t)$ entering into the rate equation for the probability $R_Z(t)$ usually differ by more than one order of magnitude. Thus, it is reasonable to use numerical methods specially adapted to the solution of stiff differential equations, e.g., the Gear method [48].

Another possible approach is based on the formal solution (4). In this case, one has to evaluate a great number of definite and improper integrals. Although the integrands are positive, they oscillate very rapidly and it is important to prevent precision loss due to truncation errors.

We used both methods in order to check the consistency. The results obtained by both alternatives are in agreement. The characteristic probability for an ion to have a specific charge as a function of time is shown in Figs. 2(a)–2(c) at three different intensities. For visual convenience, the instantaneous laser intensity is also shown on the figure. These results provide detailed information about the ionization dynamics of an ionic target. Our numerical analysis shows that barrier-suppression ionization plays a minor role in the production of highly charged ions, even for short laser pulses: Ions with $Z > 2$ are ionized before the intensity reaches the corresponding barrier-suppression value. This result is in agreement with the conclusion of Ref. [28] for long pulses.

In addition to, and aside from, other aspects, our calculations deliver the time intervals when different highly charged ions exist within the pulse (see Fig. 2). These intervals can easily be transformed into respective intensity regions. It should be mentioned that the boundaries of these intensity regions, i.e., threshold and saturation intensities, are in good quantitative agreement with the results of [21].

Another interesting question is which ion would dominate at the given intensity after the end of the laser pulse or, vice versa, which intensity is necessary to maximize the yield of a given ion. The latter dependence has been calculated and is shown in Fig. 3. The entire dependence can be fitted by a quadratic function. The two big groups of points on this
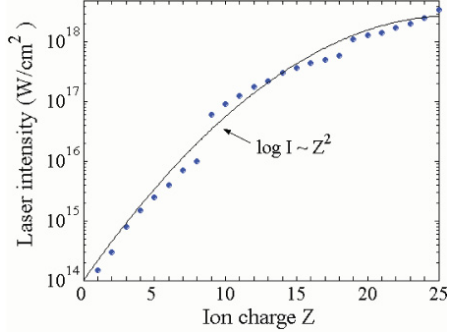
FIG. 3. (Color online) The laser intensity, which maximizes the ion yield of a specific charge state, is shown as a function of the ion charge. The thin black line corresponds to the quadratic fitting: $\log_{10} I \propto Z^2$.

figure correspond to the atomic shells $5p^6 5s^2$ and $4d^{10} 4p^6 4s^2$, subsequently ionized in our calculations.

B. Momentum distributions

The results of our simulation for the ion-momentum distributions are presented on Figs. 4, 5, and 6. It is seen from these figures that the ion-momentum distribution has a Gaussian shape. Any Gaussian-type curve can be characterized by two parameters: its width and the position of the maximum.

The dependence of the width of the ion-momentum distribution on the ionization potential I_p shown in Fig. 4 can easily be obtained as follows: For any given ion, there is an intensity that maximizes the yield of this ion (see Fig. 3). Thus, by performing the Monte Carlo simulations at this intensity, one can calculate the corresponding momentum distribution and obtain its width. It is reasonable that the width of the ion-momentum distribution increases with increasing laser intensity. At intensities of 5–7×10^{16} W/cm^2, the widths of the momentum distribution of the product ions exhibit a linear
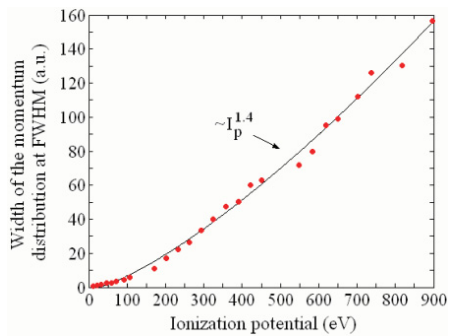
FIG. 4. (Color online) Width (FWHM) of the ion-momentum distribution as a function of ionization potential I_p. Numerical results are fitted to a power law $\propto I_p^{1.4}$ depicted by the thin black line.
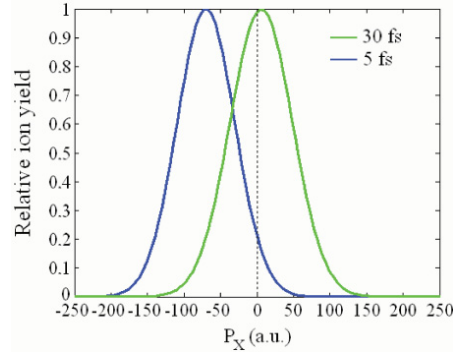
FIG. 5. (Color online) Ion-momentum distribution of Xe^{21+} at the intensity of 1.5×10^{18} W/cm^2 for two different pulse durations at FWHM. The shift of the maximum is clearly seen from the figure.

dependence on the ionization potential of the respective ions [28,29]. Such a linear dependence was analyzed theoretically using the strong-field approximation and a reasonable scaling was proposed [29]. However, our calculations show that, within a wider range of intensities (10^{14}–10^{18} W/cm^2), the width of ionic momentum distribution is proportional to $I_p^{1.4}$ (see Fig. 4).

Apart from the investigation of the widths, we predict a new effect: the shift of the maxima from zero momentum (see Fig. 5). This effect originates from the finite pulse duration and vanishes for a monochromatic field. It also vanishes when averaging over the carrier-envelope phase φ. Hence, this shift must be considered as a carrier-envelope phase effect. It would be very desirable to have a scaling for the shift. However, such a scaling is quite an intricate problem.

It is evident that ionization happens near field maxima, i.e., near minima of the vector potential. It would also appear reasonable that each ionization act occurs near its own maxima of the laser field. However, such a seemingly natural assumption is not true [see Fig. 2(c)]. For example, at the parameters of Fig. 2(c), we have one ionization event during the first half of the laser period, two events during the second half of period, etc. Thus, in order to estimate the position of the maxima at given laser-atom parameters, one has to solve the rate equations (2) first, i.e., one has to determine the subcycle ionization dynamics.

Once the ionization dynamics is known, one can easily derive the scaling of the shift of maximum. Indeed, according to momentum conservation

$$\mathbf{P} = -\sum_i \mathbf{p}_{e_i}, \qquad (8)$$

where $\mathbf{p}_e$ are the momenta of all ionized electrons after the end of the laser pulse.

Consider an electron ionized at instant of time t_0. Then, the asymptotic momentum of the electron at $t \to \infty$ reads as

$$p_{e,x} = -\int_{t_0}^{\tau_L} F(t)\, dt. \qquad (9)$$

Assuming that ionization happens exactly at field maxima $\omega t = \pi k$, one has, from Eq. (1),

$$p_{e,x} = \frac{F_0}{2\omega n_p}(-1)^{(k+1)} \sin\left(\frac{\pi k}{n_p}\right)\left(1 + \frac{1}{n_p^2}\right). \qquad (10)$$

For simplicity, we assume that $\varphi = 0$ when calculating the last equation. In order to estimate the position of the maximum, one has to sum Eq. (10) over all the relevant values of k, which should be extracted from the solution of Eqs. (2). Note that the same value of k may appear in the sum of Eq. (10) several times if there are several ionization events on the corresponding half-cycle. For example, at the intensity of 5.0×10^{17} W/cm² and for pulse duration of 30 fs (FWHM), the index k runs over the values $(2,3,3,4,4,5,6,6,9,11,12,13,14,15,17,19)$ [see Fig. 2(c)]. In this case, we have, from Eqs. (8) and (10), $P_x \approx 2.3$ a.u., whereas the calculated momentum distribution of Xe^{16+} has its maximum at $P_x \approx 5.0$ a.u. It should be noted, however, that the estimate Eq. (10) is appropriate only if each ionization act can be assigned to a certain half-cycle. If this is not the case, i.e., the new charge state appears during several half of periods, this scaling gives wrong results.

The intensity and phase dependence of the centroid is shown in Fig. 6 for short and relatively long laser pulses. Here
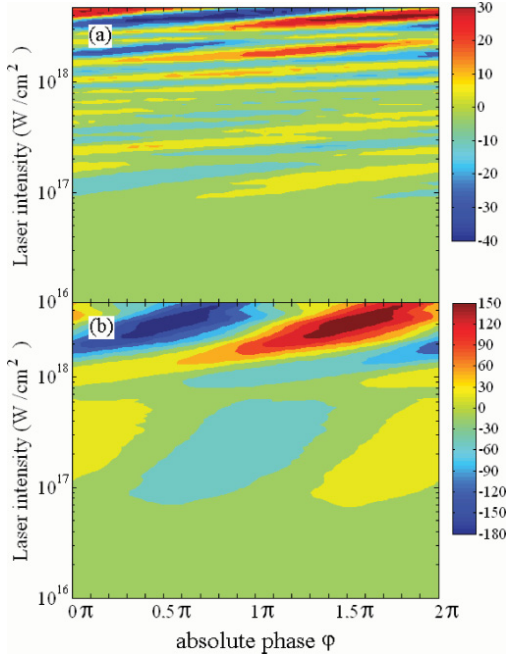

FIG. 6. (Color online) The shift of the centroid in atomic units as a function of the phase φ and intensity. At any given intensity only the distribution of the ion with the highest yield is considered. The two panels (a) and (b) correspond to the pulse duration of 30 and 6.7 fs at FWHM, respectively.

we briefly discuss both the intensity and phase dependence. It is evident from Eq. (10) that the shift of the maxima is proportional to the field strength and inversely proportional to the duration of the pulse. Because of this, the displacement of the maxima from $P_x = 0$ can be observed in long pulses [up to 30 fs at FWHM; see Fig. 6(a)] provided the intensity is high enough.

It should be mentioned that we were only discussing the momentum distribution of the charge state, which has the highest yield at the given peak intensity. The momentum distribution of other charge states, which arises after the end of the laser pulse, is also shifted. In principle, one can calculate the corresponding shifts as well. However, this calculation does not provide any additional information about the effect under consideration: As one would expect, the distributions of the lower charge states are less shifted than the distributions of the higher ones.

The strong dependence on the CEP originates from the different ionization pathways [different sets of k in Eq. (10)], which are realized at different values of the phase due to the different temporal evolution of the field. The phase dependence of the shift survives even for relatively long pulses [see Fig. 6(a)]. This may appear surprising. In fact, phase effects with respectively long pulses have been observed before in HHG under situations where contributions of different recolliding electron trajectories interfered [49]. Here the situation is completely different: The asymmetry is dominated by the ionization event occurring in the optical cycle next to the pulse maximum. Evidently, the phase effects for long pulses are hard to observe if focal averaging plays a significant role. Ion beam experiments have a distinct advantage in this respect.

V. CONCLUSIONS

In conclusion, we have investigated the total yields and the momentum distributions of highly charged ions produced by strong laser pulses at different intensities and pulse durations. We present numerical results as well as semianalytic estimates and scaling relations. A surprising result of our study is that the maximum of the longitudinal ion-momentum distribution shifts from zero momentum, even for pulses much longer than a few cycles provided the laser intensity is high enough. The magnitude of this shift is proportional to the field and inversely proportional to the pulse duration. This effect should be experimentally detectable for pulses of 25–30 fs duration at FWHM. In addition, we have demonstrated that, even for short pulses, barrier-suppression ionization plays a minor role in the production of multiply charged ions due to the temporal variation of the laser field. Consequently, tunneling is the most important mechanism of the multiple ionization.

[1] M. V. Fedorov, *Atomic and Free Electrons in a Strong Laser Field* (World Scientific, Singapore, 1997).

[2] N. B. Delone and V. P. Krainov, *Multiphoton Processes in Atoms* (Springer, Berlin, 2000), Chap. 9.

[3] W. Becker *et al.*, Adv. At. Mol. Opt. Phys. **48**, 35 (2002).

[4] D. B. Milošević and F. Ehlotzky, Adv. At. Mol. Opt. Phys. **49**, 373 (2003).

[5] A. Becker and F. H. M. Faisal, J. Phys. B: At. Mol. Opt. Phys. **38**, R1 (2005).

[6] V. V. Suran and I. P. Zapesochny, Pis'ma Zh. Tech. Fiz. **1**, 420 (1975) [Sov. Tech. Phys. Lett. **1**, 420 (1975)].

[7] A. l'Huillier, L. A. Lompré, G. Mainfray, and C. Manus, Phys. Rev. A **27**, 2503 (1983).

[8] M. Yu. Kuchiev, Pis'ma Zh. Eksp. Teor. Fiz. **45**, 319 (1987) [Sov. Phys. JETP Lett. **45**, 404 (1987)].

[9] P. B. Corkum, Phys. Rev. Lett. **71**, 1994 (1993).

[10] J. L. Krause, K. J. Schafer, and K. C. Kulander, Phys. Rev. Lett **68**, 3535 (1992).

[11] R. Dörner *et al.*, Adv. At. Mol. Opt. Phys. **48**, 1 (2002); A. Becker, R. Dörner, and R. Moshammer, J. Phys. B: At. Mol. Opt. Phys. **38**, S753 (2005).

[12] T. Weber *et al.*, Phys. Rev. Lett. **84**, 443 (2000).

[13] R. Moshammer *et al.*, Phys. Rev. Lett. **84**, 447 (2000).

[14] T. Weber *et al.*, Nature (London) **405**, 658 (2000).

[15] T. Weber *et al.*, J. Phys. B: At. Mol. Opt. Phys. **33**, L127 (2000).

[16] B. Feuerstein, R. Moshammer, and J. Ullrich, J. Phys. B: At. Mol. Opt. Phys. **33**, L823 (2000).

[17] R. Moshammer *et al.*, Phys. Rev. Lett. **91**, 113002 (2003).

[18] A. Rudenko *et al.*, J. Phys. B: At. Mol. Opt. Phys. **37**, L407 (2004).

[19] A. Rudenko, K. Zrost, B. Feuerstein, V. L. B. de Jesus, C. D. Schröter, R. Moshammer, and J. Ullrich, Phys. Rev. Lett. **93**, 253001 (2004).

[20] P. Lambropoulos and X. Tang, J. Opt. Soc. Am. **4**, 821 (1987).

[21] Briton Chang, Paul R. Bolton, and David N. Fittinghoff, Phys. Rev. A **47**, 4193 (1993).

[22] S. Augst, A. Talebpour, S. L. Chin, Y. Beaudoin, and M. Chaker, Phys. Rev. A **52**, R917 (1995).

[23] S. Larochelle, A. Talebpour, and S. L. Chin, J. Phys. B: At. Mol. Opt. Phys. **31**, 1201 (1998).

[24] A. Becker and F. H. M. Faisal, Phys. Rev. A **59**, R3182 (1999); J. Phys. B: At. Mol. Opt. Phys. **32**, L335 (1999).

[25] H. Maeda, M. Dammasch, U. Eichmann, W. Sandner, A. Becker, and F. H. M. Faisal, Phys. Rev. A **62**, 035402 (2000).

[26] H. Maeda, M. Dammasch, U. Eichmann, and W. Sandner, Phys. Rev. A **63**, 025401 (2001).

[27] S. Palaniyappan *et al.*, J. Phys. B: At. Mol. Opt. Phys. **39**, S357 (2006).

[28] K. I. Dimitriou, S. Yoshida, J. Burgdörfer, H. Shimada, H. Oyama, and Y. Yamazaki, Phys. Rev A **75**, 013418 (2007).

[29] S. Yoshida, K. I. Dimitriou, J. Burgdörfer, H. Shimada, H. Oyama, and Y. Yamazaki, J. Phys.: Conf. Ser. **163**, 012009 (2009).

[30] J. S. Cohen, Phys. Rev. A **64**, 043412 (2001).

[31] K. I. Dimitriou, D. G. Arbo, S. Yoshida, E. Persson, and J. Burgdörfer, Phys. Rev. A **70**, 061401(R) (2004).

[32] D. B. Milošević, G. G. Paulus, D. Bauer, and W. Becker, J. Phys. B: At. Mol. Opt. Phys. **39**, R203 (2006).

[33] N. Hazewindus and J. M. Van Nieuwland, United States Patent 4019989 (1977).

[34] L. D. Landau and E. M. Lifshitz, *Quantum Mechanics Non-Relativistic Theory*, 2nd ed. (Pergamon, Oxford, 1965), Sec. 77.

[35] A. M. Perelomov, V. S. Popov, and M. V. Terent'ev, Zh. Eksp. Teor. Fiz. **51**, 309 (1966) [Sov. Phys. JETP **24**, 207 (1966)].

[36] M. V. Ammosov, N. B. Delone, and V. P. Krainov, Zh. Eksp. Teor. Fiz. **91**, 2008 (1986) [Sov. Phys. JETP **64**, 1191 (1987)].

[37] V. S. Popov, Usp. Fiz. Nauk **174**, 921 (2004) [Phys. Usp. **47**, 855 (2004)].

[38] V. P. Krainov and B. Shokri, Zh. Eksp. Teor. Fiz. **107**, 1180 (1995) [JETP **80**, 657 (1995)].

[39] V. P. Krainov, J. Opt. Soc. Am. B **14**, 425 (1997).

[40] D. Bauer and P. Mulser, Phys. Rev. A **59**, 569 (1999).

[41] V. S. Popov, Zh. Eksp. Teor. Fiz. **118**, 56 (2000) [Sov. Phys. JETP **91**, 48 (2000)].

[42] X. M. Tong and C. D. Lin, J. Phys. B: At. Mol. Opt. Phys. **38**, 2593 (2005).

[43] R. J. Damburg and V. V. Kolosov, J. Phys. B: At. Mol. Opt. Phys. **9**, 3149 (1976); **11**, 1921 (1978).

[44] V. Franceschini, V. Grecchi, and H. J. Silverstone, Phys. Rev. A **32**, 1338 (1985).

[45] V. M. Vainberg, V. D. Mur, V. S. Popov, and A. V. Sergeev, Pis'ma Zh. Eksp. Teor. Fiz. **44**, 9 (1986) [Sov. Phys. JETP Lett. **44**, 9 (1986)]; Zh. Eksp. Teor. Fiz. **93**, 450 (1987) [Sov. Phys. JETP **66**, 258 (1987)].

[46] V. S. Popov *et al.*, Phys. Lett. A **124**, 77 (1987); *ibid*. **149**, 418 (1990); V. D. Mur and V. S. Popov, Laser Phys. **3**, 462 (1993).

[47] W. H. Press, S. A. Teukolsky, W. T. Vetterling, and B. P. Flannery, *Numerical Recipes in Fortran 77: The Art of Scientific Computing*, 2nd ed. (Cambridge University, Cambridge, 1992).

[48] C. W. Gear, *Numerical Initial Value Problems in Ordinary Differential Equations* (Prentice-Hall, Englewood Cliffs, NJ, 1971).

[49] G. Sansone, C. Vozzi, S. Stagira, M. Pascolini, L. Poletto, P. Villoresi, G. Tondello, S. De Silvestri, and M. Nisoli, Phys. Rev. Lett. **92**, 113904 (2004).

8.7 CEP effect in the yield of sequential ionization

Carrier–envelope phase effect in the yield of sequential ionization by an intense few-cycle laser pulse

N I Shvetsov-Shilovski[1,2,3,5], **A M Sayler**[1,2], **T Rathje**[1,2] **and G G Paulus**[1,2,4]

[1] Institute for Optics and Quantum Electronics, Friedrich-Schiller-University, Max-Wien-Platz 1, D-07743 Jena, Germany
[2] Helmholtz Institut Jena, Max-Wien-Platz 1, D-07743 Jena, Germany
[3] National Research Nuclear University MEPI, Kashirskoe shosse 31, Moscow, Russia
[4] Department of Physics, Texas A&M University, College Station, TX 77843, USA
E-mail: n79@narod.ru

Abstract. The relative yield of highly charged atomic ions produced by a short (4–6 fs at FWHM) intense (10^{14}–5×10^{18} W cm^{-2}) laser pulse was investigated by numerical solution of the rate equations. We predict oscillations of the ion yield as a function of the absolute phase. A distinctive property of this phase dependence is that it can only be observed when at least two ions have comparable yields. It is shown that with currently available laser systems the effect should be experimentally detectable for various rare gas atoms: Xe, Kr, Ar and Ne.

[5] Author to whom any correspondence should be addressed.

2 **IOP** Institute of Physics **Φ** DEUTSCHE PHYSIKALISCHE GESELLSCHAFT

Contents

1. Introduction

Double and multiple ionization of atoms and molecules is one of the most theoretically challenging strong-field phenomena. This process has been intensively investigated over the last two decades, both experimentally and theoretically. As a result of these investigations it has been found that two different physical scenarios underlie this phenomenon: sequential and nonsequential double (multiple) ionization (for reviews see [1–4]). In the process of sequential ionization, electrons are ionized sequentially and independently of one another.

In contrast to this process, electron–electron correlation is a necessary condition for nonsequential double (or multiple) ionization. The actual mechanism underlying this correlation has been the subject of extensive investigation and debate for several years. At this point it has been established that nonsequential double ionization occurs due to inelastic recollision of the ionized electron with the parent ion [5, 6]. This mechanism can be visualized by the well-known three-step model. According to this model, (i) one electron tunnels out of the atomic potential and is driven by the laser field away from the residual atom. When the field changes its direction, (ii) the electron is driven back, and on recollision with the ion core, (iii) it gives part of its kinetic energy to a second bound electron, which is then freed. Finally, both are driven by the laser field. Note that the details of this picture significantly depend on the specific atom (see, e.g., [1, 2]). Obviously, the rate of the nonsequential process is not the product of single ionization rates. It was first proposed in [7, 8] that the nonsequential mechanism contributes to double ionization.

In contrast to nonsequential ionization, which can be observed at relatively low laser intensities, sequential ionization dominates at high intensities. Sequential processes also dominate in the case of ionization by a circularly polarized laser field. For elliptical polarization the electron must depart with nonzero initial velocity perpendicular to the main axis of the polarization ellipse in order to return to its parent ion. However, this initial velocity decreases the tunneling rate. As a result, the probability of the nonsequential double ionization decreases quickly with increasing ellipticity and for a circularly polarized field, the nonsequential mechanism is essentially eliminated. At present, sequential ionization is attracting particular interest due to the constant increase in the intensity of modern lasers. Moreover, the rapid progress of the experimental technique (particularly, the advent of the cold-target recoil-ion-momentum spectroscopy COLTRIMS or REMI) has not only allowed for measurements of the total ion yield, but also the momentum distributions of the product ions [9–15].

Strange as it may seem, at present, there is a lack of theoretical studies of sequential double and multiple ionization. This particularly holds for the ion momentum distributions and for ionization by short laser pulses. At first glance, there is a considerable body of work on sequential processes, such as [16–26]. However, the vast majority is concerned with only the total ion yield. Moreover, emphasis has been put on the description of the well-known 'knee' in the yield, which appears due to the nonsequential channel. Momentum distributions of multiply charged ions generated by sequential ionization of atoms were studied in the works [24–26], two of which were experimental and theoretical investigations [24, 25] of the momentum distributions of multiply charged He, Ne and Ar ions up to the charge of $Z = 8$ generated by a long (200 fs at full-width at half-maximum (FWHM)) laser pulse with the maximum intensity of 5–7×10^{15} W cm^{-2}. In the third work [26], the momentum distributions of Xe ions up to Xe^{24+} were calculated for both relatively long and short laser pulses.

To the best of our knowledge, our previous work [26] is the only theoretical study of sequential multiple ionization by a short laser pulse, when the carrier–envelope phase (CEP) effects may be essential (for a review of these effects, see [27] and references therein). In [26], we predicted a substantial shift in the maximum (centroid) of the ion-momentum distribution along the laser polarization as a function of the CEP. This effect should be experimentally detectable with currently available laser systems even for relatively long pulses, i.e. 25–30 fs.

At first glance, it is much easier to measure the variation of ion yield with the absolute phase than to measure the phase-dependent shift of the momentum distributions. However, CEP effects are often not apparent in measurements of the total yields, because they can be washed out by the integration over momentum. Nevertheless, the effect of the absolute phase on the total yield of highly charged ions has not been studied so far. In this paper, we investigate the CEP dependence of the ion yield by solving the system of rate equations for different charge states. We perform a comprehensive analysis of the absolute phase effect for various atomic targets (Ne, Ar, Kr and Xe) over a wide range of laser intensities and formulate the conditions under which it can be observed.

2. Phase dependence of the ion yields

2.1. Theoretical approach

In our calculations, we use a short linearly polarized laser pulse with a sinus-square envelope:

$$F(t) = F_0 \sin^2(\pi t/\tau_L) \cos(\omega t + \varphi), \tag{1}$$

where ω is the carrier frequency, φ is the absolute phase and $\tau_L = (2\pi/\omega)n_p$ is the duration of the pulse; here, in turn, n_p is the number of cycles within the pulse. The pulse duration at FWHM can be estimated as one half of the τ_L: $\tau_{FWHM} \approx \tau_L/2$. Assuming that ion creation is a sequential process (i.e. there is no interaction between the electrons), we come to the following system of rate equations:

$$\frac{dr_0}{dt} = -w_0 r_0, \qquad \frac{dr_1}{dt} = w_0 r_0 - w_1 r_1, \qquad \frac{dr_2}{dt} = w_1 r_1 - w_2 r_2,$$

$$\ldots, \qquad \frac{dr_N}{dt} = w_N r_{N-1}. \tag{2}$$

Here $r_Z \equiv r_Z(t, \varphi)$ is the probability for an ion to have charge Z at time t, N is the maximum charge state that can be achieved at a given laser intensity and $w_Z \equiv w_Z(F(t, \varphi), I_Z)$ is the

4   **IOP** Institute of Physics Φ DEUTSCHE PHYSIKALISCHE GESELLSCHAFT

ionization rate for an ion with the charge Z and ionization potential I_Z. The initial conditions for the system of rate equations, equations (2), are $r_0(0, \varphi) = 1$ and $r_Z(0, \varphi) = 0$ for $Z = 1, 2, \ldots, N$. As the probability of finding a particle with some charge is equal to unity, the system (2) is constrained to the condition

$$r_0(t, \varphi) + r_1(t, \varphi) + \cdots + r_N(t, \varphi) = 1. \tag{3}$$

In order to solve system (2), we need to know the ionization probabilities. According to simple estimates, the ionization of the neutral Xe atoms, as well as that of the Xe^{1+} and Xe^{2+} ions, occurs in the barrier-suppression regime, and, strictly speaking, one needs to use ionization rates suitable for barrier-suppression ionization; see, e.g., [28, 29]. The formula of [28, 29] reduces to the usual Perelomov–Popov–Terent'ev (PPT) [30] or Ammosov–Delone–Krainov (ADK) [31] rates in the tunneling limit, when the laser field is relatively weak. The extrapolation of the tunneling formula into the barrier-suppression regime overestimates the ionization rate as compared to the barrier-suppression one. However, a substantial difference between these two formulae (say, at the level of 50%) occurs only when the laser field is at least 7–8 times greater than the corresponding barrier-suppression value, which is not true in our case. Numerical simulations show that the ionization of neutral atoms, as well as that of singly and doubly charged ions, occurs mostly at field strengths no more than 2 times stronger in comparison with the barrier-suppression fields (see figures 2(a) and (d)). Moreover, ions with $Z > 2$ are ionized well before the intensity reaches the corresponding barrier-suppression value. Thus, barrier-suppression ionization plays a minor role in the production of highly charged ions, both for long [24] and short [26] laser pulses, and the PPT or ADK formulae for the ionization probability, $w_Z(t)$, are appropriate. Thus, the tunneling rate for a level with ionization potential I_p and angular and magnetic quantum numbers equal to l and m, respectively, is given by

$$w_Z = (2I_p)(2l+1)\frac{(l+m)!}{2^m m! \, (l-m)!} C_{kl}^2 2^{2n^*-m} \left(\frac{F}{F_a}\right)^{m+1-2n^*} \exp\left(-\frac{2F_a}{3F}\right), \tag{4}$$

where $F_a = (2I_p)^{3/2}$ is the atomic field, $n^* = Z/\sqrt{(2I_p)}$ is the effective quantum number and C_{kl}^2 is the asymptotic coefficient of the atomic wave function; see [32]. We neglect the Keldysh parameter $\gamma = \omega\sqrt{2I_p}/F$ in the exponent of equation (4) and omit the pre-exponential factor $\sqrt{3\pi/F}$, because the latter arises from the averaging over the laser period.

The probabilities $r_Z(t, \varphi)$ can be calculated in various ways. In order to solve the system of the rate equations (2) numerically, it is reasonable to use the Gear method [33] or other methods adapted to the solution of stiff differential equations instead of the standard Runge–Kutta method. The fact that the system (2) is stiff becomes evident if we compare the ionization rates w_{k-1} and w_k entering the same equation for the probability $r_k(t, \varphi)$. Usually these rates differ by one or even more than one order of magnitude. Another technique is based on the simulation procedure, which was developed in [26] for the derivation of ion momentum distributions. For high laser intensities, when multiply charged ions are available and, as a consequence, the system (2) consists of a large number of equations, the latter method is faster than the former one. We used both approaches in order to check consistency. The results obtained by both methods coincide with each other.

Bearing in mind potential measurements with widely available Ti:sapphire chirped pulse amplification (CPA) systems, we perform calculations for the wavelength of 790 nm. When solving the rate equations (2), we restrict ourselves to a maximal intensity of 5×10^{18} W cm^{-2}. At this intensity the energy of an ionized electron in the final continuum state is of the order of
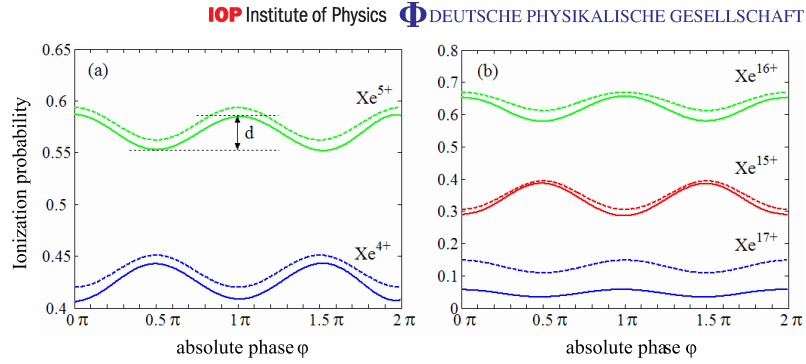
5

Figure 1. The ion yield as a function of the absolute phase φ. The two panels (a) and (b) correspond to the intensities of 3.0×10^{15} and $5.0 \times 10^{17}\,\mathrm{W\,cm^{-2}}$, respectively. The pulse duration is $5.3\,\mathrm{fs}$ at FWHM. The dashed lines show the results of the analytic model, discussed in section 3.

its rest energy and the formulae for the relativistic ionization should be used in equations (2) instead of the rate (4).

2.2. Results

Let $R_Z(\varphi) \equiv r_Z(t = \tau_\mathrm{L}, \varphi)$, $Z = 1, 2, \ldots, N$, be the yield of an ion with a charge Z at the end of the laser pulse, i.e. at $t \to \infty$. In the following, we consider only these final yields of different charge states. We investigate how the yields R_Z depend on the CEP φ. This dependence is shown in figure 1 for several charge states at two laser intensities. It is seen that the relative yields are oscillating functions of the absolute phase. The oscillation amplitude is rather complicated, not a monotonic function of the laser intensity. The minima and maxima of the yield curves correspond to $\varphi = 0$, $\pi/2$, π, $3\pi/2$ and 2π. Moreover, if the yield of the ion with a certain charge Z has a maximum, the yield of the ion $Z - 1$ has its minimum at the same phase, and vice versa. If only two different charge states can be detected after the end of the pulse, this feature can be easily explained by equation (3). In the general case, it follows from the analytic formulae; see section 3.

The oscillations of the ion yield at a given intensity can be characterized by the difference between the yields at $\varphi = 0$ and $\varphi = \pi/2$:

$$d = R_Z(0) - R_Z(\pi/2), \tag{5}$$

see figure 1. The quantity d may be negative or positive depending on the intensity and ion charge. This parameter can be considered as an absolute characteristic of the effect. It is useful to introduce the relative parameter as well:

$$\alpha = \frac{R_Z(0) - R_Z(\pi/2)}{(R_Z(0) + R_Z(\pi/2))} \equiv \frac{d}{(R_Z(0) + R_Z(\pi/2))}. \tag{6}$$

The parameters d and α are two independent characteristics. This is evident from the following example: at the intensity of $3.0 \times 10^{15}\,\mathrm{W\,cm^{-2}}$ (see figure 1(a)), for Xe^{5+} one has $d = 0.04$ and $\alpha = 0.03$. At the intensity of $5.0 \times 10^{17}\,\mathrm{W\,cm^{-2}}$ the oscillations of the Xe^{17+} yield are hardly
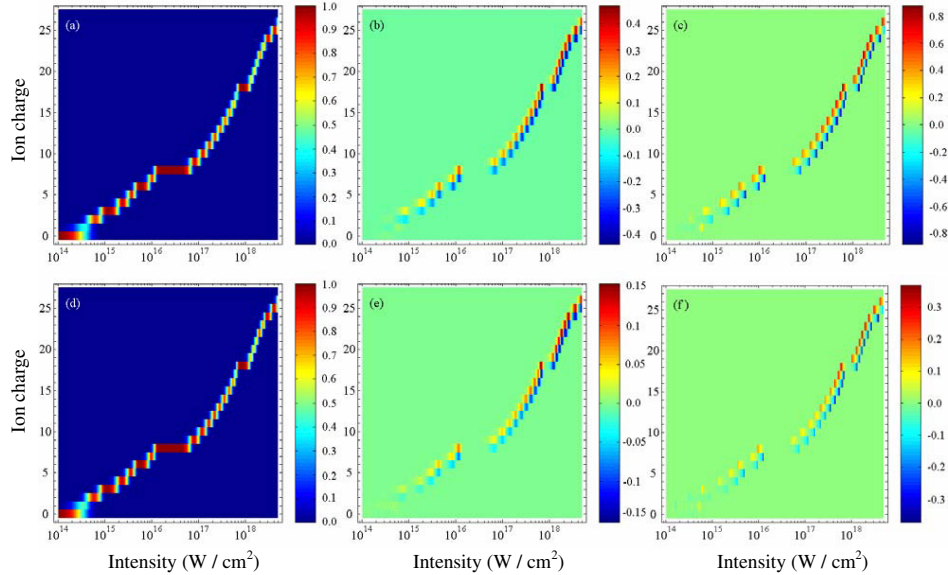
Figure 2. Results of numerical solution of the rate equations (2) for Xe ions at different intensities: (a, d) ion yields $R_Z(0)$; (b, e) absolute characteristic of the phase dependence d; (c, f) relative characteristic α. The panels (a–c) and (d–f) correspond to the pulse duration of 4.0 and 5.3 fs at FWHM, respectively.

visible from figure 1(b) and $d = 0.02$, while the relative characteristic $\alpha = 0.53$ is much greater than in the previous case due to the smaller yield.

The relative ion yield of different charge states, the difference d and the parameter α are shown in figure 2 over the range of intensities 10^{14}–5.0×10^{18} W cm^{-2} for two different pulse durations. As expected, the shorter the laser pulse, the more pronounced the absolute phase effect. We first discuss the yields, see figures 2(a) and (d). For any given ion there exists an intensity region where the yield of this ion differs from zero. The left boundary of this interval is referred to as threshold intensity (for more details, see, e.g., [17], where the corresponding field strength for a long pulse was estimated analytically), whereas to the best of our knowledge, there is no common term for the right boundary. Let us call it the depletion intensity. It is seen from figures 2(a) and (d) that only two or, at some intensities, three yields differ from zero after the end of the short laser pulse. This is also true for any given time instant within the pulse, see [26].

The striking feature of the CEP effect can be revealed if we compare panels (a) and (b) (or (d) and (e)) of figure 2: the extrema of the differences d correspond to such intensities at which the ion yields are close to each other. If, on the other hand, the yields of all available ions are substantially different at a given intensity, the corresponding absolute values of d are small. In the case when only one charge state exists after the interaction with the laser pulse, there is no noticeable absolute phase effect. Indeed, long steps in figures 2(a) and (d) for $Z = 8$
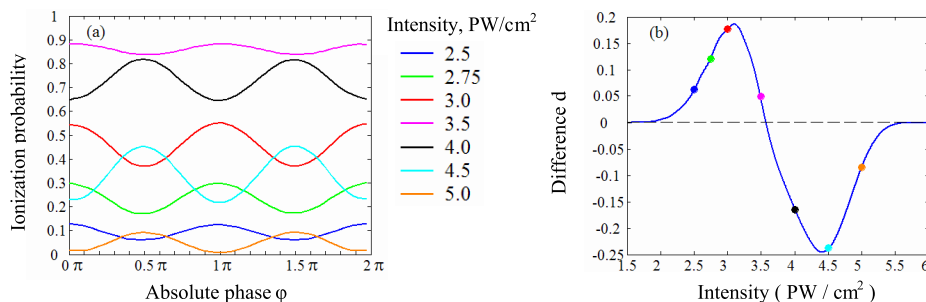
Figure 3. (a) The yield of Xe^{5+} ion as a function of the CEP at several laser intensities. (b) Absolute characteristic of the phase dependence for Xe^{5+} yield as a function of intensity. Colored circles show the values of d, which correspond to the curves of panel (a). The pulse duration is 4.0 fs at FWHM.

and $Z = 18$ in the intensity ranges of $2–4.5 \times 10^{16}$ and $6.5–9 \times 10^{17}\,W\,cm^{-2}$, respectively, give rise to the zero difference d; see figures 2(b) and (e). Such a situation occurs every time a subsequent atomic shell is completely ionized (in our case these are $5p^65s^2$ and $4d^{10}4p^64s^2$). Hence, the presence of at least two ions with comparable yield is a necessary condition for oscillations with the CEP to be detectable. This feature distinguishes the phase effect, which we predict here for the sequential multiple ionization, from the other CEP effects known from the ionization by short laser pulses.

Intensity variation has a dramatic effect on the phase dependence of the ion yield: The maxima and minima change their places. This is clearly seen from figure 3(a), where the phase dependence of Xe^{5+} yield is shown for several different intensities. As a consequence, the difference d changes its sign with increasing intensity; see figures 2(b) and (e). The evolution of d with intensity for Xe^{5+} ion is also shown in figure 3(b), which was obtained by performing a cut of figure 2(b). It is seen that near the threshold intensity, d is positive and close to zero. It increases up to a maximum with increasing intensity. After the maximum, the difference decreases, passes through zero and becomes negative. Then d decreases further, while increasing in absolute value, and has its minimum at a certain intensity. Finally, when the intensity approaches the depletion value, d is negative and tends to zero. It should be noted that, according to equation (3), at any intensity the sum of all the values of d is equal to zero; see figures 2(b) and (e).

It is seen from figures 2(c) and (f) that, in contrast to the absolute characteristic, the relative quantity α has its maxima close to the threshold and depletion intensities of each charge state. The reason is that the ion yield varies faster with intensity than the difference d. It is important to keep in mind that the parameter α can be big when the ion yield is close to zero. For this reason, in figures 2(c) and (f) we show this parameter only if the corresponding relative ion yield is more than 0.05. It is seen, however, that even with such a restriction the relative characteristic can reach a value of 0.8 for shorter pulse at high intensities.

The dependence of the CEP effect on the atomic target is illustrated by figure 4, where the absolute characteristic d is shown for Ne, Ar and Kr ions; see figure 3(e) for Xe. It is seen that the heavier the atom, the more pronounced is the phase dependence of the ion yield. This feature will be explained below; see section 3.
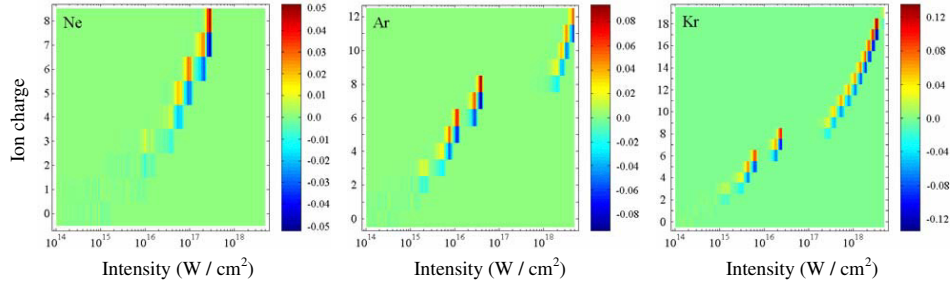
8

Figure 4. The absolute characteristic d of the CEP effect for different atomic targets. The pulse duration is 5.3 fs at FWHM.
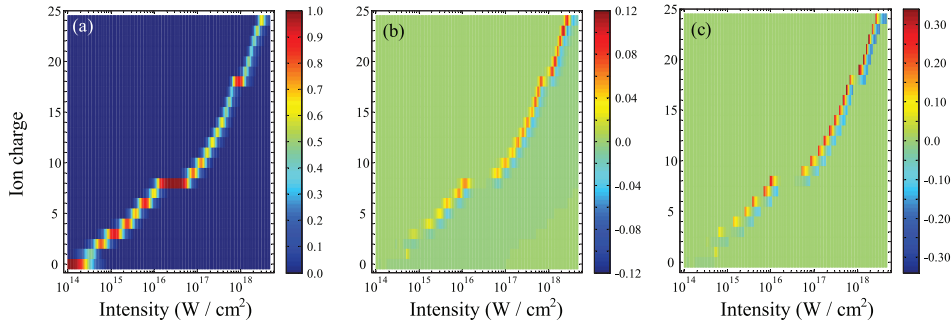

Figure 5. (a) The ion yield $R_Z(0)$, (b) the absolute characteristic d and (c) the relative α characteristic of the phase dependence after focal averaging for a pulse duration of 5.3 fs at FWHM.

2.3. Volume averaging

It is evident from this analysis that the phase dependence of ion yield is very sensitive to small variations in the laser intensity. This brings up the question: does the effect survive after focal averaging, which is inevitable in the experiment? In order to clarify whether the CEP effect can be observed in the worst possible case of 3D configuration, we integrate the yields R_Z over all space. We assume that the laser intensity is a focused beam of Gaussian spatial profile and evaluate the volume integral by changing the integration variable from volume to intensity, see [17, 34, 35]. This integrating over isointensity shells greatly simplifies the calculations.

The results of the averaging are shown in figures 5(a)–(c). It it seen that the effect is quite detectable, especially near the threshold intensities. Moreover, averaging mostly affects the negative values of d, reducing them approximately by one half, and the range of differences becomes asymmetric. These results could be expected. Indeed, for any charge state Z there is a distinct boundary between two intensity ranges, one of which corresponds to the positive and the other one to the negative values of d; see figures 2(b) and (e). Focal averaging leads to summation of the contributions from different intensities lower than a given peak value I_0. These contributions begin to compensate each other only if I_0 belongs to the second intensity range; otherwise no compensation occurs due to focal averaging and the CEP effect survives.

9

IOP Institute of Physics Φ DEUTSCHE PHYSIKALISCHE GESELLSCHAFT

3. Analytic model

Although numerical simulations have given an insight into the phase dependence of ion yield, it would be highly desirable to have an analytic model of the effect to gain a better understanding of the underlying physics. Such a model can be developed on the basis of the approximate solution of the rate equations (2), derived in [17]. This approximate solution, in turn, is based on the following formal solution of equations (2):

$$r_0(t, \varphi) = \exp\left\{-\int_{-\infty}^{t} w_0(t', \varphi)\, \mathrm{d}t'\right\},$$

$$r_1(t, \varphi) = \exp\left\{-\int_{-\infty}^{t} w_1(t', \varphi)\, \mathrm{d}t'\right\} \int_{-\infty}^{t} \exp\left\{\int_{-\infty}^{s} w_1(t', \varphi)\, \mathrm{d}t'\right\} r_0(s, \varphi) w_0(s)\, \mathrm{d}s,$$

$$r_2(t, \varphi) = \exp\left\{-\int_{-\infty}^{t} w_2(t', \varphi)\, \mathrm{d}t'\right\} \int_{-\infty}^{t} \exp\left\{\int_{-\infty}^{s} w_2(t', \varphi)\, \mathrm{d}t'\right\} r_1(s, \varphi) w_1(s, \varphi)\, \mathrm{d}s,$$

$$\dots,$$

$$r_N(t, \varphi) = \int_{-\infty}^{t} w_{N-1}(s, \varphi) r_{N-1}(s, \varphi)\, \mathrm{d}s. \tag{7}$$

Two approximations were performed in [17] to simplify equations (7): firstly, the probabilities, r_k, in the intergands of equation (7) were approximated by their decaying edges: $\exp(-\int_0^t w_{k-1}(t', \varphi)\, \mathrm{d}t')$. This is well justified, if the charge states exist sequentially in time and the temporal overlap of the different states is low, i.e. the population transfer from $Z = N$ to $Z = N + 1$ occurs quickly and all the $Z = N$ population is transferred to $Z = N + 1$ before there is a significant $Z = N + 2$ population; see [26]. Our numerical analysis of the ionization dynamics for a short laser pulse shows that the aforementioned conditions are fulfilled provided the intensity is less than ≈ 5–$7 \times 10^{17}\,\mathrm{W\,cm^{-2}}$. For example, at an intensity of $4 \times 10^{14}\,\mathrm{W\,cm^{-2}}$, $\mathrm{Xe^+}$ ionizes with 99% probability within 0.8 of the optical cycle. Secondly, the ionization rates $w_k(t, \varphi)$ are assumed to be narrow square functions of time. This is also justified, because in the case of a short pulse every ionization event occurs on one half or on two adjacent halves of the laser period, i.e. on a small fraction of the whole pulse duration τ_L. Thus, the rates $w_k(t, \varphi)$ are really narrow functions of time and, as a consequence, they may be approximated by squares of different heights.

After these approximations, the probabilities of different charge states after the end of the pulse read as (see [17])

$$R_0(\varphi) = \exp(-W_0(\varphi)),$$

$$R_1(\varphi) \approx W_0 \frac{\exp(-W_0(\varphi)) - \exp(W_1(\varphi))}{W_1(\varphi) - W_0(\varphi)},$$

$$R_2(\varphi) \approx W_1 \frac{\exp(-W_1(\varphi)) - \exp(W_2(\varphi))}{W_2(\varphi) - W_1(\varphi)}, \tag{8}$$

$$\dots,$$

$$R_N(\varphi) \approx 1 - \exp(-W_{N-1}(\varphi)),$$

10   **IOP** Institute of Physics Φ DEUTSCHE PHYSIKALISCHE GESELLSCHAFT

where

$$W_k(\varphi) = \int_0^\infty w_k(t', \varphi)\, dt'$$

is the total ionization probability for an ion with charge Z, i.e. the total area under the rate curve, which can be calculated numerically. It is seen that the dependence of the yield R_k, $k = 1, \ldots, N-1$, on the absolute phase is governed by the same dependence of the total rates W_k and W_{k-1}. This contrasts with the case of momentum distribution, where the strong dependence on the CEP originates from various ionization pathways, which are realized at different values of the phase due to different temporal evolutions of the field; see [26].

The CEP dependence of the total ionization rate with high accuracy can be approximated by the following ansatz:

$$W_k(\varphi) \approx W_k^{\pi/2} + (W_k^0 - W_k^{\pi/2})\cos^2(\varphi) \equiv W_k^0 - (W_k^0 - W_k^{\pi/2})\sin^2(\varphi), \tag{9}$$

where $W_k^0 = W_k(0)$ and $W_k^{\pi/2} = W_k(\pi/2)$. Note that sine-like ansatz is a natural one for the absolute phase dependence of the single charged ions. Ion yields calculated from equations (8) and (9) are shown in figure 1 by dashed lines. It is seen that predictions of the analytic model are in good quantitative agreement with the numerical results. The only exception is Xe^{17+} ion at the intensity of $5 \times 10^{17}\,W\,cm^{-2}$; see figure 1(b): equations (8) overestimate the ion yield by a factor of two. This disagreement is caused by the fact that at high laser intensities the charge states are not separated in time and the approximation of the ion yield by its decaying edge is no longer valid, see above. However, even in this case, the model qualitatively describes the shape of the phase dependence.

In the following, let us consider the yield of the ion with the maximal charge $Z = N$. After the substitution of equation (9) the last equation of the system (8) reads as

$$R_N(\varphi) \approx 1 - \exp(-W_{N-1}^0)\exp[-(W_{N-1}^0 - W_{N-1}^{\pi/2})\sin^2(\varphi)]. \tag{10}$$

For most intensities and ion charges the difference $(W_N^0 - W_0^{\pi/2})$ is small compared to unity. This allows us to simplify equation (10) by expanding the exponent in a Taylor series:

$$R_N \approx 1 - \exp(-W_{N-1}^0) + (W_{N-1}^0 - W_{N-1}^{\pi/2})\exp(-W_{N-1}^0)\sin^2(\varphi). \tag{11}$$

The product $(W_{N-1}^0 - W_{N-1}^{\pi/2})\exp(-W_{N-1}^0)$ in equation (11) is the oscillation amplitude of the ion yield with the absolute phase, i.e. one half of the difference d: $d/2$. We notice that the value of this amplitude is governed by the interplay of the probability W_{N-1}^0 and the difference $(W_{N-1}^0 - W_{N-1}^{\pi/2})$. If only one charge state N exists after the end of the laser pulse, the ionization probability W_{N-1}^0 is much greater than unity, and the oscillation amplitude tends to zero due to the factor of $\exp(-W_{N-1}^0)$. On the other hand, both the probabilities W_{N-1}^0 and $W_{N-1}^{\pi/2}$ and therefore their difference approach zero in the vicinity of the threshold intensity. As a result, the oscillation amplitude is again negligibly small and no phase dependence can be detected. Assuming that the difference of the probabilities $(W_{N-1}^0 - W_{N-1}^{\pi/2})$ is some fraction of W_{N-1}^0, one easily finds that the amplitude in equation (11) has its maximum at $W_{N-1}^0 = 1$ when $R_N \approx 0.63$ and therefore the yields of at least two ions substantially differ from zero.

The greater the ionization potential, the sharper the phase dependence of the total ionization rate, i.e. the more substantial the difference between the total rates W_{N-1}^0 and $W_{N-1}^{\pi/2}$. For this reason, the CEP effect in the ion yield is more pronounced for heavier atoms than for lighter ones. For example, let us consider the ionization of Ne and Xe at the same intensity

of 2.5×10^{17} W cm^{-2}, when Ne^{8+} and Xe^{13+} ions dominate in the corresponding yields. The ionization potentials of the previous charge states, i.e. Ne^{7+} and Xe^{12+}, are equal to 239.1 and 294.0 eV, respectively. For the ionization of Ne^{7+} the difference of the rates is $(W_7^0 - W_7^{\pi/2}) \approx 0.03$, whereas for Xe^{12+} this difference is $(W_{12}^0 - W_{12}^{\pi/2}) \approx 0.16$. As a result, for Xe^{13+} one has $d = 0.06$, which is six times greater than the same characteristic $d = 0.01$ for Ne^{7+}. Thus equation (11) explains all the basic features of the numerical results obtained in section 2.

4. Conclusion

In conclusion, on the basis of the rate equations we investigate the relative ion yields of sequential ionization generated by a short (4–6 fs at FWHM) intense (10^{14}–5×10^{18} W cm^{-2}) laser pulse. It is shown that the ion yields are oscillating functions of the absolute phase of the pulse, provided the pulse length is not more than 6 fs at FWHM. In contrast to other well-known CEP effects, the phase dependence of the yield can be observed only if, at the end of the laser pulse, the yields of at least two ions are comparable with each other. Despite the strong intensity dependence, the effect survives focal averaging and should be experimentally detectable. In addition to the numerical results, we present an analytic model which explains the basic features of the phase dependence.

Acknowledgments

References

[1] Dörner R *et al* 2002 *Adv. At. Mol. Opt. Phys.* **48** 1
[2] Becker A, Dörner R and Moshammer R 2005 *J. Phys. B: At. Mol. Opt. Phys.* **38** S753
[3] Agostini P and DiMauro L M 2008 *Contemp. Phys.* **49** 179
[4] Becker W and Rottke H 2008 *Contemp. Phys.* **49** 199
[5] Kuchiev M Yu 1987 *Pis'ma Zh. Eksp. Teor. Fiz* **45** 319
     Kuchiev M Yu 1987 *Sov. Phys.—JETP Lett.* **45** 404 (Engl. Transl.)
[6] Corkum P B 1993 *Phys. Rev. Lett.* **71** 1994
[7] Suran V V and Zapesochny I P 1975 *Sov. Tech.—Phys. Lett.* **51** 420
[8] l'Huillier A, Lompré L A, Mainfray G and Manus C 1983 *Phys. Rev.* A **27** 2503
[9] Weber T *et al* 2000 *Phys. Rev. Lett.* **84** 443
[10] Moshammer R *et al* 2000 *Phys. Rev. Lett.* **84** 447
[11] Weber T *et al* 2000 *Nature* **405** 658
[12] Weber T *et al* 2000 *J. Phys. B: At. Mol. Opt. Phys.* **33** L127
[13] Feuerstein B, Moshammer R and Ullrich J 2000 *J. Phys. B: At. Mol. Opt. Phys.* **33** L823
[14] Moshammer R *et al* 2003 *Phys. Rev. Lett.* **91** 113002
[15] Rudenko A *et al* 2004 *J. Phys. B.: At. Mol. Opt. Phys.* **37** L407
[16] Lambropoulos P and Tang X 1987 *J. Opt. Soc. Am.* B **4** 821
[17] Britton C, Bolton Paul R and Fittinghoff D N 1993 *Phys. Rev.* A **47** 4193

12

[18] Augst S, Talebpour A, Chin S L, Beaudoin Y and Chaker M 1995 *Phys. Rev.* A **52** R917
[19] Larochelle S, Talebpour A and Chin S L 1998 *J. Phys. B.: At. Mol. Opt. Phys.* **31** 1201
[20] Becker A and Faisal F H M 1999 *Phys. Rev.* A **59** R3182
     Becker A and Faisal F H M 1999 *J. Phys. B: At. Mol. Opt. Phys.* **32** L335
[21] Maeda H *et al* 2000 *Phys. Rev.* A **62** 035402
[22] Maeda H, Dammasch M, Eichmann U and Sandner W 2001 *Phys. Rev.* A **63** 025401
[23] Palaniyappan S *et al* 2006 *J. Phys. B.: At. Mol. Opt. Phys.* **39** S357
[24] Dimitriou K I, Yoshida S, Burgdörfer J, Shimada H, Oyama H and Yamazaki Y 2007 *Phys. Rev.* A **75** 013418
[25] Yoshida S *et al* 2009 *14th Int. Conf. on the Physics of Highly Charged Ions (HCI 2008)*
     Yoshida S *et al* 2009 *J. Phys.: Conf. Ser.* **163** 012009
[26] Shvetsov-Shilovski N I, Sayler A M, Rathje T and Paulus G G 2011 *Phys. Rev.* A **83** 033401
[27] Milošević D B, Paulus G G, Bauer D and Becker W 2006 *J. Phys. B.: At. Mol. Opt. Phys.* **39** R203
[28] Krainov V P and Shokri B 1995 *Zh. Eksp. Teor. Fiz.* **107** 1180
     Krainov V P and Shokri B 1995 *Sov. Phys.—JETP Lett.* **80** 657 (Engl. Transl.)
[29] Krainov V P 1997 *J. Opt. Soc. Am.* B **14** 425
[30] Perelomov A M, Popov V S and Terent'ev M V 1966 *Zh. Eksp. Teor. Fiz.* **51** 309
     Perelomov A M, Popov V S and Terent'ev M V 1966 *Sov. Phys.—JETP* **24** 207 (Engl. Transl.)
[31] Ammosov M V, Delone N B and Krainov V P 1986 *Zh. Eksp. Teor. Fiz.* **91** 2008
     Ammosov M V, Delone N B and Krainov V P 1987 *Sov. Phys.—JETP* **64** 1191 (Engl. Transl.)
[32] Popov V S 2004 *Usp. Fiz. Nauk* **174** 921
     Popov V S 2004 *Phys. Usp.* **47** 855 (Engl. Transl.)
[33] Gear C W 1971 *Numerical Initial Value Problems in Ordinary Differential Equations* (Englewood Cliffs, NJ:
     Prentice-Hall)
[34] Perry M D, Landen O L, Szöke A and Campbell E M 1988 *Phys. Rev.* A **37** 747
[35] Posthumus J H 2004 *Rep. Prog. Phys.* **67** 623

8.8   Ehrenfest's theorem and validity of the two-step model

Ehrenfest's theorem and the validity of the two-step model for strong-field ionization

N. I. Shvetsov-Shilovski, D. Dimitrovski, and L. B. Madsen

Lundbeck Foundation Theoretical Center for Quantum System Research, Department of Physics and Astronomy,
Aarhus University, 8000 Aarhus C, Denmark

By comparison with the solution of the time-dependent Schrödinger equation we explore the validity of the two-step semiclassical model for strong-field ionization in elliptically polarized laser pulses. We find that the discrepancy between the two-step model and the quantum theory correlates with situations where the ensemble average of the force deviates considerably from the force calculated at the average position of the trajectories of the ensemble. We identify the general trends for the applicability of the semiclassical model in terms of intensity, ellipticity, and wavelength of the laser pulse, and in terms of the properties of the atomic potential.

PACS number(s): 32.80.Fb, 32.80.Rm, 32.80.Wr

I. INTRODUCTION

Over the last three decades significant progress has been made in the investigation of phenomena arising from the interaction of strong laser fields with atoms and molecules. The phenomena include above-threshold ionization (ATI), high-order harmonic generation (HHG), and enhanced double and multiple ionization (see Refs. [1–4] for recent reviews). Along with the strong-field approximation (SFA) [5–7] and the numerical solution of the time-dependent Schrödinger equation (TDSE), semiclassical simulations are widely used in strong-field physics. We denote a model as semiclassical when it applies a classical description of the electron after it has been promoted into the continuum by the laser field, typically by tunneling ionization. The two-step [8,9] and three-step [10–12] models are the most widely known examples of such approaches to strong-field phenomena, where in some cases even the initial tunneling step is skipped by simply placing the classical electron in the external field at a chosen ionization time. The description of ionization within the two-step semiclassical model corresponds to the following physical picture [8,9]. In the first step an electron tunnels out of the atom, and in the second step, the electron moves along a classical trajectory towards a detector. Along with these two steps, the three-step model [10–12] involves the interaction of the returning electron with the parent ion, and, therefore, enables a qualitative description of the implications of rescattering processes: high-order ATI, HHG, excitation, and multiple ionization of the target.

The semiclassical models have a number of advantages. First, semiclassical simulations can help to identify in terms of classical trajectories the specific mechanism underlying the strong-field phenomena of interest. For example, the cutoffs in both high-order ATI [13] and high-harmonic spectra [14,15], the position of the maxima in the photoelectron angular distributions [16], and characteristic cutoffs for nonsequential double ionization (see, e.g., Refs. [17,18]) can be explained by such simulations. The inclusion of the Coulomb potential of the parent ion into the two-step model revealed the so-called Coulomb focusing effect [19]. More recently, different semiclassical models that account for the ionic potential were used to understand the low-energy peak structures in strong-field ionization by midinfrared laser

pulses [20–25], as well as to explain the angular shifts of the momentum distributions generated by close to circularly polarized fields [26–28].

Another appealing feature of the semiclassical models is their numerical simplicity compared to the solution of the TDSE. In fact, it appears that such models are the only computationally tractable route for some laser-atom problems such as, e.g., nonsequential double ionization of atoms by near infrared fields with elliptical [29–31] or circular polarization [32]. As the the ellipticity and wavelength increases the TDSE approach becomes increasingly impractical. The reason is that one has to accommodate (i) the description of more angular momentum states (because of the increase of ellipticity ϵ or wavelength λ) and (ii) the increase in the quiver motion proportional to λ^2. Luckily, at larger wavelengths, the application of tunneling theory for the initial ionization becomes more accurate. One way to quantify this trend is to consider the Keldysh parameter [5] and its decrease with the wavelength as $1/\lambda$ for fixed field strength, ellipticity, and ionization potential. Accordingly, models based on a quantum description of the tunneling ionization step supplemented by classical equations of motion for the propagation become attractive.

It is therefore of interest to investigate the applicability region of models based on propagation of classical trajectories for strong-field ionization. This study is particularly important in view of the rapid progress in experimental techniques, which has made it possible to study strong-field processes in completely new and unexplored regions of laser parameters. To the best of our knowledge, the validity of the trajectory-based models has not been systematically analyzed so far. In this paper we address the question about the applicability of the two-step semiclassical model of ionization by strong laser fields. Our analysis is based on a quantitative comparison of the results obtained by the two-step model with the exact solution of the TDSE. In our analysis we will apply Ehrenfest's theorem (ET) (for a textbook treatment see, e.g., Ref. [33]), which establishes the quantum-mechanical counterpart of the classical equations of motion.

The paper is organized as follows. In Sec. II we formulate the two-step semiclassical model used in our calculations. In Sec. III we discuss ET in general, and for strong-field ionization of atoms in particular. The comparison between the semiclassical model and the solution of the TDSE

(for the photoelectron momentum distributions generated by elliptically polarized laser pulses), as well as the analysis in terms of classical electron trajectories, are presented in Sec. IV. Section V establishes a correlation between the inapplicability of the two-step model and the deviation from what we define as the "strict" form of ET for an ensemble of trajectories satisfying the classical equations of motion. This deviation is quantified, and a criterion of validity of the model based on classical trajectories is formulated. In Sec. VI, using this criterion we explore the trends for the applicability of the two-step semiclassical model in terms of laser ellipticity, intensity, and wavelength. In Sec. VII we investigate the dependence of the deviation on the atomic potential, i.e., in terms of the ionization potential and potential range. The summary and conclusions of the paper are given in Sec. VIII.

II. TWO-STEP SEMICLASSICAL MODEL

According to the quantum-classical correspondence principle, quantum mechanics reduces to classical mechanics in the limit $\hbar \to 0$. In this limit, the WKB-type approximations are devised. A more elementary semiclassical approach, considered here, is to assume that the electrons, after quantum-mechanical tunneling, follow the classical equations of motion. This approach is also in accord with the limit $\hbar \to 0$ since by having position and momentum defined for the classical electron at each instant of time after tunneling, the commutators of these operators vanish, instead of being equal to $i\hbar$.

The models based on propagation of classical trajectories evolved along the following lines. Initially, these models involved a classical ensemble [34] modeling the initial atomic state before the action of the laser pulse (see, e.g., Ref. [35]). Although such purely classical models explained some qualitative features of the dynamics of strong-field ionization, it was recognized that one could improve them by adding a quantum input, i.e., by simulating that the initial ionization step follows from tunneling and employing the WKB tunneling exponent to mimic the probability of tunneling [36,37]. In what follows we discuss semiclassical models of the latter type, that is, the two-step semiclassical model.

In the two-step semiclassical model, the trajectory of the electron and its asymptotic momentum are calculated from Newton's equations of motion in the combined ionic potential and the electric field of the laser pulse. This procedure requires the specification of the initial conditions for the electron just after the escape from the atom: the tunnel exit point [26,28], and the momentum spread at the tunnel exit point of the classical ensemble modeling the electronic wave packet [38]. The results obtained within the semiclassical model depend critically on the initial conditions, but also on the precise description of the ionic potential. We utilize the approximate separation of the tunneling problem in parabolic coordinates (in the case of atomic H the separation is exact) to obtain the tunnel exit point [26]. We also include the Stark shifts of the energy levels which affect the ionization probability and the tunnel exit point [39]. Finally, the effective potential that includes the multielectron effect through the induced dipole term of the ion is taken into account. This potential affects the tunnel exit point and the subsequent propagation of the classical electronic trajectories [27,40].

Regarding the momentum composition of the classical ensemble modeling the electronic wave packet, we assume that at the tunnel exit the electron has zero initial momentum parallel to the laser field $p_{\parallel} = 0$ and nonzero initial transverse momentum $p_{\perp}$. The instants of ionization and the initial transverse momenta are distributed according to the static ionization rate [41–43] (from this point on we use atomic units):

$$w(t_0, v_0) \sim \exp\left(-\frac{2\varkappa^3}{3F}\right) \exp\left(-\frac{\varkappa p_{\perp}^2}{F}\right), \tag{1}$$

with $F = F(t_0)$ and $\varkappa^2/2 = I_p$ and where I_p denotes the Stark-shifted ionization potential. For simplicity, the preexponential factor is omitted in Eq. (1). This factor can change the total ionization yield by several orders of magnitude, but for the intensities considered it only slightly affects the shape of the momentum distribution, the quantity of interest here. In our calculations of momentum distributions we used an ensemble of 1.5×10^6 trajectories each weighted with Eq. (1). Newton's equations of motion were solved using a fourth-order Runge-Kutta method with adaptive step-size control [44].

At the end of the pulse, the trajectories with negative energy, corresponding to the bound states [45,46], are removed. Moreover, the classical trajectories corresponding to electrons with positive energies should be propagated in the ionic potential some time after the end of the pulse, so that the momenta converge. This propagation can be performed analytically to infinite times, so that the electron momentum **p** and its position **r** at the end of the laser pulse uniquely determine the asymptotic momentum **k**. For the Coulomb potential of charge Z, the asymptotic momentum **k** is [28,46]

$$\mathbf{k} = k\frac{k(\mathbf{L} \times \mathbf{a}) - \mathbf{a}}{1 + k^2 L^2}, \tag{2}$$

where the absolute value of the asymptotic momentum k can be found from energy conservation

$$\frac{p^2}{2} - \frac{Z}{r} = \frac{k^2}{2}, \tag{3}$$

and where $\mathbf{L} = \mathbf{r} \times \mathbf{p}$ and $\mathbf{a} = \mathbf{p} \times \mathbf{L} - \mathbf{r}/r$ are the angular momentum and Runge-Lenz vector, respectively. These quantities are conserved after the end of the pulse and at distances where only the Coulomb potential is important. For the case of a Yukawa potential, which is also considered below, the ensemble of trajectories is propagated after the end of the laser pulse (typically 20 laser field periods) until the electron momentum distribution converges. Each point in the momentum distributions in the semiclassical model is obtained by collecting a large number of classical trajectories with an asymptotic momentum belonging to a square-shaped bin in the momentum plane with a side length of 0.02 a.u.

III. EHRENFEST'S THEOREM

Ehrenfest's theorem gives the law of the motion satisfied by the mean values of the spatial, **r**, and the momentum, **p**, coordinates of the quantum system. For the purpose of this paper, a quantum system with a single active electron is considered. The Hamiltonian of the system reads

$$\hat{H}(t) = -\tfrac{1}{2}\nabla_{\mathbf{r}}^2 + V(\mathbf{r},t), \tag{4}$$

and the mean values of the position and momentum operators for the quantum system satisfy

$$\frac{d\langle \mathbf{r} \rangle}{dt} = \langle \mathbf{p} \rangle \qquad (5)$$

and

$$\frac{d\langle \mathbf{p} \rangle}{dt} = \langle -\nabla_{\mathbf{r}} V(\mathbf{r},t) \rangle. \qquad (6)$$

From the above equations, it seems that the average values $\langle \mathbf{r} \rangle$ and $\langle \mathbf{p} \rangle$ of the quantum system follow the classical equations of motion. This is, however, not the case because of the term $\langle -\nabla_{\mathbf{r}} V(\mathbf{r},t) \rangle$ present in Eq. (6), which reflects the *average of the force* [33]. In order that mean values $\langle \mathbf{r} \rangle$ and $\langle \mathbf{p} \rangle$ satisfy the classical equations of motion, instead of the average of the force, the *force at the average position* should appear in Eq. (6), i.e.,

$$\frac{d\langle \mathbf{p} \rangle}{dt} = -\nabla_{\mathbf{r}} V(\mathbf{r},t)|_{\mathbf{r}=\langle \mathbf{r} \rangle}. \qquad (7)$$

We refer to the system of Eqs. (5) and (7) as the "strict" form of ET. Mean values of $\mathbf{r}$ and $\mathbf{p}$ obey the classical equations of motion for quantum systems that satisfy the strict form of ET.

In cases when the potential $V(\mathbf{r},t)$ is slowly varying with respect to $\mathbf{r}$, $\nabla_{\mathbf{r}} V(\mathbf{r},t)$ can be expanded in the vicinity of $\langle \mathbf{r} \rangle$ and to second order in $(\mathbf{r} - \langle \mathbf{r} \rangle)$ as

$$\nabla_{\mathbf{r}} V(\mathbf{r},t) \approx \nabla_{\mathbf{r}} V(\mathbf{r},t)|_{\mathbf{r}=\langle \mathbf{r} \rangle} + [(\mathbf{r} - \langle \mathbf{r} \rangle) \cdot \nabla_{\mathbf{r}}](\nabla_{\mathbf{r}} V(\mathbf{r},t))|_{\mathbf{r}=\langle \mathbf{r} \rangle}$$
$$+ \tfrac{1}{2}[(\mathbf{r} - \langle \mathbf{r} \rangle) \cdot \nabla_{\mathbf{r}}]^2 (\nabla_{\mathbf{r}} V(\mathbf{r},t))|_{\mathbf{r}=\langle \mathbf{r} \rangle}. \qquad (8)$$

In a single dimension (1D), the above expression reduces to

$$\frac{\partial V(x,t)}{\partial x} \approx \frac{\partial V(x,t)}{\partial x}\bigg|_{x=\langle x \rangle} + (x - \langle x \rangle)\frac{\partial^2 V(x,t)}{\partial x^2}\bigg|_{x=\langle x \rangle}$$
$$+ \frac{1}{2}(x - \langle x \rangle)^2 \frac{\partial^3 V(x,t)}{\partial x^3}\bigg|_{x=\langle x \rangle}. \qquad (9)$$

Inserting the series (9) into Eq. (6), one obtains

$$\frac{d\langle p_x \rangle}{dt} \approx -\frac{\partial V(x,t)}{\partial x}\bigg|_{x=\langle x \rangle}$$
$$- \frac{1}{2}\frac{\partial^3 V(x,t)}{\partial x^3}\bigg|_{x=\langle x \rangle}(\langle x^2 \rangle - \langle x \rangle^2). \qquad (10)$$

From the above equation it is clear that if the dependence of a 1D Hamiltonian on the spatial coordinate is a polynomial of up to quadratic order, the second term in Eq. (10) is zero, as well as all higher-order terms. Therefore, all 1D quantum systems with Hamiltonians that are polynomials up to the second power in the spatial coordinate obey the strict form of ET.

For the three-dimensional (3D) case, inserting Eq. (8) into Eq. (6) yields

$$\frac{d\langle \mathbf{p} \rangle}{dt} \approx -\nabla_{\mathbf{r}} V(\mathbf{r},t)|_{\mathbf{r}=\langle \mathbf{r} \rangle}$$
$$- \frac{1}{2}\langle [(\mathbf{r} - \langle \mathbf{r} \rangle) \cdot \nabla_{\mathbf{r}}]^2 (\nabla_{\mathbf{r}} V(\mathbf{r},t))|_{\mathbf{r}=\langle \mathbf{r} \rangle} \rangle, \qquad (11)$$

since, as in the 1D case, the term linear in $(\mathbf{r} - \langle \mathbf{r} \rangle)$ disappears when evaluating the expectation value. The second term in the above equation reflects the lowest-order deviation from the strict form of ET. This term is different from the term appearing

in the 1D case [Eq. (10)] and includes linear combinations of terms of the type $(\langle x_i x_j \rangle - \langle x_i \rangle \langle x_j \rangle)$, $i,j = 1,2,3$ where x_i are the components of $\mathbf{r}$. Quantum systems with potentials linear in $\mathbf{r}$ such as the free particle in the time-dependent field $[\mathbf{F}(t) \cdot \mathbf{r}]$ satisfy the strict form of ET, and this is also true for quantum systems with potentials that have terms up to quadratic dependence on the components of the spatial coordinate, e.g., the 3D harmonic oscillator. All other quantum systems do not, in general, satisfy the strict form of ET, including the cases of interest for strong-field physics: atoms and molecules in a laser field. This deviation of a given quantum system from the strict form of ET can be quantified by introducing the relative deviation from the strict form of ET as

$$R_q(t) = \frac{|\nabla_{\mathbf{r}} V(\mathbf{r},t)|_{\mathbf{r}=\langle \mathbf{r} \rangle} - \langle \nabla_{\mathbf{r}} V(\mathbf{r},t) \rangle|}{|\langle \nabla_{\mathbf{r}} V(\mathbf{r},t) \rangle|}, \qquad (12)$$

where the subscript q denotes that the above measure should be evaluated quantum mechanically. Hence, to determine $R_q(t)$, it is necessary to have the exact solution of the TDSE at all times, and therefore its evaluation is impractical. On the other hand, it is interesting to gauge the validity of a certain model simulating the quantum dynamics in cases where it is impossible or very expensive in terms of computational resources to solve the TDSE. Consequently, it makes sense to monitor the validity of ET for a *classical* ensemble. For a probability distribution of a classical ensemble in phase space satisfying the Liouville equation, it can be shown that the average values of the position and momentum satisfy ET of Eqs. (5) and (6) [47]. In that way, if the corresponding quantum system satisfies the strict form of ET, so does the statistical ensemble of classical trajectories. According to Ref. [33], for the semiclassical approach of Sec. II to be valid, the mean values of the positions and momenta of the quantum system should follow the classical laws of motion to a good approximation, and the dimensions of the wave packet should be smaller than the characteristic dimension of the problem at hand. However, later it was remarked [47] that the quantum system might violate the strict form of ET and still behave essentially classically. We examine this below for the problem of strong-field ionization of atoms.

For strong-field ionization of atoms, the potential is of the form

$$V(\mathbf{r},t) = V_{\mathrm{at}}(\mathbf{r}) + \mathbf{F}(t) \cdot \mathbf{r}, \qquad (13)$$

where $V_{\mathrm{at}}(\mathbf{r})$ is the atomic potential and $\mathbf{F}(t)$ is the electric field of the laser pulse. Then for the $\mathbf{F}(t) \cdot \mathbf{r}$ part of the potential the strict form of ET is satisfied, whereas for the V_{at} part it is, in general, not.

In the following, we explore the validity of our model for strong-field ionization in elliptically polarized laser pulses by comparing it to exact solutions of the TDSE. We also examine the correlation between the deviation from the strict form of ET for the semiclassical model and the ability of the semiclassical model to mimic the quantum dynamics; that is, we examine the validity of the semiclassical model.

IV. MOMENTUM DISTRIBUTIONS IN ELLIPTICALLY POLARIZED PULSES

We start by considering momentum distributions obtained by ionization of H by elliptically polarized laser pulses. To facilitate the comparison of the semiclassical results with the results obtained from a numerical solution of the TDSE in the velocity gauge, the laser pulse is defined in terms of a vector potential $\mathbf{A}(t)$ of the form (we choose a left circularly polarized field in the xy plane)

$$\mathbf{A}(t) = \frac{F_0}{\omega} \sin^2\left(\frac{\omega t}{2n_p}\right)(-1)^{n_p}\left[-\frac{1}{\sqrt{1+\epsilon^2}} \sin(\omega t)\mathbf{e}_x + \frac{\epsilon}{\sqrt{1+\epsilon^2}} \cos(\omega t)\mathbf{e}_y \right], \quad (14)$$

where ω is the angular frequency, F_0 is the field amplitude, ϵ is the ellipticity of the pulse, n_p is the number of cycles, and $\mathbf{e}_{x,y}$ are unit vectors, the pulse is present from 0 to $2\pi n_p/\omega$. The electric field is obtained from Eq. (14) by $\mathbf{F}(t) = -\partial\mathbf{A}/\partial t$ and for $n_p = 3$ it is plotted in Fig. 1. Counting the minima in $|\mathbf{F}(t)|$ one can see that there are approximately 7 half cycles in the field with unequal duration. The maximum of the field occurs in the dominant half cycle of the pulse, located approximately from 2.5 to 3.5 (in units of $\omega t/\pi$).

Below we compare the results of semiclassical simulations with the exact solution of the TDSE. We solve the TDSE in the velocity gauge using a grid-based split-step method, where the wave function is expressed on a basis of spherical harmonics:

$$\Psi(\mathbf{r},t) = \sum_{l=0}^{l_{\max}} \sum_{m=-l}^{l} \frac{f_{lm}(r,t)}{r} Y_{lm}(\theta,\phi). \quad (15)$$

The initial state is obtained by imaginary time propagation. Then this state is evolved in time, the details being described elsewhere (see Ref. [48]). Knowing the final wave function at the end of the pulse $T = 2\pi n_p/\omega$, we can calculate the differential momentum distribution by projection onto Coulomb
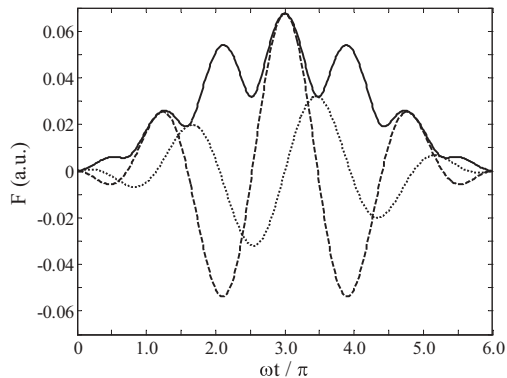
FIG. 1. The electric field of the laser pulse $\mathbf{F}(t)$: modulus of the field $|\mathbf{F}|$ (full curve), x component of $\mathbf{F}(t)$ (dashed curve), and y component of $\mathbf{F}(t)$ (dotted curve). The pulse parameters are wavelength $\lambda = 800$ nm, peak intensity 2×10^{14} W/cm^2, ellipticity $\epsilon = 0.5$, and the number of cycles $n_p = 3$.

continuum scattering states of asymptotic momentum $\mathbf{k}$:

$$\frac{\partial^3 P}{\partial k_x \partial k_y \partial k_z} = \left|\left\langle \Psi_{\mathbf{k}}^{C-} \middle| \Psi(\mathbf{r},T)\right\rangle\right|^2. \quad (16)$$

The scattering states $\Psi_{\mathbf{k}}^{C-}$ entering Eq. (16) are obtained by solving the time-independent Schrödinger equation subject to incoming wave boundary conditions. For the TDSE calculations we used a radial grid consisting of 4096 points and a time step 0.005 a.u., whereas the size of the sphere $X_{\max}$ and the maximum angular momentum $l_{\max}$ were adjusted to ensure convergence depending on the wavelength and ellipticity: These are stated in the captions of the figures showing the TDSE results.

Using the semiclassical model defined in Sec. II, we obtain the momentum distributions for a $n_p = 3$ cycle elliptically ($\epsilon = 0.5$) polarized pulse for a wavelength of 800 nm [Fig. 2(a)] and 400 nm [Fig. 3(a)]. The intensities are chosen such that the Keldysh parameters [5] are kept relatively low for 800 nm ($\gamma = 0.75$) and not substantially large for 400 nm ($\gamma = 1.51$). The momentum distributions from elliptically polarized pulses with not too low value of ellipticity have a distinctive shape with two crescents [26,28]. In cases of short, few-cycle pulses with fixed carrier-envelope phase, as employed here, only one of the crescents in the momentum distribution remains, reflecting the dominant instant of emission by the phase-stabilized laser pulse [28,49]. The maximum of the momentum distribution is angularly shifted from the minor polarization axis of the pulse in the direction of the rotation of the electric field [28,49]. In this sense, the distribution for 800 nm [Fig. 2(a)] has the expected shape, while the distribution for 400 nm [Fig. 3(a)] deviates from the expected shape (note that the maximum is in the first quadrant). To investigate whether the features in the semiclassical momentum distributions reflect the exact solution, we have performed TDSE calculations for the same pulse parameters, the results being shown in Figs. 2(b) and 3(b), respectively.

While the semiclassical model [Fig. 2(a)] agrees qualitatively with the TDSE result at $\lambda = 800$ nm [Fig. 2(b)], it is clear from Fig. 3 that there is a large discrepancy between the TDSE and the semiclassical model at 400 nm. First, the maximum in Fig. 3(b), although shifted to smaller momenta, as compared with the classical calculation, is mostly in the fourth quadrant, as expected. On top of that, in the momentum distributions by the TDSE, the ATI rings are visible, although somewhat broadened because of the short pulse duration. The latter discrepancy between the TDSE and the semiclassical model is also present in the case of 800 nm in Fig. 2; such discrepancy is expected as the semiclassical model cannot account for the interference structures in the momentum distributions. On the other hand, in Fig. 3 the position of the maximum and the overall discrepancy of the shape of momentum distributions between the semiclassical and quantum results is unexpected. In addition, we have checked that the discrepancy in Fig. 3 cannot be removed if the tunnel exit point is chosen along the field direction instead in parabolic coordinates chosen here. Equally, and in accord with Ref. [28], the overall shape of the momentum distribution for the case of Fig. 2 does not change by choosing the tunnel exit point along the field direction, although the exact angular shift in the polarization plane might
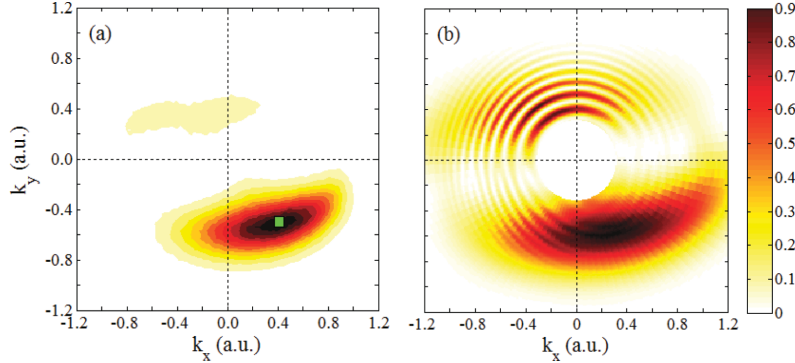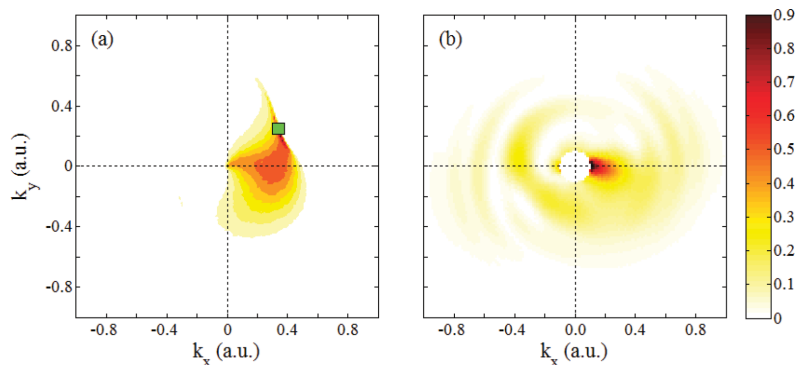
FIG. 2. (Color online) Momentum distribution (normalized to the peak value) for the H atom in the polarization plane using a laser pulse with wavelength $\lambda = 800$ nm, peak intensity 2×10^{14} W/cm^2, ellipticity $\epsilon = 0.5$, and a laser pulse duration of $n_p = 3$ cycles, obtained (a) using the semiclassical two-step model and (b) by numerical solution of the TDSE (the size of the spatial box $X_{max} = 600$ a.u., the maximum angular momentum $l_{max} = 60$). The maximum of the semiclassical momentum distribution is qualitatively indicated by a (green) square in (a).

change [26,28]. As we show here, the discrepancy between the quantum and the semiclassical result coincides with the cases when the strict form of ET is not satisfied by the ensemble of classical trajectories.

We note in passing that, contrary to the discrepancy between the TDSE and the semiclassical model in the momentum distributions at 400 nm, the energy distributions in Fig. 4, obtained both from the TDSE and the calculation within the semiclassical model, compare much more favorably. In fact, it appears that the discrepancy between the energy distributions obtained in the semiclassical model and the TDSE is small for both 800 nm [Fig. 4(a)] and 400 nm [Fig. 4(b)]. In the following, we focus on the comparison of momentum distributions obtained by the TDSE and the semiclassical model.

To investigate the reason for the appearance of peculiar structures in the first quadrant of the momentum distributions

of Fig. 3(a), we first explore the difference between time evolution of the characteristic trajectories leading to the maxima in Figs. 2(a) and 3(a), indicated qualitatively by (green) squares in the fourth and the first quadrant, respectively. The first difference is that the maximum in the momentum distribution of Fig. 2(a) stems from the initial time instant when the electric field of the laser reaches the maximum. In contrast, the maximum in Fig. 3(a) is due to mapping of many trajectories each with smaller weight into a single bin in the momentum plane. This is clearly seen from Figs. 5(a) and 5(b), which present initial conditions (i.e., instants of ionization ωt_0 and initial transverse velocity $p_\perp$) for all the trajectories leading to the bins indicated by the (green) squares, which contain the maxima of Figs. 2(a) and 3(a), respectively. This is very similar to the process of "bunching" of classical trajectories that lead to the low-energy maximum in linearly polarized infrared pulses [24].

FIG. 3. (Color online) Momentum distribution (normalized to the peak value) for the H atom in the polarization plane using a laser pulse with wavelength $\lambda = 400$ nm, peak intensity 2×10^{14} W/cm^2, ellipticity $\epsilon = 0.5$, and a laser pulse duration of $n_p = 3$ cycles, obtained (a) using the semiclassical two-step model and (b) by numerical solution of the TDSE (the size of the spatial box $X_{max} = 400$ a.u., the maximum angular momentum $l_{max} = 40$). The maximum of the semiclassical momentum distribution is qualitatively indicated by a (green) square in (a).
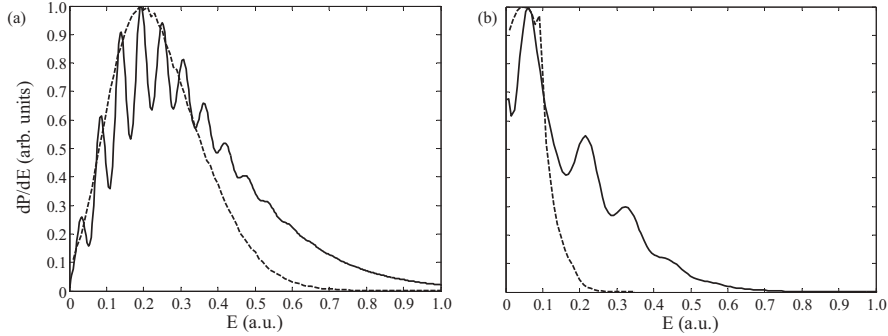
FIG. 4. Comparison of the energy distributions obtained for the H atom from the semiclassical two-step model (dashed curve) and from the TDSE (solid curve) at the wavelength of (a) $\lambda = 800$ nm, (b) $\lambda = 400$ nm. The rest of parameters are peak intensity 2×10^{14} W/cm^2, ellipticity $\epsilon = 0.5$, and number of cycles $n_p = 3$ (see also Figs. 2 and 3). The energy distributions are normalized to the peak value.

In Figs. 6(a) and 6(b) we consider the time evolution of the x and y components of the Coulomb forces acting on the characteristic trajectories that lead to the maxima in Figs. 2(a) and 3(a), respectively. The shape of the time evolution of the Coulomb force is different in the two cases, characterized by different wavelengths. More precisely, for the case of 400 nm, in addition to the maximum during the half cycle of the field when the trajectory started, an additional maximum appears in the subsequent half cycle. This is so because in the case of 400 nm the trajectories leading to the maximum in the momentum distribution, after the initial departure, come back relatively close to the Coulomb center, exhibiting soft collisions (the trajectories are plotted in Fig. 7). This leads to focusing of very many trajectories into the same momentum-space bin. In the case of the pulse at 800 nm, the characteristic trajectory does not exhibit any close collision simply because the excursion amplitude of a classical electron (proportional to F_0/ω^2) is larger than in the case of 400 nm (see Fig. 7). We have performed calculations with different number of cycles and they all show that at 400 nm the electron

trajectory leading to the maximum of the distribution always exhibits a soft collision during the first half cycle of the field after the instant of ionization.

However, such an analysis lacks predictive power. We would like to quantify at which parameters of the field and the atomic target such spurious structures in the momentum distributions from the semiclassical model appear and why. We show that one way to analyze the validity of the results obtained by the semiclassical models is through the use of ET.

V. QUANTIFICATION OF THE DEVIATION FROM THE STRICT FORM OF EHRENFEST'S THEOREM

As stated in Sec. III, the strict form of ET is valid for potentials of polynomial form up to the quadratic power in the spatial coordinate. Instead of calculating the deviation from the strict form of ET for the quantum system, here we calculate this deviation for the semiclassical model. When modeling strong-field ionization by classical trajectories, the atomic potential is a source of deviation from the strict form of
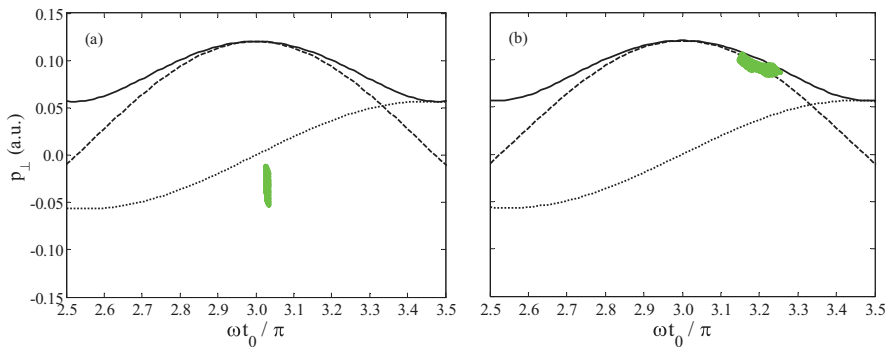

FIG. 5. (Color online) Initial conditions (instant of ionization and initial transverse velocity) for the trajectories leading to the maxima (a) in Fig. 2(a) (800 nm) and (b) in Fig. 3(a) (400 nm) are shown by shaded (green) areas. The full curve shows the modulus of the laser field $|\mathbf{F}(t)|$, whereas the dashed and the dotted curves correspond to the x and y components of $\mathbf{F}(t)$, respectively (the curves are plotted in arbitrary units).
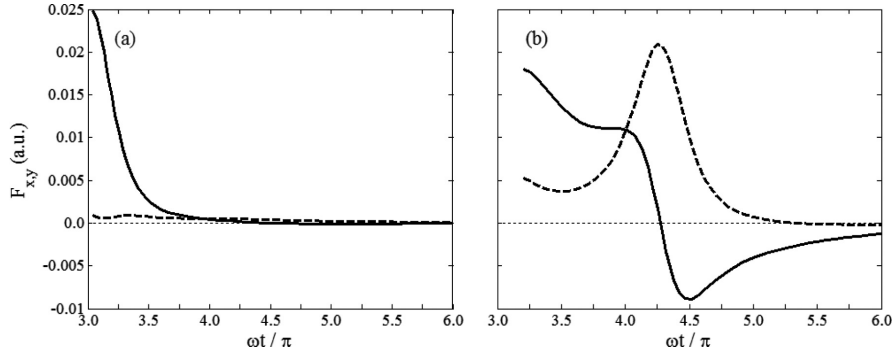
FIG. 6. Time-dependence of the x components (full curves) and the y components (long-dashed curves) of the Coulomb force for trajectories that lead to final momenta corresponding to the maxima of the momentum distributions in (a) Fig. 2(a) and (b) Fig. 3(a). The pulse parameters are as in Figs. 2 and 3, respectively (see also Fig. 1). In (b) the time axis is given in units of half-cycle duration, the pulse starts at time zero, and $\omega t/\pi = 3$ corresponds to the center of the pulse.

ET. As we see below, such deviation could be used as a measure for the quality of the semiclassical modeling. Before we start with the analysis, we discuss how to quantify the deviation from the strict form of ET for the semiclassical model. More specifically, we address the questions of which quantity is a suitable measure for the deviation from the strict form of ET and when and on which ensemble of classical trajectories to evaluate this deviation.

First, we propose to consider the relative deviation from the strict form of ET for the semiclassical ensemble to quantify the validity of the semiclassical simulation. In accord with the discussion of Sec. III [Eq. (12)], we define the relative deviation $R(t)$ from the strict form of ET for the semiclassical model as

$$R(t) = \left| \nabla_{\mathbf{r}} V(\mathbf{r},t)|_{\mathbf{r}=\langle \mathbf{r}(t)\rangle} \right.$$
$$\left. - \sum_{\mathcal{A}} w_i \nabla_{\mathbf{r}} V(\mathbf{r},t) \right| \Bigg/ \left| \sum_{\mathcal{A}} w_i \nabla_{\mathbf{r}} V(\mathbf{r},t) \right|, \quad (17)$$
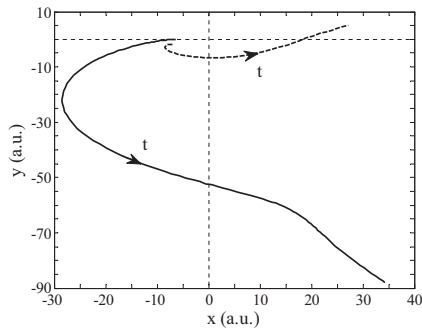
FIG. 7. Classical electron trajectories in the laser and Coulomb fields corresponding to the maxima of Fig. 2(a) ($\lambda = 800$ nm, solid curve) and of Fig. 3(a) ($\lambda = 400$ nm, dashed curve).

where $\langle \mathbf{r}(t)\rangle$ is the average position at time t, formed by the set $\mathcal{A}$ of classical trajectories

$$\langle \mathbf{r}(t)\rangle = \sum_{\mathcal{A}} w_i \mathbf{r}_i, \quad (18)$$

with w_i a weight assigned to trajectory i in $\mathcal{A}$. The potential V, defined in Eq. (13) includes both the atomic potential and the field of the pulse. Equation (17) can be read in words as force at the average position minus the average of the force divided by the average of the force. The relative deviation $R(t)$ is the measure of the deviation of ET during the time evolution of the pulse. For the whole duration of the pulse, we also monitor the *maximal relative deviation*,

$$R = \max\{R(t)\} = R(t_m), \quad (19)$$

for a given classical ensemble $\mathcal{A}$, where t is the time of the evolution during the pulse and t_m is the *time of maximal relative deviation*.

The deviation from the strict form of ET should be monitored for the whole duration of the pulse. If at some point between the electron ejection and the end of the pulse the deviation is substantial, then the semiclassical result will, in general, not reflect the solution of the TDSE; therefore, we "record" the maximum relative deviation R and the time t_m at which this occurs. The exemptions are for deviations at times around the electron ejection and at times close to the end of the pulse. At the time of electron ejection, the trajectory i is assigned a weight w_i, which is a quantum input in the model. For times close to the time of ejection, the classical electrons are close to the atomic potential and in the initial stages of their trajectory the force terms from the atomic potential are typically substantial. However, since at this stage the quantum part of the model is interfacing the classical propagation of electronic trajectories, those deviations are not important for the quality of the semiclassical prediction. We make another exemption for the times near to the end of the pulse where one considers the mapping of the classical trajectories into eigenstates of the field-free atom. When the field is turned off, the ensemble of classical trajectories model both excited

and ionized atoms. The field-free atom can be modeled by an ensemble of classical trajectories: Although the ensemble of classical trajectories does not satisfy the strict form of ET, in accord with Ref. [47], we assume that the classical model satisfactorily describes the field-free atom; without this assumption we cannot relate the momentum distributions of the quantum and the semiclassical model. Consequently, we assume that the deviation from the strict form of ET at the end of the pulse, that is, for the last half cycle of the pulse is not important for assessing the validity of the semiclassical prediction. We see below, when comparing the quantum and classical results, that indeed these deviations from the strict form of ET do not affect the possibility of the classical model to give the correct prediction.

Second, we discuss the question about which classical ensemble of trajectories to take into account when considering the deviation from the strict form of ET. In the semiclassical model, trajectories are started at different times during the pulse with a weight w_i determined by the static tunneling rate. At each instant of tunneling, the electron appears with a certain transverse initial momentum with a probability that is governed by the expression given in Eq. (1). The ejection of electrons at different times is uncorrelated because the probability of electron tunneling at the current time does not depend on the probability of tunneling at the previous times if the depletion of the initial state is negligible (this is satisfied in the cases considered here). Hence, the ensemble of independent, random events in time is used to model the quantum dynamics. In contrast, the electrons that emerge at the same time, but with different initial momenta, depend on the time of tunneling through the time-dependence of the field. The different initial momenta at a particular instant of tunneling form a set of classical trajectories that are the classical analog of the quantum wave packet formed at the tunnel exit point. Therefore, in principle, the subset of classical trajectories used for the calculation of the deviation from the strict form of ET should include all trajectories emerging from the same time during the pulse, but not necessarily from different times. For practical purposes, it is of interest to consider the ensemble of trajectories with largest weights, which also leads to the dominant features in the momentum distributions. In the following, we calculate deviations from the strict form of ET for the classical ensemble consisting of all trajectories that emerge from the dominant, most intense, half cycle of the field.

To start the analysis based on R and $R(t)$, we first reconsider the cases presented in Figs. 2 and 3. The time dependence of the relative deviation for those cases is given in Fig. 8. For the case of 800 nm (solid curve in Fig. 8), the maximal relative deviation occurs at the half cycle where the trajectories were launched and it never exceeds 0.1. On the other hand, for 400 nm (dashed curve in Fig. 8), the maximal relative deviation is considerably larger than at 800 nm and it occurs at a later stage of the time evolution of the pulse, namely at the next second cycle after the trajectories were launched. In summary, for large maximal relative deviation R (roughly exceeding 0.1) the deviation from the strict form of ET is substantial and the semiclassical model does not reflect the solution of the TDSE as in the case of 400 nm (Fig. 3). On the other hand, if $R(t)$ is kept roughly below 0.1 at all times, the deviation from the strict form of ET is minor and the semiclassical simulations capture
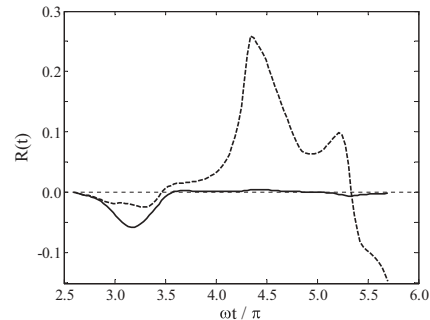

FIG. 8. Time evolution for the relative deviation $R(t)$ [Eq. (17)] between the magnitudes of the force on the average position and average of the force at ellipticity $\epsilon = 0.5$ for two wavelengths: $\lambda = 800$ nm (solid curve) and $\lambda = 400$ (dashed curve). The laser pulse duration is $n_p = 3$ cycles and the peak intensity is 2×10^{14} W/cm^2. The time axis is given in units of half-cycle duration, the pulse starts at zero, $\omega t / \pi = 3$ corresponds to the center of the pulse.

the main features of the TDSE result. In other words, in this case there are no distortions in the semiclassical momentum distributions that destroy the qualitative agreement with the result of the TDSE.

Encouraged by the success of this criterion ($R < 0.1$) for these two isolated cases, in the next sections we explore this criterion in more depth by calculating the maximal relative deviations from the strict form of ET, R, and the corresponding time of the maximal deviation, t_m, as a function of the parameters of the laser pulse (ellipticity, wavelength, and intensity) and as a function of the properties of the atomic target (ionization potential and potential range). We confront the predictions obtained analyzing R and t_m with the comparison between the TDSE and the semiclassical predictions of the momentum distributions.

VI. DEPENDENCE OF THE DEVIATION FROM THE STRICT FORM OF EHRENFEST'S THEOREM ON THE PARAMETERS OF THE PULSE

A. Ellipticity dependence

When the ellipticity ϵ is decreased, keeping all other parameters fixed, the number of recollision events is increased. One expects that R is increased because of the relative increase in the importance of the atomic potential. In the opposite direction, increasing the ellipticity leads to small R values. The maximum relative deviation R as a function of ellipticity for 400 and 800 nm is plotted in Fig. 9(a). Both curves show the expected trend of the decrease of the maximal relative deviation R as a function of the ellipticity. Until around an ellipticity of $\epsilon = 0.8$ the curve for 400 nm lies higher than the one for 800 nm. The former does not reach the level of 0.1 before the ellipticity reaches approximately 0.7. In the latter case, for almost the whole ellipticity range, excluding the interval of small ellipticities below approximately 0.2, R is less then 0.1, consistent with a good qualitative agreement between semiclassical and TDSE results.
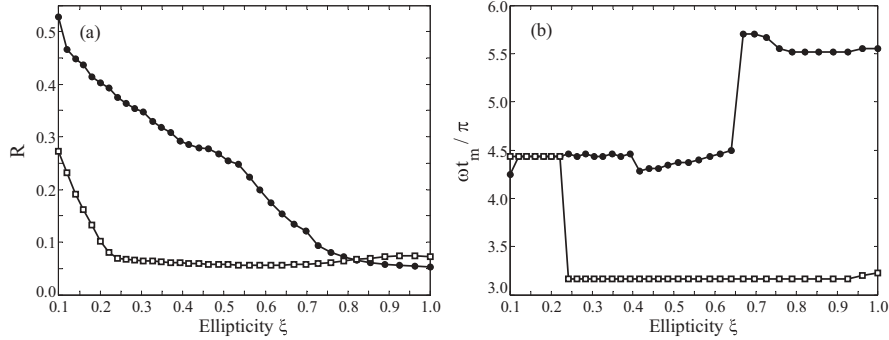
FIG. 9. (a) Maximum relative deviation R and (b) times t_m (in half-cycle units) of maximum deviation [Eq. (19)] as a function of the ellipticity of the laser pulse for the case of $\lambda = 800$ nm (open squares) and $\lambda = 400$ nm (solid circles). The laser pulse duration is $n_p = 3$ cycles, the peak intensity is 2×10^{14} W/cm^2, and the atom is H. The ensemble of trajectories included in this calculation consists of all the trajectories that emerge from the dominant, most intense central half cycle of the pulse, peaking at $\omega t / \pi = 3$.

The time instants t_m corresponding to R are plotted in Fig. 9(b). This figure clearly shows that the times of maximal relative deviation exhibit a profound threshold behavior for both wavelengths. For small ellipticities, the times of maximal relative deviation for both wavelengths are located roughly at the middle of the half cycle after the half cycle of the field where the classical ensemble was created by tunneling, indicating a return of the classical trajectories to the vicinity of the atomic potential. Then, above an ellipticity of 0.2, the time of maximal relative deviation for 800 nm changes to the cycle at which the trajectories of the ensemble are launched. If t_m is in the half cycle where the classical trajectories are launched, in accord with the discussion in Sec. IV, such deviations are ignored and it is assumed that the system satisfies the strict form of ET. More importantly, this drop in t_m coincides with the drop in R roughly below 0.1 [see Fig. 9(a)]. While R monotonically decreases, the threshold behavior of t_m clearly delimits the dynamics when the value of R is substantial or not. Equally, for the case of 400 nm t_m at around $\epsilon = 0.65$ exhibits a threshold behavior, now from the half cycle after the half cycle when the trajectories were launched to the last half cycle of the pulse. Again, in accord with the discussion in the preceding section, deviations at the end of the pulse are ignored and so it is assumed that the classical ensemble satisfies the strict form of the ET. Once again, this rapid change of the behavior of the time of the maximal relative deviation coincides with the ellipticity at which R decreases to a value below 0.1.

To check our conclusions on the validity of the semiclassical results obtained analyzing R and t_m, we compare momentum distributions obtained within the semiclassical model and by the TDSE. For comparison, we choose the cases when from our analysis we have an indication that the semiclassical results for 400 nm are valid and for the case when the semiclassical model at 800 nm fails. The comparison between the semiclassical
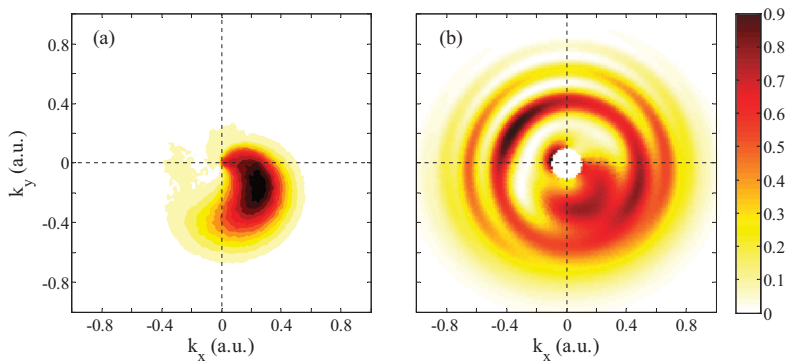

FIG. 10. (Color online) Comparison of the momentum distributions for the H atom at 400 nm for the ellipticity $\epsilon = 0.85$ obtained from (a) the semiclassical model and (b) the TDSE. The laser pulse duration is $n_p = 3$ cycles and the peak intensity is 2×10^{14} W/cm^2. The grid for the TDSE extends up to $X_{\max} = 400$ a.u., and the maximum angular momentum is $l_{\max} = 40$. The distributions are normalized to the peak value.
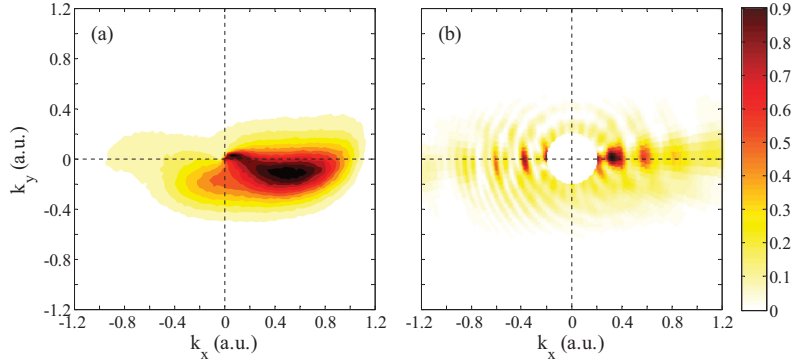
FIG. 11. (Color online) Comparison of the momentum distributions for the H atom at 800 nm for the ellipticity $\epsilon = 0.15$ obtained from (a) the semiclassical model and (b) the TDSE. The laser pulse duration is $n_p = 3$ cycles and the peak intensity is 2×10^{14} W/cm^2. The grid for the TDSE extends up to $X_{max} = 600$ a.u., and the maximum angular momentum is $l_{max} = 40$. The distributions are normalized to the peak value.

model and the TDSE for $\epsilon = 0.85$ at 400 nm and for $\epsilon = 0.15$ at 800 nm shown on Figs. 10 and 11, respectively, confirms these expectations. Namely, for $\epsilon = 0.85$ and $\lambda = 400$ nm, in accord with the analysis based on R and the corresponding time instant t_m, the semiclassical model should describe the quantum dynamics correctly. Indeed, comparing Figs. 10(a) and 10(b), we see that the overall rotation of the momentum distribution is qualitatively well reproduced by the semiclassical calculation. For $\epsilon = 0.15$ and $\lambda = 800$ nm, according to the analysis based on R and t_m (Fig. 9), we expect that the semiclassical model will not mimic the quantum results. This is confirmed in Fig. 11; the small overall rotation that the semiclassical model is pointing to is not present in the TDSE result, where the population is concentrated along the k_x axis. In cases of larger ellipticity and $\lambda = 800$ nm, the momentum distributions from the semiclassical model and the TSDE show excellent agreement, as illustrated in Fig. 12 (for

$\epsilon = 0.85$ and $\lambda = 800$ nm) and in accord with previous works of Refs. [26,28].

B. Wavelength dependence

Next, we consider the wavelength dependence, keeping all parameters of the laser pulse and the atomic target fixed; ellipticity $\epsilon = 0.5$ and intensity of 2×10^{14} W/cm^2. The maximal relative deviation R of Eq. (19), plotted in Fig. 13(a), monotonically decreases as a function of the wavelength, up to $\lambda \approx 600$ nm. From $\lambda = 600$ nm on, R slowly increases with wavelength, reaching a level of about 0.1 at $\lambda = 1600$ nm. The graph for the time of maximal relative deviation t_m [Fig. 13(b)] reveals an abrupt change in the dynamics as the wavelength is increased. First, until a wavelength around 600 nm t_m is in the half cycle after the half cycle where the classical trajectories were started, this, as in the previous subsection,
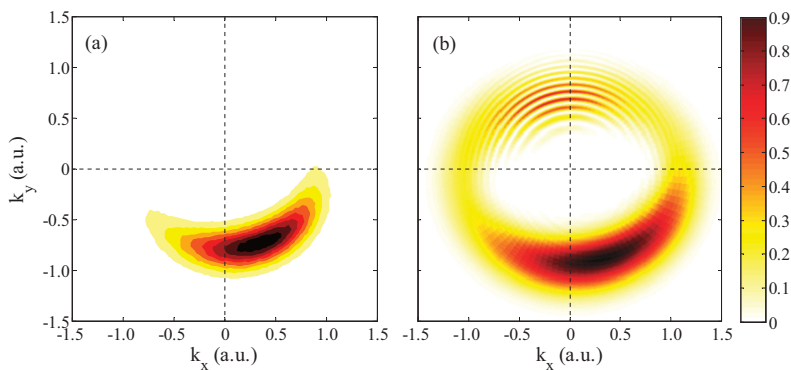

FIG. 12. (Color online) Comparison of the momentum distributions for the H atom at 800 nm for the ellipticity $\epsilon = 0.85$ obtained from (a) the semiclassical model and (b) the TDSE. The laser pulse duration is $n_p = 3$ cycles and the peak intensity is 2×10^{14} W/cm^2. The grid for the TDSE extends up to $X_{max} = 600$ a.u., and the maximum angular momentum is $l_{max} = 60$. The distributions are normalized to the peak value.
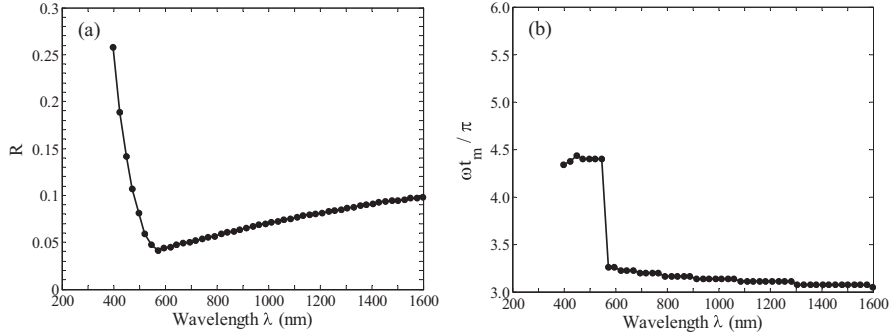
FIG. 13. (a) Maximum relative deviation R as a function of the wavelength and (b) times t_m (in units of half-cycle duration) of maximum relative deviation of ET as a function of wavelength. The laser pulse duration is $n_p = 3$ cycles, the ellipticity is $\epsilon = 0.5$, the peak intensity is 2×10^{14} W/cm², and the atom is H. The ensemble consists of classical trajectories stemming from the largest (central) half cycle of the laser pulse, peaking at $\omega t/\pi = 3$.

leads to a non-negligible value of R. For wavelengths roughly longer than 600 nm, t_m moves to the half cycle where the classical trajectories were launched. This is so because as the wavelength increases, the excursion of classical trajectories increases and they rapidly leave the region close to the origin. This again causes the force terms stemming from the potential to decrease rapidly, and therefore the deviation is most pronounced when the trajectories are launched.

As discussed previously, it is assumed that the deviations from the strict form of ET are correlating with the invalidity of the semiclassical model; therefore, for wavelengths equal to or larger then 600 nm, we expect that the results from the semiclassical model will be qualitatively similar to the results obtained from the TDSE. To test this, we consider as an example the case of $\lambda = 600$ nm in Fig. 14. As pointed out by our analysis, the case of 600 nm is at the edge of applicability of the semiclassical model from the perspective

of the deviation from the strict form of ET. More precisely, a few tens of nanometers before 600 nm, the time of maximum deviation t_m jumps; in this sense this case is at the edge of applicability. Indeed, from the comparison in Fig. 14 one sees that, qualitatively, the overall rotation in the momentum distribution is reproduced.

C. Intensity dependence

Finally, we consider the dependency of R on the laser pulse intensity, restraining ourselves to the case of 800 nm. In Fig. 15(a) the maximum relative deviation R of Eq. (19) is plotted as a function of intensity, keeping all other parameters of the three-cycle pulse fixed, wavelength of 800 nm and ellipticity $\epsilon = 0.5$. The intensity dependence in Fig. 15(a) is nonmonotonic and R exceeds 0.1 for the largest intensities considered. The nonmonotonic dependence of R on intensity
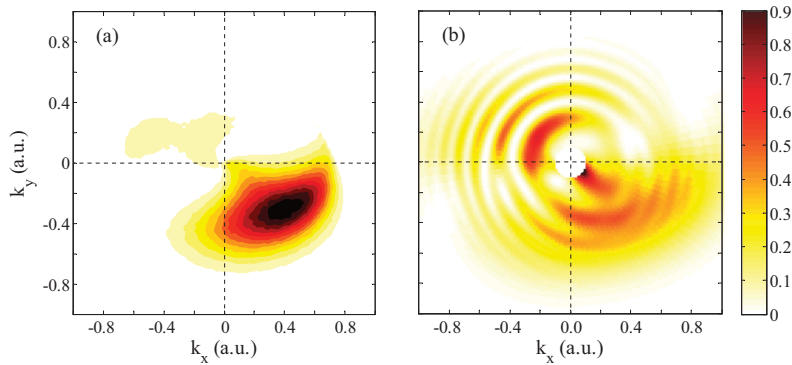

FIG. 14. (Color online) Comparison of the momentum distributions for the H atom at 600 nm obtained from (a) the semiclassical model and (b) the TDSE. The ellipticity of the pulse is $\epsilon = 0.5$, the laser pulse duration is $n_p = 3$ cycles, and the peak intensity is 2×10^{14} W/cm². The grid for the TDSE extends up to $X_{max} = 600$ a.u., and the maximum angular momentum is $l_{max} = 40$. The distributions are normalized to the peak value.
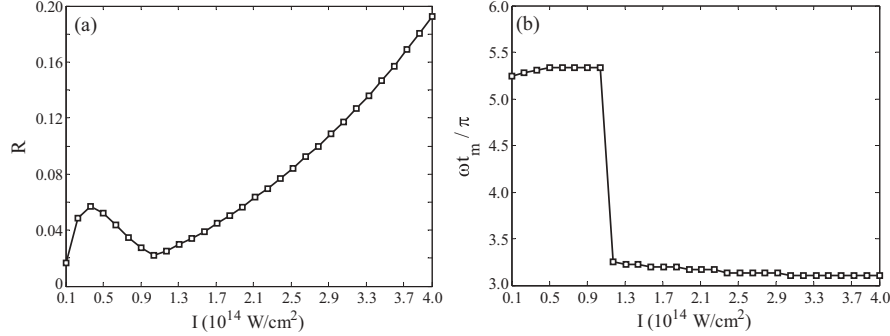
FIG. 15. (a) Maximum relative deviation R as a function of the intensity and (b) time (in units of half-cycle duration) of maximum deviation of ET as a function of intensity. The laser pulse duration is $n_p = 3$ cycles, the ellipticity is $\epsilon = 0.5$, the wavelength is 800 nm, and the atom is H. The ensemble consists of classical trajectories stemming from the largest, most intense half cycle of the pulse, peaking at $\omega t/\pi = 3$.

can be understood as follows. Normally we would expect that by decreasing intensity the classical trajectories will quickly move away from the origin, decreasing the force term from the atomic potential and thus decreasing the relative deviation. Although with the decrease of the intensity the excursion of the classical electron decreases and lower final momenta are populated, the large absolute distance of the trajectories from the atomic center is decisive for the decrease of the maximal relative deviation. Indeed, this is so for the region beginning from the highest intensities until the intensity of 1×10^{14} W/cm² [local minimum in Fig. 15(a)]. Decreasing the intensity further leads to a rise of the maximal relative deviation R, indicating that the excursion of the electronic trajectories becomes very small at the end of the pulse. However, after reaching maximum at 0.4×10^{14} W/cm², R drops again. The time t_m, plotted in Fig. 15(b) does not show a rapid change around that maximum, indicating that the dynamics stays the same. In fact at the lowest intensities considered here (below approximately 0.4×10^{14} W/cm²) the Keldysh parameter γ becomes larger than 2, suggesting the invalidity of the semiclassical model based on the static ionization rates.

At the local minimum of the curve in Fig. 15(a) (intensity 10^{14} W/cm²), the dynamics changes, since t_m in Fig. 15(b) drops from times in the last half cycle to the half cycle at which the classical trajectories are started. This is so because the tunnel exit point is closer to the origin, making the force terms of the potential larger; therefore, R is larger. Although R exceeds 0.1, the corresponding times t_m are located either in the first or in the last half cycle, so it appears that at $\lambda = 800$ nm variation in intensity will not lead to a qualitative difference between the semiclassical and the TDSE results.

VII. DEPENDENCE OF THE DEVIATION FROM THE STRICT FORM OF EHRENFEST'S THEOREM ON THE PARAMETERS OF THE ATOMIC TARGET

A. Ionization potential dependence

In Figs. 16(a) and 16(b) we give R and t_m the times of maximum relative deviation for some atomic species with

different ionization potentials for both $\lambda = 800$ nm and $\lambda = 400$ nm, respectively. The laser pulse duration is $n_p = 3$ cycles, the ellipticity is 0.5, and the intensity is 2×10^{14} W/cm². The semiclassical simulations are performed taking the static Stark shifts and effective potential that includes the induced dipole of the atomic ion [28] for all atomic species considered. To characterize the static Stark shifts and the induced dipole, we took the polarizabilities of the neutral atoms and atomic ions from Ref. [50]. The tunnel exit point is determined in parabolic coordinates [26,28].

Generally, the smaller the ionization potential, the larger is R, since the tunnel exit points ($\sim I_p/F$) for the classical ensemble of trajectories for weaker potentials are smaller, resulting in larger force terms from the atomic potential. This trend is evident in Fig. 16(a), especially for $\lambda = 800$ case. For the $\lambda = 400$ nm case, the dependence of R on I_p is not monotonic, partly because we have included the Stark shifts of the ionization potential and the induced dipole in the atomic potential, which vary nonmonotonically from one atom to the other [54]. Analyzing t_m, we find out that for $\lambda = 400$ nm, the results from the semiclassical model will be invalid for atomic species from Mg to Ar (there the t_m's are not located in the first and the last half cycle). In all other cases Fig. 16(b) suggests that the result from the semiclassical model give qualitatively correct predictions.

To isolate the dependency of the relative deviation on the ionization potential only, but also to show that at $\lambda = 800$ nm (with laser pulse duration of $n_p = 3$ cycles and ellipticity of 0.5), depending on the intensity, there will be ionization potentials for which the two-step semiclassical model will be invalid, we consider the case of an artificial hydrogen-like atom with no static Stark shift and no polarizability. Again, the tunnel exit point is determined in parabolic coordinates [26,28]. The maximum relative deviation R and the times of maximum relative deviation t_m for this case are plotted in Figs. 17(a) and 17(b), respectively. Two different intensities, 2.0×10^{14} (full curve) and 2.5×10^{13} W/cm² (dashed curve), are considered, and the calculations are performed up to the ionization potential that corresponds to the over-the-barrier ionization limit. From Fig. 17(a), we see that R is substantial
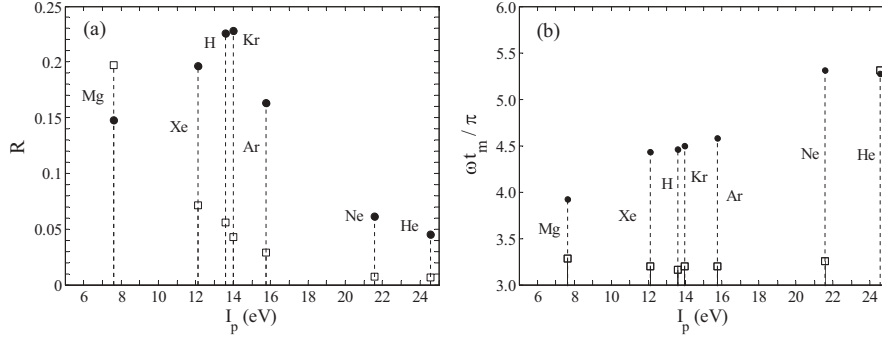
FIG. 16. Maximum relative deviation (a) and times (in units of half-cycle duration) (b) for different atomic species. The laser pulse duration is $n_p = 3$ cycles, ellipticity is 0.5, and the intensity is 2×10^{14} W/cm^2, the field peaks at $\omega t/\pi = 3$. Two different wavelengths are considered: $\lambda = 400$ nm (solid circles) and $\lambda = 800$ nm (open squares). The ensemble of classical trajectories consists of all the trajectories that emerge from the largest (central) half cycle of the pulse. We have included the static Stark shifts for the atomic species in question, as well as the induced dipole term in the effective atomic potential, taking polarizabilities from Ref. [50]

(larger than 0.1) for the lower intensity and for the smallest ionization potentials. The inspection of Fig. 17(b) reveals that for the lower intensity and for ionization potentials below approximately 11 eV the semiclassical model can be invalid, because in this case t_m occurs in the half cycle after the classical trajectories are ejected.

B. Potential with finite range

As a final dependence, we consider the range of the potential as the parameter. For this purpose, we consider the Yukawa potential $V_Y(r) = -\exp(-r/d)/r$ of range d. To isolate the influence of the potential range when propagating the classical ensemble, we assume that the classical ensemble is created by tunneling from the H atom (tunnel exit point is the same as in H) and that the classical ensemble moves

in $V_Y(r)$. To illustrate the influence of the range on the momentum distributions, we focus on the parameters used in Fig. 3: $\lambda = 400$ nm, laser pulse duration $n_p = 3$ cycles, ellipticity equal to 0.5, and intensity 2×10^{14} W/cm^2. For these parameters, the semiclassical model for H fails. In Fig. 18, momentum distributions corresponding to ranges decreasing from $d = 50$ to $d = 5$ are given. The momentum distribution in Fig. 18(a), corresponding to the range of $d = 50$, is almost indistinguishable from the result obtained for the pure Coulomb potential [Fig. 3(a)]. Decreasing the potential range, the momentum distribution smoothly changes into having the usual form (one smooth maximum in the fourth quadrant) [Fig. 18(d)]. The maximum relative deviation R and the corresponding times t_m are plotted in Figs. 19(a) and 19(b), respectively. When the range of the potential increases, R rises, reaching approximately $R = 0.2$. For $d = 5$, where the
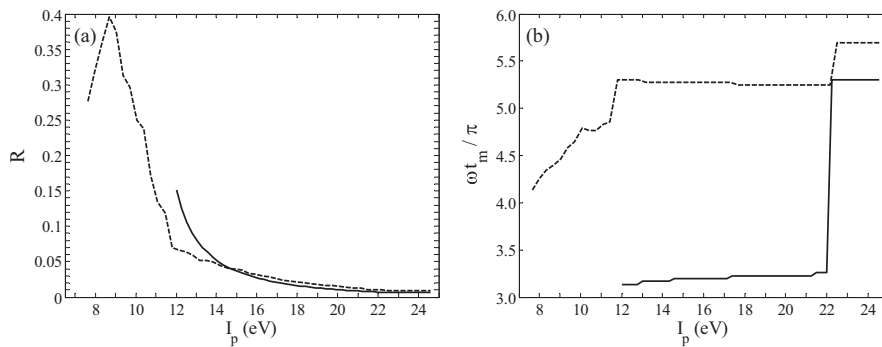

FIG. 17. (a) Maximum relative deviation and (b) times (in units of half-cycle duration) of maximum relative deviation as a function of the ionization potential for an artificial H-like atom with no static Stark shift and no polarizability. The pulse wavelength is $\lambda = 800$ nm, the laser pulse duration is $n_p = 3$ cycles, and the ellipticity is 0.5. The pulse peaks at $\omega t/\pi = 3$. Two intensities are considered: 2.0×10^{14} (full curve) and 2.5×10^{13} W/cm^2 (dashed curve). The smallest ionization potentials considered correspond to the case of over-the-barrier ionization for the particular intensity. The other pulse parameters are the same as in Fig. 16.
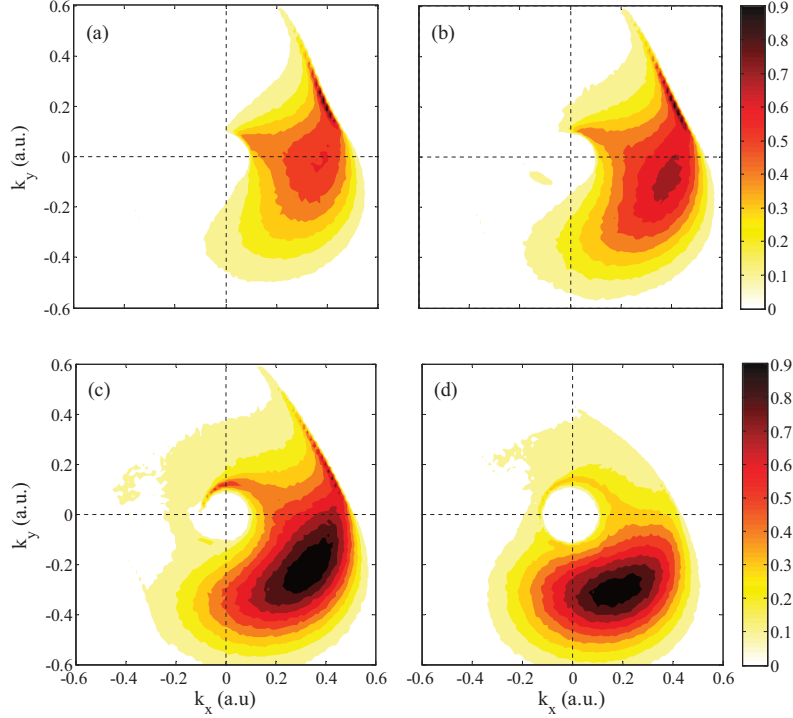
FIG. 18. (Color online) Momentum distributions in the cases of a Yukawa potential $[V_Y(r) = -\frac{\exp(-r/d)}{r}]$ with different range d: (a) $d = 50$, (b) $d = 20$, (c) $d = 10$, and (d) $d = 5$. The laser pulse duration is $n_p = 3$ cycles, the peak intensity is 2×10^{14} W/cm^2, the ellipticity of the pulse is $\epsilon = 0.5$, and the wavelength is $\lambda = 400$ nm.

momentum distribution has the usual form [Fig. 18(d)], R reaches approximately 0.1. For very short-ranged potentials ($d < 4$), the t_m's are located in the last half cycle, and then

for all larger ranges the t_m's are located in the half cycle subsequent to the half cycle where the classical trajectories were launched.
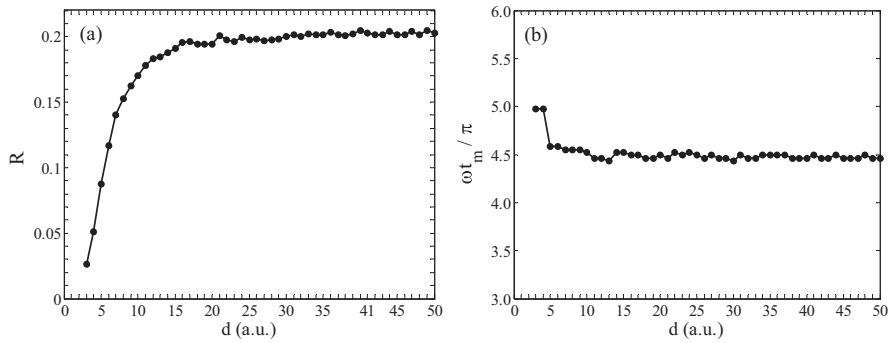
FIG. 19. Maximum relative deviation (a) and times (in units of half-cycle duration) (b) as a function of the Yukawa potential range d. The laser pulse duration is $n_p = 3$ cycles, the intensity is 2×10^{14} W/cm^2, the ellipticity of the pulse is $\epsilon = 0.5$, the pulse peaks at $\omega t/\pi = 3$, and the wavelength is $\lambda = 400$ nm. The ensemble of classical trajectories consists of all the trajectories that emerge from the largest (central) half cycle of the pulse.

EHRENFEST'S THEOREM AND THE VALIDITY OF THE . . .

VIII. SUMMARY AND CONCLUSIONS

In summary, by comparison with the accurate numerical solution of the TDSE, we have investigated the applicability of the two-step semiclassical model widely used for the description of strong-field ionization. For an ensemble of classical trajectories we have introduced a measure for the deviation from the strict form of ET. This measure is the relative deviation between the force at the average position of the classical ensemble and the average of the force [Eq. (17)]. We have found a correlation between the invalidity of the two-step model and the deviation from the strict form of ET. We showed that even substantial deviations from the strict form of ET at times close the electron ejection, as well as at the end of the pulse, do not affect the agreement between the solution of the TDSE and the two-step model. However, a substantial deviation from the strict form of ET at any other time should be considered as a manifestation of inapplicability of the two-step model, at least for the adequate description of the momentum distributions.

Specifically, we showed that if the relative deviation exceeds the level of $\approx 10\%$, the deviation from the strict form of ET is substantial, and the semiclassical model does not reflect the solution of the TDSE. We have calculated the maximal relative deviations and the times of these deviations as a function of the parameters of the laser pulse and of the atomic target: ellipticity, wavelength, intensity, ionization potential, and the potential range. By doing so, we have explored the trends of the applicability of the two-step semiclassical model. For ellipticities where rescattering is suppressed, one can expect better agreement between the two-step model and the TDSE result with increasing ellipticity, wavelength, and ionization potential, as well as with decreasing of the potential range. More precisely, for the H atom, a peak intensity of 2.0×10^{14} W/cm^2, and $\lambda = 400$ nm, the two-step model is inapplicable for the ellipticities $\epsilon < 0.65$, whereas at a wavelength of 800 nm and the same intensity the model is valid already for $\epsilon > 0.2$. For the same intensity, but for ellipticity $\epsilon = 0.5$ the semiclassical model is applicable for H at wavelengths greater than 600 nm. A similar criterion for the intensity dependence of the applicability range of the two-step model cannot be formulated, since this dependence is more complex. In addition to H, we investigated the applicability of the two-step model for the following atomic targets: Mg, Xe, Kr, Ar, Ne, and He, taking into account the corresponding Stark shifts of the initial states and polarization-induced dipole potentials as in [26–28]. We showed that for 400 nm, 2.0×10^{14} W/cm^2, and $\epsilon = 0.5$ the results of the two-step model will be valid only for Ne and He, whereas for 800 nm and the same values of intensity and ellipticity the model is applicable to all of the considered atomic species.

The results presented here can be used as a guideline for the applicability of the two-step semiclassical model for strong-field ionization, depending on the parameters of the laser pulse and the target atom.

[1] W. Becker, F. Grasbon, R. Kopold, D. B. Milošević, G. G. Paulus, and H. Walther, Adv. At. Mol. Opt. Phys. **48**, 35 (2002).

[2] D. B. Milošević and F. Ehlotzky, Adv. At. Mol. Opt. Phys. **49**, 373 (2003).

[3] A. Becker and F. H. M. Faisal, J. Phys. B **38**, R1 (2005).

[4] C. Figueira de Morisson Faria and X. Liu, J. Mod. Opt. **58**, 1076 (2011).

[5] L. V. Keldysh, Zh. Eksp. Teor. Fiz. **47**, 1945 (1964) [Sov. Phys. JETP **20**, 1307 (1965)].

[6] F. H. M. Faisal, J. Phys. B **6**, L89 (1973).

[7] H. R. Reiss, Phys. Rev. A **22**, 1786 (1980).

[8] H. B. van Linden van den Heuvell and H. G. Muller, in *Multiphoton Processes*, edited by S. J. Smith and P. L. Knight (Cambridge University Press, Cambridge, UK, 1988).

[9] T. F. Gallagher, Phys. Rev. Lett. **61**, 2304 (1988).

[10] P. B. Corkum, N. H. Burnett, and F. Brunel, Phys. Rev. Lett. **62**, 1259 (1989).

[11] K. C. Kulander, K. J. Schafer, and J. L. Krause, in *Super-Intense Laser-Atom Physics*, edited by B. Pireaux, A. L'Hullier, and K. Rzazewski (Plenum, New York, 1993).

[12] P. B. Corkum, Phys. Rev. Lett. **71**, 1994 (1993).

[13] G. G. Paulus, W. Nicklich, H. Xu, P. Lambropoulos, and H. Walther, Phys. Rev. Lett. **72**, 2851 (1994).

[14] J. L. Krause, K. J. Schafer, and K. C. Kulander, Phys. Rev. Lett. **68**, 3535 (1992).

[15] M. Lewenstein, Ph. Balcou, M. Yu. Ivanov, A. L'Huillier, and P. B. Corkum, Phys. Rev. A **49**, 2117 (1994).

[16] G. G. Paulus, W. Becker, W. Nicklich, and H. Walther, J. Phys. B **27**, L703 (1994).

[17] C. Figueira de Morisson Faria and W. Becker, Laser Phys. **13**, 1196 (2003).

[18] D. B. Milošević and W. Becker, Phys. Rev. A **68**, 065401 (2003).

[19] T. Brabec, M. Yu. Ivanov, and P. B. Corkum, Phys. Rev. A **54**, R2551 (1996).

[20] W. Quan, Z. Lin, M. Wu, H. Kang, H. Liu, X. Liu, J. Chen, J. Liu, X. T. He, S. G. Chen *et al.*, Phys. Rev. Lett. **103**, 093001 (2009).

[21] C. I. Blaga, F. Catoire, P. Colosimo, G. G. Paulus, H. G. Muller, P. Agostini, and L. F. DiMauro, Nat. Phys. **5**, 335 (2009).

[22] C. Liu and K. Z. Hatsagortsyan, Phys. Rev. Lett. **105**, 113003 (2010).

[23] Tian-Min Yan, S. V. Popruzhenko, M. J. J. Vrakking, and D. Bauer, Phys. Rev. Lett. **105**, 253002 (2010).

[24] A. Kästner, U. Saalmann, and J. M. Rost, Phys. Rev. Lett. **108**, 033201 (2012).

[25] C. Lemell, K. I. Dimitriou, X. M. Tong, S. Nagele, D. V. Kartashov, J. Burgdörfer, and S. Gräfe, Phys. Rev. A **85**, 011403(R) (2012).

[26] A. N. Pfeiffer, C. Cirelli, M. Smolarski, D. Dimitrovski, M. Abu-Samha, L. B. Madsen, and U. Keller, Nat. Phys. **8**, 76 (2012).

[27] J. Maurer, D. Dimitrovski, L. Christensen, L. B. Madsen, and H. Stapelfeldt, Phys. Rev. Lett. **109**, 123001 (2012).

[28] N. I. Shvetsov-Shilovski, D. Dimitrovski, and L. B. Madsen, Phys. Rev. A **85**, 023428 (2012).

[29] N. I. Shvetsov-Shilovski, S. P. Goreslavski, S. V. Popruzhenko, and W. Becker, Phys. Rev. A **77**, 063405 (2008).

[30] X. Wang and J. H. Eberly, Phys. Rev. Lett. **103**, 103007 (2009).

[31] X. L. Hao, G. Q. Wang, X. Y. Jia, W. D. Li, J. Liu, and J. Chen, Phys. Rev. A **80**, 023408 (2009).

[32] F. Mauger, C. Chandre, and T. Uzer, Phys. Rev. Lett. **105**, 083002 (2010).

[33] A. Messiah, *Quantum Mechanics* (Wiley, New York, 1966).

[34] R. Abrines and I. C. Percival, Proc. Phys. Soc. London **88**, 861 (1966).

[35] J. P. Hansen, J. Lu, L. B. Madsen, and H. M. Nilsen, Phys. Rev. A **64**, 033418 (2001).

[36] J. S. Cohen, Phys. Rev. A **64**, 043412 (2001).

[37] B. Hu, J. Liu, and S. Chen, Phys. Lett. A **236**, 533 (1997).

[38] A. N. Pfeiffer, C. Cirelli, A. S. Landsman, M. Smolarski, D. Dimitrovski, L. B. Madsen, and U. Keller, Phys. Rev. Lett. **109**, 083002 (2012).

[39] L. Holmegaard, J. L. Hansen, L. Kalhøj, S. L. Kragh, H. Stapelfeldt, F. Filsinger, J. Küpper, G. Meijer, D. Dimitrovski, M. Abu-samha, C. P. J. Martiny, and L. B. Madsen, Nat. Phys. **6**, 428 (2010).

[40] D. Dimitrovski, C. P. J. Martiny, and L. B. Madsen, Phys. Rev. A **82**, 053404 (2010).

[41] A. M. Perelomov, N. B. Popov, and M. V. Terent'ev, Zh. Eksp. Teor. Fiz. **50**, 1393 (1966) [Sov. Phys. JETP **23**, 924 (1966)].

[42] M. V. Ammosov, N. B. Delone, and V. P. Krainov, Zh. Eksp. Teor. Fiz. **91**, 2008 (1986) [Sov. Phys. JETP **64**, 1191 (1986)].

[43] N. B. Delone and V. P. Krainov, J. Opt. Soc. Am. B **8**, 1207 (1991).

[44] W. H. Press, S. A. Teukolsky, W. T. Vetterling, and B. P. Flannery, *Numerical Recipes in Fortran 77: The Art of Scientific Computing*, 2nd ed. (Cambridge University Press, Cambridge, 1992).

[45] T. Nubbemeyer, K. Gorling, A. Saenz, U. Eichmann, and W. Sandner, Phys. Rev. Lett. **101**, 233001 (2008).

[46] N. I. Shvetsov-Shilovski, S. P. Goreslavski, S. V. Popruzhenko, and W. Becker, Laser Phys. **19**, 1550 (2009).

[47] L. E. Ballentine, Y. Yang, and J. P. Zibin, Phys. Rev. A **50**, 2854 (1994).

[48] T. K. Kjeldsen, L. A. A. Nikolopoulos, and L. B. Madsen, Phys. Rev. A **75**, 063427 (2007).

[49] C. P. J. Martiny, M. Abu-samha, and L. B. Madsen, J. Phys. B **42**, 161001 (2009).

[50] The polarizabilities for Xe$^+$ and Kr$^+$ were taken from Ref. [51], the polarizability of Kr was taken from Ref. [52], and the polarizability of Ne$^+$ was taken from Ref. [53]. All other polarizabilities for the atoms considered in this paper were taken from Ref. [54].

[51] V. P. Shevelko and A. V. Vinogradov, Phys. Scr. **19**, 275 (1979).

[52] U. Hohm and K. Kerl, Mol. Phys. **69**, 803 (1990); **69**, 819 (1990).

[53] NIST Standard Reference Database 101. Computational Chemistry Comparison and Benchmark Database, calculation using density-functional theory, B3LYP, aug-cc-pVTZ.

[54] J. Mitroy, M. S. Safronova, and C. W. Clark, J. Phys. B **43**, 202001 (2010).

8.9 *Semiclassical two-step model with quantum input*
PHYSICAL REVIEW A **100**, 053411 (2019)

**Semiclassical two-step model with quantum input: Quantum-classical approach
to strong-field ionization**

N. I. Shvetsov-Shilovski ●* and M. Lein ●
Institut für Theoretische Physik, Leibniz Universität Hannover, D-30167 Hannover, Germany

We present a mixed quantum-classical approach to strong-field ionization—a semiclassical two-step model with quantum input. In this model the initial conditions for classical trajectories that simulate an electron wave packet after ionization are determined by the exact quantum dynamics. As a result, the model allows to overcome deficiencies of standard semiclassical approaches in describing the ionization step. The comparison with the exact numerical solution of the time-dependent Schrödinger equation shows that for ionization of a one-dimensional atom the model yields quantitative agreement with the quantum result. This applies both to the width of the photoelectron momentum distribution and to the interference structure.

I. INTRODUCTION

Strong-field physics is a fascinating field of research resulting from remarkable progress in laser technologies during the last three decades. The interaction of strong laser radiation with atoms and molecules leads to many highly nonlinear phenomena, including above-threshold ionization (ATI) along with the formation of the plateau in the energy spectrum of the photoelectrons (high-order ATI), generation of high-order harmonics of the incident field (HHG), and nonsequential double ionization (NSDI) (see, e.g., Refs. [1–5] for reviews). The main theoretical approaches used to study all these phenomena are based on the strong-field approximation (SFA) [6–8], direct numerical solution of the time-dependent Schrödinger equation (TDSE) (see, e.g, Refs. [9–14] and references therein), and the semiclassical models.

The semiclassical models apply classical mechanics to describe the motion of an electron after it has been released from an atom or molecule by a strong laser field. The most widely known examples of the semiclassical approaches are the two-step [15–17] and the three-step [18,19] models. The two-step model corresponds to the following picture of the ionization process. In the first step an electron is promoted into the continuum, typically by tunneling ionization [20–22]. In the second step the electron moves in the laser field towards a detector along a classical trajectory. In addition to these two steps, the three-step model involves the interaction of the returning electron with the parent ion. Accounting for this interaction allows the three-step model to qualitatively describe high-order ATI, HHG, and NSDI.

The semiclassical approaches have important advantages. First, the trajectory-based models, including those that take into account both the laser field and the ionic potential, are often computationally simpler than the numerical solution of the TDSE. What is even more important, the analysis of the

classical trajectories helps to understand the physical picture of the strong-field phenomenon under study.

In order to calculate the classical trajectory, it is necessary to specify the corresponding initial conditions, i.e., the starting point and the initial velocity of the electron. To obtain the former, i.e., the tunnel exit point, the separation of the tunneling problem for the Coulomb potential in parabolic coordinates can be used (see, e.g., Ref. [20]). In trajectory-based models it is often assumed that the electron starts with zero initial velocity along the laser field. Simultaneously, it can have a nonzero initial velocity in the direction perpendicular to the field. The initial transverse momenta, as well as the instants of ionization, are usually distributed in accord with the static ionization rate [23] with the field strength equal to the instantaneous field at the time of ionization.

In the standard formulation, the trajectory models used in strong-field physics are not able to describe quantum interference effects. Accounting for interference effects in trajectory-based simulations has attracted considerable interest (see, e.g., Refs. [24–27]). The recently developed quantum trajectory Monte Carlo (QTMC) [28] and semiclassical two-step (SCTS) models [29] describe interference structures in photoelectron momentum distributions of the ATI process. These models assign a certain phase to each classical trajectory, and the corresponding contributions of all the trajectories leading to a given asymptotic (final) momentum are added coherently. The QTMC model accounts for the Coulomb potential within the semiclassical perturbation theory. In contrast to this, in the SCTS model the phase associated with every trajectory is obtained using the semiclassical expression for the matrix element of the quantum-mechanical propagator (see Ref. [30]). Therefore, the SCTS model accounts for the binding potential beyond the semiclassical perturbation theory. This explains why for identical initial conditions after the ionization step the SCTS model shows closer agreement with solution of the TDSE than the QTMC model (see Ref. [29]).

The analysis of the photoelectron momentum distributions and energy spectra calculated within both the QTMC and the

---

SCTS models showed that the ATI peaks are qualitatively reproduced by the semiclassical approaches [29]. However, the semiclassical approximation does not quantitatively reproduce the amplitude of the oscillations. The photoelectron spectra calculated within the semiclassical models fall off too rapidly for energies exceeding U_p, where $U_p = F_0^2/4\omega^2$ is the ponderomotive energy, i.e., the cycle-averaged quiver energy of a free electron in an electromagnetic field (atomic units are used throughout the paper unless indicated otherwise). Here, F_0 and ω are the amplitude and the frequency of the field, respectively. This deficiency is closely related to the fact that the initial conditions usually employed in semiclassical models provide too few trajectories with large longitudinal momenta [29].

Recently several approaches to improving the quality of the initial conditions in semiclassical models have been proposed. The simplest method is to distribute the initial conditions for electron trajectories using the SFA formulas (see, e.g., Refs. [31–36]). We note that this method dates back to Refs. [37,38]. In most cases it leads to closer agreement with the TDSE. However, to the best of our knowledge, the validity of the usage of the SFA expressions in trajectory-based simulations has not been systematically analyzed so far. In this paper we consider an alternative approach: the combination of the semiclassical models with direct numerical solution of the TDSE.

A significant step in this direction has been taken with the development of the backpropagation method (see Refs. [39,40]). In this method, the wave packet of the outgoing electron obtained from the TDSE is transformed into classical trajectories. These trajectories are then propagated backwards in time, which makes it possible to retrieve the information about the tunnel exit point and the initial electron velocity. Various approximations to the distributions of the starting points and the initial velocities were analyzed by choosing different criteria to stop the backpropagating trajectories [40,41]. However, the backpropagation method requires the numerical solution of the TDSE up to some point in time after the end of the laser pulse *in the whole space*. This restricts its applicability in the case of computationally difficult strong-field problems.

A promising approach would be a combination of the SCTS model with extended virtual detector theory (EVDT) [42,43]. For the first time the concept of a virtual detector (VD) was proposed in Ref. [44] as a method for calculating momentum distributions from the time-dependent wave function. The EVDT approach combines the VD method with semiclassical simulations. The EVDT employs a network of virtual detectors that encloses an atom interacting with the external laser field. Each detector detects the wave function $\psi(\vec{r}, t) = A(\vec{r}, t) \exp[i\phi(\vec{r}, t)]$ obtained by solving the TDSE and generates a classical trajectory at the same position with the initial momentum $\vec{k}$ determined from the gradient of the phase, $\vec{k}(\vec{r}_d, t) \equiv \nabla \cdot \phi(\vec{r}_d, t) = \vec{j}(\vec{r}_d, t)/|A(\vec{r}_d, t)|^2$. Here $\vec{r}_d$ is the position of a virtual detector and $\vec{j}(\vec{r}_d, t)$ is the probability flux at this position. The latter determines the relative weight of the generated trajectory. The subsequent motion of an electron is found from the solution of Newton's equations. The final photoelectron momentum distribution is obtained by summing over all classical trajectories with their relative

weights. It should be stressed that EVDT solves the TDSE only within some restricted region centered at the atom. A network of virtual detectors is placed at the boundary of this region. This reduces the computational load of numerically difficult strong-field problems. Recently the VD approach was used for study of tunneling times [45] and longitudinal momentum distributions [46] in strong-field ionization.

Leaving the combination of the SCTS with the EVDT for future studies, in this paper we formulate an alternative quantum-classical approach: the semiclassical two-step model with quantum input (SCTSQI). To this end, we combine the SCTS model with initial conditions obtained from TDSE solutions using Gabor transforms. For simplicity, we consider ionization of a one-dimensional (1D) atom. The generalization to the real three-dimensional case is straightforward. The benefit of the 1D model, however, is that potential deficiencies of trajectory models are exposed better and, therefore, it makes the comparison with the fully quantum simulations more valuable.

The paper is organized as follows. In Sec. II we sketch our approach to solve the TDSE, we briefly review the SCTS model, and we formulate our SCTSQI approach. In Sec. III we apply our model to the ionization of a 1D model atom and present comparison with the TDSE results. The conclusions and outlook are given in Sec. IV.

II. SEMICLASSICAL TWO-STEP MODEL WITH QUANTUM INPUT

We benchmark our semiclassical model against the results obtained by direct numerical solution of the 1D TDSE and by using the SCTS model. For this reason, before formulating the SCTSQI model and discussing its outcomes, we briefly review the technique used to solve the TDSE and sketch the SCTS model. We define a few-cycle laser pulse linearly polarized along the x axis in terms of a vector potential:

$$\vec{A} = (-1)^{n+1} \frac{F_0}{\omega} \sin^2\left(\frac{\omega t}{2n}\right) \sin(\omega t + \varphi)\vec{e}_x. \quad (1)$$

Here n is the number of cycles within the pulse, φ is the carrier envelope phase, and $\vec{e}_x$ is a unit vector. The laser pulse is present between $t = 0$ and $t_f = (2\pi/\omega)n$, and its electric field $\vec{F}$ can be obtained from Eq. (1) by $\vec{F} = -\frac{d\vec{A}}{dt}$.

A. Solution of the one-dimensional time-dependent Schrödinger equation

In the velocity gauge, the 1D TDSE for an electron in the laser pulse reads as

$$i\frac{\partial}{\partial t}\Psi(x, t) = \left\{\frac{1}{2}\left(-i\frac{\partial}{\partial x} + A_x(t)\right)^2 + V(x)\right\}\Psi(x, t), \quad (2)$$

where $\Psi(x, t)$ is the time-dependent wave function in coordinate space, and a soft-core potential $V(x) = -\frac{1}{\sqrt{x^2+a^2}}$ is used, with $a = 1$ as in Ref. [47].

In the absence of the laser pulse, the 1D system satisfies the time-independent Schrödinger equation:

$$\left\{-\frac{1}{2}\frac{d^2}{dx^2} + V(x)\right\}\Psi(x) = E\Psi(x). \quad (3)$$

We solve Eq. (3) on a grid and approximate the second derivative by the well-known three-point formula. For our simulations we use a box centered at the origin and extending to $\pm x_{\max}$, i.e., $x \in [-x_{\max}, x_{\max}]$. Typically, our grid extends up to $x_{\max} = 500$ a.u. and consists of 8192 points, which corresponds to the grid spacing $dx \approx 0.1221$ a.u. The energy eigenvalues E_n and the corresponding eigenfunctions $\Psi_n(x)$ are found by a diagonalization routine designed for sparse matrices [48]. For the chosen value of a we find the ground-state energy $E_0 = -0.6698$ a.u. This value, as well as the energies of other lowest-energy bound states, coincides with the results of Ref. [47].

We solve Eq. (2) using the split-operator method [49] with the time step $\Delta t = 0.0734$ a.u. Unphysical reflections of the wave function from the grid boundary are prevented by using absorbing boundaries. More specifically, in the region $|x| \geqslant x_b$ we multiply the wave function by a mask

$$M(x) = \cos^{1/6}\left[\frac{\pi(|x| - x_b)}{2(x_{\max} - x_b)}\right]. \qquad (4)$$

Here we assume that the internal boundaries of the absorbing regions correspond to $x = \pm x_b$ (we use $x_b = 3x_{\max}/4$). This ensures that the part of the wave function in the mask region is absorbed without an effect on the inner part $|x| < x_b$. We calculate the photoelectron momentum distributions using the mask method (see Ref. [50]).

B. Semiclassical two-step model

In our semiclassical simulations the trajectory $\vec{r}(t)$ and momentum $\vec{p}(t)$ of an electron are calculated treating the electric field of the pulse $\vec{F}(t)$ and the ionic potential $V(\vec{r}, t)$ on equal footing:

$$\frac{d^2\vec{r}}{dt^2} = -\vec{F}(t) - \vec{\nabla}V(\vec{r}, t). \qquad (5)$$

In the SCTS model, every trajectory is associated with the phase of the matrix element of the semiclassical propagator [30]. For an arbitrary effective potential $V(\vec{r}, t)$ the SCTS phase reads as

$$\Phi(t_0, \vec{v}_0) = -\vec{v}_0 \cdot \vec{r}(t_0) + I_p t_0$$
$$- \int_{t_0}^{\infty} dt \left\{ \frac{p^2(t)}{2} + V[\vec{r}(t)] - \vec{r}(t) \cdot \vec{\nabla}V[\vec{r}(t)] \right\}, \qquad (6)$$

where t_0 is the ionization time, and $\vec{r}(t_0)$ and $\vec{v}_0$ are the initial electron position and velocity of an electron, respectively.

We solve Newton's equations of motion (5), in order to find the final (asymptotic) momenta of all the trajectories, and bin them in cells in momentum space according to these final momenta. If the quantum interference is taken into account, a large number of classical trajectories is needed in order to achieve convergence of electron momentum distributions. Different approaches of sampling the initial conditions can be used. In one possible approach the initial conditions, i.e., the ionization times t_0^j and transverse initial velocities $\vec{v}_{0,\perp}^j$ ($j = 1, \ldots, n_p$) of the ensemble consisting of n_p trajectories are distributed randomly, or, equivalently, a uniform grid in the $(t_0, \vec{v}_0)$ space is used. The weight of each trajectory is

determined by the corresponding tunneling probability. The latter is given by the formula for the static ionization rate [23]:

$$w(t_0, v_{0,\perp}) \sim \exp\left(-\frac{2(2I_p)^{3/2}}{3F(t_0)}\right)\exp\left(-\frac{\kappa v_{0,\perp}^2}{F(t_0)}\right), \qquad (7)$$

where $\vec{v}_{0,\perp}$ is the initial electron velocity in the direction perpendicular to the instantaneous laser field $\vec{F}(t_0)$ at the time of ionization. Here it is assumed that the electron emerges at the tunnel exit from the potential barrier formed by the instantaneous field and the ionic potential with zero initial velocity along the laser field: $\vec{v}_{0,\parallel} = 0$. Indeed, in the tunneling picture the electron velocity in the direction of tunneling must be equal to zero at the turning point. However, the tunneling makes no restriction on the perpendicular velocity. This is supported by the tunneling theory (see Ref. [20]). The contributions of the $n_{\vec{k}}$ trajectories that reach the same bin centered at a given final momentum $\vec{k}$ are added coherently. Therefore, the ionization probability is given by

$$R(\vec{k}) = \left| \sum_{j=1}^{n_{\vec{k}}} \sqrt{w(t_0^j, \vec{v}_{0,\perp}^j)} \exp\left[i\Phi(t_0^j, \vec{v}_{0,\perp}^j)\right] \right|^2. \qquad (8)$$

Alternatively, we can take into account the weight of a given trajectory before the solution of Newton's equations, i.e., already at the sampling stage. To this end, we distribute the sets of initial conditions $(t_0^j, \vec{v}_{0,\perp}^j)$ in accord with the square root of the tunneling probability (see Ref. [29] for details). We refer to this implementation of the SCTS model as the importance sampling implementation. We note that a similar approach is widely used in Monte Carlo integration (see Ref. [51]). If the trajectories are selected by importance sampling, the ionization probability in the SCTS model is calculated as

$$R(\vec{k}) = \left| \sum_{j=1}^{n_{\vec{k}}} \exp\left[i\Phi(t_0^j, \vec{v}_0^j)\right] \right|^2. \qquad (9)$$

For some laser parameters the importance sampling approach can significantly decrease the computational cost of the SCTS model. In the present work we use the important sampling implementation of the SCTS model. However, in our SCTSQI model we employ the first approach with random distribution of the initial conditions (see Sec. II B).

If the potential $V(\vec{r}, t)$ is set to the 1D soft-core potential $V(x) = -1/\sqrt{x^2 + a^2}$, the equation of motion (5) and the expression for the SCTS phase (6) reads as

$$\frac{d^2x}{dt^2} = -F_x(t) - \frac{x}{(x^2 + a^2)^{3/2}}, \qquad (10)$$

and, choosing the initial velocity as zero, we have the phase

$$\Phi(t_0, \vec{v}_0)$$
$$= I_p t_0 - \int_{t_0}^{\infty} dt \left\{ \frac{v_x^2(t)}{2} - \frac{x^2}{(x^2 + a^2)^{3/2}} - \frac{1}{\sqrt{x^2 + a^2}} \right\} dt. \qquad (11)$$

In the 1D case the ionization rate (7) is replaced by

$$w(t_0) \sim \exp\left(-\frac{2(2|E_0|)^{3/2}}{3F(t_0)}\right), \qquad (12)$$

where $E_0 = -0.6698$ a.u. is the ground-state energy in the potential $V(x)$.

We integrate the equation of motion numerically up to $t = t_f$ and find the final electron momentum k_x from its momentum $p_x(t_f)$ and position $x(t_f)$ at the end of the laser pulse. To this end, the energy conservation law can be used. Since an unbound classical electron cannot change the direction of its motion at $t \geqslant t_f$, the sign of the k_x coincides with that of $p_x(t_f)$.

In order to accomplish the formulation of the SCTS model for the 1D case, we need to calculate the postpulse phase, i.e., the contribution to the phase (11) accumulated in the asymptotic interval $[t_f, \infty]$. Indeed the phase of Eq. (11) can be decomposed as

$$\Phi(t_0, \vec{v}_0)$$
$$= I_p t_0 - \int_{t_0}^{t_f} dt \left\{ \frac{v_x^2(t)}{2} - \frac{x^2}{(x^2 + a^2)^{3/2}} - \frac{1}{\sqrt{x^2 + a^2}} \right\}$$
$$+ \Phi_f^V, \qquad (13)$$

where the postpulse phase Φ_f^V reads

$$\Phi_f^V(t_f) = -\int_{t_f}^{\infty} \left(E - \frac{x^2(t)}{[x^2(t) + a^2]^{3/2}} \right) dt \qquad (14)$$

with total energy E. As in Ref. [29], we separate the phase (14) into parts with time-independent and time-dependent integrand. The first part yields the linearly divergent contribution

$$\lim_{t \to \infty} (t_f - t)E \qquad (15)$$

that is to be disregarded, since it results in the zero phase difference for the trajectories leading to the same momentum cell. Therefore, the postpulse phase is determined by the time-dependent contribution

$$\tilde{\Phi}_f^V = \int_{t_f}^{\infty} \frac{x^2(t)}{[x^2(t) + a^2]^{3/2}} dt. \qquad (16)$$

Although the integral (16) diverges, we can isolate the divergent part as follows:

$$\tilde{\Phi}_f^V = \int_{t_f}^{\infty} \left[\frac{x^2}{(x^2 + a^2)^{3/2}} - \frac{2Et^2}{(2Et^2 + a^2)^{3/2}} \right] dt$$
$$+ \int_{t_f}^{\infty} \frac{2Et^2}{(2Et^2 + a^2)^{3/2}} dt. \qquad (17)$$

The divergent contribution, i.e., the second term of Eq. (17), depends only on the electron energy E and parameter a and, therefore, is equal for all the trajectories leading to a given bin on the p_x axis. Since we are interested in the relative phases of the interfering trajectories, this common divergent part can be omitted, and the postpulse phase can be calculated as

$$\tilde{\Phi}_f^V = \int_{t_f}^{\infty} \left[\frac{x^2}{(x^2 + a^2)^{3/2}} - \frac{2Et^2}{(2Et^2 + a^2)^{3/2}} \right] dt. \qquad (18)$$

The integral in Eq. (18) converges and can be easily calculated numerically. It depends on the electron position $x(t_f)$ and velocity $v_x(t_f)$ at the end of the pulse. In practice, we calculate this integral on a grid in the $(x(t_f), v_x(t_f))$ plane and use bilinear interpolation, in order to find its values for $x(t_f)$ and $v_x(t_f)$ that correspond to every electron trajectory.

C. Semiclassical two-step model with quantum input

Combination of the exact solution of the TDSE with a trajectory-based model is not a simple task. In order to calculate a classical trajectory, both the starting point and the initial velocity are needed. However, in accord with Heisenberg's uncertainty principle, there is a fundamental limit to the precision with which canonically conjugate variables such as position and momentum can be known. Information about *both* the position and momentum of a quantum particle can be obtained using a position-momentum quasiprobability distribution, e.g., the Wigner function or Husimi distribution (see, e.g., Ref. [52] for a textbook treatment). Here we employ the Gabor transformation [53], which is widely used for the analysis of the HHG and ATI (see, e.g., Refs. [54–57]). The Gabor transformation of a function $\tilde{\Psi}(x, t)$ near the point x_0 is defined by

$$G(x_0, p_x, t) = \frac{1}{\sqrt{2\pi}} \int_{-\infty}^{\infty} \tilde{\Psi}(x', t) \exp\left[-\frac{(x' - x_0)^2}{2\delta_0^2}\right]$$
$$\times \exp(-ip_x x') dx', \qquad (19)$$

where the exponential factor $\exp\left[-\frac{(x' - x_0)^2}{2\delta_0^2}\right]$ is a window with the width δ_0. The squared modulus of $G(x_0, p_x, t)$ describes the momentum distribution of the electron in the vicinity of $x = x_0$ at time t. In fact, $|G(x_0, p_x, t)|^2$ is nothing but the Husimi distribution [58], which can be obtained by a Gaussian smoothing of the Wigner function. In contrast to the Wigner function, the Husimi distribution is a positive-semidefinite function, which facilitates the interpretation as a quasiprobability distribution. In our SCTSQI model, we solve the TDSE in the length gauge:

$$i\frac{\partial}{\partial t}\Psi(x, t) = \left\{ -\frac{1}{2}\frac{\partial^2}{\partial x^2} + V(x) + F_x(t)x \right\}\Psi(x, t). \qquad (20)$$

We introduce two additional spatial grids consisting of N points in the absorbing regions of the computational box:

$$x_{0,\pm}^j = \mp(x_b + \Delta x \cdot j), \qquad (21)$$

where $\Delta x = (x_{max} - x_b)/N$ and $j = 0, \ldots, N$. At every step of the time propagation of the TDSE (20) we calculate the Gabor transform (19) of the absorbed part $\tilde{\Psi}(x, t) = [1 - M(x)]\Psi(x, t)$ at the points $x_{0,-}^j$ and $x_{0,+}^j$ [see Fig. 1(a)]. The TDSE is solved in the computational box $x \in [-x_{max}, x_{max}]$, whereas the Gabor transforms are calculated only for $x \in [-x_{max}, x_b]$ and $x \in [x_b, x_{max}]$. However, in the SCTSQI model the size of the computational box can be chosen much smaller than the one required to obtain accurate electron momentum distributions (see Sec. III). As a result, at every time instant t we know $G(x, p_x, t)$ on the grids in the rectangular domains $D_1 = [-x_{max}, -x_b] \times [-p_{x,max}, p_{x,max}]$ and $D_2 = [x_b, x_{max}] \times [-p_{x,max}, p_{x,max}]$ of the phase space. Here p_{max} is the maximum momentum, i.e., $p_{max} = \pi/\Delta x$,
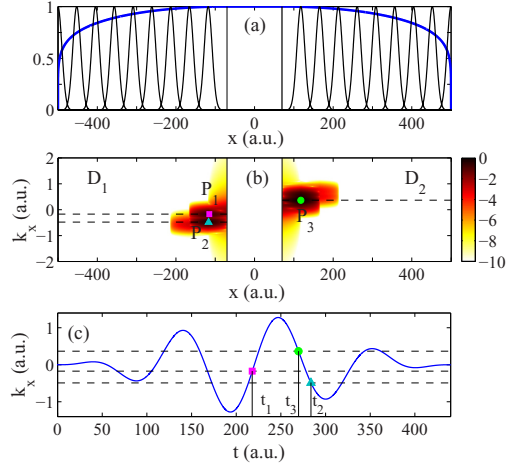
FIG. 1. (a) Scheme illustrating the structure of the computational box in the SCTSQI model. The mask function [Eq. (4)] is shown by the thick blue curve. The vertical lines correspond to the internal boundaries of the mask region. The thin black curves show the windows of the Gabor transform centered at the points $x_{0,\pm}^i$ [Eq. (21)]. (b) The Husimi quasiprobability distribution $|G(x, p_x, 3t_f/2)|^2$ calculated at $t = 3t_f/2$ for the laser pulse defined by Eq. (1) with a duration of $n = 4$ cycles, intensity of 2.0×10^{14} W/cm^2, phase $\varphi = 0$, and a wavelength of 800 nm. The Husimi distribution is calculated in the domains D_1 and D_2 of the phase space (see text). A logarithmic color scale is used. P_1–P_3 represent the three main spots of the Husimi distribution. The maxima of these spots are depicted by a (green) circle, (magenta) square, and (cyan) rectangle, respectively. (c) The final electron momentum $-A_x(t)$ in the potential-free classical model as a function of the time of ionization. The parameters of the laser pulse are the same as in (b). The vicinities of the time instants t_1, t_2, and t_3 make the main contribution to the spots P_1, P_2, and P_3, respectively [see (b)].

if the fast Fourier transform is used to calculate Eq. (19). An example of the corresponding Husimi quasiprobability distribution calculated at $t = 3t_f/2$ is shown in Fig. 1(b). At this time instant the quasiprobability distribution consists of the three main spots P_1, P_2, and P_3, whose maxima are indicated by a (green) circle, (magenta) square, and (cyan) triangle, respectively. These maxima correspond to the electron momenta k_x equal to 0.37, -0.17, and -0.48 a.u., respectively [see Fig. 1(b)]. According to the two-step model, a final electron momentum k_x corresponds to the ionization times t_0 satisfying the equation

$$k_x = -A_x(t_0). \quad (22)$$

Depending on the momentum value, this equation can have several solutions, and therefore, several different ionization times can lead to a given k_x; see Fig. 1(c), which shows the final electron momentum as a function of the ionization time. The analysis of the time evolution of the electron probability density reveals that every spot in Fig. 1(b) is mainly created within a narrow time interval that is close to only one of

the solutions of Eq. (22). The solutions of Eq. (22) that make the main contributions to the maxima of P_1, P_2, and P_3 are shown in Fig. 1(c). This fact is easy to understand, if we take into account that Fig. 1(b) is a snapshot of the dynamic quasiprobability distribution in the absorbing mask regions. Indeed, at a given time instant the contributions to the Husimi distribution from the vicinities of other solutions of Eq. (22) are either already absorbed by the mask or have not reached the absorbing regions yet. We note that aside from P_1, P_2, P_3 some other less pronounced spots are also seen in Fig. 1(b). These latter spots correspond to the contributions that by the given time instant are already mostly absorbed. The slight slope of the whole Husimi distribution that is visible in Fig. 1(b) is due to the fact that the contributions corresponding to the high values of $|k_x|$ travel larger distances before being absorbed than the ones with smaller $|k_x|$.

The value of the Gabor transform at an arbitrary point that belongs to the domain D_1 or D_2 can be obtained by a two-dimensional interpolation. We note that the application of the additional grids (21) in combination with the two-dimensional interpolation provides a computationally cheap alternative to the calculation of the Gabor transform at all the points of the main spatial grid that fall within the absorbing regions. The accuracy with which the function $G(t, x, p_x)$ is calculated depends on the number of points, N, in the grids (21) and, therefore, the convergence of the results with respect to this number must be checked.

Let N_T be the number of time steps used to solve the TDSE. At every time point t_0^m ($m = 1, \ldots, N_T$) used for the time propagation of the TDSE we randomly distribute initial positions x_0^j and momenta $p_{x,0}^j$ ($j = 1, \ldots, n_p$) of n_p classical trajectories in the domains D_1 and D_2. These trajectories are propagated according to Newton's equation of motion (10). Every trajectory is assigned with the quantum amplitude $G(t_0, x_0^j, p_{x,0}^j)$ and the phase

$$\Phi_0(t_0, x_0^j, p_{x,0}^j)$$
$$= -\int_{t_0}^{\infty} dt \left\{ \frac{v_x^2(t)}{2} - \frac{x^2}{(x^2+a^2)^{3/2}} - \frac{1}{\sqrt{x^2+a^2}} \right\}. \quad (23)$$

We note that the SCTSQI phase (23) corresponds to the phase of the matrix element of the semiclassical propagator that describes a transition from momentum $p_{x,0}^j$ at $t = t_0$ to momentum $k_x^j = k_x^j(x_0^j, p_{x,0}^j)$ at $t \to \infty$. The ionization probability in the SCTSQI model is given by

$$R(k_x) = \left| \sum_{m=1}^{N_T} \sum_{j=1}^{n_{k_x}} G(t_0^m, x_0^j, p_{x,0}^j) \exp\left[i\Phi_0(t_0^m, x_0^j, p_{x,0}^j)\right] \right|^2, \quad (24)$$

where n_{k_x} is the number of trajectories reaching the same bin centered at k_x [cf. Eq. (8)]. It should be stressed that the Gabor transform $G(t_0^m, x_0^j, p_{x,0}^j)$ is a complex function with both absolute value and phase. In order to ensure that ionized parts of the wave function reach the absorbing regions, we propagate the TDSE up to some time $t = T$, where $T > t_f$. For this reason, in the SCTSQI model we calculate classical trajectories till $t = T$ and replace t_f by T in Eq. (18) for the postpulse phase. In our simulations we have used $T = 4t_f$.
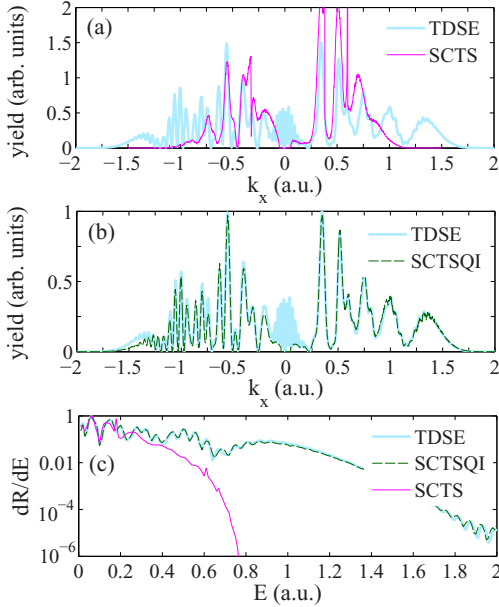
FIG. 2. Comparison of the semiclassical models with the TDSE. The parameters are the same as in Fig. 1(b). (a) The photoelectron momentum distributions for ionization of a one-dimensional model atom obtained from the SCTS model (thin magenta curve) and the solution of the TDSE (thick light blue curve). The distributions are normalized to the total ionization yield. (b) The electron momentum distributions calculated using the present SCTSQI model (dashed dark green curve) and the TDSE (thick light blue curve). The distributions are normalized to the peak values. (c) Electron energy spectra obtained from the TDSE (thick light blue curve), SCTSQI (dashed dark green curve), and the SCTS (thin magenta curve). The spectra are normalized to the peak values.

III. RESULTS AND DISCUSSION

For our numerical examples we use the intensity of 2.01×10^{14} W/cm^2 ($F_0 = 0.0757$ a.u.) and the wavelength 800 nm ($\omega = 0.057$ a.u.). This corresponds to the Keldysh parameter $\gamma = \omega\sqrt{2I_p}/F_0$ (see Ref. [6]) equal to 0.87. For simplicity, we set the absolute phase of the pulse (1) equal to zero: $\varphi = 0$.

We benchmark our SCTSQI approach against the SCTS model and the exact numerical solution of the TDSE. We implement the SCTS by solving Newton's equation of motion using a fourth-order Runge-Kutta method with adaptive step size [51]. In order to fully resolve the rich interference structure, we need to use the a momentum-space bin size of $\Delta k_x = 0.0019$ a.u. For this value of Δk_x the convergence of the interference oscillations is achieved for an ensemble consisting of 1.2×10^7 trajectories. At first, we consider photoelectron momentum distributions. In Fig. 2(a) we compare the SCTS model with the solution of the TDSE. The TDSE photoelectron momentum distribution has a rather complicated structure. This is due to the fact that the laser pulse

used in calculations is neither long nor very short. The side maxima at $k_x = -1.35$ a.u. and $k_x = 1.33$ a.u. are created due to the interference of contributions from times near the central maximum and minimum of the vector potential, respectively [see Fig. 1(c)]. The central minimum of the vector potential is also responsible for the formation of the maximum at $k_x = 1.0$ a.u. On the other hand, the ATI peaks in the electron momentum distributions are most pronounced in the range of k_x from -1.0 to -0.25 a.u. The SCTS model predicts a caustic of the momentum distribution around $k_x = 0.38$ a.u. For this reason, we normalize the distributions of Fig. 2(a) to the total ionization yield. Figure 2(a) shows that there is only a qualitative agreement between the SCTS approach and the TDSE result. Indeed, the SCTS model underestimates the width of the momentum distribution.

In Fig. 2(b) we compare the SCTSQI model with the TDSE. In our SCTSQI simulations we have used $N = 50$, $x_{max} = 500$ a.u., and $x_b = 70$ a.u. We note that in the SCTSQI approach, as well as in the SCTS model, the convergence of the electron momentum distributions must be achieved with respect to both the size of the bin and the number of trajectories. In order to achieve convergence of the momentum distribution, the bin size was chosen to be 1.5×10^{-4} a.u., and $n_p = 10^6$ trajectories were launched at every time step of the TDSE propagation. We note that in the mask method it is difficult to achieve full convergence of the TDSE momentum distribution for small momenta. The distribution in the vicinity of $k_x = 0$ is formed by the slow parts of the electron wave packet. A long propagation time is needed in order to let these parts reach the absorbing mask and, therefore, to obtain converged distribution for small k_x. Thus we do not consider the region of small k_x when comparing the SCTSQI model with the TDSE. It is clearly seen from Fig. 2(b) that for $|k_x| \gtrsim 0.15$ a.u. the SCTSQI model provides *quantitative* agreement with a fully quantum-mechanical result. This applies to both the width of the momentum distribution and the positions of the interference maxima (minima). The small remaining discrepancy in the heights of some of the interference maxima is caused by the fact that, similar to the SCTS, the SCTSQI model does not account for the preexponential factor of the semiclassical matrix element [30].

In Fig. 2(c) we present the photoelectron energy spectra obtained from the SCTS, the solution of the TDSE, and the present SCTSQI model. It is seen that the SCTSQI and the TDSE spectra are almost identical, while the spectrum predicted by the SCTS model falls off too rapidly with the increase of the electron energy. This is a direct consequence of the fact that the SCTS model underestimates the width of the electron momentum distribution [see Fig. 2(a)].

In order to further test the SCTSQI model, we calculate the electron momentum distributions for different positions of the mask x_b and fixed x_{max} of the computational box [see Fig. 3(a)]. The distributions corresponding to different values of x_b are in good quantitative agreement with each other. The same is also true for momentum distributions obtained for fixed x_b and different values of x_{max} [see Fig. 3(b)]. Here, we have used the two values $x_{max} = 500$ a.u. and $x_{max} = 200$ a.u. It should be stressed that it is impossible to obtain accurate electron momentum distributions for the small value $x_{max} = 200$ a.u. using the mask method. We also note that for the 1D
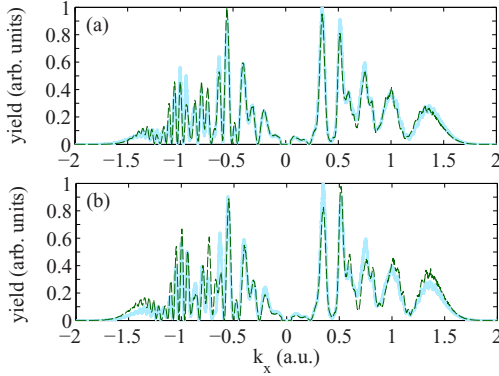
FIG. 3. The outcomes of the SCTSQI model for different internal boundaries of the absorbing mask and lengths of the computational box. The distributions are normalized to the peak values. (a) The one-dimensional momentum distributions calculated within the SCT-SQI model for the absorbing mask beginning at $x_b = 50$ a.u. (thick light blue curve) and $x_b = 100$ a.u. (dashed dark green curve). The parameters are the same as in Fig. 1(b), and the size of the computational box is $x_{\max} = 500$ a.u. (b) The one-dimensional momentum distributions obtained from the SCTSQI model for $x_{\max} = 500$ a.u. (thick light blue curve) and $x_{\max} = 200$ a.u. (dashed dark green curve). The parameters are the same as in Fig. 1(b). The absorbing mask begins at $x_b = 50$ a.u.

soft-core Coulomb potential used in this work, the smallest allowed x_b should exceed 30–40 a.u., to be outside of the region where the bound-state wave function is localized. Indeed, due to the large number of time steps, even the absorption of a small fraction of the bound-state wave function at each step will result in a severe distortion of the final momentum distribution.

Finally, we check how important is the phase of the factor $G(x, p_x, t)$ in Eq. (24). To this end, in Fig. 4 we compare the photoelectron momentum distribution calculated using the formula

$$R(k_x) = \left| \sum_{m=1}^{N_T} \sum_{j=1}^{n_{k_x}} \left| G\left(t_0^m, x_0^j, p_{x,0}^j\right) \right| \exp\left[i\Phi_0\left(t_0^m, x_0^j, p_{x,0}^j\right)\right] \right|^2, \tag{25}$$

instead of Eq. (24). We find that neglecting the phase of the Gabor transform is severe: The SCTSQI distribution cannot even be qualitatively reproduced when using Eq. (25). This result could be expected. Indeed, the factor $G(x, p_x, t)$ contains all the information about the quantum dynamics of the absorbed part of the wave packet *prior* to its conversion to the ensemble of classical trajectories. In a sense the $I_p t_0$ term in the SCTS phase [see Eq. (11)] plays the role of the phase $G(t, x, p_x)$ of the Gabor transform in Eq. (24).

We also study the role of the maximal allowed initial momentum $p_{x,\max}$. To this end, we perform the SCTSQI simulations for $p_{x,\max} = 1.0$ a.u. and $p_{x,\max} = 0.5$ a.u. [see Fig. 4(b)]. This should be compared with $p_{x,\max} = 2.0$ a.u.
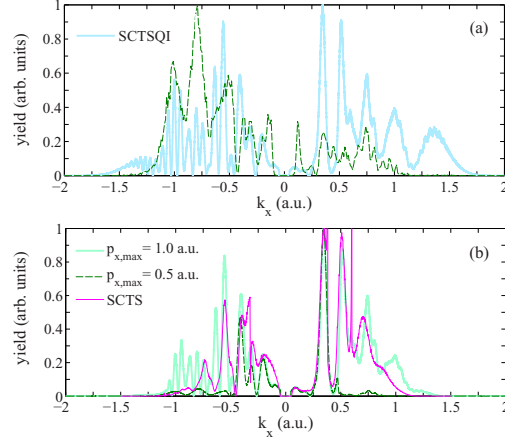

FIG. 4. (a) The photoelectron momentum distributions obtained from the SCTSQI model (thick light blue curve) and using Eq. (25), i.e., neglecting the phase of the Gabor transform (dashed dark green curve). The parameters are the same as in Figs. 1(b), 2, and 3. The size of the computational box is $x_{\max} = 500$ a.u., and the absorbing mask begins at $x_b = 50$ a.u. The distributions are normalized to the peak values. (b) The one-dimensional momentum distributions obtained from the SCTSQI model for $p_{x,\max} = 1.0$ a.u. (thick light blue curve) and $p_{x,\max} = 0.5$ a.u. (dashed dark green curve). The thin magenta curve shows the result of the SCTS model. The parameters are the same as in Figs. 1(b), 2, and 3. The distributions calculated within the SCTSQI model are normalized to the peak values, whereas the one obtained from the SCTS model is normalized to the value at $k_x = 0.35$ a.u. for visual convenience.

used above. It is seen that the width of the photoelectron momentum distribution decreases with decreasing $p_{x,\max}$. However, reducing the D_1 and D_2 domains in the p_x direction does not make the SCTSQI approach coincide with the SCTS model [see Fig. 4(b)]. This result could be expected. Indeed, electron trajectories start at different points in the SCTSQI and the SCTS models. The SCTS model relies on an expression for the tunnel exit point, whereas in the SCTSQI model every trajectory can start at any point of space in the absorbing regions. Figures 4(a) and 4(b) indicate that the phase of the Gabor transform and the maximal allowed initial momentum are equally important for reproducing of the TDSE result.

As other trajectory-based approaches, our SCTSQI model can help to illustrate the physical mechanisms underlying the strong-field process under investigation in terms of classical trajectories. In order to illustrate this point, we analyze the formation of the maximum of electron momentum distribution at $k_x = 0.35$ a.u. [see Figs. 2(a) and 2(b)]. We note that the SCTS model reproduces the position and the width of this peak, but not its relative height. First, we identify the trajectories leading to this final momentum in accord with the SCTSQI model. The analysis reveals that there are four main groups of these trajectories. In Fig. 5 we show one typical trajectory from each group (thick curves). The SCTS model also predicts four different groups of trajectories leading to
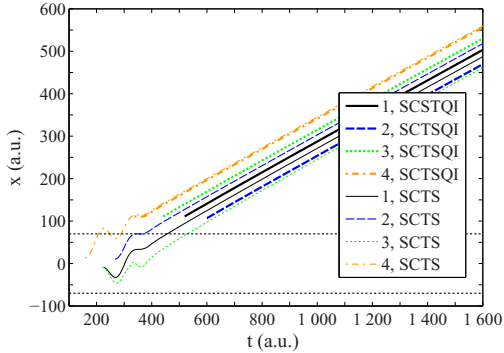
FIG. 5. Four characteristic electron trajectories leading from the SCTSQI and the SCTS models to the same final momentum $k_x = 0.35$ a.u. The parameters are the same as in Figs. 1(b), 2, and 3. The thick curves show the trajectories predicted by the SCTSQI model. The thin curves correspond to the trajectories obtained within the SCTS model. The horizontal dotted lines depict the boundaries of the absorbing regions.

$k_x = 0.35$ a.u. The corresponding characteristic trajectories are shown in Fig. 5 by thin curves. We note that the SCTS trajectories start closer to the origin and at earlier times than the trajectories in the SCTSQI model. This is easy to understand, since classical trajectories in the SCTSQI model can start only within the absorbing regions, i.e., for $|x| > x_b$, and it takes some time for the ionized part of the electron wave function to reach these regions. It is seen from Fig. 5 that the characteristic trajectories are different in the two models. In the SCTSQI model the initial conditions for the electron trajectories are determined from the solution of the TDSE. Therefore, we can expect that the SCTSQI model provides a more accurate trajectory-based picture of the formation of the electron momentum distribution than the SCTS model. This advantage of the SCTSQI approach should be used in the future for the analysis of more complex strong-field processes.

We believe that the SCTSQI model can also be applied to rescattering-induced processes, i.e., high-order ATI, HHG, and NSDI. Knowing the Gabor transform and the phases of the classical trajectories, we can reconstruct the electron wave function in both coordinate and momentum representation not only at $t \to \infty$ [see Eq. (24)], but at any time t. This wave function can be used for calculation of the elastic scattering of the electron wave packet, which is formed in an ionization process, on the parent ion, i.e., for description of the high-order ATI. Alternatively, it can be used, after adding the bound-state wave function, to calculate the expectation values of the electron dipole moment, velocity, or acceleration and, therefore, it allows us to obtain the HHG spectra. The application of the SCTSQI model to the NSDI process is more involved, since it requires solution of the two-electron TDSE, although in a smaller area of space compared to the fully quantum approach.

Finally, we discuss the computational performance of the SCTSQI approach. It should be noted that in the 1D case the

SCTSQI model is computationally more expensive than the numerical solution of the TDSE. This is easy to understand taking into account that at every time step the SCTSQI model requires calculation of a number of Gabor transforms, as well as the time propagation of a large ensemble of classical trajectories. The latter is the performance bottleneck of the method. In the present 1D implementation of the SCTSQI model we use about 2×10^{10} trajectories in total. This estimate is done based on the number of time steps needed for the propagation of the TDSE and amount of trajectories launched at every time step.

Nevertheless, we can expect that for the two-dimensional (2D) and three-dimensional (3D) cases the computational complexity of the SCTSQI model will not be higher than the one of the numerical solution of the TDSE. Indeed, for higher dimensionalities the computational costs of the solution of the TDSE increase dramatically. We note that in our SCTS model these costs can be substantially reduced using a smaller computational box compared to the one that is typically needed for solution of the TDSE. On the other hand, computational loads required for integration of Newton's equation of motion are comparable in the 1D, 2D, and 3D cases. Therefore, for higher dimensionalities numerical costs needed for calculation of the ensemble of classical trajectories become less important. In addition to this, an approach similar to the one used in the 1D case can be applied for calculation of the Gabor transform for higher dimensionalities: The Gabor transform can be first calculated on a sparse grid, and its value at any intermediate point is found using linear interpolation. We also note that the number of trajectories required for convergence of electron momentum distributions depends on the size of the bin, observable of interest, and the method used for sampling of initial conditions.

IV. CONCLUSIONS AND OUTLOOK

In conclusion, we have developed a trajectory-based approach to strong-field ionization: the semiclassical two-step model with quantum input. In the SCTSQI model every trajectory is associated with the SCTS phase and, therefore, the SCTSQI model allows us to describe quantum interference and account for the ionic potential beyond the semiclassical perturbation theory. Furthermore, the SCTSQI model corrects the inaccuracies of the SCTS model in treating the tunneling step. This has been achieved by the numerical solution of the TDSE with absorbing boundary conditions in a restricted area of space, applying the Gabor transform to the part of the wave function that is absorbed at each time step, and transforming this absorbed part into classical trajectories. The Gabor transform determines quantum amplitudes assigned to trajectories of the ensemble. Therefore, in the SCTSQI model the initial conditions of classical trajectories are governed by the exact quantum dynamics rather than by the quasistatic or SFA-based expressions as in other semiclassical approaches.

We have tested our SCTSQI model by comparing its predictions with the numerical solution of the 1D TDSE. We have shown that the SCTSQI model yields quantitative agreement with the fully quantum results. This is true not only for the widths of the electron momentum distributions,

but also for the positions of the interference maxima and minima. The model can be straightforwardly extended to the three-dimensional case. Most importantly, the SCTSQI model circumvents the nontrivial problem of choosing the initial conditions for classical trajectories. This makes the SCTSQI model extremely useful for study of strong-field ionization of molecules.

[1] N. B. Delone and V. P. Krainov, *Multiphoton Processes in Atoms* (Springer, Berlin, 2000).

[2] W. Becker, F. Grasbon, R. Kopold, D. B. Milošević, G. G. Paulus, and H. Walther, Above-threshold ionization: From classical features to quantum effects, Adv. At. Mol. Opt. Phys. **48**, 35 (2002).

[3] D. B. Milošević and F. Ehlotzky, Scattering and reaction processes in powerful laser fields, Adv. At. Mol. Opt. Phys. **49**, 373 (2003).

[4] A. Becker and F. H. M. Faisal, Intense field many-body *S*-matrix theory, J. Phys. B **38**, R1 (2005).

[5] C. Faria and X. Liu, Electron-electron correlation in strong laser fields, J. Mod. Opt. **58**, 1076 (2011).

[6] L. V. Keldysh, Ionization in the field of a strong electromagnetic wave, Zh. Eksp. Teor. Fiz. **47**, 1945 (1964) [Sov. Phys. JETP **20**, 1307 (1965)].

[7] F. H. M. Faisal, Multiple absorption of laser photons by atoms, J. Phys. B **6**, L89 (1973).

[8] H. R. Reiss, Effect of an intense electromagnetic field on a weakly bounded system, Phys. Rev. A **22**, 1786 (1980).

[9] H. G. Muller, An efficient propagation scheme for the time-dependent Schrödinger equation in the velocity gauge, Laser Phys. **9**, 138 (1999).

[10] D. Bauer and P. Koval, QPROP: A Schrödinger-solver for intense laser-atom interaction, Comput. Phys. Commun. **174**, 396 (2006).

[11] L. B. Madsen, L. A. A. Nikolopoulos, T. K. Kjeldsen, and J. Fernández, Extracting continuum information from $\Psi(t)$ in time-dependent wave-packet calculations, Phys. Rev. A **76**, 063407 (2007).

[12] A. N. Grum-Grzhimailo, B. Abeln, K. Bartschat, D. Weflen, and T. Urness, Ionization of atomic hydrogen in strong infrared laser fields, Phys. Rev. A **81**, 043408 (2010).

[13] S. Patchkovskii and H. G. Muller, Simple, accurate, and efficient implementation of 1-electron atomic time-dependent Schrödinger equation in spherical coordinates, Comput. Phys. Commun. **199**, 153 (2016).

[14] X. M. Tong, A three-dimensional time-dependent Schrödinger equation solver: An application to hydrogen atoms in an elliptical laser field, J. Phys. B **50**, 144004 (2017).

[15] H. B. van Linden van den Heuvell and H. G. Muller, in *Multiphoton processes*, edited by S. J. Smith and P. L. Knight (Cambridge University Press, Cambridge, UK, 1988).

[16] T. F. Gallagher, Above-Threshold Ionization in Low-Frequency Limit, Phys. Rev. Lett. **61**, 2304 (1988).

[17] P. B. Corkum, N. H. Burnett, and F. Brunel, Above-Threshold Ionization in the Long-Wavelength Limit, Phys. Rev. Lett. **62**, 1259 (1989).

[18] K. C. Kulander, K. J. Schafer, and J. L. Krause, in *Super-Intense Laser-Atom Physics*, edited by B. Pireaux, A. L'Hullier, and K. Rzazewski (Plenum, New York, 1993).

[19] P. B. Corkum, Plasma Perspective on Strong-Field Multiphoton Ionization, Phys. Rev. Lett. **71**, 1994 (1993).

[20] L. D. Landau and E. M. Lifshitz, *Quantum Mechanics Nonrelativistic Theory*, 2nd ed. (Pergamon, Oxford, 1965).

[21] A. M. Perelomov, V. S. Popov, and M. V. Terent'ev, Ionization of atoms in an alternating electric field, Zh. Eksp. Teor. Fiz. **50**, 1393 (1966) [Sov. Phys. JETP **23**, 924 (1966)].

[22] M. V. Ammosov, N. B. Delone, and V. P. Krainov, Tunnel ionization of complex atoms and of atomic ions in an alternating electromagnetic field, Zh. Eksp. Teor. Fiz. **91**, 2008 (1986) [Sov. Phys. JETP **64**, 1191 (1986)].

[23] N. B. Delone and V. P. Krainov, Energy and angular electron spectra for the tunnel ionization of atoms by strong low-frequency radiation, J. Opt. Soc. Am. B **8**, 1207 (1991).

[24] G. van de Sand and J.-M. Rost, Semiclassical description of multiphoton processes, Phys. Rev. A **62**, 053403 (2000).

[25] M. Spanner, Strong-Field Tunnel Ionization by Real-Valued Classical Trajectories, Phys. Rev. Lett. **90**, 233005 (2003).

[26] C. Zagoya, C.-M. Goletz, F. Grossmann, and J.-M. Rost, Dominant-interaction Hamiltonians for high-order harmonic generation in laser-assisted collisions, Phys. Rev. A **85**, 041401(R) (2012).

[27] C. Zagoya, J. Wu, M. Ronto, D. V. Shalashilin, and C. Faria, Quantum and semiclassical phase-space dynamics of a wave packet in strong fields using initial-value representations, New J. Phys. **16**, 103040 (2014).

[28] M. Li, J.-W. Geng, H. Liu, Y. Deng, C. Wu, L.-Y. Peng, Q. Gong, and Y. Liu, Classical-Quantum Correspondence for Above-Threshold Ionization, Phys. Rev. Lett. **112**, 113002 (2014).

[29] N. I. Shvetsov-Shilovski, M. Lein, L. B. Madsen, E. Räsänen, C. Lemell, J. Burgdörfer, D. G. Arbó, and K. Tőkési, Semiclassical two-step model for strong-field ionization, Phys. Rev. A **94**, 013415 (2016).

[30] W. H. Miller, Classical-limit quantum mechanics and the theory of molecular collisions, Adv. Chem. Phys. **25**, 69 (1974).

[31] T.-M. Yan, S. V. Popruzhenko, M. J. J. Vrakking, and D. Bauer, Low-Energy Structures in Strong-Field Ionization Revealed by Quantum Orbits, Phys. Rev. Lett. **105**, 253002 (2010).

[32] S. V. Popruzhenko and D. Bauer, Strong-field approximation for systems with Coulomb interaction, J. Mod. Opt. **55**, 2573 (2008).

[33] R. Boge, C. Cirelli, A. S. Landsman, S. Heuser, A. Ludwig, J. Maurer, M. Weger, L. Gallmann, and U. Keller, Probing Nonadiabatic Effects in Strong-Field Tunnel Ionization, Phys. Rev. Lett. **111**, 103003 (2013).

[34] C. Hofmann, A. S. Landsman, A. Zielinski, C. Cirelli, T. Zimmermann, A. Scrinzi, and U. Keller, Interpreting electron-momentum distributions and nonadiabaticity in strong-field ionization, Phys. Rev. A **90**, 043406 (2014).

[35] J.-W. Geng, L. Qin, M. Li, W.-H. Xiong, Y. Liu, Q. Gong, and L.-Y. Peng, Nonadiabatic tunneling ionization of atoms in elliptically polarized laser fields, J. Phys. B **47**, 204027 (2014).

[36] M. Li, J.-W. Geng, M. Han, M.-M. Liu, L.-Y. Peng, Q. Gong, and Y. Liu, Subcycle nonadiabatic strong-field tunneling ionization, Phys. Rev. A **93**, 013402 (2016).

[37] G. L. Yudin and M. Yu. Ivanov, Nonadiabatic tunnel ionization: Looking inside a laser cycle, Phys. Rev. A **64**, 013409 (2001).

[38] D. I. Bondar, Instantaneous multiphoton ionization rate and initial distribution of electron momentum, Phys. Rev. A **78**, 015405 (2008).

[39] H. Ni, U. Saalmann, and J.-M. Rost, Tunneling Ionization Time Resolved by Backpropagation, Phys. Rev. Lett. **117**, 023002 (2016).

[40] H. Ni, U. Saalmann, and J.-M. Rost, Tunneling exit characteristics from classical backpropagation of an ionized electron wave packet, Phys. Rev. A **97**, 013426 (2018).

[41] H. Ni, N. Eicke, C. Ruiz, J. Cai, F. Oppermann, N. I. Shvetsov-Shilovski, and L. W. Pi, Tunneling criteria and a nonadiabatic term for strong-field ionization, Phys. Rev. A **98**, 013411 (2018).

[42] X. Wang, J. Tian, and J. H. Eberly, Extended Virtual Detector Theory for Strong-Field Atomic Ionization, Phys. Rev. Lett. **110**, 243001 (2013).

[43] X. Wang, J. Tian, and J. H. Eberly, Virtual detector theory for strong-field atomic ionization, J. Phys. B **51**, 084002 (2018).

[44] B. Feuerstein and U. Thumm, On the computation of momentum distributions within wavepacket propagation calculations, J. Phys. B **36**, 707 (2003).

[45] N. Teeny, C. H. Keitel, and H. Bauke, Virtual-detector approach to tunnel ionization and tunneling times, Phys. Rev. A **94**, 022104 (2016).

[46] J. Tian, X. Wang, and J. H. Eberly, Numerical Detector Theory for the Longitudinal Momentum Distribution of the Elec-tron in Strong Field Ionization, Phys. Rev. Lett. **118**, 213201 (2017).

[47] J. Javanainen, J. H. Eberly, and Q. Su, Numerical simulations of multiphoton ionization and above-threshold electron spectra, Phys. Rev. A **38**, 3430 (1988).

[48] E. Anderson, Z. Bai, C. Bischof, S. Blackford, J. Demmel, J. Dongarra, J. Du. Craz, A. Greenbaum, S. Hammarling, A. McKenney, and D. Sorensen, *LAPACK User's Guide*, 3rd ed. (Society for Industrial and Applied Mathematics, Philadelphia, 1999).

[49] M. D. Feit, J. A. Fleck, and A. Steiger, Solution of the Schrödinger equation by a spectral method, J. Comput. Phys. **47**, 412 (1982).

[50] X. M. Tong, K. Hino, and N. Toshima, Phase-dependent atomic ionization in few-cycle intense laser pulse, Phys. Rev. A **74**, 031405(R) (2006).

[51] W. H. Press, S. A. Teukolsky, W. T. Vetterling, and B. P. Flannery, *Numerical Recipes in Fortran 77: The Art of Scientific Computing*, 2nd ed. (Cambridge University Press, Cambridge, UK, 1992).

[52] L. E. Ballentine, *Quantum Mechanics: A Modern Development* (World Scientific, Singapore, 1998).

[53] D. Gabor, Theory of communication, J. Inst. Electr. Eng. **93**, 429 (1946).

[54] C. C. Chirilă, I. Dreissigacker, E. V. van der Zwan, and M. Lein, Emission times in high-order harmonic generation, Phys. Rev. A **81**, 033412 (2010).

[55] K.-J. Yuan and A. D. Bandrauk, Circularly polarized attosec-ond pulses from molecular high-order harmonic generation by ultrashort intense bichromatic circularly and linearly polarized laser pulses, J. Phys. B **45**, 074001 (2012).

[56] J. Wu, B. B. Augstein, and C. Figueira de Morisson Faria, Local dynamics in high-order-harmonic generation using Bohmian trajectories, Phys. Rev. A **88**, 023415 (2013).

[57] X. F. Shu, S. B. Liu, and H. Y. Song, Phase-space analysis for ionization processes in the laser-atom interaction using Gabor transformation, Mod. Phys. Lett. B **30**, 1650147 (2016).

[58] K. Husimi, Some formal properties of the density matrix, Proc. Phys. Math. Soc. Jpn. **22**, 264 (1940).

8.10   Quantum battles in attoscience: tunneling

**THE EUROPEAN
PHYSICAL JOURNAL D**

Topical Review - Ultraintense and Ultrashort Laser Fields

Quantum battles in attoscience: tunnelling

Cornelia Hofmann[1,a], Alexander Bray[2], Werner Koch[3], Hongcheng Ni[4,5], and
Nikolay I. Shvetsov-Shilovski[6]

[1] Department of Physics and Astronomy, University College London, Gower Street, London WC1E 6BT, UK
[2] Research School of Physics, The Australian National University, Canberra, ACT 0200, Australia
[3] Weizmann Institute of Science, Rehovot, Israel
[4] State Key Laboratory of Precision Spectroscopy, East China Normal University, Shanghai 200241, China
[5] Institute for Theoretical Physics, Vienna University of Technology, 1040 Vienna, Austria
[6] Institut für Theoretische Physik, Leibniz Universität Hannover, 30167 Hannover, Germany

Abstract. What is the nature of tunnelling? This yet unanswered question is as pertinent today as it was at the dawn of quantum mechanics. This article presents a cross section of current perspectives on the interpretation, computational modelling, and numerical investigation of tunnelling processes in attosecond physics as debated in the Quantum Battles in Attoscience virtual workshop 2020.

1 Introduction

The discovery of the quantum tunnelling phenomenon almost 100 years ago has not only opened up many new avenues and applications. It has also kept quantum physics researchers busy since then, trying to define the temporal resolution of the process [1,2]. Early experiments were focused on photons tunnelling through potential barriers, such as Ref. [3] for example. But with the advent of attosecond science [4] the question *"Does tunnelling take time, and if yes, how much?"* has gained a lot of new interest, since electron dynamics often include quantum tunnelling portions, be that in biological processes such as photosynthesis [5] or charge transport in semiconductors [6], tunnelling ionisation as the first step for high-order harmonic generation (HHG) spectroscopy [7], photoelectron holography [8], laser induced electron diffraction (LIED) [9] or many more.

The temporal resolution of quantum tunnelling is still heavily debated [10–13] and thus presented an interesting topic for a debate at the Quantum Battles in Attoscience virtual workshop 2020 [14]. The aim of the *Battle* sessions was "an open debate on a contentious topic involving several early career researchers ('combatants') and the entire audience of attendees" [15]. To that effect, the combatants prepared a scaffolding structure of the debate on "tunnelling", defining three main topics: (a) Physical observables and typical experiments (presented in Sect. 2 of this article), (b) Nature of Tunnelling (see Sect. 3), and (c) Theoretical approaches to quantum tunnelling time (in Sect. 4). Each topic was introduced with an overview presentation, followed by a

free debate among all combatants, moderated by Prof. Jonathan Tennyson, UCL, and included both questions among the combatants as well as live audience questions. The result was a highly interactive and lively debate [16].

This perspective article offers a text-form of the live debate [17], supplemented with additional references and explanations.

2 Physical observables and typical experiments

The guiding questions for this first topic are:

> *What are physical observables, typical measurements, and what are the characteristic physical systems under investigation?*
> *What other aspects of these particular systems influence the interpretation of tunnelling time studies?*

2.1 Overview

When it comes to experiments investigating the temporal resolution of a quantum tunnelling particle, there are typically two kinds of experiments: (a) Bose–Einstein-Condensates (BEC) of atoms trapped in optical lattices, with various manipulations on them to measure tunnelling from one lattice site to the next [13,18]. Since the particles in question are entire atoms, their temporal resolution for the dynamics is in the range of microseconds. And (b) attosecond angular streaking (also known as attoclock) type [19–21] exper-

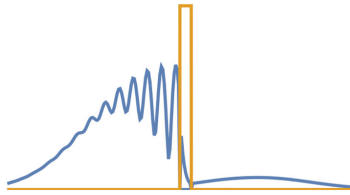[a] e-mail: c.hofmann@ucl.ac.uk (corresponding author)

Fig. 1 Idealised sketch of a wave packet hitting and partially tunnelling through a potential barrier

iments, a technique developed in strong-field attosecond physics, where electrons tunnel ionise from a bound state through the potential barrier which is created by the interaction of the strong laser field with the binding Coulomb potential of atoms. These are on the attosecond regime since electrons are tunnelling, and the main focus of the here following debate.

On a fundamental level, what we are interested in is the temporal resolution of a wave packet hitting a potential barrier, and then a part of that wave packet tunnelling through, such as schematically illustrated in Fig. 1. However, this exactly creates several challenges in trying to time this process compared to other timings of wave packets, such as for example group delay in photonics. The peak of the wave packet is not conserved, since the incoming (or bound state) wave packet is split into a reflected and a transmitted part. The potential barrier essentially acts as an energy-dependent filter, such that the spectra of the two resulting wave packets are significantly different [10]. A wave packet also always corresponds to a probability distribution, and in consequence it is difficult to define a clear starting and ending (or entrance and exit) point, more on that in Sect. 3. Furthermore, in strong-field attoscience scenarios we are tunnel ionising from a bound state, where of course parts of the wave function even in its field-free ground state always are "under" the barrier, without any tunnelling occurring. Additionally, approaches such as Wigner-like, scattering and resonance phase times [22] which are commonly applied to single-photon ionisation [23] are not applicable either, again because of the chirped propagation of the electron wave packet and the energy filtering of the potential barrier. While we are on the topic of potential barriers, it is also worthwhile noting that this classical picture of the potential barrier only emerges if the laser field is treated in the length gauge [24–27].

The physical observable for measurements (and calculations often, too) of strong-field tunnel ionisation are momentum distributions of photoelectrons [20,21,28] or momenta of atoms [13,18]. Momentum is of course a standard quantum mechanical observable corresponding to a unitary operator, whereas time itself is a parameter of the Schrödinger equation and thus not an observable as such. Therefore, a relation between measured (or calculated) momenta and the timing of the tunnelling process needs to be established through theoretical understanding of the quantum tunnelling process.

In the experiment by Fortun and co-workers a rubidium BEC is oscillating in an optical lattice. In a pump-probe-type approach, the lattice is turned off at different intervals after the initiation of the oscillation and the instantaneous momentum of the atoms carried them flying towards a position-sensitive detector. The tunnelled wave packets appeared delayed with respect to the reflected wave packets [18]. In the experiment by Ramos and co-workers, a quantum simulation of the Larmor clock [29–31], one of the well-known theoretical approaches to predicting the tunnelling time [32], was realised causing precession of the spin of the rubidium atoms while traversing a potential barrier. This spin precession was then mapped onto different states according to the angle of rotation and separated by a Stern–Gerlach measurement [13].

In attoscience experiments utilising the attoclock method [33,34], the rotation of the nearly circularly polarised vector potential **A** mimics the hand of a clock. The path of a photoelectron after tunnel ionisation is dominated by the interaction with the laser field [35], and thus neglecting all other corrections and perturbations, the final asymptotic momentum $\mathbf{p}_f$ is determined by the vector potential at the time when it first exits the potential barrier and enters the continuum t_0, through the conservation of canonical momentum

$$\mathbf{p}_f = \mathbf{p}_0 - \mathbf{A}(t_0), \tag{1}$$

where $\mathbf{p}_0$ denotes a possible initial momentum. Hence, the final momentum angle acts as a clock for the exit moment in time. However, this angle to time mapping is subject to several corrections, some easy to describe and include in calculations, others more elusive to quantify and thus the topic of ongoing research. A non-exhaustive list of corrections, approximations, and other issues include: the Coulomb force of the parent ion induces an angular shift [11,21,36,37]; the ellipticity, pulse envelope, pulse duration, and carrier-envelope-offset phase are wave form parameters which affect the photoelectron trajectories; and depletion mixes in with pulse duration and the intensity of the applied field [38,39] for topics which mostly have been dealt with in great detail and comparable results; the experiment does not have access to any "start" signal of the tunnelling process, only the exit point [10,28]; non-adiabatic effects influence the ionisation rate, energy at tunnel exit, initial momentum $\mathbf{p}_0$ distribution, and the location of said tunnel exit itself [39–43]; multi-electron-effects are ignored in most calculations [44–48]; models including non-classical characteristics of the trajectory which can be compared against experimental data are still being developed [20,38,49]; and the orbital angular momentum of the bound state has an effect on the strong-field ionisation [50–53] for issues which are more elusive (although this categorisation is not definite).

There is still a lot of work necessary to properly disentangle the different contributions which lead to various angular shifts, sketched in Fig. 2 of the measured Photoelectron Momentum Distribution (PMD), until we can
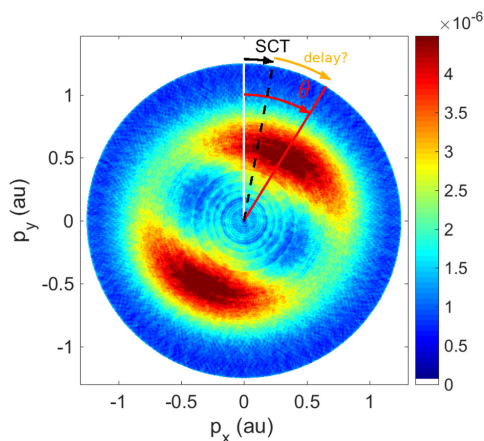
Fig. 2 Illustration of photoelectron momentum distribution for ellipticity 0.87, clockwise helicity, projected to the plane of polarisation. Single Classical Trajectory (SCT) models assuming instantaneous tunnelling predict an angle offset away from the pure $-\mathbf{A}(t_{\max})$, but the measured angle offset might be even larger than that. Adapted from [10]
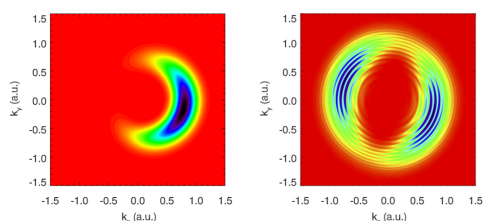

Fig. 3 Time-dependent Schrödinger equation (TDSE) calculation of photoelectron momentum distributions for hydrogen ionisation. Left: idealised attoclock with a single cycle pulse and circular polarisation leads to a unique final momentum probability distribution peak. Pulse duration ≈ 1.6 fs FWHM, peak intensity 0.86×10^{14} W/cm^2, wavelength 800 nm, with clockwise helicity. Right: A multi-cycle pulse yields two main blobs with Above Threshold Ionisation (ATI) rings from the inter-cycle-interference. Pulse duration ≈ 6 fs FWHM, peak intensity 1.5×10^{14} W/cm^2, wavelength 770 nm, with clockwise helicity. Adapted from [11,54]

be sure of the remaining angle offset and it's relation to tunnelling time.

2.2 Debate

– Figure 3 exemplifies the pulse duration and wave form dependence, as well as an energy dependence between the different ATI rings in the long pulse case, which show different angular maxima [55–

57]. This raises concerns about the validity of one single time (rather than a distribution of times) extracted typically from data, thus averaging over the energy dependence. In attoclock experiments, the carrier-envelope-offset phase (CEP) was not stabilised [20,21,28]. Additionally, the orientation of the polarisation ellipse in the lab frame was chosen such that the observable of interest (angular shift mostly parallel to the major axis of polarisation) was orthogonal to the direction with the biggest experimental noise (along the gas jet direction, thus chosen for the minor axis of polarisation) [58]. Both of these effects wash out ATI interference. For the CEP influence in particular, the interplay between ellipticity and pulse duration is critical. For the largest field strength to be following the polarisation ellipse (desired in attoclock experiments [10]) rather than the CEP [33,34], the pulse envelope must be long enough relative to the ellipticity reducing the field strength within a quarter cycle. Furthermore, ATI rings result from interference created by many laser optical cycles, highlighting the difficulty of defining a "single time", or even relative time intervals with respect to local maxima of the field strength or other possible references.

– Most often, tunnelling time calculations tend to use only a single peak point in the momentum distribution [12,38,59]. However, based on this discussion it would seem more appropriate to extract the tunnelling time from the full momentum distribution, which contains much more information regarding the tunnelling process [32,39]. We note that such work has been carried out in a recent publication [60], which assesses the whole momentum distribution instead of just a single offset angle.

– An audience question is brought in: How is the peak of the PMD determined precisely, since the maximum in a 2D distribution is not the same as the maximum in the 1D angular distribution? Of course the strictly linear angle-time relationship is only exact for circular polarisation. For any other polarisation, the elliptical geometry introduces corrections and needs to be taken into consideration [61]. These effects as well as the influence of integrating over the radial component in the 2D distribution were double-checked against. The resulting shifts in the extracted values were smaller than or of the order of the reported error bars for experimental data. Nevertheless, it is important to keep in mind that different coordinate system transforms and peak angle extraction methods lead to significant shifts in the extracted angle and thus the interpreted delay time [62]. Regarding the third component, the laser propagation direction, so far no significant difference has been found between a projection to or a cut along the polarisation plane. Of course this requires that no extra physics becomes important along this third component, for example the influence of the magnetic field must be negligible [26,63].

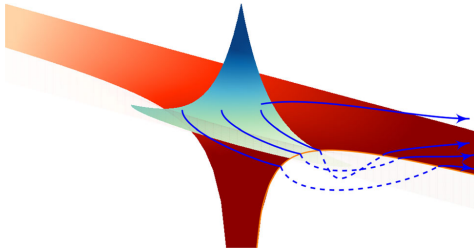Of course, an energy-resolved angular distribution would avoid the integration over at least one of

Fig. 4 A central conundrum of quantum tunnelling: Wave functions tunnel naturally but have no clear tunnel entry or exit. Real valued trajectories allow for a clearly defined tunnel entry and exit criterion but can not tunnel without excursions into the complex plane. Which of the two perspectives is the better choice?

the components and thus make the peak search less dependent on geometry and coordinate choices.

3 Nature of tunnelling

The guiding questions for the second topic are:

What is the nature of tunnelling at the classical/quantum intersection?
What is the "beginning" and "end" of tunnelling, and how do we define it?
What are classical or quantum trajectories?

3.1 Overview

Quantum tunnelling is a wave phenomenon, and the time-dependent Schrödinger equation (TDSE) is an equation for the probability amplitude wave (wave function). But this description makes it difficult to define where and when tunnelling exactly starts. Tunnelling itself is natural in quantum mechanics, it is only when we look at it from a classical perspective that there is a "forbidden" region in the potential barrier. In the classical domain, trajectories are well defined in space and time, but can they tunnel? The semiclassical models typically use classical trajectories to describe the motion of an electron after it has been released from an atom, usually by tunnelling ionisation.

Is a synthesis of these two worlds like the sketch in Fig. 4, aiming to retain the quantum physics behaviour with the clarity of trajectories, possible? It is clear that such a synthesis is not a simple task. Indeed, in order to calculate the classical trajectory, i.e., to integrate Newton's equation of motion, both starting point and the initial velocity are needed. However, Heisenberg's uncertainty principle imposes a fundamental limit to the accuracy with which the values of the position and momentum, as well as of any other canonically conjugate variables, can be simultaneously determined. Nev-

ertheless, the application of the quasiprobability distribution allows to obtain information about both the position and momentum from the wave function. The most widely known examples of quasiprobability distributions are the Wigner function and Husimi distribution. We note that the Wigner function has already been used for description of strong-field processes, see, e.g., Refs. [64–66]. However, to the best of our knowledge, the Wigner function has not yet been applied to the combination of the quantum and trajectory-based description in strong-field tunnel ionisation, although a similar method has been proposed for the case of attosecond pulse single-photon ionisation with subsequent streaking of the photoelectron wave function [67]. A recent and successful attempt of such combination was made in Ref. [49] using Gabor transform.

Doing so still begs the question, which quantity best characterises the onset of tunnelling?

3.2 Debate

– Quantum particle description is necessary for tunnelling to occur in the first place, but the potential barrier defines local properties which are significant for classical systems. So we need a combination of both, quantum tunnelling feature with the classical flavour of understanding if we aim for any kind of temporal resolution of a tunnelling process. The challenge is then to find one single picture for the entire process. Instead of relying on real-space trajectories, including complex space and time enables the tunnelling phenomenon, resulting in a quantum trajectory with clearly defined entry and exit to the barrier [68], as well as corresponding times (more on this method in Sect. 4).
  On the other hand, measurements can always only find real observables, thus fully complex calculations must find their way to the real axis somehow, where the propagation of a photoelectron wave packet is very well described by classical methods [69]. But since the experimental observables typically are momenta, purely quantum models which operate in complex space and time can still be used for the purpose of comparison, as long as they can predict a final momentum distribution.
– One huge assumption in experimental approaches based on the "attoclock" principle is the "starting time", relative to which the tunnelling delay is calculated. This is typically chosen to be the maximum of the electric field, since that moment corresponds to the highest probability of tunnelling [10]. However, this assumption might be missing out on half of the effect [41], and the tunnelling process in strong-field ionisation might be a symmetric problem relative to the (local) field maximum [70]. Publications which attempted to identify a physical starting point have found other values, typically before the maximum is reached [41,42,71,72].
– If we consider fully quantum models which describe both the tunnelling transition from bound to ionised

state and the propagation afterwards in one, it becomes important to distinguish tunnelling from over-the-barrier (OBI) ionisation. In experimental approaches it is generally not possible to *a posteriori* separate these two contributions to the total momentum distribution, and the same limitation is also true for numerical solutions of the TDSE [73].

However, in theoretical calculations based on trajectories, these two processes can easily be differentiated. The semiclassical models naturally distinguish between the tunnelling through a potential barrier and the over-barrier-ionisation. Indeed, when the field strength is so high that the potential barrier formed by the laser field and the ionic potential is suppressed, it is impossible to find the starting point of the electron trajectory using field direction model (see, e.g., Refs. [74–77]) or the separation of the static tunnelling problem in parabolic coordinates [78]. In this case it is usually assumed that the electron starts at the top of the suppressed potential barrier, and the difference between the ionisation potential and the energy at the top of the barrier $\Delta E = -I_p - V_{\max}$ is transferred to the initial longitudinal velocity of the departing electron:

$$v_{0,\parallel} = \sqrt{2\Delta E}. \qquad (2)$$

Non-adiabatic effects, i.e. effects beyond the quasistatic approximation which are due to the time-dependent changes in the strong field, also play into these definitions. For example, at which energy or distance can a photoelectron exit the potential barrier [43,79] or when does the onset of OBI occur? The so-called backpropagation method [39,42,43] is one hybrid approach which utilises the full quantum power of the TDSE for the tunnel ionisation but then retroactively adds the power of classical trajectories to also distinguish between OBI and tunnelling (more on this method in Sect. 4).

– An audience member suggests that localised position measurements would be able to distinguish tunnelling and OBI, since only OBI would be detectable.

This gedanken experiment however would require a detector positioned at the atomic potential barrier, which is unfeasible in any kind of experimental setup since detectors require some time-of-flight information and are placed a significant distance away from the interaction region, of the order of several centimetres at least [58,80]. There have been some theoretical studies using virtual detectors in combination with TDSE solutions [71,72], but those again can not distinguish of course. This is because both under-the-barrier and over-the-barrier transmission causes a probability flux of the wave function, which a hypothetical detector would be able to pick up without being able to distinguish between those two types of transmission. This remains the case also in different tunnelling scenarios such as in

a tunnelling junction where a macroscopic, position resolving detector might be feasible.

– The last point for this topic is concerning representation of a quantum wave function by using trajectories. Fundamentally, we are trying to study the behaviour of a wave function doing something interesting. In the most simple trajectory approach, the entire wave function is represented by a single simplified wave packet (i.e. a Gaussian) with the associated trajectory of its wave packet peak mapping the motion of the expectation value of the wave function (similar to a group velocity approach) [81]. However, this approach can not describe a wave packet being split into a reflected and a transmitted part, and thus would either always remain bound or the bound state is fully depleted. Trajectories representing a skewed wave packet [82] would present a more generalised version.

Even more accurate are descriptions that employ a large ensemble of trajectories following the probability distribution of the underlying wave function [83].

The question is then: Will an ensemble of (classical or quantum) trajectories not only represent an instantaneous probability distribution derived from a wave function, but also its dynamics over time? This question was addressed in Ref. [84] that studies the validity of the two-step semiclassical model disregarding quantum interference but accounting for the Coulomb field for strong-field ionisation. The Ehrenfest theorem [69] (see, e.g., Ref. [85] for a textbook treatment), which establishes quantum mechanical analogues of classical Hamiltonian equations, was applied in Ref. [84]. Furthermore, the analysis of Ref. [84] is based on a quantitative comparison of the electron momentum distributions obtained within the two-step model and by numerical solution of the TDSE. Reference [84] introduces the measure for the deviation of the dynamics of an ensemble of classical trajectories from the Ehrenfest's theorem. This measure is the relative deviation between the force at the average position of the ensemble of trajectories and the average of the forces on the ensemble. A correlation was found between the invalidity of the two-step model and the deviation of the dynamics from the Ehrenfest's theorem. The general trends for the applicability of the two-step model in terms of laser intensity, wavelength, ellipticity, as well as in terms of the potential properties are identified in [84]. However, this study is done in the two-dimensional (2D) case and needs to be extended to the 3D one.

4 Theoretical approaches to quantum tunnelling time

The guiding questions for the third and last topic are:

What are theoretical approaches used to investigate quantum tunnelling times?
What are their various characteristics, advantages and disadvantages?

4.1 Overview

For the overview, a brief and non-exhaustive list of different calculation approaches to the tunnelling time are given. They are categorised with regards to their theoretical foundation.

4.1.1 Quantum methods based on time-dependent Schrödinger equation

First are numerical solutions to TDSE. A common advantage of all these methods is that they are fully quantum calculations for the entire process. Further individual characteristics, advantages and disadvantages can be summarised as follows.

TDSE calculations which employ Coulomb vs Yukawa potentials [21,38] found that attoclock signal shows a prominent offset angle with Coulomb binding potential, while the offset angle vanishes for a Yukawa potential. This comparison offered an indirect proof of instantaneous tunnelling by comparing the results depending on the two different binding potential of the parent ion.

The numerical saddle-point method [62] uses a trajectory-free language and establishes a connection between the final momentum of the photoelectron and the numerical saddle-point time for the full Hamiltonian including the Coulomb potential. It supports the conclusion of instantaneous tunnelling. However, this method is gauge dependent.

The functional derivative method [70] investigates the instantaneous ionisation probability as a functional derivative of the total ionisation with respect to the wave form of the ionising field, but does not map directly to any experimental observables. It is gauge independent, and found vanishing delay (or vanishing delay asymmetry with respect to the local peak in the field).

Bohmian mechanics [86] present a mapping from the quantum world to the trajectory language. However, the calculation is guided by a pilot wave not pertaining solely to the (eventually) ionised part of the wave packet near the tunnel exit, thus potentially giving false tunnelling information. A separation of the (eventually) ionised part and bound part of the wave packet near the tunnel exit is, unfortunately, impossible, due to quantum nonlocality.

4.1.2 Quantum methods based on strong-field approximation

Strong-field-approximation (SFA) [87–89] based quantum methods describe ionisation as a transition from an initial state unaffected by the laser field to a Volkov state, i.e., the free electron wave function in an electromagnetic field. Therefore, the SFA disregards the
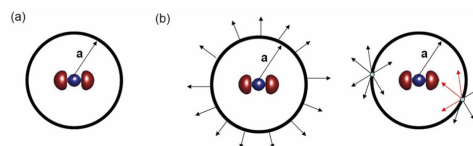

Fig. 5 Separation of space into inner (close to parent ion) and outer (far away) regions of space. Adapted from [36]
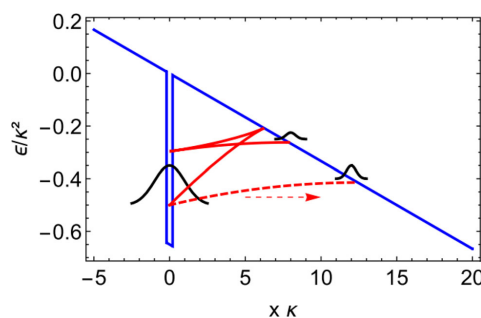

Fig. 6 Illustration of rescattering and transmitting quantum trajectories under the potential barrier. Adapted from [90]

intermediate bound states and the ionic potential (e.g., Coulomb interaction) in the final state. Presently, several SFA-based quantum approaches are developed. Typically, these approaches decide which force dominates the trajectory of a photoelectron based on its position in space and use the corresponding approximations. This separation and reduction of the acting forces allows for analytic calculations. The imaginary part of the saddle-point time in SFA calculations relates to the inverse tunnelling rate, while the real part in these models is often taken as the tunnel exit time.

The analytic R-Matrix (ARM) method [36,38] separates space into an inner region (Coulomb & Laser field considered) and an outer region (Coulomb field neglected, eikonal-Volkov approximation), as illustrated in Fig. 5. The disadvantage of this method is the challenge of choosing proper integration contours for each trajectory.

The under-barrier recollision theory [90] specifically includes interference between under-barrier rescattered and direct trajectories, as shown in Fig. 6. This leads to a shift in the momentum wave packet peak, which can be interpreted as a delay. However, this method ignores Coulomb corrections.

4.1.3 Hybrid quantum-classical method

The backpropagation method [39,42,43] is a hybrid quantum-classical approach offering a unique perspective on the tunnelling process. It combines a fully quantum calculation of the ionisation process with for-
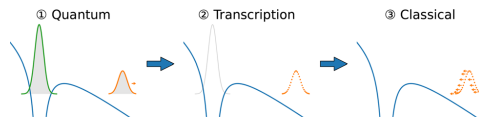
Fig. 7 Concept of the backpropagation method

ward propagation utilising TDSE solution, followed by a transcription of the resulting ionised quantum wave packet into classical trajectories, and a subsequent propagation of the trajectories backward in time, see Fig. 7 for a sketch. Another variant of the backpropagation method would be putting a sphere of virtual detectors [91–96] around the target, where the flux is converted into classical trajectories during the laser pulse on the fly [53,97].

Why backpropagation? Firstly, as everyone agrees, tunnelling is a purely quantum process. Introducing a tunnelling barrier into the description of tunnelling ionisation, however, brings in clearly classical elements into the picture. Namely, tunnelling is now depicted with local tunnelling exit positions and momenta, which calls for a classical formulation. Secondly, due to quantum nonlocality, the portion of the wave packet that would eventually be freed and the portion that would finally remain bound can not be separated during the tunnelling process. A separation is only possible in the far field, when these two portions are spatially detached. These are exactly the design philosophy of the backpropagation method, a hybridisation of quantum forward and classical backward propagation. It combines the advantages of the quantum and classical methods by offering the capability to include the full Hamiltonian and quantum tunnelling dynamics while retaining the local information from the classical trajectories. It also naturally includes nonadiabatic tunnelling effects, automatically remove the offset angle from Coulomb effects, and retrieves the electron characteristics at the tunnel exit.

The classical backpropagating trajectories may be stopped whenever a certain condition is met, which defines the tunnel exit, yielding highly differential information of the tunnel exit. In this manner, the backpropagation method may act as a common ground to compare different definitions of tunnelling. It was found that a vanishing tunnelling time results if the tunnel exit is defined in the momentum space when the velocity of the trajectory vanishes in the instantaneous field direction (the velocity criterion), while defining the tunnel exit as a certain position in the coordinate space (the position criterion) gives rise to a finite tunnelling time [39,43]. Different definitions of the tunnel exit were thus believed to be the origin of the tunnelling time debate. It was further argued that the position criterion leads to inconsistencies and difficulties and thus the velocity criterion is favoured as the definition of the tunnel exit, and the tunnelling time delay should thus vanish [39,43].

The backpropagation method has further enabled a study of the tunnelling time delay induced by orbital deformation [53] and a subcycle time resolution of the linear laser momentum transfer, where a coupling between the nondipole and nonadiabatic tunnelling effects was found [97].

4.1.4 Semiclassical methods

Semiclassical methods apply classical trajectories to describe the motion of an electron after it has been released from an atom or molecule by the laser pulse. The two-step [98–100] and the three-step [101,102] models are the most widely known examples of the semiclassical approaches. These models do not account for the effect of the ionic potential on the electron motion in the continuum. Presently there are many trajectory-based models that do account for the ionic potential in the classical equations of motion. Among these are: Trajectory-based Coulomb SFA (TCSFA) [103,104], Quantum trajectory Monte-Carlo method (QTMC) [105], Coulomb quantum orbit strong-field approximation (CQSFA) [106–111], semiclassical two-step model (SCTS) [112], Quasistatic Wigner method [20], etc. The three-step model using complex classical trajectories [68] and the classical Keldysh-Rutherford model [37] are closely related to this group of models.

Using a purely classical description of the electron motion it is not possible to describe the quantum interference effect in the photoelectron momentum distributions and energy spectra. Recently substantial progress has been achieved along these lines. Along with some other approaches, the TCSFA, QTMC, CQSFA, and SCTS models account for interference effects. In these approaches every classical trajectory is assigned to a certain phase, and the contributions of different trajectories leading to a given final electron momentum are added coherently.

The TCSFA extends the well-known Coulomb-corrected strong-field approximation (CCSFA) [113, 114] by treating the laser field and the Coulomb force acting on the electron from the ion on an equal footing. The TCSFA accounts for the Coulomb potential in the phase of every trajectory within the semiclassical perturbation theory. The same approach is used in the QTMC model. In contrast to this, the SCTS and the CQSFA models account for the Coulomb potential beyond the semiclassical perturbation theory.

The quasistatic Wigner method [20] employs the concept of the dominant quantum path. Using the space-time propagator, the quasistatic Wigner method considers the propagation of the electron wave function that originates from the initial bound state in the classically forbidden domain. The quasistatic description of the laser field is used in Ref. [20]. The phase of the quantum mechanical propagator determines the most dominant path along the tunnel channel, and therefore, determines the Wigner trajectory. The Wigner trajectory is merged with the corresponding classical trajectory in the continuum, see Ref. [20]. In this way the
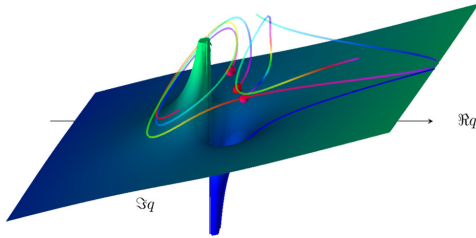
Fig. 8 Schematic depiction of trajectories in complex space surrounding the singularity of the 1D radial Coulomb potential. Note the repulsive nature of the potential in the negative half of the plane. Orbiting trajectories result from propagation in complex time prior to ionisation [68]

quasistatic Wigner method determines the initial conditions for the classical trajectory. It should be emphasised that the initial conditions include not only an initial momentum, but also a time delay. However, this method reduces the wave packet to a single trajectory. It should also be noted that the Wigner time is ill-defined in the tunnelling process [10].

Since real-valued trajectories are not able to describe tunnel ionisation, the complex-time-and-space model [68] employs complex trajectories, as illustrated in Fig. 8. This approach was applied to the HHG process in Ref. [68]. All components of the three-step model are described in Ref. [68] within a single consistent trajectory framework. The trajectories are sampled from an initial Coulomb eigenstate, and the time propagation is performed using the final value coherent state propagator (see Ref. [115]). As a result, the model provides a unified and seamless trajectory description of the ground state, tunnelling, and collision process. The model shows quantitative agreement with fully quantum results. However, the contour in the plane of complex time, which is necessary to implement the model, has to be chosen manually.

4.1.5 Classical methods

And finally, purely classical models are still also developed and used often. The Keldysh-Rutherford model [37] applies the famous Rutherford scattering formula taking the vector potential of the laser pulse as the asymptotic electron velocity and the Keldysh tunnelling width as the impact parameter. The model was tested by comparison of its predictions with the numerical solution of the TDSE using the hydrogenic potential and the screened (Yukawa) potential. In the latter case the action of the Coulomb field was gradually switched off. The striking similarity between the attoclock offset angle and the Rutherford scattering angle was revealed in Ref. [37]. The Keldysh-Rutherford model suggests that the offset angle has a largely Coulombic origin [37]. Therefore, the model is questioning the interpretation of this angle in terms of a finite tunnelling

time. However, the Keldysh-Rutherford model completely neglects nonadiabatic effects, and is also limited in its validity to short pulse durations and (relatively) weak intensities which are outside the typical parameter range of experiments to date. Therefore, some further work along this direction is needed.

Classical trajectory Monte Carlo (CTMC) methods [28,45] are the classical cousin of QTMC, and often employed where interference effects are not of any key interest. Since the calculations are computationally cheap compared to TDSE solutions and fewer trajectories are needed than in QTMC to reach similar statistical quality, these methods are able to fully include the ion Coulomb potential together with the laser field during the propagation after the tunnel exit, as well as various non-adiabatic effects [116], certain multi-electron effects [47] including Stark shift and an induced dipole in the parent ion [45].

4.2 Debate

– Regarding the complex-time-and-space method [68], the question is raised how exactly the integration contour is chosen manually. Every time a trajectory orbits the singularity at the nucleus, there is a possibility for the quantum trajectory to be emitted from the bound wave packet and leave as part of the ionisation wave packet. The exact choice for after how many orbits an ionisation event happens is done by comparing to the full quantum result, for sections of initial coordinate space. Observables are then computed from the resulting trajectories. The number of loops is a discrete choice and not a fully tunable parameter. While there is a choice to match the quantum result, each discrete choice yields significantly different results, so the agreement with TDSE calculations is not entirely by construction. The interpretation of this choice is not clear yet from a physical point of view.

When it comes to separating the eventually bound from the eventually ionised part of the wave packet, trajectories far from the core in the long time limit are considered ionised. Searching for conditions (zero momentum for example) along those eventually ionised trajectories yields two complex times, labelled as tunnel entry and exit, where the difference can be interpreted as tunnelling time, see Fig. 9a. Alternatively, the difference to the field maximum can be computed, as shown in Fig. 9b. This may be required to compare the results to experiments where tunnel entry times may not be accessible but it does ignore a significant contribution to the total tunnelling time. As Fig. 9 shows, the time required for tunnelling is nonzero in both real and imaginary components. Furthermore, a single averaged result may be insufficient to characterise the tunnelling process as the distribution of times is wide and asymmetric.

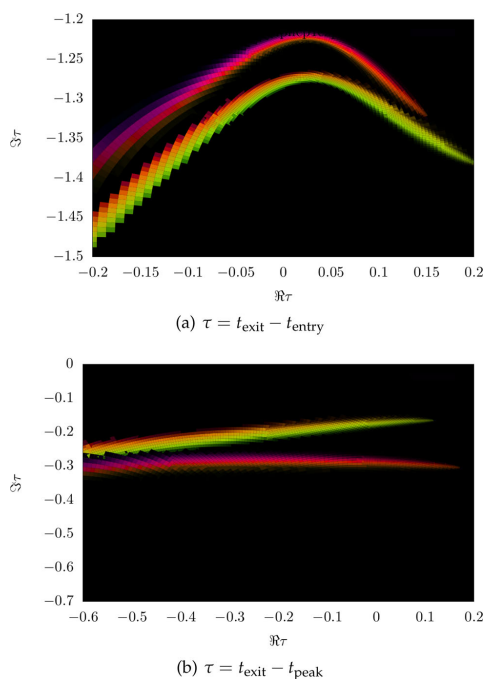Two distinct classical processes are found, and the

(a) $\tau = t_{\mathrm{exit}} - t_{\mathrm{entry}}$

(b) $\tau = t_{\mathrm{exit}} - t_{\mathrm{peak}}$

Fig. 9 Tunnelling time distribution extracted from the complex-time-and-space method for a half cycle pulse, with wavelength $\lambda = 1033$ nm, ionisation potential $I_p = 13.6$ eV (hydrogen), intensity $I = 1.9 \times 10^{14}$ W/cm^2, resulting in a Keldysh parameter of $\gamma = 0.6$. Brightness encodes probability magnitude and colour encodes phase of the trajectory. Two distinct distributions belonging to two separate classical processes in the trajectory ensemble are visible in both plots

two references (entry point or field maximum) for the tunnelling delay time differ significantly.

– An audience member asks what the effect of excited states on an attoclock measurement is. This was dealt with in the [21] study since molecular hydrogen had to be split into atomic hydrogen. In their extended data figures & tables, it is shown how initial bound states 1s or 2s result in completely different final momentum distributions. Photoelectrons ionised from 2s have much smaller absolute momenta, their distribution shows a different structure, and the event is less likely to happen. Therefore, contributions from different initial states can be separated.

– Already in Sect. 3, combined approaches which offer quantum behaviour with trajectory insight have been identified as beneficial for many strong-field (tunnelling) phenomena models.

Typically, the SCTS model requires large ensembles

of classical trajectories to resolve fine interference details. These trajectories are propagated, and their final momenta are binned in cells in momentum space. This is often referred to as "shooting method' [103], although this approach has nothing to do with the shooting method for solving a boundary value problem. In contrast to the TCSFA, QTMC, and SCTS, the CQSFA method finds all the trajectories corresponding to the given final momentum. This approach is often called the solution of the "inverse problem" and it allows to bypass the necessity of large ensembles of trajectories. However, the solution of the inverse problem is a non-trivial task, and, furthermore, is generally less versatile than the "shooting method".

Any trajectory-based model requires specification of initial conditions, i.e., the initial electron velocity and the starting point of the classical trajectory. Indeed, these initial conditions are needed to integrate the Newton's equations of motion. The starting point, i.e., the tunnel exit, is found using the separation of the tunnelling problem in parabolic coordinates [78]. The Stark shift of the energy level that has an effect on both the tunnel exit and ionisation probability was also taken into account in the SCTS. It is generally considered in the semiclassical models that the electron departs with zero initial velocity along the laser polarisation direction $v_{0,\parallel} = 0$ and an arbitrary initial velocity $v_{0,\perp}$ in the perpendicular direction. The ionisation times and the initial transverse velocities are distributed in accord with the static ionisation rate:

$$w\left(t_0, v_{0,\perp}\right) \sim \exp\left(-\frac{2\kappa^3}{3F\left(t_0\right)}\right) \exp\left(-\frac{\kappa v_{0,\perp}^2}{F\left(t_0\right)}\right) (3)$$

with $\kappa = \sqrt{2I_p}$. The quasistatic approximation is used in Eq. (3), i.e., the static field strength F is replaced by the instantaneous value $F\left(t_0\right)$. The quasistatic approximation is used in both QTMC and the SCTS.

We note that many trajectory-based models use the SFA formulas instead of Eq. (3) to distribute the initial conditions of classical trajectories, see, e.g., Refs. [103,116–119]. This allows to investigate nonadiabatic effects in above-threshold ionisation and often leads to a better agreement with the numerical solution of the TDSE.

Recently, the SFA-based formulas as distributions of the initial conditions have been validated in a systematic way [60]. It is found that a combination of SFA initial conditions with complex weight and a trajectory model of SCTS provides the best solution for obtaining the most accurate attoclock signal [60]. The SCTS model has not been extended to the over-the-barrier ionisation (barrier-suppression regime) yet. Such an extension can be easily done as discussed above, see Eq. (2).

Recently an efficient extension and modification of the SCTS model was proposed [119]. In its orig-

inal formulation the SCTS model uses the phase of the semiclassical matrix element [120–122] (see Refs. [123,124] for a textbook treatment), but completely disregards the pre-exponential factor of the bound-continuum transition matrix element. The influence of this pre-exponential factor was for the first time studied in Ref. [119]. The modulus of the pre-exponential factor corresponds to the mapping from initial conditions for electron trajectories to the components of the final momentum. It affects the weights of classical trajectories. The phase of the pre-exponential factor modifies the interference structures. This phase is known as a Maslov phase and can be viewed as a case of Gouy's phase anomaly, see Ref. [119]. Furthermore, a novel approach to the inverse problem applying a clustering algorithm was proposed in [119]. The modified version of the SCTS demonstrates excellent agreement with numerical solution of the TDSE for both photoelectron momentum distributions and energy spectra. It was found that the account for the pre-exponential factor is crucial for the quantitative agreement with the TDSE. This novel version of the SCTS can be applied not only to linearly polarised laser fields, but also to non-cylindrically-symmetric ones, e.g., bicircular laser pulses [119].

The recent semiclassical two-step model with quantum input (SCTSQI) [49] is a mixed quantum-classical approach that combines the SCTS with the numerical solution of the TDSE. To perform the synthesis of the trajectory-based approach with the TDSE, the Gabor transformation of the wave function $\Psi(x,t)$

$$G(x_0, p_x, t) = \frac{1}{\sqrt{2\pi}} \int_{-\infty}^{\infty} \Psi(x', t) \exp\left[-\frac{(x'-x_0)^2}{2\delta_0^2}\right] \times \exp(-ip_x x')\, dx', \qquad (4)$$

was used in the SCTSQI [49]. Here x_0 is the point in the vicinity of which the Gabor transform is calculated and $\exp\left[-\frac{(x'-x_0)^2}{2\delta_0^2}\right]$ is a Gaussian window of the width δ_0. The quantity $|G(x_0, p_x, t)|^2$ describes the momentum distribution of the electron near the point x_0 at time t. This is nothing just the Husimi distribution, which can be also obtained by Gaussian smoothing of the Wigner function.

In Ref. [49] the Gabor transform (4) was used in combination with the absorbing boundaries that prevent the unphysical reflections of the wave function from the grid boundary. More specifically, the Gabor transform was applied to the part of the wave function that is absorbed at every time step of the solution of the TDSE. Figure 10 shows an example of the corresponding Husimi distribution calculated at the end of a few-cycle laser pulse. This absorbed part is transformed in the ensemble of classical trajectories that is propagated using classical equations of motion. Therefore, initial positions and
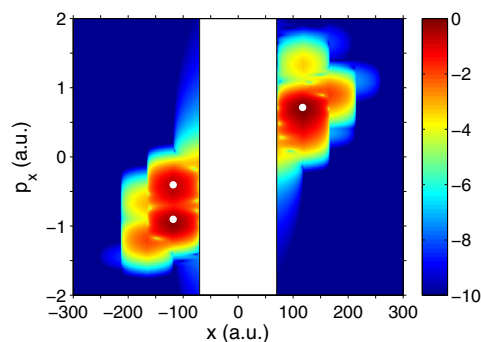

Fig. 10 The Husimi distribution $|G(x, p_x, t)|^2$ in the absorbing mask regions calculated for ionisation of 1D model atom at the end of the laser pulse with a duration of 4 optical cycles, intensity of $2.0 \times 10^{14}\,\mathrm{W/cm^2}$, and a wavelength of 800 nm. A logarithmic colour scale is used. The three main maxima of the Husimi distribution are shown by white circles

momenta of classical trajectories used to simulate an electron wave packet are extracted from the exact quantum dynamics. It is clear that the convergence with respect to the position of the absorbing boundaries and the number of trajectories launched at every time step should be checked in this approach. The absorbing boundaries must be far enough to not affect the bound part of the wave function. The SCTSQI yields quantitative agreement with quantum results [49]. What is even more important, it corrects the inaccuracies of the standard trajectory-based approaches in description of the ionisation step and circumvents the complicated problem of choosing the initial conditions.

However, future work is needed to turn the SCTSQI model in a powerful tool for studies of tunnelling. First, the model formulated for the one-dimensional (1D) model atom should be generalised to the three-dimensional case (3D). To describe fine details of interference patterns accurately enough, large numbers of classical trajectories are needed in the SCTSQI. In addition to this, the ensembles of trajectories are launched at every step of the time propagation. As the result, the SCTSQI model includes all possible trajectories, and it is not always easy to distinguish between them. This hampers the understanding of the strong-field phenomena that is expected to be provided by the SCTSQI model and its future extensions. Therefore, the number of trajectories has to be reduced in the SCTSQI approach, e.g., by using more sophisticated sampling techniques.

– A mask function which is absorbing the wave function over a spatial extension, such as in the SCTSQI method for example, will lead to a decreasing total probability of the wave packet. This must be mon-

itored over the course of the calculation to ensure it does not introduce unwanted artefacts through the choice of position or steepness of the absorbing mask. The efficiency of this also depends on the ionisation probability which determines how much of the wave function is going to hit the absorbing boundary.

5 Outlook

It is evident that much remains to be done to further improve our general understanding of the tunnelling process as well as the interaction between the strong laser light and the target atom (or molecule, surface, liquid, . . .) in order to tackle the underlying reasons for why so many approaches reach opposing conclusions. Given the lack of a clear, agreed upon definition of the onset and conclusion of tunnelling, it is perhaps unsurprising that there is also not a clear pattern between classical or quantum methods in their various predictions regarding instantaneous or finite tunnelling time, let alone numerical values. More than anything, this debate has demonstrated the need to find a common ground on which to compare the vast range of theoretical approaches and experimental setups. One of the few prevailing themes of this debate that most everyone could agree on is that a combination of classical and quantum theory is required for describing tunnelling processes in order to be able to interpret the experimental evidence.

Author contributions

All authors were involved in the live debate and the preparation of the manuscript. All authors have read and approved the final manuscript.

Data Availability Statement This manuscript has no associated data or the data will not be deposited. [Authors' comment: The datasets discussed in this current study are available from the corresponding author or co-authors on reasonable request.]

References

1. E. Hauge, J. Støvneng, Rev. Mod. Phys. **61**, 917 (1989)
2. R. Landauer, T. Martin, Rev. Mod. Phys. **66**, 217 (1994)
3. A.M. Steinberg, P.G. Kwiat, R.Y. Chiao, Phys. Rev. Lett. **71**, 708 (1993)
4. P.B. Corkum, F. Krausz, Nat. Phys. **3**, 381 (2007)
5. E.D. Filho, K.H.P. Jubilato, R.M. Ricotta, 1–10 (2019). arXiv:1911.02606
6. J. Teuscher, J.C. Brauer, A. Stepanov, A. Solano, A. Boziki, M. Chergui, J.P. Wolf, U. Rothlisberger, N. Banerji, J.E. Moser, Struct. Dyn. **4**, 061503 (2017)
7. B.D. Bruner, H. Soifer, D. Shafir, V. Serbinenko, O. Smirnova, N. Dudovich, J. Phys. B: At. Mol. Opt. Phys. **48**, 174006 (2015)
8. Y. Huismans, A. Rouzée, A. Gijsbertsen, J.H. Jungmann, A.S. Smolkowska, P.S.W.M. Logman, F. Lépine, C. Cauchy, S. Zamith, T. Marchenko et al., Science (New York, N.Y.) **331**, 61 (2011)
9. M. Meckel, D. Comtois, D. Zeidler, A. Staudte, D. Pavicic, H.C. Bandulet, H. Pepin, J.C. Kieffer, R. Dorner, D.M. Villeneuve et al., Science **320**, 1478 (2008). arXiv:1002.1037
10. C. Hofmann, A.S. Landsman, U. Keller, J. Mod. Opt. **66**, 1052 (2019). arXiv:1901.07015
11. A.S. Kheifets, J. Phys. B: At. Mol. Opt. Phys. **53**, 072001 (2020)
12. U. Satya Sainadh, R.T. Sang, I.V. Litvinyuk, J. Phys. Photonics **2**, 042002 (2020)
13. R. Ramos, D. Spierings, I. Racicot, A.M. Steinberg, Nature **583**, 529 (2020). arXiv:1907.13523
14. E. Hauge, Can one speak about tunneling times in polite society?, in *Proceedings of the Adriatico Research Conference on Tunneling and Its Implications*, ed. by D. Mugnai, A. Ranfagni, L. Schulman (World Scientific, Singapore, 1997)
15. Quantum battles in attoscience 2020. https://www.quantumbattles.com/
16. C.F.D.M. Faria, A. Brown, Fostering academic debate in an online world (2020). https://physicsworld.com/a/fostering-academic-debate-in-an-online-world/
17. Quantum battles in attoscience: Battle 1 (2020). https://youtu.be/COXjc1GVXhs

18. A. Fortun, C. Cabrera-Gutiérrez, G. Condon, E. Michon, J. Billy, D. Guéry-Odelin, Phys. Rev. Lett. **117**, 010401 (2016). arXiv:1603.03655

19. A. Landsman, M. Weger, J. Maurer, R. Boge, A. Ludwig, S. Heuser, C. Cirelli, L. Gallmann, U. Keller, 11 (2013). arXiv e-prints arXiv1301.2766

20. N. Camus, E. Yakaboylu, L. Fechner, M. Klaiber, M. Laux, Y. Mi, K.Z. Hatsagortsyan, T. Pfeifer, C.H. Keitel, R. Moshammer, Phys. Rev. Lett. **119**, 023201 (2017). arXiv:1611.03701

21. U.S. Sainadh, H. Xu, X. Wang, A. Atia-Tul-Noor, W.C. Wallace, N. Douguet, A. Bray, I. Ivanov, K. Bartschat, A. Kheifets et al., Nature (2019). arXiv:1707.05445

22. M. Isinger, R.J. Squibb, D. Busto, S. Zhong, A. Harth, D. Kroon, S. Nandi, C.L. Arnold, M. Miranda, J.M. Dahlström et al., Science **358**, 893 (2017). arXiv:1709.01780

23. L. Gallmann, I. Jordan, H.J. Wörner, L. Castiglioni, M. Hengsberger, J. Osterwalder, C.A. Arrell, M. Chergui, E. Liberatore, U. Rothlisberger et al., Struct. Dyn. **4**, 061502 (2017)

24. H. Reiss, Phys. Rev. Lett. **101**, 043002 (2008)

25. H.R. Reiss, Phys. Rev. Lett. **101**, 159901 (2008)

26. H.R. Reiss, J. Phys. B: At. Mol. Opt. Phys. **47**, 204006 (2014)

27. H.R. Reiss, Eur. Phys. J. D **75**, 158 (2021)

28. A.S. Landsman, M. Weger, J. Maurer, R. Boge, A. Ludwig, S. Heuser, C. Cirelli, L. Gallmann, U. Keller, Optica **1**, 343 (2014). arXiv:1301.2766

29. M. Büttiker, Phys. Rev. B **27**, 6178 (1983)

30. A. Baz', Sov. J. Nucl. Phys. **4**, 182 (1967)

31. V. Rybachenko, Sov. J. Nucl. Phys. **5**, 635 (1967)

32. A.S. Landsman, U. Keller, Phys. Rep. **547**, 1 (2015)

33. P. Eckle, M. Smolarski, P. Schlup, J. Biegert, A. Staudte, M. Schöffler, H.G. Muller, R. Dörner, U. Keller, Nat. Phys. **4**, 565 (2008)

34. P. Eckle, A.N. Pfeiffer, C. Cirelli, A. Staudte, R. Dörner, H.G. Muller, M. Büttiker, U. Keller, Science **322**, 1525 (2008)

35. C. Hofmann, A.S. Landsman, U. Keller, Attoclock revisited on electron tunnelling time (2019). https://doi.org/10.6084/m9.figshare.8040410.v1

36. L. Torlina, O. Smirnova, Phys. Rev. A **86**, 043408 (2012)

37. A.W. Bray, S. Eckart, A.S. Kheifets, Phys. Rev. Lett. **121**, 123201 (2018)

38. L. Torlina, F. Morales, J. Kaushal, I. Ivanov, A. Kheifets, A. Zielinski, A. Scrinzi, H.G. Muller, S. Sukiasyan, M. Ivanov et al., Nat. Phys. **11**, 503 (2015). arXiv:1402.5620v1

39. H. Ni, U. Saalmann, J.M. Rost, Phys. Rev. A **97**, 013426 (2018)

40. I.A. Ivanov, A.S. Kheifets, Phys. Rev. A **89**, 021402 (2014). arXiv:1309.7436

41. M. Klaiber, K.Z. Hatsagortsyan, C.H. Keitel, Phys. Rev. Lett. **114**, 083001 (2015). arXiv:1408.5712v1

42. H. Ni, U. Saalmann, J.M. Rost, Phys. Rev. Lett. **117**, 023002 (2016)

43. H. Ni, N. Eicke, C. Ruiz, J. Cai, F. Oppermann, N.I. Shvetsov-Shilovski, L.W. Pi, Phys. Rev. A **98**, 013411 (2018)

44. M. Lezius, V. Blanchet, D.M. Rayner, D.M. Villeneuve, A. Stolow, M.Y. Ivanov, Phys. Rev. Lett. **86**, 51 (2001)

45. A.N. Pfeiffer, C. Cirelli, M. Smolarski, D. Dimitrovski, M. Abu-samha, L.B. Madsen, U. Keller, Nat. Phys. **8**, 76 (2012)

46. N.I. Shvetsov-Shilovski, D. Dimitrovski, L.B. Madsen, Phys. Rev. A **85**, 23428 (2012)

47. A. Emmanouilidou, A. Chen, C. Hofmann, U. Keller, A.S. Landsman, J. Phys. B: At. Mol. Opt. Phys. **48**, 245602 (2015). arXiv:1505.07385v1

48. V.P. Majety, A. Scrinzi, J. Mod. Opt. **0340**, 1 (2017)

49. N.I. Shvetsov-Shilovski, M. Lein, Phys. Rev. A **100**, 053411 (2019). arXiv:1907.01231

50. S. Beiser, M. Klaiber, I.Y. Kiyan, Phys. Rev. A **70**, 11402 (2004)

51. I. Barth, O. Smirnova, Phys. Rev. A **84**, 063415 (2011). arXiv:1304.4875

52. T. Herath, L. Yan, S.K. Lee, W. Li, Phys. Rev. Lett. **109**, 043004 (2012)

53. K. Liu, H. Ni, K. Renziehausen, J.M. Rost, I. Barth, Phys. Rev. Lett. **121**, 203201 (2018)

54. A.W. Bray, Phd thesis, Australian National University (2020). http://hdl.handle.net/1885/203824

55. H. Xie, M. Li, S. Luo, Y. Li, Y. Zhou, W. Cao, P. Lu, Phys. Rev. A **96**, 063421 (2017)

56. N. Eicke, M. Lein, Phys. Rev. A **99**, 031402 (2019)

57. M.H. Yuan, X.B. Bian, Phys. Rev. A **101**, 013412 (2020)

58. R. Dörner, V. Mergel, O. Jagutzki, L. Spielberger, J. Ullrich, R. Moshammer, H. Schmidt-Böcking, Phys. Rep. **330**, 95 (2000)

59. A.S. Landsman, U. Keller, J. Phys. B: At. Mol. Opt. Phys. **47**, 204024 (2014)

60. Y. Ma, J. Zhou, P. Lu, H. Ni, J. Wu, J. Phys. B: At. Mol. Opt. Phys. (2021). https://doi.org/10.1088/1361-6455/ac0d3e

61. C. Hofmann, A.S. Landsman, C. Cirelli, A.N. Pfeiffer, U. Keller, J. Phys. B: At. Mol. Opt. Phys. **46**, 125601 (2013)

62. N. Eicke, M. Lein, Phys. Rev. A **97**, 031402 (2018)

63. A. Ludwig, J. Maurer, B.W. Mayer, C.R. Phillips, L. Gallmann, U. Keller, Phys. Rev. Lett. **113**, 243001 (2014). arXiv:1408.2336

64. A. Czirják, R. Kopold, W. Becker, M. Kleber, W. Schleich, Opt. Commun. **179**, 29 (2000)

65. S. Gräfe, J. Doose, J. Burgdörfer, J. Phys. B: At. Mol. Opt. Phys. **45**, 055002 (2012)

66. H. Chomet, D. Sarkar, C. Figueira de Morisson Faria, New J. Phys. **21**, 123004 (2019). arXiv:1907.12503

67. T. Zimmermann, L. Ortmann, C. Hofmann, J.M. Rost, A.S. Landsman (2018). arXiv:1804.09583

68. W. Koch, D.J. Tannor, Ann. Phys. 168288 (2020). arXiv:1907.12897

69. P. Ehrenfest, Z. Phys. **45**, 455 (1927)

70. I.A. Ivanov, C. Hofmann, L. Ortmann, A.S. Landsman, C.H. Nam, K.T. Kim, Commun. Phys. **1**, 81 (2018). arXiv:1804.06556

71. N. Teeny, E. Yakaboylu, H. Bauke, C.H. Keitel, Phys. Rev. Lett. **116**, 1 (2016). arXiv:1502.05917

72. N. Teeny, C.H. Keitel, H. Bauke, Phys. Rev. A **94**, 022104 (2016). arXiv:1605.06411

73. V.P. Krainov, J. Opt. Soc. Am. B **14**, 425 (2008)

74. T. Brabec, M.Y. Ivanov, P.B. Corkum, Phys. Rev. A **54**, R2551 (1996)

75. J. Chen, C.H. Nam, Phys. Rev. A **66**, 053415 (2002)

76. N.B. Delone, V.P. Krainov, J. Opt. Soc. Am. B **8**, 1207 (1991)

77. C. Lemell, K.I. Dimitriou, X.M. Tong, S. Nagele, D.V. Kartashov, J. Burgdörfer, S. Gräfe, Phys. Rev. A **85**, 011403 (2012)

78. L.D. Landau, E.M. Lifshitz, *Quantum Mechanics*, 2nd edn. (Pergamon Press Ltd, Oxford, 1965)

79. V.D. Mur, S.V. Popruzhenko, V.S. Popov, J. Exp. Theor. Phys. **92**, 777 (2001)

80. M. Weger, J. Maurer, A. Ludwig, L. Gallmann, U. Keller, Opt. Express **21**, 21981 (2013). arXiv:1301.2766

81. E.J. Heller, J. Chem. Phys. **65**, 4979 (1976)

82. E.J. Heller, J. Chem. Phys. **62**, 1544 (1975)

83. M.F. Herman, E. Kluk, Chem. Phys. **91**, 27 (1984)

84. N.I. Shvetsov-Shilovski, D. Dimitrovski, L.B. Madsen, Phys. Rev. A **87**, 013427 (2013)

85. A. Messiah, *Quantum Mechanics* (Wiley, New York, 1966)

86. N. Douguet, K. Bartschat, Phys. Rev. A **97**, 013402 (2018). arXiv:1712.07100

87. L.V. Keldysh, Zh Eksp, Teor. Fiz. **47**, 1945 (1964)

88. F.H.M. Faisal, J. Phys. B: At. Mol. Phys. **6**, L89 (1973)

89. H.R. Reiss, Phys. Rev. A **22**, 1786 (1980)

90. M. Klaiber, K.Z. Hatsagortsyan, C.H. Keitel, Phys. Rev. Lett. **120**, 013201 (2018)

91. B. Feuerstein, U. Thumm, J. Phys. B: At. Mol. Opt. Phys. **36**, 707 (2003)

92. X. Wang, J. Tian, J.H. Eberly, Phys. Rev. Lett. **110**, 243001 (2013)

93. X. Wang, J. Tian, J.H. Eberly, J. Phys. B: At. Mol. Opt. Phys. **51**, 084002 (2018)

94. R.H. Xu, X. Wang, AIP Adv. **11**, 025124 (2021)

95. J.P. Wang, F. He, Phys. Rev. A **95**, 043420 (2017)

96. Q. Zhang, G. Basnayake, A. Winney, Y.F. Lin, D. Debrah, S.K. Lee, W. Li, Phys. Rev. A **96**, 023422 (2017)

97. H. Ni, S. Brennecke, X. Gao, P.L. He, S. Donsa, I. Bezinová, F. He, J. Wu, M. Lein, X.M. Tong et al., Phys. Rev. Lett. **125**, 073202 (2020)

98. H. van Linden van den, H. Muller, in *Multiphoton Processes*. ed. by S.J. Smith, P.L. Knight (Cambridge University Press, Cambridge, 1988)

99. T.F. Gallagher, Phys. Rev. Lett. **61**, 2304 (1988)

100. P.B. Corkum, N.H. Burnett, F. Brunel, Phys. Rev. Lett. **62**, 1259 (1989)

101. K.C. Kulander, K.J. Schafer, J.L. Krause, in *Super-Intense Laser-Atom Physics*. ed. by B. Piraux, K. Huillier, K. Rzazewski (Plenum, New York, 1993)

102. P.B. Corkum, Phys. Rev. Lett. **71**, 1994 (1993)

103. T.M. Yan, S.V. Popruzhenko, M.J.J. Vrakking, D. Bauer, Phys. Rev. Lett. **105**, 253002 (2010)

104. T.M. Yan, D. Bauer, Phys. Rev. A **86**, 053403 (2012)

105. M. Li, J.W. Geng, H. Liu, Y. Deng, C. Wu, L.Y. Peng, Q. Gong, Y. Liu, Phys. Rev. Lett. **112**, 113002 (2014)

106. X.Y. Lai, C. Poli, H. Schomerus, C. Faria, Phys. Rev. A **92**, 043407 (2015)

107. X. Lai, S. Yu, Y. Huang, L. Hua, C. Gong, W. Quan, C. Faria, X. Liu, Phys. Rev. A **96**, 013414 (2017)

108. A.S. Maxwell, A. Al-Jawahiry, T. Das, C. Faria, Phys. Rev. A **96**, 023420 (2017)

109. A.S. Maxwell, A. Al-Jawahiry, X.Y. Lai, C. Faria, J. Phys. B: At. Mol. Opt. Phys. **51**, 044004 (2018)

110. A.S. Maxwell, S.V. Popruzhenko, C. Faria, Phys. Rev. A **98**, 063423 (2018)

111. A.S. Maxwell, C. Faria, J. Phys. B: At. Mol. Opt. Phys. **51**, 124001 (2018)

112. N.I. Shvetsov-Shilovski, M. Lein, L.B. Madsen, E. Räsänen, C. Lemell, J. Burgdörfer, D.G. Arbó, K. Tőkési, Phys. Rev. A **94**, 013415 (2016). arXiv:1604.05123

113. S. Popruzhenko, D. Bauer, J. Mod. Opt. **55**, 2573 (2008)

114. S.V. Popruzhenko, G.G. Paulus, D. Bauer, Phys. Rev. A **77**, 053409 (2008)

115. N. Zamstein, D.J. Tannor, J. Chem. Phys. **140**, 041105 (2014). https://doi.org/10.1063/1.4862898

116. C. Hofmann, A.S. Landsman, A. Zielinski, C. Cirelli, T. Zimmermann, A. Scrinzi, U. Keller, Phys. Rev. A **90**, 043406 (2014)

117. R. Boge, C. Cirelli, A.S. Landsman, S. Heuser, A. Ludwig, J. Maurer, M. Weger, L. Gallmann, U. Keller, Phys. Rev. Lett. **111**, 103003 (2013)

118. J.W. Geng, L. Qin, M. Li, W.H. Xiong, Y. Liu, Q. Gong, L.Y. Peng, J. Phys. B: At. Mol. Opt. Phys. **47**, 204027 (2014)

119. S. Brennecke, N. Eicke, M. Lein, Phys. Rev. Lett. **124**, 153202 (2020)

120. W. Miller, Adv. Chem. Phys. **25**, 69 (1974)

121. M.W. Walser, T. Brabec, J. Phys. B: Atomic Mol. Opt. Phys. **36**, 3025 (2003)

122. M. Spanner, Phys. Rev. Lett. **90**, 233005 (2003)

123. D. Tannor, *Introduction to Quantum Mechanics: A Time-Dependent Perspective* (University Science Books, Sausalito, 2007)

124. F. Grossmann, *Theoretical Femtosecond Physics. Atoms and Molecules in Strong Laser Fields* (Springer, Berlin, 2008)

8.11 *Multielectron polarization effects*

Multielectron polarization effects in strong-field ionization: Narrowing of momentum distributions and imprints in interference structures

N. I. Shvetsov-Shilovski,[1,*] M. Lein,[1] and L. B. Madsen[2]

[1]*Institut für Theoretische Physik, Leibniz Universität Hannover, D-30167 Hannover, Germany*
[2]*Department of Physics and Astronomy, Aarhus University, 8000 Århus C, Denmark*

We extend the semiclassical two-step model [Phys. Rev. A **94**, 013415 (2016)] to include a multielectron polarization-induced dipole potential. Using this model we investigate the imprints of multielectron effects in the momentum distributions of photoelectrons ionized by a linearly polarized laser pulse. We predict narrowing of the longitudinal momentum distributions due to electron focusing by the induced dipole potential. We show that the polarization of the core also modifies interference structures in the photoelectron momentum distributions. Specifically, the number of fanlike interference structures in the low-energy part of the electron momentum distribution may be altered. We analyze the mechanisms underlying this interference effect. The account of the multielectron dipole potential seems to improve the agreement between theory and experiment.

I. INTRODUCTION

Advances in laser technologies, especially the advent of table-top intense femtosecond optical laser systems have led to the remarkable progress in strong-field physics that studies the interaction of strong laser radiation with atoms and molecules. This interaction results in such phenomena as above-threshold ionization (ATI), high-order harmonic generation (HHG), nonsequential double ionization (NSDI), etc. (see Refs. [1–4] for reviews). In atomic ATI an electron absorbs more photons than necessary for ionization. The kinetic-energy spectrum generated by the ATI process consists of two distinct parts: a rapidly decaying low-energy part of the spectrum that ends at an energy around $2U_p$, where $U_p = F^2/4\omega^2$ is the ponderomotive energy (atomic units are used throughout the paper unless indicated otherwise); this part is followed by the high-energy plateau extending up to $\sim 10U_p$, which is often several orders of magnitude less intense than the maximum of the low-energy part. The part of the spectrum below $2U_p$ is mainly formed by electrons that do not undergo hard recollisions with their parent ions. These electrons are usually referred to as direct electrons. The spectrum of the direct electrons can be described by the two-step model for ionization [5–7]. In the first step of this model an electron is promoted to the continuum by tunneling ionization [8–10], and in the second step it moves along a classical trajectory in the laser field. In contrast to this, the high-energy plateau arises due to rescattered electrons that are driven back by the laser field to their parent ions and scatter by large angles. The qualitative description of the rescattering processes is provided by the three-step model [11,12], which includes the interaction of the returning electron with the parent ion as the third step. The concept of rescattering also provides the basis of the mechanisms responsible for HHG and NSDI. Indeed, the returning electron can recombine with the residual

ion, resulting in emission of high-frequency radiation, or as an alternative, if the energy of the rescattered electron is high enough, it can liberate another electron from the parent ion.

The main theoretical approaches to strong-field phenomena include the direct numerical solution of the time-dependent Schrödinger equation (TDSE) (see, e.g., Refs. [13–21]), the strong-field approximation (SFA) [22–25], and semiclassical models employing classical equations of motion to describe the electron motion in the continuum (see, e.g., Refs. [26–35]). The two- and the three-step models are the most well-known examples of the semiclassical approaches. All these theoretical methods are usually based on the single-active-electron approximation (SAE). Within the SAE, the ionization is considered as a one-electron process, i.e., an atom (or molecule) in the laser field is replaced by a single electron that interacts with the laser field and an effective potential. The latter is optimized to reproduce the ground state and singly excited states. Although SAE allows an understanding of the major features of ATI and HHG (see, e.g., Refs. [1,36]), the role of multielectron (ME) effects in these processes has recently been attracting considerable attention (see recent Refs. [37,38] and references therein).

Among the theoretical approaches capable to account for ME effects in strong-field processes are the time-dependent density-functional theory [39] (see Ref. [40] for a textbook treatment), multiconfiguration time-dependent Hartree-Fock theory [41,42], time-dependent restricted-active-space self-consistent-field theory [43], time-dependent complete-active-space self-consistent-field theory [44], time-dependent *R*-matrix theory [45,46], *R*-matrix method with time dependence [47,48], time-dependent configuration-interaction-singles [49,50], time-dependent restricted-active space configuration-interaction methods [51,52], time-dependent analytical *R*-matrix theory [53], and various semiclassical models (see, e.g., Refs. [31–35,37]). The advantages of the semiclassical approaches, such as their relative numerical simplicity and the ability to provide an illustrative

—————
*n79@narod.ru

physical picture of the phenomena under study, are particularly important in investigations of complex ME dynamics.

Laser-induced polarization of the ionic core is one of the well-known examples of ME effects. During the last years, significant progress has been achieved in studies of the polarization effects in ATI (see Refs. [54], [31–35], and [37]). The effective potential for the outer electron that takes into account the laser field, the Coulomb potential as well as the polarization effects of the inner core [see Eq. (2) in Sec. II] was found in Refs. [55,56] and [54] within the adiabatic approximation. It was shown that the Schrödinger equation with this effective potential and accounting for the Stark shift of the ionization potential can be approximately separated in the parabolic coordinates [31]. This separation procedure results in a certain tunneling geometry. The corresponding physical picture was named tunnel ionization in parabolic coordinates with induced dipole and Stark shift (TIPIS). The semiclassical model based on the TIPIS approach was validated by comparison with *ab initio* results [31,32] and experiments [26–31,33–35]. It was shown that for different atoms and molecules (Ar, Mg, naphthalene, etc.) the photoelectron momentum distributions are highly sensitive to ME effects as captured by the induced dipole of the atomic core [31–35].

Most of the studies mentioned here deal with circularly or close to circularly polarized laser fields. The reason is that the potential of Refs. [54,55] that is used in semiclassical simulations is valid at large and intermediate distances and not at short distances. It is well known that the rescattering processes are suppressed in close to circularly polarized laser fields [57], and, therefore, the vast majority of the electron trajectories do not return to the vicinity of the ionic core. However, this is certainly not the case for linearly polarized field. This raises the question regarding the applicability of the TIPIS model for linear polarization of the laser field. As a result, there is a lack of theoretical studies of the ME polarization effects in ATI with linearly polarized field.

To the best of our knowledge, Ref. [37] is the only application of the potential of Refs. [54,55] to semiclassical simulations of ATI processes in linearly polarized fields. That study focuses on the modification of the low-energy structures [58,59] and the very low-energy structures [59,60] due to polarization effects. It was shown that the relative yields of LES and VLES are enhanced due to the effect of the polarized ionic core on the recolliding electrons [37]. To the best of our knowledge, the impact of the polarization of the ionic core on the whole direct part of the spectrum has not been investigated so far. Furthermore, the applicability of the semiclassical model with the potential of Refs. [54,55] was not discussed in Ref. [37]. Finally, quantum interference was disregarded in all the trajectory-based studies of Refs. [31–35,37]. Since the ME potential affects both the tunnel exit point and the electron dynamics in the continuum [32], an imprint of the polarization effects in the interference patterns of the momentum distributions can be expected.

In this paper we apply the TIPIS model to ATI and momentum distributions in linearly polarized laser fields and analyze the applicability of this model. In order to study the interference effects due to the polarization of the ionic core, we combine the TIPIS approach with the semiclassical two-step model (SCTS) [61]. The SCTS model describes

quantum interference and accounts for the ionic potential beyond semiclassical perturbation theory. Recently this model was applied to the study of the intra-half-cycle interference of low energy photoelectrons [62], to the analysis of the interference patterns emerging in strong-field photoelectron holography (see Refs. [63,64]), and to the investigation of the subcycle interference upon ionization by counter-rotating two-color fields [65]. Using the semiclassical approach we calculate the photoelectron momentum distributions and energy spectra of the ATI in linearly polarized laser field with the account for the ME polarization potential and interference. We then analyze both the dynamic and interference effects induced by the polarization of the ionic core.

The paper is organized as follows. In Sec. II we briefly review the TIPIS model, discuss its application to the case of linear polarization, and formulate our combined model. In Sec. III we calculate photoelectron momentum distributions and energy spectra, identify the imprints of the ME polarization effect, and reveal by trajectory analysis the physical mechanisms underlying the formation of these imprints. The conclusions are given in Sec. IV.

II. MODEL

A detailed derivation of the TIPIS model as well as its applications to simulations of the photoelectron momentum distributions in elliptically polarized fields are presented in Ref. [32]. Here we repeat the main points to make the presentation self-contained. We next combine the TIPIS approach with the SCTS model. By doing so we develop a two-step semiclassical model for strong-field ionization with the inclusion of the Stark shift, the Coulomb potential, and the polarization induced dipole potential, capable of describing quantum interference.

A. TIPIS model and its application to linearly polarized laser fields

In semiclassical simulations the trajectory of an electron $\vec{r}(t)$ is calculated using Newton's equation of motion:

$$\frac{d^2\vec{r}}{dt^2} = -\vec{F}(t) - \vec{\nabla}V(\vec{r}, t), \qquad (1)$$

where $\vec{F}(t)$ is the electric field of the laser pulse, and the ionic potential $V(\vec{r}, t)$ is given by

$$V(\vec{r}, t) = -\frac{Z}{r} - \frac{\alpha_I \vec{F}(t) \cdot \vec{r}}{r^3}. \qquad (2)$$

Here Z is the ion charge. In Eq. (2) the ME effect is taken into account through the induced dipole potential [$\frac{\alpha_I \vec{F} \cdot \vec{r}}{r^3}$], where α_I is the static polarizability of the ion. As in Ref. [32], we refer to the second term of Eq. (2) as the ME term. It is important to stress that the potential of Eq. (2) is valid only at large and intermediate distances (see Refs. [54–56]).

In order to integrate Eq. (1), we need the starting point of the trajectory and the initial velocity of the electron. To obtain the former, i.e., the tunnel exit point, the approximate separation of variables in the static tunneling problem in parabolic coordinates is used in the TIPIS model. If the static field acts along the z axis, we define the parabolic

coordinates as $\xi = r + z$, $\eta = r - z$, and $\phi = \arctan(y/x)$. Then the approximate separation is valid in the limit $\xi/\eta << 1$ [31]. The tunnel exit point z_e is then found as $z_e \approx -\eta_e/2$, where η_e is the solution of the following equation:

$$-\frac{\beta_2(F)}{2\eta} + \frac{m^2 - 1}{8\eta^2} - \frac{F\eta}{8} + \frac{\alpha_I F}{\eta^2} = -\frac{I_p(F)}{4}, \quad (3)$$

where $I_p(F)$ is the ionization potential, m is the magnetic quantum number of the initial state, and

$$\beta_2(F) = Z - (1 + |m|)\frac{\sqrt{2I_p(F)}}{2} \quad (4)$$

is the separation constant [32]. The TIPIS model accounts for the Stark shift of the ionization potential:

$$I_p(F) = I_p(0) + (\vec{\mu}_N - \vec{\mu}_I) \cdot \vec{F} + \frac{1}{2}(\alpha_N - \alpha_I)F^2, \quad (5)$$

where $I_p(0)$ is the field-free ionization potential, $\vec{\mu}_N$ and $\vec{\mu}_I$ are the dipole moments of an atom (molecule) and of its ion, respectively, and α_N is the static polarizability of an atom (molecule). For atoms the term linear in $\vec{F}$ is absent in Eq. (5). The static field F in Eqs. (3), (4), and (5) should be interpreted as the instantaneous value of the laser field $F(t_0)$ at the time of ionization denoted by t_0.

We assume that the electron starts with zero initial velocity along the direction of the laser field: $v_{0,z} = 0$. It can, however, have a nonzero initial velocity $\vec{v}_{0,\perp}$ in the perpendicular direction. The ionization time t_0 and the initial transverse velocity $\vec{v}_{0,\perp}$ completely determine the electron trajectory. We distribute t_0 and $\vec{v}_{0,\perp}$ according to the static ionization rate [66]:

$$w(t_0, v_{0,\perp}) \sim \exp\left[-\frac{2\kappa^3}{3F(t_0)}\right] \exp\left[-\frac{\kappa v_{0,\perp}^2}{F(t_0)}\right] \quad (6)$$

with $\kappa = \sqrt{2I_p(F)}$. We omit the preexponential factor in Eq. (6), since for atoms it only slightly affects the shape of the photoelectron momentum distributions that we are interested in.

As the ME term of the potential Eq. (2) vanishes at $t \geqslant t_f$, where t_f is the time at which the laser pulse terminates, after the end of the pulse an electron moves in the Coulomb field only. The asymptotic momentum of the electron $\vec{k}$ can be found from its momentum $\vec{p}(t_f)$ and position $\vec{r}(t_f)$ at the end of the laser pulse (see Refs. [32,67]):

$$\vec{k} = k\frac{k(\vec{L} \times \vec{a}) - \vec{a}}{1 + k^2L^2}. \quad (7)$$

Here $\vec{L} = \vec{r}(t_f) \times \vec{p}(t_f)$ and $\vec{a} = \vec{p}(t_f) \times \vec{L} - Z\vec{r}(t_f)/r(t_f)$ are the angular momentum and Runge-Lenz vector, respectively. The magnitude of the asymptotic momentum can be found from energy conservation

$$\frac{k^2}{2} = \frac{p^2(t_f)}{2} - \frac{Z}{r(t_f)} \quad (8)$$

at the end of the laser pulse. Equipped with the ensemble of $(t_0, v_{0,\perp})$, and the corresponding values of the asymptotic momenta, we are now ready to combine the TIPIS approach with the SCTS model.

B. Combination of the TIPIS approach with the SCTS model

In order to study the ME polarization-induced interference effects, we combine the TIPIS approach with the SCTS model. In the SCTS model every classical trajectory is associated with a phase. The latter is calculated using the semiclassical expression for the matrix element of the quantum mechanical propagator [68–70]. For an arbitrary effective potential $V(\vec{r}, t)$ this phase is given (see Ref. [61]):

$$\Phi(t_0, \vec{v}_0) = -\vec{v}_0 \cdot \vec{r}(t_0) + I_p t_0$$
$$- \int_{t_0}^{\infty} dt \left\{ \frac{p^2(t)}{2} + V[\vec{r}(t)] - \vec{r}(t) \cdot \vec{\nabla}V[\vec{r}(t)] \right\}. \quad (9)$$

If $V(\vec{r}, t)$ is set to the potential of Eq. (2), the expression for the phase $\Phi(t_0, \vec{v}_0)$ reads as

$$\Phi(t_0, \vec{v}_0) = -\vec{v}_0 \cdot \vec{r}(t_0) + I_p t_0$$
$$- \int_{t_0}^{\infty} dt \left\{ \frac{p^2(t)}{2} - \frac{2Z}{r} - \frac{3\alpha_I \vec{F}(t) \cdot \vec{r}}{r^3} \right\}. \quad (10)$$

For our simulations we use an importance sampling implementation of the SCTS model. In this approach we distribute ionization times t_0^j and initial velocities $v_0^j (j = 1, \ldots, n_p)$ according to the square root of the tunneling probability [Eq. (6)]. We solve the equations of motion (1) and find the final (asymptotic) momenta of all n_p trajectories in the ensemble. Then we bin the trajectories in cells in momentum space according to their final momenta. The amplitudes associated with the trajectories reaching the same bin that is centered at a given final momentum $\vec{k}$ are added coherently, and the ionization probability is given by (see Ref. [61]):

$$\frac{dR}{d^3k} = \left| \sum_{j=1}^{n_p} \exp\left[i\Phi(t_0^j, \vec{v}_0^j)\right] \right|^2. \quad (11)$$

We note that convergence both with respect to the size of the momentum bin and the number of the trajectories must be achieved. The bin size and the number of trajectories in the ensemble needed for convergence strongly depend on the laser-atom parameters. All results provided below have been checked for convergence and the computational parameters are explicitly given in the illustrative examples.

III. RESULTS AND DISCUSSION

In our simulations we use a few-cycle laser pulse linearly polarized along the z axis and defined in terms of a vector potential:

$$\vec{A}(t) = (-1)^{n+1}\frac{F_0}{\omega} \sin^2\left(\frac{\omega t}{2n}\right) \sin(\omega t)\vec{e}_z, \quad (12)$$

where $\vec{e}_z$ is a unit vector, F_0 is the field strength, ω is the angular frequency, and n is the number of cycles within the pulse present between $t = 0$ and $t = t_f$, where $t_f = 2\pi n/\omega$. The electric field is obtained from Eq. (12) by $\vec{F}(t) = -\frac{d\vec{A}}{dt}$. We
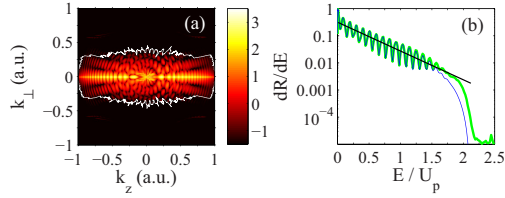
FIG. 1. (a) The two-dimensional photoelectron momentum distribution [Eq. (11)] for the Mg atom ionized by a laser pulse with an intensity of 3.0×10^{13} W/cm^2, wavelength of 1600 nm, and duration of $n = 8$ cycles. The white curve shows the boundary of the domain that can be reliably calculated using the TIPIS model. The laser field is linearly polarized along the z axis. The distribution is normalized to the total ionization yield. A logarithmic color scale in arbitrary units is used. (b) Electron energy spectra calculated without any restriction on the electron trajectories [thick (green) curve] and with the exclusion of the trajectories that approach the parent ion to the distances less than 5.0 a.u. [thin (blue) curve]. The slope of the spectra is qualitatively shown by the thin black line.

solve the equations of motion (1) using a fourth-order Runge-Kutta method with adaptive stepsize control [71].

Here we restrict ourselves to the case of atoms. Apart from the fact that the potential of Eq. (2) is inapplicable at small distances, the range of applicability of the TIPIS model is restricted by two conditions (see Ref. [32]). First, the field-induced term of Eq. (5) should not exceed 10–20% of the first term, and this introduces an upper bound for the magnitude of the laser intensity. At the same time, the intensity must not be too low: since in the TIPIS model the ionization probability is described by the tunneling formula [Eq. (6)], the Keldysh parameter $\gamma = \omega\kappa/F$ [22] should be less or of the order of one. We also note that the using of static polarizabilities is justified for large wavelengths λ. The choice of the atomic species and the laser parameters for which (i) the ME effects are more pronounced and (ii) the TIPIS model is applicable, is thoroughly discussed in Ref. [32].

We perform our simulations for Mg and Ca. For the Mg atom, $I_p = 0.28$ a.u., $\alpha_N = 71.33$ a.u., and $\alpha_I = 35.00$ a.u., whereas for Ca $I_p = 0.22$ a.u., $\alpha_N = 169.0$ a.u., and $\alpha_I = 74.11$ a.u. (see Ref. [72] for the values of polarizabilities). Note that these atoms have similar ionization potentials, but for Ca the static ionic polarizability that enters the ME term is approximately two times larger than the one for Mg. We do the simulations for the intensities of 3.0×10^{13} W/cm^2 (Mg) and 1.0×10^{13} W/cm^2 (Ca) and use the wavelength 1600 nm for both atoms. The corresponding Keldysh parameters for Mg and Ca are equal to $\gamma = 0.73$ and $\gamma = 1.13$, respectively.

First, we analyze the applicability of the TIPIS model to the case of linear polarization. In Ref. [37] a cutoff was introduced at a radial distance where the core polarization cancels the laser field. At the distances smaller than the cutoff radius the electron does not experience polarization effects. This approach follows the reasoning of Ref. [56], which was based on considerations of a behavior similar to that of a large metallic-like system.

Here we also introduce a cutoff radius r_C. However, in contrast to Ref. [37], we disregard all the trajectories entering

the sphere $r \leqslant r_C$. By doing so we prevent the electron trajectories from reaching the vicinity of the residual ion. The elimination of the returning trajectories leads to the depletion of some parts of the photoelectron momentum distributions. It is clear that these depleted parts cannot be reliably calculated within the TIPIS model. However, these domains usually correspond to the upper boundary of the direct ionization spectrum and do not involve its main part containing most of the yield. This point is illustrated by Figs. 1(a) and 1(b). In Fig. 1(a) we show the photoelecton momentum distribution calculated taking into account all the trajectories of the ensemble. The white curve in Fig. 1(a) shows the boundary of the part of the momentum distribution that is reliably reproduced when the trajectories entering the area $r \leqslant r_C$ are excluded. The electron energy spectra calculated with and without the elimination of the returning trajectories are compared in Fig. 1(b). If the photoelectron momentum distribution [Eq. (11)] is available, the energy spectrum can be calculated as

$$\frac{dR}{dE} = 2\pi\sqrt{(2E)}\int_0^\pi d\theta \sin\theta \frac{dR}{d^3k}[\vec{k}(\theta)]. \qquad (13)$$

For the parameters of Fig. 1 we need the bin size equal to 6.25×10^{-4} a.u. and an ensemble of 3.2 billion trajectories to achieve convergence. The latter was controlled by comparison of the energy spectra within the energy range in which signal decreases to 10^{-5} of its maximum. In our simulations we have chosen the cutoff radius equal to $r_C = 5.0$ a.u., but for the parameters considered here the results only weakly depend on the particular value of r_C in the range from 3.0 to 7.0 a.u. Figure 1(b) clearly shows that almost the whole direct part of the electron spectrum is unaffected by the exclusion of the returning trajectories. Taking into account these findings, in what follows we do not impose the condition $r < r_C$. We note, however, that at different laser-atom parameters the applicability of the TIPIS model to the case of linear polarization may be not as favorable as in Figs. 1(a) and 1(b). An analysis similar to the one presented here is, therefore, needed for any set of laser parameters before application of the TIPIS model to linearly polarized fields.

In Figs. 2(a) and 2(b) we present the two-dimensional photoelectron momentum distributions in the $(k_z, k_\perp)$ plane calculated within the semiclassical model accounting for laser and Coulomb field only [panels (a) and (c)] and with account of the ME potential [panels (b) and (d)]. The first and the second row of Fig. 2, i.e., panels [(a), (b)] and [(c), (d)] show the results for Mg and Ca, respectively. The size of the bin and the number of trajectories are the same as for Fig. 1. We note that the lack of the inversion symmetry of the two-dimensional momentum distributions that can be seen in Figs. 1(a) and 2 (as well as in Figs. 6 and 7) results from the finite duration of the laser pulse. Careful analysis of the results shown in Fig. 2 reveals that the presence of the ME term leads to two different effects: a narrowing of the longitudinal momentum distributions and a modification of the interference patterns. As we shall describe in detail later, the ME-induced dipole potential can alter the fanlike interference structures in the momentum distributions at low energy [Fig. 7(c) and 7(d)].

We first consider the narrowing effect. In order to illustrate this effect, we calculate the longitudinal momentum distributions dR/dk_z with and without the ME term [see
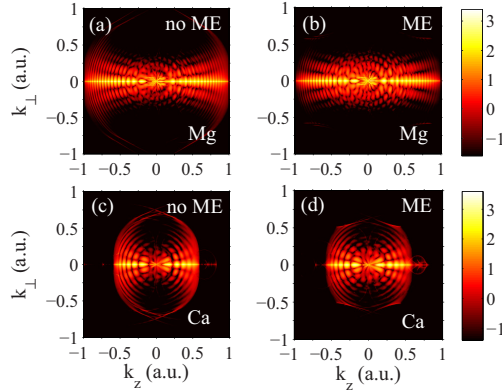
FIG. 2. The two-dimensional photoelectron momentum distributions for Mg [(a), (b)] and Ca [(c), (d)] ionized by a laser pulse with a duration of $n = 8$ cycles at a wavelength of 1600 nm. Panels (a, b) and (c, d) correspond to the intensities 3.0×10^{13} W/cm^2 and 1.0×10^{13} W/cm^2, respectively, implying the Keldysh parameters 0.71 and 1.13. The left column [panels (a) and (c)] show the distributions calculated ignoring the ME terms in Eqs. (2), (3), and (10). The right column [panels (b) and (d)] displays the distributions obtained with account of the ME terms in all equations. The distributions are normalized to the total ionization yield. A logarithmic color scale in arbitrary units is used. The laser field is linearly polarized along the z axis.
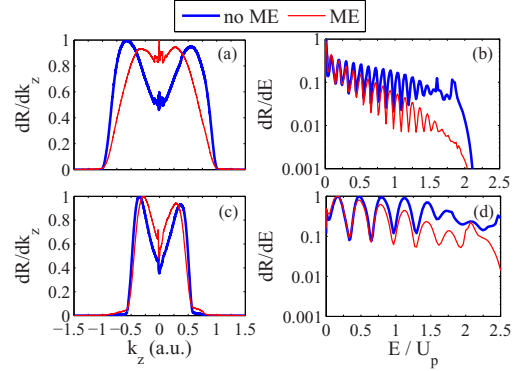

FIG. 3. Longitudinal momentum distributions [panels (a) and (c)] and energy spectra [panels (b) and (d)] of the photoelectrons for ionization of Mg [panels (a) and (b)] and Ca [panels (c) and (d)]. Red (thin) and blue (thick) curves correspond to the semiclassical simulations with and without ME term, respectively. The panels [(a) and (b)] and [(c) and (d)] correspond to the intensities 3.0×10^{13} W/cm^2 and 1.0×10^{13} W/cm^2, respectively. The wavelength and pulse durations are as in Figs. 1 and 2. The energy spectra and the longitudinal distributions are normalized to the peak value.

Figs. 3(a) and 3(c)]. The widths of the longitudinal momentum distributions are insensitive to the interference terms, which are, therefore, not included in Figs. 3(a) and 3(c). Furthermore, the narrowing of the two-dimensional distributions leads to the change of the slope of the electron energy spectra [Fig. 1(b)]. The spectra calculated with account of the ME term fall off more rapidly with electron energy than the ones calculated neglecting the polarization effects [see Figs. 3(b) and 3(d)]. It is also seen from Figs. 3(a) and 3(c) that the account of the ME term leads to partial filling of the dip at zero longitudinal momentum.

In order to understand the mechanism responsible for the narrowing of the longitudinal momentum distributions, we analyze electron trajectories ending up in a bin centered at some final momentum $\vec{k} = (k_z, k_\perp)$. We consider ionization of Mg [see Figs. 2(a) and 2(b)], and we choose $\vec{k}$ to be equal to $\vec{k}_0 = (0.86, 0.31)$ a.u. In the importance sampling approach, where the weight of every trajectory is accounted for already at the sampling stage and the photoelectron distribution is given by Eq. (11), the presence of the ME term reduces the number of trajectories reaching this bin by a factor of five. Therefore, the ionization probability at $\vec{k} = \vec{k}_0$ is substantially decreased due to the polarization of the residual ion. First we consider the trajectories leading to this bin neglecting the ME effect, i.e., when the electrons move in the laser and Coulomb fields. The analysis of these trajectories shows that there are three main groups of them starting from three different domains of the $(t_0, v_{0,\perp})$ space. We refer to these trajectories as no. 1, no. 2, and no. 3, respectively. In Fig. 4 we plot one characteristic trajectory from each group when the ME term is disregarded

in Eq. (1) (dashed curves). In the same plot we show the trajectories resulting when the ME term is taken into account while the initial conditions are unchanged (solid curves). Table I presents detailed quantitative information about these trajectories: Their times of start $t_0^{(j)}$, initial transverse velocities
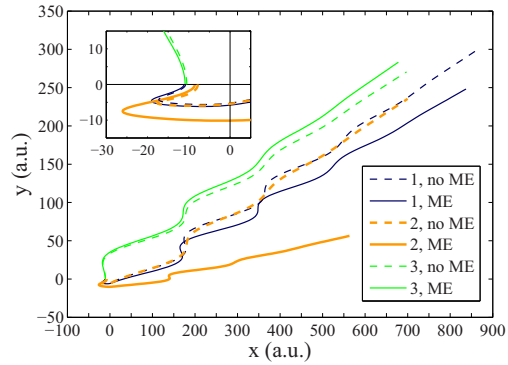

FIG. 4. Three characteristic electron trajectories leading in the absence of the ME potential to the same final momentum $\vec{k}_0 = (0.86, 0.31)$ a.u. The parameters correspond to the ionization of Mg by a laser pulse with a duration of $n = 8$ cycles, intensity of 3.0×10^{13} W/cm^2, and wavelength of 1600 nm. The dashed curves show the trajectories calculated ignoring the ME potential, i.e., when accounting for only the laser and Coulomb fields. The solid curves depict the trajectories moving in the laser field and the full potential of Eq. (2) including the ME term. The inset shows a zoom-in of the initial part of the electron trajectories.

TABLE I. The kinematic characteristics of the trajectories shown in Fig. 4. The table presents the times of start ωt_0^j, initial transverse velocities $v_{0,\perp}^{(j)}$, starting points $z_0^{(j)}$, and the final asymptotic momenta $\vec{k}_L^{(j)}$, $\vec{k}_{CL}^{(j)}$, and $\vec{k}^{(j)}$ that correspond to the motion in the laser field only, in the laser and Coulomb fields, and in the laser field and the full potential of Eq. (2), respectively.

j	$\omega t_0^{(j)}$ (rad)	$v_{0,\perp}^{(j)}$ (a.u.)	$z_0^{(j)}$ (a.u.)	$\vec{k}_L^{(j)}$ (a.u.)	$\vec{k}_{CL}^{(j)}$ (a.u.)	$\vec{k}^{(j)}$ (a.u.)
1	19.49	-0.10	-10.78	$(0.54, -0.10)$	$(0.84, 0.31)$	$(0.81, 0.26)$
2	25.50	-0.14	-7.78	$(0.37, -0.14)$	$(0.86, 0.31)$	$(0.70, 0.09)$
3	25.86	0.46	-10.49	$(0.67, 0.46)$	$(0.86, 0.31)$	$(0.84, 0.32)$

$v_{0,\perp}^{(j)}$, the tunnel exit points $z_0^{(j)}$, as well as the corresponding asymptotic momenta of the electron moving in the laser field only $\vec{k}_L^{(j)}$, in both laser and Coulomb fields $\vec{k}_{CL}^{(j)}$, and, the asymptotic momentum $\vec{k}^{(j)}$ that corresponds to the case when the entire potential of Eq. (2) is included into the equations of motion (1) [here $j = 1, 2$ and 3]. It is seen from Table I and Fig. 1 that, in contrast to the trajectories no. 1 and no. 3, trajectory no. 2 is strongly affected by the ME potential. The reason is that this trajectory has the smallest exit point (see Table I and inset in Fig. 1) and, simultaneously, its initial transverse velocity $v_{0,\perp} = -0.14$ a.u. is not large (comparable to the value $v_{0,\perp} = -0.10$ a.u. for the trajectory no. 1). Indeed, the force acting on the electron due to the ME polarization effect decays as $1/r^2$ with increasing r [see Eq. (2)]. For brevity, we call this force the ME force. It is clear that the ME force can affect the electron motion only at the initial parts of the electron trajectory close to its starting point (i.e., close to the tunnel exit). The smaller the distance to the tunnel exit, the stronger the effect of the ME force on the trajectory.

It is seen that for trajectory no. 2 both longitudinal and transverse components of the asymptotic momentum $\vec{k}$ are reduced due to the ME force when compared to the corresponding components of the momenta $\vec{k}^{(1)}$ and $\vec{k}^{(3)}$. As a result, trajectory no. 2 will not end up in any bin of the momentum space close to $\vec{k}_0$. Instead, it will lead to another bin with smaller k_z. It is worth noting that for close to circularly polarized fields the ME effect manifests itself in the rotation of the two-dimensional momentum distribution towards the minor axis of the polarization ellipse [31].

If the Coulomb and the ME forces are small compared to the laser field, these forces can be considered as small perturbations. Based on this idea analytical estimates of the effects of the Coulomb and ME forces were obtained in Ref. [32] for the asymptotic electron momenta by integrating both Coulomb and ME forces along the trajectory generated by a constant field $\vec{F}(t_0)$ at the time of ionization. In linearly polarized fields these estimates may be inapplicable even for the trajectories that are not substantially affected by the ME force (e.g., trajectory no. 1). This becomes clear already from the fact that the Coulomb potential changes the sign of the transverse momentum component (cf. $\vec{k}_C$ and $\vec{k}$ for the trajectory no. 1). We note, however, that the sign of the ME contribution to the final electron momentum is predicted correctly by the estimates of Ref. [32].

As the narrowing of the momentum distributions due to the polarization of the ionic core is a pronounced effect, we may expect that the inclusion of the ME term will be important to explain experimental data. In Figs. 5(a) and 5(b) we show the results of our semiclassical simulations for Ar

$(I_p = 0.58$ a.u., $\alpha_I = 7.2$ a.u.) by the eight-cycle laser pulse with intensity 5.0×10^{14} W/cm^2 and wavelength 800 nm. These parameters are close to those used in the experiment of Ref. [73]. Convergence was achieved at 1.6 billion trajectories and the bin size equal to 1.3×10^{-3} a.u. Since the interference oscillations are strong and the narrowing effect is weaker for Ar than for Mg or Ca, we again neglect quantum interference when calculating the longitudinal momentum distributions [see Fig. 5(a)]. The narrowing of the longitudinal distribution and the change of the slope of the energy spectra are clearly seen from Figs. 5(a) and 5(b). The experimental photoelectron momentum distributions of Ref. [73] are narrower than the corresponding theoretical results based on the solution of the TDSE within the SAE (see Refs. [74,75]). This suggests that polarization effects may be important in resolving the remaining subtle discrepancy between the experiment [73] and theory.

Let us finally discuss the interference effects caused by the laser-induced polarization of the atomic residual. It is seen from Figs. 2(a) and 2(b) that the changes of the interference patterns due to the ME terms in the equations of motion [Eq. (1)] and phase [Eq. (10)] are not very strong. These changes are only visible in the first and partially the second ATI peaks, as well as in the vicinity of the k_z axis. In order to understand the mechanism of the ME polarization-induced interference effect, we compare the photoelectron momentum distributions calculated without considering the ME effects [Fig. 6(a)], with the account of the ME term only in the equations of motion [Fig. 6(b)], and with the full account of the ME effects, i.e., by including the ME terms in the equations of motion and in the phase of Eq. (10) [Fig. 6(c)]. It is seen that the interference
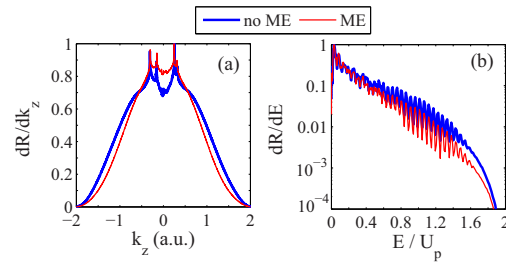

FIG. 5. Longitudinal momentum distributions (a) and electron energy spectra (b) calculated for ionization of Ar by a Ti:sapphire laser pulse (800 nm) with a duration of eight cycles and intensity 5.0×10^{14} W/cm^2. Red (thin) and blue (thick) curves correspond to the semiclassical simulations with and without ME term, respectively.
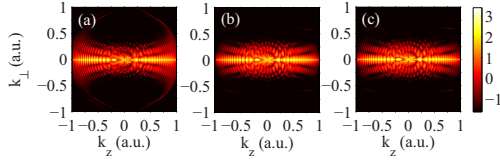
FIG. 6. The two-dimensional photoelectron momentum distributions for ionization of Mg calculated (a) ignoring ME polarization potential, (b) accounting for the ME force in the equations of motion [Eq. (1)], but disregarding the ME potential in the phase [Eq. (10)], and (c) with the full account of the ME term. The laser parameters are as in Figs. 1(a) and 1(b). The distributions are normalized to the total ionization yield. A logarithmic color scale in arbitrary units is used.

structures change mainly due to the presence of the ME term in the Newton's equations (1), i.e., due to the change of the electron trajectories caused by the polarization of the core.

At first glance, the facts that for Mg and Ca the polarization-induced changes of the interference patterns (i) are relatively weak and (ii) originate due to the dynamic effect may appear counterintuitive. Indeed, due to the relatively high values of α_I for Mg and Ca, the ME term in the integrand of Eq. (10) seems to have a sufficiently large value to produce substantial contribution to the phases of trajectories shown in Fig. 1. Therefore, we could expect substantial modification of the interference patterns for the parameters of Fig. 2 when including the ME potential. The detailed analysis of the trajectories interfering in different bins shows, however, while the ME phases are large, they have very similar magnitudes and, hence, they do not change the interference. The reason for this is the following. In order for two trajectories to interfere maximally, they must have comparable weights. Since the tunneling probability [Eq. (6)] is a sharp function of the electric field $F(t_0)$ at the time of start, the interfering trajectories start at the time instants that correspond to similar values of the instantaneous field. Furthermore, the contribution of the ME term to the phase (10) is mostly created on the initial part of the electron trajectory close to the tunnel exit. The latter depends only on the parameters of the atomic (molecular) species and the laser field at the time of ionization [see Eq. (3)]. As a result, the interfering trajectories have similar values of the ME contributions to the phase, $- \int_{t_0}^{\infty} \alpha_I \vec{F} \cdot \vec{r}/r^3 \, dt$, and the *difference* of these contributions, which is the quantity relevant for the interference, is small. Nevertheless, for atoms and molecules with larger values of the ionic polarizability α_I this difference can reach significant values, and, therefore, produce considerable changes of the interference patterns. To illustrate this point, in Figs. 7(a) and 7(b) we show the two-dimensional photoelectron momentum distributions for ionization of Ba ($\alpha_I = 124.15$ a.u., see Ref. [72]) calculated without considering the ME term in the phase and with [Eq. (10)] account of this term, respectively. The bin size and the number of trajectories in the ensemble are the same as for Fig. 1. In order to enhance intracycle interference, we consider here a shorter pulse with a duration of $n = 4$ cycles (cf. to $n = 8$ in Figs. 1–6). It is seen from Figs. 7(a) and 7(b) that the presence of the ME term in the phase of Eq. (10) leads to changes in the
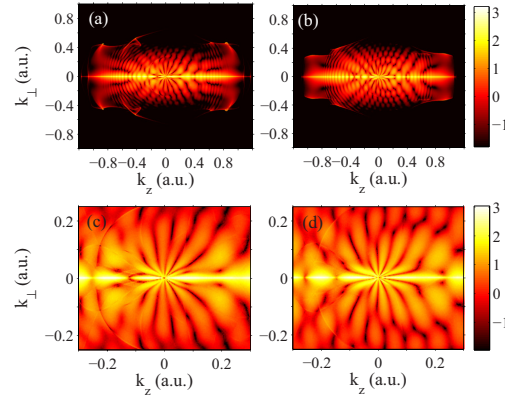

FIG. 7. Two-dimensional electron momentum distributions for the Ba atom ionized by a laser pulse with a duration of $n = 4$ cycles, wavelength of 1600 nm, and an intensity of $3.0 \times 10^{13} \, \text{W/cm}^2$ calculated [(a) and (c)] disregarding the ME term in the phase [Eq. (10)], and [(b) and (d)] with the account of this term. Panels (c) and (d) show the magnification for $k_z \leqslant 0.3$ a.u and $k_\perp \leqslant 0.25$ a.u. of the distributions shown in (a) and (b), respectively. For both distributions the ME force is included in the equations of motion. The distributions are normalized to the total ionization yield. A logarithmic color scale in arbitrary units is used.

interference pattern. For example, the number of radial nodal lines in the fanlike interference structure for $|k| \leqslant 0.25$ a.u. is different in the distributions calculated without and with the ME term in the phase [cf. Figs. 7(c) and 7(d)]. In Fig. 7(c), we see six fanlike structures for $k_\perp > 0$, while the presence of the ME contribution reduces the number of such structures to five in Fig. 7(d).

IV. CONCLUSIONS AND OUTLOOK

We have investigated ME effects as described by a laser-induced dipole polarization potential on photoelectron momentum distributions from strong-field ionization in a linearly polarized laser field. To this end, we have applied semiclassical simulations based on the TIPIS model [31]. We have analyzed the applicability of the TIPIS approach to the case of linear polarization. We have proposed a simple procedure that allows to find the domain in the photoelectron momentum distributions that can be reliably calculated by the TIPIS model. For the atomic species and laser parameters considered here this domain includes the whole direct part of the ATI spectrum. In order to study the polarization-induced interference efffects, we have combined the TIPIS approach with the SCTS model [61].

We predict a pronounced narrowing of the photoelectron momentum distributions in the longitudinal direction parallel with the laser polarization. By analyzing the characteristic electron trajectories we have studied the mechanism underlying the narrowing effect. We have shown that the narrowing is caused by the polarization-induced dipole force on electrons that start relatively close to the origin.

We have also revealed the polarization-induced modification of interference effects in the photoelectron momentum distributions. This effect is found to be pronounced for atoms with relatively high static polarizabilities, and it was found to change the number of fanlike interference structures at low energy in the two dimensional electron momentum distribution. Due to the rapid progress in experimental techniques, it is now possible to study photoelectron momentum distributions with high resolution (see, e.g., Ref. [76]), and, therefore, ME effects will have to be taken into account for accurate description of experimental data, in particular for larger molecules with large polarizabilities.

[1] W. Becker, F. Grasbon, R. Kopold, D. B. Milošević, G. G. Paulus, and H. Walther, Above-threshold ionization: From classical features to quantum effects, Adv. At. Mol. Opt. Phys. **48**, 35 (2002).

[2] D. B. Milošević and F. Ehlotzky, Scattering and reaction processes in powerful laser fields, Adv. At. Mol. Opt. Phys. **49**, 373 (2003).

[3] A. Becker and F. H. M. Faisal, Intense field many-body S-matrix theory, J. Phys. B **38**, R1 (2005).

[4] C. Faria and X. Liu, Electron-electron correlation in strong laser fields, J. Mod. Opt. **58**, 1076 (2011).

[5] H. B. van Linden van den Heuvell and H. G. Muller, in *Multiphoton processes*, edited by S. J. Smith and P. L. Knight, Multiphoton ionization in the long-wavelength limit (Cambridge University, Cambridge, 1988), p. 25.

[6] T. F. Gallagher, Above-Threshold Ionization in Low-Frequency Limit, Phys. Rev. Lett. **61**, 2304 (1988).

[7] P. B. Corkum, N. H. Burnett, and F. Brunel, Above-Threshold Ionization in the Long-Wavelength Limit, Phys. Rev. Lett. **62**, 1259 (1989).

[8] L. D. Landau and E. M. Lifshitz, *Quantum Mechanics Nonrelativistic Theory*, 3rd ed. (Pergamon, Oxford, 1991), Chap. 10, pp. 289–299.

[9] A. M. Perelomov, V. S. Popov, and M. V. Terent'ev, Ionization of atoms in an alternating electric field, Zh. Eksp. Teor. Fiz. **50**, 1393 (1966) [Sov. Phys. JETP **23**, 924 (1966)].

[10] M. V. Ammosov, N. B. Delone, and V. P. Krainov, Tunnel ionization of complex atoms and of atomic ions in an alternating electromagnetic field, Zh. Eksp. Teor. Fiz. **91**, 2008 (1986) [Sov. Phys. JETP **64**, 1191 (1986)].

[11] K. C. Kulander, K. J. Schafer, and J. L. Krause, in *Super-Intense Laser-Atom Physics*, edited by B. Pireaux, A. L'Huillier, and K. Rzazewski, Dynamics of short-pulse excitation, ionization, and harmonic conversion (Plenum, New York, 1993), p. 95.

[12] P. B. Corkum, Plasma Perspective on Strong-Field Multiphoton Ionization, Phys. Rev. Lett. **71**, 1994 (1993).

[13] K. J. LaGatutta, Laser effect in photoionization: Numerical solution of coupled equations for a three-dimensional Coulomb potential, J. Opt. Soc. Am. B **7**, 639 (1990).

[14] E. Cormier and P. Lambropoulos, Effect of a strong dressing field on the polarizability of atomic helium at harmonic frequencies, J. Phys. B **30**, 77 (1997).

[15] M. Nurhuda and F. H. M. Faisal, Numerical solution of time-dependent Schrödinger eqnution for multiphoton processes: A matrix iterative method, Phys. Rev. A **60**, 3125 (1999).

[16] H. G. Muller, An efficient propagation scheme for the time-dependent Schrödinger equation in the velocity gauge, Laser Phys. **9**, 138 (1999).

[17] D. Bauer and P. Koval, Qprop: A Schrödinger-solver for intense laser-atom interaction, Comput. Phys. Commun. **174**, 396 (2006).

[18] L. B. Madsen, L. A. A. Nikolopoulos, T. K. Kjeldsen, and J. Fernández, Extracting continuum information from Ψ(t) in time-dependent wave-packet calculations, Phys. Rev. A **76**, 063407 (2007).

[19] A. N. Grum-Grzhimailo, B. Abeln, K. Bartschat, D. Weflen, and T. Urness, Ionization of atomic hydrogen in strong infrared laser fields, Phys. Rev. A **81**, 043408 (2010).

[20] S. Patchkovskii and H. G. Muller, Simple, accurate, and efficient implementation of 1-electron atomic time-dependent Schrödinger equation in spherical coordinates, Comput. Phys. Commun. **199**, 153 (2016).

[21] X. M. Tong, A three-dimensional time-dependent Schrödinger equation solver: An application to hydrogen atoms in an elliptical laser field, J. Phys. B **50**, 144004 (2017).

[22] L. V. Keldysh, Ionization in the field of a strong electromagnetic wave, Zh. Eksp. Teor. Fiz. **47**, 1945 (1964) [Sov. Phys. JETP **20**, 1307 (1965)].

[23] F. H. M. Faisal, Multiple absorption of laser photons by atoms, J. Phys. B **6**, L89 (1973).

[24] H. R. Reiss, Effect of an intense electromagnetic field on a weakly bounded system, Phys. Rev. A **22**, 1786 (1980).

[25] M. Lewenstein, P. Balcou, M. Yu. Ivanov, A. L. Huillier, and P. B. Corkum, Theory of high-harmonic generation by low-frequency laser fields, Phys. Rev. A **49**, 2117 (1994).

[26] B. Hu, J. Liu, and S.-G. Chen, Plateau in above-threshold-ionization spectra and chaotic behavior in rescattering processes, Phys. Lett. A **236**, 533 (1997).

[27] L.-B. Fu, J. Liu, J. Chen, and S.-G. Chen, Classical collisional trajectories as the source of strong-field double ionization of helium in the knee regime, Phys. Rev. A **63**, 043416 (2001).

[28] J. Chen and C. H. Nam, Ion momentum distributions for He single and double ionization in strong laser fields, Phys. Rev. A **66**, 053415 (2002).

[29] R. Panfili, S. L. Haan, and J. H. Eberly, Slow-Down Collisions and Nonsequential Double Ionization in Classical Simulations, Phys. Rev. Lett. **89**, 113001 (2002).

[30] P. J. Ho and J. H. Eberly, Classical Effects of Laser Pulse Duration on Strong-Field Double Ionization, Phys. Rev. Lett. **95**, 193002 (2005).

[31] A. N. Pfeiffer, C. Cirelli, M. Smolarski, D. Dimitrovski, M. Abusamha, L. B. Madsen, and U. Keller, Attoclock reveals geometry for laser-induced tunneling, Nat. Phys. **8**, 76 (2012).

[32] N. I. Shvetsov-Shilovski, D. Dimitrovski, and L. B. Madsen, Ionization in elliptically polarized pulses: Multielectron polarization effects and asymmetry of photoelectron momentum distributions, Phys. Rev. A **85**, 023428 (2012).

[33] D. Dimitrovski, J. Maurer, H. Stapelfeldt, and L. B. Madsen, Low-Energy Photoelectrons in Strong-Field Ionization by Laser Pulses with Large Ellipticity, Phys. Rev. Lett. **113**, 103005 (2014).

[34] D. Dimitrovski and L. B. Madsen, Theory of low-energy photoelectrons in strong-field ionization by laser pulses with large ellipticity, Phys. Rev. A **91**, 033409 (2015).

[35] D. Dimitrovski, J. Maurer, H. Stapelfeldt, and L. B. Madsen, Observation of low-energy electrons in the photoelectron energy distribution from strong-field ionization of naphtalene by circularly polarized pulses, J. Phys. B **48**, 121001 (2015).

[36] F. Grossmann, *Theoretical Femtosecond Physics. Atoms and Molecules in Strong Laser Fields* (Springer-Verlag, Berlin, 2008).

[37] H.-P. Kang, S.-P. Xu, Y.-L. Wang, S.-G. Yu, X.-Y. Zhao, X.-L. Hao, X.-Y. Lai, T. Pfeifer, X.-J. Liu, J. Chen, Y. Cheng, and Z.-Z. Xu, Polarization effects in above-threshold ionization with a mid-infrared strong laser field, J. Phys. B **51**, 105601 (2018).

[38] C.-T. Le, V.-H. Hoang, L.-P. Tran, and V.-H. Le, Effect of the dynamic core polarization of CO molecules on high-order harmonic generation, Phys. Rev. A **97**, 043405 (2018).

[39] E. Runge and E. K. U. Gross, Density-Functional Theory for Time-Dependent Systems, Phys. Rev. Lett. **52**, 997 (1984).

[40] C. A. Ullrich, *Time-Dependent Density-Functional Theory: Concepts and Applications* (Oxford University Press, Oxford, 2012).

[41] J. Zanghellini, M. Kitzler, T. Brabec, and A. Scrinzi, Testing the multi-configuration time-dependent Hartree-Fock method, J. Phys. B **37**, 763 (2004).

[42] J. Caillat, J. Zanghellini, M. Kitzler, O. Koch, W. Kreuzer, and A. Scrinzi, Correlated multielectron systems in strong laser fields: A multiconfiguration time-dependent Hartree-Fock approach, Phys. Rev. A **71**, 012712 (2005).

[43] H. Miyagi and L. B. Madsen, Time-dependent restricted-active-space self-consistent-field theory for laser-driven many-electron dynamics, Phys. Rev. A **87**, 062511 (2013).

[44] T. Sato and K. L. Ishikawa, Time-dependent complete-active-space self-consistent-field method, Phys. Rev. A **88**, 023402 (2013).

[45] P. G. Burke and V. M. Burke, Time-dependent R-matrix theory of multiphoton processes, J. Phys. B **30**, L383 (1997).

[46] M. A. Lysaght, H. W. van der Hart, and P. G. Burke, Time-dependent R-matrix theory for ultrafast atomic processes, Phys. Rev. A **79**, 053411 (2009).

[47] L. A. A. Nikolopoulos, J. S. Parker, and K. T. Taylor, Combined R-matrix eigenstate basis set and finite-difference propagation method for the time-dependent Schrödinger equation: The one-electron case, Phys. Rev. A **78**, 063420 (2008).

[48] L. R. Moore, M. A. Lysaght, L. A. A. Nikolopoulos, J. S. Parker, H. W. van der Hart, and K. T. Taylor, The RMT method for many-electron atomic systems in intense short-pulse laser light, J. Mod. Opt. **58**, 1132 (2011).

[49] N. Rohringer, A. Gordon, and R. Santra, Configuration-interaction-based time-dependent orbital approach for *ab initio* treatment of electronic dynamics in a strong optical laser field, Phys. Rev. A **74**, 043420 (2006).

[50] S. Pabst, L. Greenman, D. A. Mazziotti, and R. Santra, Impact of multichannel and multipole effects on the cooper minimum in the high-order-harmonic spectrum of argon, Phys. Rev. A **85**, 023411 (2012).

[51] D. Hochstuhl and M. Bonitz, Time-dependent restricted-active-space configuration-interaction method for the photoionization of many-electron atoms, Phys. Rev. A **86**, 053424 (2012).

[52] S. Bauch, L. K. Sørensen, and L. B. Madsen, Time-dependent generalized-active-space configuration-interaction approach to photoionization dynamics of atoms and molecules, Phys. Rev. A **90**, 062508 (2014).

[53] L. Torlina and O. Smirnova, Time-dependent analytical R-matrix approach for strong-field dynamics. I. One-electron systems, Phys. Rev. A **86**, 043408 (2012).

[54] D. Dimitrovski, C. P. J. Martiny, and L. B. Madsen, Strong-field ionization of polar molecules: Stark-shift-corrected strong-field approximation, Phys. Rev. A **82**, 053404 (2010).

[55] T. Brabec, M. Côté, P. Boulanger, and L. Ramunno, Theory of Tunnel Ionization in Complex Systems, Phys. Rev. Lett. **95**, 073001 (2005).

[56] Z. X. Zhao and T. Brabec, Tunnel ionization in complex systems, J. Mod. Opt. **54**, 981 (2007).

[57] P. Dietrich, N. H. Burnett, M. Ivanov, and P. B. Corkum, High-harmonic generation and correlated two-electron multiphoton ionization with elliptically polarized light, Phys. Rev. A **50**, R3585 (1994).

[58] C. I. Blaga, F. Catoire, P. Colosimo, G. G. Paulus, H. G. Muller, P. Agostini, and L. F. DiMauro, Strong-field photoionization revisited, Nat. Phys. **5**, 335 (2009).

[59] W. Quan, Z. Lin, M. Wu, H. Kang, H. Liu, X. Liu, J. Chen, J. Liu, X. T. He, S. G. Chen, H. Xiong, L. Guo, H. Xu, Y. Fu, Y. Cheng, and Z. Z. Xu, Classical Aspects in Above-Threshold Ionization with a Midinfrared Strong Laser Field, Phys. Rev. Lett. **103**, 093001 (2009).

[60] C. Y. Wu, Y. D. Yang, Y. Q. Liu, Q. H. Gong, M. Wu, X. Liu, X. L. Hao, W. D. Li, X. T. He, and J. Chen, Characteristic Spectrum of Very Low-Energy Photoelectron from Above-Threshold Ionization in the Tunneling Regime, Phys. Rev. Lett. **109**, 043001 (2012).

[61] N. I. Shvetsov-Shilovski, M. Lein, L. B. Madsen, E. Räsänen, C. Lemell, J. Burgdörfer, D. G. Arbó, and K. Tőkési, Semiclassical two-step model for strong-field ionization, Phys. Rev. A **94**, 013415 (2016).

[62] H. Xie, M. Li, Y. Li, Y. Zhou, and P. Lu, Intra-half-cycle interference of low-energy photoelectron in strong midinfrared laser fields, Opt. Express **24**, 27726 (2016).

[63] S. G. Walt, N. Bhargava Ram, M. Atala, N. I. Shvetsov-Shilovski, A. von Conta, D. Baykusheva, M. Lein, and H. J. Wörner, Dynamics of valence-shell electrons and nuclei probed by strong-field holography and rescattering, Nat. Commun. **8**, 15651 (2017).

[64] N. I. Shvetsov-Shilovski and M. Lein, Effects of the Coulomb potential in interference patterns of strong-field holography with photoelectrons, Phys. Rev. A **97**, 013411 (2018).

[65] S. Eckart, M. Kunitski, I. Ivanov, M. Richter, K. Fehre, A. Hartung, J. Rist, K. Henrichs, D. Trabert, N. Schlott, L. Ph. H.

Schmidt, T. Jahnke, M. S. Schöffler, A. Kheifets, and R. Dörner, Subcycle interference upon tunnel ionization by counter-rotating two-color fields, Phys. Rev. A **97**, 041402 (2018).

[66] N. B. Delone and V. P. Krainov, Energy and angular electron spectra for the tunnel ionization of atoms by strong low-frequency radiation, J. Opt. Soc. Am. B **8**, 1207 (1991).

[67] N. I. Shvetsov-Shilovski, S. P. Goreslavski, S. V. Popruzhenko, and W. Becker, Capture into Rydberg states and momentum distributions of ionized electrons, Laser Phys. **19**, 1550 (2009).

[68] W. H. Miller, Classical-limit quantum mechanics and the theory of molecular collisions, Adv. Chem. Phys. **25**, 69 (1974).

[69] M. Walser and T. Brabec, Semiclassical path integral theory of strong-laser-field physics, J. Phys. B **36**, 3025 (2003).

[70] M. Spanner, Strong Field Tunnel Ionization by Real-Valued Classical Trajectories, Phys. Rev. Lett. **90**, 233005 (2003).

[71] W. H. Press, S. A. Teukolsky, W. T. Vetterling, and B. P. Flannery, *Numerical Recipes in Fortran 77: The Art of Scientific Computing*, 2nd ed. (Cambridge University Press, Cambridge, 1992).

[72] J. Mitroy, M. S. Safronova, and C. W. Clark, Theory and applications of atomic and ionic polarizabilities, J. Phys. B. **43**, 202001 (2010).

[73] A. Rudenko, K. Zrost, C. D. Schröter, V. L. B. de Jesus, B. Feuerstein, R. Moshammer, and J. Ullrich, Resonant structures in the low-energy electron continuum for single ionization of atoms in the tunneling regime, J. Phys. B **37**, L407 (2004).

[74] T. Morishita, Z. Chen, S. Watanabe, and C. D. Lin, Two-dimensional electron momentum spectra of argon ionized by short intense lasers: Comparison of theory with experiment, Phys. Rev. A **75**, 023407 (2007).

[75] M. Abu-Samha and L. B. Madsen, Momentum distributions of selected rare-gas atoms probed by intense femtosecond laser pulses, J. Phys. B **44**, 235601 (2011).

[76] Ph. A. Korneev, S. V. Popruzhenko, S. P Goreslavski, T.-M. Yan, D. Bauer, W. Becker, M. Kübel, M. F. Kling, C. Rödel, M. Wünsche, and G. G. Paulus, Interference Carpets in Above-Threshold Ionization: From the Coulomb-Free to the Coulomb-Dominated Regime, Phys. Rev. Lett. **108**, 223601 (2012).

8.12   Reconstruction of a single-active-electron potential

Reconstruction of a single-active-electron potential from electron momentum distribution produced by strong-field ionization using optimization technique

N I Shvetsov-Shilovski[*]

Institut für Theoretische Physik, Leibniz Universität Hannover, D-30167, Hannover, Germany

E-mail: n79@narod.ru

CrossMark

Abstract

We present a method for retrieving of single-active electron potential in an atom or molecule from a given momentum distribution of photoelectrons ionized by a strong laser field. In this method the potential varying within certain limits is found as the result of the optimization procedure aimed at reproducing the given momentum distribution. The optimization using numerical solution of the time-dependent Schrödinger equation for ionization of a model one-dimensional atom shows the good accuracy of the potential reconstruction method. This applies to different ways used for representing of the potential under reconstruction, including a parametrization and determination of the potential by specifying its values on a spatial grid.

Keywords: strong-field ionization, derivative-free optimization, photoelectron momentum distributions, single-active electron potential

(Some figures may appear in colour only in the online journal)

1. Introduction

The advances in laser technologies during the last decades have allowed to study the variety of phenomena arising from the interaction of strong laser radiation with matter, see, e.g. [1, 2] for recent reviews. These phenomena include above-threshold ionization (ATI), formation of the high-energy plateau in the ATI spectrum (high-order ATI), generation of high-order harmonics (HHG), nonsequential double ionization (NSDI), etc (see [3–6] for reviews). It was shown in the studies of the ATI process that the vast majority of the photoelectrons do not recollide with their parent ions. These electrons are referred to as direct electrons. They are detected with the energies below $2U_\mathrm{p}$, where $U_\mathrm{p} = F_0^2/\omega^2$ is the ponderomotive

energy. Here F_0 is the field strength and ω is the angular frequency (atomic units are used throughout the paper). There are also rescattered electrons that due to oscillations of the laser field come back to their parent ions and rescatter on them by large angles. The rescattered electrons form the high-energy plateau in the ATI spectrum, i.e. they are responsible for the high-order ATI.

The development of laser technologies has also given rise to a number of techniques aimed at time-resolved molecular imaging, including, laser-induced Coulomb explosion imaging [7–10], laser-assisted electron diffraction [11, 12], high-order harmonic orbital tomography [13, 14], laser-induced electron diffraction [15–17], strong-field photoelectron holography [18], see [19] for review. The correct interpretation of the imaging experiments, as well as the understanding of the HHG, NSDI, and other phenomena in intense laser fields, requires an accurate description of strong-field ionization of various quantum systems. Among the main theoretical approaches used to describe ionization of atoms by strong laser pulses are the

strong-field approximation [20–22], the semiclassical models [23–27], and the direct numerical solution of the time-dependent Schrödinger equation (TDSE) (see, e.g. [28–31]) in single-active electron (SAE) approximation [32, 33]. Within the SAE the strong-field ionization of many-electron atom or molecule is described as an interaction of only one active electron with the laser radiation. This active electron moves in the combined effective potential and the electric field of the laser pulse. In many cases the solution of the TDSE within the SAE gives good agreement with experimental data. In situations where the multielectron effects are important, the SAE is still valuable, since it provides a necessary benchmark for the analysis of the results of multielectron calculations. On the other hand, if the multielectron simulations are not feasible, the SAE remains the only possible approach. Therefore, it is important to obtain suitable SAE potentials for various systems.

In this paper we focus on the atomic case only. The SAE potential designed for a multielectron atom should account for the presence of the atomic nucleus and approximately describe the effect of other electrons. The calculation of such a potential is a non-trivial task. Indeed, the widely used potential by Tong and Lin [34] was obtained using density-functional theory. This potential has a singularity at $r \to 0$. The same is true for the other well-known potential [35] and the SAE potentials obtained recently by fitting to the effective Kohn–Sham potentials [36]. However, the presence of this singularity causes problems, if the TDSE is solved with the split-operator method [37] employing fast Fourier transform. To avoid this singularity, the SAE potential can be converted into a pseudo potential using an approach developed by Troullier and Martins [38]. Nevertheless, while the pseudopotential can be successfully applied to description of the direct electrons, it faces challenges in describing the rescattering process (see [39] for details). Therefore, development of approaches aimed at calculation of the SAE potentials is of great interest.

The SAE potentials are often constructed as analytic functions that depend on one or a few parameters. While one parameter of the potential allows to reproduce only one bound-state energy, the presence of several parameters makes it possible to recover the predefined energies of few different bound states. Usually, the parameters of a model potential are adjusted using an optimization technique. This suggests to obtain the SAE potential as a result of some optimization procedure. Indeed, in reference [40] the atomic potentials were retrieved from differential electron scattering cross section using genetic algorithm. The differential cross sections can in turn be extracted from momentum distributions of the rescattered electrons. Nevertheless, since the potential experienced by the ionized electron is encoded in the measured photoelectron momentum distribution (PMD), it should be possible to optimize the unknown SAE potential in order to directly reproduce a given PMD generated by strong-field ionization of an atom.

In this paper we develop such an approach to retrieval of the SAE potentials. We assume that the given momentum distribution is measured in an experiment and refer to it as the target PMD (TPMD). The TPMD is considered as a goal that is to be achieved by an optimization algorithm considering the

unknown values of the potential (or expansion coefficients of the potential in a given basis) as parameters that are optimized. It should be stressed that there is a substantial difference between the approach proposed here and the quantum optimal control theory (QOCT), see [41, 42] for reviews. The latter provides a powerful theoretical approach to the optimization and control of various quantum phenomena, including those in strong laser fields (see, e.g. [43–46]). Indeed, the QOCT treats the electric field of the laser pulse as a control function, whereas the effective potential experienced by an electron is to be predefined and does not change in optimization.

Any optimization requires a specification of a measure that allows to identify whether the optimization target is achieved. Since a PMD is a picture, it is natural to specify such a measure using tools employed in image analysis and pattern recognition. Therefore, the measures applied to compare different digital images or videos (see, e.g. [47, 48]) can be used to estimate the similarity of the two PMD's: the result of current iteration of an optimization algorithm and the target distribution. However, a valid choice of the specific measure and its application to comparison of the PMD's require thorough studies. For this reason, we leave the application of image recognition tools for future investigations. In this paper we retrieve the SAE potential from momentum distribution produced in ionization of a one-dimensional (1D) model atom. The 1D momentum distribution is a function of only one variable (momentum component along one spatial axis). Therefore, the widely-known measures used in variation calculus and functional analysis (see, e.g. [49]) can be applied for comparison of different PMD's. In our optimization-based approach only momentum distributions of the direct electrons are used. The optimization technique relying on the distributions of rescattered electrons will be the subject of further studies.

The paper is organized as follows. In section 2 we briefly discuss our approach to solve the 1D TDSE, measures used to compare electron momentum distributions, and derivative-free optimization algorithms. In section 3 we apply our method to retrieve the soft-core Coulomb potential from the PMD's produced by ionization of a 1D model atom. We test our approach for two different ways of representing the unknown potential and discuss various optimization strategies. The conclusions and outlook are given in section 4.

2. Comparison of electron momentum distributions and optimization

2.1. Numerical solution of the TDSE

We define a few-cycle laser pulse linearly polarized along the *x*-axis by specifying its vector-potential:

$$\mathbf{A}(t) = (-1)^{n_{\mathrm{p}}+1} \frac{F_0}{\omega} \sin^2\left(\frac{\omega t}{2n_{\mathrm{p}}}\right) \sin(\omega t + \varphi)\, \mathbf{e}_x, \quad (1)$$

where n_{p} is number of optical cycles within the pulse, φ is the carrier envelope phase, $\mathbf{e}_x$ is a unit vector, and the laser pulse is present between $t = 0$ and $T = (2\pi/\omega)\, n_{\mathrm{p}}$. The electric field can be calculated from vector-potential (1) by $\mathbf{F} = -\mathrm{d}\mathbf{A}/\mathrm{d}t$. In the velocity gauge, the 1D TDSE for an electron interacting

with the lase pulse is given by

$$i\frac{\partial}{\partial t}\Psi(x,t) = \left[\frac{1}{2}\left(-i\frac{\partial}{\partial x} + A_x(t)\right)^2 + V(x)\right]\Psi(x,t), \quad (2)$$

where $\Psi(x,t)$ is the time-dependent wave function in coordinate representation and $V(x)$ is the SAE potential. In the absence of the electric field, the time-independent Schrödinger equation reads as

$$\left[-\frac{1}{2}\frac{d^2}{dx^2} + V(x)\right]\Psi(x) = E\Psi(x), \quad (3)$$

where $\Psi(x)$ and E are the eigenfunction and the corresponding energy eigenvalue, respectively. The eigenvalue problem (3) is solved on a grid using the three-step formula to approximate the second derivative. Hence, the diagonalization routine developed for sparse matrices [50] can be used. Alternatively, the ground state and the first few excited states can be found by imaginary time propagation (see, e.g. [51, 52]). The computational box is centered at $x = 0$ and extends to $\pm x_{\max}$, i.e. $x \in [-x_{\max}, x_{\max}]$. Typically, we set $x_{\max} = 250.0$ a.u. and use a grid consisting of $N = 4096$ points, what corresponds to the grid spacing $dx = 0.1225$ a.u.

The well-known split-operator method [37] is used to solve the TDSE (2). The time step is $\Delta t = 0.055$ a.u.. We prevent unphysical reflections from the boundary of the grid by using absorbing boundaries, i.e. at every step of the time propagation we multiply the wave function in the region $|x| > x_b$ by the mask:

$$M(x) = \cos^{1/6}\left[\frac{\pi(|x| - x_b)}{2(x_{\max} - x_b)}\right] \quad (4)$$

with $x_b = 3x_{\max}/4$. Hence, $x = \pm x_b$ correspond to the internal boundaries of the absorbing regions. As the result, at every time step the part of the wave function in the mask region is absorbed without any effect on the $|x| < x_b$ domain. We calculate the electron momentum distributions using the mask method [53].

2.2. Comparison of electron momentum distributions and optimization algorithms

The optimization procedure developed here is based on comparison of the 1D electron momentum distributions, which are functions of one variable. The following metrics are widely used to calculate the distance between continuous functions $f(x)$ and $g(x)$ defined for $x \in [a, b]$:

$$\rho_1[f(x), g(x)] = \max_{x \in [a,b]} |f(x) - g(x)| \quad (5)$$

and

$$\rho_2[f(x), g(x)] = \left\{\int_a^b dx[f(x) - g(x)]^2\right\}^{1/2}, \quad (6)$$

see, e.g. [49] for a textbook treatment. We use metric (6) as a measure of difference between two PMD's. We note that before calculating the distance (6) we normalize electron momentum distributions to the total ionization yield (i.e. the

area under the graph of the PMD). Therefore, our optimization procedure relies only on the shape of momentum distributions, but not on the ionization probabilities. We believe that similar approach when applied to the 3D case will help to facilitate the retrieval of the unknown potential from experimental electron momentum distributions.

Since the derivatives of the similarity measure with respect to unknown potential values (or any other parameters used to represent the potential) can be calculated only numerically, it is not practical to use any gradient-based optimization method. Instead, it is appropriate to use a derivative-free optimization technique, see [54, 55] for recent reviews. We apply particle swarm optimization method [56, 57], surrogate optimization technique [58], and pattern search method [59–61]. The MATLAB system [62] is used for simulations.

3. Results and discussion

3.1. Reconstruction of SAE potential on a grid

In this work we reconstruct the soft-core Coulomb potential:

$$V(x) = \frac{Z}{\sqrt{x^2 + a}} \quad (7)$$

with $Z = 1.0$ and $a = 1.0$, see [63]. At first, we do not use any parametrization to represent the potential (7). Instead, we determine the potential that is to be retrieved by specifying its values in certain points of the x-axis. The potential values in any other points are found by interpolation. Here we use cubic spline interpolation [64]. As many other SAE potentials the potential $V(x)$ changes more rapidly for small values of x. Therefore, it is natural to use a non-uniform grid to represent the potential (7).

Here we apply the following grid used for development of generalized pseudospectral methods:

$$x = \gamma\frac{1 + x_0}{1 - x_0 + x_0^m}, \quad (8)$$

where $x_0^m = 2\gamma/x_{\max}$ and γ is the mapping parameter [65–67]. Equation (8) transforms a uniform grid within the domain $x_0 \in [-1.0, 1.0]$ to a nonuniform grid in the domain $x \in [0, x_{\max}]$. The points of this grid are to be reflected with respect to $x = 0$ and thus a nonuniform grid in the whole range $x \in [-x_{\max}, x_{\max}]$ is obtained. Then the question arises: how many points of the grid (8) are required to represent the potential with sufficient accuracy? To answer this question, we choose different numbers of points for the uniform grid in the range $[-1.0, 1.0]$, find the corresponding point of the nonuniform grid (8), and calculate the potential values at these points. For each number of points of the nonuniform grid we interpolate the potential $V(x)$ at every point of the dense uniform grid with N points. For this interpolated potential we find energy eigenvalues and the corresponding eigenfunctions, solve the TDSE for a given laser pulse, and calculate electron momentum distributions. We next compare these PMD's with the reference momentum distribution obtained in the case that the potential (7) is directly calculated on the dense uniform grid consisting of N points, see figure 1. It is seen that about
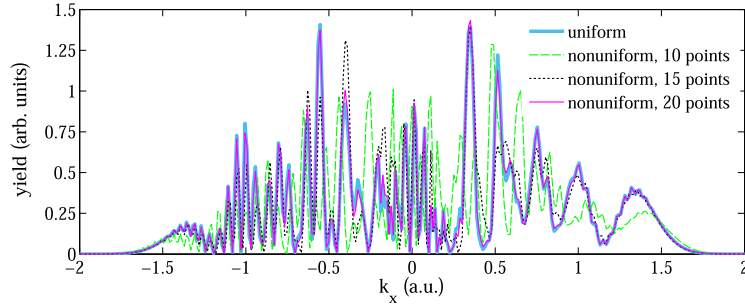
Figure 1. The electron momentum distributions for ionization of a 1D atom by a laser pulse with a duration of $n_p = 4$ cycles, wavelength of 800 nm, phase $\varphi = 0$, and intensity of 2.0×10^{14} W cm^{-2}. The distributions are obtained from the solution of the TDSE (2) with the potential (7) calculated on a uniform grid consisting of $N = 4096$ points (thick light-blue curve), as well as with the same potential determined by its values on the non-uniform grid (8) with $\gamma = 20.5$ consisting of 10 (dashed green curve), 15 (dotted black curve), and 20 (thin magenta curve) points.

20 points of the nonuniform grid (8) is sufficient to reproduce the reference PMD accurately enough. Indeed, the difference between these distributions calculated in accord with the measure (6) is about 0.01. Taking into account that the potential $V(x)$ is an even function, the number of the points can be reduced by a factor of two, i.e. only 10 points are needed.

Using the nonuniform grid we first attempt to reconstruct the unknown potential using the ground state and the first excited state energies only. Such an attempt may raise questions. Indeed, it is well-known that even in the 1D case the potential cannot be unambiguously determined from one or a few energy eigenvalues. Only a symmetric *reflectionless* potential can be restored based on its *complete set* of the bound state energies [68]. However, it is evident that the optimization of a 'black-box' function that depends on 10–20 parameters is a difficult numerical problem. An optimization algorithm used to solve this problem requires an initial approximation to the maximum (minimum). The success of the optimization and the convergence speed critically depend on the quality of the initial approximation. It turns out that satisfactory initial approximations can often be obtained as a result of optimization of only a few bound state energies.

The optimization methods also require the specification of the boundaries, within which the optimization parameters (in this case, the values of the potential in the grid points) can vary. We specify these ranges by sandwiching the unknown potential between the two known potential functions. As these functions we use

$$V_{1,2}(x) = \frac{Z_{1,2}}{\sqrt{x^2 + a_{1,2}}}. \qquad (9)$$

At first, we chose $Z_{1,2} = 1.0$ and a_1 and a_2 equal to 0.4 and 1.5, respectively. Therefore, $V_1(x)$ is the lower boundary for the potential $V(x)$ that is to be retrieved, whereas $V_2(x)$ is the upper boundary. The SAE potential reconstructed by optimization the ground state energy is shown in figure 2(a) together with the boundaries $V_1(x)$ and $V_2(x)$. For the optimization we use the particle swarm method. It is seen that the obtained

potential is in a good quantitative agreement with the one that we wanted to reconstruct. However, the situation changes dramatically, if the boundaries for the potential values under reconstruction are not as tight as in the example shown in figure 2(a). In figure 2(b) we display *one* of the potentials that can be obtained by optimization of the bound state energy in the case where the lower boundary for the potential values is again given by $V_1(x)$, but the upper boundary is chosen to be zero: $V_2(x) = 0$. It should be stressed that the optimization result is not unique for the chosen boundaries. The successive runs of the optimization algorithms lead to a whole family of the potentials with very close ground state energies. This agrees with the conclusions of [68]. It is seen that there is even no qualitative agreement between the potential shown in figure 2(b) and the soft-core Coulomb potential (7) that is to be reconstructed.

We now turn to the retrieval of the potential from the electron momentum distributions. At first, we use the same boundaries for the unknown potential values as in the example shown in figure 2(a). We minimize the difference as defined by the measure (6) between the PMD calculated for a potential defined by its values in the grid points and the PMD obtained for the potential (7) with the same laser pulse. The minimum value of the metric ρ_2 [PMD, TPMD] obtained in optimization is 0.019. The potential retrieved in the optimization procedure is shown in figure 3(a). It is seen that the obtained potential almost coincides with the soft-core Coulomb potential (7) we wanted to reconstruct. The same is true for the distributions calculated for the retrieved potential and the potential (7), see figure 3(b).

The question arises how sensitive is the optimization result to a change in the boundaries $V_1(x)$ and $V_2(x)$. To answer this question, we perform another optimization with the broader boundaries for the allowed potential values. Specifically, we sandwich the potential that is to be retrieved by $V_1(x)$ and $V_2(x)$ with $a_{1,2} = 1.0$ and Z_1 and Z_2 equal to 2.0 and 0.5, respectively. The optimization result for these broader boundaries quantitatively agrees with the potential (7), see
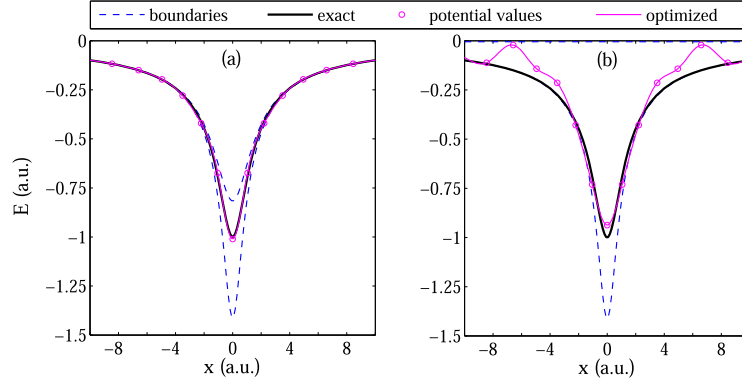
Figure 2. The values of the SAE potential on the non-uniform grid (8) (magenta circles) reconstructed by optimization of the bound state and first excited states energies only, boundaries for the potential values (dashed blue curves), the potential obtained by spline interpolation based on the reconstructed values (thin magenta curve), and the soft-core Coulomb potential (thick black curve). Panel (a) shows the optimization result for the case where the optimized potential values are bounded by the potentials (9) with $Z_{1,2} = 1.0$ and a_1 and a_2 equal to 0.4 and 1.5, respectively. Panel (b) displays the potential obtained for the optimization parameters restricted by $V_1(x)$ calculated from equation (9) with $Z_1 = 1.0$ and $a_1 = 0.4$ and $V_2(x) = 0$. The parameters are the same as in figure 1.
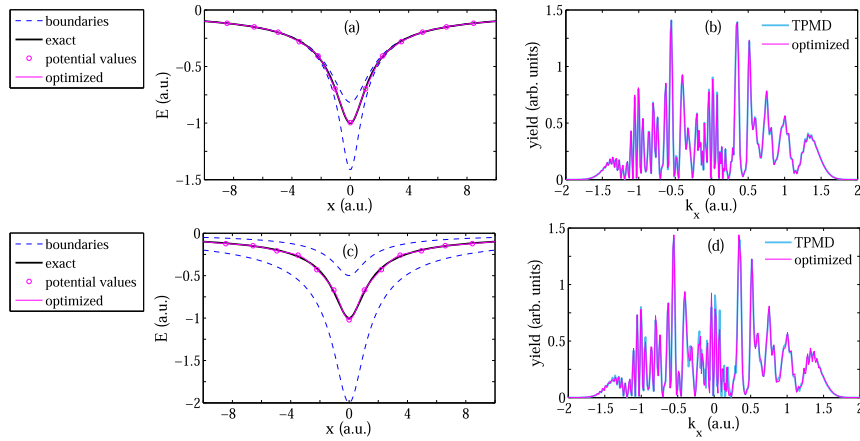

Figure 3. (a) and (c) The values of the SAE potential (magenta circles) reconstructed by optimization of the electron momentum distribution, boundaries for the potential values (dashed blue curves), the potential obtained by spline interpolation using the reconstructed values (thin magenta curve), and the soft-core Coulomb potential (thick black curve). (b) and (d) The PMD calculated using the optimized potential (thin magenta curve) and the TPMD (thick light-blue curve). Panels (a) and (b) show the optimization results for the case where the allowed potential values are bounded by the potentials $V_{1,2}(x)$ (equation (9)) with $Z_{1,2} = 1.0$ and a_1 and a_2 equal to 0.4 and 1.5, respectively. Panels (c) and (d) correspond to the boundaries $V_{1,2}(x)$ for the potential values given by (9) with $a_{1,2} = 1.0$ and Z_1 and Z_2 equal to 0.5 and 2.0, respectively. The potential under reconstruction is determined by its values on the grid (8) with 20 points. The laser parameters are the same as in figures 1 and 2.

figure 3(c). The same is also true for the electron momentum distributions, see figure 3(d). The minimum value of the metric (6) obtained in optimization with these broader boundaries is 0.03, which is only slightly higher than in the previous case.

We are now able to address the more important questions to the optimization-based approach, namely, how vulnerable

is it to intensity fluctuations that are inevitable in an experiment? Can the actual laser intensity be restored by applying the optimization technique? In order to answer the first question, we try to retrieve the potential at the intensity of 1.0×10^{14} W cm^{-2} using the TPMD calculated for the higher intensity of 2.0×10^{14} W cm^{-2}. The potential obtained in such
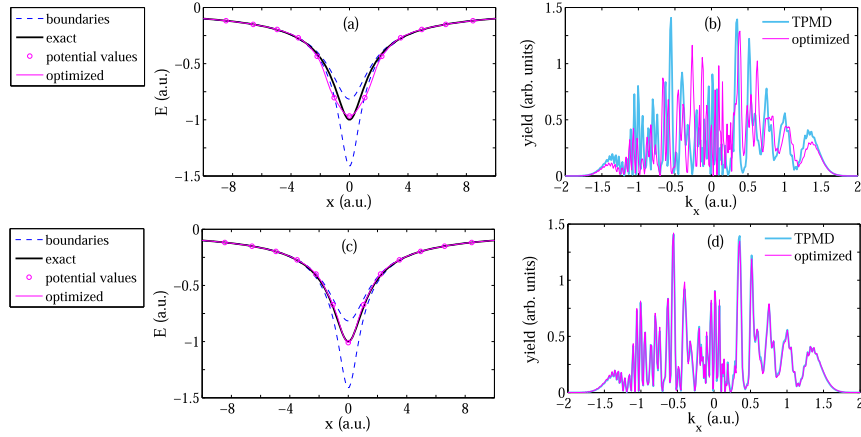
Figure 4. (a) and (c) The values of the SAE potential on the non-uniform grid (8) with 20 points (magenta circles) reconstructed by optimization of the PMD, boundaries for the potential values (dashed blue curves), the potential obtained by spline interpolation based on the reconstructed values (thin magenta curve), and the soft-core Coulomb potential (thick black curve). (b) and (d) The PMD calculated using the optimized potential (thin magenta curve) and the TPMD (thick light-blue curve). Panels (a) and (b) correspond to the case where the TPMD is calculated for the intensity of 2.0×10^{14} W cm^{-2} and the optimization of the momentum distributions is performed at the intensity of 1.0×10^{14} W cm^{-2}. Panels (c) and (d) show the results obtained treating the field strength F_0 as an additional parameter that is to be optimized. The boundaries for the optimized potential values are given by equation (9) with $Z_{1,2} = 1.0$ and a_1 and a_2 equal to 0.4 and 1.5, respectively. The parameters are the same as in figures 1–3.

an optimization is shown in figure 4(a). It is seen that this potential substantially differs from the potential (7) we expected to reconstruct. Indeed, the minimum obtained value of the metric (6) is 0.61, and the PMD calculated for the retrieved potential does not agree with the target one, see figure 4(b). To generalize our approach to the case where the TPMD is obtained at different laser intensity, we add the field strength to the parameter set that is to be optimized. This allows us to reconstruct the actual value of the laser intensity, at which the TPMD that we want to reproduce in optimization is obtained. In this case, the surrogate optimization turns out to be slightly more efficient than the particle swarm method. The results of this modified approach are shown in figures 4(c) and (d). It is seen from figure 4(c) that the retrieved potential is in a quantitative agreement with the soft-core Coulomb potential (7) used to calculate the TPMD. The same is true for the resulting electron momentum distribution, see figure 4(d). The difference between the momentum distributions ρ_2 [PMD, TPMD] comes to only 0.032. The optimized value of the field strength is 0.0763 a.u., whereas the exact value of F_0 equals to 0.0755 a.u.. Although these results are encouraging, it is clear that further studies are needed to completely tackle the question regarding the intensity fluctuations. To mimic a real experimental situation, it is necessary to average the PMD over the intensity distribution within the focal volume at every iteration of the optimization process. We leave this modification of the proposed method for further studies implying the generalization to the 3D case.

The results shown in figures 2–4 were obtained for the non-uniform grid (8) in the range $[-x_{max}, x_{max}]$. However, the

typical molecular potential we intend to reconstruct has a long-range Coulomb asymptotic at large distance: $V(r) \rightarrow 1/r$ at $r \rightarrow \infty$. Therefore, there is no need to find the values of the potential at large x, and an optimization of the potential values at $x \rightarrow \infty$ leads to a waste of computational resources. At the same time, it is highly desirable to have a denser grid for small x, where the potential can vary significantly. To address both these issues, from this point on we use a smaller computational box $[-x_C, x_C]$ setting $V(x) = 1/|x|$ for $|x| > x_C$. Typically, we chose $x_C = 10.0$ a.u. and use uniform grid within the range $[-x_C, x_C]$. The optimization results are shown in figures 5(a) and (b). It is seen from figure 5(a) that retrieved potential agrees well with the soft-core Coulomb potential (7). The optimization results in a measure (6) equal to 0.04 what corresponds to a good agreement between the obtained and target electron momentum distributions, see figure 5(b). A different optimization method was used here. At first, we performed an optimization of the bound state and first excited state energies. As mentioned above, such optimization results in a family of different potentials, unless the boundaries for the potential values are close to each other. Some of these potentials resemble the desired potential (7), whereas the others are very different from it and do not match the Coulomb asymptote at $x = \pm x_C$. Then we use all the obtained potentials as an initial approximation for the second optimization procedure that minimize the difference between the corresponding PMD and the target one. For the second optimization we use the pattern search algorithm (Hook–Jeeves method [59]), see, e.g. [60, 61] for reviews. This combined two-step approach to optimization of the PMD turns out to be computationally more

N I Shvetsov-Shilovski

efficient than particle swarm optimization we used before and many other gradient-free optimization methods, including simulated annealing, genetic algorithms, and surrogate optimization, if these methods start from a random initial approximation.

The optimization results presented in figures 5(a) and (b) were obtained for 20 grid points in the range $[-x_C, x_C]$ (i.e. for 10 grid points for $x \in [0, x_C]$). This corresponds to the grid spacing $\mathrm{d}x = 1.0$ a.u.. Suppose that we need better resolution along the x axis, e.g. $\mathrm{d}x = 0.5$ a.u., what corresponds to 20 grid points between 0 and x_C. The most efficient way to perform the optimization of the PMD on a denser grid is to use the results obtained for a sparser grid as an initial approximation. In doing so the potential values in the points of a denser grid can be restored by interpolation. The results of the application of this approach are shown in figures 5(c) and (d). Note that for $\mathrm{d}x = 0.5$ a.u. we achieve a perfect agreement between the retrieved potential and the desired soft-core Coulomb potential (7). The corresponding PMD's are also almost indistinguishable from each other, see figure 5(d). The optimization algorithm terminates when the distance ρ_2 [PMD, TPMD] reduces to 0.0042.

3.2. Reconstruction of parametrized potential

Up to this point we have not used any parametrization to represent the unknown SAE potential. It is clear, however, that this parametrization-free approach being extended to the two-dimensional and especially the 3D case will become a very difficult computational task. Indeed, such an extension will lead to a necessity of optimization of a function that depends on hundred of variables. We note that this task is feasible with modern computational facilities and optimization algorithms. Such problems arise, for example, in research on magnetically confined plasmas for fusion energy, see, e.g. [69, 70]. It is nevertheless of interest to test the optimization-based algorithm in the case where the unknown potential is in some way parametrized. It is natural to express the SAE potential as

$$V(x) = V_0(x) \left[1 + V_{1p}(x) \right], \qquad (10)$$

where $V_0(x)$ is a known potential with correct asymptotic behavior and the potential $V_1(x)$ is to be parametrized and determined. Here we choose $V_0(x) = Z_0 / (x^4 + a_0)^{\frac{1}{4}}$ with $Z_0 = 1.0$ and $a_0 = 1000.0$ what corresponds to a very shallow and wide potential well, which is substantially different from the potential (7) that should be restored. The question thus arises how to parametrize the potential $V_1(x)$ in the best possible way.

Since we know the potential $V(x)$ we want to reconstruct, this question is easy to answer. Indeed, by trying different options and applying standard curve fitting routines [62], we find that the rational interpolation can be used to approximate the function $V_{1p}(x) = V(x) / V_0(x) - 1$ with a good accuracy. Therefore, the potential $V_{1p}(x)$ can be represented as a quotient of two polynomials $P_m(x)$ and $Q_n(x)$:

$$V_{1p}(x) = \frac{P_m(x)}{Q_n(x)}. \qquad (11)$$

It is clear that since $V_{1p}(x) \to 0$ at $x \to 0$, the inequality $m < n$ should be fulfilled. It is easy to see that the measure ρ_2 of the difference between the corresponding momentum distribution and the target one dramatically changes for different choices of the m and n. If, for example, $m = 0$ and $n = 2$, the minimum value of the ρ_2 that can be achieved is equal to 0.29. This corresponds to $V_{1p}(x) = p_1 / (x^2 + q_1)$ with $p_1 = 29.99$ and $q_1 = 3.62$. The linear function in the nominator ($m = 1$) and the quadratic function in the denominator ($n = 2$), i.e. $V_{1p}(x) = (p_1 x + p_2) / (x^2 + q_1 x + q_2)$, allow to reduce the measure (6) to 0.047. This value is achieved for $p_1 = -1.15$, $p_2 = 36.90$, $q_1 = 0.92$, and $q_2 = 23.95$. The minimum value of the ρ_2 we have obtained using the equation (11) is equal to 0.01. It corresponds to the constant in the numerator and the fourth-order polynomial in the denominator of the quotient (11):

$$V_{1p}(x) = \frac{p_1}{x^4 + q_1 x^3 + q_2 x^2 + q_3 x + q_4}, \qquad (12)$$

where $p_1 = 1261.0$, $q_1 = -9.747$, $q_2 = 66.5$, $q_3 = 10.4$, and $q_4 = 138.7$. It should be noted that not all of the coefficients in the denominator of this formula are positive. When using the optimization-based method in practice, a series of optimizations applying different ways to parametrize the unknown potential should be performed. This will allow to compare the optimization results and to choose the best way of the parametrization similarly to what we do here with the fitting of the known potential.

We now try to recover the parameter values in the parametrization (12) by optimizing the PMD. At first glance it would seem that optimization of function (12) depending on only 5 parameters is a simple task compared to the one performed in section 3.1. But this is not the case, since negative values of the parameters q_i ($i = 1, \ldots, 4$) may lead to $1 + V_{1p}(x) < 0$ and, therefore, $V(x) > 0$ for certain ranges of x. To prevent this situation, we use constrained optimization. Specifically, instead of minimizing the measure (6) alone, we now look for a minimum of

$$\rho_2 \left[\text{PMD}, \text{TPMD} \right] + w \cdot V_m^2 \left[1 + \text{sgn}(V_m) \right], \qquad (13)$$

where V_m is the maximum value of $V(x)$ in the interval $[0, x_0]$, and w is some weight factor. Typically, we use w in the range between 5.0 and 20.0. We allow for the following ranges of the optimization parameters: $p_1 \in [-2000.0, 2000.0]$ and $q_i \in [-100.0, 100.0]$ ($i = 1, \ldots, 4$). To speed up the simulations, we again perform the optimization in two steps, i.e. we use the results obtained in optimization of the ground state, first, and second excited states energies as initial approximations for the optimization of the PMD. The retrieved potential and the corresponding electron momentum distribution are shown in figures 6(a) and (b), respectively. The following parameter values were obtained: $p_1 = 403.44$, $q_1 = 3.08$, $q_2 = 17.03$, $q_3 = 35.57$, and $q_4 = 80.45$. The difference ρ_2 between the resulting PMD and the TPMD is 0.0164, what is higher than the one corresponding to the parameters obtained by approximation of the known function $V_{1p}(x)$. Therefore, some local minimum, albeit quite close to the desired global one, is found in optimization. It is seen that the retrieved potential agrees
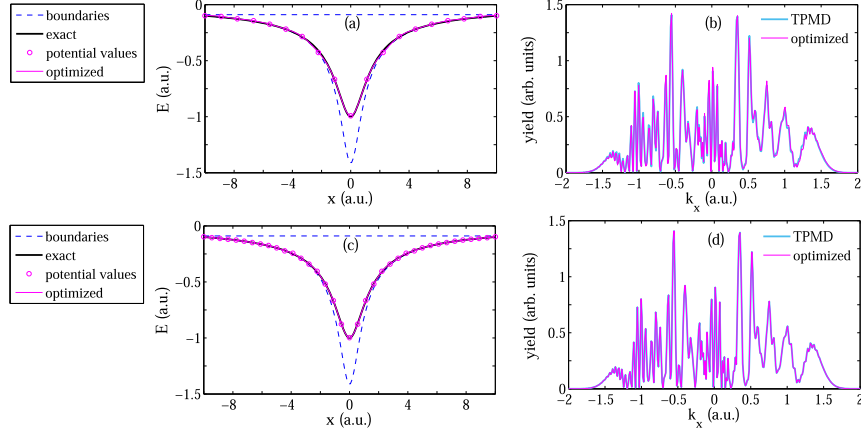
Figure 5. Panels (a) and (b) show the same as figures 3(a) and (b) for the optimization parameters varying in wider ranges and the potential determined by the values on the uniform grid consisting of 10 points between 0 and 10.0 a.u.. Panels (c) and (d) display the optimization results for the same grid consisting of 20 points. The optimization parameters are bounded by the potential $V_1(x)$ calculated from equation (9) with $Z_1 = 1.0$ and $a_1 = 0.4$ and $V_2(x) = -0.09$ a.u.. The parameters are the same as in figures 1–3.
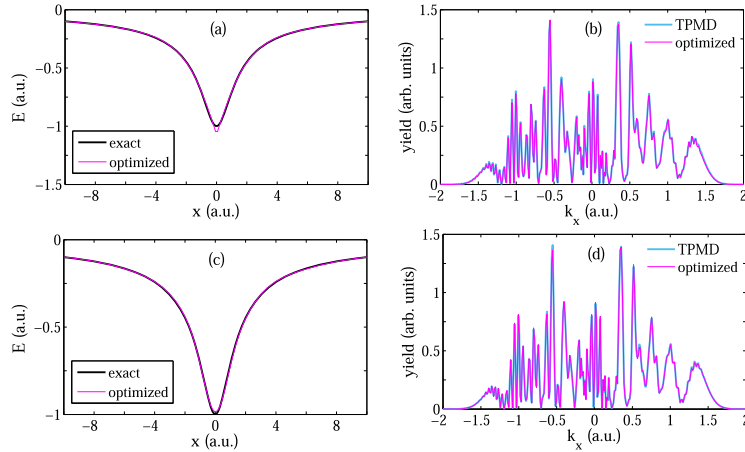
Figure 6. Optimization results for parametrized SAE potential. Panels (a) and (c) show the reconstructed potentials (thin magenta curve) and the soft-core Coulomb potential (thick black curve). Panels (b) and (d) display the comparison of the PMD's obtained from the TDSE with the retrieved (thin magenta curve) and the exact (thick light-blue curve) SAE potentials. Panels ((a), (b)) and ((c), (d)) correspond to the parametrization (12) and (14), respectively. The laser parameters are the same as in figures 1–3.

well with the exact result, see figure 6(a). The same is also true for the electron momentum distributions (see figure 6(b)). As a next step in testing the method, we represent our potential as a sum of a few Gaussian functions:

$$V_{1p}(x) = \sum_{k=1}^{k_{\max}} a_k \exp\left[-\frac{(x - b_k)^2}{c_k^2}\right]. \qquad (14)$$

The representation (14) is obviously more flexible, i.e. it allows for finer variations of the potential function, as compared to the one applying rational function. Here we choose $k_{\max} = 5$ what corresponds to 15 parameters to be optimized. It should be stressed that in contrast to all other examples shown in this paper, here we do not assume any symmetry of the potential $V(x)$. Indeed, the allowed values of the optimization parameters are: $a_k \in [-4.0, 4.0]$, $b_k \in [-20.0, 20.0]$, and

$c_k \in [0, 100.0]$ $(k = 1, \ldots, 5)$. As an initial approximation for the optimization of the PMD's we use the potential shown in figure 6(a), i.e. the one obtained with parametrization (11). The optimization results are presented in figures 6(c) and (d). As expected, a better agreement between the retrieved potential and the exact one can be achieved with parametrization (14). However, the measure (6) remains practically unchanged: ρ_2 [PMD, TPMD] = 0.0159.

The examples above demonstrate that in the 1D case the parametrization of the potential does not offer any decisive advantages compared to the direct representation on a grid. Nevertheless, it is shown that the optimization-based method also works in the case, where the potential is determined by a number of parameters. This is essential in view of the possible extension of the approach onto the 3D case, where parametrization of the unknown potential is expected to become particularly important.

4. Conclusions and outlook

In conclusion, we have developed a method capable to retrieve the SAE potential in an atom from a given momentum distribution of photoelectrons ionized by a strong laser pulse. In this method the potential is found by minimization of the difference between the given momentum distribution and the one obtained from the solution of the TDSE with the SAE potential that varies in the optimization process. The unknown potential is either represented by a set of its values in points of a spatial grid, or by a set of parameters. We have shown that the optimization can be performed using a number of different derivative-free techniques, including particle swarm method, surrogate optimization, and pattern search. It is found that the most efficient approach is based on the use of potentials obtained in optimization of a few bound-state energies as initial approximations for the optimization of the PMD.

We have tested our method by reconstructing of the soft-core Coulomb potential from the corresponding PMD generated in ionization of a 1D atom by a strong few-cycle laser field. It is shown that the retrieved SAE potential is in a quantitative agreement with the potential we aimed to reconstruct. This is true for both ways used to represent the potential under reconstruction. In the case where the potential is represented by its values on a grid the spatial resolution can be effectively improved by using the optimization results on a sparse grid as an initial approximation for optimization on the dense grid. This allows to avoid severe computational costs when optimizing a function depending on a few dozens of variables.

It is clear that the measured electron momentum distributions are affected by focal averaging. We have shown that the actual laser intensity can be restored together with the SAE potential in the optimization approach. Nevertheless, further work is needed to fully explore the question how sensitive is the proposed method to the focal averaging. Furthermore, extension of the method to the real 3D case require a reliable measure used to compare different momentum distributions. To this end, the tools of image analysis and pattern recognition can be applied. It remains to be studied which of these tools are the most appropriate for the problem at hand.

Furthermore, we have restricted ourselves by the optimization of only one part of the PMD created by the direct electrons. However, our preliminary results show that the momentum distribution of the rescattered photoelectrons are more sensitive optimization target that can be used for the retrieval of the potential. This suggests to develop a method optimizing the distributions of the rescattered electrons. It is obviously more difficult to obtain suitable SAE potentials for molecules than for atoms. To the best of our knowledge, the SAE potentials are presently available only for some simple molecules (see, e.g. [71–76]). Therefore, it would be of interest to extend the proposed optimization technique to the molecular case. Future studies are required to address the issues listed here. Developments in these directions have already begun. We believe that the advent of the method for retrieval of the SAE potential from the electron momentum distribution will be an important step forward in the studies of strong-field ionization.

Acknowledgments

Data availability statement

All data that support the findings of this study are included within the article (and any supplementary files).

ORCID iDs

N I Shvetsov-Shilovski ⓘ https://orcid.org/0000-0002-8825-9302

References

[1] Kitzler M and Gräfe S (ed) 2016 *Ultrafast Dynamics Driven by Intense Light Pulses* (*From Atoms to Solids, from Lasers to Intense X-Rays*) (Berlin: Springe)
[2] Lin C D, Le A-T, Jin C and Wei H 2018 *Attosecond and Strong-Field Physics* (*Principles and Applications*) (Cambridge: Cambridge University Press)
[3] Becker W, Grasbon F, Kopold R, Milošević D B, Paulus G G and Walther H 2002 Above-threshold ionization: from classical features to quantum effects *Adv. At. Mol. Opt. Phys.* **48** 35
[4] Milošević D B and Ehlotzky F 2003 Scattering and reaction processes in powerful laser fields *Adv. At. Mol. Opt. Phys.* **49** 373
[5] Becker A and Faisal F H M 2005 Intense-field many-body *S*-matrix theory *J. Phys. B: At. Mol. Opt. Phys.* **38** R1
[6] Faria C and Liu X 2011 Electron–electron correlation in strong laser fields *J. Mod. Opt.* **58** 1076
[7] Frasinski L J, Codling K, Hatherly P, Barr J, Ross I N and Toner W T 1987 Femtosecond dynamics of multielectron dissociative ionization by use of a picosecond laser *Phys. Rev. Lett.* **58** 2424
[8] Cornaggia C, Lavancier J, Normand D, Morellec J, Agostini P, Chambaret J P and Antonetti A 1991 Multielectron

dissociative ionization of diatomic molecules in an intense femtosecond laser field *Phys. Rev.* A **44** 4499

[9] Posthumus J H, Frasinski L J, Giles A J and Codling K 1995 Dissociative ionization of molecules in intense laser fields: a method of predicting ion kinetic energies and appearance intensities *J. Phys. B: At. Mol. Opt. Phys.* **28** L349

[10] Cornaggia C, Schmidt M and Normand D 1995 Laser-induced nuclear motions in the Coulomb explosion of $C_2H_2^+$ ions *Phys. Rev. A* **51** 1431

[11] Kanya R, Morimoto Y and Yamanouchi K 2010 Observation of laser-assisted electron–atom scattering in femtosecond intense laser fields *Phys. Rev. Lett.* **105** 123202

[12] Morimoto Y, Kanya R and Yamanouchi K 2014 Laser-assisted electron diffraction for femtosecond molecular imaging *J. Chem. Phys.* **140** 064201

[13] Itatani J, Levesque J, Zeidler D, Niikura H, Pépin H, Kieffer J C, Corkum P B and Villeneuve D M 2004 Tomographic imaging of molecular orbitals *Nature* **432** 867

[14] Haessler S *et al* 2010 Attosecond imaging of molecular electronic wavepackets *Nat. Phys.* **6** 200

[15] Meckel M *et al* 2008 Laser-induced electron tunneling and diffraction *Science* **320** 1478

[16] Blaga C I, Xu J, DiChiara A D, Sistrunk E, Zhang K, Agostini P, Miller T A, DiMauro L F and Lin C D 2012 Imaging ultrafast molecular dynamics with laser-induced electron diffraction *Nature* **483** 194

[17] Pullen M G *et al* 2015 Imaging an aligned polyatomic molecule with laser-induced electron diffraction *Nat. Commun.* **6** 7262

[18] Huismans Y *et al* 2011 Time-resolved holography with photoelectrons *Science* **331** 61

[19] Xu J, Blaga C I, Agostini P and DiMauro L F 2016 Time-resolved molecular imaging *J. Phys. B: At. Mol. Opt. Phys.* **49** 112001

[20] Keldysh L V 1965 Ionization in the field of a strong electromagnetic wave *Sov. Phys. JETP* **20** 1307

[21] Faisal F H M 1973 Multiple absorption of laser photons by atoms *J. Phys. B: At. Mol. Phys.* **6** L89

[22] Reiss H R 1980 Effect of an intense electromagnetic field on a weakly bound system *Phys. Rev. A* **22** 1786

[23] van Linden van den Heuvell H B and Muller H G 1988 *Multiphoton Processes Studies in Modern Optic s* ed S J Smith and P L Knight (Cambrige: Cambrige University Press)

[24] Gallagher T F 1988 Above-Threshold ionization in low-frequency limit *Phys. Rev. Lett.* **61** 2304

[25] Corkum P B, Burnett N H and Brunel F 1989 Above-threshold ionization in the long-wavelength limit *Phys. Rev. Lett.* **62** 1259

[26] Kulander K C, Schafer K J, Krause J L, Pireaux B, L'Hullier A and Rzazewski K 1993 *Super-Intense Laser–Atom Physics* (New York: Plenum)

[27] Corkum P B 1993 Plasma perspective on strong field multiphoton ionization *Phys. Rev. Lett.* **71** 1994

[28] Muller H G 1999 An efficient propagation scheme for the time-dependent Schrödinger equation in the velocity gauge *Laser Phys.* **9** 138

[29] Bauer D and Koval P 2006 Qprop: a Schrödinger-solver for intense laser–atom interaction *Comput. Phys. Commun.* **174** 396

[30] Madsen L B, Nikolopoulos L A A, Kjeldsen T K and Fernández J 2007 Extracting continuum information from $\Psi(t)$ in time-dependent wave-packet calculations *Phys. Rev. A* **76** 063407

[31] Tong X-M 2017 A three-dimensional time-dependent Schrödinger equation solver: an application to hydrogen atoms in an elliptical laser field *J. Phys. B: At. Mol. Opt. Phys.* **50** 144004

[32] Kulander K C 1988 Time-dependent theory of multiphoton ionization of xenon *Phys. Rev. A* **38** 778

[33] Kulander K C, Schafer K J and Krause J L 1991 Single-active electron calculation of multiphoton process in krypton *Int. J. Quantum Chem.* **40** 415

[34] Tong X M and Lin C D 2005 Empirical formula for static field ionization rates of atoms and molecules by lasers in the barrier-suppression regime *J. Phys. B: At. Mol. Opt. Phys.* **38** 2593–600

[35] Muller H G and Kooiman F C 1998 Bunching and focusing of tunneling wave packets in enhancement of high-order above-threshold ionization *Phys. Rev. Lett.* **81** 1207

[36] Reiff R, Joyce T, Jaroń-Becker A and Becker A 2020 Single-active electron calculations of high-order harmonic generation from valence shells in atoms for quantitative comparison with TDDFT calculations *J. Phys. Commun.* **4** 065011

[37] Feit M D, Fleck J A and Steiger A 1982 Solution of the Schrödinger equation by a spectral method *J. Comput. Phys.* **47** 412

[38] Troullier N and Martins J L 1991 Efficient pseudopotentials for plane-wave calculations *Phys. Rev. B* **43** 1993

[39] Eicke N T 2020 Momentum distributions from bichromatic ionization of atoms and molecules *PhD Thesis* Leibniz University, Hannover, Germany

[40] Xu J, Zhou H-L, Chen Z and Lin C D 2009 Genetic-algorithm implementation of atomic potential reconstruction from differential electron scattering cross sections *Phys. Rev. A* **79** 052508

[41] Werschnik J and Gross E K U 2007 Quantum optimal control theory *J. Phys. B: At. Mol. Opt. Phys.* **40** R175

[42] Brif C, Chakrabarti R and Rabitz H 2010 Control of quantum phenomena: past, present and future *New J. Phys.* **12** 075008

[43] Castro A, Räsänen E, Rubio A and Gross E K U 2009 Femtosecond laser pulse shaping for enhanced ionization *Europhys. Lett.* **87** 53001

[44] Solanpää J, Budagosky J A, Shvetsov-Shilovski N I, Castro A, Rubio A and Räsänen E 2014 Optimal control of high-harmonic generation by intense few-cycle pulses *Phys. Rev. A* **90** 053402

[45] Shvetsov-Shilovski N I, Madsen L B and Räsänen E 2015 Suppression of strong-field ionization by optimal pulse shaping: application to hydrogen and the hydrogen molecular ion *Phys. Rev. A* **91** 023425

[46] Goetz R E, Karamatskou A, Santra R and Koch C P 2016 Quantum optimal control of photoelectron spectra and angular distributions *Phys. Rev. A* **93** 013413

[47] Wang Z, Bovik A C, Sheikh H R and Simoncelli E P 2003 Image quality assessment: from error visibility to structure similarity *IEEE Trans. Image Process.* **13** 600

[48] Buldas A, Kronmaa A and Laanoja R 2013 *Keyless Signature's Infrastructure: How to Build Global Distributed Hash-Trees* (Berlin: Springer)

[49] Kolmogorov A N, Fomin S V and Silverman R A 1975 *Introductory Real Analysis* (New York: Dover)

[50] Anderson E *et al* 1999 *LAPACK User's Guide* 3rd edn (Philadelphia: Society for Industrial and Applied Mathematics)

[51] Kjeldsen T K 2007 Wave packet dynamics studied by *ab initio* methods: application to strong-field ionization of atoms and molecules *PhD Thesis* Århus: University of Århus, Denmark

[52] Bauer D (ed) 2017 *Computational Strong-Field Quantum Dynamics* (Berlin: de Gruyter & Co)

[53] Tong X M, Hino K and Toshima N 2006 Phase-dependent atomic ionization in few-cycle intense laser pulse *Phys. Rev. A* **74** 031405(R)

[54] Rios L M and Sahinidis N V 2013 Derivative-free optimization: a review of algorithms and comparison of software implementations *J Glob Optim.* **56** 1247

[55] Larson J, Menickelly M and Wild S M 2019 Derivative-free optimization methods *Acta Numer.* **28** 287

[56] Kennedy J and Eberhart R 1995 Particle swarm optimization *Proc. of IEEE Int. Conf. on Neural Networks* vol 4

[57] Shi Y and Eberhart R C 1998 A modified particle swarm optimizer *Proc. of IEEE Int. Conf. on Evolutionary Computation*

[58] Gutmann H-M 2001 A radial basis function method for global optimization *J. Glob. Optim.* **19** 201

[59] Hooke R and Jeeves T A 1961 'Direct search' solution of numerical and statistical problems *J. Acm* **8** 212

[60] Kolda T G, Lewis R M and Torczon V 2003 V Optimization by direct search: new perspectives on some classical and modern methods *SIAM Rev.* **45** 385

[61] Audet C and Dennis J E 2003 Analysis of generalized pattern searches *SIAM J. Optimiz.* **13** 889

[62] The MathWorks Inc. MATLAB Version 9.9.0 (R2020b) *Natick, Massachusetts* mathworks.com

[63] Javanainen J, Eberly J H and Su Q 1988 Numerical simulations of multiphoton ionization and above-threshold electron spectra *Phys. Rev.* A **38** 3430

[64] Press W H, Teukolsky S A, Vetterling W T and Flannery B P 1992 *Numerical Recipes in Fortran 77: The Art of Scientific Computing* 2nd edn (Cambridge: Cambridge University Press)

[65] Wang J, Chu S-I and Laughlin C 1994 Multiphoton detachment of H$^-$. II. Intensity-dependent photodetachment rates and threshold behavior-complex-scaling generalized pseudospectral method *Phys. Rev.* A **50** 3208

[66] Yao G and Chu S-I 1993 Generalized pseudospectral methods with mappings for bound and resonance state problems *Chem. Phys. Lett.* **204** 381

[67] Tong X-M and Chu S-I 1997 Theoretical study of multiple high-order harmonic generation by intense ultrashort pulsed laser fields: a new generalized pseudospectral time-dependent method *Chem. Phys.* **217** 119

[68] Thacker H B, Quigg C and Rosner J L 1978 Inverse scattering problem for quarkonium systems. II. Applications to ψ and Υ families *Phys. Rev.* D **18** 287

[69] Spong D A *et al* 2001 Physics issues of compact drift optimized stellarators *Nucl. Fusion* **41** 711

[70] Drevlak M, Beidler C D, Geiger J, Helander P and Turkin Y 2019 Optimisation of stellarator equilibria with ROSE *Nucl. Fusion* **59** 016010

[71] Miller K J and Green A E S 1974 Energy levels and potential energy curves for H_2, N_2, and O_2 with an independent particle model *J. Chem. Phys.* **60** 2617

[72] Abu-samha M and Madsen L B 2010 Single-active-electron potentials for molecules in intense fields *Phys. Rev.* A **81** 033416

[73] Zhao S F, Jin C, Le A-T, Jiang T F and Lin C D 2010 Determination of structure parameters in strong-field tunneling ionization theory of molecules *Phys. Rev.* A **81** 033423

[74] Kästner A, Grossmann F and Schmidt R 2010 Reliability of soft-core approximations in theoretical studies of molecules in intense laser fields *Phys. Rev.* A **81** 023414

[75] Peters M, Nguyen-Dang T T, Charron E, Keller A and Atabek O 2012 Laser-induced electron diffraction: a tool for molecular orbital imaging *Phys. Rev.* A **85** 053417

[76] Lv H, Zuo W, Zhao L, Xu H, Jin M and Ding D 2016 Comparative study on atomic and molecular Rydberg-state excitation in strong infrared laser fields *Phys. Rev.* A **93** 033415

8.13   *Optimal control of high-harmonic generation*

Optimal control of high-harmonic generation by intense few-cycle pulses

J. Solanpää,[1,*] J. A. Budagosky,[2] N. I. Shvetsov-Shilovski,[1] A. Castro,[2,3] A. Rubio,[4,5] and E. Räsänen[1,†]

[1]*Department of Physics, Tampere University of Technology, Tampere FI-33101, Finland*
[2]*Institute for Biocomputation and Physics of Complex Systems (BIFI) and Zaragoza Center for Advanced Modeling (ZCAM),*
University of Zaragoza, E-50009 Zaragoza, Spain
[3]*ARAID Foundation, María de Luna 11, Edificio CEEI Aragón, Zaragoza E-50018, Spain*
[4]*Max Planck Institute for the Structure and Dynamics of Matter, 22761 Hamburg, Germany*
[5]*Nano-Bio Spectroscopy Group and ETSF, Departamento de Física de Materiales, CFM CSIC-UPV/EHU-MPC and DIPC,*
Universidad del País Vasco, E-20018 San Sebastián, Spain

At the core of attosecond science lies the ability to generate laser pulses of subfemtosecond duration. In tabletop devices the process relies on high-harmonic generation, where a major challenge is to obtain high yields and high cutoff energies required for the generation of attosecond pulses. We develop a computational method that can simultaneously resolve these issues by optimizing the driving pulses using quantum optimal control theory. Our target functional, an integral over the harmonic yield over a desired energy range, leads to a remarkable cutoff extension and yield enhancement for a one-dimensional model H atom. The physical enhancement process is shown to be twofold: the cutoff extension is of classical origin, whereas the yield enhancement arises from increased tunneling probability. The scheme is directly applicable to more realistic models and, within straightforward refinements, also to experimental verification.

PACS number(s): 32.80.Rm, 42.65.Ky, 42.65.Re, 42.79.Nv

The revolution of attosecond science, i.e., monitoring and controlling the dynamics of electrons in their native time scale, relies on the generation of laser pulses with duration of a few dozen attoseconds [1]. Such pulses can be generated by using large-scale free-electron laser facilities [2] or in tabletop devices using high-harmonic generation (HHG), an ultrafast frequency conversion process [1]. Using tabletop devices, however, comes with a price: the generated attosecond pulses are often too long and they suffer from low intensity [1].

A high-harmonic spectrum has an energy range of nearly constant intensity (plateau), which ends in a distinctive cutoff [3]. Attosecond pulses are formed from the harmonics on the plateau [1]. Hence, the low amplitude of the pulses is due to low harmonic yield and the pulse duration is determined by the cutoff energy (the higher the energy, the shorter the pulse) [1]. The objectives of increasing the yield and reducing the pulse duration can be addressed by temporal shaping of the driving pulse—already experimentally realizable either with multicolor fields or with more sophisticated techniques [4]. Yet a crucial question remains unanswered: how to find the optimal shape of the driving pulse to enhance HHG.

Numerous previous studies have tackled the issues of cutoff and yield; for a recent review see, e.g., Refs. [5,6]. The main scheme behind the cutoff extension has been using two-color laser fields [7,8] or chirped pulses [9–11], but also steepening of the carrier wave [12] or even using a sawtooth pulse should extend the cutoff [13]. In addition, combined temporal and spatial synthesis of the driving field has been shown to extend the cutoff [14]. A previous study based on quantum optimal control theory (QOCT), for example, demonstrated some cutoff extension, albeit with a low yield, by maximizing the ground-state occupation at the end of the pulse [15].

Yield increase of the plateau has been accomplished, e.g., by two-color fields [16–21] and also by using a mixture of two target gases [22]. In a separate work [23], some of the authors of the present work addressed the selective enhancement of harmonic peaks; selective harmonic enhancement has been studied using QOCT also in Ref. [24], and experimentally, e.g., in Ref. [25]. Recently also the attosecond pulse generation has been optimized using genetic algorithms [26].

In this paper, we provide an efficient computational method to *simultaneously* enhance both the yield and the cutoff energy of the harmonic plateau by optimizing the driving pulses with QOCT [27–29]. The optimal pulses are found by maximizing the target functional, an integral over the harmonic yield over a desired energy range. Surprisingly, the enhancements are achieved with fixed-fluence pulses; i.e., the search is performed over the set of pulses with equal duration and fixed fluence (integrated intensity). We examine in detail the physical origin behind the enhancement, which is found to be of classical nature to a significant extent.

To demonstrate our method, we use one-dimensional hydrogen with the soft-Coulomb potential [30] $V(x) = -1/\sqrt{x^2+1}$ as our model system and the laser-electron interaction is calculated in the dipole approximation. The harmonic spectra are calculated from the Fourier transform of the dipole acceleration $\ddot{d}(\omega)$ as $S(\omega) = |\ddot{d}(\omega)|^2/\omega^2$ as suggested in Ref. [31]. Unless otherwise specified, Hartree atomic units (a.u.) are used throughout the paper, i.e., $\hbar = q_e = m_e = 1/(4\pi\epsilon_0) = 1$. The time-evolution operator is calculated using the exponential midpoint rule [32] with the Lanczos algorithm [33] for the operator exponential; during time propagation we also use imaginary absorbing boundaries. We use box sizes of 4000–6000, grid spacings of 0.2–0.3, and time steps of 0.03–0.05; the parameters have been checked to ensure full convergence. Most of the calculations—including QOCT discussed below—are done in length gauge using the OCTOPUS code [34].

In QOCT one solves for a laser pulse $\epsilon(t)$ that maximizes a target functional $J_1[\epsilon]$. To optimize the harmonic spectrum,

---

*janne@solanpaa.fi
†esa.rasanen@tut.fi

we have implemented a target of the form

$$J_1[\epsilon] = \int_{\omega_a}^{\omega_b} |\ddot{d}[\epsilon](\omega)|^2 \, d\omega, \tag{1}$$

where $[\omega_a, \omega_b]$ is the frequency range for the desired enhancement of the HHG spectrum. The field ϵ is represented by a set of parameters, and maximization of the functional defined in Eq. (1) amounts to a function maximization for those parameters. We have used both a gradient-free algorithm (NEWUOA [35]) and the gradient-based Broyden-Fletcher-Goldfarb-Shannon (BFGS) algorithm [36] (the expression for the gradient is supplied by the QOCT). As we will see, both algorithms provide similar enhancements in the harmonic spectrum. The optimized pulses are constrained by (i) a finite number of frequencies with the maximum frequency ω_{max}, (ii) a fixed pulse length, and (iii) a fixed fluence which is set to that of a single-frequency *reference* pulse, whose shape is shown in the figures below. For each set of pulse constraints, we begin the optimization from several (5–10) random initial pulses and report here the best result; it is important to note that QOCT always converges into a *local* maximum in the parameter space.

First we apply the NEWUOA algorithm to optimize a laser pulse for HHG in the target interval $\omega \in [1.3, 4]$ a.u. The pulse length is fixed to $T = 1104$ (26.7 fs) and the carrier frequency of the reference pulse is $\omega = 0.0569$ a.u. (wavelength $\lambda \approx 800$ nm corresponding to the typical range of Ti:sapphire lasers), which we choose to keep as the maximum allowed frequency of the optimized pulse to prevent the formation of complicated pulses with high-frequency components. The peak intensity of the reference pulse is 6×10^{13} W/cm^2, and the fluence is kept constant in the optimization. The reference and optimized pulses are shown in Fig. 1(a) as red (light gray) and blue (dark gray) lines, respectively. The optimized harmonic spectrum in Fig. 1(b) completely fulfills the desired target, and in addition to the cutoff extension, the yield is also increased by several orders of magnitude.

Next we comment on the two most obvious characteristics of the optimized pulse in Fig. 1(a). First, it is important to note that the high-intensity half cycle in the beginning is not responsible for the significant increase in the HHG yield and cutoff. If this part were later in the pulse, the cutoff would be at $\omega \approx 2.5$ a.u. A similar effect is seen if, e.g., the last low-intensity peak is missing. Second, as shown in the inset of Fig. 1(a), the optimized pulse contains lower-frequency components. Indeed, the standard theoretical HHG considerations predict that lower frequencies should lead to higher cutoff energy due to higher ponderomotive energy. However, merely using low-frequency single-color pulses produces very low yields. It is the shaped multifrequency pulses that produce both the large cutoff and high intensities. Furthermore, in the case of HHG resulting from pulses that have a single carrier frequency, the harmonic peaks are equally separated by twice the carrier frequency. In the case of optimized pulses, however, we find no connection between the frequency components in the pulse and the HHG peak separations. This is expected in view of the complexity of the optimized pulse in the time-frequency plane, even though we applied rather simple pulse constraints as explained above.
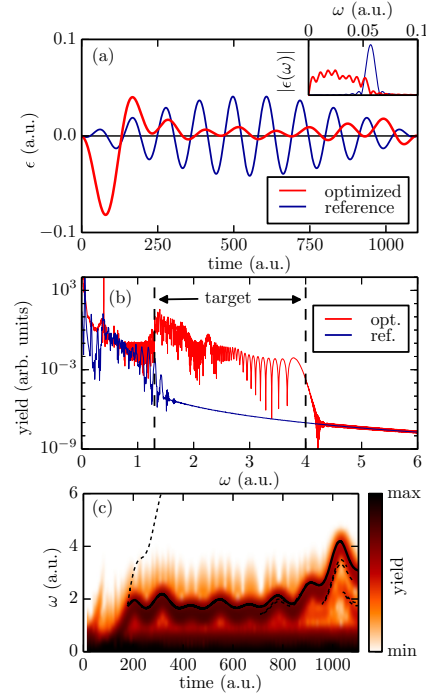

FIG. 1. (Color online) Optimization results for the HHG spectrum with the target range $\omega \in [1.3, 4]$ a.u. The pulse length is $T = 1104$ a.u. and the frequency of the reference pulse is $\omega = 0.0569$ a.u., equal to the maximum frequency in the optimization. The fluence is kept constant. (a) Optimized [red (light gray)] and reference [blue (dark gray)] pulses and their frequencies (inset). (b) High-harmonic spectra for optimized [red (light gray)] and reference [blue (dark gray)] pulses. The target range is shown with vertical dashed lines. (c) Quantum-mechanical time-dependent harmonic spectrum in log scale [color (gray scale)] and return energies calculated from the semiclassical model (solid line). Spurious branches from a uniform tunneling rate are shown with dashed lines (see text).

The emission process is further demonstrated in Fig. 1(c), where the color (gray scale) image shows the time-frequency map of the quantum dipole acceleration, $\ddot{d}(t, \omega)$. The time-frequency map is calculated as a discrete short-time Fourier transform (STFT) [37] using the Blackman window function [38]. In essence, the time axis is split into multiple overlapping windows, and the dipole acceleration is Fourier transformed in each window. Finally, we plot the quantity $S(t, \omega) = |\ddot{d}(t, \omega)|^2 / \omega^2$ in log scale in analog with the harmonic yield; here t corresponds to the middle of each time window of the STFTs. $S(t, \omega)$ essentially describes HHG *in time*. Bicubic interpolation is used for slight visual improvements. The cutoff extension up to $\omega \lesssim 2.5$ a.u. occurs throughout the pulse as it is the effect of the high-intensity peak. The full extension up to $\omega = 4$ a.u., however, occurs only at the end of the pulse. This

clarifies the above-mentioned fact that the complete structure of the optimized pulse is important.

Next we examine the physical origin of the cutoff extension in more detail by employing semiclassical simulations. An ensemble of classical trajectories is propagated with initial times t_0 distributed according to either a uniform tunneling rate $w(t_0) \sim 1$ or exponential tunneling rate $w(t_0) \sim \exp\{-[2(2I_p)^{3/2}]/[3|\epsilon(t_0)|]\}$ [39–41], where $I_p = 0.669$ a.u. is the ionization potential of our system. At the tunnel exit obtained from the classical turning point equation $V(x) + F_x(t)x = -I_p$, the velocity is set to zero and the electron is propagated classically. Upon return of the tunneled electron to the origin, a photon is emitted with frequency corresponding to the kinetic energy of the electron; also later returns are recorded and taken into account. Note that in contrast to the three-step (simple man) model [42], where the electron starts from the origin and moves in the laser field only, the electron in our model starts at the tunnel exit and moves in the combined force field of the laser and the atomic potential. It should be noted that in contrast to our semiclassical simulation taking the atomic potential into account, the three-step model underestimates the cutoff energy. For the parameters of Fig. 2 the cutoff calculated from the three-step model corresponds to 3.2 a.u. (compare to 4.2 a.u. predicted by semiclassical simulations with binding potential shown in Fig. 2).

The return energy maps of the semiclassical model as a function of the return time (solid curves) are compared with the time-dependent harmonic spectrum in Fig. 1(c). Due to the pulse shape, the electron can return only once to the origin. With uniform tunneling distribution, the semiclassical model exhibits a few spurious branches (dashed black curves), which are suppressed when using the exponential tunneling rate. The remarkable agreement between the semiclassical and quantum descriptions highlights the classical origin of the cutoff extension.

In Fig. 2(a) we show a BFGS-optimized pulse [red (light gray)] with the same reference pulse [blue (dark gray)] as in Fig. 1. The target range is now $\omega \in [1,5]$ a.u., i.e., considerably larger than in the previous case. Despite a slightly more complicated temporal shape of the optimized pulse, the resulting HHG spectrum [Fig. 2(b)] is similar to the first case. Now, however, the optimized pulse allows multiple returns of the electron to the origin as shown in Fig. 2(c) when using an exponential tunneling rate. Not all of the quantum-mechanical harmonic emissions can be found in the semiclassical model with exponential tunneling distribution. They are, however, allowed by the semiclassical model and visible when using a uniform tunneling rate. Therefore, the semiclassical picture does agree with the quantum description, but the exponential tunneling distribution does not produce all tunneling events.

Next we double the pulse length while keeping the peak intensity of the reference pulse, the maximum frequency, and the target HHG range the same (note that the fluence is also doubled). The BFGS-optimized pulse of Fig. 3(a) now leads to complete extension of the cutoff all the way up to $\omega = 5$ a.u., as demonstrated in Fig. 3(b). This is likely due to higher fluence and more freedom in the shaping of the longer pulse.

The effect of late returns [see, e.g., Fig. 2(c)] can be analyzed in the semiclassical picture. The harmonic spectrum can be calculated as a histogram of the electron energies
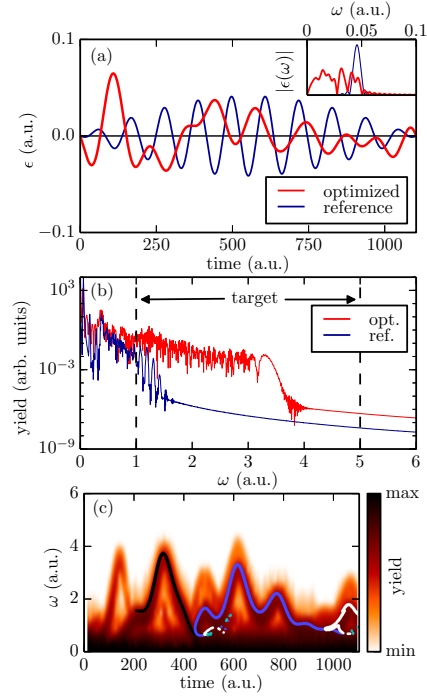

FIG. 2. (Color online) Same as Fig. 1 but for an extended target range (up to $\omega = 5$ a.u.) and for the gradient-based BFGS optimization algorithm. In (c), energies of an electron calculated from the semiclassical model upon its first, second, third, and fourth return to the origin are shown with black, blue (medium gray), white, and cyan (light gray) curves, respectively.
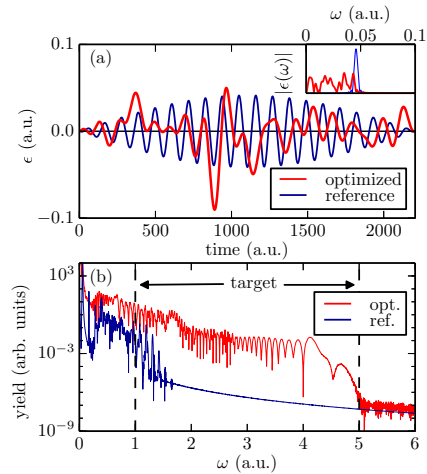

FIG. 3. (Color online) Same as Figs. 2(a) and 2(b) but for a longer pulse with $T = 2209$ a.u. (53.5 fs).

upon return to the origin with weights from the exponential tunneling rate (see above). The resulting spectra demonstrate varying contributions of late returns between different pulses. Even in the case of pulse of Fig. 2(a), where late returns are evident, their contributions to the spectra in the semiclassical models are minimal. In contrast, for the optimal pulse of Fig. 3, also the second return plays an important role in enhanced HHG.

The yield increase can be attributed to the increased tunneling probability compared to the reference pulses. Indeed, the yield increase of comparable, albeit slightly larger, magnitude can be found when using single-frequency pulses with the same maximum amplitude as in the optimized pulses, but the extension of the cutoff does not reach the optimized results. Sensitivity of HHG to the pulse amplitude has been previously reported in, e.g., Refs. [18,43]. The sensitivity is also obvious from the analytic factorization of the HHG rates in Ref. [44]. We emphasize that the yield increase of the presented optimized HHG arises from an increased tunneling rate, not from resonances as, e.g., in Ref. [16]: in our case a minimum of seven-photon absorption would be required, which is highly unlikely.

Finally, we verify which stationary states are involved in the enhanced HHG process. For this purpose, we solve the time-dependent Schrödinger equation in *momentum space and velocity gauge* by expanding the state in terms of the eigenstates of the field-free Hamiltonian [45]. Note that the occupations are gauge dependent. We find that approximately four lowest bound states are essential for the enhanced HHG, but ten are required for (nearly) full convergence of the spectrum; the numbers are similar for reference pulses. However, in the optimized HHG much of the electron density reaches high-energy continuum states, whereas for the reference pulse the electron occupation is mostly in the bound states and in the low-energy continuum (see Fig. 4).

To summarize, we have developed an optimal-control scheme to simultaneously enhance both the yield and the cutoff energy of HHG. Our target functional, an integral over the harmonic yield in a desired energy range, leads to a significant increase in the HHG yield and cutoff energy within two different optimization algorithms. Furthermore, we have shown through semiclassical studies that the extension of the cutoff is of classical origin. Instead, the increase in the harmonic yield is found to be due to increased
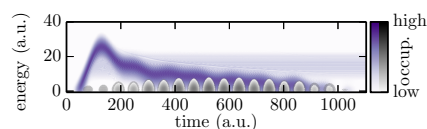

FIG. 4. (Color online) Occupations (log scale) of stationary states in velocity gauge for the reference (gray bulb-shaped structures at the bottom) and optimized (colored structures elsewhere) pulse of Fig. 1.

tunneling probability arising from increased peak amplitudes, while the fluence is kept constant in the optimization. We note that in higher-dimensional models, the harmonic yield will be affected by transversal spreading of the electron wave packet. However, our preliminary results (not shown here) demonstrate even the one-dimensional-optimized pulses provide qualitatively similar cutoff extension and no significant loss of yield also when applied to a two-dimensional model; we expect a similar tendency also for three dimensions. In addition, by doing the optimization within the same dimensionality, there can be additional degrees of freedom in the pulse regarding, e.g., polarization, number of frequency components, and pulse sources, which will help counter the issue of wave packet spreading.

We leave the detailed analysis of realistic pulse constraints to three-dimensional and many-electron models, where such analysis will be more relevant. With such refinements, we expect our method to be usable also in experimental applications, which can have direct implications in the development of efficient, flexible, and tunable light-emitting tabletop devices.

[1] See, e.g., P. B. Corkum and F. Krausz, Nat. Phys. **3**, 381 (2007).

[2] See, e.g., B. W. J. McNeil and N. R. Thompson, Nat. Photonics **4**, 814 (2010), and references therein.

[3] See, e.g., A. Scrinzi and H. G. Muller, in *Strong Field Laser Physics*, edited by T. Brabec (Springer, New York, 2008).

[4] See, e.g., A. Wirth, M. T. Hassan, I. Grgura, J. Gagnon, A. Moulet, T. T. Luu, S. Pabst, R. Santra, Z. A. Alahmed, A. M. Azzeer *et al.*, Science **334**, 195 (2011). H. Fattahi, H. G. Barros, M. Gorjan, T. Nubbemeyer, B. Alsaif, C. Y. Teisset, M. Schultze, S. Prinz, M. Haefner, M. Ueffing *et al.*, Optica **1**, 45 (2014).

[5] C. Winterfeldt, C. Spielmann, and G. Gerber, Rev. Mod. Phys. **80**, 117 (2008).

[6] M. Kohler, T. Pfeifer, K. Hatsagortsyan, and C. Keitel, in *Advances in Atomic, Molecular, and Optical Physics*, Vol. 61, edited by E. A. Paul Berman and C. Lin (Academic Press, New York, 2012).

[7] T. Shao, G. Zhao, B. Wen, and H. Yang, Phys. Rev. A **82**, 063838 (2010).

[8] Z. Zeng, Y. Cheng, X. Song, R. Li, and Z. Xu, Phys. Rev. Lett. **98**, 203901 (2007).

[9] D. G. Lee, J.-H. Kim, K.-H. Hong, and C. H. Nam, Phys. Rev. Lett. **87**, 243902 (2001).

[10] J. J. Carrera and Shih-I Chu, Phys. Rev. A **75**, 033807 (2007).

[11] Y. Xiang, Y. Niu, and S. Gong, Phys. Rev. A **79**, 053419 (2009).

[12] S. B. P. Radnor, L. E. Chipperfield, P. Kinsler, and G. H. C. New, Phys. Rev. A **77**, 033806 (2008).

[13] L. E. Chipperfield, J. S. Robinson, J. W. G. Tisch, and J. P. Marangos, Phys. Rev. Lett. **102**, 063003 (2009).

[14] J. A. Pérez-Hernández, M. F. Ciappina, M. Lewenstein, L. Roso, and A. Zaïr, Phys. Rev. Lett. **110**, 053001 (2013).

[15] E. Räsänen and L. B. Madsen, Phys. Rev. A **86**, 033426 (2012).

[16] K. L. Ishikawa, Phys. Rev. Lett. **91**, 043002 (2003).

[17] K. L. Ishikawa, Phys. Rev. A **70**, 013412 (2004).

[18] I. J. Kim, C. M. Kim, H. T. Kim, G. H. Lee, Y. S. Lee, J. Y. Park, D. J. Cho, and C. H. Nam, Phys. Rev. Lett. **94**, 243901 (2005).

[19] F. Brizuela, C. M. Heyl, P. Rudawski, D. Kroon, L. Rading, J. M. Dahlström, J. Mauritsson, P. Johnsson, C. L. Arnold, and A. L'Huillier, Sci. Rep. **3**, 1410 (2013).

[20] E. Mansten, J. M. Dahlström, P. Johnsson, M. Swoboda, A. L'Huillier, and J. Mauritsson, New J. Phys. **10**, 083041 (2008).

[21] A. Fleischer and N. Moiseyev, Phys. Rev. A **77**, 010102 (2008).

[22] E. J. Takahashi, T. Kanai, K. L. Ishikawa, Y. Nabekawa, and K. Midorikawa, Phys. Rev. Lett. **99**, 053904 (2007).

[23] A. Castro, A. Rubio, and E. K. U. Gross (unpublished).

[24] I. Schaefer and R. Kosloff, Phys. Rev. A **86**, 063417 (2012).

[25] P. Wei, J. Miao, Z. Zeng, C. Li, X. Ge, R. Li, and Z. Xu, Phys. Rev. Lett. **110**, 233903 (2013).

[26] E. Balogh, B. Bódi, V. Tosa, E. Goulielmakis, K. Varjú, and P. Dombi, Phys. Rev. A **90**, 023855 (2014).

[27] A. P. Peirce, M. A. Dahleh, and H. Rabitz, Phys. Rev. A **37**, 4950 (1988).

[28] R. Kosloff, S. Rice, P. Gaspard, S. Tersigni, and D. Tannor, Chem. Phys. **139**, 201 (1989).

[29] For a recent review on QOCT, see, e.g., J. Werschnik and E. K. U. Gross, J. Phys. B **40**, R175 (2007); C. Brif, R. Chakrabarti, and H. Rabitz, New J. Phys. **12**, 075008 (2010).

[30] J. Javanainen, J. H. Eberly, and Q. Su, Phys. Rev. A **38**, 3430 (1988).

[31] J. C. Baggesen and L. B. Madsen, J. Phys. B **44**, 115601 (2011).

[32] See, e.g., A. Castro, M. A. L. Marques, and A. Rubio, J. Chem. Phys. **121**, 3425 (2004).

[33] M. Hochbruck and C. Lubich, SIAM J. Numer. Anal. **34**, 1911 (1977).

[34] M. A. Marques, A. Castro, G. F. Bertsch, and A. Rubio, Comput. Phys. Commun. **151**, 60 (2003); A. Castro, H. Appel, M. Oliveira, C. A. Rozzi, X. Andrade, F. Lorenzen, M. A. L. Marques, E. K. U. Gross, and A. Rubio, Phys. Status Solidi B **243**, 2465 (2006).

[35] M. J. D. Powell, IMA J. Numer. Anal. **28**, 649 (2008).

[36] R. Fletcher, *Practical Methods of Optimization*, 2nd ed. (Wiley, New York, 2000).

[37] J. B. Allen, IEEE Trans. Acoust., Speech, Signal Process. **ASSP-25**, 235 (1977).

[38] R. B. Blackman and J. W. Tukey, *The Measurement of Power Spectra* (Dover, New York, 1958).

[39] A. Perelomov, V. Popov, and M. Terent'ev, Zh. Eksp. Teor. Fiz. **50**, 1393 (1966) [Sov. Phys. JETP **23**, 924 (1966)].

[40] M. Ammosov, N. Delone, and V. Krainov, Zh. Eksp. Teor. Fiz. **91**, 2008 (1986) [Sov. Phys. JETP **64**, 1191 (1986)].

[41] N. B. Delone and V. P. Krainov, J. Opt. Soc. Am. B **8**, 1207 (1991).

[42] P. B. Corkum, Phys. Rev. Lett. **71**, 1994 (1993).

[43] J. M. Dahlström, A. L'Huillier, and J. Mauritsson, J. Phys. B **44**, 095602 (2011).

[44] M. V. Frolov, N. L. Manakov, T. S. Sarantseva, M. Y. Emelin, M. Y. Ryabikin, and A. F. Starace, Phys. Rev. Lett. **102**, 243901 (2009).

[45] N. I. Shvetsov-Shilovski, E. Räsänen, G. G. Paulus, and L. B. Madsen, Phys. Rev. A **89**, 043431 (2014).

[46] F. Prez and B. E. Granger, Comput. Sci. Eng. **9**, 21 (2007).

[47] J. D. Hunter, Comput. Sci. Eng. **9**, 90 (2007).

[48] E. Jones, T. Oliphant, P. Peterson *et al.*, www.scipy.org (2011); T. E. Oliphant, Comput. Sci. Eng. **9**, 10 (2007).

8.14   Suppression of strong-field ionization

Suppression of strong-field ionization by optimal pulse shaping: Application to hydrogen and the hydrogen molecular ion

N. I. Shvetsov-Shilovski,[1] L. B. Madsen,[2] and E. Räsänen[1]

[1]*Department of Physics, Tampere University of Technology, FI-33101, Tampere, Finland*
[2]*Department of Physics and Astronomy, Aarhus University, 8000 Aarhus C, Denmark*

We investigate the ability of quantum optimal control theory to shape pulses suppressing strong-field ionization of a hydrogen atom and a H_2^+ molecule. We show that considerable suppression of the ionization yield can be achieved for both H and H_2^+ with optimal pulse shaping for a fixed fluence and pulse length. The mechanisms responsible for ionization suppression and the shape of the optimized pulse are different for infrared and ultraviolet laser fields. In the low-frequency regime the optimized pulse reduces the ionization yield by suppressing the highest peaks of the laser field. For the higher laser frequencies considered the ionization yield of H can be decreased by exciting low-lying resonances.

I. INTRODUCTION

The remarkable progress in laser technology during the last two decades has made it possible to monitor, manipulate, and control electron dynamics in real time. Weak extreme ultraviolet laser pulses with a duration of several dozens of attoseconds, as well as strong infrared pulses of femtosecond duration, are extensively used for these purposes [1]. Recently it was demonstrated that few-femtosecond pulses of a predefined shape can be synthesized using several control knobs, including beam sizes, chirps, and time delays in the respective frequency ranges [2,3]. The use of these tailored pulses opens up new prospects for manipulation of the electron motion on the atomic scale. The control of electron dynamics on its natural time scale implies a great diversity of possible applications, e.g., in femtochemistry, where some reactions occur on the femtosecond and, in some cases, the attosecond time scale [4].

One of the most challenging problems in femtochemistry is the laser control of chemical dynamics (see, e.g., Ref. [5] for a recent review). This problem has a variety of applications and perspectives, including photoassociation [6], enhancement of molecular bond breaking in the electronic ground state [7,8], control of the branching ratio in photofragmentation (see, e.g., Refs. [9–11]), and possible creation of molecules which cannot be created by other means. It is customary to distinguish between weak-field and strong-field laser control. Strong-field control is often more efficient than control using weak laser fields [5]. For example, laser intensities higher than 10^{13} W/cm^2 are required to control branching ratios in photofragmentation of CH_2BrCl more efficiently than is possible using weak fields [5,11,12]. However, it was experimentally found in Ref. [12] that the fragments of the molecule resulting from photofragmentation are ionized when using a strong field. The same problem arises in the control of electron localization in molecular dissociation [13], where undesired ionization limits the outcome. Hence, we face a situation where the strong field is desirable because of the potentially larger degree of control in a given process. At the same time the use of a strong field has the undesirable side effect of increased ionization, impeding control. Therefore, suppression of undesired ionization produced by a strong laser

pulse is an important step towards establishing laser control as a versatile tool in femtochemistry and strong-field physics.

A powerful theoretical approach to the control of quantum phenomena also in a strong field is provided by the quantum optimal control theory (QOCT) [14,15] (see Refs. [16] and [17] for recent reviews). For example, very recently QOCT was successfully applied to extend the cutoff energy and the yield of high-order harmonics [18] and to control electric dipole transitions in a real multilevel system consisting of hyperfine levels in the electronic ground state of the OH molecule [19]. The *inverse* problem to the one we discuss here, i.e., enhancement of the ionization yield, was studied in Ref. [20] by applying QOCT to H_2^+ with a fixed internuclear distance. The duration of the laser pulse and its total energy (fluence) were fixed in the optimization process to the same values as in the initial (nonoptimized) pulse. Considerable enhancement of ionization was achieved for both parallel and perpendicular orientations of the molecular axis with respect to the laser polarization. It was shown that the magnitude of the obtained enhancement and the shape of the optimized pulse depend on the constraints imposed on the laser frequency during optimization. When only low frequencies are allowed, the optimized pulse simply increases the field strength in one of its half-cycles and, in order to keep the fluence fixed, decreases the field strength of other half-cycles. If higher frequencies are allowed in the QOCT procedure, the optimized field has a more complicated structure and, as a consequence, drives the molecule through intermediate states [20]. As a result, ionization can be enhanced by resonance transitions.

Ionization suppression by pulse shaping for a fixed fluence and duration of the pulse was analyzed in Ref. [21] for a one-dimensional (1D) model H atom on the basis of QOCT. From here on we refer to the (near-) infrared fields as low-frequency fields and the ultraviolet fields as high-frequency fields. Significant suppression of ionization yield was achieved in Ref. [21] in both low-frequency and high-frequency regimes with respective physical mechanisms: in the first case, the ionization dynamics takes place in the tunneling regime and the suppression was achieved by a reduction of the peak laser intensity, which significantly decreases the probability of tunneling ionization [22]. This mechanism is opposite to

the one revealed in Ref. [20] for maximizing ionization in the tunneling regime. In contrast to this, complex excitation and de-excitation processes during the action of laser pulses prevent ionization efficiently in the high-frequency regime. To the best of our knowledge, studies on ionization suppression for three-dimensional (3D) atoms or molecules have not been carried out so far, and a quantitative assessment of the ionization suppression and its controllability in a real system is the topic of the present work.

In this paper we investigate the ability of the QOCT to suppress the ionization of H and H_2^+ by optimization of the shape of the laser pulse while keeping the pulse energy and duration fixed to some initial reference values. In the case of H we focus on both low-frequency and high-frequency regimes. Due to the numerical complexity of the application of the QOCT, we restrict our consideration of H_2^+ to the case of a fixed internuclear distance as in Ref. [20]. Since we fix the internuclear distance, the results of our simulations are applicable only for ultrashort laser pulses, so that nuclear motion can be neglected.

The paper is organized as follows. In Sec. II we briefly discuss the QOCT and its application to ionization suppression. In Sec. III we investigate suppression of the ionization yield in H. We analyze the physical mechanisms underlying ionization suppression by pulse shaping. In Sec. IV we study suppression of the ionization process in H_2^+. The conclusions of the paper are given in Sec. V. Atomic units ($\hbar = m = e = 1$) are used throughout unless indicated otherwise.

II. QUANTUM OPTIMAL CONTROL THEORY AND ITS APPLICATION TO IONIZATION SUPPRESSION

Before presenting and discussing the results of our simulations, we briefly sketch the numerical technique used. The main question that is addressed in the QOCT can be formulated as follows: What is the external time-dependent field that maximizes the transition probability to a prescribed final state from the given initial state? The usual formulation of the problem in QOCT is to find extremal points of the functional consisting of three terms (see, e.g., Ref. [16]). The first term is the target functional, which can be expressed as the expectation value of the so-called target operator being maximized at the end of the laser pulse. The second term of the functional is a constraint imposed on the field (a fixed fluence in our case), and the third one is a Lagrange multiplier that ensures the fulfillment of the time-dependent Schrödinger equation (TDSE).

Since our goal is to suppress the ionization yield, we need to maximize the population in the bound states of the system of interest at the end of the laser pulse. However, optimization in this formulation often becomes numerically difficult [20]. Following Ref. [21], we define the ionization yield as unity minus the projection onto several of the lowest eigenstates. In most cases this yield is very close to the one calculated taking into account only the ground state in the optimization. The exception is provided by H in the high-frequency regime (see Sec. III A). But even in this case the difference between the ground-state occupation and the total occupation of all the bound states does not exceed 10%–20%. In view of the above, we use a projection onto the ground state $|\Psi_0\rangle$ as a

target operator $\hat{O} = |\Psi_0\rangle\langle\Psi_0|$, and hence, the first term of the functional maximized in the QOCT is given by

$$J_1 = \langle\Psi(T)|\hat{O}|\Psi(T)\rangle = |\langle\Psi(T)|\Psi_0\rangle|^2, \tag{1}$$

where $|\Psi(t)\rangle$ is the time-dependent wave function, and the laser pulse ends at $t = T$.

Several QOCT algorithms have been developed (see, e.g., Refs. [15–20], and [23–26]). The applicability and efficiency of these schemes crucially depend on the specific target functional and constraints put on the laser field. When the maximal allowed frequency of the field is relatively high, the scheme of Werschnik and Gross [26], WG05, is very efficient. Therefore, we use this scheme for ionization suppression of H in the high-frequency regime. The WG05 scheme is based on multiple forward-backward propagations of the TDSE. This scheme does not use an expansion of the laser field in a basis: The temporal shape of the pulse is varied freely during the optimization process. The frequency constraints are expressed in the WG05 scheme using a filter function [16]. Note that the condition $\int_0^T F(t)dt = 0$ for physically meaningful laser fields, $F(t)$ (see, e.g., Refs. [27] and [28]), is not automatically fulfilled in the WG05 algorithm: The scheme can sometimes result in a nonzero integral of the optimized laser field. In this case the optimized pulse has to be modified by adding some function $\epsilon(t)$ such that $\int_0^T [F(t) + \epsilon(t)]dt = 0$. However, this modification generally worsens the optimization result as pointed out in Sec. III B.

For H in the tunneling regime and for H_2^+ at high laser intensities we are interested in relatively low frequencies and we use the direct optimization scheme [20]. In this scheme, a merit function,

$$M(p) = \langle\Psi_p(T)|\hat{O}|\Psi_p(T)\rangle, \tag{2}$$

is maximized in the set of parameters of the laser pulse p using a derivative-free algorithm (e.g., the Nelder-Mead algorithm [29]), and the laser field $F(t)$ is expressed in the Fourier basis,

$$F(t) = \sum_{n=1}^{N}\left[\alpha_n\sqrt{\frac{2}{T}}\cos(\omega_n t) + \beta_n\sqrt{\frac{2}{T}}\sin(\omega_n t)\right], \tag{3}$$

where $\omega_n = 2\pi n/T$. The condition $\int_0^T F(t)dt = 0$ is automatically fulfilled for the field given by Eq. (3). Moreover, by imposing the constraint $\sum_{n=1}^{N}\beta_n = 0$, we set $F(0) = F(T)$. The sum over n in Eq. (3) is truncated with the maximum allowed frequency, which, in turn, has to be chosen from physical considerations.

The QOCT schemes discussed here are based on the *ab initio* numerical solution of the TDSE; i.e., no approximations are done to obtain the time-dependent wave function $|\Psi(t)\rangle$. The TDSE is solved in the length gauge using the OCTOPUS code [30]. By using sufficiently large simulation boxes we ensure that only a negligible fraction of the electron density reaches the box boundaries. Nevertheless, we used the $\sin^2$ absorbing potential in order to absorb this small fraction. The size and shape of the simulation box, the grid spacing, and the time step are tailored for each specific case to ensure convergence and are given below.

III. SUPPRESSION OF IONIZATION YIELD OF H

A. Reference data and the high-frequency regime

Before we present and discuss the QOCT results, we produce an extensive set of reference data on ionization of H using nonoptimized pulses. To this end, we solve the TDSE for an H atom irradiated with a single-frequency laser pulse with the sinusoidal envelope,

$$F(t) = -F_0 \sin\left(\frac{\pi t}{2\tau_0}\right)\cos(\omega t), \qquad (4)$$

where F_0 is the field strength, ω is the carrier angular frequency, and $\tau_0 = 103.35$ a.u., corresponding to the pulse duration of $T = 2\tau_0 = 206.71$ a.u. (5 fs). The TDSE is solved on a 3D Cartesian grid. The Coulomb singularity is avoided by using the Troullier-Martins pseudopotential [31] with a core radius equal to 1.25 a.u. This leads to the correct ground-state energy of -0.5 a.u. For the simulations we use a sphere with radius 18 a.u., grid spacing 0.3 a.u., and time step 0.04 a.u. We calculate the occupations of the 20 lowest eigenstates and define the ionization yield as 1 minus the total occupation of these states. The frequencies ω under consideration do not exceed the ionization potential (0.5 a.u.), so we are not in the stabilization regime [32,33].

The total bound-state occupation and the occupation of the ground state at the end of the laser pulse given by Eq. (4) as a function of the field strength F_0 are shown over the range of frequencies between $\omega = 0.2$ a.u. (228 nm) and $\omega = 0.5$ a.u. (91 nm) in Figs. 1(a) and 1(b), respectively. Figure 1(c) presents ionization yields as functions of F_0 over the same range of laser frequencies.

As expected, at a fixed frequency the total bound-state occupation decreases with the field strength, and hence, the ionization yield increases. However, the frequency dependence of both the total bound-state and the ground-state occupations is not monotonic. Before we proceed further, recall that the
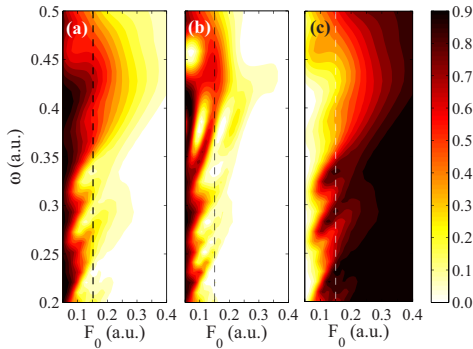

FIG. 1. (Color online) (a) Total bound-state occupation, (b) ground-state occupation, and (c) ionization yield (arbitrary units) of an H atom at the end of the laser pulse given by Eq. (4) as functions of the pulse amplitude F_0 and the frequency ω. The pulse length is $T = 206.71$ a.u. (5 fs), and the number of cycles ranges from 7 to 16 for $\omega = 0.2$ a.u. and $\omega = 0.5$ a.u., respectively.
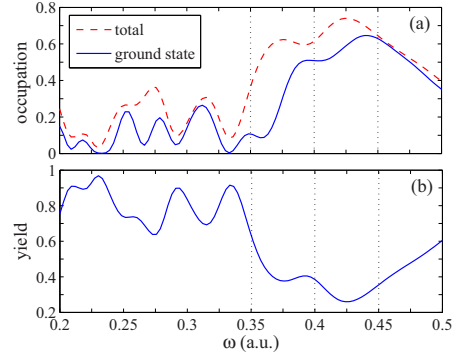

FIG. 2. (Color online) (a) Total bound-state [dashed (red) curve] and ground-state [solid (blue) curve] occupations in H at the end of the laser pulse as a function of the pulse frequency. (b) Ionization yield as a function of pulse frequency. The field strength is $F_0 = 0.15$ a.u., and the pulse length is as in Fig. 1. Dashed vertical lines indicate the frequencies studied in Fig. 3.

tunneling and the multiphoton regimes correspond to $\gamma \ll 1$ and $\gamma \gg 1$, respectively. Here $\gamma = \omega\kappa/F_0$ is the Keldysh parameter [34], where, in turn, $\kappa = \sqrt{2I_p}$, with I_p being the ionization potential. For $F_0 = 0.4$ a.u. the range of frequencies $0.2 \leqslant \omega \leqslant 0.5$ a.u. (see Fig. 1) corresponds to the following range of Keldysh parameters: $0.5 \leqslant \gamma \leqslant 1.24$. Note that for $F_0 = 0.05$ a.u. the same frequency range corresponds to $4.0 \leqslant \gamma \leqslant 10.0$. The variation of the ground-state occupation for fixed ω and increasing F_0 indicates that intermediate resonances play a role in the ionization process when $\gamma > 1$.

The dependence of the occupations and the ionization yield on the laser frequency is further illustrated in Fig. 2, obtained by a cut of Figs. 1(a)–1(c) at $F_0 = 0.15$ a.u. (shown by dashed lines). Both occupations demonstrate oscillating behavior as functions of the laser frequency and have their two highest local maxima in the range between $\omega = 0.35$ a.u. and $\omega = 0.45$ a.u. The local maxima of the total bound-state occupation are larger and more pronounced than those of the ground-state occupation. Note that for the frequencies and pulse durations used the changes in the number of photons required for ionization (channel closings) are not visible in the results.

In order to understand these frequency dependencies, we can analyze the occupations of all the bound states for several laser pulses with fixed amplitude $F = 0.15$ a.u. and different frequencies in the range of $0.2 \leqslant \omega \leqslant 0.5$ a.u. The occupations of some of the bound states during the pulses given by Eq. (4), with $F = 0.15$ a.u. and $\omega = 0.33, 0.4, 0.45,$ and 0.5 a.u. (see dashed lines in Fig. 2), are shown in Figs. 3(a), 3(c), 3(e), and 3(g), respectively. The corresponding total bound-state occupations along with the continuum populations are shown in Figs. 3(b), 3(d), 3(f), and 3(h). Note that it is physically meaningful to calculate the population in the continuum during the laser pulse using the length gauge [35]. It is clear that two resonances are excited within the frequency range discussed here: Rabi-like oscillations are seen in all the figures, but they
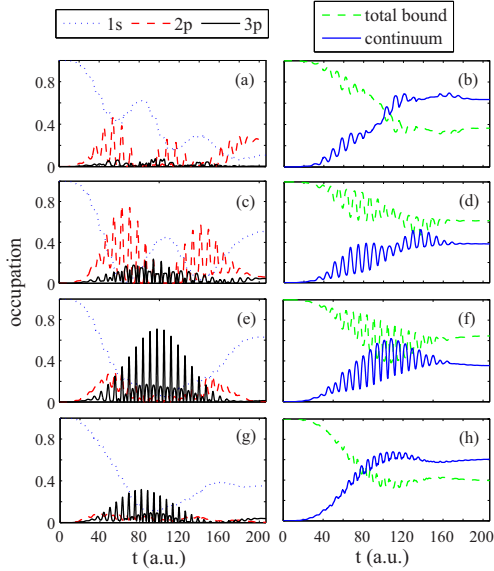
FIG. 3. (Color online) Occupations of some of the lowest states [(a), (c), (e), and (g)], and total bound-state occupations along with continuum populations [(b), (d), (f), and (h)] in H during a laser pulse with $F_0 = 0.15$ a.u. for four laser frequencies: (a, b) 0.35 a.u., (c, d) 0.4 a.u., (e, f) 0.45 a.u., and (g, h) 0.5 a.u. The pulse length is as in Figs. 1 and 2.

are most pronounced for $\omega \approx 0.40$ a.u. [Figs. 3(c) and 3(d)] and for $\omega \approx 0.45$ a.u. [Figs. 3(e) and 3(f)].

The first resonance, at $\omega \approx 0.40$ a.u. [Fig. 3(c)], corresponds to the $1s \leftrightarrow 2p$ transition. The difference in the resonant frequency from the energy gap between the $1s$ and the $2p$ levels (0.375 a.u.) is due to the ac Stark shift (see Ref. [36] for a review). Indeed, the ac Stark shift of the $1s$ state is negative, while the $2p$ state is shifted upwards; see Ref. [37], where these shifts are calculated from the real parts of complex Floquet energies [38] over a range of frequencies for a long pulse with amplitude $F_0 = 0.12$ a.u., somewhat lower than that of interest here. The imaginary parts of the Floquet energies give the corresponding ionization rates. The second resonance, at $\omega \approx 0.45$ a.u. [Fig. 3(e)], corresponds to the $1s \leftrightarrow 3p$ transition. Separate calculations (not shown here) reveal that the oscillations of both the ground-state and the total bound-state occupations for $\omega \leqslant 0.3$ a.u. are absent for a many-cycle rectangular pulse and the field strengths considered here. Therefore, the oscillations clearly visible in Figs. 2(a) and 2(b) for $\omega \leqslant 0.3$ a.u. are produced by the pulse envelope.

The ionization probability of the $1s$ state is higher than those of the $2p$ and $3p$ states for the frequencies considered in Fig. 3 (see Ref. [37]). For this reason, the excitation of resonances with these states allows an increase in the ground-state population at the end of the laser pulse, provided that the electron density is transferred back to the $1s$ state [see

Figs. 3(a), 3(c), 3(e), and 3(g)]. The numerical solution of the TDSE shows that, due to the presence of the pulse envelope, this is always the case in our study. It should be stressed that the absolute maximum of the total bound-state occupation at $\omega = 0.42$ a.u. [Fig. 2(a)] corresponds to the situation when substantial occupations of both the $2p$ and the $3p$ states are observed during the laser pulse. Indeed, the frequency $\omega = 0.42$ a.u is confined between the resonant frequencies $\omega \approx 0.40$ a.u. and $\omega \approx 0.45$ a.u., which are close to each other. It would appear natural that (i) the QOCT algorithm will shape the pulse in order to excite both resonances, and (ii) the total bound-state population at the end of the optimized pulse will be larger than the maximum of the curve shown in Fig. 2(a), which is equal to 0.74.

B. Ionization suppression in the high-frequency regime

Application of the WG05 algorithm starting from several initial pulses with different frequencies and equal amplitudes shows that the optimized pulse does excite both resonances. However, the total bound-state population at the end of this pulse does not exceed the maximum of the corresponding curve in Fig. 2. As an initial guess we use the laser pulse of Eq. (4) with $\omega = 0.4$ a.u., which is very close to the resonant frequency of the $1s \leftrightarrow 2p$ transition. The occupations of the ground state and the total bound state at the end of the initial pulse are equal to 0.50 and 0.61, respectively. Using a filter function we restrict frequencies allowed in the optimization process to $\omega \leqslant 0.5$ a.u. The initial and optimized laser pulses and their Fourier spectra are shown in Figs. 4(a) and 4(b), respectively. It is noteworthy that the peak intensity of the optimized field is higher than that of the initial field [see Fig. 4(a)].

The populations of several bound states at the end of the optimized pulse are depicted in Fig. 4(c). It is seen that the optimized pulse enhances population transfer between the $1s$ and the $3p$ states and suppresses the $1s \leftrightarrow 2p$ transition, especially after the maximum of the pulse envelope. Figure 4(d) shows the total bound-state occupation and the population in the continuum during the optimized pulse. Although the ground-state occupation (0.69) [see Fig. 4(d)] at the end of the optimized pulse is higher than the maximum of the corresponding frequency dependence (0.65; see Fig. 2), the total bound-state occupation after the optimized field, 0.72, is less than the maximum value, 0.74, accessible simply by changing the frequency of the initial pulse to $\omega = 0.42$ a.u. Significantly stronger suppression of the ionization yield has been obtained for a 1D model atom [21].

In order to further test the ability of the QOCT to suppress ionization in the high-frequency regime, we changed the target operator $\hat{O}$ to a local one [16] in order to maximize the electron density in the vicinity of the atomic core. This leads to results (not shown) similar to those in Fig. 4(a) with a total bound-state occupation, again less than 0.74.

The above results may be summed up as follows: The QOCT identifies and exploits the correct physical mechanism that needs to be used in order to suppress ionization for high laser frequencies, which couple resonantly to excited states. However, it is sometimes difficult with the QOCT to improve the result of the brute force optimization (e.g., of a simple frequency scan). In this respect, the practical benefit
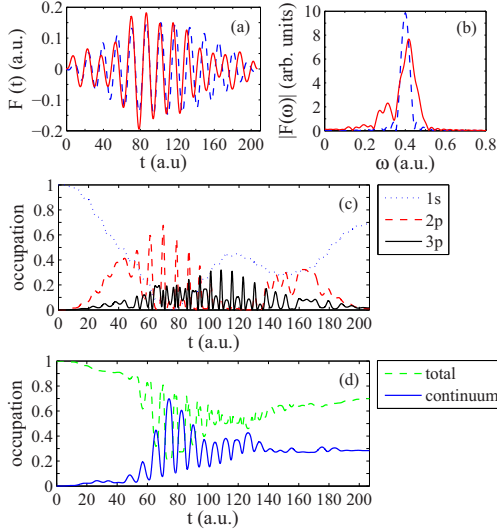
FIG. 4. (Color online) (a) Initial laser pulse with $F_0 = 0.15$ a.u. and $\omega = 0.4$ a.u. [dashed (blue) curve] and optimized pulse [solid (red) curve] with a fixed fluence equal to 1.16 a.u. (b) Fourier spectra of the pulses. (c) Occupations of some of the bound states during the optimized pulse. (d) Total bound-state occupation and the population in the continuum during the optimized pulse.
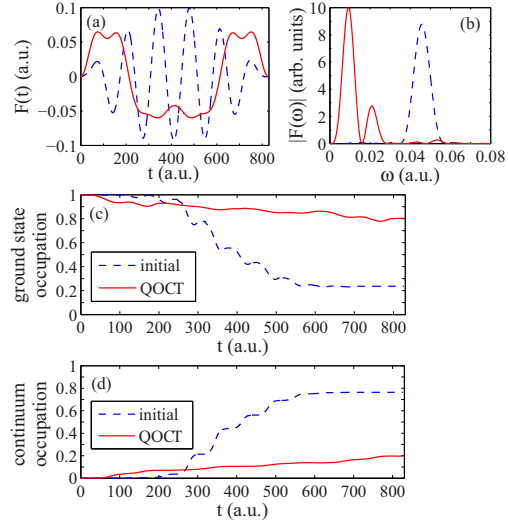

FIG. 5. (Color online) (a) Initial laser pulse with $F_0 = 0.1$ a.u. and $\omega = 0.0459$ a.u. [dashed (blue) curve] and optimized pulse [solid (red) curve]. The pulse fluence is fixed to 2.07 a.u. (b) Fourier spectra of the pulses. (c) Time dependence of the ground-state occupation in an H atom for the initial pulse [dashed (blue) curve] and the same dependence for the optimized pulse [solid (red) curve]. (d) Continuum occupation during the initial [dashed (blue) curve] and the optimized [solid (red) curve] laser pulses.

of the QOCT scheme is questionable, at least in the applied high-frequency regime.

C. Ionization suppression in the low-frequency regime

In the low-frequency (tunneling) regime, the ionization suppression for 3D H is numerically a tedious task due to the use of a direct optimization scheme (see Sec. II) that typically requires hundreds (500–800) of TDSE solutions. For example, a single optimization for a 20-fs laser pulse takes about 30 days of parallel work for eight modern CPUs with the parameters of the simulation box as in Sec. III B and a time step of 0.1 a.u. For this reason, we present only one example of the application of the QOCT to ionization suppression of H in this regime. The laser field is now given by Eq. (3), and the amplitude and the frequency of an initial pulse are equal to 0.1 and 0.0459 a.u., respectively. This corresponds to the Keldysh parameter $\gamma = 0.46$. As in the high-frequency regime, we keep the fluence of the pulse fixed to $\int_0^T F^2(t)dt = 2.07$ a.u. The threshold frequency was set to $\omega_{max} = 1.4\omega = 0.0659$ a.u.

The initial and optimized laser pulses and their Fourier spectra are shown in Figs. 5(a) and 5(b), respectively. Figure 5(c) presents the time dependencies of the corresponding ground-state occupations. The populations in the continuum during both initial and optimized pulses are shown in Fig. 5(d). It is seen that in the tunneling regime the ionization yield can be considerably suppressed: The yield produced by the initial pulse is about 0.76, whereas the same yield for the optimized pulse is about 0.20. This performance can

be qualitatively compared with the result for a 1D model atom in Ref. [21], where the ionization yield dropped in the optimization process from an initial value of 0.37 down to 0.06.

The ionization rate in the tunneling regime is given to the exponential accuracy by [22]

$$w(t_0) \sim \exp\left(-\frac{2\kappa^3}{3F}\right), \qquad (5)$$

with $F = F(t_0)$, where t_0 is ionization instant. It is seen from Eq. (5) that a lower field amplitude leads to a smaller ionization yield in an exponentially sensitive manner. This clarifies the physical mechanism responsible for ionization suppression in the tunneling regime. The mechanism is similar to the case of a 1D model atom in Ref. [21]. In essence, QOCT decreases the peak intensities of the pulse [see Fig. 5(a)], leading to a flatter overall pulse profile. Since the fluence of the pulse is fixed, the peaks at $t \leqslant 200$ a.u. and $t \geqslant 650$ a.u. become larger. Consequently, the Fourier spectrum of the pulse shifts to lower frequencies [Fig. 5(b)].

IV. IONIZATION SUPPRESSION IN THE H_2^+ MOLECULE

In this section we consider ionization suppression in H_2^+. We set the internuclear distance to the equilibrium value of 2.0 a.u., where the electronic binding energy is equal to -0.6 a.u. We consider the pulse length ≈ 5 fs. In order to have reasonable values for the initial ionization yields produced
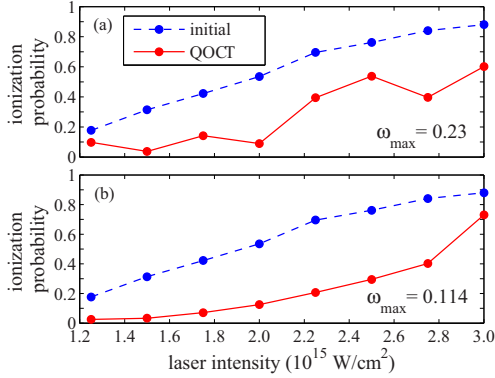
FIG. 6. (Color online) Intensity dependence of the ionization yield of an H_2^+ molecule for the initial [dashed (blue) curve] and optimized [solid (red) curve] laser pulses. The internuclear axis is parallel to the polarization direction. The frequency of all initial pulses is $\omega = 0.114$ a.u. The fluence and the pulse duration are fixed to 3.1 and 206.71 a.u. (5 fs), respectively. The maximum frequency allowed in the optimization is (a) $\omega_{max} = 0.23$ a.u. and (b) $\omega_{max} = 0.114$ a.u.
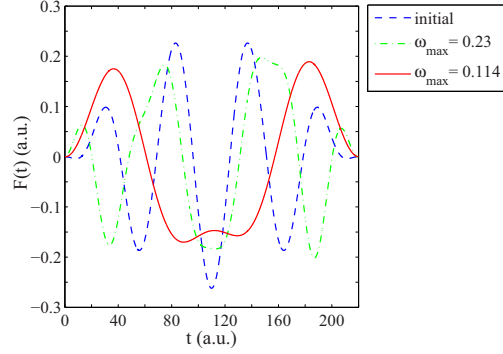

FIG. 7. (Color online) Initial laser pulse [dashed (blue) curve] for $\omega = 0.114$ a.u. and two optimized pulses [dash-dotted (green) curve and solid (red) curve] that suppress the ionization of the H_2^+ molecule at the intensity of 2.25×10^{15} W/cm^2. Dash-dotted (green) and solid (red) curves correspond to $\omega_{max} = 0.23$ a.u. and $\omega_{max} = 0.114$ a.u., respectively.

by such short pulses [see Eq. (5)], we set the peak intensity range of the initial pulse as high as $1.25 \times 10^{15} - 3.0 \times 10^{15}$ W/cm^2. For the frequency of the initial pulse $\omega = 0.114$ a.u., the chosen intensity range corresponds to the tunneling regime with $\gamma = 0.66$–0.43.

As for H in the low-frequency regime, we apply the direct optimization scheme in order to suppress ionization of H_2^+. We consider the case where the internuclear axis is parallel to the polarization direction. A combination of two Troullier-Martins pseudopotentials [31] was used in order to model the potential experienced by an electron in an H_2^+ ion. For the simulations we used a cylindrical box with the length of 30 a.u. along the polarization direction and the radius $R = 12$ a.u. The grid spacing and the time step are 0.3 and 0.03 a.u., respectively.

In Fig. 6(a) we show the intensity dependence of the ionization yield for the nonoptimized and optimized pulses. The maximum frequency allowed in the optimization is $\omega_{max} = 2\omega = 0.23$ a.u. Figure 7 shows the pulses at the intensity 2.25×10^{15} W/cm^2. It is seen in Fig. 6(a) that considerable suppression of the ionization can be achieved at most of the intensities. For example, at the intensity of 2.0×10^{15} W/cm^2 the ionization yield produced by the nonoptimized pulse is 0.53, whereas the same yield for the optimized pulse is only 0.08. It is seen that for optimized pulses the dependence of the ionization yield on the intensity is not monotonic. The nonmonotonic behavior arises from the fact that QOCT always converges to a *local* extremum in the parameter space. To find a "better" result, several optimizations with different initial conditions should be tried as, e.g., in Ref. [18]. In the present case, we were restricted to only one optimization with each laser intensity due to computational limitations.

In Fig. 6(b) we show the optimization results for a lower maximal allowed frequency, $\omega_{max} = \omega = 0.114$ a.u. Figure 7

shows the nonoptimized and optimized pulses at the intensity 2.25×10^{15} W/cm^2. The generally better results in this case [Fig. 6(b)] can be understood if we take into account that the mechanism underlying the ionization suppression in H_2^+ is the same as the one discussed in Sec. III B; i.e., QOCT decreases the intensity of the main peaks of the laser pulse. A larger ω_{max} allows for additional freedom in the pulse shaping for the purpose of maximizing the target functional. However, this additional freedom in the optimization process may sometimes result in other local maxima corresponding to less efficient suppression of the high peaks of the laser pulse and, as a consequence, to larger ionization (see Fig. 7). Similar results (not shown here) are found if the H_2^+ molecule is oriented *perpendicularly* to the polarization direction.

Because of the numerical complexity here we do not consider ionization suppression in the H_2^+ molecule in the high-frequency regime. However, the shape of the optimized pulse as well as the mechanism underlying the ionization suppression in the high-frequency regime may differ for the H_2^+ molecule compared to the H atom. The reason is that for high frequencies the suppression of the ionization yield is very sensitive to the resonances (see Sec. III A), and they are different in H_2^+ and H. The ionization suppression for high laser frequencies along with the consideration of the movement of the nuclei in H_2^+ will be the subject of future studies.

V. CONCLUSIONS AND OUTLOOK

In conclusion, we have applied QOCT to tailor short, strong laser pulses to suppress strong-field ionization of H and H_2^+. The possibility of suppressing ionization is of importance for femtochemistry and strong-field physics, since undesired ionization produced by strong laser pulses used, e.g., to control the electron density in molecular dissociation or the branching ratio in photofragmentation, may seriously limit the ability to obtain the desired degree of control and experimental outcomes. The experimental realization of the pulses needed

seems within reach in view of the remarkable technological progress that has been achieved in the generation of strong few-cycle laser pulses with a predefined shape [2,3].

Suppression of tunneling ionization was investigated for H_2^+, whereas for H we have considered both low-frequency (tunneling), and high-frequency regimes. We have shown that a significant decrease in the ionization yield can be achieved in both cases by varying the temporal shape of the laser pulse while keeping the fluence and pulse duration fixed. The shape of the optimized pulse and the physical mechanism responsible for the ionization suppression are different in low-frequency and high-frequency regimes. In the low-frequency regime, a decrease in the ionization yield for both H and H_2^+ can be achieved by suppression of the highest peaks of the laser pulse, for which the tunneling probability is maximal.

It is shown that for H in the high-frequency regime the optimized pulse suppresses the ionization by using a resonant population transfer between the ground state ($1s$) and some of the excited states ($2p$ and $3p$). However, it is difficult to improve the result of a brute force "single-frequency" optimization by using the QOCT in an attempt to maximize

the ground-state occupation or the electron density near the atomic core at the end of the pulse.

The results of our fully 3D real-space calculations can be used as a benchmark for further studies of the suppression of strong-field ionization by optimal pulse shaping. A natural, albeit challenging next step could be the inclusion of the nuclear motion in order to better mimic, e.g., pump-probe experiments. Developments in this direction are on the way.

ACKNOWLEDGMENTS

[1] F. Krausz and M. Ivanov, Rev. Mod. Phys. **81**, 163 (2009).

[2] A. Wirth, M. Th. Hassan, I. Grguraš, J. Gagnon, A. Moulet, T. T. Luu, S. Pabst, R. Santra, Z. A. Alahmed, A. M. Azzeer *et al.*, Science **334**, 195 (2011).

[3] M. Th. Hassan, A. Wirth, I. Grguraš, A. Moulet, T. T. Luu, J. Gagnon, V. Pervak, and E. Goulielmakis, Rev. Sci. Instrum. **83**, 111301 (2012).

[4] M. F. Kling and M. J. J. Vrakking, Annu. Rev. Phys. Chem. **59**, 463 (2008).

[5] N. E. Henriksen, Chem. Phys. **442**, 2 (2014).

[6] C. P. Koch and M. Shapiro, Chem. Rev. **112**, 4928 (2012).

[7] S. Chelkowski, A. D. Bandrauk, and P. B. Corkum, Phys. Rev. Lett. **65**, 2355 (1990).

[8] T. Witte, T. Hornung, L. Windhorn, D. Proch, R. de Vivie-Riedle, M. Motzkus, and K. L. Kompa, J. Chem. Phys. **118**, 2021 (2003).

[9] T. S. Rose, M. J. Rosker, and A. H. Zewail, J. Chem. Phys. **88**, 6672 (1988).

[10] A. K. Tiwari, K. B. Møller, and N. E. Henriksen, Phys. Rev. A **78**, 065402 (2008).

[11] C. C. Shu, T. Rozgonyi, L. Gonzáles, and N. E. Henriksen, J. Chem. Phys. **136**, 174303 (2012).

[12] N. H. Damrauer, C. Dietl, G. Krampert, S.-H. Lee, K.-H. Jung, and G. Gerber, Eur. Phys. J. D **20**, 71 (2002).

[13] M. F. Kling, Ch. Siedschlag, A. J. Verhoef, J. I. Knan, M. Schultze, Th. Uphues, Y. Ni, M. Uiberacker, M. Drescher, F. Krausz, and M. J. J. Vrakking, Science **312**, 246 (2006).

[14] A. P. Peirce, M. A. Daleh, and H. Rabitz, Phys. Rev. A **37**, 4950 (1988).

[15] R. Kosloff, S. A. Rice, P. Gaspard, S. Tersigni, and D. J. Tannor, Chem. Phys. **139**, 201 (1989).

[16] J. Werschnik and E. K. U. Gross, J. Phys. B **40**, R175 (2007).

[17] C. Brif, R. Chakrabarti, and H. Rabitz, New J. Phys. **12**, 075008 (2010).

[18] J. Solanpää, J. A. Budagosky, N. I. Shvetsov-Shilovski, A. Castro, A. Rubio, and E. Räsänen, Phys. Rev. A **90**, 053402 (2014).

[19] M. Lysebo and L. Veseth, Phys. Rev. A **90**, 063427 (2014).

[20] A. Castro, E. Räsänen, A. Rubio, and E. K. U. Gross, Europhys. Lett. **87**, 53001 (2009).

[21] E. Räsänen and L. B. Madsen, Phys. Rev. A **86**, 033426 (2012).

[22] L. D. Landau and E. M. Lifschitz, *Quantum Mechanics Nonrelativistic Theory*, 2nd ed. (Pergamon, Oxford, UK, 1965).

[23] D. Tannor, V. Kazakov, and V. Orlov, in *Time-Dependent Quantum Molecular Dynamics*, edited by J. Broeckhove and L. Lathouweres (Plenum, New York, 1992).

[24] W. Zhu, J. Botina, and H. Rabitz, J. Chem. Phys. **108**, 1953 (1998).

[25] S. E. Sklarz and D. J. Tannor, Phys. Rev. A **66**, 053619 (2002).

[26] J. Werschnik and E. K. U. Gross, J. Opt. B **7**, S300 (2005).

[27] L. B. Madsen, Phys. Rev. A **65**, 053417 (2002).

[28] D. B. Milošević, G. G. Paulus, D. Bauer, and W. Becker, J. Phys. B **39**, R203 (2006).

[29] J. A. Nelder and R. Mead, Comput. J. **7**, 308 (1965).

[30] M. A. Marques, A. Castro, G. F. Bertsch, and A. Rubio, Comput. Phys. Commun. **151**, 60 (2003).

[31] N. Troullier and J. L. Martins, Phys. Rev. B **43**, 1993 (1991).

[32] M. Gavrila, J. Phys. B **35**, R147 (2002).

[33] A. M. Popov, O. V. Tikhonova, and E. A. Volkova, J. Phys. B **36**, R125 (2003).

[34] L. V. Keldysh, Zh. Eksp. Teor. Fiz. **47**, 1945 (1964) [Sov. Phys. JETP **20**, 1307 (1965)].

[35] L. B. Madsen and D. Dimitrovski, Phys. Rev. A **78**, 023403 (2008).

[36] N. B. Delone and V. P. Krainov, Usp. Fiz. Nauk **169**, 753 (1999); Phys. Usp. **42**, 669 (1999).

[37] M. G. Girju, K. Hristov, O. Kidun, and D. Bauer, J. Phys. B **40**, 4165 (2007).

[38] R. M. Potvliege, Comput. Phys. Commun. **114**, 42 (1998).

8.15   *Dynamics of valence-shell electrons*
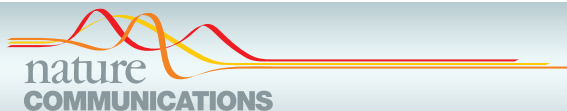
ARTICLE

Dynamics of valence-shell electrons and nuclei probed by strong-field holography and rescattering

Samuel G. Walt[1], Niraghatam Bhargava Ram[1], Marcos Atala[1,†], Nikolay I. Shvetsov-Shilovski[2], Aaron von Conta[1], Denitsa Baykusheva[1], Manfred Lein[2] & Hans Jakob Wörner[1]

Strong-field photoelectron holography and laser-induced electron diffraction (LIED) are two powerful emerging methods for probing the ultrafast dynamics of molecules. However, both of them have remained restricted to static systems and to nuclear dynamics induced by strong-field ionization. Here we extend these promising methods to image purely electronic valence-shell dynamics in molecules using photoelectron holography. In the same experiment, we use LIED and photoelectron holography simultaneously, to observe coupled electronic-rotational dynamics taking place on similar timescales. These results offer perspectives for imaging ultrafast dynamics of molecules on femtosecond to attosecond timescales.

[1] Laboratorium für Physikalische Chemie, ETH Zürich, Vladimir-Prelog-Weg 2, HCI E 237, 8093 Zürich, Switzerland. [2] Institut für Theoretische Physik, Leibniz Universität Hannover, 30167 Hannover, Germany. † Present address: Max Planck Institute for the Structure and Dynamics of Matter, Center for Free Electron Laser Science, Luruper Chaussee 149, 22761 Hamburg, Germany. Correspondence and requests for materials should be addressed to H.J.W. (email: hwoerner@ethz.ch).

Time-resolved measurements of molecular dynamics have made substantial progress over the past years. In particular, electronic dynamics in atoms and molecules have become accessible through recent developments in attosecond and strong-field science[1-10]. This fundamental progress has so far remained restricted to methods relying on spectroscopy, rather than diffraction. In other words, electronic dynamics have been recorded by measuring either the time-dependent populations of electronic eigenstates or their accumulated phase differences, which does not provide any structural information about electronic wave functions. However, the interaction of a molecule with a strong laser field naturally provides access to structure by inducing rescattering between the laser-driven photoelectron wave packet and the parent ion. This so-called laser-induced electron diffraction (LIED)[11,12] has been used to probe the structure of static atoms and molecules[13-20], and to obtain evidence of nuclear dynamics following strong-field ionization[21]. Photoelectron holography, which results from interference between electrons that have scattered from the parent ion and those that have not, has also been used to interrogate the structure of static atoms and molecules[22-24], and to reveal nuclear dynamics following ionization[25]. Although the imprint of electronic dynamics on photoelectron distributions has been reported for neutral atoms[26], it is not obvious whether the distributions can be interpreted in terms of LIED or holography. As far as molecules are concerned, electronic dynamics have so far escaped observation by any of these powerful methods. As LIED and holography rely both on the wave nature of the electron and on rescattering, they are expected to be sensitive to small variations of the molecular structure. Earlier work on electron interference without rescattering[27-30] has already revealed the sensitivity to the symmetry of the bound state.

In this study, we transpose photoelectron holography and LIED from static systems to probing coupled electronic and nuclear dynamics in molecules. We first concentrate on purely electronic dynamics and show that a valence-shell electron wave packet leads to a very strong contrast modulation of the holographic fringes. Our calculations trace the origin of this effect to the time dependence of the momentum-space electron wavefunction, which modulates the amplitude ratio and the relative phases of scattering and non-scattering trajectories. We then investigate the manifestation of coupled electronic and nuclear dynamics taking place on similar time scales. We find signatures of both types of dynamics in photoelectron holography, but LIED is found to be almost exclusively sensitive to the nuclear dynamics. These results suggest avenues for disentangling electronic and nuclear dynamics in molecules, which is particularly interesting in the case of non-adiabatic dynamics, such as those occurring at conical intersections[31].

Results

Experiment. We use impulsive stimulated Raman scattering to prepare a coupled electronic and rotational wave packet in the neutral NO molecule. A supersonic molecular beam was formed by expanding a 1% mixture of NO with helium through a pulsed Even–Lavie valve. Several rotational states within the $^2\Pi_{1/2}$ ground electronic state and the $^2\Pi_{3/2}$ first excited electronic state (separated by 15 meV) are impulsively prepared by a non-resonant laser pulse (800 nm, 145 fs, $4 \times 10^{13}\,W\,cm^{-2}$ peak intensity). The long duration of the laser pulse is chosen to avoid the preparation of vibrational wave packets in NO and NO^+ (periods of 17 and 14 fs, respectively). The wave packet is subsequently probed by strong-field ionization (800 nm, 35 fs, $2.3 \times 10^{14}\,W\,cm^{-2}$) and the photoions and photoelectrons are detected by a velocity-map-imaging spectrometer[32,33]. We also recorded ion time-of-flight measurements (Fig. 1a) by adding $<1\%$ Xe to the NO/He mixture and the NO^+ signal was normalized to the Xe^+ signal, to eliminate fluctuations of laser parameters and gas-jet density.

Figure 1a shows the normalized NO^+ yield as a function of the pump–probe delay. The rapid regular oscillation originates from the electronic dynamics, illustrated in the inset, whereas the two features around 5 and 10 ps correspond to rotational revivals. The amplitude modulations observed around 8–9.5 ps are a characteristic signature of multi-level quantum beats[34,35]. Figure 1b shows a cut through the three-dimensional photoelectron momentum distribution recorded at a delay of 1.56 ps. Details about the processing of the photoelectron momentum images are given in the Methods section. Figures 1c,d show normalized differences, defined as $S(t_1, t_2) = 2(D(t_2) - D(t_1))/(D(t_2) + D(t_1))$ of photoelectron momentum distributions D recorded at the local minimum (delay t_1) and maximum (delay t_2) of the photoelectron (or NO^+) yield that are dominated by either purely electronic or electronic and rotational dynamics, respectively. The corresponding values of t_1 and t_2 are given in the caption of Fig. 1. The purely electronic valence-shell dynamics (Fig. 1c) appears as a pronounced modulation of a holographic pattern, whereas the rotational dynamics manifests itself by additionally modifying the angular distribution of rescattered photoelectrons, clearly visible at the highest momenta of Fig. 1d.

Electronic dynamics. We first concentrate on the purely electronic dynamics. Figure 2a (reproduced from Fig. 1c) shows stripes of alternating orange and yellow colours extending from the centre towards the border of the momentum distribution. We attribute these structures to photoelectron holography, previously observed for stationary states of atoms[22,23,36]. This assignment is substantiated by comparing the observed fringe pattern with the quantitative prediction of holography. Using the vertical ionization potential of NO and the conditions of our experiments leads to the prediction of regions of constructive (black) and destructive (white) interference calculated following the simple model outlined in ref. 36. These fringes arise from the interference between quantum trajectories of (signal) electrons that have scattered forward from the parent ion and (reference) electrons that have passed by the parent ion without scattering. The lack of quantitative agreement between the experiment and the simple model mainly originates from the absence of the Coulomb potential in the latter, as we further discuss below.

The sudden loss of fringe visibility with increasing momentum constitutes further evidence of the holographic origin of the fringes. The green circle in Fig. 2a marks the maximal momentum that can be acquired by electrons that do not scatter. The blue line represents the $1/e^2$ full width of the tunnelling filter, defined by

$$G\left(p_x^2 + p_y^2\right) = e^{-\frac{(p_x^2 + p_y^2)\tau}{2}}, \tag{1}$$

where p_x and p_y are momentum components perpendicular to the laser-field direction and $\tau = \sqrt{2I_p}/F$, where I_p represents the ionization potential and F is the instantaneous field strength at the moment of ionization. The fringes are only observed within the area defined by the green circle, showing that they involve non-scattered electrons. More precisely, we find that the fringes are even limited to the area within the blue curve, showing that the maximal lateral momentum of the electron wave packet is indeed limited by the tunneling filter, lending support to the concept proposed in refs 15,37. We emphasize that the
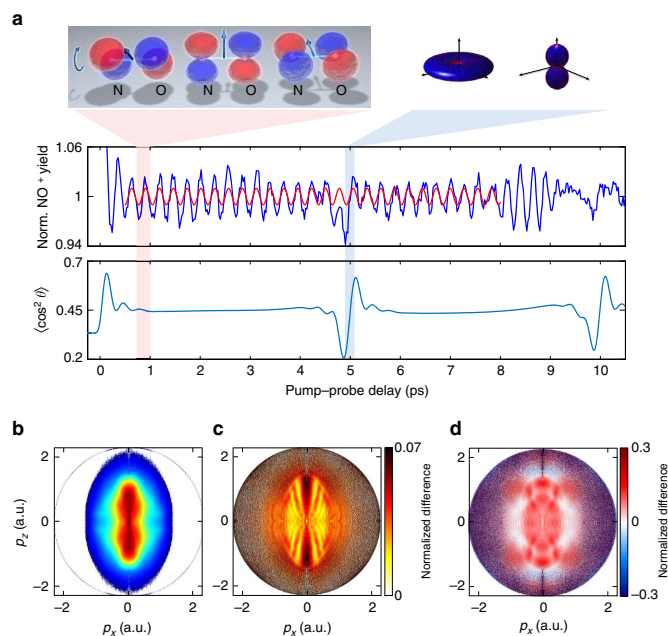
ARTICLE

Figure 1 | Discerning electronic and nuclear dynamics. (**a**) The top panel illustrates the prepared electronic and rotational dynamics with the left part showing the time-evolution of the one-electron wave function in NO and the right part illustrating the molecular-axis distribution. The wave function can be chosen real-valued with opposite signs (red and blue) by multiplication with a global phase factor that corresponds to a physically irrelevant shift of the absolute energy scale. The middle panel shows the time-dependent normalized NO^+ yield (blue line) and a sine function with a period of 277 fs (red line). The lowest panel shows the calculated alignment dynamics expressed by $\langle \cos^2\theta \rangle$ (including volume averaging). (**b**) Photoelectron momentum distribution of excited NO molecules recorded at a delay of 1.56 ps. Normalized difference $S(t_1, t_2)$ (defined in the text) of momentum distributions measured at the minimum and maximum of the NO^+ signal dominated by electronic dynamics (**c**, $t_1 = 1.56$ ps and $t_2 = 1.72$ ps, respectively) or around the rotational revival (**d**, at $t_1 = 4.91$ ps and $t_2 = 5.10$ ps, respectively). a.u., atomic units.

holographic fringes observed in Fig. 2a are barely visible in the inverted photoelectron momentum distributions themselves (Fig. 1b). They only become visible in the normalized differences. Figure 2b shows how the contrast of the holographic fringes evolves in time over one period of the electronic dynamics. The holographic fringes in the normalized-difference images modulate with a contrast close to 100%.

A weak signature of the electronic dynamics can also be observed outside the green circle of Fig. 2a, that is, in the region dominated by the electrons that have scattered backwards from the parent ion. We note that the noise along the central vertical line is an artifact of the inversion procedure. The nearly constant value of the difference signal observed in this region shows that the electronic dynamics does not change the angular distribution function of the rescattered electrons. However, the total signal of the rescattered electrons modulates in time with approximately the same contrast as the total signal. We thus conclude that the electronic dynamics in NO causes a variation of the rescattering probability, but it hardly affects the shape of the photoelectron distribution in the rescattering region. In contrast, the shape of the holographic pattern shows a strong signature of the electronic dynamics.

Model for time-dependent photoelectron holography. We now introduce a model for time-dependent photoelectron holography and use it to explain our observations. Figure 3a shows the temporal

evolution of the time-dependent orbital describing the unpaired electron of NO. The displayed orbital wavefunction corresponds to one of two possible values of the spin projection quantum number ($\Sigma = +1/2$). The orbital corresponding to the opposite value of Σ rotates in the opposite direction[8] and is omitted here for clarity. As holography results from the interference of scattered and non-scattered trajectories, we focus on the momentum distribution of electrons perpendicular to the direction of tunnelling, also called lateral momentum distribution. We determine this quantity for the time-dependent electronic wave packet by building on the concept of partial-Fourier transformation for strong-field ionization[38]. The laser field is linearly polarized along the z axis. A cut through the one-electron density in the xy plane at the distance $z_0 = -1.83$ Å from the origin is shown on the front face of each cube in Fig. 3a. z_0 corresponds to the position of the local maximum of the combined Coulomb and laser-field potentials using the peak electric field strength. The two-dimensional Fourier transform of the wave function at $z = z_0$, multiplied by the tunnelling filter (equation 1) leads to the lateral-momentum distribution of the continuum photoelectron wave packet after tunnelling, shown in Fig. 3b:

$$\Phi(p_x, p_y, z_0, t) \approx \left| \frac{1}{2\pi} \iint \Psi(x, y, z_0, t) e^{ixp_x + iyp_y} dxdy \right.$$
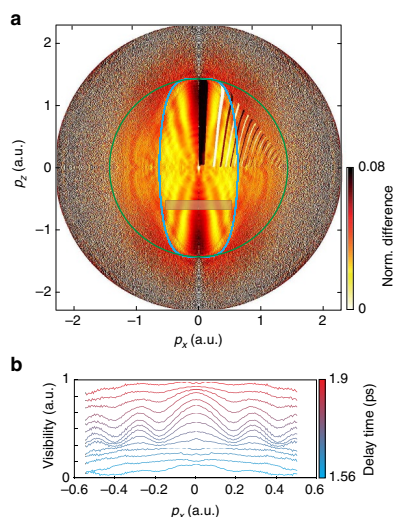$$\left. \times G\left(p_x^2 + p_y^2\right) \right|^2. \tag{2}$$

Figure 2 | Time-dependent photoelectron holography. (**a**) Normalized difference $S(t_1, t_2)$ between delays $t_1 = 1.56$ ps and $t_2 = 1.72$ ps, dominated by electronic dynamics. The added curves are discussed in the text. The polarization of both laser pulses was parallel to the p_z axis. (**b**) Lineouts of the holographic pattern obtained by integrating the signal inside the grey box in **a** over p_z, but recorded at the indicated delays that sample one period of the electronic dynamics and are referenced to a delay of 1.05 ps.

The corresponding angle-averaged distribution function $M(p_r, t)$, shown in Fig. 3c, is defined by

$$M(p_r, t) = \frac{\Phi'(p_r, z_0, t)}{\Phi'(p_r = 0, z_0, t = t_0)}, \qquad (3)$$

where

$$\Phi'(p_r, z_0, t) = \frac{\oint_{p_r} \Phi(p_x, p_y, z_0, t)\,\mathrm{d}s}{\oint_{p_r} \mathrm{d}s} \qquad (4)$$

and $p_r^2 = p_x^2 + p_y^2$.

The time-evolving lateral-momentum distribution shown in Fig. 3b has a transparent physical interpretation. As time evolves, the orbital wave function of the unpaired electron shown in Fig. 3a rotates around the molecular axis, leading to the periodic appearance and disappearance of a nodal plane containing the direction of tunnelling (z).

We further support the interpretation of the observed holographic fringes by turning to classical-trajectory calculations[39] that are described in more detail in the Methods section. We consider the two cases where the one-electron density is aligned either parallel to the polarization direction of the ionizing laser pulse ($t = t_0$) or perpendicular to it ($t = t_0 + T/2$). We propagate classical trajectories in the combined Coulomb and laser field, using the experimental parameters for the latter. The initial momenta sample the distribution function derived above for the highest-occupied molecular orbital of NO obtained from quantum-chemical calculations using the GAMESS package. Figure 4 shows the calculated final momentum distributions at the detector for (a) the electron density being aligned along the direction of the ionizing laser polarization, (b) the electron density being aligned perpendicular to this direction and (c) the
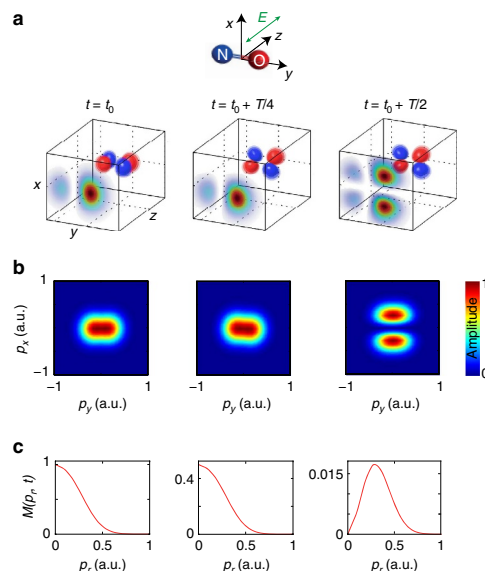

Figure 3 | Model for time-dependent photoelectron holography. (**a**) Temporal evolution of the one-electron wave function of NO and cut through the density along the vertical plane located at the maximum of the laser + Coulomb potential. (**b**) Lateral-momentum distributions obtained by 2D-Fourier transformation of the wave-function cuts shown in **a** and multiplication with the tunnelling filter. (**c**) Distribution function of lateral momentum norms $M(p_r, t)$ of **b**.

normalized difference of (a) and (b). The momentum distribution (a) shows the characteristic features of strong-field ionization by a near-infrared laser pulse, that is, the above-threshold ionization peaks, which extend up to $2U_p$ and the holographic fringes. The momentum distribution (b) is significantly weaker in amplitude (note the different colour scales), broader in the lateral-momentum direction and additionally displays a node at $p_x = 0$. This feature reflects the nodal plane of the molecular orbital, which contains the laser polarization in this specific configuration. This feature is not visible in the experimental data, because the fraction of excited molecules is on the order of 1% (refs 34,35) and the molecules are not aligned at the considered delays, whereas 100% excitation and perfect alignment was assumed in the calculations.

Figure 4c shows the normalized difference of Fig. 4a,b and is in excellent agreement with the experimental result (Fig. 2a). In particular, the calculation nicely displays all characteristic properties of the experimentally observed holographic structures. Interestingly, the comparison of these calculations with the simple model from ref. 36 shows the same discrepancies as Fig. 2a, that is, the model overestimates the spacing of the holographic fringes along the lateral-momentum direction. The improved agreement between the experiment and our trajectory calculations must therefore originate from the inclusion of the Coulomb potential in the latter.

These complete three-dimensional trajectory calculations further show that the electronic dynamics indeed modulate the contrast of the holographic fringes. As the calculations were done using a purely Coulombic potential, the observed time-dependent
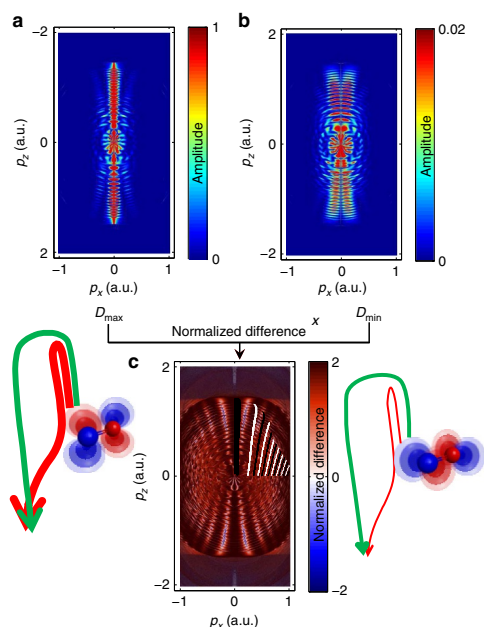
ARTICLE

Figure 4 | Classical trajectory calculations. Calculated momentum distribution for the cases where the electron density of the highest-occupied molecular orbital (HOMO) is aligned (**a**) along the polarization direction of the ionizing laser field or (**b**) perpendicular to it. (**c**) The normalized difference of the momentum distributions shown in **a**,**b**.

holography can be uniquely attributed to the time-dependent momentum-space structure of the outermost orbital of NO as illustrated in Fig. 3. The time dependence of the orbital is translated into a time-dependent lateral-momentum distribution of the photoelectron wave packet after tunneling, which results in a high contrast modulation of the holographic fringes. The good agreement between theory (Fig. 4c) and experiment (Fig. 2a) also shows that the molecular properties of the potential seen by the continuum electron are not crucial in defining the observed holographic pattern. This insensitivity may turn out to be an advantageous filter that makes time-dependent photoelectron holography specifically sensitive to a particular aspect of the electronic dynamics that it records, that is, the lateral momentum distribution.

Coupled electronic and nuclear dynamics. We now turn to the observation of coupled nuclear and electronic dynamics occurring around a rotational revival. Figure 1a compares the measured NO^+ signal with calculations of the rotational dynamics of NO. At the early delays discussed so far (1–4 ps), rotational dynamics can be neglected, because the axis distribution does not change over the period of the electronic dynamics. In contrast, electronic and nuclear dynamics occur on similar time scales around a rotational revival, which offers the opportunity to study the manifestation of coupled electronic and nuclear dynamics. Figure 5a compares the photoelectron yield integrated over all momenta around the revival of the rotational dynamics (top) with the extrapolated electronic quantum beat (centre) and the

calculated rotational dynamics (bottom) taken from Fig. 1a. These calculations have been done with the methods described in refs 34,35. They include the rotational levels of both populated electronic states of NO and fully account for the coupled electronic and rotational dynamics on the relevant time scales.

Figures 5b–d show normalized differences of photoelectron momentum distributions $S(t_2, t_1)$, $S(t_2, t_3)$ and $S(t_2, t_4)$, respectively. These delays were chosen to highlight the different manifestations of coupled electronic and nuclear dynamics. The delays t_1 and t_2 both lie close to the minimum of $\langle\cos^2\theta\rangle$, which means that the axis distribution undergoes little change within this time interval. However, the interval $[t_1, t_2]$ samples a significant fraction of the electronic quantum beat. Between t_2 and t_3, both electronic and nuclear dynamics evolve. Between t_2 and t_4, the electronic dynamics have evolved for half of a period and the rotational dynamics have undergone their maximal evolution, from anti-alignment to alignment.

We first note that the minimum of the photoelectron and NO^+ yield (t_2) lies between the minima of $\langle\cos^2\theta\rangle$ (close to t_1) and that of the extrapolated purely electronic quantum beat (close to t_3). This is a first indication that both electronic and nuclear dynamics influence the ionization probability. Much more details are visible in the photoelectron images. We focus our discussion on three aspects of these images. First, Fig. 5b–d all display holographic signatures similar to those of Fig. 2a. These features coincide with the location of the measured main holographic maxima in Fig. 2a, which are reproduced here as black dashed lines. The excellent agreement shows that the structures observed in Fig. 5b–d also correspond to photoelectron holography. These holographic fringes are not unexpected because all three intervals sample substantial fractions of an electronic quantum beat.

Second, each of these six main holographic fringes displays an additional extremum in the radial dimension, which was not observed in Fig. 2a. Comparing Fig. 5b with Fig. 5c,d, we observe a maximum along the radial dimension in the case of Fig. 5b and a minimum in Fig. 5c,d. These radial extrema cannot be explained by purely electronic dynamics because of the differences observed in comparison with Fig. 2a. We note that normalized-difference images evaluated between delays sampling fractions of the purely electronic quantum beat in the range of 1–2 ps all look qualitatively identical to Fig. 2a (not shown). The additional structures on top of the holographic fringes can therefore only originate from the simultaneous effect of electronic and nuclear dynamics, which is thus found to leave a characteristic imprint on time-dependent photoelectron holography.

Third, Fig. 5d additionally shows pronounced structures in the region of the rescattered photoelectrons (outside the green circle). This shows that the distribution shape of the rescattered electrons with energies above $2U_p$ is also modulated, which was clearly not observed during the purely electronic dynamics (compare Figs 2a and 5d). We further investigate this aspect by analysing the rescattered electrons. Outside the green circle in Fig. 5d, alternating regions of negative (blue) and positive (red) colour are observed. We analyse this region using the LIED approach illustrated with a black circle and arrow[21,40,41]. Electrons that have elastically scattered with the momentum $|\mathbf{p}_s|$ in the direction α acquire the additional momentum $\mathbf{p}_L = -\mathbf{A}(t_r)$ from the laser field, equal to the opposite value of the vector potential at the moment of rescattering (t_r). The value of the normalized difference along such circles is displayed in Fig. 5f and compared with calculations (Fig. 5e). We use the variational Schwinger method implemented in ePolyScat[42,43] to accurately solve the scattering problem of electrons from aligned NO^+ molecules. Our calculations also take into account the angle-dependent strong-field ionization rate of NO[44] and the
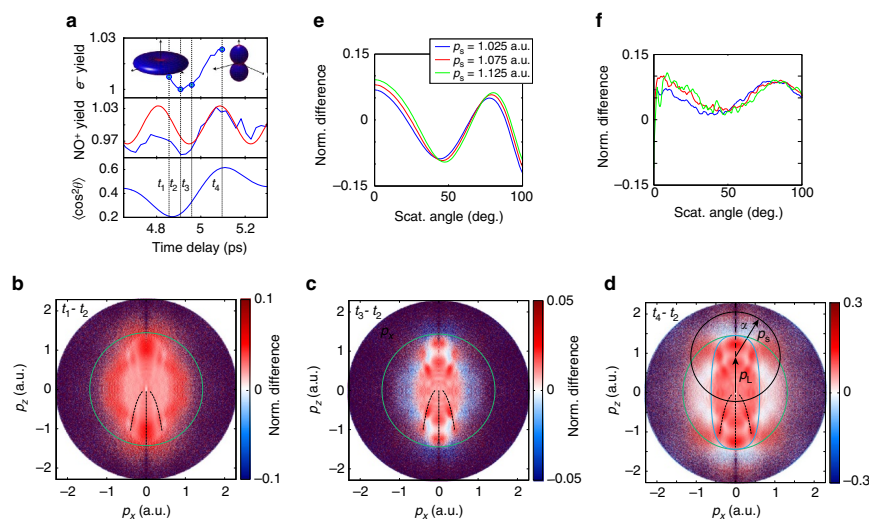
ARTICLE   NATURE COMMUNICATIONS | DOI: 10.1038/ncomms15651

Figure 5 | Manifestation of coupled electronic-nuclear dynamics in holography and LIED. (**a**) Normalized photoelectron yield integrated over all momenta around the first revival (top), NO^+ yield in blue and extrapolated electronic quantum beat in red (middle) and calculated alignment dynamics (bottom). (**b**) Normalized difference $S(t_2, t_1)$ for $t_1 = 4.86$ ps and $t_2 = 4.91$ ps. The green circle indicates the $2U_p$ limit. The black dashed lines indicate the position of the maximum of the holographic pattern of Fig. 2a. (**c**) $S(t_2, t_3)$ for $t_3 = 4.96$ ps. (**d**) $S(t_2, t_4)$ for $t_4 = 5.10$ ps, the blue line is the same as in Fig. 2a. The black circle indicates the final momentum of photoelectrons with a scattering momentum $|p_s|$ and scattering angle α ($\alpha = 0$ corresponds to back-scattering). (**e**) Calculated normalized difference of rescattered electron distributions for different scattering momenta. (**f**) Experimental normalized differences as a function of the scattering angle for the same scattering momenta as in **e**, smoothed over a $10°$ range, using the same colour coding as in **e**.

molecular-axis distribution corresponding to our experimental conditions. The prediction shown in Fig. 5e qualitatively agrees with the experimental result in Fig. 5f. Both the general shape of the curves and the shift of the minimum to larger angles for increasing scattering momenta are well reproduced. The calculation however overestimates the contrast of the normalized difference, which can originate from the limited accuracy of the electron-molecule scattering calculations and/or the strong-field ionization rates. We have verified that uncertainties in the molecular axis distributions cannot explain the observed discrepancy.

Discussion
We have reported on the observation of valence-shell electron and coupled electronic-nuclear dynamics using strong-field photoelectron holography and rescattering. We will separate our conclusions into two parts, that is, conclusions that we expect to be general and conclusions that we view as specific to the broad class of radicals (such as NO, NO_2, OH and so on). We have shown that photoelectron holography can be used as a probe of valence-shell dynamics in molecules, and that it is particularly sensitive to the components of the momentum wave function perpendicular to the direction of tunnelling. These components indeed control the relative probability and phase of rescattering relative to non-rescattering trajectories, which directly control the contrast and structure of the holographic pattern, respectively. We have further shown that coupled electronic and nuclear dynamics leave a characteristic imprint on the holographic pattern. This suggests the application of photoelectron holography to probe coupled electronic and nuclear dynamics in polyatomic molecules. We expect these two conclusions to be general. As NO has a single unpaired electron, we expect some of

our observations to apply to radicals. Specifically, we have observed that the electronic dynamics leave no signature on the angular-distribution shape of the rescattered electrons (see Fig. 2a), such that LIED provides a virtually background-free measurement of nuclear dynamics. This observation constitutes an experimental demonstration of the fundamental quantum-mechanical principle that the laser-driven electron wave packet must be described as scattering from its parent ion, rather than from the neutral molecule. In systems featuring a single unpaired electron, such as NO, the parent ion does not display electronic dynamics, resulting in a delay-independent LIED. In the more frequent case of closed-shell molecules, the returning electron will scatter off an ion supporting electronic dynamics, such as charge migration[10]. Our results suggest that in this case, the electronic dynamics of the neutral molecule will be observable in holography, which will however additionally contain signatures of the ionic dynamics (both electronic and nuclear), contributed by the rescattering quantum trajectories. In contrast to holography, LIED will mainly reflect the dynamics of the ion, because the angle dependence of the rescattered electrons is dominated by the elastic-scattering cross-section[41]. More broadly, these considerations show how the fundamental principles uncovered in our pump–probe experiment can be transferred to the regime of sub-cycle temporal resolution to observe, for example, coupled structural and electronic rearrangements on femtosecond to attosecond timescales.

Methods
Data processing. The two-dimensional photoelectron momentum images were processed as follows. A constant background was subtracted from the entire image to account for dark counts and residual stray light. Then, the images were symmetrized. Finally, two-dimensional momentum distributions were obtained by iterative Abel inversion using a computer program developed in our group[33].

ARTICLE

A typical photoelectron momentum distribution is shown in Fig. 1b. The momentum distributions shown in Figs 1c,d,2a and 5b–d are normalized differences between distributions measured at two different pump–probe delays, as defined in the text. The analysis of the LIED signals proceeded as follows. For a given photoelectron momentum at rescattering $\mathbf{p}_s$, the corresponding time of rescattering t_s was determined using the long trajectories in the classical recollision model (see, for example, ref. 41). The short trajectories were discarded, because they are suppressed by the lower strong-field ionization rate at the corresponding times of ionization. The additional momentum shift $\mathbf{p}_L$ that the electrons acquire from the laser field after rescattering was calculated according to $\mathbf{p}_L = -\mathbf{A}(t_r)$, using the vector potential corresponding to the laser field used in our experiment.

Trajectory calculations. We calculate photoelectron momentum distributions for different times during the electronic wave-packet dynamics using the semiclassical two-step model for strong-field ionization[39], which is a Monte-Carlo method involving interfering trajectories. Electron trajectories are launched throughout the laser pulse with probabilities corresponding to the instantaneous tunnel ionization rate. As initial conditions we use the lateral momentum distributions derived above (see equation 3) in combination with zero initial momentum along the field and initial electron position at the tunnel exit of a triangular barrier determined by the instantaneous electric field. As the method[39] is based on Newtonian trajectories moving in a cylindrically symmetric potential formed by the laser field and a Coulomb potential, the simulation can be restricted to trajectories in a plane containing the field direction. However, electrons departing towards opposite sides at the time of ionization may end up with the same final momentum and interfere. Thus, initial conditions for both negative and positive lateral momenta must be defined. The lateral distribution is chosen to be symmetric in both cases that we consider, $t = t_0$ and $t = t_0 + T/2$. In the former case, the initial phases are taken equal on both sides, but in the latter case a π phase difference is used, in view of the orbital symmetry (see Fig. 3a,b). Similarly, in the former case, the initial phases have a π difference for opposite directions of the ionizing field and they are taken equal for both field directions in the latter case. The laser parameters for the simulation are the experimental ones except that a short $\sin^2$-shaped envelope with total length of eight optical cycles is used instead of the longer experimental pulses.

References

1. Drescher, M. *et al.* Time-resolved atomic innershell spectroscopy. *Nature* **419**, 803–807 (2002).
2. Goulielmakis, E. *et al.* Real-time observation of valence electron motion. *Nature* **466**, 739–743 (2010).
3. Mauritsson, J. *et al.* Attosecond electron spectroscopy using a novel interferometric pump-probe technique. *Phys. Rev. Lett.* **105**, 053001 (2010).
4. Holmegaard, L. *et al.* Photoelectron angular distributions from strong-field ionization of oriented molecules. *Nat. Phys.* **6**, 428–432 (2010).
5. Wörner, H. J. & Corkum, P. B. Imaging and controlling multielectron dynamics by laser-induced tunnel ionization. *J. Phys. B* **44**, 041001 (2011).
6. Fleischer, A. *et al.* Probing angular correlations in sequential double ionization. *Phys. Rev. Lett.* **107**, 113003 (2011).
7. Lux, C. *et al.* Circular dichroism in the photoelectron angular distributions of camphor and fenchone from multiphoton ionization with femtosecond laser pulses. *Angew. Chem. Int. Ed.* **51**, 5001–5005 (2012).
8. Kraus, P. M. *et al.* High-harmonic probing of electronic coherence in dynamically aligned molecules. *Phys. Rev. Lett.* **111**, 243005 (2013).
9. Ott, C. *et al.* Reconstruction and control of a time-dependent two-electron wave packet. *Nature* **516**, 374–378 (2014).
10. Kraus, P. M. *et al.* Measurement and laser control of attosecond charge migration in ionized iodoacetylene. *Science* **350**, 790–795 (2015).
11. Zuo, T., Bandrauk, A. D. & Corkum, P. B. Laser-induced electron diffraction: a new tool for probing ultrafast molecular dynamics. *Chem. Phys. Lett.* **259**, 313–320 (1996).
12. Lein, M., Marangos, J. P. & Knight, P. L. Electron diffraction in above-threshold ionization of molecules. *Phys. Rev. A* **66**, 051404 (2002).
13. Ray, D. *et al.* Large-angle electron diffraction structure in laser-induced rescattering from rare gases. *Phys. Rev. Lett.* **100**, 143002 (2008).
14. Okunishi, M. *et al.* Experimental retrieval of target structure information from laser-induced rescattered photoelectron momentum distributions. *Phys. Rev. Lett.* **100**, 143001–143004 (2008).
15. Meckel, M. *et al.* Laser induced electron tunnelling and diffraction. *Science* **320**, 1478–1482 (2008).
16. Okunishi, M., Niikura, H., Lucchese, R. R., Morishita, T. & Ueda, K. Extracting electron-ion differential scattering cross sections for partially aligned molecules by laser-induced rescattering photoelectron spectroscopy. *Phys. Rev. Lett.* **106**, 063001 (2011).
17. Xu, J. *et al.* Diffraction using laser-driven broadband electron wave packets. *Nat. Commun.* **5**, 4635 (2014).
18. Pullen, M. G. *et al.* Imaging an aligned polyatomic molecule with laser-induced electron diffraction. *Nat. Commun.* **6**, 7262 (2015).
19. Pullen, M. G. *et al.* Influence of orbital symmetry on diffraction imaging with rescattering electron wave packets. *Nat. Commun.* **7**, 11922 (2016).
20. Ito, Y. *et al.* Extracting conformational structure information of benzene molecules via laser-induced electron diffraction. *Struct. Dyn.* **3**, 034303 (2016).
21. Blaga, C. I. *et al.* Imaging ultrafast molecular dynamics with laser-induced electron diffraction. *Nature* **483**, 194–197 (2012).
22. Huismans, Y. *et al.* Time-resolved holography with photoelectrons. *Science* **331**, 61–64 (2011).
23. Hickstein, D. D. *et al.* Direct visualization of laser-driven electron multiple scattering and tunneling distance in strong-field ionization. *Phys. Rev. Lett.* **109**, 073004 (2012).
24. Meckel, M. *et al.* Signatures of the continuum electron phase in molecular strong-field photoelectron holography. *Nat. Phys.* **10**, 594–600 (2014).
25. Haertelt, M., Bian, X.-B., Spanner, M., Staudte, A. & Corkum, P. B. Probing molecular dynamics by laser-induced backscattering holography. *Phys. Rev. Lett.* **116**, 133001 (2016).
26. Hultgren, H., Eklund, M., Hanstorp, D. & Kiyan, I. Y. Electron dynamics in the ground state of a laser-generated carbon atom. *Phys. Rev. A* **87**, 031404 (2013).
27. Gribakin, G. F. & Kuchiev, M. Y. Multiphoton detachment of electrons from negative ions. *Phys. Rev. A* **55**, 3760–3771 (1997).
28. Reichle, R., Helm, H. & Kiyan, I. Y. Photodetachment of H^- in a strong infrared laser field. *Phys. Rev. Lett.* **87**, 243001 (2001).
29. Lindner, F. *et al.* Attosecond double-slit experiment. *Phys. Rev. Lett.* **95**, 040401 (2005).
30. Bergues, B., Ansari, Z., Hanstorp, D. & Kiyan, I. Y. Photodetachment in a strong laser field: an experimental test of keldysh-like theories. *Phys. Rev. A* **75**, 063415 (2007).
31. Wörner, H. J. *et al.* Conical intersection dynamics in NO_2 probed by homodyne high-harmonic spectroscopy. *Science* **334**, 208–212 (2011).
32. Walt, S. G. *et al.* Role of multi-electron effects in the asymmetry of strong-field ionization and fragmentation of polar molecules: the methyl halide series. *J. Phys. Chem. A* **119**, 11772–11782 (2015).
33. Walt, S. G. *Imaging Electronic Structure and Dynamics of Molecules Through Strong-Field Ionization, Rescattering and Holography.* PhD thesis, ETH Zurich (2015).
34. Baykusheva, D., Kraus, P. M., Zhang, S. B., Rohringer, N. & Wörner, H. J. The sensitivities of high-harmonic generation and strong-field ionization to coupled electronic and nuclear dynamics. *Farad. Disc.* **171**, 113–132 (2014).
35. Zhang, S. B., Baykusheva, D., Kraus, P. M., Wörner, H. J. & Rohringer, N. Theoretical study of molecular electronic and rotational coherences by high-order-harmonic generation. *Phys. Rev. A* **91**, 023421 (2015).
36. Bian, X.-B. *et al.* Subcycle interference dynamics of time-resolved photoelectron holography with midinfrared laser pulses. *Phys. Rev. A* **84**, 043420 (2011).
37. Spanner, M., Simova, O., Corkum, P. B. & Ivanov, M. Y. Reading diffraction images in strong field ionization of diatomic molecules. *J. Phys. B* **37**, L243–L250 (2004).
38. Murray, R., Liu, W.-K. & Ivanov, M. Y. Partial fourier-transform approach to tunnel ionization: atomic systems. *Phys. Rev. A* **81**, 023413 (2010).
39. Shvetsov-Shilovski, N. I. *et al.* Semiclassical two-step model for strong-field ionization. *Phys. Rev. A* **94**, 013415 (2016).
40. Chen, Z., Le, A.-T., Morishita, T. & Lin, C. D. Quantitative rescattering theory for laser-induced high-energy plateau photoelectron spectra. *Phys. Rev. A* **79**, 033409 (2009).
41. Lin, C. D., Le, A.-T., Chen, Z., Morishita, T. & Lucchese, R. Strong-field rescattering physics: self-imaging of a molecule by its own electrons. *J. Phys. B* **43**, 122001 (2010).
42. Gianturco, F. A., Lucchese, R. R. & Sanna, N. Calculation of low-energy elastic cross sections for electron-CF_4 scattering. *J. Chem. Phys.* **100**, 6464–6471 (1994).
43. Natalense, A. P. P. & Lucchese, R. R. Cross section and asymmetry parameter calculation for sulfur 1s photoionization of SF_6. *J. Chem. Phys.* **111**, 5344–5348 (1999).
44. Saito, R., Tolstikhin, O. I., Madsen, L. B. & Morishita, T. Structure factors for tunneling ionization rates of diatomic molecules. *Atom. Data Nuclear Data Tables* **103**, 4–49 (2015).

ARTICLE

Author contributions

Additional information

How to cite this article: Walt, S. G. *et al.* Dynamics of valence-shell electrons and nuclei probed by strong-field holography and rescattering. *Nat. Commun.* **8,** 15651 doi: 10.1038/ncomms15651 (2017).

Publisher's note: Springer Nature remains neutral with regard to jurisdictional claims in published maps and institutional affiliations.

8.16   Effects of the Coulomb potential in interference patterns
PHYSICAL REVIEW A **97**, 013411 (2018)

**Effects of the Coulomb potential in interference patterns of strong-field
holography with photoelectrons**

N. I. Shvetsov-Shilovski[*] and M. Lein
Institut für Theoretische Physik and Centre for Quantum Engineering and Space-Time Research,
Leibniz Universität Hannover, D-30167 Hannover, Germany

Using the semiclassical two-step model for strong-field ionization we investigate the interference structures emerging in strong-field photoelectron holography, taking into account the Coulomb potential of the atomic core. For every kind of the interference pattern predicted by the three-step model, we calculate the corresponding structure in the presence of the Coulomb field, showing that the Coulomb potential modifies the interference patterns significantly.

I. INTRODUCTION

Development of techniques capable of tracing molecular dynamics involves fundamental and technological problems of great complexity that need to be solved. The reason is that the dynamic imaging techniques are to operate at subangstrom spatial scales with femtosecond time resolution. The continuous progress in laser technologies, especially the advent of the technology of pulse compression, as well as the advances in the development of free-electron lasers, have given rise to a variety of techniques aimed at time-resolved molecular imaging. Among these are optical pump-probe spectroscopy, time-resolved electron and x-ray diffraction, and ultrafast x-ray spectroscopy (see Ref. [1] for recent review).

During the last three decades a breakthrough in laser technology has been achieved: table-top intense femtosecond laser systems operating at various wavelengths have become available in many laboratories all over the world. This has led to the emergence of such fields of research as strong-field, ultrafast, and attosecond physics (see Ref. [2] for review). It was found that the interaction of intense laser radiation with atoms and molecules leads to a plethora of highly nonlinear phenomena. Among these are above-threshold ionization (ATI) and the formation of the high-energy plateau in the electron energy spectrum (high-order ATI), generation of high-order harmonics (HHG), nonsequential double ionization (NSDI), etc. (see Refs. [3–6] for recent reviews). The main theoretical approaches used in strong-field physics are the direct numerical solution of the time-dependent Schrödinger equation (TDSE) (see, e.g., Refs. [7–9] and references therein), the strong-field approximation (SFA) [10–12], and semiclassical models using classical description of the electron after it has been promoted to the continuum, typically by tunneling ionization [13–15]. The widely known semiclassical approaches are the two-step [16–18] and the three-step models [19,20].

The studies of ATI have shown that the vast majority of electrons reach the detector without recolliding with their parent ions. These electrons are referred to as direct ones and they have energies below $2U_p$, where $U_p = F^2/4\omega^2$ is the ponderomotive energy (atomic units are used throughout the paper unless indicated otherwise). There are also electrons that are driven back to their parent ions and scatter off them by angles close to $180°$. The high-energy plateau in the ATI spectrum is created due to these rescattered electrons. The rescattering scenario led to an understanding of the physical mechanisms responsible for HHG and NSDI. The returning electron can recombine with the parent ion and emit high-order harmonics [20,21]. As an alternative, if this electron has enough energy, it can release another electron from the atomic ion (see Ref. [22] for review). These rescattering-induced processes can be qualitatively described within the three-step model. In the first step of this model an electron tunnels out of an atom, and in the second step it moves along a classical trajectory in the laser field only. The third step involves the interaction of the returning electron with the parent ion.

Some of the phenomena mentioned here may be used for the development of new ways of time-resolved molecular imaging. Indeed, new ultrafast laser-based imaging techniques have been proposed recently: laser-assisted electron diffraction [23,24], laser-induced Coulomb explosion imaging [25–28], laser induced electron diffraction [29–32], high-order harmonic orbital tomography [33,34], and strong-field photoelectron holography (SFPH) [35].

Using the full coherence of the electron motion after ionization, the SFPH method puts into practice the idea of holography [36]. It was shown in Ref. [35] that a photoelectron holographic pattern can be clearly recorded in experiment. The hologram is created by the interference between a reference (direct) electron and a signal (rescattered) one. The SFPH method of molecular imaging has several important advantages. First, although free-electron lasers were used in some of the SFPH experiments (see Refs. [35,37]), this method can be realized in a table-top experiment. Second, the hologram that is recorded in SFPH encodes temporal and spatial information not only about the ion but about the recolliding electron as well. Last but not least, attosecond time resolution can be achieved for the photoelectron dynamics. Indeed, the signal and reference

---

[*]n79@narod.ru

electronic wave packets that produce the holographic patterns can be ionized in the same quarter cycle of the oscillating laser field. As a result, subcycle time resolution can be achieved even for long laser pulses.

For these reasons, the SFPH has been studied extensively in the last few years, both experimentally (see, e.g., Refs. [38–42]) and theoretically [35,37–39,41,43–49]. Among the theoretical approaches used to analyze the holographic structures are the semiclassical model that accounts for the laser field only [41,43–46], direct numerical solution of the TDSE [35,38,39,41,43], the modified version of the SFA that accounts for the rescattering [35,37], the Coulomb-corrected strong-field approximation (CCSFA) [35,37], and the Coulomb quantum orbit strong-field approximation (CQSFA) [48,49] (see Ref. [50] for the foundations of the CQSFA method). The holograms obtained from the solution of the TDSE agree with the experimental data. This is particularly true for the spacing between the side lobes (fringes) of the holographic structure emerging when both the signal and reference electrons are generated on the same quarter of cycle. However, it is difficult to interpret the hologram from the solution of the TDSE.

The three-step semiclassical model was adapted for calculation of the SFPH (see Refs. [43–46]). Different types of subcycle interference structures were predicted by this model [43]. Indeed, while the first studies of the SFPH considered only the interference of the reference and signal waves that are born in the same quarter cycle of the laser field, the signal and reference electrons can also originate from different quarter cycles, leading to different holographic patterns. Despite the appealing physical picture of the SFPH provided by the three-step model, it is well known that neglecting the Coulomb potential is severe (see, e.g., Refs. [51–53]). Note that the same is true for the modified version of the SFA. Furthermore, the simulations of the SFPH within three-step model were performed assuming that the starting point of the classical trajectory is independent of the field strength [43–46]. In contrast to this, it is natural to assume that electrons tunnel through a potential barrier with time-dependent width due to the oscillations of the laser field. It is known that the proper choice of the initial conditions for classical trajectories is important [54,55].

The study of the electron trajectories calculated within the CCSFA showed that the trajectories responsible for the emergence of the interference structure can indeed be considered as reference and scattered wave packets [35]. The CCSFA approach reproduces the shape of the interference fringes and the spacing between them. Finally, the CCSFA simulations have given important insight into the role of the Coulomb potential in the SFPH [35,37]. The same is also true for the CQSFA theory that has allowed for the identification and isolation of many types of interference patterns in the photoelectron momentum distributions. The distortion of different kinds of interfering trajectories along with the change of the phase difference between them due to the presence of the ionic potential were studied in Ref. [49]. However, no direct comparison of the interference structures predicted by the three-step model with those calculated taking the Coulomb potential into account has been made so far.

Moreover, not all the principal types of interference structures predicted by the three-step model were considered in

Refs. [35,37,49]. To the best of our knowledge, the effects of the Coulomb potential in the interference structures emerging due to the hard collisions of the signal electron with the atomic core have not been analyzed so far. Recall that hard collisions require small impact parameters and result in large changes of electron momenta including backward scattering. The interference of direct with *backscattered* electrons has been proposed in Ref. [44] as a particularly sensitive probe of the molecular structure. The holograms for H_2 and N_2 measured recently in Ref. [41] revealed a fishbonelike structure that was claimed to originate from backward scattering.

In this paper we revisit the holographic interferences calculated using the three-step model, in order to (i) understand how the time-dependent exit point affects the interference patterns and (ii) obtain a benchmark for comparison with the case when the Coulomb field is taken into account. We then calculate all major types of interference structures in the presence of the Coulomb potential, including those that involve hard collisions of the signal electron (backward scattering). Our analysis is based on the semiclassical two-step model (SCTS) that describes quantum interference and accounts for the Coulomb potential beyond the semiclassical perturbation theory (see Ref. [56]).

The paper is organized as follows. In Sec. II we discuss the three-step model and its application to the SFPH when the starting point of the classical trajectories is time independent, and when it depends on time. We formulate our approach to calculation of the SFPH with the Coulomb field in Sec. III. In Sec. IV we analyze formation of the interference structures in the presence of the Coulomb potential. The conclusions of the paper are given in Sec. V.

II. STRONG-FIELD PHOTOELECTRON HOLOGRAPHY IN THE THREE-STEP MODEL

A. Application of the three-step model to strong-field photoelectron holography

The application of the three-step model to the SFPH is reported in Refs. [43–47]. Here we repeat the main points that are important for the following discussion. For simplicity, and in order to be consistent with Refs. [43–45], in this section we consider only one cycle of a linearly polarized cosinelike laser field: $\vec{F}(t) = F_0 \cos(\omega t) \vec{e}_x$ between $\omega t = 0$ and 2π. Here $\vec{e}_x$ is the unit vector in the polarization direction, F_0 is the field strength, and ω is the frequency. Newton's equation of motion for an electron moving in this field can be easily solved analytically. The velocity $\vec{v}(t)$ and the position $\vec{r}(t)$ of an electron launched at time t_0 are given by

$$\vec{v}(t) = \{v_x(t_0) + p_F \sin(\omega t_0) - p_F \sin(\omega t)\}\vec{e}_x + v_y(t_0)\vec{e}_y + v_z(t_0)\vec{e}_z, \tag{1}$$

and

$$\vec{r}(t) = \left\{ x_0(t) + \frac{F_0}{\omega^2}(\omega t - \omega t_0)\sin(\omega t_0) \right. \\ \left. + \frac{F_0}{\omega^2}[\cos(\omega t) - \cos(\omega t_0)] \right\}\vec{e}_x \\ + v_y(t_0)(t - t_0)\vec{e}_y + v_z(t_0)(t - t_0)\vec{e}_z. \tag{2}$$

Here $\vec{v}(t_0) = v_x(t_0)\vec{e}_x + v_y(t_0)\vec{e}_y + v_z(t_0)\vec{e}_z$, $\vec{r}(t_0) = x(t_0)\vec{e}_x + y(t_0)\vec{e}_y + z(t_0)\vec{e}_z$, and $p_F = F_0/\omega$. Due to the cylindrical symmetry with respect to the polarization direction, we leave out the z component of both $\vec{r}(t)$ and $\vec{v}(t)$ in what follows and consider electron motion in two spatial dimensions.

We assume that the electron starts with zero initial velocity along the laser field $v_x(t_0) = 0$, but its initial transverse velocity $v_y(t_0) \equiv v_{0,\perp}$ can be arbitrary. An electron starting with zero initial transverse velocity at a time instant t_0^{sig} within a certain fraction of the laser period can return to the parent ion [i.e., to the point $(x = 0, y = 0)$]. Upon its return this signal electron is elastically scattered from the atomic core by an angle θ_0 (see, e.g., Ref. [57]). The scattering event is assumed to be instantaneous, and the scattering angle θ_0 is randomly distributed between 0 and $360°$.

The time of return t_1 of the signal electron can be found from the equation

$$x(t_0^{\mathrm{sig}}) + \frac{F_0}{\omega^2}(\omega t_1 - \omega t_0^{\mathrm{sig}})\sin(\omega t_0^{\mathrm{sig}})$$
$$+ \frac{F_0}{\omega^2}\left[\cos(\omega t_1) - \cos(\omega t_0^{\mathrm{sig}})\right] = 0. \tag{3}$$

Since the signal electron returns to the core with the velocity

$$V_1 = -p_F\left[\sin(\omega t_1) - \sin(\omega t_0^{\mathrm{sig}})\right], \tag{4}$$

its velocity at time $t > t_1$ is given by

$$\vec{V}(t) = [V_1 \cos\theta_0 + p_F \sin(\omega t_1) - p_F \sin(\omega t)]\vec{e}_x$$
$$+ V_1 \sin\theta_0 \vec{e}_y. \tag{5}$$

From Eq. (5) we obtain the asymptotic (final) momentum of the signal electron:

$$\vec{p} = [V_1 \cos\theta_0 + p_F \sin(\omega t_1)]\vec{e}_x + V_1 \sin\theta_0 \vec{e}_y. \tag{6}$$

The asymptotic momentum of a reference electron starting at time t_0^{ref} with initial transverse velocity $v_{0,\perp}$ reads as

$$\vec{p} = p_F \sin(\omega t_0^{\mathrm{ref}})\vec{e}_x + v_{0,\perp}\vec{e}_y. \tag{7}$$

For both signal and reference trajectories to lead to the same final momentum $\vec{p} = (p_x, p_y)$, their velocities at any time $t > t_1$ must be equal [43]. Indeed, from Eqs. (5) and (6) it follows that for $t > t_1$

$$\vec{V}(t) = [p_x - p_F \sin(\omega t)]\vec{e}_x + p_y\vec{e}_y. \tag{8}$$

The same expression is also valid for the reference electron [cf. Eqs. (1) and (7)].

When the three-step model is applied to the SFPH, the phase associated with an electron trajectory starting at time t_0 is determined by the classical action (see Refs. [43–47]) $S(t_0,t) = \int_{t_0}^{t}(\vec{v}^2(t')/2 + I_p)dt'$, where I_p is the ionization potential. Therefore, the phases of the signal and reference electrons are given by

$$S^{\mathrm{sig}}(t) = \frac{1}{2}\int_{t_0^{\mathrm{sig}}}^{t_1} v_x^2(t')dt' + \frac{1}{2}\int_{t_1}^{t}[p_x - p_F\sin(\omega t')]^2 dt'$$
$$+ I_p(t - t_0^{\mathrm{sig}}) + \frac{p_y^2}{2}(t - t_1) \tag{9}$$

and

$$S^{\mathrm{ref}}(t) = \frac{1}{2}\int_{t_0^{\mathrm{ref}}}^{t_1} v_x^2(t')dt' + \frac{1}{2}\int_{t_1}^{t}[p_x - p_F\sin(\omega t')]^2 dt'$$
$$+ I_p(t - t_0^{\mathrm{ref}}) + \frac{p_y^2}{2}(t - t_0^{\mathrm{ref}}), \tag{10}$$

respectively. Finally, the phase difference between the signal and reference waves reads as (see Refs. [43–47])

$$\Delta S = \frac{1}{2}\int_{t_0^{\mathrm{sig}}}^{t_1} v_x^2(t')dt' - \frac{1}{2}\int_{t_0^{\mathrm{ref}}}^{t_1} v_x^2(t')dt'$$
$$- I_p(t_0^{\mathrm{sig}} - t_0^{\mathrm{ref}}) - \frac{p_y^2}{2}(t_1 - t_0^{\mathrm{ref}}). \tag{11}$$

In order to calculate the phase difference (11) at a given final momentum $\vec{p}$, it is necessary to find the corresponding values of t_0^{ref}, t_0^{sig}, and t_1. For $|p_x| < p_F$ the equation $p_x = p_F \sin(\omega t_0^{\mathrm{ref}})$ [see Eq. (7)] has two solutions in the range $0 \leqslant \omega t_0^{\mathrm{ref}} < 2\pi$. For $p_x \geqslant 0$ we have $\omega t_{0,1}^{\mathrm{ref}} = \arcsin(p_x/p_F)$ and $\omega t_{0,2}^{\mathrm{ref}} = \pi - \arcsin(p_x/p_F)$. For negative p_x the solutions are given by $\omega t_{0,1}^{\mathrm{ref}} = \pi + \arcsin(|p_x|/p_F)$ and $\omega t_{0,2}^{\mathrm{ref}} = 2\pi - \arcsin(|p_x|/p_F)$.

Retrieving the corresponding t_0^{sig} and t_1 is more cumbersome. It is worthwhile to solve Eq. (3) first, i.e., to find the function $t_1 = t_1(t_0^{\mathrm{sig}})$ at every point of some grid for the time of start t_0^{sig}. For some values of ionization time Eq. (3) has multiple solutions, which correspond to so-called late returns of the ionized electron to the ion. Knowing $t_1 = t_1(t_0^{\mathrm{sig}})$ on some grid we can calculate $V_1(t_0^{\mathrm{sig}})$ on the same grid [see Eq. (4)]. Then the values of t_1 and V_1 at any intermediate point can be found by interpolation. From Eqs. (4) and (8) it follows that

$$\{p_x - p_F \sin[\omega t_1(t_0^{\mathrm{sig}})]\}^2 + p_y^2$$
$$= p_F^2\{\sin[\omega t_1(t_0^{\mathrm{sig}})] - \sin[\omega t_0^{\mathrm{sig}}]\}^2. \tag{12}$$

By solving this equation numerically we can find the time of start t_0^{sig} that leads to a given $\vec{p}$, and then evaluate the corresponding values of $t_1(t_0^{\mathrm{sig}})$ and $V_1(t_0^{\mathrm{sig}},t_1)$. Finally, Eq. (6) allows us to determine the instantaneous scattering angle.

The algorithm described here is not the only possible approach to calculation of interferometric structures. An alternative method treats t_0^{sig} and θ_0 as new independent variables. For every time of start t_0^{sig} the corresponding recollision time is again found from Eq. (3). Then for any pair $(t_0^{\mathrm{sig}},\theta_0)$ the asymptotic momentum can be found from Eq. (6). By doing so for a sufficiently large number of trajectories specified by t_0^{sig} and θ_0, we can obtain reliable statistics in the (p_x, p_y) plane. Finally, these signal trajectories with the corresponding phases are binned according to their asymptotic momenta in cells in momentum space. After the phase of the reference electron leading to a given cell is found, we can calculate the phase difference ΔS associated with this cell.

Instead of dividing the (p_x, p_y) plane into cells, interpolation on the nonuniform grid can be applied to find the value of S^{sig} for any given momentum $\vec{p}$. However, for the laser-atom parameters used in this paper, the results of such interpolation converge slowly with increasing number of sets $(t_0^{\mathrm{sig}},\theta_0)$.
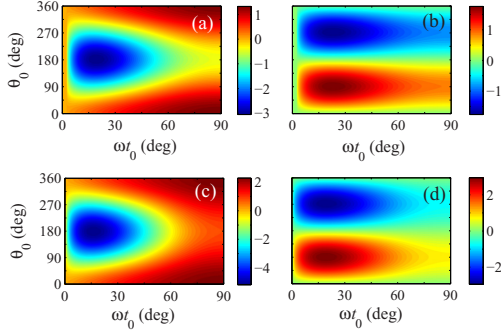
FIG. 1. Asymptotic electron momentum components as functions of the ionization time and the instantaneous scattering angle for the H atom ionized by the first quarter of a cosinelike field with a wavelength of 800 nm (Ti:sapphire laser) polarized along the x axis. The left column, that is, panels (a) and (c), shows the p_x component. The right column [panels (b) and (d)] shows the p_y component. Panels (a, b) and (c, d) correspond to the intensities of 2.0 and 6.0×10^{14} W/cm^2, respectively.
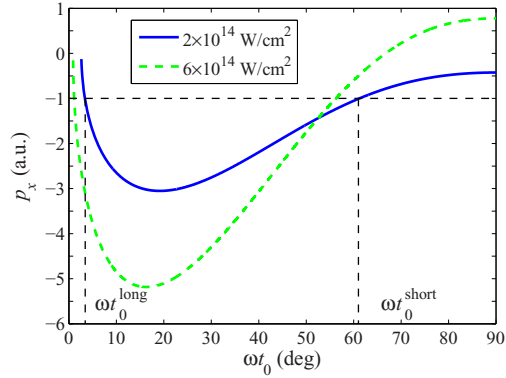

FIG. 2. The p_x component of the asymptotic electron momentum as a function of ionization time for the scattering angle $\theta_0 = 180°$ (backward scattering). The parameters are as in Fig. 1. The blue (solid) and green (dashed) curves correspond to the intensities of 2.0 and 6.0×10^{14} W/cm^2, respectively.

Moreover, before convergence is achieved, the interferometric structures calculated within this approach show some spurious structures, which could be confused with the true interference patterns. For this reason, we use bins on the (p_x, p_y) plane when implementing the second approach with t_0^{sig} and θ_0 being the independent variables. We have used both approaches to check the consistency. The results obtained within both methods are in agreement.

Four major different types of interference structures are usually discussed (see Ref. [43]). Two of these types correspond to forward scattering of a signal electron, whereas two other types involve its backward scattering. Nevertheless, in all these four types the signal electron starts from the first quarter of the laser period $0 \leqslant \omega t_0 \leqslant 90°$. Therefore, we start our analysis with the kinematics of the signal electron launched in the first quarter of the cycle.

B. Interference structures for the time-independent exit point

Let us first consider the simplest case that is usually assumed when the three-step model is used to calculate holographic interference patterns [43–46]: the tunnel exit is equal for all ionization times and it is determined by the amplitude of the laser field: $x_0 = I_p/F_0$. Figure 1 shows the asymptotic momentum components of such a signal electron as functions of the start time and instantaneous scattering angle for ionization of the H atom at a wavelength of 800 nm and two laser intensities: 2×10^{14} and 6×10^{14} W/cm^2. For most values of the scattering angle θ_0, the p_x component of the asymptotic momentum has a minimum as a function of ωt_0. This minimum (maximum of the absolute value) is particularly pronounced for the backward scattered electrons: $90 \leqslant \theta_0 \leqslant 270°$. Nevertheless, it may also exist for forward scattered electrons, i.e., for $0 \leqslant \theta_0 < 90°$ (or $270 < \theta_0 \leqslant 360°$). The presence of this minimum implies that for some values of the final momentum $\vec{p}$ there are two

different ionization times corresponding to this angle θ_0^* [see Fig. 2 where the cuts of Figs. 1(a) and 1(b) at $\theta_0 = 180°$ are shown]. These two ionization times correspond to different electron trajectories. Depending on whether the signal electron is ionized before the minimum or after it, we refer to the corresponding trajectory as a long or short one. Therefore, it is necessary to distinguish the interference structures created by reference and long signal trajectories from those produced by reference and short signal trajectories. This issue was also discussed in Ref. [46].

The first and widely discussed type of the holographic interference emerges when both reference and signal electrons are launched in the first quarter of the optical cycle [see Fig. 3(a)]. For brevity, we refer to this kind of interference as type A. Usually it is also assumed that the signal electron is scattered forward. The interference pattern of the second kind [type B, Fig. 3(b)] is produced when the signal electron is launched on the first quarter of the cycle, whereas the reference electron is generated in the second quarter. The interference structures [i.e., $\cos(\Delta S)$, where ΔS is given by Eq. (11)] of types A and B are shown in Figs. 3(c) and 3(d). For the cosinelike field discussed here they emerge in the half plane $p_x > 0$. In contrast to Refs. [43–46], we do not restrict our consideration to forward scattered electrons only. Instead, we allow for all instantaneous scattering angles θ_0. The short and long signal trajectories should be separated in calculations. The averaging over the phase differences that correspond to the long and short trajectories ending up at a given $\vec{p}$ leads to the results shown in Figs. 3(e) and 3(f): the false substructures are clearly visible on the edges of the interference patterns. In contrast to this, Figs. 3(c) and 3(d) were obtained by considering only the long trajectories for the momenta at the edges of the structure.

When the reference electron is launched in the third quarter of the cycle, we refer to the corresponding structure as interference type C. In the case when the reference trajectory starts in the fourth quarter, we classify the interference structure as type
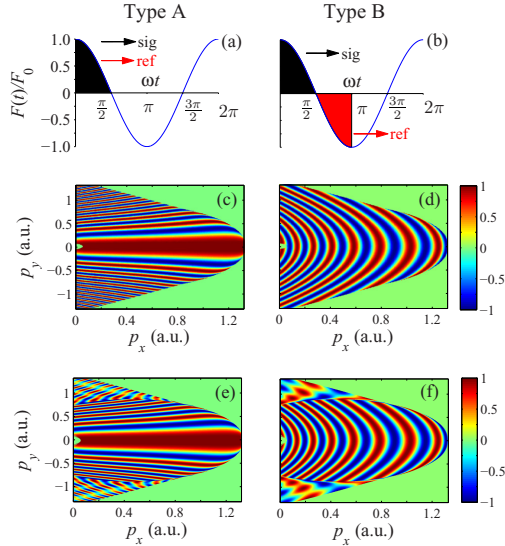
FIG. 3. Forward scattering holographic interference patterns calculated within the three-step model for ionization of the H atom by the laser field with a wavelength of 800 nm and intensity of 2.0×10^{14} W/cm^2. Panels (a) and (b) illustrate formation of the interferences of types A and B, respectively. Panels (c) and (d) present the interference structure of types A and B, respectively. The same structures calculated without separation of different forward scattered signal trajectories leading to the same final momenta are shown in panels (e) and (f), respectively.
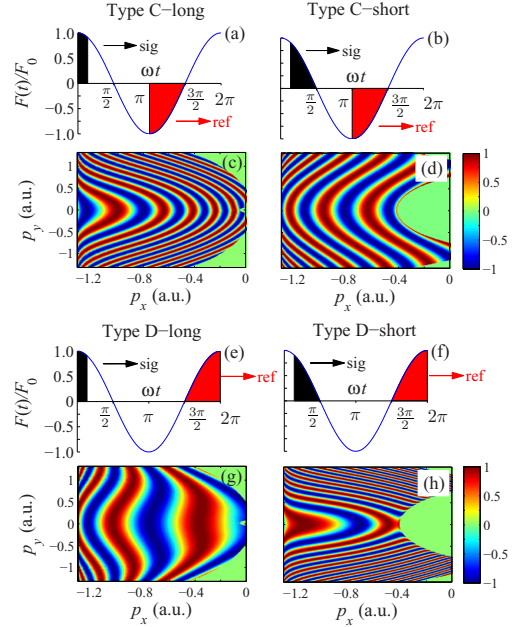

FIG. 4. Backward scattering holographic interferences predicted by the three-step model. Panels (a), (b), (e), and (f) show schematic illustration of the structures of types C-long, C-short, D-long, and D-short, respectively. Panels (c), (d), (g), and (h) present the corresponding interference patterns. The parameters are as in Fig. 3.

D. In order to distinguish between the patterns created by long and short signal trajectories, we add the word "long" or "short." Thus we consider the following types of holographic patterns: C-long, C-short, D-long, and D-short [see Figs. 4(a), 4(b) 4(e), and 4(f), respectively]. The corresponding interference structures calculated at the intensity of 2.0×10^{14} W/cm^2 are shown in Figs. 4(c), 4(d), 4(g), and 4(h). Note that, in contrast to Refs. [43–46], when calculating the structures of types C-long and D-long we do not restrict ourselves to backward scattered electrons only, i.e., we assume $0 \leqslant \theta_0 \leqslant 360°$. However, only the backward scattered electrons are taken into account in calculations of the patterns of types C-short and D-short. This is due to the fact that the interference of the short forward scattered electrons with the reference ones results in a different kind of interference structure emerging in a small part of the (p_x, p_y) plane. This structure is outside of the scope of the present paper.

Special attention must be given to the area of the (p_x, p_y) plane in Figs. 4(d) and 4(h), where the interference structure is absent. The vanishing of the interference structure occurs due to the fact that not all the values of the p_x component can be reached by short trajectories [see Figs. 1(a) and 1(b)]. This effect is particularly pronounced at lower intensities and disappears with increasing field strength. Interference structures of all six types discussed here are shown in Fig. 5 at the

higher intensity 6.0×10^{14} W/cm^2. With increasing intensity the interference stripes become narrower and their number increases dramatically. At this higher intensity the holographic structures of types C-short and D-short fill the half of the plane $-F_0/\omega < p_x < 0$ completely.

C. Interferometric structures for the time-dependent exit point

Next, we analyze the interference structures calculated assuming that the starting point of the trajectory depends on time $x_0(t) = -I_p/F(t)$. First, we recalculate p_x and p_y components as functions of ωt_0^{sig} and θ_0 [see Figs. 6(a) and 6(b)]. The results differ dramatically from the case of constant x_0 [cf. Figs. 1(c) and 1(d)]. Indeed, the function $p_x = p_x(\omega t_0, \theta_0)$ has now two minima. Accordingly, the p_y component has two maxima for $0 \leqslant \theta_0 \leqslant 180°$ and two minima for $180 \leqslant \theta_0 \leqslant 360°$. The second extremum of p_x and p_y in the vicinity of $\omega t_0 = 90°$ gives rise to another kind of interference structures. Here we do not consider this second extremum and, therefore, account only for the electrons launched at $\omega t_0 \leqslant 67°$.

The corresponding interference patterns are shown in Figs. 7(a)–7(f). It is seen that the structures of types A and B occupy a larger area on the (p_x, p_y) plane compared to those shown in Figs. 5(a) and 5(b). The caustics that are hardly visible in Fig. 7(a) and better seen in Fig. 7(b) arise due to the discontinuity of the $\omega t_0(p_x, p_y)$ found from Eq. (3) for x_0
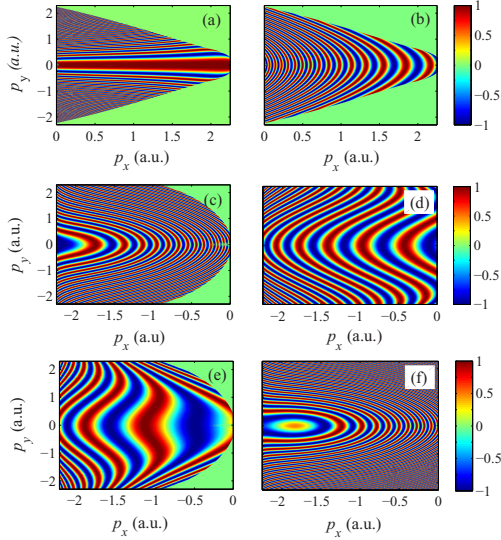
FIG. 5. Holographic interference patterns obtained from the three-step model for ionization of H by a Ti:sapphire laser (800 nm) at the intensity 6.0×10^{14} W/cm^2. Panels (a), (b), (c), (d), (e), and (f) show the interference structures of types A, B, C-long, C-short, D-long, and D-short, respectively.

depending on t_0. The time-dependent exit point leads to the decrease of the area occupied by the interference structures of types C-short and D-short [see Figs. 7(d) and 7(f)]. In this respect, the account for the time dependence in the expression for the exit point has a similar effect as the decrease of the laser intensity. This result is expected, because the maximum value F_0 of the laser field $F(t)$ was used when calculating Fig. 1 with fixed x_0.

III. CALCULATION OF THE HOLOGRAPHIC INTERFERENCE PATTERNS WITH COULOMB POTENTIAL

In order to calculate the holographic interference patterns in the presence of the Coulomb field, we use an adapted version of the SCTS model. Here we sketch the main points of our approach focusing on the differences in the implementation
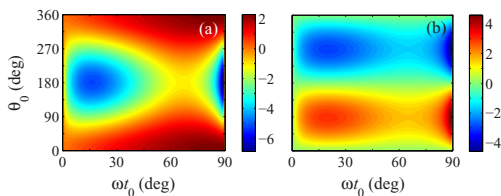

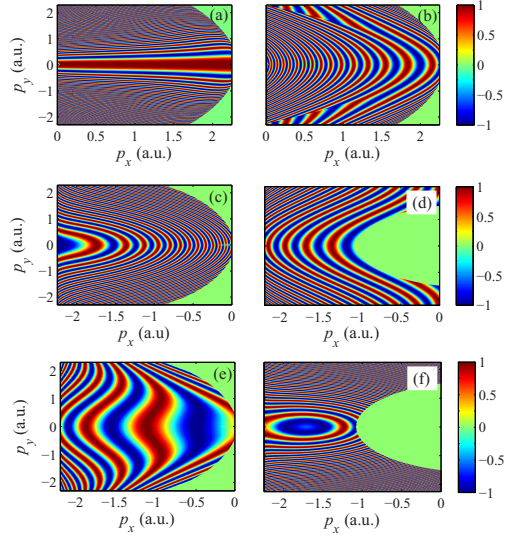FIG. 6. Same as Fig. 1 for the time-dependent exit point and intensity 6.0×10^{14} W/cm^2.

FIG. 7. Same as Fig. 5 for the time-dependent exit point.

compared to Ref. [56]. As in any semiclassical approach, the trajectory $\vec{r}(t)$ and momentum $\vec{p}(t)$ of an electron in the SCTS model are calculated using Newton's equation of motion:

$$\frac{d^2\vec{r}}{dt^2} = -\vec{F}(t) - \frac{Z\vec{r}(t)}{r^3(t)}, \tag{13}$$

where Z is the ionic charge ($Z = 1$ for the H atom). In our simulations we solve Eq. (13) for the electrons launched on the central period of the Ti:sapphire laser pulse (800 nm) with the full duration of eight optical cycles. In order to integrate Eq. (13), we need to specify initial conditions, i.e., the initial velocity and position. To this end, one could use the separation of the static tunneling problem in parabolic coordinates [13,58,59]. However, in the present paper we use the simplest formula for the tunnel exit neglecting the Coulomb potential: $x_0 = -I_p/F(t_0)$ to allow for direct comparison with the results of the three-step model.

We assume that the electron starts with zero initial velocity along the laser polarization $v_x(t_0) = 0$ and nonzero initial velocity $v_{0,\perp}$ in the transverse direction. The SCTS considers an ensemble of classical trajectories with different t_0 and $v_{0,\perp}$. Since in this paper we are interested in the holographic interference structures rather than in calculation of the momentum distributions, we disregard trajectory weights and distribute the trajectories uniformly.

Following the SCTS model we associate every trajectory with the phase of the semiclassical propagator (see Refs. [60–62]). For the Coulomb potential this phase is given by

$$\Phi(t_0, \vec{v}_0) = -\vec{v}_0 \cdot \vec{r}(t_0) + I_p t_0 - \int_{t_0}^{\infty} dt \left\{ \frac{p^2(t)}{2} - \frac{2Z}{r(t)} \right\} \tag{14}$$
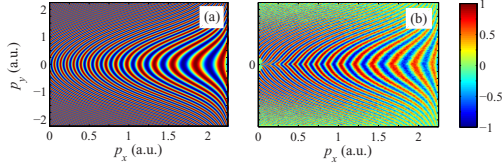
FIG. 8. Interference pattern for intracycle interference obtained (a) from the three-step model and (b) in the presence of the Coulomb potential. The parameters are as in Fig. 5.

(see Ref. [56]). Once the asymptotic momenta of all the trajectories in the ensemble are found, we bin them in cells in momentum space. Finally, the amplitudes $\exp[i\Phi(t_0^j, \vec{v}_0^j)]$ with $j = 1, \ldots, n_p$ associated with all n_p trajectories ending up in a given bin located at $\vec{p} = (p_x, p_y)$ can be added coherently. However, it is easy to see that the quantity

$$Q = \left| \sum_{j=1}^{n_p} \exp\left[i\Phi\left(t_0^j, \vec{v}_0^j\right)\right] \right|^2, \tag{15}$$

which is similar to the ionization probability calculated according to the importance sampling implementation of the SCTS model, is not sufficient to obtain the phase difference between signal and reference electrons we are interested in. Indeed, for calculation of interference patterns similar to those shown in Figs. 3, 4, 5, and 7, we have to isolate *only one* kind of rescattered and *only one* kind of direct trajectories. In the presence of the Coulomb field this is not an easy task. Nevertheless, this objective can be accomplished by careful choice of initial conditions, i.e., of t_0 and $v_{0,\perp}$.

Once the necessary isolation of different kinds of trajectories is achieved, in any bin of the momentum space we have N trajectories of one kind with phases Φ_0^i ($i = 1, \ldots, N$) and M trajectories of another kind with phases Φ_1^k ($k = 1, \ldots, M$). Then we calculate the average cosine of the phase difference $\langle \cos(\Phi_0 - \Phi_1) \rangle$ in every bin of the momentum plane.

IV. STRONG-FIELD PHOTOELECTRON HOLOGRAPHY WITH THE COULOMB POTENTIAL

We begin our analysis of effects of the Coulomb potential with the intracycle interference, i.e., the interference of reference (direct) electrons starting from two different quarters of the laser period (see, e.g., Refs. [63–66] and [43,49]). This type of interference does not belong to the category of holography as it does not require rescattering. For this reason it is not shown in Figs. 3–5. The corresponding interference patterns produced by the reference electrons launched on the first and on the second quarter of the period calculated within the three-step model and with the account for the Coulomb field are shown in Figs. 8(a) and 8(b), respectively. It is apparent that the Coulomb field creates characteristic kinks in the vicinity of $p_y = 0$. The interference pattern of Fig. 8(b) is similar to the structures that are seen in the momentum distributions calculated in Ref. [49].

To understand the formation of the interference patterns in the presence of the Coulomb field, one must note that the reference trajectories are considered to be those that pass the

core at large distances and undergo small-angle scattering, whereas the signal trajectories are those that pass the parent ion at small distances and undergo large-angle scattering causing a sign change of the momentum in the y direction. Therefore, it appears natural to consider the electrons obeying the condition $v_{0,\perp}\, p_y \geqslant 0$ as reference electrons and to use only these when calculating the intracycle interference structure shown in Fig. 8(b). However, this restriction is not sufficient to calculate interference patterns properly. The reason is the nontrivial dependence of the final electron momentum on the initial conditions in the presence of the Coulomb field. Indeed, the calculation of the p_y component as a function of t_0 and $v_{0,\perp}$ shows that for each time of start t_0 there is a smallest positive initial transverse velocity $v_{0,\perp}^+(t_0)$ [largest negative $v_{0,\perp}^-(t_0)$] leading to $p_y \geqslant 0$ [$p_y \leqslant 0$]. This implies that $p_y \geqslant 0$ [$p_y \leqslant 0$] for any $v_{0,\perp} > v_{0,\perp}^+(t_0)$ [$v_{0,\perp} < v_{0,\perp}^-(t_0)$]. Moreover, for certain ranges of ionization time t_0, the y component of the final momentum is not a sign-constant function over the intervals $v_{0,\perp}^-(t_0) < v_{0,\perp} \leqslant v_{0,\perp}^+(t_0)$. As a result, some trajectories launched with $0 < v_{0,\perp} \leqslant v_{0,\perp}^+(t_0)$ [$0 > v_{0,\perp} \geqslant v_{0,\perp}^-(t_0)$] are detected with $p_y \geqslant 0$ [$p_y < 0$]. These trajectories interfere with those starting from another quarter of the cycle with $v_{0,\perp} > v_{0,\perp}^+(t_0)$ [$v_{0,\perp} < v_{0,\perp}^-(t_0)$] and, therefore, create an additional interference pattern in some part of the (p_x, p_y) plane. This pattern should not be mixed with the main one created solely by the electrons with $v_{0,\perp} > v_{0,\perp}^+(t_0)$ [$v_{0,\perp} < v_{0,\perp}^-(t_0)$]. Accordingly, from this point on we exclude the reference trajectories not obeying the condition $v_{0,\perp} > v_{0,\perp}^+(t_0)$ [$v_{0,\perp} < v_{0,\perp}^-(t_0)$].

Another significant point is that the first quarter of the laser cycle alone is no longer sufficient to produce the whole interference pattern when the Coulomb field is taken into account. The interference structure shown in Fig. 8(b) was calculated by considering the range of ionization times ωt_0 between -10 and $90°$. This shift of the left boundary compared to the case of the three-step model is caused by the change of the final electron momentum due to the Coulomb potential. The magnitude of this shift can be easily estimated by treating the Coulomb field as a perturbation. Its contribution to the asymptotic momentum is calculated by integrating the Coulomb force along the trajectory governed by the laser field only [53,67]. For not very large transverse velocities $v_{0,\perp} < \sqrt{2I_p}$ the corresponding integral can be evaluated analytically. As a result, for the cosinelike field $\vec{F}(t) = F_0 \cos(\omega t)\vec{e}_x$ the x component of the final momentum $\vec{p}$ can be estimated as (see Ref. [67] for details)

$$p_x \approx \frac{F_0}{\omega}\sin(\omega t_0) + \pi\frac{F_0\cos(\omega t_0)}{(2I_p)^{3/2}}. \tag{16}$$

It is easy to see that Eq. (16) can be rewritten as

$$p_x \approx F_0\sqrt{\frac{1}{\omega^2} + \frac{\pi^2}{(2I_p)^3}}\cos(\omega t_0 - \alpha), \tag{17}$$

where

$$\alpha = \arctan\left[\frac{(2I_p)^{3/2}}{\omega\pi}\right]. \tag{18}$$

The left edge of the intracycle interference structure in the three-step model is located at $p_x = 0$ [see Fig. 3(a)], corresponding to $\omega t_0 = 0$. In the presence of the Coulomb potential, it follows from Eq. (17) that for p_x to be equal to zero $\omega t_0 = \alpha + \frac{\pi}{2} + \pi k$, where k is an integer number. Therefore, the ionization time closest to $\omega t_0 = 0$ that leads to $p_x = 0$ is estimated as

$$\omega t_0^\star \approx -\frac{\pi}{2} + \arctan\left[\frac{(2I_p)^{3/2}}{\omega\pi}\right] = -\operatorname{arccot}\left[\frac{(2I_p)^{3/2}}{\omega\pi}\right]. \tag{19}$$

For the parameters of Fig. 8 this estimate yields $\omega t_0^\star = -10.2°$. Note that Eq. (19) does not depend on the field strength. More accurate expressions for the asymptotic momentum of a direct electron moving in laser and Coulomb fields were obtained recently [68,69]. Furthermore, analytical estimates for the final momenta of different kinds of rescattered electrons were also derived in Refs. [68,69]. However, the simple formula (16) is sufficient to understand the formation of the holographic interference patterns. Note that the vast majority of the reference trajectories starting in the vicinity of $\omega t_0 = \frac{\pi}{2}$ are only weakly affected by the Coulomb field. For this reason, we do not shift the right boundary of the first quarter (the left boundary of the second quarter) of the cycle.

In the three-step model, the interference structure of type A corresponds to the situation when both signal and reference electrons are launched within the first quarter of the laser period. In contrast to type A, the structure of type B is created by the signal electrons launched on the first quarter of the cycle and the reference trajectories starting on the second quarter. When the Coulomb field is taken into account, the signal trajectories must obey the condition $v_{0,\perp} p_y < 0$. Furthermore, the x component of the final momentum must be positive, since the interference patterns of type A and B emerge in the half plane $p_x > 0$. However, these conditions are not sufficient to produce the proper interference pattern (similarly to the case of the intracycle interference). The reason is that the mapping from the $(t_0, v_{0,\perp})$ plane to the (p_x, p_y) plane is not a one-to-one function in the domain where the condition for the signal trajectories $v_{0,\perp} p_y < 0$ is fulfilled. Different initial conditions $(t_0, v_{0,\perp})$ can lead to the same final momentum $\vec{p}$. As the result, several different interference patterns can emerge in the same area of the (p_x, p_y) plane. These patterns must be separated. Note that already in the three-step model it is necessary to restrict the initial conditions in order to ensure a one-to-one mapping to the final momentum and, hence, to separate different interference patterns emerging for the same final momenta $\vec{p}$. Within the three-step model this restriction is achieved by considering different quarters of the optical cycle (see Sec. II B).

In order to separate different interference patterns in the presence of the Coulomb field, we identify the domains of initial conditions, where the mapping $(t_0, v_{0,\perp}) \to (p_x, p_y)$ is a one-to-one function. As a result, we find that interference patterns similar to those obtained within the three-step model also emerge when the Coulomb field is taken into account. Figures 9(a) and 9(b) show the x and y components of the final electron momentum as functions of t_0 and $v_{0,\perp} \geqslant 0$, respectively. The domain of the $(t_0, v_{0,\perp})$ plane that gives rise
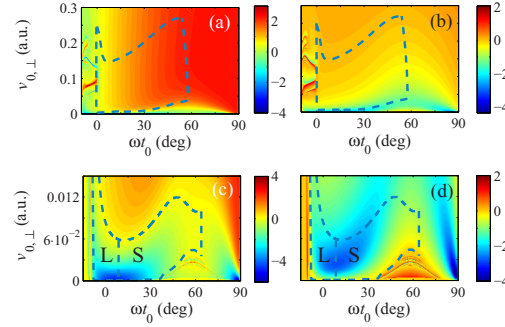

FIG. 9. Asymptotic electron momentum components as functions of the ionization time and the initial transverse velocity calculated in the presence of the Coulomb potential. The parameters are as in Fig. 5. Panels (a) and (c) show the p_x component. Panels (b) and (d) display the p_y component. The blue (dashed) curves in panels (a) and (b) show the boundary of the domain that gives rise to the signal electrons responsible for the lower half ($p_y < 0$) of the interference patterns of types A and B. The letters "L" and "R" in panels (c) and (d) mark the domains responsible for the long and short signal trajectories, respectively. The boundaries of these domains are indicated by blue (dashed) curves.

to the relevant interference patterns similar to the one predicted by the three-step model is shown by the blue (dashed) curves in Figs. 9(a) and 9(b). The corresponding interference patterns of types A and B at the intensity of 6.0×10^{14} W/cm^2 are shown Figs. 10(a) and 10(b). It is apparent that the Coulomb potential changes the interference structure substantially. This is true for the positions of the interference maxima and minima, as well as for their spacing. For type B the interference stripes show kinks at $p_y = 0$, similar as in intracycle interference, Fig. 8(b), but pointing in the opposite direction.

To obtain the interference structures of types C and D, we calculate the interference of the signal electrons with $v_{0,\perp} p_y < 0$ starting from the first quarter with the reference electrons starting from the third or the fourth quarter of the cycle. The interference patterns of types C and D correspond to negative p_x.

The x and y components of the final electron momentum as functions of $\omega t_0 \in [-10°, 90°]$ and small positive $v_{0,\perp}$ are shown in Figs. 9(c) and 9(d). It is seen that both p_x and p_y components have two pronounced minima as in the case of the electron motion in the laser field only. The second minimum close to $\omega t_0 = 90°$ is due to the time-dependent exit point [see Fig. 6]. Here we again consider only the left minimum of p_x and p_y. The position of this minimum weakly depends on the initial transverse velocity. For the parameters considered the minimum is achieved at $\omega t_0 \approx 18.3°$. Thus, by analogy with the electron kinematics within the three-step model, we can again distinguish between long and short signal trajectories. The corresponding domains on the $(t_0, v_{0,\perp})$ plane are marked in Figs. 9(c) and 9(d) by the letters "L" and "R", respectively. The boundaries of these domains are shown by blue (dashed) curves. With signal trajectories from these domains, we calculate interferences of types C-long,
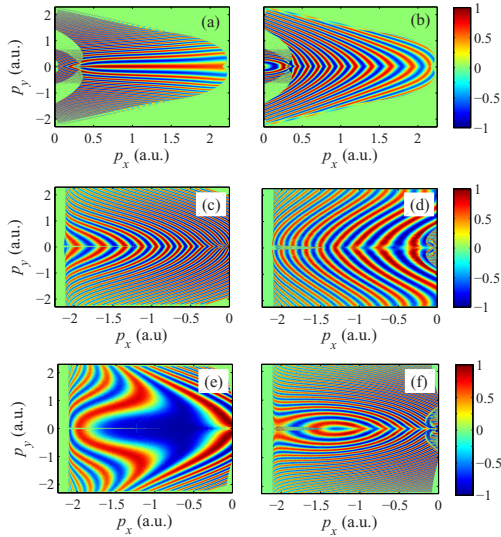
FIG. 10. Holographic interference patterns of types A (a), B (b), C-long (c), C-short (d), D-long (e), and D-short (f) in the presence of the Coulomb potential. The parameters are as in Fig. 5.

parameters under investigation, the corresponding interference structures are almost identical to those presented here.

V. CONCLUSIONS

In conclusion, we have investigated subcycle interference structures emerging in strong-field photoelectron holography using semiclassical approaches. First, we have calculated these structures within the three-step model. Following Ref. [43] we assumed initially that all classical electron trajectories start at the same point, which is determined as the tunnel exit at the maximum of the field. We found it important to distinguish between long and short rescattered trajectories when calculating the interference structures involving backscattering. This is in agreement with the conclusion of Ref. [46].

We have found that the interference structures change significantly when the time dependence of the tunnel exit is taken into account. Specifically, some interference patterns expand, whereas others may shrink compared to those calculated with the time-independent exit point. This is due to the substantial change in kinematics of the signal electron.

In order to calculate the interference patterns in the presence of the Coulomb potential, we have developed a computational approach based on the SCTS model, which describes quantum interference including the Coulomb potential beyond the semiclassical perturbation theory. We have identified the specific groups of trajectories responsible for each kind of holographic structure. Finally, for every type of interference structure predicted by the three-step model we have presented its counterpart emerging in the presence of the Coulomb potential. In addition to changing the positions and the widths of the interference stripes, the Coulomb potential can manifest itself in three other effects. These are the shift of the interference pattern as a whole, the filling of the parts of the interference structure that are missing when the Coulomb potential is neglected, and the characteristic kink of the interference stripes at zero transverse momentum. In measurable momentum distributions, several of the interference structures will usually be overlaid on top of each other. Furthermore, it remains to be studied which of the holographic structures are less vulnerable to focal averaging and thus more visible under experimental observation. Therefore, future work is needed to shed light on the question of which of the Coulomb effects are observable in momentum distributions.

C-short, D-long, and D-short. As for the reference electrons, we proceed similarly to the cases of the intracycle interference and types A and B. Note that we shift the left boundary of the third quarter of the cycle by $10.2°$ to earlier times when calculating the structure of type C. The results are presented in Figs. 10(c)–10(f). The patterns shown here should be compared with those presented in Figs. 7(c)–7(f). It is seen that the Coulomb potential has three main effects on the interference patterns. First, it shifts the interference pattern as a whole. Second, it fills the parts of the interference structures that are absent when the Coulomb field is neglected. Third, the presence of the Coulomb potential results in the characteristic kinks of the interference stripes at $p_y = 0$. We attribute these kinks to the Coulomb focusing effect (see Ref. [70]).

Finally, we have checked the sensitivity of the results to changes in the exit point. To this end, we have recalculated the results shown using the expression for the tunnel exit that results from the separation of the time-independent Schrödinger equation in parabolic coordinates. For the

[1] J. Xu, C. I. Blaga, P. Agostini, and L. F. DiMauro, Time-resolved molecular imaging, J. Phys. B **49**, 112001 (2016).

[2] F. Krausz and M. Ivanov, Attosecond physics, Rev. Mod. Phys. **81**, 163 (2009).

[3] W. Becker, F. Grasbon, R. Kopold, D. B. Milošević, G. G. Paulus, and H. Walther, Above-threshold ionization: From classical features to quantum effects, Adv. At. Mol. Opt. Phys. **48**, 35 (2002).

[4] D. B. Milošević and F. Ehlotzky, Scattering and reaction processes in powerful laser fields, Adv. At. Mol. Opt. Phys. **49**, 373 (2003).

[5] A. Becker and F. H. M. Faisal, Intense field many-body S-matrix theory, J. Phys. B **38**, R1 (2005).

[6] C. Figueira de Morisson Faria and X. Liu, Electron-electron correlation in strong laser fields, J. Mod. Opt. **58**, 1076 (2011).

N. I. SHVETSOV-SHILOVSKI AND M. LEIN   PHYSICAL REVIEW A **97**, 013411 (2018)

[7] H. G. Muller, An efficient propagation scheme for the time-dependent Schrödinger equation in the velocity gauge, Laser Phys. **9**, 138 (1999).

[8] D. Bauer and P. Koval, Qprop: A Schrödinger-solver for intense laser–atom interaction, Comput. Phys. Commun. **174**, 396 (2006).

[9] L. B. Madsen, L. A. A. Nikolopoulos, T. K. Kjeldsen, and J. Fernández, Extracting continuum information from $\Psi(t)$ in time-dependent wave-packet calculations, Phys. Rev. A **76**, 063407 (2007).

[10] L. V. Keldysh, Ionization in the field of a strong electromagnetic wave, Zh. Eksp. Teor. Fiz. 47, 1945 (1964) [Sov. Phys. JETP **20**, 1307 (1965)].

[11] F. H. M. Faisal, Multiple absorption of laser photons by atoms, J. Phys. B **6**, L89 (1973).

[12] H. R. Reiss, Effect of an intense electromagnetic field on a weakly bounded system, Phys. Rev. A **22**, 1786 (1980).

[13] L. D. Landau and E. M. Lifshitz, *Quantum Mechanics Non-relativistic Theory*, 2nd ed. (Pergamon Press, Oxford, 1965).

[14] A. M. Perelomov, V. S. Popov, and M. V. Terent'ev, Ionization of atoms in an alternating electric field, Zh. Eksp. Teor. Fiz. **50**, 1393 (1966) [Sov. Phys. JETP **23**, 924 (1966)].

[15] M. V. Ammosov, N. B. Delone, and V. P. Krainov, Tunnel ionization of complex atoms and of atomic ions in an alternating electromagnetic field, Zh. Eksp. Teor. Fiz. **91**, 2008 (1986) [Sov. Phys. JETP **64**, 1191 (1986)].

[16] H. B. van Linden, van den Heuvell, and H. G. Muller, in *Multiphoton Processes*, edited by S. J. Smith and P. L. Knight (Cambridge University Press, Cambridge, England, 1988).

[17] T. F. Gallagher, Above-Threshold Ionization in Low-Frequency Limit, Phys. Rev. Lett. **61**, 2304 (1988).

[18] P. B. Corkum, N. H. Burnett, and F. Brunel, Above-Threshold Ionization in the Long-Wavelength Limit, Phys. Rev. Lett. **62**, 1259 (1989).

[19] K. C. Kulander, K. J. Schafer, and J. L. Krause, in *Super-Intense Laser-Atom Physics*, edited by B. Pireaux, A. L'Hullier, and K. Rzazewski (Plenum, New York, 1993).

[20] P. B. Corkum, Plasma Perspective on Strong-Field Multiphoton Ionization, Phys. Rev. Lett. **71**, 1994 (1993).

[21] J. L. Krause, K. J. Schafer, and K. C. Kulander, High-Order Harmonic Generation from Atoms and Ions in the High Intensity Regime, Phys. Rev. Lett. **68**, 3535 (1992).

[22] A. Becker, R. Dörner, and R. Moshammer, Multiple fragmentation of atoms in femtosecond laser pulses, J. Phys. B **38**, S753 (2005).

[23] R. Kanya, Y. Morimoto, and K. Yamanouchi, Observation of Laser-Assisted Electron-Atom Scattering in Femtosecond Intense Laser Fields, Phys. Rev. Lett. **105**, 123202 (2010).

[24] Y. Morimoto, R. Kanya, and K. Yamanouchi, Laser-assisted electron diffraction for femtosecond molecular imaging, J. Chem. Phys. **140**, 064201 (2014).

[25] L. J. Frasinski, K. Codling, P. Hatherly, J. Barr, I. N. Ross, and W. T. Toner, Femtosecond Dynamics of Multielectron Dissociative Ionization by Use of a Picosecond Laser, Phys. Rev. Lett. **58**, 2424 (1987).

[26] C. Cornaggia, J. Lavancier, D. Normand, J. Morellec, P. Agostini, J. P. Chambaret, and A. Antonetti, Multielectron dissociative ionization of diatomic molecules in an intense femtosecond laser field, Phys. Rev. A **44**, 4499 (1991).

[27] J. H. Posthumus, L. J. Frasinski, A. J. Giles, and K. Codling, Dissociative ionization of molecules in intense laser fields: A method of predicting ion kinetic energies and appearance intensities, J. Phys. B **28**, L349 (1995).

[28] C. Cornaggia, M. Schmidt, and D. Normand, Laser-induced nuclear motions in the Coulomb explosion of $C_2H_2^+$ ions, Phys. Rev. A **51**, 1431 (1995).

[29] M. Lein, J. P. Marangos, and P. L. Knight, Electron diffraction in above-threshold ionization of molecules, Phys. Rev. A **66**, 051404 (2002).

[30] M. Meckel, D. Comtois, D. Zeidler, A. Staudte, D. Pavičić, H. C. Bandulet, H. Pépin, J. C. Kieffer, R. Dörner, D. M. Villeneuve, and P. B. Corkum, Laser-induced electron tunneling and diffraction, Science **320**, 1478 (2008).

[31] C. I. Blaga, J. Xu, A. D. DiChiara, E. Sistrunk, K. Zhang, P. Agostini, T. A. Miller, L. F. DiMauro, and C. D. Lin, Imaging ultrafast molecular dynamics with laser-induced electron diffraction, Nature (London) **483**, 194 (2012).

[32] M. G. Pullen, B. Wolter, A. T. Le, M. Baudisch, M. Hemmer, A. Senftleben, C. D. Schröter, J. Ullrich, R. Moshammer, C. D. Lin, and J. Biegert, Imaging an aligned polyatomic molecule with laser-induced electron diffraction, Nat. Commun. **6**, 7262 (2015).

[33] J. Itatani, J. Levesque, D. Zeidler, H. Niikura, H. Pépin, J. C. Kieffer, P. B. Corkum, and D. M. Villeneuve, Tomographic imaging of molecular orbitals, Nature (London) **432**, 867 (2004).

[34] S. Haessler, J. Caillat, W. Boutu, C. Giovanetti-Teixeira, T. Ruchon, T. Auguste, Z. Diveki, P. Breger, A. Maquet, B. Carrè, R. Taïeb, and P. Salières, Attosecond imaging of molecular electronic wavepackets, Nat. Phys. **6**, 200 (2010).

[35] Y. Huismans, A. Rouzée, A. Gijsbertsen, J. H. Jungmann, A. S. Smolkowska, P. S. W. M. Logman, F. Lépine, C. Cauchy, S. Zamith, T. Marchenko *et al.*, Time-resolved holography with photoelectrons, Science **331**, 61 (2011).

[36] D. Gabor, *Nobel Lectures, Physics 1971–1980* (World Scientific, Singapore, 1992).

[37] Y. Huismans, A. Gijsbertsen, A. S. Smolkowska, J. H. Jungmann, A. Rouzée, P. S. W. M. Logman, F. Lépine, C. Cauchy, S. Zamith, T. Marchenko *et al.*, Scaling Laws for Photoelectron Holography in the Midinfrared Wavelength Regime, Phys. Rev. Lett. **109**, 013002 (2012).

[38] T. Marchenko, Y. Huismans, K. J. Schafer, and M. J. J. Vrakking, Criteria for the observation of strong-field photoelectron holography, Phys. Rev. A **84**, 053427 (2011).

[39] D. D. Hickstein, P. Ranitovic, S. Witte, X.-M. Tong, Y. Huismans, P. Arpin, X. Zhou, K. E. Keister, C. W. Hogle, B. Zhang *et al.*, Direct Visualization of Laser-Driven Electron Multiple Scattering and Tunneling Distance in Strong-Field Ionization, Phys. Rev. Lett. **109**, 073004 (2012).

[40] M. Meckel, A. Staudte, S. Patchkovskii, D. M. Villeneuve, P. B. Corkum, R. Dörner, and M. Spanner, Signatures of the continuum electron phase in molecular strong-field photoelectron holography, Nat. Phys. **10**, 594 (2014).

[41] M. Haertelt, X.-B. Bian, M. Spanner, A. Staudte, and P. B. Corkum, Probing Molecular Dynamics by Laser-Induced Backscattering Holography, Phys. Rev. Lett. **116**, 133001 (2016).

[42] S. G. Walt, N. Bhargava Ram, M. Atala, N. I. Shvestov-Shilovski, A. von Conta, D. Baykusheva, M. Lein, and H. J.

Wörner, Dynamics of valence-shell electrons and nuclei probed by strong-field holography and rescattering, Nat. Commun. **8**, 15651 (2017).

[43] X.-B. Bian, Y. Huismans, O. Smirnova, K.-J. Yuan, M. J. J. Vrakking, and A. D. Bandrauk, Subcycle interference dynamics of time-resolved photoelectron holography with midinfrared laser pulses, Phys. Rev. A **84**, 043420 (2011).

[44] X-B. Bian and A. D. Bandrauk, Attosecond Time-Resolved Imaging of Molecular Structure by Photoelectron Holography, Phys. Rev. Lett. **108**, 263003 (2012).

[45] X.-B. Bian and A. D. Bandrauk, Orientation-dependent forward-backward photoelectron holography from asymmetric molecules, Phys. Rev. A **89**, 033423 (2014).

[46] M. Li, J. Yian, X. Sun, J. Yu, Q. Gong, and Y. Liu, Recollision-induced subcycle interference of molecules in strong laser fields, Phys. Rev. A **89**, 033425 (2014).

[47] M. Li, X. Sun, X. Xie, Y. Shao, Y. Deng, C. Wu, Q. Gong, and Y. Liu, Revealing backward rescattering photoelectron interference of molecules in strong infrared laser fields, Sci. Rep. **5**, 8519 (2015).

[48] X.-Y. Lai, S.-G. Yu, Y.-Y. Huang, L.-Q. Hua, C. Gong, W. Quan, C. Faria, and X.-J. Liu, Near-threshold photoelectron holography beyond the strong-field approximation, Phys. Rev. A **96**, 013414 (2017).

[49] A. S. Maxwell, A. Al-Jawahiry, T. Das, and C. Faria, Coulomb-corrected quantum interference in above-threshold ionization: Working towards multi-trajectory electron holography, Phys. Rev. A **96**, 023420 (2017).

[50] X. Y. Lai, C. Poli, H. Schomerus, and C. Faria, Influence of the Coulomb potential on above-threshold ionization: A quantum-orbit analysis beyond the strong-field approximation, Phys. Rev. A **92**, 043407 (2015).

[51] M. Bashkansky, P. H. Bucksbaum, and D. W. Schumacher, Asymmetries in Above-Threshold Ionization, Phys. Rev. Lett. **60**, 2458 (1988).

[52] G. G. Paulus, F. Grasbon, A. Dreischuh, H. Walther, R. Kopold, and W. Becker, Above-Threshold Ionization by an Elliptically Polarized Field: Interplay Between Electronic Quantum Trajectories, Phys. Rev. Lett. **84**, 3791 (2000).

[53] S. P. Goreslavski, G. G. Paulus, S. V. Popruzhenko, and N. I. Shvetsov-Shilovski, Coulomb Asymmetry in Above-Threshold Ionization, Phys. Rev. Lett. **93**, 233002 (2004).

[54] A. N. Pfeiffer, C. Cirelli, M. Smolarski, D. Dimitrovski, M. Abu-Samha, L. B. Madsen, and U. Keller, Attoclock reveals geometry for laser-induced tunneling, Nat. Phys. **8**, 76 (2012).

[55] N. I. Shvetsov-Shilovski, D. Dimitrovski, and L. B. Madsen, Ionization in elliptically polarized pulses: Multielectron polarization effects and asymmetry of photoelectron momentum distributions, Phys. Rev. A **85**, 023428 (2012).

[56] N. I. Shvetsov-Shilovski, M. Lein, L. B. Madsen, E. Räsänen, C. Lemell, J. Burgdörfer, D. G. Arbó, and K. Tőkési, Semiclassical two-step model for strong-field ionization, Phys. Rev. A **94**, 013415 (2016).

[57] G. G. Paulus, W. Becker, W. Nicklich, and H. Walther, Rescattering effects in above-threshold ionization: A classical model, J. Phys. B **27**, L703 (1994).

[58] C. Z. Bisgaard and L. B. Madsen, Tunneling ionization of atoms, Am. J. Phys. **72**, 249 (2004).

[59] D. Dimitrovski, C. P. J. Martiny, and L. B. Madsen, Strong-field ionization of polar molecules: Stark-shift-corrected strong-field approximation, Phys. Rev. A **82**, 053404 (2010).

[60] W. H. Miller, Classical-limit quantum mechanics and the theory of molecular collisions, Adv. Chem. Phys. **25**, 69 (1974).

[61] M. Walser and T. Brabec, Semiclassical path integral theory of strong-laser-field physics, J. Phys. B **36**, 3025 (2003).

[62] M. Spanner, Strong Field Tunnel Ionization by Real-Valued Classical Trajectories, Phys. Rev. Lett. **90**, 233005 (2003).

[63] G. F. Gribakin and M. Yu. Kuchiev, Multiphoton detachment of electrons from negative ions, Phys. Rev. A **55**, 3760 (1997).

[64] F. Lindner, M. G. Schätzel, H. Walther, A. Baltuška, E. Goulielmakis, F. Krausz, D. B. Milošević, D. Bauer, W. Becker, and G. G. Paulus, Attosecond Double-Slit Experiment, Phys. Rev. Lett. **95**, 040401 (2005).

[65] R. Gopal, K. Simeonidis, R. Moshammer, Th. Ergler, M. Dürr, M. Kurka, K.-U. Kühnel, S. Tschuch, C.-D. Schröter, D. Bauer, and J. Ullrich, Three-Dimensional Momentum Imaging of Electron Wave Packet Interference in Few-Cycle Laser Pulses, Phys. Rev. Lett. **103**, 053001 (2009).

[66] D. G. Arbó, K. L. Ishikawa, K. Schiessl, E. Persson, and J. Burgdörfer, Intracycle and intercycle interferences in above-threshold ionization: The time grating, Phys. Rev. A **81**, 021403(R) (2010).

[67] N. I. Shvetsov-Shilovski, S. P. Goreslavski, S. V. Popruzhenko, and W. Becker, Capture into Rydberg states and momentum distributions of ionized electrons, Laser Phys. **19**, 1550 (2009).

[68] W. Becker, S. P. Goreslavski, D. B. Milošević, and G. G. Paulus, Low-energy electron rescattering in laser-induced ionization, J. Phys. B **47**, 204022 (2014).

[69] S. A. Kelvich, W. Becker, and S. P. Goreslavski, Coulomb focusing and defocusing in above-threshold ionization spectra produced by strong mid-IR laser pulses, Phys. Rev. A **93**, 033411 (2016).

[70] T. Brabec, M. Yu. Ivanov, and P. B. Corkum, Coulomb focusing in intense field atomic processes, Phys. Rev. A **54**, R2551 (1996).

8.17   Deep learning for retrieval of the internuclear distance
PHYSICAL REVIEW A **105**, L021102 (2022)

Deep learning for retrieval of the internuclear distance in a molecule from interference patterns in photoelectron momentum distributions

N. I. Shvetsov-Shilovski [*] and M. Lein

Institut für Theoretische Physik, Leibniz Universität Hannover, 30167 Hannover, Germany

We use a convolutional neural network to retrieve the internuclear distance in the two-dimensional H_2^+ molecule ionized by a strong few-cycle laser pulse based on the photoelectron momentum distribution. We show that a neural network trained on a relatively small dataset consisting of a few thousand images can predict the internuclear distance with an absolute error less than 0.1 a.u. Deep learning allows us to retrieve more than one parameter from a given momentum distribution. Specifically, we used a convolutional neural network to retrieve both the internuclear distance and the laser intensity. We study the effect of focal averaging, and we find that the convolutional neural network trained using the focal averaged electron momentum distributions also shows a good performance in reconstructing the internuclear distance.

I. INTRODUCTION

Development of techniques aimed at visualization of electronic and molecular dynamics in real time will open new horizons in many branches of modern science and technology. Many different techniques for time-resolved molecular imaging have been proposed thus far (see Ref. [1] for a review). The emergence and availability of table-top intense femtosecond laser systems has led to several new time-resolved imaging techniques using the highly nonlinear phenomena originating from interaction of strong laser pulses with atoms and molecules (see, e.g., Refs. [2,3] for review of these phenomena and the whole field of strong-field physics). Examples are laser-assisted electron diffraction [4,5], laser induced Coulomb explosion imaging [6–9], high-order harmonic orbital tomography [10,11], laser-induced electron diffraction (LIED) [12–15], and strong-field photoelectron holography (SFPH) [16]. The two latter methods analyze momentum distributions of electrons from strong-field ionization. The recent experimental achievements in LIED and SFPH (see, e.g., Refs. [17,18]) suggest that future experiments will aim at extracting the information about nuclear motion in a molecule from electron momentum distributions.

The understanding of the outcomes of these forthcoming experiments requires thorough theoretical studies of the effects of nuclear motion on the photoelectron momentum distributions. Such theoretical studies are already on the way. For instance, it was shown in Ref. [17] that the different nuclear wave packet dynamics in hydrogen and deuterium molecules leads to a difference in bond length, which, in turn, transforms into a shift of the holographic fringe at certain electron momenta. Before analyzing the imprints of the nuclear motion in momentum distributions, it is useful to study the distributions for fixed nuclei with varying internuclear distance. In the present paper we address this problem using methods of

machine learning, which is "a subfield of Computer Science wherein machines learn to perform tasks for which they were not explicitly programed" [19].

Machine learning, and more specifically deep learning (see, e.g., Refs. [20,21] for textbook treatments), has been successfully applied to the prediction of the flux of high-order harmonics for different experimental parameters [22], the prediction of the ground-state energy of an electron in various two-dimensional (2D) confining potentials [23], and the reconstruction of the intensity and the carrier-envelope phase (CEP) of ultrashort laser pulses from 2D images, namely from frequency-resolved optical gating traces [24] and from dispersion scan traces [25]. Recently a deep neural network was also applied to develop an efficient numerical implementation of the trajectory-based Coulomb-corrected strong-field approximation (TCSFA) (see Refs. [26,27] for the foundations of the TCSFA method) [28]. In all these examples the application of machine learning allowed the avoidance of heavy computational costs that would be inevitable when solving these problems using traditional ways.

Very recently the convolutional neural networks (CNN) were used to predict high-order harmonic generation (HHG) spectra for model di- and triatomic molecules for randomly chosen parameters. The latter include laser intensity, internuclear distance, and orientation of the molecule [29]. Furthermore, it was shown in Ref. [29] that the CNN can be used for solving inverse problems: determination of molecular and laser parameters, as well as classification of molecules based on their HHG spectrum (or time-dependent dipole acceleration) alone. These problems are hard to solve by manually inspecting a variety of complex spectra. On the other hand, classification is one of the typical tasks of machine learning. A similar situation is found for the problem of the present work. In this paper we train a CNN to predict the internuclear distance in the 2D model H_2^+ molecule from a given photoelectron momentum distribution (PMD). Application of a CNN is not the only possible way to retrieve the internuclear distance from electron momentum distributions. This problem

can be also solved by directly comparing the given PMD with a precalculated set of momentum distributions corresponding to various internuclear distances. However, the direct comparison is not expected to perform well when used on momentum distributions that it has not explicitly trained for. Therefore, we focus on the CNN in this paper. Although the CNN will also face problems when tested on distributions it has not been trained for, it is of interest to address this question quantitatively.

The momentum distributions that are needed to train the CNN are calculated from the direct numerical solution of the time-dependent Schrödinger equation (TDSE). We show that a good accuracy of the predictions can be achieved even for relatively small sets of training data. We then study the effect of the focal averaging on the retrieval of the internuclear distance with the CNN.

II. MODEL

A. Solution of time-dependent Schrödinger equation

For the calculations we use a few-cycle linearly polarized laser pulse that is defined in terms of the vector-potential and present between $t = 0$ and $t_f = (2\pi/\omega)n_p$:

$$\vec{A}(t) = (-1)^{n_p} \frac{F_0}{\omega} \sin^2\left(\frac{\omega t}{2n_p}\right) \sin(\omega t + \varphi)\vec{e}_x. \quad (1)$$

Here $\vec{e}_x$ is a unit vector in the polarization direction (x axis), n_p is the number of optical cycles within the pulse, and φ is the CEP. The electric field is to be obtained from Eq. (1) as $\vec{F}(t) = -d\vec{A}/dt$. We do our simulations for $\varphi = 0$.

In the velocity gauge, the 2D TDSE for an electron interacting with the laser pulse is given by

$$i\frac{\partial}{\partial t}\Psi(x, y, t) = \left\{-\frac{1}{2}\left(\frac{\partial}{\partial x^2} + \frac{\partial}{\partial y^2}\right) - iA_x(t)\frac{\partial}{\partial x} + V(x, y)\right\}\Psi(x, y, t), \quad (2)$$

where $\Psi(x, y, t)$ is the coordinate-space wave function and $V(x, y)$ is the soft-core binding potential of the model H_2^+ molecular ion in the frozen nuclei approximation:

$$V(x, y) = -\frac{1}{\sqrt{(x - R/2)^2 + y^2 + a}} - \frac{1}{\sqrt{(x + R/2)^2 + y^2 + a}}. \quad (3)$$

Here, R is the internuclear distance and $a = 0.64$ is the soft-core parameter. We use the Feit-Fleck-Steiger split-operator method [30] to solve the TDSE Eq. (2). The ground-state wave function was obtained by imaginary time propagation. Our computational box was centered at ($x = 0, y = 0$) and extends over $x \in [-400, 400]$ a.u. and $y \in [-200, 200]$ a.u. We use equal grid spacings for x and y coordinates, $\Delta x = \Delta y = 0.1954$ a.u.

The wave function was propagated from the beginning of the laser pulse $t = 0$ to $t = 4t_f$ with the time step $\Delta t = 0.0184$ a.u. We apply absorbing boundaries to prevent unphysical reflections of the wave packet from the boundary of the computational grid, i.e., at every time step the wave function

is multiplied by the mask:

$$M(x, y) = \begin{cases} 1 & \text{for } r \leqslant r_b \\ \exp[-\beta(r - r_b)^2] & \text{for } r > r_b \end{cases}. \quad (4)$$

Here, $r = \sqrt{x^2 + y^2}$, $r_b = 150$ a.u. and $\beta = 10^{-4}$. We note that at the intensity of 4.0×10^{14} W/cm^2 and for the wavelength of 800 nm, the characteristic amplitude of the laser-induced electron quiver motion is $F_0/\omega^2 = 32.8$ a.u. Therefore, the position of the absorbing boundary r_b exceeds this value by a factor of 4.5. The photoelectron momentum distributions are calculated by using the mask method [12,31].

B. Architecture of convolutional neural network

The choice of architecture of a neural network should account for the structure of the data used for learning and the desired output. In our case the data used for learning are the pairs consisting of the PMD (image) and the corresponding internuclear distance R (label). Bearing in mind that the H_2^+ molecule is ionized by a laser field linearly polarized along the internuclear axis, we assume that every PMD has the aspect ratio 2 : 1. The details of the necessary image preprocessing are given in Sec. III. We train the neural network to solve the regression problem, i.e., to predict the internuclear distance R from a given PMD.

The deep neural network that we use for the problem at hand consists of five nonreducing convolutional layers, each followed by a reducing average pooling layer. Each of the nonreducing convolutional layers operates with 32 filters with sizes of 3×3 pixels. These convolution layers produce new images "feature maps" (see, e.g., Ref. [21]). The number of these new images equals the number of filters. The values of the filter matrices are to be determined through the training process, i.e., they play the same role as the trainable weights of an ordinary artificial neural network. After performing the convolution operation, all the convolutional layers apply the rectified linear unit (ReLU) activation function, which is defined as $\text{ReLU}(x) = \max(0, x)$. The average pooling layers divide the images they get into pooling regions with sizes of 2×2 pixels and calculate averaged values in every region. Therefore, each average pooling layer reduces the size of the image by a factor of 2. The last average pooling layer is connected to the dropout layer that randomly sets its input elements, i.e., output of the preceding layer, to zero with a certain probability. This probability is chosen to be equal to 0.2. The dropout layer allows us to avoid overfitting. The output of the dropout layer is fed to a fully connected layer that produces only one single value: the internuclear distance R. This is the output value of the whole neural network.

III. NUMERICAL EXPERIMENTS AND RESULTS

The photoelectron momentum distributions calculated from the solution of the TDSE (2) for three different internuclear distances are shown in Figs. 1(a), 1(c), and 1(e). It is seen that the shape of the distribution changes considerably with increasing R. However, the quantification of the corresponding changes in the PMDs is a nontrivial task. This makes application of neural networks particularly appropriate. In order to train the neural network, we first need to produce a
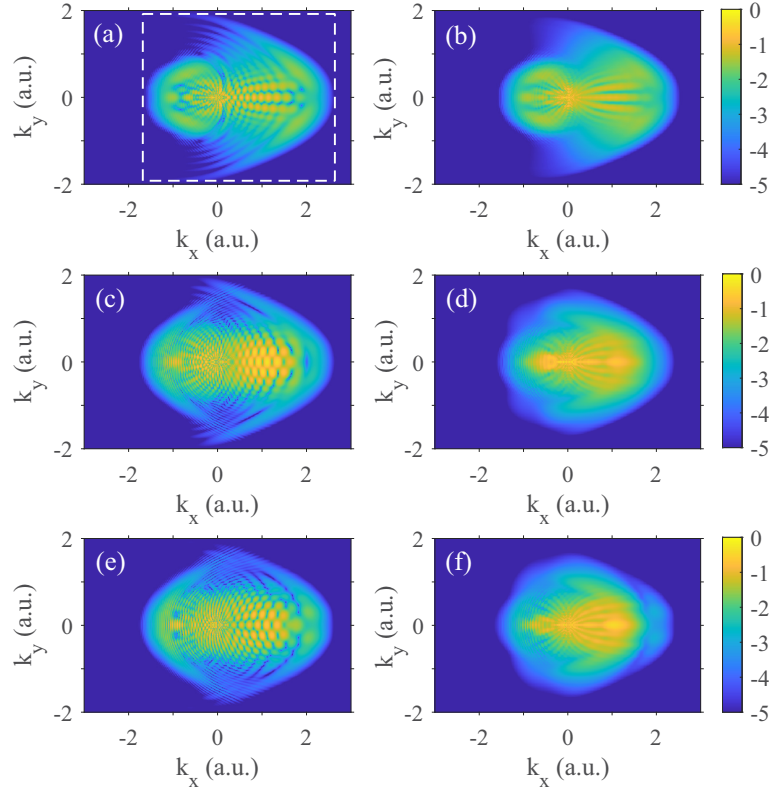
FIG. 1. Electron momentum distributions for ionization of the H_2^+ molecule by a laser pulse with a duration of $n_p = 2$ cycles and wavelength of $\lambda = 800$ nm obtained from numerical solution of the TDSE. (a), (b) correspond to the internuclear distance 2.0 a.u.; (c), (d) correspond to the internuclear distance 5.0 a.u.; (e), (f) correspond to the internuclear distance 6.0 a.u. The left column [(a), (c), and (e)] show the distributions calculated at fixed intensity of 4.0×10^{14} W/cm^2. The right column [(b), (d), and (f)] displays the distributions averaged over the focal volume for the same peak intensity of 4.0×10^{14} W/cm^2. The laser field is linearly polarized along the x axis. The distributions are normalized to the maximum value. Shown is the decimal logarithm of the distribution, see text.

set of training data. To this end, we solve the TDSE, Eq. (2), for N random internuclear distances $R_k \in [1.0, 8.0]$ a.u. and peak laser intensities $I_k \in [1.0, 4.0] \times 10^{14}$ W/cm^2, where $k = 1, ..., N$, and we calculate the corresponding electron momentum distributions. Since the solution of the 2D TDSE takes a few hours on four to eight modern cores working in parallel, the formation of a large training set is computationally expensive. Here we use $N = 3000$. About one week is needed to create such a data set using a computer cluster. We note that our data set is relatively small (compared with $N = 200000$ and $N = 30000$ used in Refs. [23] and [29], respectively). Nevertheless, for the problem at hand even such a modest data set allows us to obtain satisfactory results.

The PMD calculated from the solution of the TDSE is a matrix of size 4096×2048. The usage of matrices of such sizes as an input for a convolutional neural network will lead to a slow training process. For this reason, we first modify the matrix of the PMD as follows.

We find the absolute maximum PMD$_{max}$ of the distribution and calculate the decimal logarithm of the normalized PMD: $W = \log_{10}(\text{PMD}/\text{PMD}_{max})$. We set $W = -5$ for all values that are smaller than -5. We note that in doing so we consider not only the low-energy part of the distribution created by the electrons that do not experience hard recollisions with their parent ions, but also the beginning of the high-energy part of the PMD. This high-energy part is formed due to electrons that are driven back by the laser field to their parent ions and rescatter from them. Classically, the boundary between low- and high-energy parts of the PMD corresponds to the momentum $k = 2\sqrt{U_p}$, where U_p is the ponderomotive potential. For the parameters of Fig. 1, this estimate yields $k \approx 1.87$ a.u. Then we find a rectangular area such that the values of W at the boundary of the rectangle are just above -5. This rectangle is shown by the dashed lines in Fig. 1(a). The image within the rectangle is resized to 256×128 by using bicubic interpolation. Finally, all the elements of the matrix
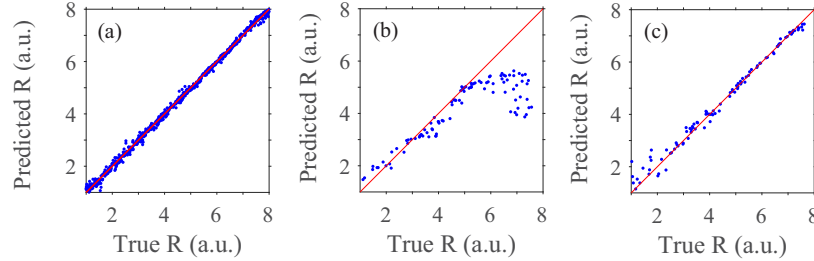
FIG. 2. Plot of predicted vs true internuclear distances illustrating the performance of neural networks. (a) Neural network trained on a set of distributions that were calculated with fixed laser intensities (not focal averaged), see text. (b) The same neural network as in (a), but receiving focal averaged momentum distributions as test images. (c) The neural network trained on a set of focal averaged distributions and tested on another independent set of focal averaged distributions.

are rescaled so that the minimum value corresponds to zero and the maximum one is mapped to 255. The resulting matrix of the size of 256×128 is used as an input for the CNN.

We split our data set into training and test sets in the ratio 0.75:0.25. Only data from the training set were used for training of the neural network. The goal of training is the minimization of the loss function, i.e., the measure of deviation (in our case the mean squared error) between predictions of the neural network and expected outcomes for the training set. The MATLAB package [32] is used for the calculations. The training of a neural network is performed on a modern PC using a graphic processing unit and takes only a few minutes. The prediction of the internuclear distance from one single image when the CNN is fully operational takes us about 0.024 sec on a PC. Therefore, the validation procedure for a test set consisting of 750 images requires only 18 sec.

The results of the application of the trained neural network to the test data are presented in Fig. 2(a). It is clearly seen that the neural network can successfully predict the internuclear distance. We characterize the quality of the neural network by the mean absolute error (MAE) between the predicted and true values of R over the test data set - a measure, which is different from the loss function (mean squared error) used in the training process. The neural network predicts the internuclear distance with the MAE of 0.07 a.u. We have found that another neural network that uses solely the low-energy part of the PMDs ($0 < k_x < \sqrt{2U_p}$, $|k_y| < \sqrt{U_p}$) shows slightly worse results: the corresponding MAE of R is equal to 0.12 a.u. This implies that the recognition of the internuclear distance with the neural network relies mostly on the interference patterns in the low-energy part of the momentum distributions, i.e., on the holographic patterns [16], but the accuracy can be enhanced by including high-energy electrons.

It is clear that the shape of the PMDs depends not only on R, but also on the laser parameters, especially on the intensity I. Deep learning allows us to retrieve more than one parameter from a given PMD. Using the same training data set, we have trained another CNN that is able to retrieve both the internuclear distance and the laser intensity. The MAEs provided by this neural network for R and I are equal to 0.07 a.u. and 0.05×10^{14} W/cm^2, respectively. It is seen that the error for R coincides with the one obtained using the very first neural network aimed at the retrieval of only the internuclear

distance. We therefore conclude that the ability of the CNN to retrieve both parameters does not affect the accuracy with which the internuclear distance is retrieved.

It is well-known that the intensity fluctuates in an experiment. This raises the question: How vulnerable is the performance of the trained neural network to the effect of focal averaging? To answer this question, we calculate a number of electron momentum distributions averaged over the focal volume and use them to test our neural network trained on the distributions obtained for *fixed* laser intensities. For a peak intensity I_0, the focal-volume averaged distribution $dP/d\vec{k}$ can be calculated as [35]

$$\frac{dP}{d^3k} = \int_0^{I_0} \frac{dP(I)}{d^3k}\left(-\frac{\partial V}{\partial I}\right)dI, \tag{5}$$

where $dP(I)/d^3k$ is the momentum distribution for a fixed intensity I, and $(\partial V/\partial I)dI$ is the focal volume element that corresponds to intensities between I and $I + dI$. We assume that the laser beam has Lorentzian spatial distribution of the intensity along the propagation direction and Gaussian intensity profile in the transverse direction (see, e.g., Refs. [3,33,34]). The focal volume element for such a beam is given by [35]:

$$\left(-\frac{\partial V}{\partial I}\right)dI \sim \frac{I_0}{I}\left(\frac{I_0}{I} + 2\right)\sqrt{\frac{I_0}{I} - 1}\,dI. \tag{6}$$

Obviously, the calculation of the focal-volume averaged distribution requires a number of TDSE solutions for different intensities $I < I_0$, and therefore is computationally demanding. For this reason, we calculate only $N_a = 100$ focal volume averaged PMDs for random internuclear distances $R_k \in [1.0, 8.0]$ a.u. and peak intensities $I_k \in [1.0, 4.0] \times 10^{14}$ W/cm^2 ($k = 1, ..., N_a$).

Figure 2(b) illustrates the performance of the neural network on this test set. We see that the performance of the CNN for the averaged PMDs is not as good as for the non-averaged PMDs. The MAE on this test set reaches the value of 0.83 a.u., which is still better than the value 1.4 a.u. that we find in an approach based on direct comparison with the training set. However, it is seen that the neural network works relatively well for PMDs that correspond to the internuclear distances less than 5.0 a.u. Indeed, the MAE calculated for the

focal-volume averaged PMDs with $R < 5.0$ a.u. is equal to 0.24 a.u. The unsatisfactory performance of the CNN for focal averaged PMDs with $R > 5.0$ a.u. can be understood from a close inspection of Figs. 1(a)–1(f). It is seen that the averaged distributions for $R = 5.0$ a.u. and $R = 6.0$ a.u. shown in Figs. 1(d) and 1(f), respectively, are similar to each other, especially in their low-energy parts, i.e., for $0 < k_x < \sqrt{2U_p}$ and $|k_y| < \sqrt{U_p}$. Simultaneously, these distributions are not too similar to their counterparts calculated for fixed laser intensity [cf. Figs. 1(c) and 1(d), as well as Figs. 1(e) and 1(f)]. In contrast to this, the averaged distributions corresponding to smaller values of R resemble the PMDs for same internuclear distances and fixed intensities [cf. Figs. 1(a) and 1(b)]. All this explains why the CNN trained with the distributions for fixed intensities underestimates large internuclear distances by treating them as $R \lesssim 5.0$ a.u. Aiming at a CNN that is able to map different PMDs (averaged and unaveraged) to the same R would indeed imply a non-bijective mapping.

In order to understand whether the internuclear distance can be reliably retrieved from the focal averaged momentum distributions using deep learning, we train another CNN. This second neural network has the same architecture as the first one, but it is trained on a set of averaged PMDs. A set of $N_a = 100$ distributions is too small to train a neural network. Therefore, the data set should be augmented. To this end, we apply 2D interpolation on an irregular grid (see, e.g., Ref. [36]) in the (R, I_0) plane formed by the N_a points. As a result, we produce a set of 6000 focal averaged electron momentum distributions and use them to train our new CNN. In order to have a test set independent of the initial N_a focal averaged momentum distributions, we produce another $N_a = 100$ of averaged PMDs for random internuclear distances and peak laser intensities using direct numerical solution of the TDSE and Eq. (5). We find that the CNN trained on the set of intensity averaged PMDs shows a rather good performance, see Fig. 2(c). It it also seen from Fig. 2(c) that the performance of the CNN is slightly worse for small internuclear distances as compared to larger values of R. We attribute this to the fact that the interpolation accuracy for the focal volume averaged momentum distributions is slightly worse for small internuclear distances. Nevertheless, the MAE on the independent test set is about 0.14 a.u. This result clearly shows that neural networks can be used to retrieve the unknown internuclear distance from a given electron momentum distribution even if the latter is affected by focal averaging.

When applied to a real experimental situation it would be desirable for a neural network to possess some transferability, i.e., to predict correct results even for PMDs obtained at parameters that are beyond the range of the training data. The neural networks trained here show only limited transferability. This is seen from the example of our first neural network trained on nonaveraged PMDs. The application of this neural network to a new set of PMDs obtained for internuclear distances $8.0 < R \leqslant 12.0$ a.u., i.e., outside of the training range $1.0 \leqslant R \leqslant 8.0$ a.u., leads to an MAE of 3.0 a.u. If our neural network is applied to images reflected about the vertical axis (corresponding to a change of the CEP by π), we find an MAE of 1.4 a.u. Slightly better results are achieved in the case where the neural network is applied to distributions obtained for a nonzero angles between the molecular axis and polarization

direction. The corresponding MAE is 0.9 a.u. We note that an approach based on the direct comparison of a given PMD with a precalculated set of the distributions shows worse results in terms of transferability. Here we find MAEs of 5.1, 1.6, and 1.4 a.u., respectively. The transferability problem of the neural network can be solved by the transfer learning technique (see, e.g., Ref. [37] for details). This approach was successfully used in Ref. [29]. The application of this technique to the retrieval of the internuclear distance will be a subject of further studies.

It should also be noted that the application of the neural network to the problem at hand is not without shortcomings. Since any neural network works as a "blackbox", i.e., it is not clear how the neural network takes its decisions, it is often difficult to assess whether it works properly for a given input image. On the other hand, the so-called visualization methods of deep neural networks that allow to explain the decisions of the CNNs are being actively developed nowadays (see, e.g., Ref. [38] for a review). Overall, there are reasons to believe that CNNs have a high potential for extracting various molecular properties from the electron momentum distributions produced by strong-field ionization.

IV. CONCLUSIONS AND OUTLOOK

In conclusion, we have investigated the capabilities of deep learning for retrieval of the internuclear distance in the H_2^+ molecule from a given 2D electron momentum distribution generated by a strong laser pulse. We have shown that the neural network trained on a few thousand images is able to predict the internuclear distance with a MAE less than 0.1 a.u. In addition to this, the CNN can be trained to retrieve more than one parameter from a given PMD. We have used the neural network to predict both the internuclear distance and the intensity of the laser pulse. Furthermore, we have studied the effect of focal averaging on the retrieval of the internuclear distance with a neural network. It is shown that the CNN trained on a set of focal averaged distributions also performs well.

The electron momentum distributions are sensitive not only to intensity fluctuations, but also to the changes of other laser parameters. For short laser pulses the variations of the CEP can change the resulting PMDs significantly. Therefore, the effect of the CEP on the retrieval of the internuclear distance needs to be studied. Moreover, it is of interest to look "inside" the CNN and analyze what features of the holographic structures allow the network to classify the images. This can be done by application of the visualization methods developed for the CNNs. Finally, the transferability of the neural networks designed for the problem at hand should be improved. These questions will be the subject of further studies. Progress in these directions is important for the development of SFPH and for the whole field of time-resolved molecular imaging.

[1] J. Xu, C. I. Blaga, P. Agostini, and L. F. DiMauro, Time-resolved molecular imaging, J. Phys. B **49**, 112001 (2016).

[2] M. Kitzler and S. Gräfe (Eds.), *Ultrafast Dynamics Driven by Intense Light Pulses. From Atoms to Solids, From Lasers to Intense X-rays* (Springer, Cham, 2016).

[3] C. D. Lin, A.-T. Le, C. Jin, and H. Wei, *Attosecond and Strong-Field Physics. Principles and Applications* (Cambridge University Press, Cambridge, 2018).

[4] R. Kanya, Y. Morimoto, and K. Yamanouchi, Observation of Laser-Assisted Electron-Atom Scattering in Femtosecond Intense Laser Fields, Phys. Rev. Lett. **105**, 123202 (2010).

[5] Y. Morimoto, R. Kanya, and K. Yamanouchi, Laser-assisted electron diffraction for femtosecond molecular imaging, J. Chem. Phys. **140**, 064201 (2014).

[6] L. J. Frasinski, K. Codling, P. Hatherly, J. Barr, I. N. Ross, and W. T. Toner, Femtosecond Dynamics of Multielectron Dissociative Ionization by use of a Picosecond Laser, Phys. Rev. Lett. **58**, 2424 (1987).

[7] C. Cornaggia, J. Lavancier, D. Normand, J. Morellec, P. Agostini, J. P. Chambaret, and A. Antonetti, Multielectron dissociative ionization of diatomic molecules in an intense femtosecond laser field, Phys. Rev. A **44**, 4499 (1991).

[8] J. H. Posthumus, L. J. Frasinski, A. J. Giles, and K. Codling, Dissociative ionization of molecules in intense laser fields: a method of predicting ion kinetic energies and appearance intensities, J. Phys. B **28**, L349 (1995).

[9] C. Cornaggia, M. Schmidt, and D. Normand, Laser-induced nuclear motions in the Coulomb explosion of $C_2H_2^+$ ions, Phys. Rev. A **51**, 1431 (1995).

[10] J. Itatani, J. Levesque, D. Zeidler, H. Niikura, H. Pépin, J. C. Kieffer, P. B. Corkum, D. M. Villeneuve, Tomographic imaging of molecular orbitals, Nature (London) **432**, 867 (2004).

[11] S. Haessler, J. Caillat, W. Boutu, C. Giovanetti-Teixeira, T. Ruchon, T. Auguste, Z. Diveki, P. Breger, A. Maquet, B. Carrè, R. Taïeb, and P. Salières, Attosecond imaging of molecular electronic wave packets, Nat. Phys. **6**, 200 (2010).

[12] M. Lein, J. P. Marangos, P. L. Knight, Electron diffraction in above-threshold ionization of molecules, Phys. Rev. A **66**, 051404(R) (2002).

[13] M. Meckel, D. Comtois, D. Zeidler, A. Staudte, D. Pavičić, H. C. Bandulet, H. Pépin, J. C. Kieffer, R. Dörner, D. M. Villeneuve, and P. B. Corkum, Laser-induced electron tunneling and diffraction, Science **320**, 1478 (2008).

[14] C. I. Blaga, J. Xu, A. D. DiChiara, E. Sistrunk, K. Zhang, P. Agostini, T. A. Miller, L. F. DiMauro, and C. D. Lin, Imaging ultrafast molecular dynamics with laser-induced electron diffraction, Nature (London) **483**, 194 (2012).

[15] M. G. Pullen, B. Wolter, A. T. Le, M. Baudisch, M. Hemmer, A. Senftleben, C. D. Schröter, J. Ullrich, R. Moshammer, C. D. Lin, J. Biegert, Imaging an aligned polyatomic molecule with laser-induced electron diffraction, Nat. Commun. **6**, 7262 (2015).

[16] Y. Huismans, A. Rouzée, A. Gijsbertsen, J. H. Jungmann, A. S. Smolkowska, P. S. W. M. Logman, F. Lépine, C. Cauchy, S. Zamith, T. Marchenko *et al.*, Time-Resolved Holography with Photoelectrons, Science **331**, 61 (2011).

[17] M. Haertelt, X-B. Bian, M. Spanner, A. Staudte, and P. B. Corkum, Probing Molecular Dynamics by Laser-Induced Backscattering Holography, Phys. Rev. Lett. **116**, 133001 (2016).

[18] S. G. Walt, N. Ram, M. Atala, N. I. Shvetsov-Shilovski, A. von Conta, D. Baykusheva, M. Lein, and H. J. Wörner, Dynamics of valence-shell electrons and nuclei probed by strong-field holography and rescattering, Nat. Commun. **8**, 15651 (2017).

[19] A. W. Trask, *Grokking Deep Learning* (Manning, Shelter Island, NY, 2019).

[20] S. Raschka, *Python Machine Learning* (Packt, Birmingham, UK, 2016).

[21] P. Kim, *MATLAB Deep Learning: With Machine Learning, Neural Networks and Artificial Intelligence* (Apress, Seoul, South Korea, 2017).

[22] A. M. M. Gherman, K. Kovách, M. V. Cristea, and V. Toşa, Artificial neural network trained to predict high-harmonic flux, Appl. Sci. **8**, 2106 (2018).

[23] K. Mills, M. Spanner, and I. Tamblyn, Deep learning and the Schrödinger equation, Phys. Rev. A **96**, 042113 (2017).

[24] T. Zahavy, A. Dikopoltsev, D. Moss, G. I. Haham, O. Cohen, S. Mannor, and M. Segev, Deep learning reconstruction of ultrashort pulses, Optica **5**, 666 (2018).

[25] S. Kleinert, A. Tajalli, T. Nagy, and U. Morgner, Rapid phase retrieval of ultrashort pulses from disbersion scan traces using deep neural networks, Opt. Lett. **44**, 979 (2019).

[26] T.-M. Yan, S. V. Popruzhenko, M. J. J. Vrakking, and D. Bauer, Low-Energy Structures in Strong Field Ionization Revealed by Quantum Orbits, Phys. Rev. Lett. **105**, 253002 (2010).

[27] T.-M. Yan and D. Bauer, Sub-barrier Coulomb effects on the interference pattern in tunneling-ionization photoelectron spectra, Phys. Rev. A **86**, 053403 (2012).

[28] X. Liu, G. Zhang, J. Li, G. Shi, M. Zhou, B. Huang, Y. Tang, X. Song, and W. Yang, Deep Learning for Feynman's Path Integral in Strong-Field Time-Dependent Dynamics, Phys. Rev. Lett. **124**, 113202 (2020).

[29] M. Lytova, M. Spanner, and I. Tamblyn, Deep learning and high harmonic generation, arXiv:2012.10328 v2 (2021).

[30] M. D. Feit, J. A. Fleck, and A. Steiger, Solution of the Schrödinger equation by a spectral method, J. Comput. Phys. **47**, 412 (1982).

[31] X. M. Tong, K. Hino, and N. Toshima, Phase-dependent atomic ionization in few-cycle intense laser pulse, Phys. Rev. A **74**, 031405(R) (2006).

[32] MATLAB, version 9.10.0 (R2021a). The MathWorks Inc., Natick, Massachusetts, 2021.

[33] A. E. Siegman, *Lasers* (University Science Books, Sausalito, CA, 1986).

[34] S. Augst, D. D. Meyerhofer, D. Strickland, and S. L. Chin, Laser ionization of noble gases by Coulomb-barrier suppression, J. Opt. Soc. Am. B **8**, 858 (1991).

[35] T. Morishita, Z. Chen, S. Watanabe, and C. D. Lin, Two-dimensional electron momentum spectra of argon ionized by short intense lasers: Comparison of theory with experiment, Phys. Rev. A **75**, 023407 (2007).

[36] W. H. Press, S. A. Teukolsky, W. T. Vetterling, and B. P. Flannery, *Numerical Recipes. The Art of Scientific Computing*, 3rd ed. (Cambridge University Press, Cambridge, 2007).

[37] I. Goodfellow, Y. Benqio, and A. Courville, *Deep Learning* (The MIT Press, Cambridge, MA, 2016).

[38] A. Shahroudnejad, A survey on understanding, visualizations, and explanation of deep neural networks, arXiv:2102.01792 (2021).